

User's Short Reports

You can jump to the first article of the beamline by clicking titles.

USER'S SHORT REPORTS

1. CONTENTS FOR EXPERIMENTAL PROGRESS REPORTS

<u>Title</u>	<u>First Author</u>	<u>Proposal number</u>	<u>Page</u>
<u>BL-1A</u>			
Determination of Ca-As Bonding at the CaF_2/GaAs Interface	Yasuko YAMADA	87-Y003	112
Oxygen K-edge EXAFS Measurements on SiO_2 Film	Satoshi MAEYAMA	87-Y003	113
Synchrotron Radiation Photoemission Spectroscopy of Ga-insulator Interfaces for GaAs Lateral Epitaxial Growth	Masaharu OSHIMA	87-Y003	114
Performance of a Grating/Crystal Monochromator Using a Multilayer Mirror-grating Combination	Satoshi MAEYAMA	87-Y003	115
Performance of a Grating/Crystal Monochromator in 50 eV - 900 eV	Tomoaki KAWAMURA	87-Y003	116
Performance of a Grating/Crystal Monochromator in 2.5 keV - 4 keV	Tomoaki KAWAMURA	87-Y003	117
<u>BL-1B</u>			
A New Soft-X-Ray Plate: Ag/Chalcogenide Film	Yasushi UTSUGI	87-Y003	118
Photon Stimulated Desorption in the Soft X-Ray Region	Toru MURASHITA	87-Y003	119
<u>BL-1C</u>			
Synchrotron Radiation Excited Etching of Si and SiO_2 by Use of SF_6+O_2 Reaction Gases	Tsuneo URISU	87-Y003	120
<u>BL-2A</u>			
X-Ray Fluorescence Analysis of Third Period Elements Using Undulator Radiation	Atsuo IIDA	86-138	121
<u>BL-2B</u>			
Soft-X-Ray p.A Scattering by Light Element Solids	Tadasu SUZUKI	86-068	122
Reflectivity Measurement of W/Be Multilayer Mirror for Soft X-Rays	Yuichi UTSUMI	87-003	123
X-Ray Contact Microscopy of Human Chromosome	Kunio SHINOHARA	86-023	124
A Preliminary Experiment of a Soft X-Ray Microscope	Sadao AOKI	85-087	125
A Performance Test of a Soft X-Ray Microscope	Yasushi KAGOSHIMA	87-103	126
<u>BL-4A</u>			
Nuclear Magnetic Resonance Study of Irradiation Effects on Br-dCMP Caused by Soft-X-Rays around K Absorption Edge of Br	Kaoru TAKAKURA	86-100	127
Strand Breaks in 5-Bromouracil-substituted DNA by 12.40 and 13.55 keV Photons	Kotaro HIEDA	86-099	128

Induction of Chromosome Aberrations in Human Lymphocytes by Synchrotron-produced Monochromatic X-Rays	Masao SASAKI	85-025	129
SR Micro Beam X-Ray Analysis	Yohichi GOHSHI	87-058	130
Determination of the Composition of Mixed Chemical States by X-Ray Fluorescence Detection Using Chemical Shift of Absorption Edge	Kenji SAKURAI	87-053	131
Chemical State Imaging by X-Ray Fluorescence Detection Using Chemical Shift of Absorption Edge	Kenji SAKURAI	87-053	132
Analysis of Micro Constituents in Sea Water Using Monochromatized X-Rays from Synchrotron Radiation	Masafumi ISHIKAWA	86-039	133
X-Ray Fluorescence (XRF) Analysis of Different Parts of a Single Strand of Hair	Takao SUZUKI	87-057	134
Application of Synchrotron Radiation to Archaeological Objects (I) - Nondestructive X-Ray Fluorescence Spectroscopic Imaging of Artistic Patterns -	Izumi NAKAI	87-056	135
Application of Synchrotron Radiation to Archaeological Objects (II) - SR X-Ray Fluorescence Analysis of Ancient Artifacts of Glass and Glaze -	Akihiko MOCHIZUKI	87-056	136
Near Surface Analysis of GaAlAs Using Grazing Incidence X-Ray Fluorescence	Atsuo IIDA	86-041	137
Grazing Incidence X-Ray Fluorescence Analysis of Layered Structure	Atsuo IIDA	86-041	138
Photoacoustic Extended X-Ray Absorption Fine Structure (PA-EXAFS)	Tsutomu MASUJIMA	86-020	139
Depth-profiling by Phase Analysis of Photoacoustic X-Ray Absorption Spectroscopy	Tsutomu MASUJIMA	86-020	140
<u>BL-4B</u>			
Fundamental Characteristics of New Powder Diffractometer	Ryosei UNO	87-061	141
X-Ray Powder Diffraction Study of the High-Tc Superconductors	Izumi NAKAI	85-148	142
Profile Analysis on the Basic of the Energy Dispersive Spectra at High Pressure and Temperature	Takamitsu YAMANAKA	87-062	143
Application of RDF Analysis Employing Anomalous X-Ray Scattering to Structural Studies of Binary $\text{GeSe}_x\text{Se}_{1-x}$ Glasses	Akihiko NUKUI	87-063	144
<u>BL-4C</u>			
X-Ray Study on Configurational Fibonacci Superlattices	Kousei KAMIGAKI	86-056	145
High Resolution Investigation of Rod-shaped Scattering from (111) Si Surface by Triple-axis Diffractometer	Nobuo KASHIWAGURA	86-051	146

A Be-cylinder Type High-pressure Apparatus for X-Ray Diffraction	Yasuhiko FUJII	85-082	147
A XANES Spectroscopy of Ni(II)-Fe(II) Hybrid Hemoglobins	Naoya SHIBAYAMA	87-065	148
Local Structure in Orthorhombic and Tetragonal $\text{Ba}_2\text{YCu}_3\text{O}_x$: The Role of Oxygen Vacancies in High T_c Superconductivity	Hiroyuki OYANAGI	87-003	149
Valence Study of Orthorhombic and Tetragonal $\text{Ba}_2\text{YCu}_3\text{O}_x$: The Role of Oxygen Vacancies in High T_c Superconductivity	Hiroyuki OYANAGI	87-003	150
Molecular Arrangement of Langmuir-blodgett Monolayers Studied by Surface-sensitive X-Ray Absorption Spectroscopy	Hiroyuki OYANAGI	87-065	151
Si/Ge/Si Monolayer Heterostructure on Si(100) Studied by Surface-sensitive EXAFS	Hiroyuki OYANAGI	87-065	152
Structural Studies of (Ga,In)(As,P) Alloys and $(\text{InAs})_m(\text{GaAs})_n$ Strained Layer Superlattices	Hiroyuki OYANAGI	87-065	153
Bond Length Relaxation Around Isoelectronic Dopants in InP Studied by Fluorescence-detected EXAFS	Hiroyuki OYANAGI	87-065	154
<u>BL-6A</u>			
Crystal Structure Analysis of ω -Amino Acid: Pyruvate Aminotransferase Preliminary Result from 2.3 Å Resolution Electron Density MAP	Nobuhisa WATANABE	85-022 87-028	155
High Resolution Data Collection of Streptomyces Erythraeus Trypsin Using the Imaging Plate Mounted in a Weissenberg Camera	Takashi YAMANE	86-022	156
Diffraction Experiments of Hydrogenase at Two Wavelengths	Yoshiki HIGUCHI	86-042	157
Development of a Rapid Laue-diffraction Technique for Protein Crystallography	Yishinori SATOW	87-059	158
<u>BL-6B</u>			
High Pressure Equation of State of α -MN to 42 GPa	Kenichi TAKEMURA	85-122	159
Phase Transitions of Black Phosphorus and Black Phosphorus-arsenic Alloy at Very Low Temperatures and High Pressures	Ichimin SHIROTANI	86-114	160
X-Ray Diffraction Study under Pressure Using an Imaging Plate	Osamu SHIMOMURA	85-122	161
<u>BL-6C</u>			
Preliminary Study of Charge Density Wave in Chromium	Masahiro MORI	85-120	162
Low Temperature and High Pressure X-Ray Study on the Pressure-induced Phase Transition of Amorphous Semiconductors	Kazuhiko TSUJI	86-112	163
Intensity of X-Ray (222) Line in InSb under High Pressure	Bin OKAI	85-083	164

A New Kind of Interference Fringe Induced by X-Ray Resonant Scattering	Masami YOSHIKAWA	87-071	165
Absolute Lattice Parameter Measurement of GaAs Crystals Using Monochromatic Synchrotron Radiation	Koji USUDA		166
<u>BL-7A</u>			
A Soft X-Ray Beam Line (20-1000 eV) with a Plane Grating Monochromator for Surface Studies	Hidetoshi NAMBA		167
<u>BL-7B</u>			
UPS Studies of 2X1 Reconstructed Surface of Diamond (111)	Hidetoshi NAMBA		168
A VUV Beam Line (5-45 eV) with a 1m Seya-Namioka Monochromator for Surface Studies	Hidetoshi NAMBA		169
<u>BL-7C</u>			
Ce L ₁₁₁ EXAFS Study of CeO ₂ -Stabilized Tetragonal ZrO ₂	Fumiyuki MARUMO	85-014	170
EXAFS Study of Relaxation of a Cu ⁺ Impurity in Alkali Halides	Takatoshi MURATA	86-059	171
Local Structure around Br Atoms in AgBr-Ag O-GeO Glasses	Hideki MORIKAWA	86-084	172
The Mechanism of Solution Strengthening by C and N in Austenitic Steel	Nobuhiko KONDOH	86-018	173
High Pressure-induced Polymorphism in Vanadium Oxides	Ayako TOKIWA	87-004	174
Zn EXAFS Measurements under High Pressure Conditions Using a Diamond Anvil Cell	Shigeho SUENO	87-007	175
EXAFS and XANES Studies of Cobalt(III)-EDTA Complex	Hideto SAKANE	85-111	176
Coordination of Fe in Garnets by EXAFS Spectroscopy	Yasunori TABIRA	86-083	177
The Local Structure of a Vanadate in Supported Vanadium Oxide Catalysts. II.	Tsunehiro TANAKA	85-101	178
Structure of Ultrafine Iron Oxides on Activated Carbon Fiber	Katsumi KANEKO	86-011	179
The Structure Change of P ₂ O ₅ -V ₂ O ₅ during the C ₄ H ₈ Oxidation Reaction	Kiyotaka ASAKURA	86-013	180
An EXAFS Study of Co-Mn/SiO ₂ Bimetallic Solvated Metal Atom Dispersed Catalysts	Hiroyoshi KANAI	86-085	181
EXAFS Studies on the Se-Nb Catalyst Obtained by Use of the Two-step Fixation Reaction	Kiyotaka ASAKURA	87-013	182
Determination of the Environmental Structure around a Specific Atom in Disordered Materials by the Anomalous X-Ray Scattering	Yoshio WASEDA	86-063	183

Vanadium K-edge X-Ray Absorption Spectroscopy of the Reduced and Thionine-oxidised Forms of the VFe Protein of the Vanadium Nitrogenase from Azotobacter Chroococcum	Judith M. ARBER	86-097	184
<u>BL-8C</u>			
A High-speed Digital Subtraction Angiography System for Phantom and Small Animal Studies	Ken UEDA	86-Y018	186
High Resolution Tomography Employing an X-Ray Sensing Pickup Tube	Tatsumi HIRANO	86-Y018	187
X-Ray Sensing Pickup Tube	Yoshio SUZUKI	86-Y014	188
<u>BL-9A</u>			
Investigation of System Reliability on the BL-9A SR Lithography Beamline	Koichi OKADA	87-Y001	189
<u>BL-9C</u>			
Interfacial Superstructure of a-Si/Si(111)-7×7 and a-Si/Ge _{0.2} Si _{0.8} (111)-5×5 Studied by Grazing Incidence X-Ray Diffraction	Koichi AKIMOTO	87-Y001	190
Interfacial Superstructure between an Epitaxial Si(111) Layer and a B($\sqrt{3}\times\sqrt{3}$)/Si(111) Substrate Studied by Grazing Incidence X-Ray Diffraction	Koichi AKIMOTO	87-Y001	191
Investigation of the Interface Structure between Al and GaAs(001) by Grazing Incidence X-Ray Diffraction	Jun'ichiro MIZUKI	87-Y001	192
X-Ray Topography of 6 inch Diameter Si Crystal	Tomohisa KITANO	87-Y001	193
Fluorescence EXAFS Study of AlGaAs Doped with Se Donor Impurities	Tomohisa KITANO	87-Y001	194
Fluorescence EXAFS Study of Zn Doped LEC InP Crystal	Tomohisa KITANO	87-Y001	195
<u>BL-10A</u>			
Determination of Fe and Ni Ordering in Tetrataenite from Saint Severin Meteorite Using Synchrotron Radiation	Tokuhei TAGAI	85-064	196
Crystal Structure of KBSi ₃ O ₈ Microcrystal	Mitsuyoshi KIMATA	85-075	197
Structure Study on the Single Crystal of Cu-Al-Ni γ_1 ' Martensite Phase	Jinhua YE	87-077	198
Dynamical Diffraction and Anomalous Transmission of Thermally Scattered X-Rays in a Perfect Germanium Crystal	Yasuji KASHIWASE	87-067	199
Photon Counting in X-Ray Diffraction	Kazutoshi GOUHARA	86-058	200
<u>BL-10B</u>			
EXAFS Study on Local Structure Changes of Amorphous Alloy	Toshio NASU	85-002	201
EXAFS and XANES Study of the Bi ₂ O ₃ -Gd ₂ O ₃ Solid Solution	Kichiro KOTO	85-012	202

Chain Structure of Liquid Selenium Systems (II)	Hirohisa ENDO	85-103	203
An EXAFS Study of Nickel(II) Complexes Containing Carbohydrates; A Novel C-2 Epimerization of Aldoses Promoted by Nickel(II) Diamine Complexes Involving a Stereospecific Rearrangement of Carbon Skeleton	Tomoaki TANASE	85-104	204
EXAFS and XANES Studies on Martensitic Transformation in Iron Base Alloys	Osamu YAMADA	85-107	205
Disordered Effect in Pentanary Alloy Semiconductor AlGaInPAs	Shun-ichi GONDA	85-108	206
X-Ray Absorption Study of Linear-chain Semiconductor $(\text{NbSe}_4)_3\text{I}$	Mitsuru IZUMI	85-112	207
X-Ray Absorption Study of Quasi-one Dimensional Conductor NbS_x ($x \sim 3$)	Toshiaki IWAZUMI	85-113	208
Short-range Order Investigation in $a\text{-Ge}_{1-x}\text{Sn}_x\text{O}$ by EXAFS	Hiroaki MYOREN	86-003	209
EXAFS Study on the Structure Changes of GeTe_2 Films	Keiji TSUNETOMO	86-003	210
EXAFS Study on Premartensitic Phase in A-15 Compounds	Kazuya KAMON	86-005	211
Local Structure of the $\alpha\text{-AgI}_{1-x}\text{Br}_x$ Solid-solution	Akira YOSHIASA	86-007	212
EXAFS and XANES Studies on $\text{Na}_2\text{O-B}_2\text{O}_3$ Glasses Containing Copper Ion	Xu QIANG	86-078	213
Study of the Electronic Structures of Highly Conductive Phthalocyaninato Nickel Complexes by Polarized XANES Spectra	Haruo KURODA	86-079	214
Crystallization of Gd_2O_3 Stabilized Zirconia from Gel by EXAFS	Kichiro KOTO	86-089	215
EXAFS Study of the Perovskite Type $\text{SrCo}_{1-x}\text{Mn}_x\text{O}_3$ Solid Solution	Akira YOSHIASA	86-090	216
Local Crystal Structure of Exchanged Ions in Zeolite	Yasushige KURODA	86-093	217
Structure Studies of Niobium and Tantalum Oxides by EXAFS	Takashi USHIKUBO	87-Y004 86-Y003 86-Y016	218
XANES and EXAFS of High T_c Superconductive Ceramics	Haruo KURODA	87-U002	219
EXAFS Observation of Vapor Quenched Fe-Ag and Fe-Ti Alloys	Yoji NAKAMURA	86-087	220
Local Structure in the Pre-martensitic State of AuCd Alloy	Yukio NODA	86-088	221
Fe K-edge XANES Study of the Metamict State in Oxide Minerals	Junji AKIMOTO	84-052	222
EXAFS/XANES Analysis of Selenium Compounds	Takuji KAWASHIMA	87-008	223
EXAFS Study on the Local Structural Rearrangement of Amorphous Cu-Zr Alloy during the Crystallization Process	Hiromi YAMASHITA	85-102	224

Studies on the Structure of Molybdenum(V) Species in Aqueous Acidic Solution by EXAFS	Kunihiko YOKOI	85-015	225
Solute Structure of Copper(II) Perchlorate Aqueous Solution in Liquid and Glassy States: Its Concentration Dependence	Masaharu NOMURA	85-021	226
Solvation Structure of Cu(II) in Liquid Ammonia	Toshio YAMAGUCHI	85-021 87-023	227
Solvation of Ag(I) in Some N-donor Solvents	Toshio YAMAGUCHI	85-021 87-023	228
Structure of Bis (2,3-Alkanedione Dioximato) Nickel(II) in Solid and Pyridine Solution by the EXAFS Method	Seichi YAMASHITA	86-008	229
Structure of Zinc Bromide Complexes in Glassy Aqueous Solutions	Toshio YAMAGUCHI	87-023	230
EXAFS Studies on Mo, Co-Mo, and Ni-Mo Supported Catalysts for Hydrotreating of Petroleum II. The Deactivation Behavior of Molybdenum Catalysts Used for Hydrotreating Coal-derived Liquid	Nobuyuki MATSUBAYASHI	85-006	231
EXAFS Studies on the Metal-support Interaction in the Pd-supported Nb System	Kiyotaka ASAKURA	85-019	232
EXAFS Studies of Silica-supported Metal Catalyst I. Effect of Additives Such as Ti, Nb and Ta on the Surface Structure of Supported Metal	Takakazu FUKUSHIMA	85-105	233
Thermal Expansion and Debye Temperature of FCC Metals	Toshihiko YOKOYAMA	85-106	234
High Pressure In-situ EXAFS Studies on the Catalytic Reaction Mechanism the Oxidation of Co on the Co(II) Oxide Cluster	Kiyotaka ASAKURA	85-110	235
EXAFS Characterization of Zeolite-encapsulated Rh and Bimetallic RhFe Carbonyl Cluster Catalysts	Masaru ICHIKAWA	86-001	236
An XANES and EXAFS Study of Gold Catalysts	Hiroyuki KAGEYAMA	86-002	237
EXAFS Study on the Structure of Catalysts for Photodecomposition of Water	Akihiko KUDO	86-004	238
EXAFS Study on the Structure of the ZSM-5-attached one Atomic ZrO ₂ Catalyst	Kiyotaka ASAKURA	86-012	239
An EXAFS Study of the Local Structure of Iron-Tin Composite Oxides	Satoshi YOSHIDA	86-086	240
Characterization of Supported RhFe and PtFe Bimetallic Carbonyl Clusters and Their Catalytic Functions	Masaru ICHIKAWA	87-002	241
EXAFS Studies of Supported Ultra Fine Metal Particles I. Effect of Additives and Supports on the Morphology of Rh	Takakazu FUKUSHIMA	87-010	242
EXAFS Studies on the Structure of the Attached Rh Dimer Carbene Complex	Kiyotaka ASAKURA	87-011	243
The Structure Studies on the TiO ₂ One-atomic Layer by Means of EXAFS	Kiyotaka ASAKURA	87-012	244
The Structure of Mo(CO) ₆ Supported in the Zeolite NaY	Kiyotaka ASAKURA	87-014	245

Studies on the Structure of Bimetallic Colloidal Catalysts	Naoki TOSHIMA	87-016	246
EXAFS Study on Local Structures of Active Site on Mo Supported Catalysts for Hydrocracking and Hydrogenation Activities I. The Effect of Presulfiding Condition	Nobuyuki MATSUBAYASHI	87-024	247
EXAFS Study of Selenocysteine Structure	Yuzuru HIRAGI	86-016	248
X-Ray Absorption Study on the Type II Copper-depleted Cucumber Ascorbate Oxidase	Takeshi SAKURAI	86-091	249
EXAFS and XANES of the Metallic Components in Plant Leaves	Masayasu KURAHASHI	86-094	250
 <u>BL-10C</u>			
Small-angle Scattering from Polymer Solutions Using Synchrotron Radiation	Hiroyuki TAGAWA	85-066	251
Study on the Size and Shape of Fine Particles of Semiconductors by Means of X-Ray Small-angle Scattering	Tadashi ITOH	85-119	252
Aggregation Process of β -Casein	Kanji KAJIWARA	86-025	253
Small-angle X-Ray Scattering Study on Higher-order Structures of Chromatin in Solution	Yoji INOKO	86-027	254
X-Ray Solution Scattering Studies on Solubilized Bacteriorhodopsin II	Mikio KATAOKA	86-028	255
Microsegregated Structure in the Silk Fibroin from Bombyx Mori	Masanobu NAGURA	86-029	256
Structural Studies on Aldolase by Means of Time-resolved X-Ray Scattering	Mamoru SATO	86-030	257
Lyotropic Mesophase of Imogolite Observed by Small-angle X-Ray Scattering	Kanji KAJIWARA	86-060	258
Effects of Ionic Strength, Temperature and the Coenzyme on the Quarternary Structure and Activity of Tryptophanase	Yuzuru HIRAGI	86-103	259
The Structure of P2 Myelin Protein in the Solution	Michio KIMURA	86-104	260
X-Ray Solution Scattering Studies on Phytochrome Phototransformation	Satoru TOKUTOMI	86-106	261
Small-angle X-Ray Scattering Study of Aggregation Process of Cucumber Green Mottle Mosaic Virus Protein	Yoh SANO	86-107	262
Structural Behavior of Troponin-C Upon Calcium Ion Binding	Tetsuro FUJISAWA	87-033	263
Micelle Structure of Polyethylene Glycol Monoether Liquid Crystal	Hiroshi URAKAWA	87-084	264
Multiply Charged Xe Ions Produced in 4.1 - 8.0 keV X-Rays	Tadao TONUMA	86-134	265
X-Ray Raman Scattering as a Tool for Structure Determination	Kazuyuki TOHJI	87-066	266
Surface structure Analysis of $\text{Si}(111)\sqrt{3}\times\sqrt{3}$ -Bi by X-Ray Diffraction	Toshio TAKAHASHI	87-085	267

BL-11A

Multiple-photoionization of Cs and Ba Atoms Due to Creation of 4d-hole States	Tetsuo NAGATA	85-090	268
2p-shell Photoionization of K and Ca Atoms	Takashi MATSUO	85-090	269
Threshold Photoionization of Kr 3d Subshell	Tatsuji HAYAISHI	86-073	270
Investigation of Fragmentation Processes Following Inner-core Level Excitation of $\text{Pb}(\text{CH}_3)_4$ and $\text{Sn}(\text{CH}_3)_4$ in the Vapor Phase	Shin-ichi NAGAOKA	87-105	271
S K and $L_{2,3}$ Absorption Spectra of $\text{Ni}(\text{mnt})_2$	Koichi KIKUCHI	85-144	272
Polarized S K and $L_{2,3}$ Absorption Spectra of $(\text{TMTTF})_2\text{ClO}_4$	Koichi KIKUCHI	86-143	273
Optical Constants of SiC in the Soft X-Ray Region; Determined from Eight Samples	Mihiro YANAGIHARA	85-095	274
Optical Constants in the Soft X-Ray Region	Naoto KIHARA		275
Reflectivity of Multilayer Reflectors in 0.1 - 1 keV Region	Koujun YAMASHITA	85-137	276
Optical Constants of Highly Reflective Materials for Soft X-Ray Multilayer Mirrors	Masaki YAMAMOTO	85-095	277
Resuscitation of Carbon-contaminated Mirrors and Gratings by Oxygen-discharge Cleaning	Tsuneharu KOIDE	85-097	278

BL-11B

STE Luminescence Excitation Spectra near the K and Cl 1s Edges in KCl and KBr	Mihiro YANAGIHARA	85-094	279
Direct Observation System for Two-dimensional X-Ray Photoelectron Diffraction (XPED) Patterns	Eisaku NAKAMURA	85-096	280
Polarization-dependent S K-edge XANES for Sulfur on Nickel II. $(5\sqrt{3}\times 2)\text{S}/\text{Ni}(111)$ and $p(2\times 2)\text{S}/\text{Ni}(111)$	Yoshinori KITAJIMA	85-092	281
Surface EXAFS of $(5\sqrt{3}\times 2)\text{S}/\text{Ni}(111)$	Yoshinori KITAJIMA	85-092	282
Ru L-edge X-Ray Absorption Studies on $\text{Ru}_3(\text{CO})_{12}$ Adsorption and the Formation of Ru-Cu Bimetallics on Cu(111)	T.K. SHAM	86-080	283
Surface EXAFS and XANES of S/Fe Systems I. Measurement of X-Ray Absorption Spectra of $c(2\times 2)\text{S}/\text{Fe}(100)$	Yoshinori KITAJIMA	86-142	284
Enhanced Killing on <u>E.Coli</u> and Bacteriophage by X-Rays at Resonance Energy of Phosphorus K-absorption Edge	Hiroshi MAEZAWA	86-101	285
Strand Breaks in PBR322 DNA Induced by Monoenergetic X-Rays around K-absorption Edge of Phosphorus	Kotaro HIEDA	86-098	286
Irradiation Effects of Monochromatic Soft X-Rays around K-shell Absorption Edge of Phosphorus on Yeast Cells	Katsumi KOBAYASHI	86-102	287

BL-11C

Piezorefectivity of Na ⁺ 2p Core Excitation in NaCl	Masatada YURI	86-071	288
The Optical Spectra of α -Al ₂ O ₃ Single Crystals in VUV Region	Tetsuhiko TOMIKI	86-070	289
VUV Spectra of CdIn ₂ S ₄ and Cd _x InGaS _{x+3} (x=1,2,3) Single Crystals	Takeo TAKIZAWA	87-110	290
VUV Reflection Spectra of Paratellurite, TeO ₂	Takeo TAKIZAWA	87-110	291

BL-11D

Angle-resolved Photoemission Study of Oxygen Adsorption on Ni(110) at 300 K	Yasuo SAKISAKA	84-080	292
Angle-resolved Photoemission from the Ni(110)(1×2)-H Surface at 80 K	Yasuo SAKISAKA	84-080	293
Angle-resolved Photoemission Study of Oxygen Adsorption on Ni(110) at 80 K	Yasuo SAKISAKA	84-080	294
4f-electron Densities of States in Light Rare-earth Halides Studied by Resonant Photoemission Spectroscopy	Atsushi FUJIMORI	86-146	295
Photoelectron Spectra of La- and Ce-compounds	Takaaki HANYU	86-148	296
Near-normal Reflectance Spectra of CeO ₂	Tsuneaki MIYAHARA	85-131	297
Photoemission Studies of Neutron-irradiated Graphite	Kazutoshi YAGI	86-149	298
Angle-resolved Photoemission Study of Cr(110). Energy-band Dispersions and Magnetic-phase Transition	Yasuo SAKISAKA	86-150	299
Angle-resolved Photoemission Study of NO Chemisorption on Ag(111)	Kazuyuki EDAMOTO	86-151	300
Resonant Photoemission Study of High-Tc Superconductors	Takashi TAKAHASHI	87-U001	301

BL-12A

Photodissociation of the Doubly Excited States of H ₂	Shin ARAI	85-089	302
Kinetic Energy Analysis of Photofragments Produced in Dissociative Photoionization of O ₂ in the VUV Region	Masatoshi UKAI	85-143	303
Vacuum-ultraviolet Absorption of Cl ₂ and HCl between 33 and 105 nm	Shin YOKOYAMA	86-072	304
Synchrotron Radiation-assisted Photochemical Etching of GaAs	Shingo TERAKADO		305

BL-12B

Photoelectric Absorption Measurements in the Focal Scanning Mode of the 6VOPE Facility and Its Application to Krypton in the VUV Region	Kenji ITO	85-088	306
Absorption Spectrum of the Neon Atom in the Vacuum-ultraviolet Region	Kenji ITO	85-088	307

High-resolution Measurements of Photoabsorption Coefficients for Carbon Monoxide Absorption Bands between 94.0 nm and 100.4 nm	Kouichi YOSHINO	85-088	308
High Resolution Absorption Spectra of H ₂ O and D ₂ O the V.U.V Region	Yumio MORIOKA	85-088	309
<u>BL-12C</u>			
Basic Characteristics of Microchannel Plates for Plasma X-Ray Diagnostics	Naohiro YAMAGUCHI	85-145	310
Deep Submicron Pattern Replication and Measurement of Temperature Rise Distribution for X-Ray Mask Membrane in SR Lithography	Ichiro MORI		311
A Method of Pattern Reduction in SR X-Ray Lithography	Shigeo SUZUKI		312
<u>BL-14A</u>			
Crystal Structure Analysis of Pseudomonas Isoamylase	Kunio MIKI	85-114	313
Use of Apoenzyme Crystal in Structure Analysis of Serratia Protease	Yoshio KATSUYA	86-034	314
Intensity Measurements with Short Wave-length X-Rays; Structure Refinement of Ilmenite	Masataka OHGAKI	86-062	315
A Single Crystal Diffraction Study of the Natural Zeolite Cowlesite	Gilberto ARTIOLI	87-086	316
The Structural Study on the SMSI Catalysts by Means of the Polarized Total Reflectance Fluorescent EXAFS Method(2)	Kiyotaka ASAKURA	85-011	317
Measurement of a Cerium K-edge EXAFS Spectrum of Cerium Oxide	Yoshinori SATOW	85-020	318
Development of a PPAC and Construction of an ALCD	Hiroyuki TAKAHASHI	85-073	319
<u>BL-14B</u>			
Dynamical Phenomena in Grazing-incidence X-Ray Diffraction by Perfect Crystals	Osami SAKATA	86-076	320
Angle-dispersive X-Ray Diffraction by Water Molecules	Hiroshi TAKEUCHI	86-125	321
<u>BL-14C</u>			
Nuclear Excitation by Synchrotron Radiation	Takeshi MUKOYAMA	85-074	322
In Situ Observation of the Structure Change in Vacancy-rich TiO _x (x=0.84, 1.0, 1.25) at High Pressures and Temperatures	Toru FUJIMURA	85-081K	323
High Resolution Momentum Density Measurement for Silicon Using 29.5 keV Synchrotron Radiation	Fumitake ITOH	86-124	324
<u>BL-15A</u>			
Time-resolved X-Ray Studies of the Aggregation of Bleached Rhodopsin	Toshiaki HAMANAKA	85-026	325

X-Ray Diffraction Studies of Glutaraldehyde and Triton X-100 Treated Purple Membrane during Its Photocycle	Tomoya URUGA	86-035	326
Development of Specimen Chamber for Light Irradiation at Low Temperature and Its Application to Bacteriorhodopsin Photocycle III	Fumio TOKUNAGA	85-028 87-036	327
X-Ray Diffraction of Bacteriorhodopsin with Nitrated Tyrosine Residues III	Fumio TOKUNAGA	85-029	328
Changes in the Equatorial Intensities on Activation of Overstretched Frog Skeletal Muscle	Naoto YAGI	85-030	329
An X-Ray Diffraction Study of Chemically Skinned Cardiac Muscle	Yasutake SAEKI	85-032 87-043	330
X-Ray Diffraction of Skeletal Muscle under the Inhibitory Action of 2,3-Butanedione-2-Monoxime	Keisuke HORIUTI	87-045	331
Effect of Slow Length Changes on the Equatorial X-Ray Diffraction Intensities of Frog Skeletal Muscle at Short and Long Sarcomere Lengths	Hiroyuki IWAMOTO	85-031	332
Use of Skeletal Muscle Fiber Bundle as a Material for Dynamic X-Ray Diffraction Studies	Hiroyuki IWAMOTO	87-044	333
Analysis of the Intensity Change of the Actin-based Layer Lines in the Two-dimensional X-Ray Diffraction Pattern from a Frog Skeletal Muscle during Isometric Contraction	Katsuzo WAKABAYASHI	85-042	334
Intensity Changes of the Second Actin Layer-line Reflection and the Equatorial Reflection at the High Radial Position of 0.21 nm^{-1} from Tetanized Frog Skeletal Muscles with Non-overlap Sarcomere Length	Katsuzo WAKABAYASHI	87-041	335
Intensity Change of the 7.2 nm Myosin Meridional Reflection from Tetanized Frog Skeletal Muscle during Sinusoidal Length Changes	Katsuzo WAKABAYASHI	86-036	336
Diffraction Studies of Muscle Contraction by Sinusoidal Length Change - Theoretical Model and Explanation of Experimental Results -	Toshio MITSUI	86-036	337
Small Angle X-Ray Diffraction of a Molluscan Smooth Muscle Contracting Tonically in Response to Acetylcholine	Yoshiko TAJIMA	86-038	338
Time-resolved Small-angle X-Ray Scattering Study of Tobacco Mosaic Virus Protein Association Induced by Salt Concentration Jump	Hideo INOUE	85-116	339
Conformational Change of Ovomacroglobulin Caused by Interaction with Chymotrypsin	Hideo ARAKAWA	85-117	340
Stopped-flow X-Ray Scattering Study VII. Dissociation of Hemocyanin from Limulus Polyhemus and Panulirus Japonicus	Yoshihiko IGARASHI	85-117	341
Slow Change of $P_{\beta'}$ Structure after Temperature Jump across Main Transition in Dimyristoylphosphatidylcholine	Morio AKIYAMA	86-037	342

Dynamical Structure Change during Reversion in Al-Zn Alloys	Kozo OSAMURA	86-065	343
Dynamical Structures during Decomposition in Al-Li Alloys	Tatsuo SATO	86-066	344
Time-resolved Small Angle X-Ray Scattering of Polyethylene under Stretching Process	Toshiro KOJIMA		345
Development of a Stretching Device of Synthetic Polymers for Time-resolved X-Ray Scattering	Toshiro KOJIMA		346
Imaging Analysis by Photoacoustic X-Ray Absorption Spectroscopy	Tsutomu MASUJIMA	86-020	347
X-Ray Photoacoustic Effect of Gas Phase	Tsutomu MASUJIMA	86-020	348
Photoacoustic Dosimetry (PAD) - Test of Metal Powder as Targets -	Masaharu HOSHI	86-020	349
Correlation Photoacoustic Measurement with Synchrotron Radiation as Exciting Source	Yoshinori SUGITANI	86-020	350
<u>BL-15B</u>			
Non-destructive Investigation of the Surface-damaged-layer of (Mn, Zn) Ferrite by X-Ray Diffraction near Absorption-edge	Yoshiro AKAGI	85-Y029	351
X-Ray Topographic and Goniometric Study of Lattice Mismatches in InAlAs Films on InP Substrates	Osamu NITTONO	86-129	352
Direct Observation of Lattice Defects in Solid Helium by SR X-Ray Topography	Hideji SUZUKI	86-131	353
Section Topography Using a High-order Reflection and Its Application	Yoshimitsu SUGITA	86-152	354
Generation of Lattice Defects in Ice at a Temperature Close to the Melting Point	Takeo HONDOH	87-095	355
Structural Study of GaAs/AlAs Superlattices	Susumu NANA0	86-130	356
X-Ray Parametric Frequency Conversion	Kazumichi NAMIKAWA	87-098	357
<u>BL-15C</u>			
X-Ray Topography of LEC GaAs Crystal (I)	Tomohisa KITANO		358
X-Ray Topography of LEC GaAs Crystal (II)	Tomohisa KITANO		359
Time-resolved X-Ray Measurement System for Studying the Structural Change under Laser Irradiation	Seiji KAWADO		360
Observation of Microdefects in a Thin Silicon Crystal by Means of Ultra-plane Wave Topography	Yoshinori CHIKAURA	85-118	361
<u>BL-16</u>			
A New Grazing Incidence Monochromator for Undulator Radiation, MMM(Muramatsu-Maezawa Monochromator)-22. (1) Design Concept	Hideki MAEZAWA	87-104	362

A New Grazing Incidence Monochromator for Undulator Radiation, MMM(Muramatsu-Maezawa Monochromator)-22. (2) Optical Designing	Yasuji MURAMATSU	87-104	363
A New Grazing Incidence Monochromator for Undulator Radiation, MMM(Muramatsu-Maezawa Monochromator)-22. (3) Mechanical Designing	Yasuji MURAMATSU	87-104	364
<u>AR</u>			
Measurements of Pressure Dependence of Debye Temperature of Aluminum	Akihito MATSUMURO	86-055	365
Structure of Liquid Gallium under Pressure	Kazuhiko TSUJI	87-094	366
Measurement of Ni_2SiO_4 Olivine-Spinel Transformation Kinetics at High Pressure and Temperature	David C. RUBIE	87-102	367
Hydrostatic Compression of MgO-FeO to 6.2 GPa: X-Ray Measurement Using Synchrotron Radiation	M.H. MANGHNANI	86-041	368
High Pressure Generation with a Multiple Anvil System Using Sintered Diamond Anvils	Eiji OHTANI	86-121	369
Animal Experiments by K-edge Subtraction Angiography Using SR	Izumi ANNO	85-038	370
X-Ray K-edge Subtraction Television System	Kiwamu SUZUKI	87-046	371

DETERMINATION OF Ca-As BONDING AT THE CaF_2/GaAs INTERFACE

Yasuko YAMADA, Masaharu OSHIMA, Satoshi MAEYAMA, Tomoaki KAWAMURA,
Tuneaki MIYAHARA+

NTT Applied Electronics Laboratories, Midori-cho, Musashino-shi, Tokyo 180
+ Photon Factory, National Laboratory for High Energy Physics, Oho-machi, Thukuba-gun, Ibaraki 300

Introduction

Calcium fluoride is an insulator which is lattice matched with GaAs to a high degree. These properties make a CaF_2 a technologically important material since it can be grown on GaAs as an epitaxial insulator. In order to understand the bonding at the CaF_2/GaAs interface, this system was studied using photoelectron spectroscopy with synchrotron radiation.

Experimental

The experiments were carried out at the BL-1A beam line. To obtain a minimum depth resolution, the radiation was tuned to a photon energy of about 120 eV. GaAs surface was cleaned by Ar-ion bombardment and then annealed at 600 C. Surface reconstruction was checked by LEED method. CaF_2 films were grown on this surface by deposition of a disordered film at room temperature and subsequently recrystallized by annealing at 600 C.

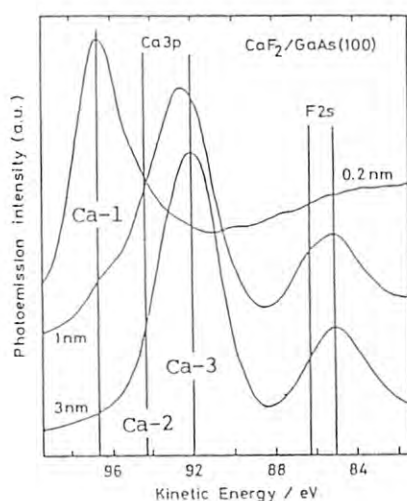


Fig. 1 Photoelectron spectra from Ca3p and F2s core levels for $\text{CaF}_2/\text{GaAs}(100)$

Results and discussion

Figure 1 shows photoelectron spectra from Ca3p and F2s core levels. At the first stage of CaF_2 growth, the dissociation reaction of CaF_2 was caused and F atoms were removed so that Ca atoms remained on the surface with 2.3 eV binding energy shift. Considering photoelectron spectra from Ga3d and As3d core levels, it is concluded that this shift comes from production of Ca-As bonding. For 1 nm coverage, CaF_2 films grow on the transition layer containing Ca-As bonding. At this stage, Ca3p spectrum consists of three components (Ca-1, Ca-2, and Ca-3).

Figure 2 shows the structural model for the $\text{CaF}_2/\text{GaAs}(100)$ interface. There are three bonding states of Ca. Ca-1 stands for the Ca atom in GaAs lattice occupying Ga position, Ca-2 for the Ca atom surrounded As and F atoms, and Ca-3 for the Ca atom in CaF_2 lattice. This interface is not abrupt. It is not Ga atom, but As atom that is involved in the interfacial bonding. Therefore the control of Ga/As ratio and As state on clean GaAs surface might be a key role for production of interface with good quality.

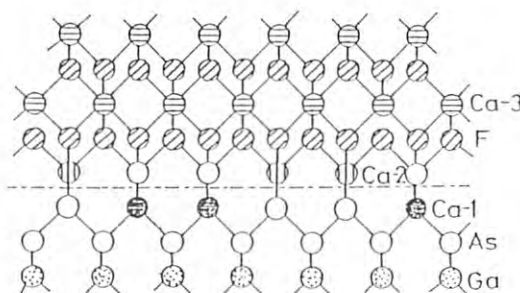


Fig. 2 The structural model for the $\text{CaF}_2/\text{GaAs}(100)$ interface

OXYGEN K-EDGE EXAFS MEASUREMENTS ON SiO_2 FILM

Satoshi MAEYAMA, Tomoaki KAWAMURA, Masaharu OSHIMA and Tuneaki MIYAHARA*
 NTT Applied Electronics Laboratories, Musashino-shi, Tokyo 180
 *KEK, Photon Factory, Oho-machi, Tukuba-gun, Ibaraki 305

Introduction

One of our goals for surface analysis at Beamline 1A in Photon Factory is to perform EXAFS analysis for SiO_2 gate oxides because SiO_2 film is a key material for silicon device technology. Recently, the monochromatized beam in the region of oxygen k-edge has become available for experiments at the Beamline 1A. In this study this beam was applied to measuring EXAFS of SiO_2 film for considering the best detection technique for EXAFS above oxygen K-edge.

Experimental

The sample used for the experiments was a SiO_2 thermally grown on Si to a thickness about 1000Å. Oxygen k-edge EXAFS measurements by means of three detection techniques (Auger electron yield, secondary electron yield and fluorescence yield) were performed at the Beamline 1A with a Grating/Crystal Monochromator and a multi-functional surface analysis system. The O_{KLL} Auger electron with kinetic energy of $504 \pm 8.5\text{eV}$ and the secondary electron of $8.5 \pm 8.5\text{eV}$ from the sample were detected by an electron analyzer equipped in the surface analysis system. A Si(Li) detector connected with the beam line end was utilized for recording O K(523eV) fluorescence yield.

Results and Discussion

Figures 1 show EXAFS spectra obtained with three detection techniques. The fluorescence(FY) spectrum was recorded with hundred times longer data acquisition time than that in the Auger electron yield(AY) and the secondary electron yield(SY) detection because of its poor sensitivity for light elements. Nevertheless, this FY spectrum has still the worst signal-to-noise ratio among three spectra. The AY spectrum has a serious problem of interfering photoemission peaks($\text{Si}2\text{s}$ and $\text{Si}2\text{p}$). Therefore, it is difficult to analysis the AY and the FY spectrum. In the case of the SY spectrum with the background in the pre-edge, the pre-edge background can be eliminated by subtracting the SY spectrum of a clean Si from that of the sample¹⁾. Figure 2 shows the Fourier transform of EXAFS oscillation obtained from the SY spectrum using calculated phase shift²⁾. The derived O-Si bond length in the SiO_2 film is 1.60Å, which is in good agreement with that determined from other diffraction technique¹⁾.

References

- 1)J.Stöhr, L.Johansson, I.Lindau and P.Pianetta, Phys.Rev., B20, 664 (1979)
- 2)B.K.Teo and P.A.Lee, J.Am.Chem.Soc., 101, 2815 (1979)

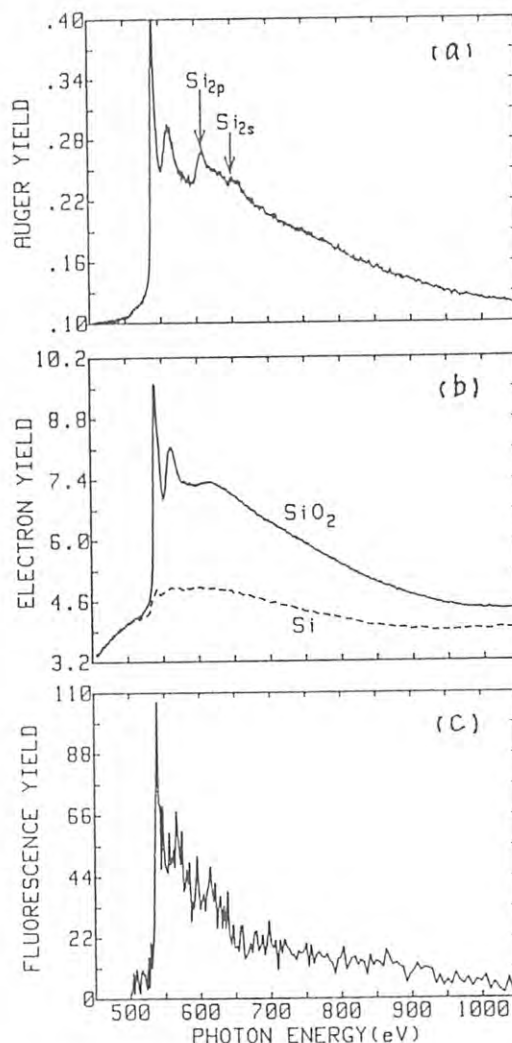


Fig.1. EXAFS spectra above O K-edge for SiO_2 film: (a) O_{KLL} Auger electron yield. (b) Secondary electron yield. (c) O K fluorescence yield.

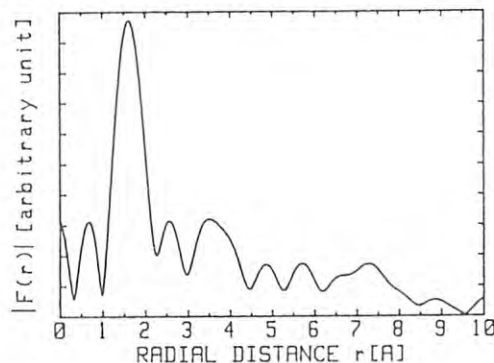


Fig.2. Fourier transform of secondary electron yield EXAFS spectrum of SiO_2 .

SYNCHROTRON RADIATION PHOTOEMISSION SPECTROSCOPY OF Ga-INSULATOR INTERFACES FOR GaAs LATERAL EPITAXIAL GROWTH

Masaharu OSHIMA, Yoshihiro KUBAYASHI*, Tomoaki KAWAMURA,
Satoshi MAEYAMA, Yukinobu SHINODA*, and Tsuneaki MIYAHARA**

NTT Applied Electronics Laboratories, Musashino-shi, Tokyo 180,

* NTT Basic Research Laboratories, Musashino-shi, Tokyo 180,

** KEK, Photon Factory, Oho-machi, Tsukuba-gun, Ibaraki 305

Introduction

GaAs lateral epitaxial growth on insulators such as glass substrates is a promising technique for developing 3 D devices and new function devices. In order to realize a high lateral growth rate, the lateral growth mechanism must be clearly understood from the viewpoints of surface migration and interfacial reaction. In this study, in situ SRPES was performed in order to understand the Ga-insulator interfacial reaction. Furthermore, surface migration rates were evaluated in order to investigate the relationships involved.

Experimental

Experiments were carried out using an in situ multi-technique surface analysis system at BL-1A of the Photon Factory. Photon energy was set at 120 eV to obtain very surface sensitive information of the interfaces. Samples were 150 Å Sm_2O_3 , MgO , Al_2O_3 , TiO_2 , SiO_2 , and Ta_2O_5 layers deposited on Si wafers. Three step Ga deposition and following annealing were performed to observe the Ga-insulator interfacial reactions at each step.

Results and discussion

Surface sensitive PES results indicate that only Ga on TiO_2 , which has larger formation energy per oxygen atom than Ga_2O_3 , is heavily oxidized, and that interfacial TiO_2 is strongly reduced to metallic Ti, as shown in Fig. 1. The large metallic peak suggests that metallic Ti atoms might diffuse out from the interface and exist on top of the Ga overlayer. Furthermore, this quite small $\text{Ti}3p$ oxide peak indicate that the TiO_2 surface is almost covered with the Ga islands at about 10 Å deposition. On the annealed surface, more than two-thirds of $\text{Ga}3d$ peak is in the incompletely oxidized state, and almost all the

$\text{Ti}3p$ peak is in the TiO_2 state with a small amount of TiO state. This annealing feature can be explained by a ball-up of GaTi complex oxides, taking into consideration the TEM and SEM images of islands.

In order to investigate the relationship between these interfacial reactions and GaAs crystal growth on various insulators, MOCVD GaAs growth was conducted. Striking coincidence of the surface migration rate; $\text{SiO}_2 \gg \text{Ta}_2\text{O}_5 > \text{Al}_2\text{O}_3 > \text{TiO}_2$ with the Ga-insulator interfacial reactions; $\text{SiO}_2 < \text{Ta}_2\text{O}_5 < \text{Al}_2\text{O}_3 < \text{TiO}_2$ was observed, indicating that Ga-insulator reaction is dominant in the surface migration process.

We also observed surface treatment effect by Ar sputtering which is useful to diminish the Ga-insulator interaction. This treatment changes the Ga growth mode from "Island growth" to "Layer-like growth". This may be due to an increase in surface energy caused by sputtering-induced dangling bonds.

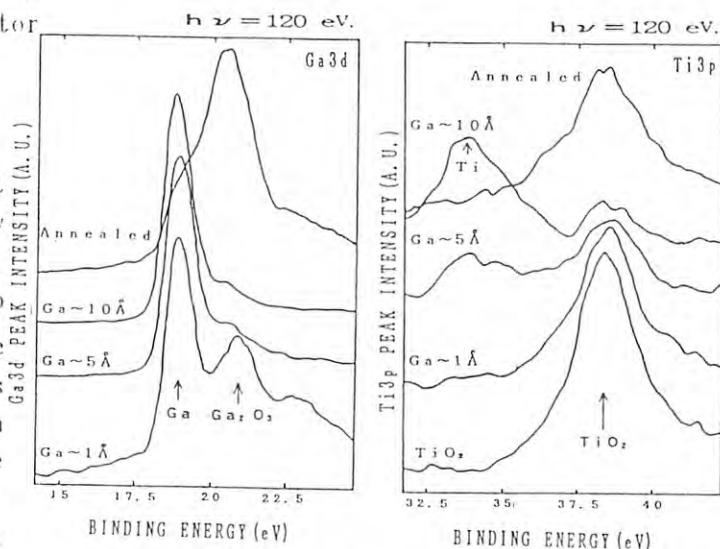


Fig. 1 Ga3d and Ti3p spectra of Ga-deposited and annealed TiO_2 surfaces. Photon energy was 120 eV.

PERFORMANCE OF A GRATING/CRYSTAL MONOCHROMATOR USING A MULTILAYER MIRROR-GRATING COMBINATION

Satoshi MAEYAMA, Tomoaki KAWAMURA, Masaharu OSHIMA, Yoshikazu ISHII and Tuneaki MIYAHARA*
 NTT Applied Electronics Laboratories, Musashino-shi, Tokyo 180
 *KEK, Photon Factory, Oho-machi, Tukuba-gun, Ibaraki 305

Introduction

In order to monochromatize the energy region which is almost difficult to cover using either crystals or gratings, the authors have a plan to employ multilayers as diffracting elements of a Grating/Crystal Monochromator (GCM)¹⁾ installed at Beamline 1A in the Photon Factory. For the first step of realizing the multilayer monochromator, transmission function of GCM using a multilayer mirror in combination with a grating was investigated.

Experimental

The multilayer used for a 4 degree incidence mirror of GCM was deposited on a very flat pylex glass substrate by sputtering method. The multilayer coating consists of 6 layer pairs of C(114Å) and W(25Å). Transmission function of GCM using the multilayer mirror-grating(2400g/mm) combination was measured by mean of output from an electron multiplier with a polypropylen window set at the beam line end. In addition, O K fluorescence radiation from a SiO₂ film was recorded with a Si(Li) detector.

Results

Figure 1 shows the transmission function of GCM using the multilayer mirror. The increment of monochromatized beam flux was observed at about 850eV in the transmission function. This phenomenon is thought to be caused by diffraction effect of multilayer used as a mirror, since this effect was not observed at all when a Pt mirror was used in stead of the multilayer. Figure 2 shows the calculated reflectivity profile of this multilayer based on the dynamical theory²⁾. The diffraction effect was confirmed by comparing the calculated result and the experimental result.

Figure 3 shows the O K fluorescence yield spectrum above the O K-edge for the SiO₂ film. Although EXAFS oscillation is not clear due to the bad signal-to-noise ratio, there is a broad peak near 850eV which is not due to EXAFS oscillation. This yield increment can be attributed to the increased incident beam flux correspond to the transmission function in Fig.1.

In conclusion, we observed the diffraction effect of the multilayer used as the mirror of GCM in the energy range of 850eV.

References

- 1)W.R.Hunter, R.T.Williams, J.C.Rife, J.P.Kirkland and M.N.Kabler, Nucl.Instr. and Meth., **195**, 141 (1982)
- 2)J.H.Underwood and T.W.Barbee, Appl.Opt., **20**, 3027 (1981)

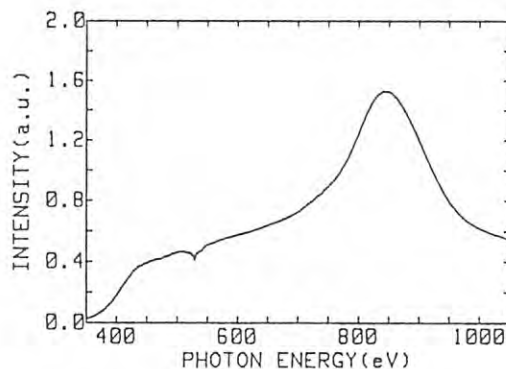


Fig.1. Transmission function measured by means of output from electron multiplier.

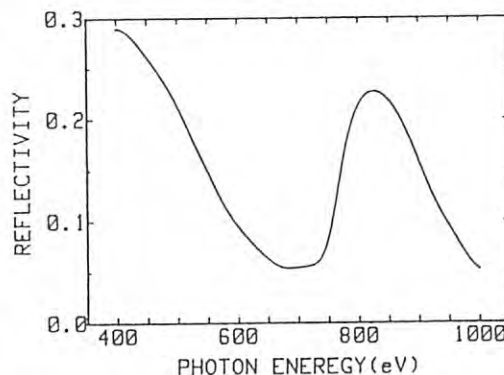


Fig.2. Calculated reflectivity of d=139Å multilayer.

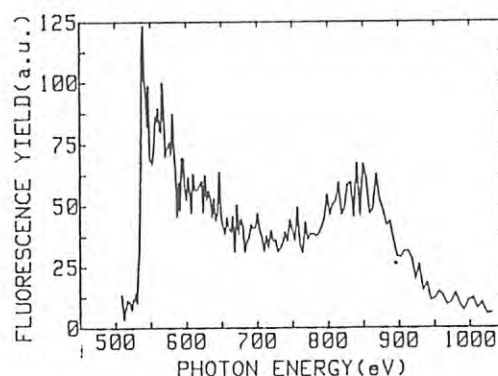


Fig.3. O K fluorescence yield spectrum above O K-edge for SiO₂ film.

PERFORMANCE OF A GRATING/CRYSTAL MONOCHROMATOR IN 50eV -900eV

Tomoaki KAWAMURA, Satoshi MAEYAMA, Masaharu OSHIMA, Yoshikazu ISHII
and Tsuneaki MIYAHARA

NTT Applied Electronics Laboratories, Midori-cho, Musashino-shi, Tokyo 180

*National Laboratory for high Energy Physics, Photon Factory, Oho-machi, Tsukuba-gun,
Ibaraki 305

Introduction

The surface analysis beamline BL-1A was constructed to provide the wide range monochromatic beam from VUV to soft X-ray for characterization with photoemission and EXAFS. Last year, we performed the monochromatization in VUV region from 20eV to 250eV by using a 1200 g/mm grating⁽¹⁾. In this report, monochromatic properties in higher energy region below 900 eV is described.

Experimental and Result

A 1200 g/mm grating with 1 degree blaze angle and a 2400 g/mm grating with 2 degree were used for monochromatization. Photon energy range was set by changing the incident angle to a plane mirror and gratings between 80 and 86 degree. Figure 1 shows the output flux measured by an Au photocathode placed at the downstream side of the exit slit. The solid lines mean the output flux of the 1200 g/mm grating and dashed line means the output of the 2400 g/mm grating. The maximum flux was obtained at about 100eV with the combination of the 80 degree incidence angle and the 1200 grating. In the case of the 2400 grating, the range of 400eV -900eV was covered although the photocurrent was smaller than 0.1nA measured by the Au photocathode.

To confirm the possibility of the "on blaze" operation by the GCM, the blaze condition monochromatization was tried. The result shows that in the 2400 g/mm grating case, the maximum value is obtained at the energy position of "blaze condition" but the maximum was far from the "on blaze condition" in the case of the 1200 grating. This is due to the rapidly decreasing reflectivity of the

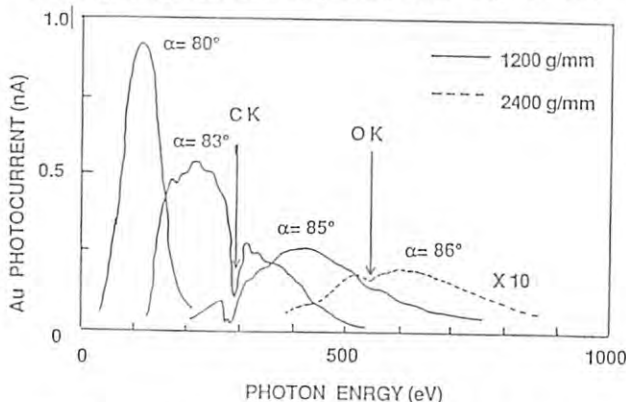


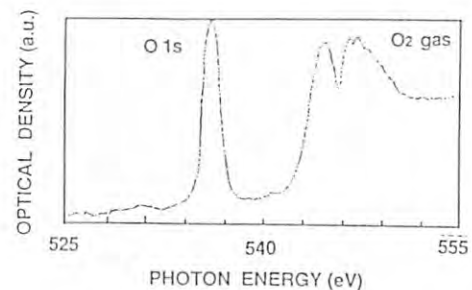
Fig.1 Output Flux of GCM measured by an Au photocathode

grating and the plane mirror, which strongly depends on the increasing of the energy and incident angle for the grating and plane mirror.

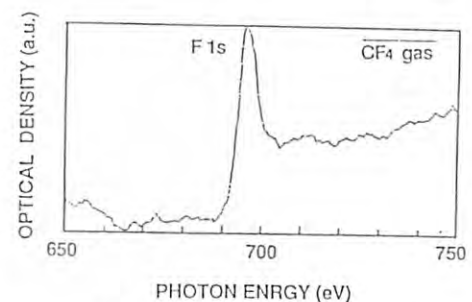
The energy resolution was measured by several gases such as Kr, Ar, O₂, CF₄ and Ne. In the 1200 g/mm grating case, the resolutions were 600-400 in 100eV to 250eV from Kr M_{4,5} (92eV) and Ar L_{2,3} (230eV) absorption. In the higher energy region, the O K-edge, F K-edge and Ne K-Edge absorption was measured with the 2400 g/mm grating. The resolution of 350 and 250 was obtained from O(540eV) and F K-edge (800eV) peaks. Near the Ne K-edge (870eV) case, a small jump derived from the absorption edge was observed and the upper limit of the monochromatization was estimated about 900eV in this arrangement.

For the monochromatization with the gratings, the improvement will be expected with the low emittance operation which decreases the source size. The effect of low emittance will be measured in near future.

(1) Kawamura, Maeyama, Oshima, Ishii and Miyahara, Photon Factory Activity Report, 1986, pl18



(a) O K-edge Absorption



(b) F K-edge Absorption

Fig.2 Absorption spectra of O K-edge and F K-edge

PERFORMANCE OF A GRATING/CRYSTAL MONOCHROMATOR IN 2.5 KeV - 4KeV

Tomoaki KAWAMURA, Satoshi MAEYAMA, Masaharu OSHIMA and Tsuneaki MIYAHARA*

NTT Applied Electronics Laboratories, Midori-cho, Musashino-shi, Tokyo, 180

*National Laboratory for High Energy Physics, Photon Factory, Oho-machi, Tsukuba-gun, Ibaraki, 305

Introduction

The wide range monochromatized beam from VUV to soft X-ray is required for characterization of the solid materials by using photoemission and EXAFS, required. A grating/crystal monochromator (GCM) was installed at the beamline BL-1A for this purpose, and the preliminary results with gratings had been reported⁽¹⁾ in the lower region than 250 eV. On the other hand, the different technique such as the maximum peak search method and the roll adjustment in vacuum are required to obtain the monochromatization. In this study,

the monochromatization with crystals are performed.

Experimental and Results

A set of InSb (111) crystals were chosen for monochromatization in 1.7 keV - 4 keV region. Figure 1 shows the arrangement for energy scanning with two crystals in GCM. In this arrangement, the 1st crystal is moved along both rotational and translational axes, and the 2nd crystal is moved only along rotational axis in order to obtain the monochromatic energy beam at the required value. Since we have a problem concerning the 2nd crystal instability due to the vibration of air-bearing system, we stopped the air-bearing of 2nd crystal, and translate only the 1st crystal.

Because of the lack of the peak search feedback system in hardware, the maximum peak search was carried out in software. Figure 2 shows the sequence of this maximum peak search method. In addition, the roll adjustment in vacuum was carried out by using an original crystal holder and a new manipulator.

Figure 3 shows the preliminary result of monochromatization in 2.5 keV - 4 keV. The steep decrease in intensity below 2.5 keV region is due to the incomplete roll adjustment of 1st and 2nd crystals. The monochromatized region should expand between 1.7 keV and 4 keV with more precise roll adjustment of 1st and 2nd crystals.

(1) Kawamura, Maeyama, Oshima, Ishii and Miyahara, Photon Factory Activity Report, 1986 pl18

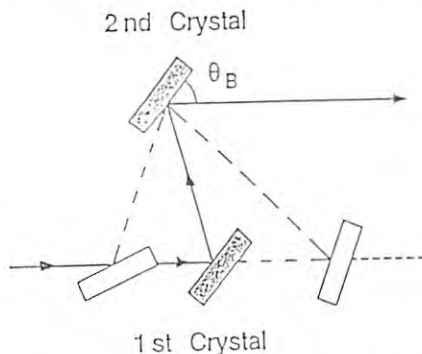
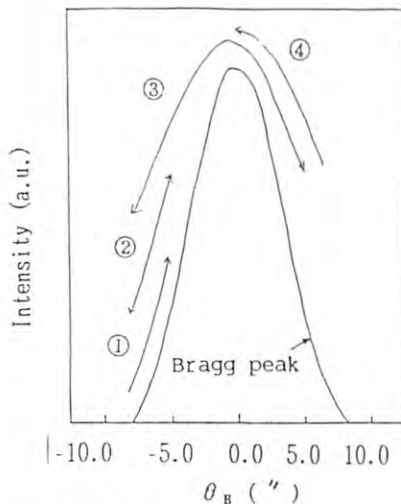


Fig.1 crystal arrangement for energy scanning



- (1) Rough scanning
- (2) Determining the scan direction
- (3) Measuring the peak profile
- (4) Setting the peak position

Fig.2 Sequence of the maximum peak search method

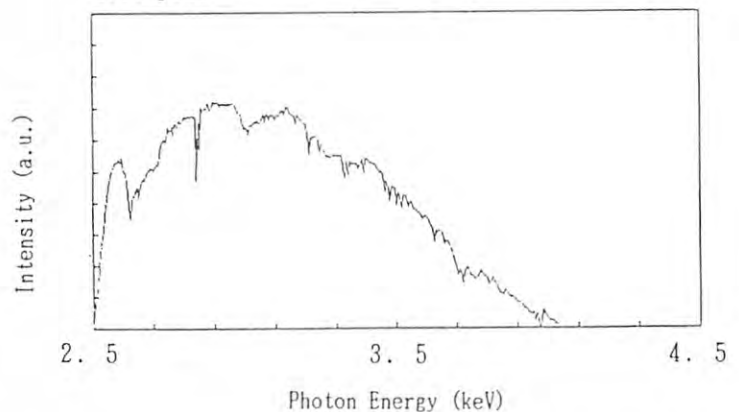


Fig.3 Output flux of InSb(111) monochromatization

A NEW SOFT-X-RAY PLATE : Ag/CHALCOGENIDE FILM

YASUSHI UTSUGI and KUNIO SAITO

NTT Electrical Communications Laboratories,
3-1, Morinosato Wakamiya, Atsugi-shi 243-01

INTRODUCTION

Real-time monitoring of high-resolution x-ray images is needed for the possible development of future soft-x-ray microscope systems, such as x-ray holography.¹⁾ Currently available x-ray detectors (polymer resist, silver halide film, photocathode tube and some semiconductor devices) cannot produce real-time monitoring of adequate resolution. Some of these techniques can provide high resolution characteristics only by using treatment, such as wet development following x-ray exposure. This report proposes a new soft-x-ray imaging plate of Ag/chalcogenide film, which offers the possibility of the real-time soft-x-ray microscope (with near-molecular resolution).

EXPERIMENTAL

Exposure experiments were conducted in the beam line BL-1B at the PHOTON FACTORY. A synchrotron radiation beam of soft x rays (2- to 10-Å wavelength) was collimated Ag/chalcogenide film through x-ray masks constructed with 0.4- μm thick Au film. The gap between the mask and the sample was adjusted to approximately 20 μm . The 1500-Å thick Ag/chalcogenide film was fabricated with Ag plating on a sputtered Ge-Se film surface. Auger analysis revealed a 200-Å thick Ag-Se film of the surface.

RESULTS AND DISCUSSIONS

Film color effectively changed only with x-ray exposure. The exposure-dose dependence of the film's optical characteristics were measured with a He-Ne laser (wavelength : 633 nm) and recorded in Fig. 1. The maximum change in transmittance is $\Delta T/T = 0.9$ and in reflectance is $\Delta R/R = -0.5$. As seen in Fig. 1, dynamic ranges are large, making neutral tints available. Utilizing this phenomenon, the phase-diffraction gratings were fabricated on the film by

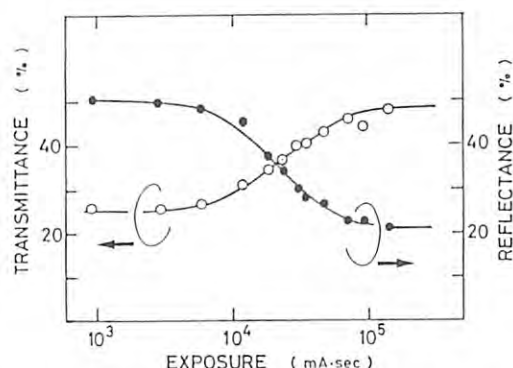


Fig. 1 X-ray exposure dependence of optical characteristics.

replicating the grating patterns on the Au mask. (Fig. 2) Also shown are the diffraction (0th, 1st, 2nd order) light beams produced from the He-Ne laser beam incidence on the gratings. A larger spatial frequency of the grating caused a larger diffraction angle. The diffraction efficiency characteristics of the 1st-order diffraction light is given in Fig. 3. Efficiency increased to a maximum of 7 % with x-ray exposure. The spatial frequency dependence of the diffraction efficiency was due to the grating quality in the Au mask. He-Ne laser beam irradiation did not damage the the phase diffraction gratings.

In conclusion, it is possible to realize real-time monitoring system of the fine x-ray images, using soft x rays as the imaging radiation, Ag/chalcogenide film as the imaging detector, and a He-Ne laser as the image-reconstructing light.

References

- 1) M. Howells, J. Kirz, D. Sayre and G. Schmahl, Phys. Today, **38**, No 8, 22 (1985)

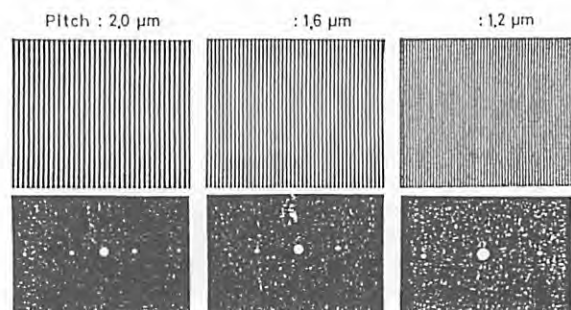


Fig. 2 Phase diffraction gratings on Ag/chalcogenide film (upper) and diffraction light beam images (lower).

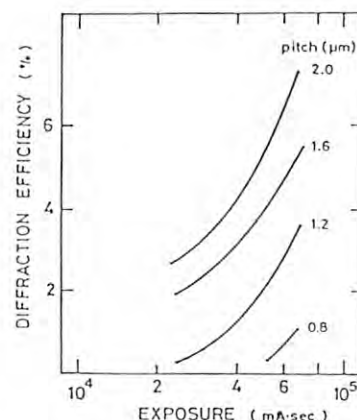


Fig. 3 Dependences of diffraction efficiency on x-ray exposure.

PHOTON STIMULATED DESORPTION IN THE SOFT X-RAY REGION

T.Murashita, T.Kaneko, H.Yoshihara, and M.Kobayashi *

NTT LSI Laboratories, Atsugi-shi, Kanagawa 243-01 Japan

*Photon Factory, National Laboratory for High Energy Physics, Oho-machi, Tsukuba-gun, Ibaraki 305 Japan

When synchrotron radiation (SR) irradiates vacuum ducts, outgassing occurs violently from those ducts. This phenomenon is known as photon stimulated desorption (PSD) and is one of the major problems in ultra-high vacuum systems using SR. PSD has been investigated in many SR facilities, but most of these studies have been carried out using hard X-ray.⁹ Meanwhile, PSD in the soft X-ray region has been largely neglected. In the soft X-ray region, the mass absorption coefficient is larger than that in the hard X-ray region. For this reason, soft X-rays are absorbed in the vicinity of the sample surface and hardly effect the inner part of the sample. It is thus thought that the behavior of PSD in soft X-ray is different from that in hard X-ray. This is one reason we wish to focus on PSD in the soft X-ray region. In this letter, a PSD measurement apparatus placed on the BL-1B beamline for studying soft X-ray effects is presented.

In the soft X-ray beamline BL-1B, SR beam is deflected by 2° using a flat SiC mirror to eliminate the hard X-ray. The calculated SR spectrum is shown in Fig.1. The SR beam is collimated and shaped by a perforated shield placed in downstream of the mirror 10x10 mm area on the sample surface. This perforated shield is made of oxygen-free copper and located 3 m upstream from the sample. This permits outgassing from the sample to be measured without any outgassing interference from the perforated shield.

Figure 2 shows a schematic view of the PSD measurement apparatus. Outgassing from the sample irradiated by SR beam is detected by the throughput method and the PSD coefficient η (molecules/photon) is calculated from the data. Nude ionization gauges are mounted in the port that can trap photons and photoelectrons, to prevent any influence from these particles. Vacuum pumping system consisted of two turbomolecular pumps connected in tandem to efficiently pump the light-mass gas molecules. Sample and shield-pipes can be moved independently in the vacuum chamber. The shield-pipe is located immediately in front of the sample and the SR beam passing through this pipe irradiates the sample.

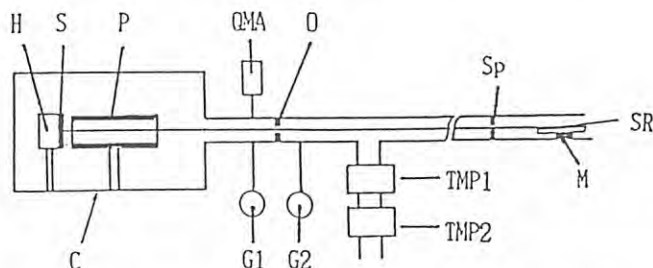


Fig.2 A schematic view of the PSD measurement apparatus
M:mirror, Sp:perforated shield, O:orifice, G:nude ionization gauge, QMA:mass analyzer, P:shield-pipe, S:sample, H:heatsink, C:chamber, TMP:turbomolecular pump

One of the shield-pipes is made of single-crystal Si whose surface is polished by chemical etching. This pipe traps more than 90 % of the SR photons reflected, and the photoelectrons emitted from the irradiated sample surface. This pipe then prevents outgassing from the interior wall of the chamber. Figure 3 shows the experimental results of the shield-pipe effect on PSD coefficient η measurement. The sample is oxygen-free copper. When shield-pipe is in position (A), the η values are exactly obtained. By contrast, those are high without shield-pipe (B) by influence from the chamber. It is clear from Fig.3 that the PSD coefficient can be exactly measured using the shield-pipe.

- 1) O.Grobner, A.G.Mathewson, H.Stoti and P.Strubin: Vacuum 33, 397 (1983)

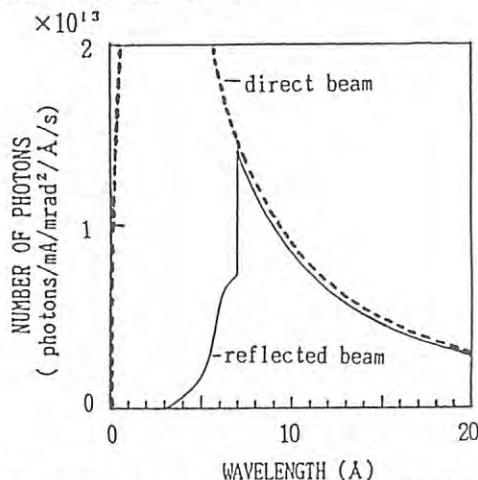


Fig.1 The calculated spectrum of SR deflected by 2° using a flat SiC mirror

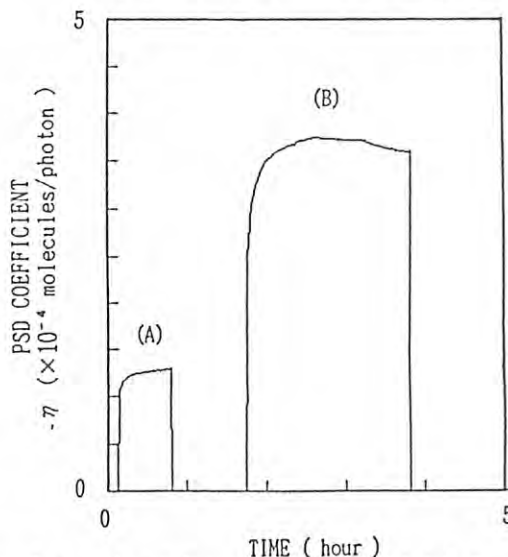


Fig.3 Experimental results of the shield-pipe effect on PSD coefficient measurement
(A) with shield-pipe and (B) without shield-pipe

Synchrotron Radiation Excited Etching of Si and SiO₂ by Use of SF₆+O₂ Reaction Gases.

Tsuneo Urisu, Hakaru Kyuragi, Mamoru Kitamura, Hideo Akiya.
NTT LSI Laboratories
3-1, Morinosato Wakamiya, Atsugi-shi,
Kanagawa, 243-01 JAPAN.

Introduction

The synchrotron radiation, which is an intensive light source from X-ray to vacuum ultraviolet, is expected to be an excellent light source of photoexcited semiconductor processes(1,2). In the present work, to assure this feasibility of the SR, the etching of Si and SiO₂ by use of SF₆+O₂ reaction gases have been conducted at the beam line BL-1C.

Experiments and Results.

The white beam of the SR radiation with about 5x10mm² spot size impinged perpendicularly on the surface of the Si substrate or SiO₂ film thermally deposited on Si. The etching gas SF₆ or mixture of SF₆ and O₂ was fed into reaction chamber.

Figure 1 shows observed etching rates. Both Si and SiO₂ showed almost equal etching rate without oxygen addition. However, it was found that the dependence on the oxygen concentration was quite different between Si and SiO₂.

The etching rate of SiO₂ gradually decreased with increasing oxygen concentration. On the other hand, the etching rate of Si rapidly decreased to zero with slight addition of oxygen. This indicates that extremely large etching selectivity ratio is realized between Si and SiO₂. Furthermore, the etching selectivity is quite different from that in rf plasma etching, where etching rate of Si is about

two orders of magnitudes larger than SiO₂. The second interesting point with this system is in the excitation mechanism. In the etching of SiO₂, it was observed that the etching proceeded only in the irradiated area. On the other hand, in etching of Si, a relatively broad etched pattern extending to the nonirradiated area was observed. This indicates that the etching proceeds through the excitation of the substrate surface or adsorbed molecules in the SiO₂, and the excitation of gas phase molecules is an important mechanism in Si etching.

Figure 2 shows the cross sectional view of the SiO₂ etched pattern. The polysilicon film (200 nm thickness) with through-hole pattern (0.5 μm diameter) was used as the etching mask. No undercutting of the sidewall is observed, indicating that, as a result of the surface excitation mechanism and good directivity of the light beam, the etching proceeds only in the direction of the light beam. So the anisotropic etching is realized in the SiO₂ etching.

References

- (1) H. Kyuragi and T. Urisu: J. Appl. Phys. 61 2035 (1987)
- (2) T. Urisu and H. Kyuragi: to be published in J. Vac. Sci. & Technol, B., Sept. /Oct. (1987)

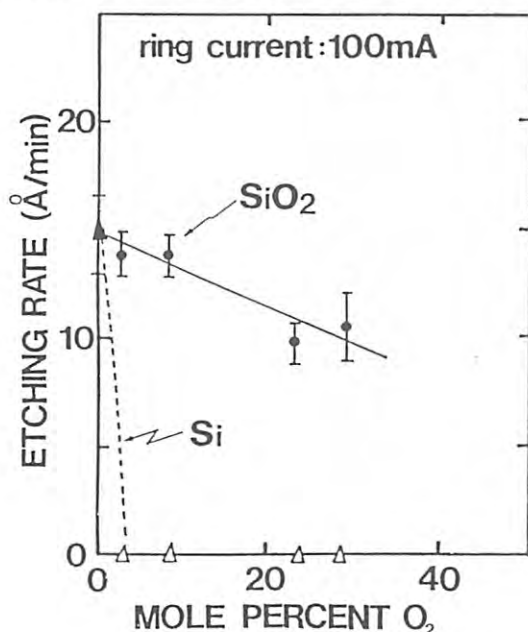


Figure 1

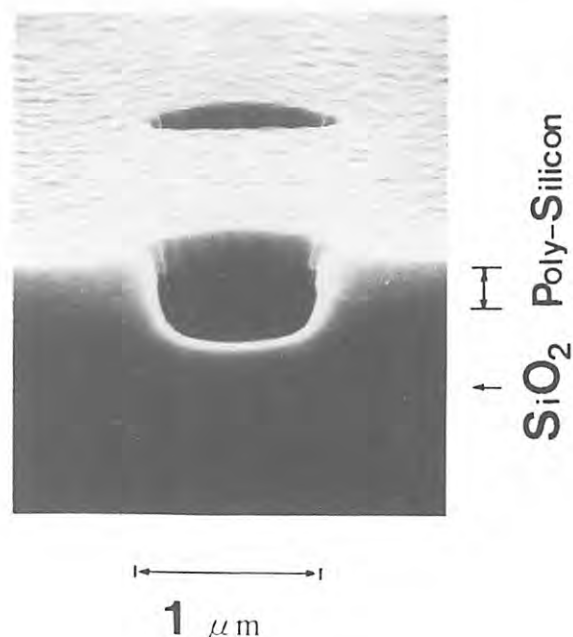


Figure 2

X-RAY FLUORESCENCE ANALYSIS OF THIRD PERIOD ELEMENTS USING UNDULATOR RADIATION

Atsuo IIDA, Tetsuya ISHIKAWA and Hideki MAEZAWA

Photon Factory, National Laboratory for High Energy Physics, Oho-machi, Tsukubagun, Ibaraki 305

INTRODUCTION

Elements of third period from Na to Cl have been difficult to analyze with high sensitivity by the X-ray fluorescence technique. Since the double crystal monochromator has been installed in the undulator beamline (BL-2A)¹⁾, the highly monochromatized and high intensity X-rays with energy range from 1 keV to 4 keV has been now available. Undulator is essentially suitable for the micro and trace element analysis²⁾. Furthermore, there is a possibility of studying the threshold effect on the X-ray emission spectrum³⁾. In this report, the preliminary results of X-ray fluorescence (XRF) analysis using monochromatic undulator radiation is described.

EXPERIMENTAL

Undulator radiation was monochromatized by the InSb (111) double crystal monochromator. The beam size at the sample was about 1 x 1 mm. A Si(Li) detector (energy dispersive mode) and a linear focusing crystal spectrometer (wavelength dispersive mode) equipped with a curved ADP crystal were used for the energy analysis of emitted X-rays.

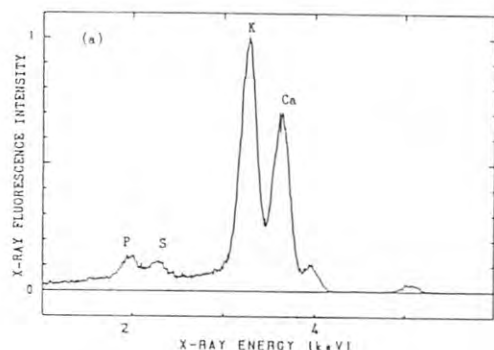


Fig.1 Energy dispersive X-ray fluorescence spectra. 5 keV(a), 2.5 keV(b) and 2 keV(c) excitation energy.

Results and Discussion

(1) Energy dispersive XRF: Fig.1(a), (b) and (c) show the spectra from Sargasso (NIES certified reference material) excited with 5 keV, 2.5 keV and 2 keV X-rays respectively. Enhancement in the sensitivity for Mg through S by the tunable X-ray source is clearly demonstrated.

(2) Wavelength dispersive XRF: Fig.2 shows the spectrum from a GaAlAs epitaxial layer. It is difficult to separate these lines by the Si(Li) detector due to the poor energy resolution, the advantage of the wavelength spectrometer is evident. Fig. 3 shows the typical Si Ka spectrum from the silicon wafer. As the excitation energy lowered down to around the Si K absorption edge, the satellite peak ($K\alpha_{3,4}$) disappeared. The effect of the excitation energy on the X-ray emission spectrum was shown.

The relatively large beam size degrades the detection performance of the curved crystal spectrometer. Improvements are now underway.

References

- 1) PF Activity Report, 1986 #4, p91
- 2) A. Iida et al., Adv. in X-ray Anal. 29(1986)427
- 3) R.D.Deslattes et al., Phys. Rev. 27(1983)923

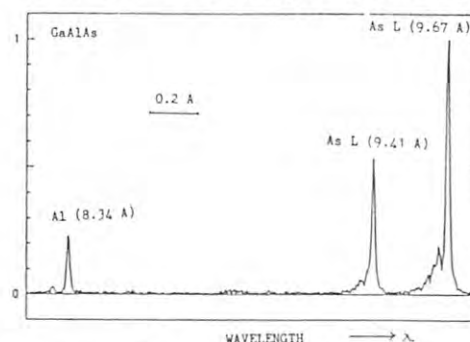


Fig.2 Wavelength dispersive X-ray fluorescence spectrum from GaAlAs.

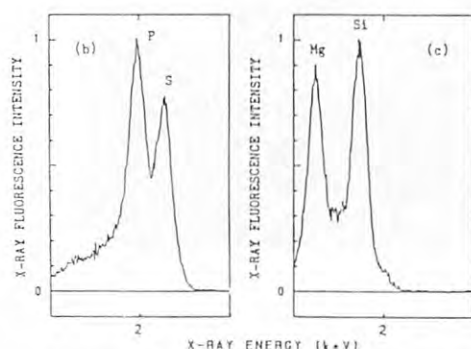


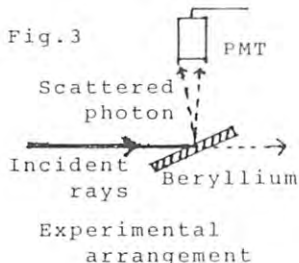
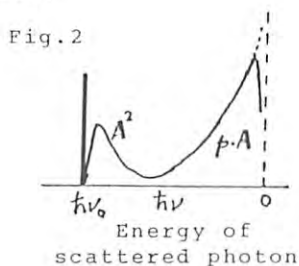
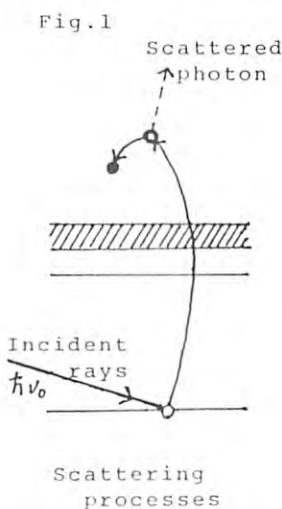
Fig.3 Si Ka X-ray emission spectra with 2.4 keV (solid line) and 1.87 keV (broken line) excitation energy.

SOFT-X-RAY p.A SCATTERING BY LIGHT ELEMENT SOLIDS

Tadas SUZUKI, Koichi MORI,^oYasuo IGUCHI and[†]Hideki MAEZAWADepartment of Physics, Sophia University
Kioi-cho, Chiyoda-ku, Tokyo 102^o Institute of Applied Physics, The University of Tsukuba
Sakura-mura, Niiharu-gun, Ibaraki-ken 300-31[†] Photon Factory, National Laboratory for High Energy Physics
Oho-machi, Tsukuba-gun, Ibaraki-ken 305Introduction

Inelastic soft-X-ray scattering by inner-shell electrons in solids of light elements has not been fully investigated either theoretically or experimentally. Recently Ohmura and Suzuki¹⁾ computed the cross section of the scattering under the condition of $2\pi a/\lambda_0 < 1$ and $10I \geq h\nu_0 \geq I$, where λ_0 and $h\nu_0$ are the wavelength and the energy of the incident X-rays and a and I are the radius and the ionization energy of the inner-shell electron, respectively. As can be seen in Fig.2, which is an example of the computed results, the scattering intensity increases towards larger energy region. This tendency reflects the off-resonant p.A term contribution in the Hamiltonian. The p.A term contribution is not negligible compared with the A^2 -term under the above mentioned condition.²⁾

Therefore, an experiment using the monochromatic intense radiation from an undulator equipped in a synchrotron orbit would be useful to confirm the stated theoretical results.

Experiment and Results

Soft-X-rays generated through an undulator and monochromatized by two-crystal monochromator were guided onto a polycrystalline beryllium plate of 5 mm thick with an incident angle of 20° . Wavelength of the X-rays were 30.6\AA . The scattered radiation was detected at 90° to the polarization direction of incident rays. A photomultiplier with good sensitivity for 300nm to 900nm was used.

Raw spectrum including thermal noise of the detector and other background signals is shown in Fig.4. After extracting the specimen from the path of incident rays, similar measurements were repeated. Net signal the disturbing noises subtracted is shown in Fig.5. Too small net signals, which should correspond to small scattering cross section, do not allow us to say anything in detail. However, the result gives us a clue to further investigation.

References

- 1) Y. Ohmura and T. Suzuki: J. Phys. Soc. Japan **53** (1984) 2807
- 2) T. Suzuki: "Advances in X-Ray Spectroscopy" ed. by C. Bonnelle and C. Mande (Pergamon Press, Oxford 1982) Ch.23

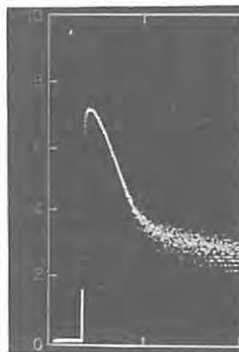


Fig.4



Fig.5

Reflectivity Measurement of W/Be Multilayer Mirror for Soft X-rays

Yuichi Utsumi, Hakaru Kyuragi, Mamoru Kitamura,

Tsuneo Urisu and*Hideki Maezawa

NTT LSI Laboratories, Morinosato-Wakamiya, Atsugi-si, Kanagawa 243-01

*Photon Factory, National Laboratory for High Energy Physics,
Oho-machi, Tsukubagun, Ibaraki 305Introduction

W and Be multilayer mirrors are expected to have high reflectivity in the energy range from 500eV to 2500 eV, which is important for x-ray lithography, as beryllium has the highest transmissivity in this energy range among applicable materials. However, optical characteristics for multilayers containing Be layers have not been investigated so far. In this work, reflectivities of W/Be multilayer have been measured using synchrotron radiation (950-1250eV) and compared with calculations.

Experimental

The W/Be multilayer were deposited by sputtering technique using a neutral Ar atom beam (1). An advantage of this technique is that the substrate does not suffer from radiation damage by ionized particles. Targets and mechano-chemically polished Si substrates were cooled by water, and substrates were reciprocated to obtain uniform film thickness. Reflectivities of the fabricated W/Be multilayer mirror were measured in the range 900eV-1250eV, using synchrotron radiation monochromatized by a 10m grazing incidence monochromator at beamline BL-2.

The measurement system is shown schematically in Fig.1. Resolution of the monochromator was 0.007Å and beam divergence was less than 0.8 mrad. The design parameters of this multilayer are N (number of layers)=30, d (period)=77.0Å and λ (thickness of reflective layer divided by the period)=0.50. The multilayer mirror was set in a chamber kept at a vacuum higher than 2.0×10^{-4} Pa. The grazing incidence angle of synchrotron radiation to the mirror was 5.0 degrees. The incident and reflected SR beam intensities were measured by photo-multiplier at (A) and (B) positions respectively in Fig.1.

Results and Discussion

Figure 2(a) shows the observed dependence of the reflectivity on photon energy. The observed peak reflectivity was about 30%. This value is about 75% of the calculated value (b) assuming ideal W/Be multilayer structure. This peak reflectivity decrease is attributed to two factors: the most important factor is interface roughness and the other factor is the increase in the absorption coefficient of the transmissive Be layer due to oxygen contamination (20 - 30at%) from the sputtering atmosphere.

The effect of interface roughness on reflectivity was calculated assuming that interface roughness was given by the Gaussian distribution with standard deviation σ , which was preliminarily determined to be 2.5Å by observed x-ray (Cu K α 1.54Å) diffraction curve. The reduction of peak reflectivity due to 25at% oxygen contamination was 4.8% of the ideal peak value. The calculated reflectivity curve (Fig.2(c)) considering these two effects was in fairly good agreement with the observed curve as shown in Fig.2.

Reference

- (1) J. Franks, J. Vac. Sci. Technol. 16, 181 (1979)

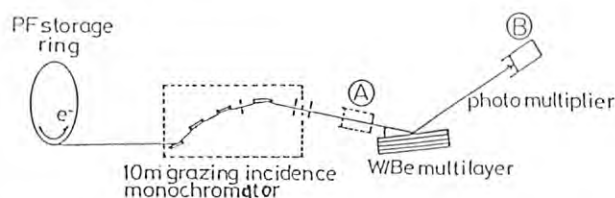


Fig.1 Schematic arrangement of reflectivity measurement system.

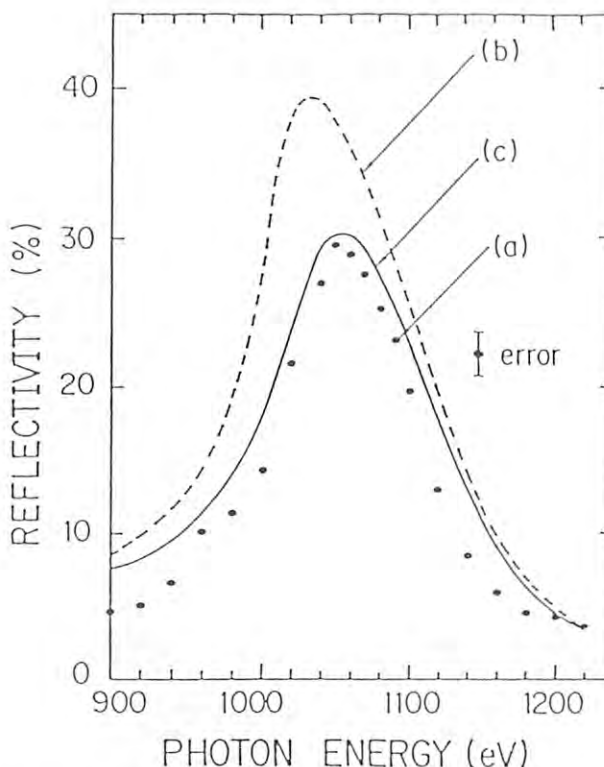


Fig.2 Observed and calculated reflectivities of W/Be mirror.

X-RAY CONTACT MICROSCOPY OF HUMAN CHROMOSOME

Kunio SHINOHARA, Hisako NAKANO, Makoto WATANABE*, Yasuhito KINJO*, Sachiko KIKUCHI**,
Yasushi KAGOSHIMA***, Katsumi KOBAYASHI***, and Hideki MAEZAWA***

Tokyo Metropolitan Institute of Medical Science, Bunkyo-ku, Tokyo 113

*Tokyo Metropolitan Isotope Research Institute, Setagaya-ku, Tokyo 158

**Toshiba VLSI Research Center, Saiwai-ku, Kawasaki-shi, Kanagawa 210

***Photon Factory, National Laboratory for High Energy Physics, Oho-machi, Ibaraki 305, Japan.

Introduction

X-ray contact microscopy of intact biological specimen using polymethylmethacrylate (PMMA) requires intense monochromatic radiation such as undulator radiation. As a step to observe intact biological materials, we have observed unstained human chromosomes dried with no fixative by x-ray contact microscopy using undulator radiation.

Materials and Methods

Chromosomes from human lymphocytes (RPMI 1788) were spread on a surface of distilled water and whole-mounted on PMMA(1). They were dried immediately without fixation. The PMMA with chromosomes was exposed to the 2.98 nm monochromatic undulator radiation from BL-2B at the Photon Factory, National Laboratory for High Energy Physics, in a vacuum (10^{-7} – 10^{-8} Torr). A zone plate monochromator (stopping material, tantalum; thickness, 1 μ m; innermost diameter, 62.9 μ m; outermost diameter, 2 mm) was installed. The exposure (972 mA·min) was expressed as ring current (mA) \times time (min). The exposed specimens were treated as described elsewhere(2). Briefly, chromosomes were removed with sodium hypochlorite from the PMMA. The PMMA was developed with a mixture of methylisobutylketone and isopropanol. The developed images were observed either with differential interference microscope or with transmission electron microscope by replica method with the plasma polymerization-film in a glow discharge.

Results and Discussion

X-ray image of chromosomes was observed in differential interference microscope (Fig. 1) and in transmission electron microscope (Fig. 2). Fig. 3 shows a stretched portion of a chromosome as seen in transmission electron microscope. We can see a superbeads structure of a chromatic fibril.

In this report, we demonstrated that the observation of human chromosomes dried with no fixative was possible at high resolution without further staining process which may induce artifact. We are now planning to try to observe these chromosomes in a wet condition.

References

- 1) M. Watanabe and N. Tanaka: Jpn. J. Genetics 47 (1972) 1.
- 2) K. Shinohara et al.: Photochem. Photobiol. 44 (1986) 401.

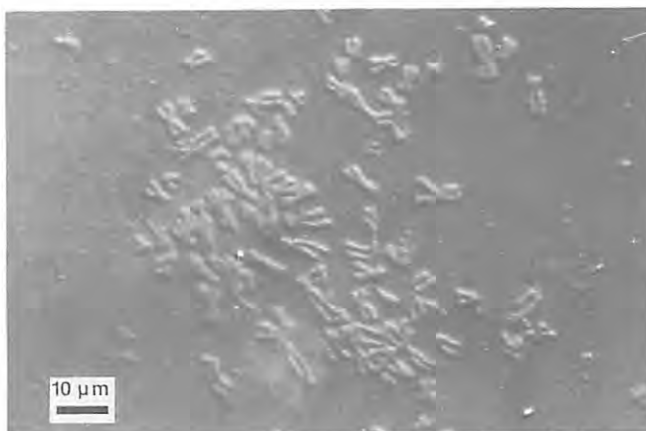


Fig. 1

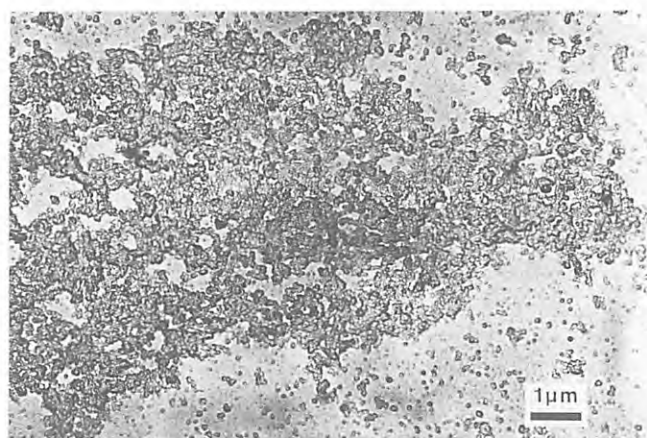


Fig. 2

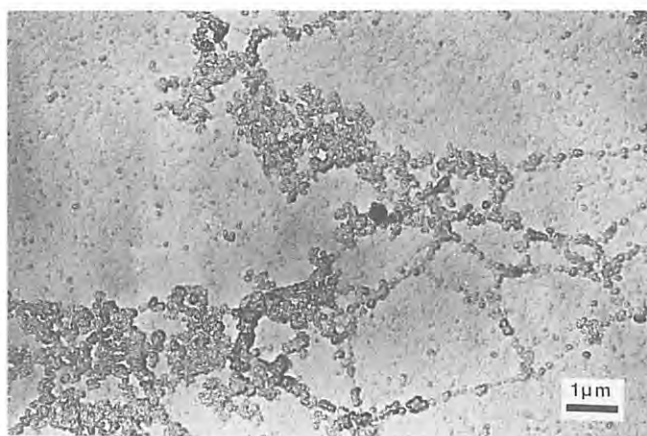


Fig. 3

A PRELIMINARY EXPERIMENT OF A SOFT X-RAY MICROSCOPE

Sadao AOKI, Yasushi KAGOSHIMA, Masami KAKUCHI*
Hideki MAEZAWA**, Kazuyuki HYODO** and Masami ANDO**

Institute of Applied Physics, University of Tsukuba
Sakura, Ibaraki 305

*NTT Electrical Communications Laboratories
Tohkai, Ibaraki 319-11

**Photon Factory, National Laboratory for High Energy Physics,
Oho, Ibaraki 305

High resolution soft x-ray microscopes have been studied in some pioneering works and the feasibility of the soft x-ray microscope has been demonstrated in them.^{1,2)} In those microscopes a Fresnel zone plate is used as an optical element and synchrotron radiation as an x-ray source. However, since a zone plate needs a high brilliant x-ray source because of its low efficiency, the undulator radiation seems to be suitable for the soft x-ray microscope.

A schematic optical system of the zone plate soft x-ray microscope is shown in Fig.1. The optical system consists of a condenser zone plate, a pinhole, an object zone plate and a screen. An incident x-ray beam radiated from the undulator is focused on an object plane by the condenser zone plate and illuminates the object on the pinhole. The pinhole works as a stopper so that the undiffracted direct beam through the condenser zone plate may not reach the screen and disturb an imaging area. The object zone plate generates a magnified image of the object on the screen.

Numerical parameters of the optical system were calculated by taking following conditions into account:

- 1) wavelength range : 20~30Å
 - 2) magnification : 150~200
 - 3) theoretical resolution limit : 0.25μm.
- The condition 1) means the wavelength range of the first harmonic of the undulator radiation. The condition 2) was imposed to be able to observe a magnified image on the microchannel plate. The condition 3) was determined by the narrowest annular width of the zone plate. Numerical parameters thus obtained are shown in table 1.

As a stopping material of a zone plate against an x-ray beam tantalum was chosen because of its properties as follow. Tantalum has as high absorption coefficients as gold in the soft x-ray region. The residual stress is four times higher than that of gold and can be successfully controlled by the sputtering conditions. The reactive ion-etching (RIE) process can be applied for the patterning of tantalum.

A preliminary experiment was performed at station BL-2B using the undulator radiation with the optical system mentioned above and zone plates shown in table 1. Fig.2 shows a magnified image of a copper mesh #1000, which was used as a model sample. The wavelength was 24Å, the film used was FUJI MINICOPY FILM, exposure time was 4 seconds at the ring current of 157mA and the magnification was 180. A pair of black crossed lines corresponds to that of the mesh, where the line width was 7.5μm.

A white blurry circle covering over the image corresponds to the defocused image of a 20μm-diam. pinhole.

References

- 1) B.Niemann, et al., Nucl. Instr. and Meth. A246 (1986) 675.
- 2) H.Rarback, et.al., Nucl. Instr. and Meth. A246 (1986) 159.

Table 1

	condenser zone plate	object zone plate
radius of innermost zone $r_1(\mu\text{m})$	15.8	5.0
diameter of zone plate $D=2r_n(\mu\text{m})$	1000.0	100.0
number of zones N	1000	100
width of outermost zone $\delta r_n(\mu\text{m})$	0.25	0.25

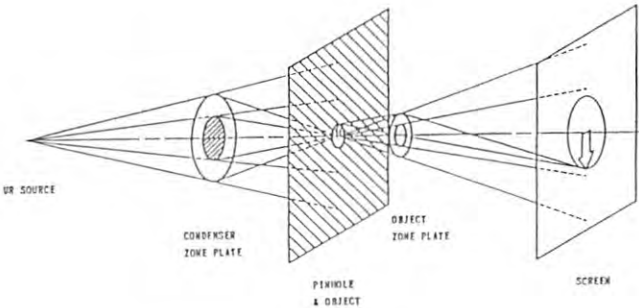


Fig. 1

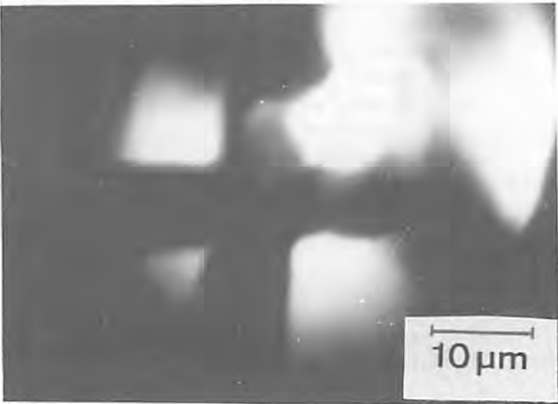


Fig. 2

A PERFORMANCE TEST OF A SOFT X-RAY MICROSCOPE

Yasushi KAGOSHIMA, Sadao AOKI, Masami KAKUSHI*
Hideki MAEZAWA**, Kazuyuki HYODO**, and Masami ANDO**

Institute of Applied Physics, University of Tsukuba
Sakura, Ibaraki 305

*NTT Electrical Communications Laboratories
Tohkai, Ibaraki 319-11

**Photon Factory, National Laboratory for High Energy Physics,
Oho, Ibaraki 305

A soft x-ray microscope with zone plates has been studied in a beamline of a soft x-ray undulator at the Photon Factory. A preliminary experiment was performed and a magnified image of a model sample (copper mesh #1000) was already obtained.^{1,2)} However, the imaging performance such as the resolving power has not been evaluated exactly yet. Therefore an experiment was made by using grating patterns with various pitches to evaluate the resolving power.

Fig.1 shows a schematic drawing of the soft x-ray microscope installed in station BL-2B. An incident X-ray beam radiated from the undulator comes from the left and enters into vacuum chambers constructed on an optical bench. The soft x-ray microscope system consists of four parts, i.e., a condenser chamber, an object chamber, a photodiode chamber and a photographic chamber. There are two gate valves, a top valve and an end valve. The top valve isolates the microscope system from the upstream beamline for vacuum. The end valve isolates the microscope system into two parts so that only the photographic chamber can be independent of other front chambers.

An experiment was performed by using the test grating patterns with various pitches which were made to evaluate the resolving power of the soft x-ray microscope. The grating patterns were made of tantalum and the pitches were from $2.0\mu\text{m}$ to $0.4\mu\text{m}$. Magnified images of these grating patterns were taken. In this experiment a $0.6\mu\text{m}$ pitch grating pattern was resolved. Fig.2 shows a SEM magnified image and an x-ray magnified image of a $1.0\mu\text{m}$ pitch grating pattern. The wavelength was 29.8\AA , the film used was FUJI MINICOPY FILM, the exposure time was 4 seconds at the ring current of 163mA and the magnification was 140.

A performance test made by using test grating patterns with various pitches. A $0.6\mu\text{m}$ pitch grating pattern was resolved. The result shows that the resolving power of the soft x-ray microscope was estimated to be $0.3\mu\text{m}$. From the fact that the theoretical resolution limit of the soft x-ray microscope is about $0.3\mu\text{m}$, the experimental limit attained is very close to the theoretical one. Furthermore, the system of the zone plate soft x-ray microscope with the undulator radiation is feasible to observe micron-order samples. By using the finer structural zone plate, the resolution will be improved.

References

- 1) S.Aoki et al.: to be published in Proceedings of X-ray Microscopy 86. (National Taiwan

university, 1986)

- 2) S.Aoki et al.: Photon Factory Activity Report 1987.

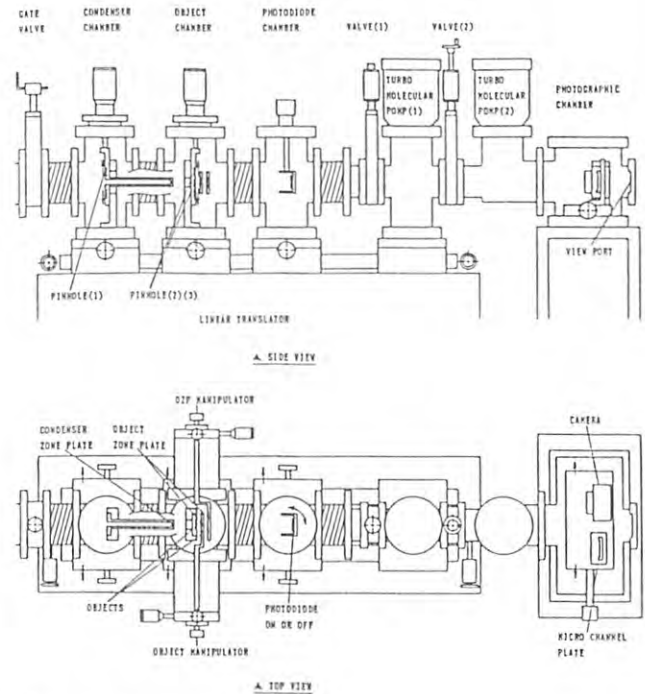


Fig.1

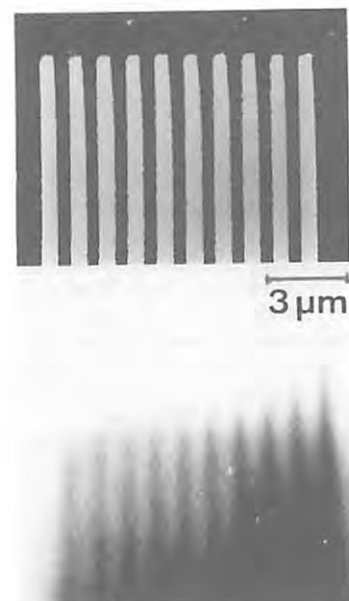


Fig.2

NUCLEAR MAGNETIC RESONANCE STUDY OF IRRADIATION EFFECTS ON Br-dCMP
CAUSED BY SOFT-X-RAYS AROUND K ABSORPTION EDGE OF Br

Kaoru TAKAKURA, Kotaro HIEDA⁺, Hiroshi MAEZAWA⁺⁺ and Katsumi KOBAYASHI⁺⁺⁺

Department of Physics, College of Liberal Arts, International Christian
University, Osawa, Mitaka-shi, Tokyo 181

⁺Department of Physics, Faculty of Science, Rikkyo (St. Paul's) University
Nishiikebukuro, Toshima-ku, Tokyo 171

⁺⁺Department of Radiation Oncology, School of Medicine, Tokai University,
Bouseidai, Isehara-shi, Kanagawa 259-11

⁺⁺⁺Photon Factory, National Laboratory for High Energy Physics, Oho-machi,
Tsukuba-gun, Ibaraki 305

Introduction

It is important to know the mechanism and the possibility of enhanced killing of bromo-substituted phage and cells by irradiation with soft-X-rays around K absorption edge of Br. For the purpose, the radiation products of Br compound mononucleotide, Br-dCMP, caused by mono-energetic X-rays, just above and below the K-absorption edge of bromine (13.47 KeV) were analysed by nuclear magnetic resonance (NMR) and high-performance liquid chromatography.

Experimental and Results

5-Bromo-2'-Deoxycytidine-5'-monophosphate (Br-dCMP) purchased from Sigma Co.Ltd. was dissolved in D₂O at concentration of 5 mg/ml. 200 μ l of the solution was irradiated in a plastic cell. Mono-energetic synchrotron radiation at Photon Factory was used as a radiation source. Two wavelengths, 0.919 Å (13.49 KeV) and 0.923 Å (13.43 KeV) were selected for irradiation. The chromatography employed a C₁₈ reverse phase column, 10 mm in diameter by 100 mm in length (Waters μ bondapak C₁₈). Elution was by 0.007 M K₂HPO₄ solution (pH 7.8). The spectra were monitored by optical detection at 260 nm. FT-NMR spectra were recorded at 21°C on a Varian XL-300 spectrometer.

The chromatogram of Br-dCMP irradiated with 0.923 Å soft-X-ray was shown in Fig.1. The amount of dCMP (peak b in Fig.1) increased as increasing the dose, suggesting the debromination from Br-dCMP by irradiation. Another two peaks (peak a and peak c) for unknown radiation-products were observed in the chromatogram. The chromatogram of Br-dCMP irradiated with 0.919 Å soft-X-ray was almost the same as that with 0.923 Å, though the debromination was somewhat effective in 0.923 Å irradiation (shown in Fig.2). dCMP in D₂O solution was also irradiated with 0.919 Å and 0.923 Å soft-X-rays. Isolation of cytosine from dCMP was observed apparently in the both case of 0.919 Å and 0.923 Å irradiation, as though no isolation of cytosine from Br-dCMP was observed. From these results it may be suggested that the bromine combined to Br-dCMP has a role to protect the isolation of base from the mononucleotide.

Phosphorus-NMR (P-NMR) and proton-NMR (H-NMR) were measured for Br-dCMP in D₂O solution. The H-NMR spectra of Br-dCMP irradiated with 0.919 Å and 0.923 Å soft-X-rays had almost no change comparing with that of control. However, in the P-NMR spectrum of irradiated Br-dCMP two new peaks were observed (peak A and B in Fig.3), revealing the radiation-products from Br-dCMP irradiated with soft-X-rays. Further investigation to identify the products is advanced.

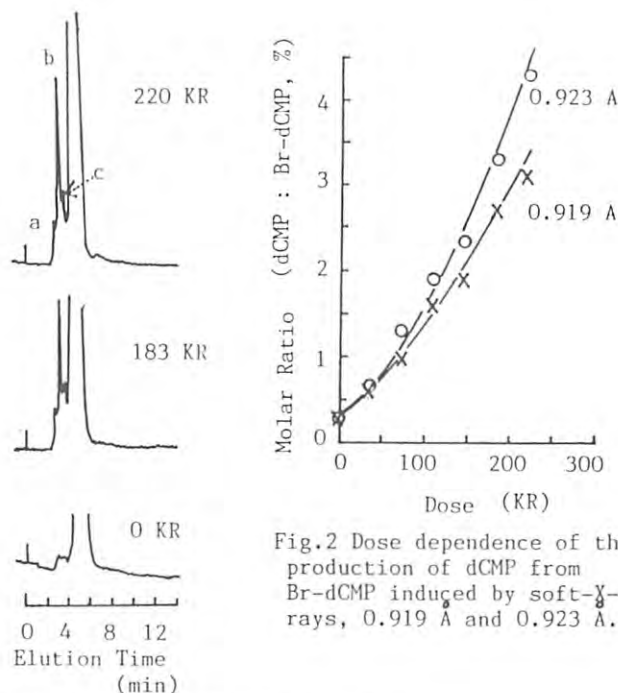


Fig.1 The chromatogram of Br-dCMP irradiated with 0.923 Å soft-X-ray. Irradiation doses on the surface of samples are 220 KR, 183 KR and 0 KR (control).

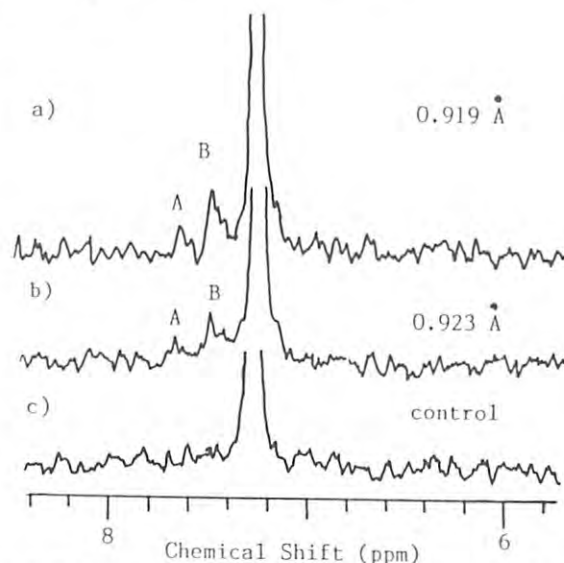


Fig.3 P-NMR spectra of Br-dCMP in D₂O solution irradiated with soft-X-rays, a) 0.919 Å, 155 KR on the surface of sample, b) 0.923 Å, 155 KR on the surface of sample, c) control.

STRAND BREAKS IN 5-BROMOURACIL-SUBSTITUTED DNA BY 12.40 AND 13.55 KEV PHOTONS

Kotaro HIEDA, Soichi HAYASHI, Ichiro MAEDA[†], Hiroshi MAEZAWA^{††},
Katsumi KOBAYASHI[‡] and Takashi ITO^{‡‡}

Department of Physics, Faculty of Science, Rikkyo University,
Nishi-Ikebukuro, Toshima-ku, Tokyo 171

[†]Nippon Kougaku K.K.,

Marunouchi, Chiyoda-ku, Tokyo 100

^{††}Department of Radiation Oncology, School of Medicine, Tokai University,
Bohseidai, Isehara, Kanagawa 259-11

[‡]Photon Factory, National Institute for High Energy Physics,
Oho-machi, Tsukuba-gun, Ibaraki 305

^{‡‡}Institute of Physics, College of Arts and Sciences, University of Tokyo,
Komaba, Meguro-ku, Tokyo 153

Introduction

Monoenergetic X-rays just above K-absorption edge of bromine (13.47 keV, 0.920 Å) produce predominantly K-shell ionization followed by Auger cascade in bromine. X-ray induced Auger cascade of bromine produces enhancement in killing of bromouracil(BU)-labelled phages and cells. The enhancement of killing may mean the enhanced production of DNA damage by Auger cascade. Recently, Hieda et al.¹⁾ measured single-strand breaks of BU-substituted pBR322 plasmid DNA after irradiation in the dry state with monoenergetic X-rays at 12.40 and 13.55 keV just below and above K-absorption edge of bromine. Unexpectedly, induction of single-strand breaks versus exposure dose (R) was same at both energies. However, the DNA sample was proved to be contaminated with CsCl and the results were distorted by the contamination. In this report we describe recent results using DNA sample without contamination.

Materials and Methods

BU-substituted DNA was isolated from *E. coli* B/r (thy⁻) cells carrying pBR322 cultured in BU containing mineral medium. Non-substituted DNA was isolated from *E. coli* HB101 cells carrying pBR322 cultured in L-broth. Isolation was performed by alkaline method and CsCl/ethidium bromide density gradient. Isolated DNA was dialyzed, filtered by Molcut (Millipore), and finally dissolved in 3 mM Tris-HCl and 0.3 mM EDTA, pH 8.0. Aliquot of 1 μ l containing 1 μ g DNA and 0.5 μ g buffer solute was spotted on polypropylene strip and dried in air. Samples in dry N₂ gas were irradiated with monoenergetic X-rays at BL-4A. Redissolved DNA was electrophoresed in agarose gel and three DNA forms (Form I, II and III) were separated. Single- and double-strand breaks were determined as a conversion from Form I to Form II and that from Form I to Form III, respectively.

Results

Form I fraction was decreased exponentially

with dose and Form III fraction was increased linearly with dose. Exposure doses in R measured by a free air ionization chamber were converted to absorbed doses in Gy by conversion factors calculated from mass energy-absorption coefficient tabulated by Hubbell²⁾ and elemental compositions of the samples which consist of 1 μ g of BU-substituted or non-substituted DNA and 0.5 μ g buffer solute. Absorbed doses giving one strand break, D₀, were calculated from dose-effect curves and tabulated in Table I.

For single-strand break, D₀ were almost same (7~8 kGy) regardless of photon energy and BU-substitution. 7~8 kGy (=kJ/kg) equals 206~234 eV/pBR322 molecule. This means that one single-strand break is induced by absorption of energy of about 220 eV per molecule which is provided mainly by secondary electrons. K-shell ionization of bromine has little effect because number of K-shell ionization of bromine per D₀ per molecule was calculated at only 0.02.

For double-strand breaks of BU-substituted DNA, D₀ at 13.55 keV was 0.827 times smaller than that at 12.40 keV. This decrease in D₀ may be caused by K-shell ionization of bromine (calculated at 0.57 ionization per D₀ per molecule) that leads efficiently to double-strand break.

References

- 1) K.Hieda, I.Maeda, H.Maezawa, K.Kobayashi, Photon Factory Activity Report 84/85, p.IV-22 (1986)
- 2) J.H.Hubbell, Int. J. Appl. Radiat. Isot., **33**, 1269 (1982)

Table I Absorbed dose (D₀) giving one strand break in a pBR322 DNA molecule after irradiation of monoenergetic X-rays at 12.40 and 13.55 keV.

X-ray energy (keV)	D ₀ (kGy)			
	Single-strand break		Double-strand break	
	T [‡]	BU [‡]	T	BU
12.40	7.6	8.0	200	266
13.55	7.0	7.7	276	220
(12.40/13.55)	1.09	1.04	0.72	1.21

[‡] T:Non-substituted DNA. BU:BU-substituted DNA.

INDUCTION OF CHROMOSOME ABERRATIONS IN HUMAN LYMPHOCYTES BY
SYNCHROTRON-PRODUCED MONOCHROMATIC X-RAYSMasao SASAKI¹, Yousuke EJIMA¹, Katsumi KOBAYASHI², Kotarou HIEDA³,
Hiroshi MAEZAWA⁴, Yoshiya FURUSAWA⁴, Takeshi YAMADA⁵ and Takashi ITO⁶¹Radiation Biology Center, Kyoto University, Sakyou-ku, Kyoto²Photon Factory, National Laboratory for High Energy Physics, Tsukuba-gun, Ibaraki³Faculty of Science, Rikkyo University, Toshima-ku, Tokyo⁴Tokai University Medical School, Isehara-shi, Kanagawa⁵National Institute of Radiological Sciences, Chiba-shi, Chiba⁶College of General Education, University of Tokyo, Meguro-ku, TokyoIntroduction

The formation of chromosome structural rearrangements have been closely linked to the expression of a variety of specific cellular injuries in cells exposed to ionizing radiations. In view of the formation of the generalized model of radiation action, the underlying mechanisms, particularly the microstructure of energy deposition and its involvement in the formation of chromosome structural rearrangements are particularly intriguing.

Monochromatic X-rays of sufficiently long wavelength generate photoelectrons having discrete initial energy and range. Recently, extensive studies have been made by Goodhead and his coworkers for the induction of mutations, chromosome aberrations and cell killing by aluminium and carbon K characteristic X-rays^{1,2}. Goodhead postulate an hypothesis called "threshold-energy repair-saturation model".

In this paper, we report the chromosomal response of human lymphocytes exposed *in vitro* to synchrotron produced monoenergetic X-rays. The efficiency and LET dependence of chromosome aberration formation were consistent with the pairwise interaction of sublesions produced with limited spatial proximity.

Experimental and Results

Monolayers of human peripheral blood lymphocytes were irradiated with the synchrotron-produced monochromatic X-rays with varying wavelengths, and the chromosome aberrations were studied in relation to the quality of radiations. For comparison, similar experiments were made with ⁶⁰Co γ -rays, and 50 kVp and 200 kVp orthovoltage X-rays.

The efficiency of chromosome aberration formation increased with increase of wavelength, which was represented by an increase of the α term when the dose-response relations were fitted to the linear-quadratic model, $Y=C+\alpha D+\beta D^2$. Figure 1 shows the LET dependence of the α term for dicentric formation (solid symbols). Data on chrome, aluminium and carbon K-characteristic X-rays in the literatures (open symbols) are also included for comparison. The efficiency first arises, subsequently falls and then arises again with a peak LET at around 2-3 keV/ μ m.

This unique LET dependence can not readily be explained by the recently proposed concept on radiation action, "threshold-energy repair-saturation model" of Goodhead (1980)³, but rather consistent with the idea that the

chromosome exchange aberrations, probably also mutation and cell inactivation which may have different target size and peak efficiency, arise as a consequence of pairwise interaction of two lesions, e.g., DNA double strand breaks, but the elemental chromatin fiber with 30-34 nm diameter, rather than DNA duplex itself, constitutes a unit of damage interaction in the formation of chromosome aberrations. The fall of the efficiency may be a consequence of a limited track segments as compared with the diameter of elemental fibers and their intranuclear geometry. The second raise may be the results of non-uniform distribution of dose to cell nucleus due to the strong attenuation during the pass through the cells. Our results thus raises a proposition that the relative biological effectiveness (RBE) should be considered separately for electrons and heavy charged particles as well as for the biological endpoints with different target size. We were now led to a new concept of the recombination-mediated damage fixation, which constitute a testable proposition for future experiments.

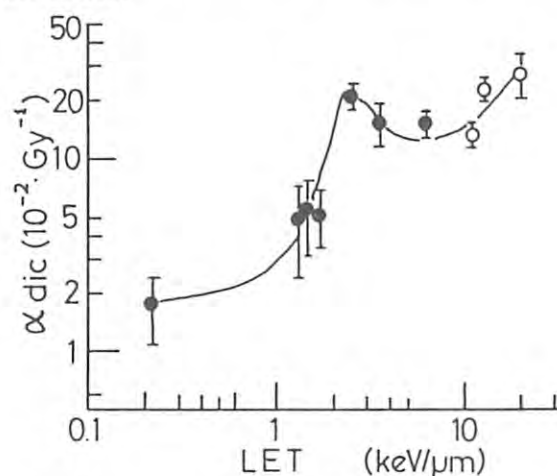


Figure 1. The linear component, α term, of the dose-response relationship for dicentric formation plotted against the LET. Open circles are data replotted from Virsik *et al.* (1980) on the chrome (Cr), aluminium (Al) and carbon (C) K-characteristic X-rays.

References

- 1) D.T. Goodhead and J. Thacker: *Int. J. Radiat. Biol.* 31 (1977) 541.
- 2) R. Cox, J. Thacker and D.T. Goodhead: *Int. J. Radiat. Biol.* 31 (1977) 561.
- 3) D.T. Goodhead: *Radiat. Res.* 91 (1982) 45.

SR MICRO BEAM X-RAY ANALYSIS

Y. Gohshi, S. Aoki*, A. Iida**, S. Hayakawa, K. Sakurai

Department of Industrial Chemistry, Faculty of Engineering, University of Tokyo, Hongo, Tokyo 113

*Institute of Applied Physics, University of Tsukuba, Sakura, Ibaraki 305,

**Photon Factory, National Laboratory for High Energy Physics, Oho-mach, Ibaraki 305

Introduction

A focused synchrotron radiation(SR) source is expected to realize X-ray analysis with spatial resolution¹. We developed a 10 keV scanning X-ray fluorescence(XRF) microprobe using Wolter type 1 optics as a focusing system². In this report, the performance of the optical system and the micro and trace XRF analysis are described.

Experimental

Experiments were performed on the BL-4A with a white SR. A schematic beam line layout is shown in Fig.1(a). Two Wolter type 1 mirror systems were used, and each system consisted of an ellipsoidal and a hyperboloidal mirror. Mirror surfaces were coated with Pt, and the average glancing angle was 7 mrad to reflect the X-rays up to 10 keV. The first optical system(condenser mirror system) was designed to demagnify the source 1/20, and the second optical system (focusing mirror system) was designed to demagnify the image 1/13. At the first focal plane(F1), a pinhole of 60 μm in diameter with 0.1 mm thick Ta was placed, which defined the final beam size.

A SR XRF microprobe consisted of the optical system, an energy dispersive XRF(EDXRF) system and a scanning system of samples(Fig. 1(b)). A micro and trace XRF analysis was realized under atmospheric condition.

Results and Discussion

The performance of the optical system was examined. The smallest beam size was obtained when the reflecting parts of the mirror were restricted by the slits before the condenser mirror system. The estimated beam size was 10 μm (V) * 30 μm (H). The difference between the observed size and the designed one(4.6 μm in diameter) was thought to be caused by the error in the mirror shape and the incomplete alignment of the optical system. The photon flux of the focused beam measured by an ionization chamber was much less than the designed value with the small beam size.

The minimum detection limit(MDL) was estimated by the measurement of a reference sample. For Mn, the MDL in relative concentration and in absolute amount was 6 ppm and about 0.1 pg respectively. Improvements in the optical system will increase the beam intensity and the signal. The background was mainly from the lower energy part of the incident X-rays, which will be reduced with the monochromatic excitation.

Cr patterns of 20 μm , 10 μm and 4 μm in width were measured and the pattern of 4 μm was quite recognizable (Fig. 2). The practical resolution of this microprobe was better than 10 μm .

Improvements in the optical system are now in progress.

References

- 1) C. J. Sparks: Synchrotron Radiation Research, eds. H. Winick and S. Doniach (Plenum, New York, 1980) chap.14.
- 2) Y. Gohshi, S. Aoki, A. Iida, S. Hayakawa, H. Yamaji and K. Sakurai, Japan. J. Appl. Phys. 26 (1987) L1260

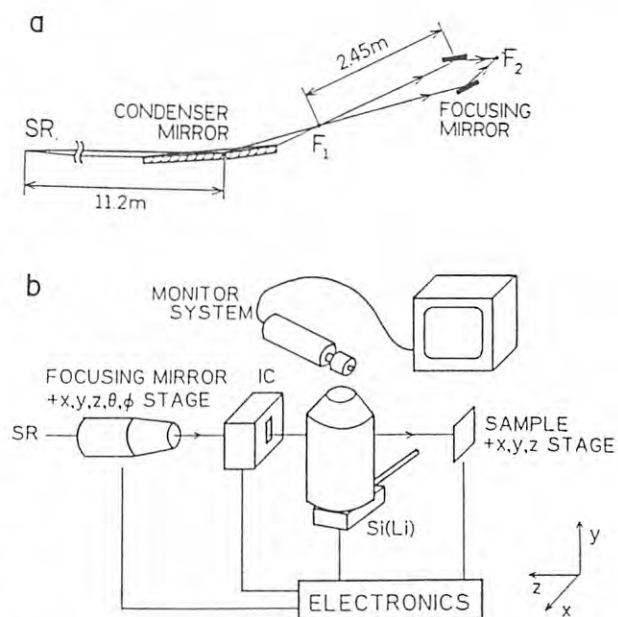


Fig. 1 a: A schematic beamline layout, and b: A schematic arrangement in the hutch.
IC : ionization chamber

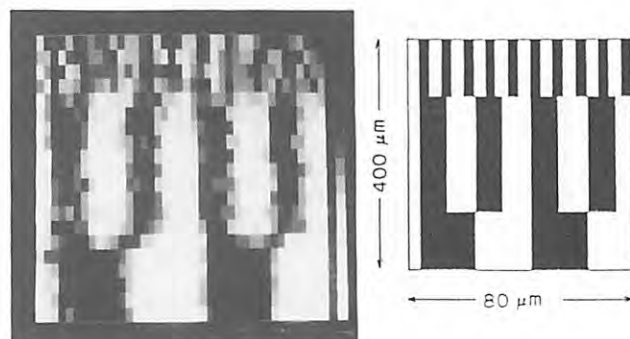


Fig. 2 Cr K α image of the Cr deposited patterns and the field examined. 40 * 20 points

DETERMINATION OF THE COMPOSITION OF MIXED CHEMICAL STATES
BY X-RAY FLUORESCENCE DETECTION
USING CHEMICAL SHIFT OF ABSORPTION EDGE

Kenji Sakurai, Atsuo Iida*, and Yohichi Gohshi

Department of Industrial Chemistry, Faculty of Engineering, University of Tokyo, Hongo, Tokyo 113

*Photon Factory, National Laboratory for High Energy Physics, Oho-machi, Tsukuba-gun, Ibaraki 305

Introduction

The selectively induced X-ray emission spectroscopy (SIXES) is the analytical technique based on the detection of the fluorescent X-rays due to the selective excitation of specific chemical species by tunable synchrotron radiation (SR). The present method, compared with the conventional transmission experiment, is particularly suitable for the measurement of trace elements of less than 10^{-10} g because of its high sensitivity.¹⁾ One of the most feasible application of SIXES is the determination of the concentration of specific chemical species in a mixture containing several chemical states.

Experimental

Mixed samples containing FeO and Fe₂O₃ with various ratio were prepared as pellets of ca. 150 mg/cm². Total concentration of iron in each pellet was 2.5 %. The experiment was carried out on the beam line 4A. The energy dispersive XRF system with a Si(Li) detector was used.²⁾ The horizontal axis was adopted for the channel cut crystal monochromator (Si 111). The energy resolution of incident X-rays was estimated to be 1.5 eV at the iron absorption edge (7.111 keV).

Results and Discussion

Absorption spectra of iron from the mixed powder samples of iron oxides are shown in Fig.1. The intensity of the Fe K α X-ray fluorescence is measured as a function of the incident energy. The absorption edge systematically shifts to higher energy as the concentration of Fe₂O₃ increases. Total concentration of iron is determined by the fluorescence intensity above edge, and the concentration of each chemical

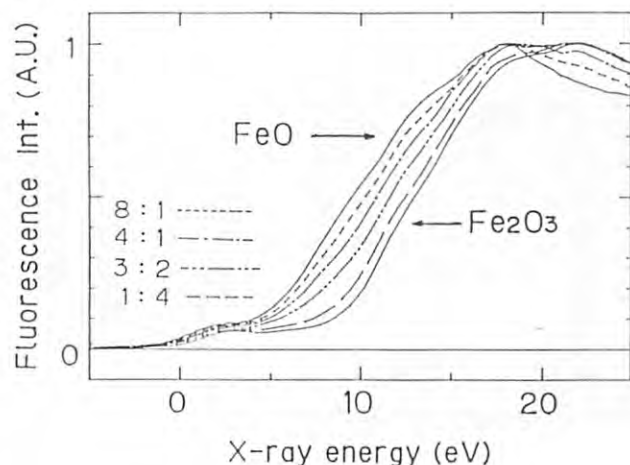


Fig.1 Near edge absorption spectrum of the mixture of iron oxides taken by SIXES.

species can be determined using the chemical shift of absorption edge.

Figure 2 shows the relationship between the chemical shift of the edge (i.e. the energy of the mid-point of the curve) and the concentration of iron(III). Calculated calibration curve is based on the experimental results of pure Fe₂O₃ and FeO. Determination of the mixed ratio of the unknown sample can be performed using the calibration curve in Fig.2, although it is not linear due to the difference in the shape of the curves for FeO and Fe₂O₃.

However, experimental results directly obtained from Fig.1 do not agree with the calculated calibration curve. It was found that this was due to the particle size effect of the X-ray fluorescence intensity. Since the particle size of Fe₂O₃ (< a few μ m) was smaller than that of FeO (a few tens of μ m) in our case, iron fluorescent X-rays from Fe₂O₃ is more intense than that from FeO provided that the same quantity of iron was contained. These data were, however, successfully corrected as shown in Fig.2 using the fluorescence intensity measured far above the absorption edge, where fluorescence intensity does not depend on chemical natures.

Precision of the present technique depends on the values of the chemical shifts, and error in the determination of the absorption edge mainly due to the counting statistics. Since the differences between the edge energy of FeO and Fe₂O₃ is about 3.5 eV, the mixed ratio of each chemical state in the mixture can be determined within ± 6 % error, assuming that the absorption edge is determined within ± 0.2 eV.

References

- 1) Photon Factory Activity Report 1986 137
- 2) A.Iida et al., Adv.in X-ray Anal. 28(1985)61

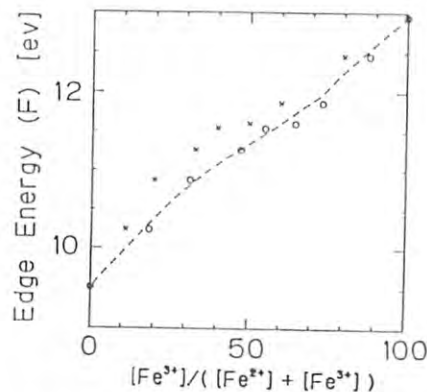


Fig.2 Quantitative analysis of the mixture of iron oxides. Energy of the absorption edge was defined as the mid-point of the normalized absorption curve. Calculated calibration curve is shown by the broken line. Open circles and crosses show the raw and corrected experimental results respectively.

CHEMICAL STATE IMAGING BY X-RAY FLUORESCENCE DETECTION USING CHEMICAL SHIFT OF ABSORPTION EDGE

Kenji Sakurai, Atsuo Iida*, Mamoru Takahashi, and Yohichi Gohshi

Department of Industrial Chemistry, Faculty of Engineering, University of Tokyo, Hongo, Tokyo 113
*Photon Factory, National Laboratory for High Energy Physics, Oho-machi, Tsukuba-gun, Ibaraki 305

Introduction

The fluorescent X-rays is abruptly emitted from the chemical species as the energy of the incident X-rays crosses the absorption edge of interest. Since the energy of absorption edges are affected by the chemical environment of the element, specific chemical species can be almost selectively excited by tuning the incident energy. In this report, determination of the spatial distribution of specific chemical species using the selectively induced X-ray emission spectroscopy (SIXES)¹⁾ is described. The present technique is decidedly superior to the absorption imaging technique²⁾ in the sensitivity.

Experimental

The experiment was carried out on the beam line 4A and 6B. The horizontal axis was adopted for the channel cut crystal monochromator (Si 111). The intensity of fluorescent X-rays was measured by a Si(Li) detector.

Results and Discussion

Near edge absorption spectra of iron oxides taken by X-ray fluorescence detection are shown in Fig.1. The absorption edge systematically shifts to higher energy as the oxidation number increases. While both FeO and Fe₂O₃ are excited at the higher energy (E_H), the intensity of the fluorescence signal from Fe₂O₃ is far lower than that from FeO at the lower energy (E_L).

The intensity distribution of Fe K α from the model sample, which contains both FeO and Fe₂O₃, were measured with 250 μ m x 500 μ m incident X-rays. Results obtained at the incident energy E_H and E_L are shown in Fig.2. By using the reference spectra shown in Fig.1, the spatial

distributions of FeO and Fe₂O₃ are determined independently, and are shown^{2,3)} in Fig.3. The results are in good agreement with the distribution confirmed by the optical microscope.

For the imaging of the chemical state by the present technique, not only the two dimensional scanning of the sample using a point shaped beam but also the tomographic approach using a line shaped beam³⁾ are promising. The latter approach is based on the the image reconstruction from the projection. Sample used was thin film of Cr and Cr₂O₃ on a glass. Preliminary measurement was made³⁾ with 8mm x 100 μ m incident X-rays, and Cr image obtained are shown in Fig.4.

References

- 1) K. Sakurai et al., submitted to Anal. Sci.
- 2) J. Kinney et al., Appl. Optics 25(1986)4583
- 3) N. Gurker: X-ray Spectrom. 8(1979)149

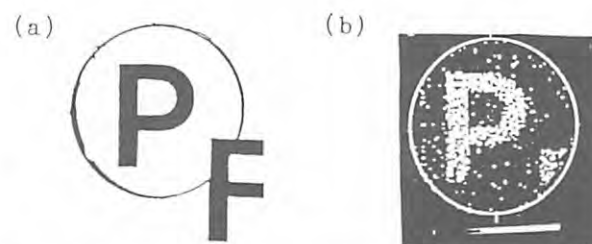


Fig.4 (a) Optical microscope image of the sample. Region measured is shown in circle. Cr was deposited drawing the letters of 'PF', and Cr₂O₃ was deposited around them. (b) Cr image processed by the image reconstruction technique.

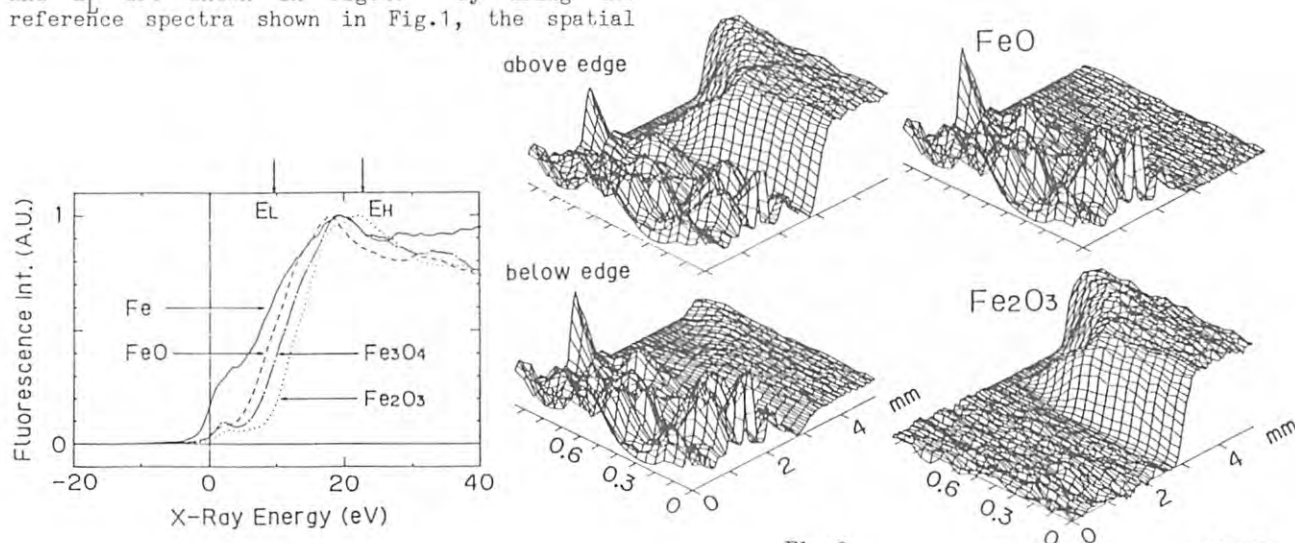


Fig.1 Near edge absorption spectra of iron oxides.

ANALYSIS OF MICRO CONSTITUENTS IN SEA WATER USING MONOCHROMATIZED X-RAYS FROM SYNCHROTRON RADIATION

Masafumi ISHIKAWA* and Atsuo IIDA**

* Division of Marine Radioecology, National Institute of Radiological Sciences, Isozaki 3609, Nakaminato-shi, Ibaraki-ken, 311-12, Japan

** KEK, National Laboratory for High Energy Physics, Oho-machi, Ibaraki-ken, 305, Japan

INTRODUCTION

The aim of this study is to represent the natural dynamics of the elemental quantity in sea water adjacent Japan. For this trace level multi-elemental analysis, synchrotron (1) monochromatized X-rays seemed to be effective. Experimental condition on the incident beam energy was the main focus in our previous paper. Since Na-DBDTC (2) replaced by APDC seemed to be advantageous, sea water samples were preconcentrated through this chelating process under the beam condition.

Elemental results will supply particular data, especially for locality problem, in which the basic concern of radioecology is to obtain detailed concentration factors of elements for the evaluation of radiation dose to men.

I. EXPERIMENTAL

1) Sampling, Preparation and Targeting

Sample sea waters were collected at Onagawa(off-shore), Miyagi, and at Nakaminato(coastal), Ibaraki, every month during the period from May 1986 to Aug. 1987.

After filtration by 0.45 μ m membrane filter, 1 liter of sea water was treated with Na-DBDTC(Sodium Di-benzyl Di-thio Carbamate), passed through a chromosorb column so as to adsorb chelates onto it, then eluted with organic solvent(CHCl_3 :EtOH=1:1) onto 2 μ m Makrofol backing. Finally, it was dried to a deposit on a ceramic hot plate at 60 $^{\circ}\text{C}$.

2) Layout, Bombardment and X-ray Analysis

As for the system installed in the BL-4A, reference, should be made to the report by Y. Gohshi (3). A monochromatized 20 keV beam of $1.0_3 \times 1.0$ mm² was introduced to the target under 10^{-3} torr for 2000 sec.

Peak identification was made manually, presenting three point standards on a calibration curve, and the peak area on the background was determined by a computer program EDAP2. The area was converted to into ppb concentration.

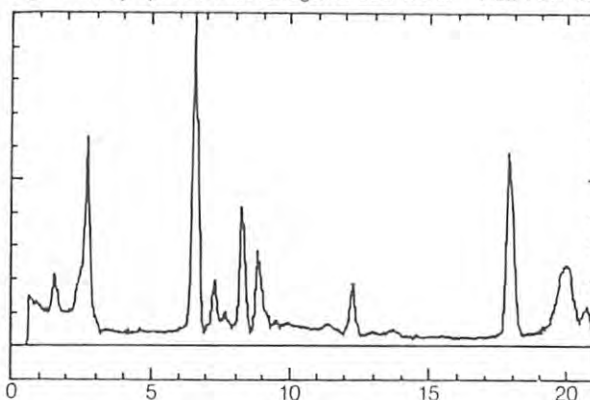
II. RESULTS AND DISCUSSION

According to the previous report (1) stating that SRXRF was particularly effective for sea water analysis, this method was applied to obtain the variation of elemental quality and quantity through the year.

Advantage of Na-DBDTC was compared with APDC(Ammonium Pyrrolidine Dithio Carbamate). Recovery of elements was reasonably similar for the two chelating reagents. However, the former was remarkably effective concerning the handling of sea water especially for the column separation with chromosorb and the final stage of the target preparation.

Because in the APDC method, several tens of mg of activated carbon are weighed into a plastic bottle after the HF treatment. This process is rather difficult in the actual handling of sea

Fig. 1 X-ray spectrum of Onagawa sea water FILE: SR138



water. Also the method requires a small amount of 2N-HNO_3 for the elution of elements from the activated carbon surface, and preparation of a small deposit onto a 2 μ m Makrofol film is again difficult.

From these points of view, Na-DBDTC method makes it possible to elute accumulated elements from chromosorb surface with organic solvent of MeOH and CHCl_3 (=1:1), and the solvent does not damage the Makrofol film, consequently it is easily evaporated from the film surface.

During the period from May 1986 to Aug. 1987, sea water samples were collected monthly at Onagawa, Miyagi, and at Nakaminato. Discussions on details of annual variation of elemental quantity for the two sampling stations are still underway. Characteristic X-ray spectrum from the Onagawa site is shown in Fig. 1. Sea water showed its elemental amount as follows; (unit in ppb)

elem.	S	K	Ca	Ti	V	Cr	Mn	Fe	Ni
conc.	1.9	60	87	1.9	2.2	1.6	1.4	58.3	5.3
Cu	Zn	As	Se	Br	Sr	Zr	Hg	Pb	U
11.2	11.6	0.6	0.8	18.6	1.8	1.6	0.01	0.02	0.02

Nearly 20 elements were determined sufficiently at the level of ppb. Compared to (1), the latter sea waters as previously reported, elemental quantities are relatively higher for the Nakaminato sea water. It may be due to the reason that the sample from Nakaminato contains many particulates, because it is a coastal water, although both water samples had been filtrated preliminarily through a membrane filter HA.

These data will supply effective information when the radiation dose to men is evaluated from the environmental radioisotopes.

REFERENCES

1. M. Ishikawa and A. Iida: PF Activity Report 1986
2. A. Prange and A. Knoechel: Analytica Chimica Acta, **172**, 79-100(1985)
3. Y. Goshi and A. Iida: PF Activity Report, 1982/1983

X-RAY FLUORESCENCE (XRF) ANALYSIS OF DIFFERENT PARTS OF A SINGLE STRAND OF HAIR

Takao SUZUKI*, Naoki SAITOH*, Yohchi GOHSHI**

*National Research Institute of Police Science

**Dept. of Industrial Chemistry, Faculty of Engineering, University of Tokyo

Introduction

A study of trace element in human hair is one of the useful means of investigating environmental influences, pathological histories, nutritive conditions of a human body and individual characteristics.

The experiment was conducted to analyse each part of a single hair from the root to its top by SR excited X-ray fluorescence.

Experiment

Hair samples of black hair and white hair were collected from two adult males and two adult females, were washed by the IAEA method with acetone and distilled water. Samples of single hair 10cm(male) and 15cm(female) cut 5cm pieces and each of them was set in a holder as shown in Fig.1. The monochromated SR beam irradiated an analysing part of a single strand of hair at 1mm in length. The analysing position of the hair was scanned by a holder moving system with 2.5μ step. X-ray fluorescence spectra were measured by Si(Li) detector. Measuring time was 500 seconds. Energy of SR was 16.5keV.

Results and Discussion

Detected elements were S, Ca, Ti, Cr, Ni, Zn, Hg, Pb, Br and Sr. Fig.2 represents the variation of trace elements S, Ca, Zn concentrations as a function of distance from the scalp.

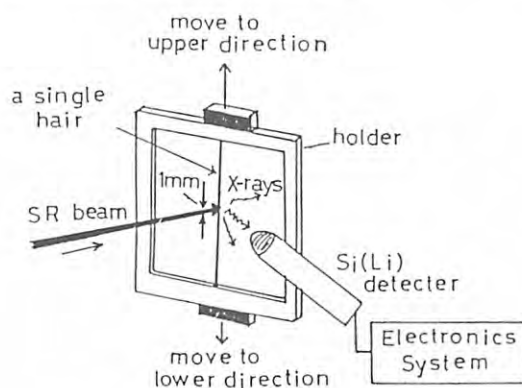


Fig.1 Schematic diagram of the experimental system.

Concentration of S seems to increase from a hair root to its top. A similar tendency was observed in Ca and Zn.

Concentration of Ca in white hairs was lower by 20% to 70% than that in black hairs of the same person.

In the case of female M.S., concentration of Ca in black hairs was by 1200ppm to 1700ppm in between 20mm and 80mm from the scalp. In her white hairs, by 800ppm to 1200ppm in the same range. Concentration of Zn in her black hairs was by 200ppm to 260ppm and in white hairs by 170ppm to 220ppm in the same range as in Ca.

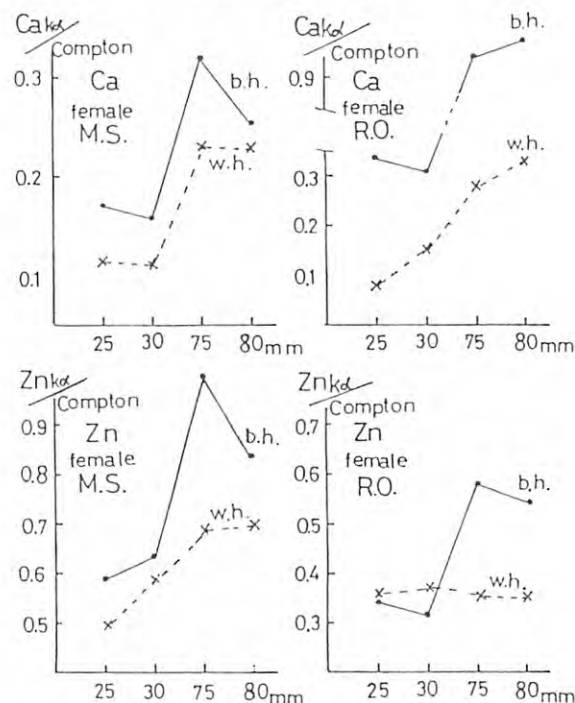
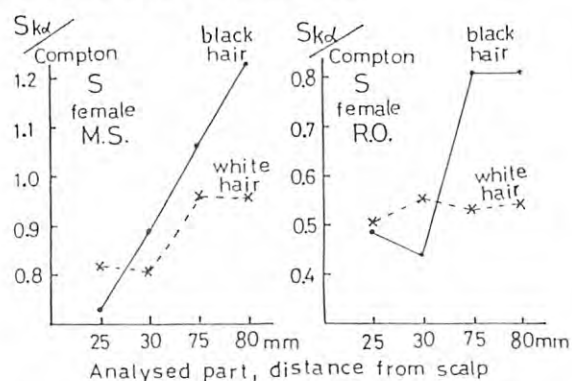


Fig.2 Variation of trace elements S, Ca, Zn concentration as function of distance from the scalp.

APPLICATION OF SYNCHROTRON RADIATION TO ARCHAEOLOGICAL OBJECTS (I) NONDESTRUCTIVE X-RAY FLUORESCENCE SPECTROSCOPIC IMAGING OF ARTISTIC PATTERNS

Izumi NAKAI, Akihiko MOCHIZUKI, Takuji KAWASHIMA, Shinjiro HAYAKAWA*, Yoichi GOSHI* and Atsuo IIDA**

* Department of Chemistry, The University of Tsukuba, Ibaraki 305

** Department of Industrial Chemistry, Faculty of Engineering, University of Tokyo, Hongo, Tokyo 113

Photon Factory, National Laboratory for High Energy Physics, Oho-machi, Ibaraki 305

Introduction

X-ray Fluorescence (XRF) technique has been widely used in the chemical analysis of ancient artifacts, because the method enable us to carry out a nondestructive rapid multielemental analysis of the samples. It is expected that application of SR X-ray to the XRF analysis will greatly improve its analytical ability because of the high brightness, polarization, and wavelength tunability of the SR X-ray. Besides, there is a hidden advantage of the utilization of SR: i.e. the SR facility provides spatial freedom, which allows truly nondestructive analysis of large artifacts such as sculptures, paintings etc. This is owing to the following advantages of the SR: the light source is far away from the samples and the SR beam is a highly collimated parallel beam. Therefore, it is expected that the SR becomes an ideal light source for XRF analysis of archaeological objects. Taking these advantages, we have started the following research programs in order to establish the experimental procedures of archaeometric analysis and to apply the technique to the practical problems in archaeology.

1) Two dimensional chemical imaging of artistic pattern This technique is used for the transformation of artistic pattern into two dimensional chemical compositional image. The technique is particularly useful when the pattern is complicated or very small.

2) Multielemental bulk analysis for provenance investigation Capability of rapid and non-destructive multielemental analysis allows to investigate a large number of samples, which are necessary for provenance investigation and documentation of ancient trade routes. Highly polarized and energy-tunable radiation allow to analyze a trace amount of desired element, which can be a fingerprint element for the above purposes.

3) Chemical speciation of colorant element of archaeological objects by measuring chemical shift of X-ray absorption edge by detection of XRF Knowledge of the oxidation state of coloring elements in pigments, glaze etc. will provide useful information on the technology of the production of artifacts such as firing temperature of potteries or origin of raw materials. This paper reports a preliminary result of the research project (1) and that of the project (2) is presented in the succeeding page. Project (3) is currently underway.

Experimental

The measurement were carried out at BL-4A using the XRF-analysis facilities. Samples were excited by monochromated X-ray at either 8 keV or 20 keV using Si(111) channel cut crystal. The analysis was made by energy dispersive mode using a Si(Li) detector. Because of the small divergence of the SR beam, a fine parallel beam of desirable size was obtained by a simple set of vertical and horizontal slits. During the two dimensional analysis the sample was placed on a

remote controlled X-Y stage with pulse motors (ca. 2.5 u/pulse) and the analyzed point was monitored with a TV camera. The intensity data were stored in a PC9801 personal computer.

Results and Discussion

Figure 1 shows photographs of the samples used in the present study: (a) a china dish made at "Kutani", a famous Japanese pottery producing district; (b) a fragment of enamel glassware (10 - 14c) excavated at a site of Egypt.

The intensity data were processed with the personal computer into two dimensional image on a color display. Figure 2 show the examples of the images. The intensity were scaled with 9 colors depending on the magnitude. The Fe K α image in Fig. 2a corresponds well with the Chinese characters "Kutani" painted with red color on the backside of the dish indicating that the colorant is Fe₂O₃, i.e. Indian red.

On the other hand, Fig. 2b and 2c are Pb L α image and Au L α image of the enamel glass, respectively. The line-drawing on the glass (inside the mark on Fig. 1b) corresponds to the Pb indicating the use of lead glass. Figure 2c shows that the surface of the glass is decorated with gold. Consequently, a one-to-one correspondence between artistic design and their chemical composition provides useful information for understanding the decoration technique of glass during the Middle Ages in Egypt. A further analysis is now in progress.

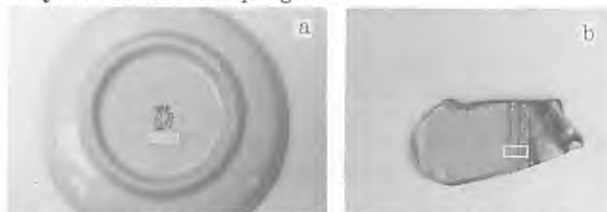


Fig. 1. Samples used in the chemical imaging.
(a) china dish (b) enamel glass

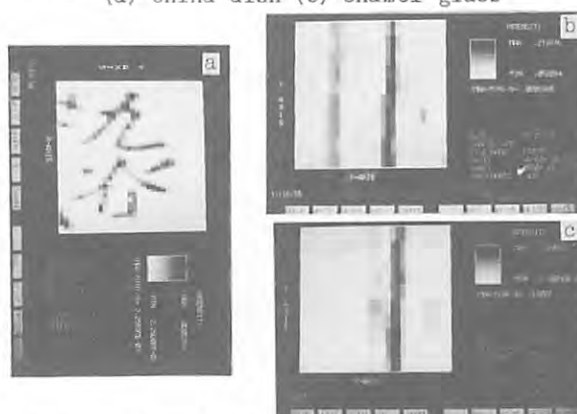


Fig. 2. Results of the chemical imaging.
(a) Fe K α image of the sample (a).
(b) Pb L α image of the sample (b).
(c) Au L α image of the sample (b).

APPLICATION OF SYNCHROTRON RADIATION TO ARCHAEOLOGICAL OBJECTS (II)
— SR X-ray Fluorescence Analysis of Ancient Artifacts of Glass and Glaze —

Akihiko MOCHIZUKI, Izumi NAKAI, Takuji KAWASHIMA, Shinjiro HAYAKAWA*, Yohichi GOHSHI*
and Atsuo IIDA**

Department of Chemistry, The University of Tsukuba, Ibaraki 305

*Department of Industrial Chemistry, Faculty of Engineering, University of Tokyo, Hongo, Tokyo 113
**Photon Factory, National Laboratory for High Energy Physics, Oho-machi, Ibaraki 305

Introduction

A wide selection of methods of chemical analysis have been employed for archaeological objects and works of art. The artifacts of ancient glass and glaze have been studied by X-ray fluorescence analysis, emission spectrography, neutron activation analysis and so on. The colorant of ancient glass and glaze have been studied, but there have been a little information as to their origins, trading routes, distributions, etc. Since SRXRF analysis is a nondestructive method and superior to the above methods in some respects, this method is excellent for obtaining these information.

In this paper, we attempted the application of SRXRF analysis to ancient glass and glaze artifacts excavated in Egypt and Japan.

Experimental

Measurements were made using the energy dispersive XRF system installed at BL-4A in Photon Factory. Samples were set on a sample holder and were excited by monochromated X-ray with a Si(111) crystal at 20.0keV in air. X-ray fluorescence spectra were measured by a Si(Li) detector.

Samples used were as follows.

1. Group A: Samples excavated at a site of Egypt. The samples were produced between ca.10c. and 14c. Eighty samples (134 analyzed points) were composed of glass wares, glass beads, glass bracelets, glaze of potteries and so on.

2. Group B: Samples excavated in the sites of Okayama Prefecture, Japan. Forty four samples (58 analyzed points) were glaze of potteries, which were produced in Japan or imported from China, etc. between the period of ancient burial mound and the Edo period (ca.6c.~18c.).

Results

About 52 percent of the samples of Group A and 20 percent of Group B show strong spectra of lead and belong to the category of lead glass and glaze. The other samples are alkali-lime glass or glaze.

The relationship between the colors of measured samples and their colorants are given in Table 1. The color of glass or glaze is blue in the presence of copper, but it grows green with the increase of lead concentration. Copper detected in the samples tinted with red is probably univalent. Colorless or pale green samples contain a little iron and/or a large amount of manganese which acts as a decolorant of the green color of iron. The strong characteristic line assigned to gold ($AuL\alpha$) explains the golden color of the samples which are known as "luster".

The representative XRF patterns of alkali-lime glass or glaze are shown in Fig. 1. Classification of the samples of alkali-lime glass and glaze based on the Zr/Rb-Sr/Rb ratios is given in Fig. 2. It is difficult to classify the lead glass and glaze based on the similar systematics

because the peaks of rubidium, strontium and zirconium were hidden by the peaks of lead. Most samples are classified into two types I and II which correspond to Group A and Group B, respectively. Six samples of Group A do not fall in either type and are classified into three types III, IV and V. These samples seem to be imported from other districts. But this is uncertain because of the shortage of number of the samples analyzed and lack of the analytical data of the similar samples excavated in the origins.

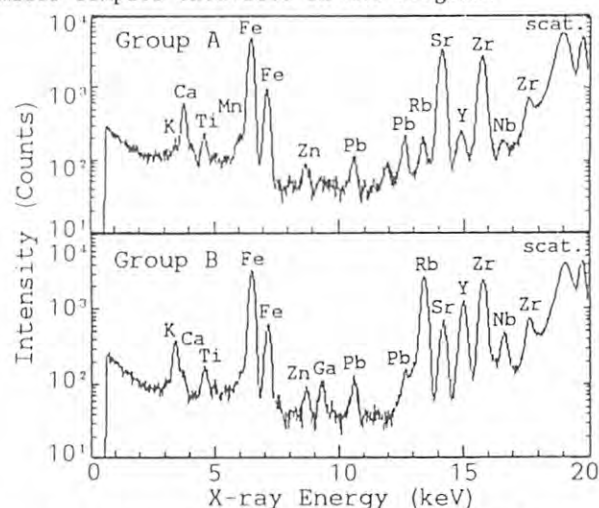


Fig. 1 Representative X-ray spectra of alkali-lime glass or glaze.

Table 1 The relationship between the colors of measured samples and their colorants.

color	colorant	color	colorant
green	Fe, Pb+Cu	black	Fe(+Mn)
red	Cu	deep blue	Co
blue	Cu	gold	Au
violet	Mn	brown	Fe
yellow	Fe, Ti?	colorless	Fe+Mn, nothing

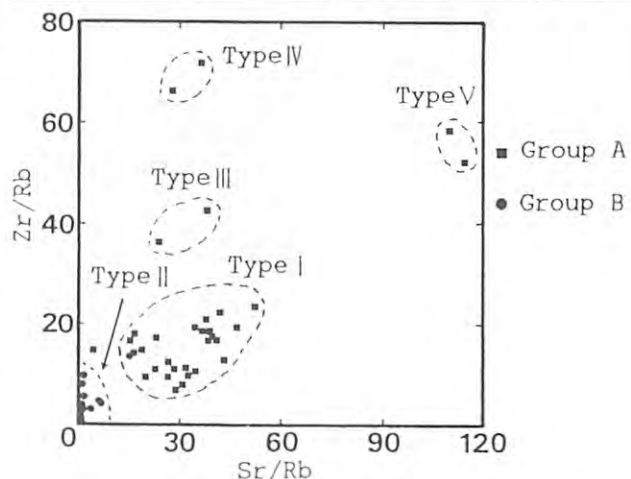


Fig. 2 Classification of the samples of alkali-lime glass and glaze based on Zr/Rb-Sr/Rb ratios.

NEAR SURFACE ANALYSIS OF GaAlAs USING GRAZING INCIDENCE X-RAY FLUORESCENCE

Atuso IIDA, Kenji SAKURAI and Yohichi GOHSHI

Photon Factory, National Laboratory for High Energy Physics, Oho-machi, Tsukubagun, Ibaraki 305
 Department of Industrial Chemistry, University of Tokyo, Hongo, Tokyo 113

INTRODUCTION

Grazing incidence X-ray fluorescence analysis is a useful technique for the analysis of the thin film and the surface of the material. The trace impurity near the semiconductor surface and the liquid-air interface of the polymer solution were successfully analyzed¹⁻³⁾. X-ray fluorescence analysis is also useful for the determination of major and minor elements with precision. In this report, the surface elemental composition of a GaAlAs epilayer was studied using the grazing incident X-ray fluorescence.

Experimental

The experiments were carried out at BL-4A. Fig. 1 shows the side view of the experimental arrangement. The energy of the monochromated synchrotron X-rays was fixed at 13 keV, which is high enough to excite Ga K and As K lines. The sample was mounted on a goniometer with a horizontal rotation axis. The X-ray fluorescence intensities were measured by a Si(Li) detector as a function of the glancing angle. The Si(Li) detector was set at the right angle to the incident beam with a slight inclination to the horizontal plane. Due to the poor energy resolution of the Si(Li) detector, Ga $K\beta$ and As $K\alpha$ lines overlap each other.

A $\text{Ga}_{1-x}\text{Al}_x\text{As}$ epilayer ($x=0.298$) was used for the sample. The epitaxial layer of 3.5 μm thick was grown on the GaAs wafer by the liquid phase epitaxy using the sliding boat technique. A mirror polished GaAs wafer was also used for the reference sample.

Results and discussion

Fig. 2 (a), (b) shows the intensities of the reflected X-rays and the ratio of the X-ray fluorescence signals ($\text{As } K\alpha + \text{Ga } K\beta$)/ $\text{Ga } K\alpha$ from the GaAs wafer and GaAlAs epilayer respectively. Since the surface of the epitaxial wafer shows the "waves" pattern, the reflection curve of Fig. 2(b) is rather broad compared to that of Fig. 2(a). While the intensity ratio obtained from the GaAs wafer

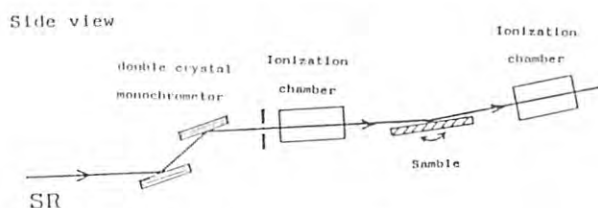


Fig.1 Experimental arrangement.

in Fig. 2(a) is constant and shows no angular dependence, that in Fig. 2(b) decreases at the lower angle. The comparison between the observed Ga K and As K intensities showed that the variation in the ratio in Fig. 2(b) was not due to the enhancement of the Ga concentration but was mainly due to the reduction of the As concentration. Since the penetration depth of the incident X-rays is less than a hundred Å in the angular range below the critical angle, the concentration of As atoms is reduced near the surface. Quantitative analysis shows that the As exhausted region is about 100 Å. The sublimation of the As atoms seems to occur during the cooling process after the epitaxial growth at 800°C.

The variation in stoichiometry at the surface of the compound semiconductor has been studied mainly by ion channeling and secondary ion mass spectrometry, but the present method has possibility of quantitative analysis of surface stoichiometry nondestructively.

References

- 1) A. Iida et al. : Nucl. Instr. and Methods, A246(1986)736
- 2) J. M. Bloch et al. : Phys. Rev. Lett. 54(1985)1039
- 3) A. Iida et al. : Photon Factory Activity Report #4(1987)140

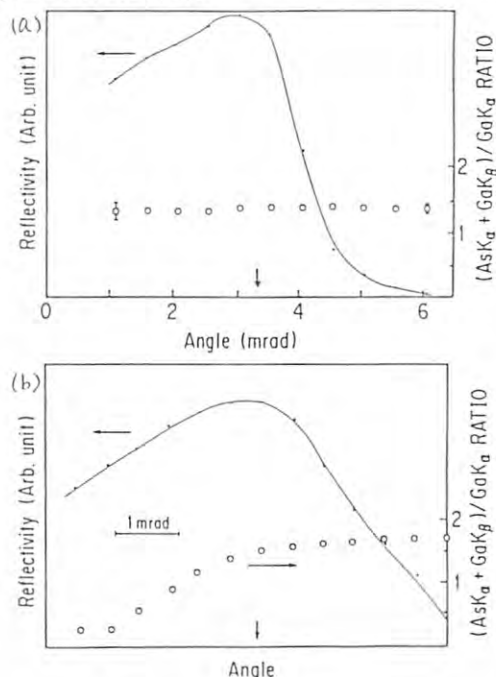


Fig.2 The angular dependence of the ratio of the X-ray fluorescence intensities and the reflectivity from the GaAs wafer (a) and GaAlAs epilayer (b).

GRAZING INCIDENCE X-RAY FLUORESCENCE ANALYSIS OF LAYERED STRUCTURE

Atsuo IIDA, Hideki HASHIMOTO

Photon Factory, National Laboratory for High Energy Physics, Ohomachi, Tsukubagun, Ibaraki 305
Toray Research Center, Sonoyama, Ohtsu, Shiga 520

Introduction

X-ray fluorescence analysis under the grazing incidence condition is useful for both the highly sensitive analysis of the solution sample¹⁾ and the near-surface depth profiling²⁾. To make quantitative analysis, however, there is a difficulty in the evaluation of the fluorescence intensity when the sample has the layered structure. Since an interference between the incident and reflected X-rays occurs in the thin film as well as above the substrate, it modifies the electric field resulting in the intensity modulation of the emitted X-rays.

In this report, the interference effect on the X-ray fluorescence intensity is demonstrated.

Experimental

The beam line 4A was used. The SR beam was monochromated by a double crystal monochromator. The sample was mounted on a goniometer with a horizontal rotation axis. The intensity of the reflected beam and the X-ray fluorescence signal were measured as a function of the glancing angle by an ionization chamber and by a Si(Li) detector respectively. Experimental details are described elsewhere³⁾. Samples used were a Si wafer covered with a 1.2 μm thick resist polymer and a layered structure with 34 Å of Ni, 843 Å of C and 111 Å of Fe on a Si wafer.

Results and Discussion

Fig. 1 shows the reflected intensity from the polymer sample as a function of the glancing angle. Below the critical angle of the polymer (2.15 mrad for 9.6 keV incident X-rays), the incident X-rays reflected almost totally at the polymer surface. As the glancing angle increases, the incident beam reaches the substrate of Si wafer and is totally reflected. Since the critical angle of the Si is 3.2 mrad, the interference between the incident and the reflected X-rays occurs between these two critical angles resulting in the intensity modulation. For the thick overlayer, however, the period of the modulation is smaller than the angular resolution of the present optics, only the hump in the reflection curve is observed.

To analyze the interference phenomenon quantitatively, the layered structure was measured. Fig. 2 shows the Ni and Fe fluorescence intensities as a function of the glancing angle. At the low angle, only the Ni layer was excited because the incident X-rays were totally reflected at the surface. After the incident X-rays penetrate deeply into the C layer, the Fe layer was also excited and the

standing wave is formed in the C layer resulting in the intensity modulation. The angle region, where the interference occurs, is between the critical angles of C and Fe (3.4 mrad and 6.0 mrad for 9 keV X-rays respectively). The calculated result is in good agreement with Fig. 2, which shows the direct evidence of the interference phenomenon in the layered structure. Detailed analysis shows that it is possible to analyze the thickness and the mass of each layer by analyzing the period and the phase of the X-ray fluorescence intensity modulation.

The authors would like to thank Mr. A. Mikuni for the fabrication of the sample.

References

- 1) A. Iida et al., Anal. Chem. 58(1986)394
- 2) A. Iida et al., Nucl. Instr. and Methods A246(1986)736
- 3) A. Iida et al., This Activity Report

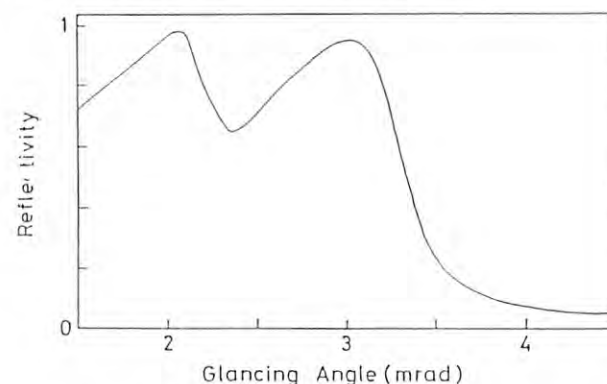


Fig. 1. The angular dependence of the reflected intensity from the Si wafer covered with the resist polymer.

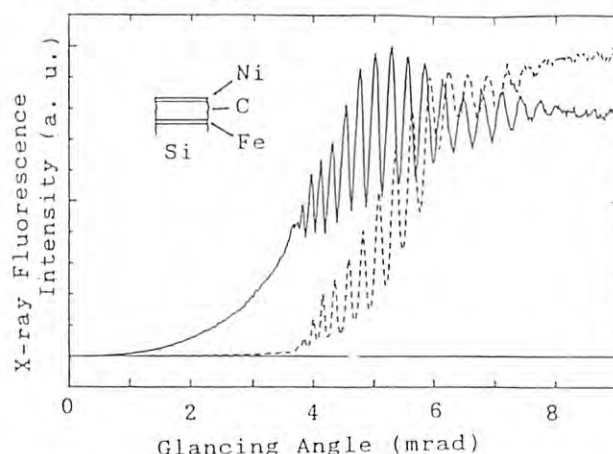


Fig. 2. The angular dependence of the fluorescence intensities from the Ni/C/Fe film on the Si wafer. Ni K (solid line) and Fe K (dotted line)

Photoacoustic Extended X-ray Absorption Fine Structure(PA-EXAFS)

Tsutomu Masujima¹, Hiroshi Kawata², Mikio Kataoka³, Masaharu Nomura², Katsumi Kobayashi²,
Masaharu Hoshi⁴, Chieko Nagoshi⁵, Shuzo Uehara⁶, Takayuki Sano⁷, Hisanobu Yoshida¹,
Sachiko Sakura⁸, Hideo Imai⁸, and Masami Ando²

1.Inst. Pharmaceutical Sci., Hiroshima Univ. School of Medicine, Kasumi, Hiroshima 734

2.KEK, National Laboratory for High Energy Physics, Oho-machi, Ibaraki 305

3.Dep. of Physics, Faculty of Sci., Tohoku Univ., Sendai, Miyagi 980

4.Research Inst. for Nuclear Medicine and Biology, Hiroshima Univ., Kasumi, Hiroshima 734

5.Inst. for Nuclear Study, Univ. of Tokyo, Tanashi, Tokyo 188

6.Lab. of Physics, School of Health Sci., Kyushu Univ., Maidashi, Higashiku, Fukuoka 812

7.Faculty of Sci., Hiroshima Univ., Higashi-senda, Hiroshima 730

8.Faculty of Pharmaceutical Sci., Fukuyama Univ., Higashimura-cho, Fukuyama 729-02

Introduction

The heat generation by monochromatic X-ray irradiation was detected by photoacoustic method using the synchrotron radiation at PF¹⁾ and the K-edge absorption was also found in the spectra.²⁾ Recently, the fine structure at K-edge region which is well known as extended X-ray absorption fine structure(EXAFS) was also found in the photoacoustic X-ray absorption spectra.

Experimental

The monochromatic X-ray was obtained by silicon (111) channel cut double crystal monochromator using white X-ray at Beam Line 4A. The photoacoustic cell was detailed elsewhere.¹⁾ The ion chambers were set to the both side of the photoacoustic cell just like sandwich, in order to compare the spectrum by photoacoustic X-ray absorption spectroscopy(PAXAS) and usual absorption spectrum, simultaneously. The chopper at chopping frequency at 10 Hz was set at the up-stream of these detectors. Copper foil (5 μ m thick) was used as a sample.

Results and Discussion

Figure 1 is the PAXAS spectrum and the absorption spectrum of the Cu sample. Quite corresponding fine structure shows that the information of EXAFS is also reflected in the PAXAS spectrum, in other word, the heat production process also includes the EXAFS. The only difference is the monotonous increasing trend of PAXAS signal intensity along with the photon energy increase. This is also seen in the previous rough PAXAS spectrum and seems to be concluded that the amount of heat depends also on the absolute photon energy. The more the photon energy is, the higher the PAXAS signal is. Figure 2 shows the Fourier transform of these data. Face center cubic lattice gives the nearest neighbor atomic distance of 2.6 Å and the second nearest neighbor atomic distance of 3.6 Å and the peaks were seen in these region. The shoulder around 5 Å seems to be the effect of included noise. The

ratio of the structure amplitude to the K-edge absorption amplitude is smaller for PA-EXAFS than for absorption spectrum. This should be due to the fact that the heat generation process includes some multi-processes which can be converted to the heat. Photoacoustic method can be applied any types of shapes and states of the samples and also to non-destructive depth-profiling. Thus this finding expands the methodology of EXAFS much wider than before. Now, various samples are under the study.

Acknowledgement The authors are grateful to Dr. A. Iida(PF) for his kind help in the use of BL4A.

References

- 1)T.Masujima, H.Kawata,et al., PF Activity Report, 4,314(1986) & Chem. Lett., 1987,973.
- 2)T.Masujima, M.Hoshi, et al., PF Activity Report, 4,315(1986).

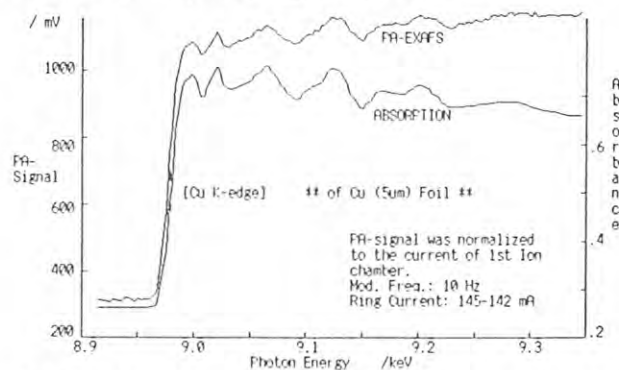


Figure 1. Photoacoustic EXAFS spectrum and absorption spectrum of copper foil.

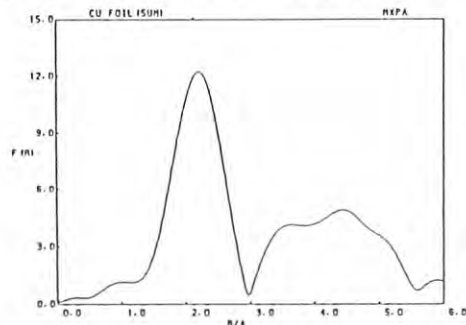


Figure 2. Fourier transform of $k\chi(k)$ of Cu foil.

Depth-Profiling by Phase Analysis of Photoacoustic X-ray Absorption Spectroscopy

Tsutomu Masujima¹, Hideaki Shiwaku¹, Hisanobu Yoshida¹, Hideo Imai², Mikio Kataoka³,
Masaharu Hoshi⁴, Takayuki Sano⁵, Tetsuya Ikeda⁶, Hiroshi Makihara⁶,
Hiroshi Kawata⁷, Yoshiyuki Amemiya⁷, Katsumi Kobayashi⁷ and Masami Ando⁷

- 1.Inst. Pharmaceutical Sci., Hiroshima Univ. School of Medicine, Kasumi, Hiroshima 734
- 2.Faculty of Pharmaceutical Sciences, Fukuyama Univ., Higashi-muracho, Fukuyama 729-02
- 3.Dept. of Physics, Faculty of Sci., Tohoku Univ., Sendai, Miyagi 980
- 4.Research Inst. for Nuclear Medicine and Biology, Hiroshima Univ. Kasumi, Hiroshima 734
- 5.Faculty of Science, Hiroshima Univ., Higashi-senda, Hiroshima 730
- 6.Mitsubishi Heavy Ind. Ltd., Technical Head Quarters, Hiroshima Technical Inst.,
Kan-on-shinmachi, Hiroshima 733
- 7.KEK, National Laboratory for High Energy Physics, Oho-machi, Ibaraki 305

Introduction

One of the unique application of photoacoustic spectroscopy is depth-profiling. The heat which was generated by the X-ray absorption under the surface, propagates to the surface. The time which was needed for propagation can be detected as the phase-lag. Phase analysis together with the intensity can reveal the subsurface structure without destructive treatment of samples. X-ray edge absorption is quite suitable for this purpose¹⁾ because of the specificity and discontinuity of absorption profile.

Experimental

Ni-plated Cu foil (10 μm thick) was used as a model sample. The setting of apparatus is the same as that of photoacoustic EXAFS¹⁾. The experiments were performed at white X-ray Beam Line 4A. The calibration of phase-lag using Ni foils of various thickness was studied by separate experiment. One side of a Ni foil which was painted in black was glued on the glass plate (1mm thick) by optically transparent epoxy resin. From the bottom of the glass plate, He-Ne laser beam was irradiated in order to generate the heat wave at the bottom of the attached Ni foil. The heat propagate onto the surface and contribute to the photoacoustic signal with certain phase-lag (at 27.6 Hz) which depend on the thickness of the foils.

Results and Discussion

Figure 1 shows the calibration curve of phase-lag for the Ni foils of various thickness. This result suggests the capability to estimate the thickness of plated materials on the metal. Figure 2 shows the PAXAS spectrum of Ni-plated Cu. In the photoacoustic amplitude spectrum, EXAFS of Cu at the subsurface of sample was still detected clearly. This means that PAXAS method can be applied even for the EXAFS analysis of subsurface materials. The phase spectrum shows sudden change at the K-edge points of Ni and Cu. The phase-lag when the heat was generated mainly at Cu area at subsurface, shows lower shift. According

to Fig. 2, the phase-lag is 4.6 ± 1 degree at 10 Hz. This value is converted to 7.6 ± 1.7 degree at 27.6 Hz which is equal to be 0.5-2 μm of Ni-plate. This value was consistent with the data of 0.65 μm of Ni-plate layer which was estimated by the weight analysis.

More general method is under the development.

Reference

- 1) T.Masujima, H.Kawata, M.Kataoka, M.Nomura, K.Kobayashi, M.Hoshi, C.Nagoshi, S.Uehara, T.Sano, H.Yoshida, S.Sakura, H.Imai, and M.Ando, Photon Factory Activity Report, 5(1987) in press.

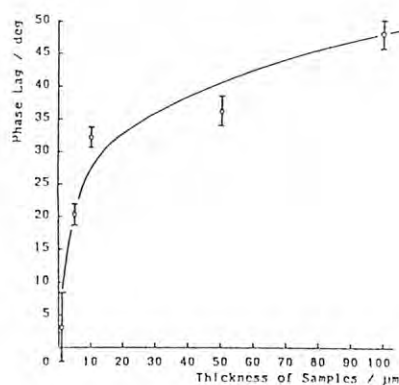


Figure 1. The dependence of phase-lag on the thickness of Ni foil. (chopping freq. 27.6 Hz)

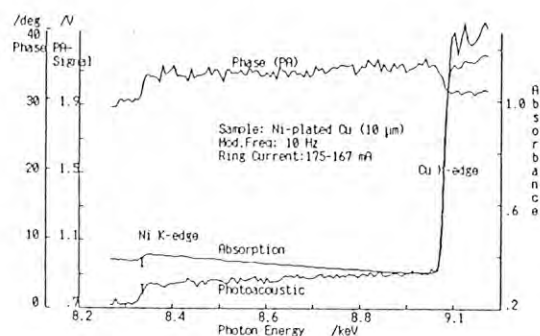


Figure 2. The photoacoustic X-ray absorption spectrum of Ni-plated Cu foil. (10 μm thick; chopping freq. 10 Hz)

FUNDAMENTAL CHARACTERISTICS OF NEW POWDER DIFFRACTMETER

Ryosei UNO, Haruo OZAWA, Takamitsu YAMANAKA⁺, Kazumasa OHSUMI⁺⁺ and Akihiko NUKUI⁺⁺⁺

College of Humanities and Sciences, Nihon University, Setagaya, Tokyo 156

+ College of General Education, Osaka University, Toyonaka, Osaka 560

++ Photon Factory, National Laboratory for High Energy Physics, Tsukuba-gun, Ibaraki 305

+++ National Institute for Research in Inorganic Materials, Niihari-gun, Ibaraki 305

Introduction

In this January, a newly designed powder diffractometer for the Photon Factory (PFPD) was constructed. The PFPD is characterized by the easiness of the alignment for the incident beam and the change of the wavelength, and the high accuracy of the goniometer. In this report, the basic specification is described.

Experimentals

The PFPD system is shown in Fig. 1. The X-ray path around the monochromator, the monitor and the sample holder is evacuated to about 10 Pa. The energy dispersive X-ray diffractometry can be readily carried out by the displacement of the monochromator.

A special slit system is prepared to align the optical axis through the monochromator and the goniometer with the SOR beam, within the error of 6×10^{-6} rad. The origin of 2θ was determined within the error of $\pm 10^{-3}$ deg.

The monochromator is a Si(111) monolithic one with fixed exit beam position¹⁾. However, it was founded that the exit beam shifted by about 200 μm in the range of the wavelength from 1.0 to 2.5 Å. The resolution of the encoder attached directly to the axis is 0.001° . The wavelength was determined from the absorption edge of Cu or the high angle diffraction lines of NBS standard Si powder. The accuracy estimated was about 10^{-5} by the scattering angle and about 10^{-6} from the diffraction.

We have used the scattered X-ray from an Al foil for monitoring. We obtained a good result that the integrated intensity of Si(111) was independent of the width of the incident beam, within 1 %.

θ and 2θ of the goniometer are measured by rotatory encoders attached directly to the axis. Their resolution is 0.0005° . A powder specimen can be spun at about 1 rev/s. The goniometer

covers the angle range from -40° to 150° for 2θ and from -10° to 190° for θ .

Results

The results for Si(111) at several wavelengths are shown in Table. The peak intensity was several tenths higher than those obtained by Parrish²⁾ at the 0.2 mm incident slit. The diffraction profile normalized by the monitor intensity is shown in Fig. 2 with a fitted pseudo-Voigt function. We found that the fraction of the Gaussian increased with the slit width at a fixed wavelength.

Discussion

The accuracy of the goniometer was higher than expected. It is useful for experiments taking advantage of the anomalous dispersion and high resolution measurements.

References

- 1) P. Spieker, M. Ando and N. Kamiya: Nuclear Instr. Method Phys. Res. 222(1984) 196.
- 2) W. Parrish and M. Hart: Transactions Am. Cryst. Assoc. 21(1985) 51.

Table

λ (Å)	current (mA)	I_p ¹⁾ cps	I_m ²⁾ cps	2θ (°)	FWHM (°)	I^3
1.48858	165	5000	2500	27.465	0.0537	0.1196
1.29869	195	11800	3600	23.894	0.0597	0.2285
0.95405	230	13100	1400	17.488	0.0637	0.6732

- 1) the intensity of the line at the peak.
- 2) the intensity of monitor at the peak.
- 3) the integrated intensity normalized by the monitor intensity.

condition of measurement :

R.S. = 0.2 mm, Soller slit = 2° .

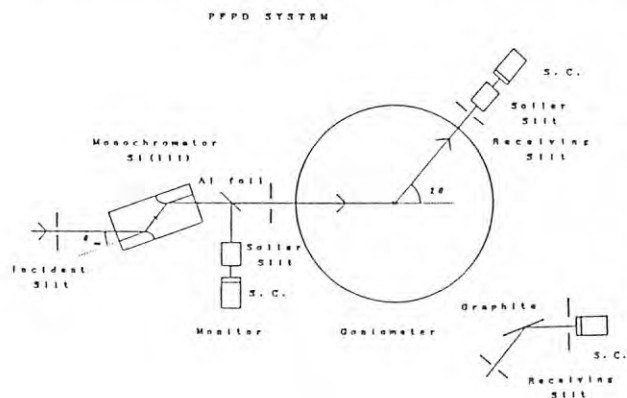


Fig. 1

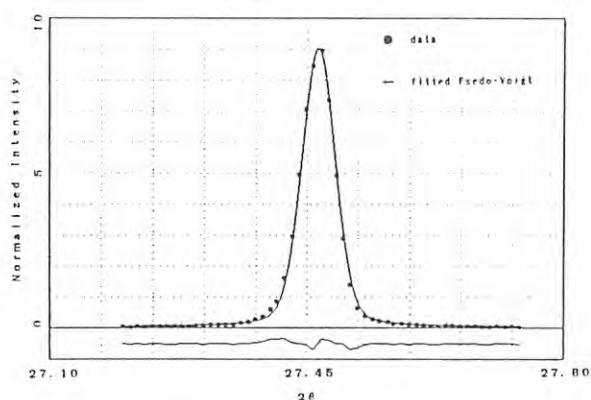


Fig. 2 $\lambda = 1.48858\text{Å}$ $R_{wp} = 2.8\%$

X-ray powder diffraction study of the High-Tc superconductors

Izumi NAKAI, Katsuhiro IMAI, Takuji KAWASHIMA, Takamitsu YAMANAKA[†],
Ryousei UNO[‡], and Kazumasa OHSUMI[§]

[†] Department of Chemistry, The University of Tsukuba, Ibaraki 305

[‡] College of General Education, Osaka University, Toyonaka, Osaka 560

[§] College of Humanities and Science, Nihon University, Setagaya, Tokyo 156

[§] KEK, National Laboratory for High Energy Physics, Ibaraki 305

Introduction

The high Tc superconductor $\text{Ba}_2\text{YCu}_3\text{O}_{7-y}$ shows a reversible orthorhombic-tetragonal transition with temperature. A large number of studies indicate that the phase transition is related to the appearance of superconductivity. Since the high temperature tetragonal phase is quenchable, a study of the structural transition around the transition temperature can be performed by the powder X-ray diffraction method using quenched samples. However, the powder diffraction data related to the phase transition exhibit a complicated pattern. So it is difficult to carry out accurate analysis by using conventional X-ray source because of its optical limitation such as interference from $\text{K}\alpha_2$ component.

It was expected that highly collimated synchrotron radiation (SR) would enable the performance of a high-resolution diffraction study on the phase transition. Therefore, we have applied this technique to the above problem. This study has also been made to examine the general capability of the powder diffraction technique by using the SR source.

Experimental

Four kinds of $\text{Ba}_2\text{YCu}_3\text{O}_{7-y}$ samples synthesized under different conditions were used for measurements. One sample was obtained by annealing $\text{Ba}_2\text{YCu}_3\text{O}_{7-y}$ at low temperature in O_2 gas flow (designated as sample A) and the others were obtained by quenching at 600, 700 and 850°C (samples B, C, D, respectively). These samples were mounted on glass plates and used for the measurements.

The measurements were performed at BL-4B station by using a Rigaku vertical-type diffractometer designed for PF. The wavelength of radiation was set at 1.4914\AA by using Si(111) channel-cut monochromator and a 0.3mm divergence slit was employed. During the data collection, samples were kept rotating by spinner and the sample room was held at high vacuum.

Intensity data were collected by using 2 θ - θ step scan method with 0.01° (in 2θ) step width for 5 sec, from 31.00° to 32.20° . The range includes the three strongest diffraction lines whose profile is sensitive to the phase transition.

Results and Discussion

Fig.1 shows a comparison of the powder diffraction patterns from conventional X-ray tube (a: $\text{CuK}\alpha$ radiation) and synchrotron radiation (b). Peak separation of the pattern (b) is much clearer than that of the pattern (a) demonstrating high resolution of the SR diffraction data. Taking this advantage, a pattern fitting analysis was attempted to study the phase transition. Pseudo-Voigt function was employed for the analysis.

The results for the sample A and D are shown in Fig.2. As can be seen from Fig.2, the (103) and (110) peaks overlap for the orthorhombic

phase (a), and the (103) and (013) peaks overlap for the tetragonal phase (b). It was found that the (103) peak shifts to lower angle with the increase in the synthesis temperature.

Although the process of the shifting of the (103) line was clearly observed, the pattern fitting analysis was difficult for the samples B and C. The reason is ascribed to the fact that these samples were obtained by quenching at around the transition temperature, so they include both orthorhombic and tetragonal phases. In addition, the distortion of the structure due to the phase transition appears to cause the broadening of the diffraction peaks. Besides, the quality of the samples used were not so good because the method of synthesis had not been established when these samples were synthesized. However, it will be possible to obtain much higher resolution patterns and hence good fitting result if we would use the samples with better quality.

The present analysis has indicated that the pattern change is due to the structural transition accompanying change in their unit cells from the low temperature orthorhombic phase ($c/3=a<b$) to the high temperature tetragonal phase ($a=b>c/3$).

This study was carried out as a preliminary experiment of our research program on structure analysis of inorganic chalcogenides by using synchrotron X-ray powder data (PF proposal No.85-148). Further application of this method to mineralogical problems is currently under way.

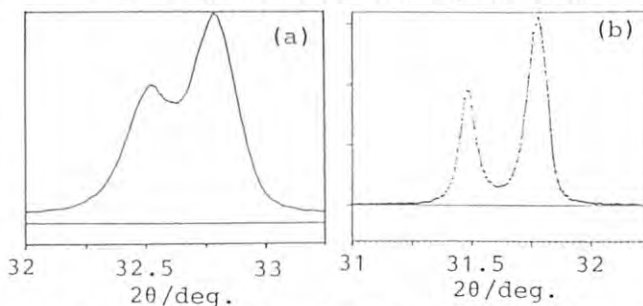


Fig.1. A comparison of X-ray powder diffraction patterns obtained by using conventional X-ray tube (a) and SR (b).

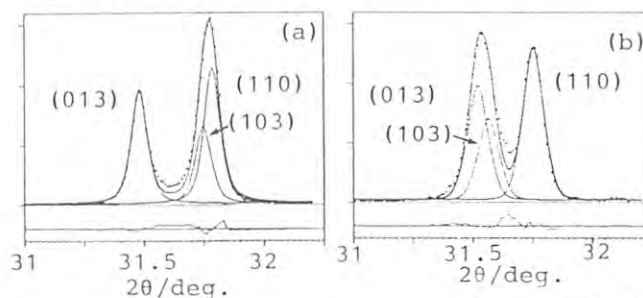


Fig.2. Results of the pattern fitting analysis for sample A (a) and sample D (b).

PROFILE ANALYSIS ON THE BASIC OF THE ENERGY DISPERSIVE SPECTRA AT HIGH PRESSURE AND TEMPERATURE

Takamitsu YAMANAKA and Kiyoshi OGATA*

College of General Education, Osaka University,
1-1 Machikaneyama-cho, Toyonaka, Osaka 560* Production Engineering Research Laboratory, Hitachi, Ltd.,
292 Yoshida-cho, Totsuka, Yokohama 244Introduction

X-ray diffraction experiments with polychromatic photons can be made in terms of its energy dispersive (ED) measurement under the condition of a fixed optical geometry. The Synchrotron Radiation (SR) X-ray has following excellent properties for the ED measurement: a) the smooth white radiation without any characteristic lines, b) the high intensity through the wide energy range, c) the high collimated beam providing the high energy resolution. These superiorities in the SR X-ray characteristics has been reported for the ED powder profile refinement.

The ED method is also capable for the fast spectra measurement and time dependent experiment particularly in studies of phase transformations at elevated temperatures and/or high pressures.

Profile of the ED spectra.

The diffraction intensity $y(E_i)$ by the ED method is expressed by the following equation, in consideration of the relation, $E_{hkl} = 12.983/(2d_{hkl} \sin \theta) \text{ keV}$ at the Bragg angle θ .

$$I_{hkl} = I_0(E_h) \cdot \rho \cdot [(1 + \cos^2 \theta) / \sin^2 2\theta \cdot \cos \theta] \\ |F_{hkl}|^2 \cdot \exp(-2B \cdot E_h^2 \sin^2 \theta / h^2 c^2) A(E_h)$$

Since the number of photons varies with the energy E_i , a source brightness calculated by the second order Bessel function directly contributes to the intensity $I_0(E_i)$. Mass absorption coefficient as a function of energy $A(E_i)$ is calculated.

An intrinsic Ge SSD has a large dynamic range from 2 to 100 KeV. A counting efficiency at each channel has been tested in advance by an radio active isotope. The correction of the counting loss and test of energy resolution caused by the dead time of the linear amplifier are made. An absorption edge of Ge is present at 11.1 KeV, at which the counting efficiency indicates a discontinuity. Photon counting correction is made for the escape peaks at the energy $E_i - E_f$, where E_f is a energy of the X-ray fluorescence of Ge. Compton peaks caused by the X-ray recoil are subtracted from the ED spectra, which is eminent especially at high energies under the conditions of light elements in the sample. An ED spectra after the intensity data process including the subtraction

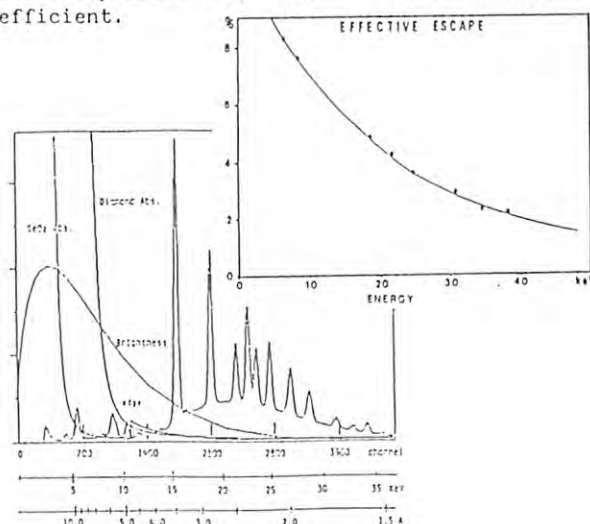
of the background is expressed by the pseudo-Voigt function, which is a sum of Gaussian and Lorentzen function. FWHM's of the diffraction peaks varies with E_i .

A computer program for the ED spectrum pattern fitting on the basis of the profile deconvolution procedure has been written in FORTRAN for a microcomputer. The fitting routine in the program takes into account of the following parameters: scale factor lattice constant, sample thickness related to the absorption correction structure factors, shape function (pseudo-Voigt function), UVW parameters of the FWHM, asymmetry parameters of the peak shape, parameters of a FWHM increment with energy. Three different reliability factor (R_{WD} , R_D , R_F) were functioned.

ED spectra of GeO_2 at pressure and temperature.

The ED measurement is applied for powder diffractions under high pressures and temperatures using a diamond anvil pressure cell. Platinum ring heater and thermocouple are installed in the cell. The maximum pressure 550°C. NaCl powder was also placed in the cell for an internal standard of the pressure calibrant. In order to avoid the effect of the grain growth on the diffraction intensity, the diamond anvil is oscillated around the incident beam.

The ED pattern fitting experiments regarding GeO_2 polymorphs trigonal ($P32_1$, $z = 3$) and tetragonal ($P4_2/mnm$, $z = 2$) phases, have been performed at high temperatures and pressures. Their lattice constants were also calculated from the peak position, providing their compressibility and thermal expansion coefficient.



APPLICATION OF RDF ANALYSIS EMPLOYING ANOMALOUS X-RAY SCATTERING TO STRUCTURAL STUDIES OF BINARY $\text{Ge}_x\text{Se}_{1-x}$ GLASSES

Akihiko NUKUI¹, Ken YUKINO³, Yasushi HASEGAWA¹, Yutaka SHIMIZUGAWA², Hideki MORIKAWA²,
Haruo OZAWA³, Ryousei UNO³ and Kazumasa OHSUMI⁴

¹National Institute for Research in Inorganic Materials, Sakura-mura, Niihari-gun, Ibaraki 305

²Hitachi Co. Ltd., Horiguchi 832-2, Katsuta-shi, Ibaraki 312

³The Tokyo Institute of Technology, Nagatsudachou 4259, Midori-ku, Yokohama-shi 227

⁴The Nippon University, Sakurajousui 3-25-40, Setagaya-ku, Tokyo 156

⁵National Laboratory for High Energy Physics, Ohho-machi, Tsukuba-gun, Ibaraki 305

INTRODUCTION

The Radial Distribution Function (RDF) analysis employing anomalous X-ray scattering, which give essential improvements to structural studies of non-crystalline solid, become available by using X-rays from Synchrotron Radiation (SR). The present study concern with the structural studies on a series of Ge-Se glasses in the Selenium-rich compositions, which allows formation of glass by quenching from the melt, by applying the RDF employing anomalous scattering at Ge and Se absorption edges.

EXPERIMENTAL

Chemical compositions of glasses used are $x=0.5, 0.10, 0.15, 0.20, 0.25$ and 0.30 for $\text{Ge}_x\text{Se}_{1-x}$. All data were taken on beam line IV, which was equipped with a Si(220) two crystal, parallel setting monochromator. Measurements were carried out at mainly three different wave lengths:

$\lambda_1 = 1.1917 \text{ \AA}$ (far from both absorption edges)

$\lambda_2 = 1.1170 \text{ \AA}$ (Ge absorption edge, 1.1165 \AA)

$\lambda_3 = 0.9807 \text{ \AA}$ (Se absorption edge, 0.9798 \AA)

At near the Se edge, a flat graphite monochromator was used to eliminate the Ge and part of the Se K fluorescence, and the Compton scattering.

RESULTS AND DISCUSSION

The superposition of distances between different types of atom pairs in experimental RDF can be removed to individual pair distribution functions by employing the anomalous X-ray scattering according to Krogh-Moe¹⁾. The practical data analysis is given at another paper²⁾. In analysis we use the differential intensities which based on differences between intensities taken at far from absorption edge of Ge(or Se) and at Ge(or Se) absorption edge, in order to subtract the contribution of Ge-Ge or Se-Se pair. Then we can obtain the Partial Pair RDF (PPRDF), $\Delta 4\pi r^2 \rho(r)_{\text{Ge(Se)}}$, which reflects the local atomic arrangements around the Ge atoms (or the Se atoms), by Fourier transformation of the differential intensities.

Figure 1 and 2 show the Differential Interference Function (DIF), $\Delta s(s)_{\text{Ge(Se)}}$, $s = 4\pi \sin \theta / \lambda$ and the Partial Pair RDF of $\text{Ge}_{0.15}\text{Se}_{0.85}$ obtained by the experiments employed X-rays with three different wave lengths.

The most RDF studies of non-crystalline Ge-Se system have been done by a single scattering experiment of electron or X-ray diffraction, excepting for Fuoss's study³⁾ by employed anomalous X-ray scattering. As the results, two different structural models were subsequently proposed for the non-crystalline Ge-Se system with different

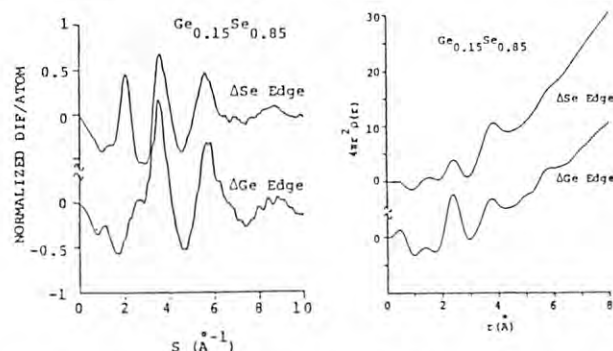


Fig. 1 Differential interference functions, $\text{DIF}_{\text{Ge(Se)}}$ deduced from the data taken at 1.1917 and 0.9807 Å (upper curve) and at 1.1917 and 1.1170 Å (lower curve).

Fig. 2 Partial Pair RDF $\rho_{\text{Ge(Se)}}$ calculated by Fourier transformation of DIF_{Ge} (upper curve) and of DIF_{Se} (lower curve).

Table 1. Structural data deduced from PPRDF_(GeSe)

	Atomic Distances		Coordination
	1st Peak	2nd Peak	Numbers
RDF _{far}	2.36 Å* (2.36)	3.74 Å* (3.77)	2.4* (2.35)
RDF _{Se}	2.36	3.75	2.1
RDF _{Ge}	2.36	3.71	3.9

* Average Values and () ; Malaurent et al.

Ge/Se ratio, because the RDF resulted from the single scattered data reflected the weighted sum of every pair of constituent atoms. In order to compare with the such the data, we calculated the RDF resulted from using only the X-rays of $\lambda_1 = 1.1917 \text{ \AA}$. As can be seen in Table 1, the average structural data obtained here are almost the same those reported by Malaurent et al.. On the other hand, the first-neighbor peak areas in PPRDF_{Ge(Se)} were calculated to be 3.9 atoms for Ge and 2.1 atoms for Se. The first-neighbor distances around Ge were 2.36, and that around Se, 2.36 Å, respectively.

Integrating the results of other samples, it concluded that the Ge-Se glasses of Selenium-rich compositions were consisted basically with four-fold coordination around Ge atom and two-fold coordination around Se atom. Thus we can discuss more detailed and exact structures from the experimental facts by applying the present method instead of the estimation deduced from the normal RDF.

REFERENCES

- 1) J. Krogh-Moe, Acta Chem. Scand. **20** (1966) 2890.
- 2) A. Nukui, Y. Shimizugawa, H. Morikawa, and K. Ohsumi, J. Non-Cryst. Solids, Special Issue (in press, 1987).
- 3) P.H. Fuoss, P. Eisenberger, W.K. Warburton and A. Bienenstock, Phys. Rev. Lett. **46** (1981) 1537.
- 4) J.C. Malaurent and J. Dixmier, J. Non-Cryst. Solids **35 & 36** (1980) 1227.

X-RAY STUDY ON CONFIGURATIONAL FIBONACCI SUPERLATTICES

Kousei KAMIGAKI, Hirofumi SAKASHITA, Hikaru TERAUCHI, and CPG*

Department of Physics, Kwansei-Gakuin University, Nishinomiya 662, Japan

*Crystal Physics Group at the Photon Factory

Introduction

In 1984, Shechtman et al.¹⁾ discovered the new ordered phase with icosahedral symmetry in quenched Al-Mn alloy. The new phase can be explained in terms of three-dimensional quasi-periodic lattice called by "quasi-crystal". Strong interest has been focused on its electronic state because quasi-crystal has only an orientational order and the intermediate property between a periodic lattice and an amorphous state. The theoretical studies of the electronic state of the one-dimensional (1-D) quasi-crystal with an incommensurate potential have been carried out. Recently, Merlin et al.²⁾ succeeded in the synthesis of the 1-D quasi-crystal by molecular beam epitaxy (MBE), namely "Fibonacci superlattice". Their crystal is composed of two different semiconductor layers of GaAs and AlAs, which form the Fibonacci sequence. The ratio of the layer thickness is the golden mean τ ($= (1+\sqrt{5})/2$), which gives a "self-similarity". "Self-similarity" is the most interesting property of the Fibonacci sequence and gives many singularities to the physical property of the 1-D quasi-crystals. Todd et al.³⁾ have clearly shown the self-similarity characterized by τ on the x-ray diffraction patterns using synchrotron radiation.

In the present, we have synthesized new Fibonacci superlattices in which the ratio of the layer thickness is not τ (called by "configurational Fibonacci superlattice"), and have discussed the "self-similarity" of the x-ray diffraction pattern of our superlattices.

Experimental

The crystal is designed in the following manner.

$$S_n = S_{n-1} : S_{n-2}$$

with $S_1 = A$, $S_2 = BC$, $n = 14$,

$$\begin{array}{ll} A : \text{Al}_{0.5}\text{Ga}_{0.5}\text{As} & ; 5a_{\text{AlGaAs}} \\ B : \text{GaAs} & ; 5a_{\text{GaAs}} \\ C : \text{AlAs} & ; 5a_{\text{AlAs}} \end{array}$$

where respective lattice constants of composites are denoted by a_{AlGaAs} , a_{GaAs} and a_{AlAs} , respectively. Note that the ratio of layer thickness is not τ .

The crystal were grown by the Riber 2300 R&D MBE system. The alloy composition and layer thickness were determined by the monitoring the specularly reflected electron beam oscillations of reflection high-energy diffraction. The substrate temperature was kept at 550°C during growth and its rate was about 1 monolayer/s.

X-ray diffraction measurements were performed at the station 4C by Huber high-precision 4-circle diffractometer with analyser.

Results

Figure 1 shows an x-ray diffraction pattern around the (004) reflection in very narrow q region along the layer stacking direction. An inset shows a diffraction pattern observed by conventional diffractometer. The region between peaks -2 and -3 is expanded in main part of figure. Very fine structure can be seen. Apparently, every peak positions can be characterized by τ . This fact implies that "configurational Fibonacci superlattice" shows the "self-similarity" characterized by golden mean τ even though the ratio of layer thickness is not τ . The studies of other Fibonacci lattices are in progress.

References

- 1) D. Shechtman, I. Blech, D. Gratias and J. W. Cahn, Phys. Rev. Lett., **53**, 1951 (1984).
- 2) R. Merlin, K. Bajema, Roy Clark, F.-Y. Juang and P. K. Bhattacharya, Phys. Rev. Lett., **55**, 1768 (1985).
- 3) J. Todd, R. Merlin, Roy Clark, K. M. Mohanty and J. D. Axe, Phys. Rev. Lett., **57**, 1157 (1986).

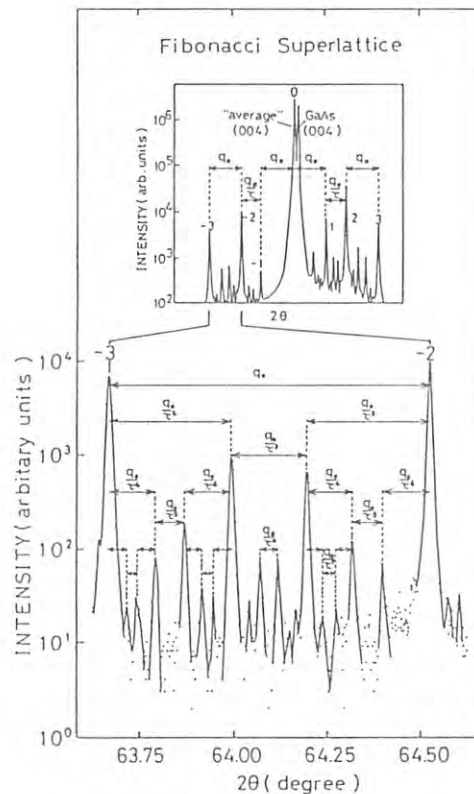


Fig. 1. X-ray diffraction pattern around the (004) reflection along the layer stacking direction. An inset shows the diffraction pattern at lower resolution.

High Resolution Investigation of Rod-Shaped Scattering from (111) Si Surface by Triple-Axis Diffractometer

Nobuo KASHIWAGURA, Yasuharu KASHIHARA*, Makoto SAKATA*, Jimpei HARADA*, Stephen W. Wilkins** and Andrew W. Stevenson**

Department of Basic Sciences, Faculty of Engineering, Gifu University, Yanagido, Gifu 501-11, Japan.

*Department of Applied Physics, Nagoya University, Chikusa-ku, Nagoya 464, Japan.

**CSIRO, Division of Materials Science and Technology, Gate 5 Normanby Road, Clayton, Locked Bag 33, Clayton, Victoria 3168, Australia.

Introduction

By using a high resolution triple-axis x-ray spectrometer, a rod-shaped scattering due to crystal truncation (RSCT)^{1),2),3),4)}, which is elongated along the normal of a crystal surface through a Bragg point, was investigated for two (111) silicon wafers of which surfaces were differently processed.

Experimental and Results

One of the samples (sample B) had been lapped by #1200 Al₂O₃ abrasive powder, and then chemically etched by an amount of 30 μ m. The surface of the other sample (sample A) was polished mechano-chemically after above treatment. No special attention has been paid for protecting against oxidation of the surface.

A 1.54Å radiation, monochromated by a sagittal focusing double crystal monochromator of Si 111, was employed at beam line 4-C. A vertical type Huber 4-circle diffractometer with a Si crystal analyzer of the (111) surface was installed to the beam line.

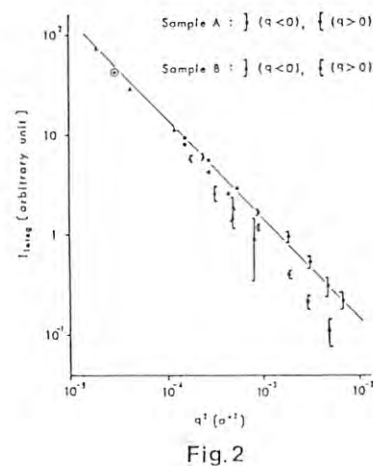
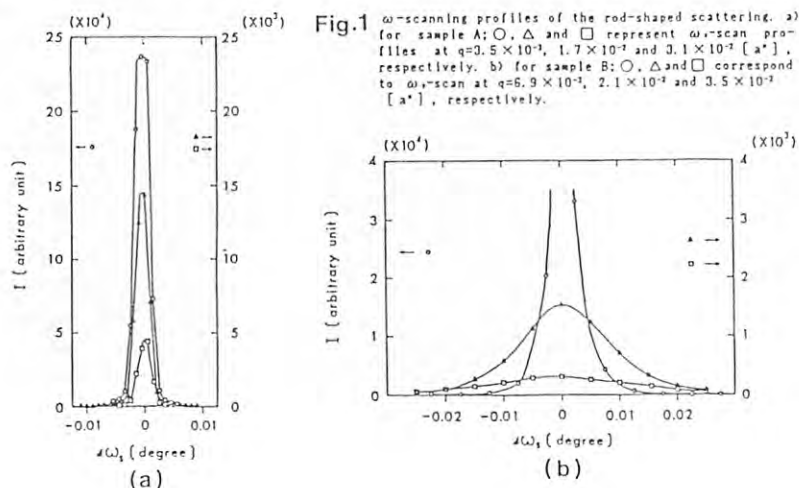
Fig.1 shows the comparison of the ω -scan profiles of the rod-shaped scattering from the sample A with those from the sample B for several different values of q ($|q|$ represents the distance from the 111 Bragg point along the [111] direction in the unit of the reciprocal lattice a^*). The FWHM values are very narrow and about 12 seconds in arc (including instrumental broadening) and are independent of $|q|$ for the sample A, while it gets broader and broader with the increase of $|q|$ for the sample B. If the angular divergence of the RSCT is measured with the center at the 111 Bragg point, it is estimated to be about 2.3 degree. The profile

of the scattering in reciprocal space is, therefore, of a cone-shape with a solid angle of about 2.3 degree. In general, the scattering from a surface truncation is not of a rod-shape but a cone-shape, and the solid angle depends directly upon the mean-square surface roughness of the crystal.

Fig.2 shows the integrated intensity distribution along the central axis of the RSCT for the sample A and sample B, where I_{int} represents the intensity integrated along each ω -scan direction. There is a considerable asymmetry between the intensity distribution for $q < 0$ and that for $q > 0$, especially for sample A. This asymmetric intensity distribution has recently been identified as being due to the effects of a lattice expansion perpendicular to the surface in addition to the existence of a slight atomic density undulation at the interface between the Si crystal and the amorphous SiO₂ layer⁵⁾. It should be pointed out that the extent of falling off of the intensity along the RSCT is different for sample A to that of sample B. This might be attributed to the fact that sample A could be expected to have a larger coherent region than sample B.

References

- 1) J. Harada, N. Kashiwagura, M. Sakata and H. Miyatake: to be published in J. Appl. Phys.
- 2) S. R. Andrews and R. A. Cowley: J. Phys. C, Solid State Phys. 18 (1985) 6427.
- 3) I. K. Robinson: Phys. Rev. B33 (1986) 3830.
- 4) A. Iida and K. Kohra: Phys. Stat. Sol. (a) 51 (1979) 533.
- 5) Y. Kashiwara, K. Kawamura, N. Kashiwagura and J. Harada: Jpn. J. Appl. Phys. 26 (1987) L1029.



A Be-CYLINDER TYPE HIGH-PRESSURE APPARATUS FOR X-RAY DIFFRACTION

Yasuhiko FUJII, Nozomu HAMAYA, Yoshihiro KUROIWA*
 Susumu SHIMOMURA, Tadashi MATSUSHITA**, and Satoshi SASAKI

Faculty of Engineering Science, Osaka University
 Toyonaka, Osaka 560

* Institute of Applied Physics, University of Tsukuba
 Sakura-mura, Niihari-gun, Ibaraki 305

** Photon Factory, National Laboratory for High Energy Physics
 Oho-machi, Tsukuba-gun, Ibaraki 305

For x-ray diffraction studies of phase transitions driven by pressure, we have developed a new high-pressure apparatus which has special capabilities of controlling pressure with precision of ± 2 bars and of performing 1) a quick change in pressure applied to a sample. This apparatus consists of three major parts connected with high-pressure tubings:

(1) Pressure generator It has been specially designed for high-precision pressure control in both loading and unloading processes with three hand pumps. The first pump is used to raise pressure up to 2 kbar and higher pressures up to 10 kbar can be reached by an intensifier driven with the second pump. The third one is employed to regulate the back-pressure exerted on a check valve for a smooth pressure release. The mixture of the castor oil and methanol is used as pressure-transmitting fluid. The pressure is measured with a Bourdon gauge.

(2) Fast valve It performs opening/closing of the pressure circuit connected between the generator and the cell within a second. This function made with a pneumatic valve is utilized to execute a sudden application of desired magnitude of pressure to a sample and also a sudden release for studying kinetics of phase transition.

(3) High-pressure cell Its structure is illustrated in Fig. 1. A conical Be cylinder(A) with taper angle 1.5 degrees of arc has dimensions of 30mm in length, 2mm in inside diameter, and 8mm in outside diameter. It is press-fitted into a supporting jacket(B), made out of copper-beryllium alloy. The pressure seal is made by

line contact of 60° cones at both edges of the Be cylinder against two other 59° cones of the tube(D) and the sample holder(C). With the aid of a simple finite-element-stress-analysis on a Be cylinder, the vertical width of x-ray window(E) on the supporting jacket was determined to be 2.4mm for the maximum pressure 5.2 kbar. As also shown in Fig. 1, the supporting jacket has the openings of 120° and $\pm 15^\circ$ in the horizontal and vertical directions, respectively, for incident and diffracted x-ray beams. Figure 2 shows the pressure cell mounted on a large circle of a four-circle diffractometer (Huber 5020.4)²⁾ installed on BL-4C at the Photon Factory. One can also see the manganin gauge attached to the cell which monitors pressure applied to the sample.

In cooperation with the high pressure-controllability $\Delta P = \pm 2$ bars of the present apparatus and the high momentum resolution capability $\Delta Q/Q = 5 \times 10^{-4}$ of the SRX diffractometer, we have carried out an experiment on the commensurate-incommensurate phase transition in ferroelastic crystal $[N(CH_3)_4]_2MnCl_4$. Our purpose is to explore any transient lock-in phase possibly existent in the previously-reported incommensurate phase. The results will appear elsewhere.

References

- 1) N. Hamaya, Y. Kuroiwa, and Y. Fujii: To be published in Nucl. Instrum. & Meth. (1987).
- 2) H. Iwasaki et al.: Photon Factory Activity Rept. #4 (1986) 160.

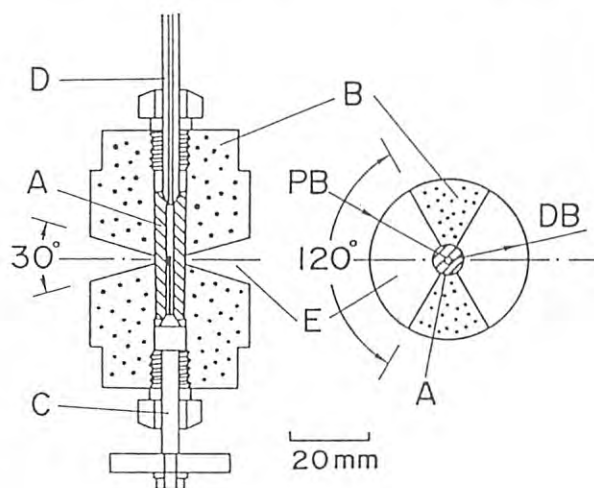


Fig. 1

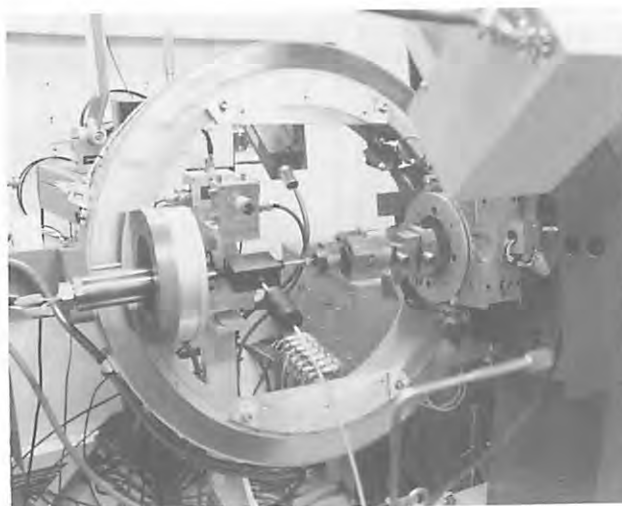


Fig. 2

A XANES SPECTROSCOPY OF Ni(II)-Fe(II) HYBRID HEMOGLOBINS

Naoya SHIBAYAMA, Satoshi SAIGO, Hiroyuki OYANAGI*,
Tetsutaro IIZUKA** and Tadashi MATSUSHITA***

Jichi Medical School, Minamikawachi, Tochigi 329-04

*Electrotechnical Laboratory, Sakuramura, Niiharigun, Ibaraki 305

**The Institute of Chemical and Physical Research, Wakoshi, Saitama 351-01

***Photon Factory, National Laboratory for High Energy Physics,
Ohomachi, Tsukubagun, Ibarki 305

Introduction

Human adult hemoglobin (HbA) is a tetrameric metalloprotein and is composed of two α and β subunits. Each subunit enfolds a prosthetic group, a heme [Fe(II) protoporphyrin IX], of which the primary coordinate bond to the globin moiety is formed between the Fe(II) atom and the nitrogen atom of the proximal histidine residue. Recently, artificial metal-substituted hybrid Hbs, in which the hemes in either α or β subunits are substituted with Ni(II) protoporphyrin IX (Ni-PPIX), have been prepared and characterized by various spectroscopic methods. Since the Ni X-ray absorption K-edge is well separated from the Fe K-edge, it is possible to investigate the local structure separately for the α and β subunits by use of Ni (or Fe) XANES spectra.

Experimental Procedures

Ni(II)-Fe(II) hybrid Hbs were prepared as previously described¹⁾. A sagittally bent crystal monochromator and a fluorescence-detection spectrometer were employed for XANES measurements. Scattered X-rays were eliminated by use of a Si(Li) detector fitted with a Co filter. Measurements were carried out at 80 K. The concentration of all samples was several mM for Ni atoms. The buffer used was 20 mM Tris-HCl at pH 7.4 (before freezing). Oxygen-bound Ni(II)-Fe(II) hybrid Hbs were deoxygenated by flushing with nitrogen gas and by adding a small amount of dithionite under nitrogen flux.

Results and Discussion

Ni(II)-Fe(II) hybrid Hbs, α_2 (Ni) β_2 (Fe) and α_2 (Fe) β_2 (Ni), exhibit quite different Ni XANES spectra as shown in Fig. 1 (solid lines). Previous spectrophotometric studies on Ni(II)-Fe(II) hybrid Hbs have revealed that four-coordinated Ni-PPIX with no axial ligand is predominant in α_2 (Ni) β_2 (Fe), while Ni-PPIX in the β subunits is always five-coordinated with the proximal histidine as an axial ligand. Such a difference in coordination number could be due to a considerably low affinity of Ni-PPIX for a nitrogen base. In Fig. 1, Ni XANES spectra of four-coordinated Ni-PPIX in dimethylformamide and six-coordinated Ni-PPIX in piperidine are also presented for comparison (broken lines). One of the most significant differences between the four-coordinated Ni-PPIX and the five-coordinated (or six-coordinated) Ni-PPIX is a

shoulder (denoted by A) on a rising absorption curve, which has been previously reported as typical absorption of square-planar four-coordinated Ni(II) complexes²⁾.

Although no large difference is observed between hybrid Hbs and their model compounds, the XANES spectra of hybrid Hbs seem to be slightly broader than those of the corresponding model compounds. In the case of α_2 (Ni) β_2 (Fe), the broadening can be caused by a small amount of thermally mixed five-coordinated Ni-PPIX in the α subunits. On the other hand, differences observed between α_2 (Fe) β_2 (Ni) and Ni-PPIX in piperidine may be attributed to structural differences between the five-coordinated square-pyramidal and six-coordinated square-bipyramidal Ni-PPIX.

References

- 1) N. Shibayama, H. Morimoto and G. Miyazaki, J. Mol. Biol. 192, 323 (1986)
- 2) U. C. Srivastava and H. L. Nigam, Coord. Chem. Rev. 9, 275 (1972-1973)

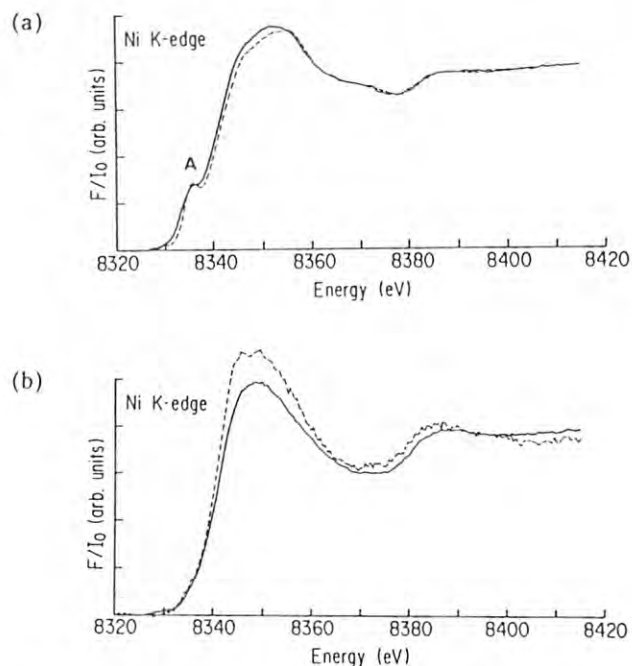


Fig. 1 XANES spectra of Ni(II)-Fe(II) hybrid hemoglobins and their model compounds.

(a) α_2 (Ni) β_2 (Fe) (solid line) and Ni-PPIX in dimethylformamide (broken line).

(b) α_2 (Fe) β_2 (Ni) (solid line) and Ni-PPIX in piperidine (broken line).

Local Structure in Orthorhombic and Tetragonal $\text{Ba}_2\text{YCu}_3\text{O}_y$: The Role of Oxygen Vacancies in High T_c Superconductivity

Hiroiyuki OYANAGI, Hideo IHARA, Toshiya MATSUBARA*,
Tadashi MATSUSHITA**, Masayuki HIRABAYASHI, Madoka TOKUMOTO,
Keizo MURATA, Norio TERADA, Kiyoshi SENZAKI, Takafumi YAO,
Hiroshi IWASAKI** and Yoichi KIMURA

Electrotechnical Laboratory, Sakuramura, Niiharigun, Ibaraki 305

**Research & Development Division, Asahi Glass Co., Ltd., Kanagawaku, Yokohama*

***National Laboratory for High Energy Physics, Ohomachi, Tsukubagun, Ibaraki 305*

Introduction

Since the first report on a possible high T_c (30 K) superconductivity in the Ba-La-Cu-O system by Bednortz and Muller¹⁾, a number of studies were aimed at understanding the nature of high T_c superconductivity. The purpose of this project is to study the role of oxygen vacancies in superconducting properties of $\text{Ba}_2\text{YCu}_3\text{O}_y$ from microscopic viewpoints. In the present study, (1) the local structure of $\text{Ba}_2\text{YCu}_3\text{O}_y$ and (2) Cu-O stretching vibrations were analyzed by Cu K-EXAFS²⁾.

Experimental and Results

$\text{Ba}_2\text{YCu}_3\text{O}_y$ ($6.22 < y < 6.96$) samples were prepared by controlling the cooling temperature after sintering pressed pellets at 930 °C. In Fig. 1, the magnitude of Fourier transform of EXAFS for orthorhombic $\text{Ba}_2\text{YCu}_3\text{O}_{6.87}$ ($T_c = 90$ K) and tetragonal $\text{Ba}_2\text{YCu}_3\text{O}_{6.36}$ (non-superconducting) are shown. Bold and fine lines indicate the results for $\text{Ba}_2\text{YCu}_3\text{O}_{6.87}$ and $\text{Ba}_2\text{YCu}_3\text{O}_{6.36}$. The first peak is due to the Cu-O distance (1.96 Å) and more distant peaks are the Cu-Ba(Y) and second nearest Cu-Cu distances. On going from the orthorhombic to tetragonal structure, (1) radial distribution narrows, (2) the Cu-Ba(Y)

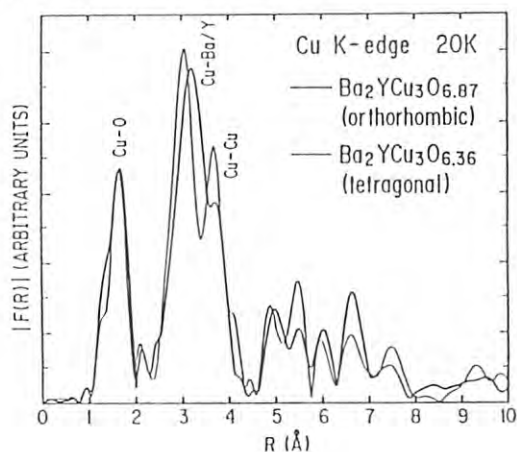


Fig. 1

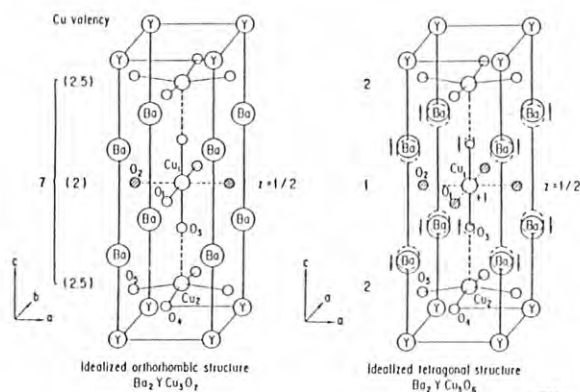


Fig. 2

distance decreases by *ca.* 0.13 Å and (3) the Cu-O and Cu-Cu distances are essentially unchanged.

In Fig. 2, the crystal structures of idealized orthorhombic $\text{Ba}_2\text{YCu}_3\text{O}_7$ and tetragonal $\text{Ba}_2\text{YCu}_3\text{O}_6$. Ordered oxygen vacancies in orthorhombic $\text{Ba}_2\text{YCu}_3\text{O}_7$ form the O-Cu₁-O linear chain, which is not present in tetragonal $\text{Ba}_2\text{YCu}_3\text{O}_6$. The orthorhombic distortion displaces Ba(Y) atoms along the *c*-axis. Oxygen vacancies modify the local structure around Cu species both in *basal planes* and *linear chain*. As a result, the structural disorder are introduced *within and between* basal planes. The temperature dependence of the mean relative displacement for Cu-O bond is larger in the orthorhombic phase than in the tetragonal phase, implying that antisymmetric (breathing mode) Cu-O stretching vibration is suppressed in the tetragonal phase.

References

- 1) J.G. Bednortz and K.A. Muller: *Z. Phys.* B64 (1986) 189.
- 2) H. Oyanagi, H. Ihara, T. Matsubara, M. Tokumoto, T. Matsushita, M. Hirabayashi, K. Murata, N. Terada, K. Senzaki, T. Yao, H. Iwasaki and Y. Kimura, *Jpn. J. Appl. Phys.* 26 (1987) L1233.

Valence Study of Orthorhombic and Tetragonal $\text{Ba}_2\text{YCu}_3\text{O}_y$: The Role of Oxygen Vacancies in High T_c Superconductivity

Hiroyuki OYANAGI, Hideo IHARA, Toshiya MATSUBARA*, Madoka TOKUMOTO
Tadashi MATSUSHITA**, Masayuki HIRABAYASHI, Keizo MURATA,
Norio TERADA, Takafumi YAO, Hiroshi IWASAKI** and Yoichi KIMURA

Electrotechnical Laboratory, Sakuramura, Niiharigun, Ibaraki 305

**Research & Development Division, Asahi Glass Co., Ltd., Kanagawaku, Yokohama 221*

***National Laboratory for High Energy Physics, Ohomachi, Tsukubagun, Ibaraki 305*

Introduction

A strong correlation has been found between the oxygen content y in $\text{Ba}_2\text{YCu}_3\text{O}_y$ and T_c , i.e., high T_c superconductivity (90 K) degrades to lower value (50-60 K) at the critical oxygen content $y=6.7-6.8^1$. We have investigated the local structure of orthorhombic and tetragonal $\text{Ba}_2\text{YCu}_3\text{O}_y$ and found that oxygen vacancies affect both structure and electronic states. The purpose of this project is to systematically investigate the valency of Cu ions in $\text{Ba}_2\text{YCu}_3\text{O}_y$ as a function of y using near-edge X-ray absorption spectroscopy²⁾.

Experimental and Results

Orthorhombic $\text{Ba}_2\text{YCu}_3\text{O}_y$ showed a high value of T_c (90 K) for $y>6.8$ and lower T_c value (50-60 K) for $y<6.7$. The tetragonal phase with $y<6.3$ is non-superconducting and shows a semiconductive temperature dependence of resistivity.^{1,2)} Cu-K near-edge spectra of $\text{Ba}_2\text{YCu}_3\text{O}_y$ ($6.22<y<6.96$) are shown in Fig. 1. The average position of absorption lies at a similar position to that of CuO indicating that the Cu valency is primarily divalent. However, with the decrease of oxygen content, the characteristic feature A grows at 8982.5 eV. This sharp $1s-4p\pi^*$ bound state transition lies at

Fig. 1

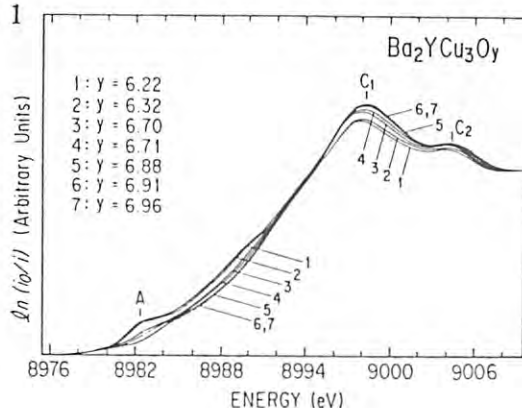
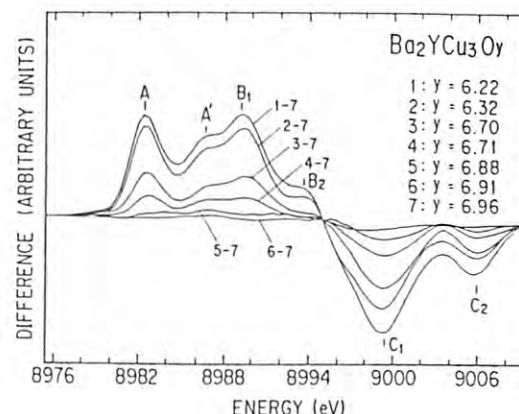


Fig. 2



the same energy as that of Cu_2O , 3.4 eV lower than that of CuO, which indicates that oxygen vacancies create Cu^+ species at the two-fold coordinated Cu_1 sites on the $z=1/2$ plane.

In Fig. 2, difference spectra demonstrate the systematic change of near-edge spectra as the average Cu valency varies from 2.31 ($y=6.96$) to 1.81 ($y=6.22$). The positive region (8975-8996 eV) increases with the decrease of y while the negative region (8996-9018 eV) decreases. These spectra measure the formation of Cu^+ as a positive part and the decrease of $\text{Cu}^{2+}/\text{Cu}^{3+}$ as a negative part. We find that the formation of Cu^+ is enhanced at the critical oxygen content or Cu valency for 90 K superconductivity although whether oxygen vacancies create Cu^{3+} (d^8) states or O (2p) holes is not settled yet.

References

- 1) M. Tokumoto, H. Ihara, T. Matsubara, M. Hirabayashi, N. Terada, H. Oyanagi, K. Murata and Y. Kimura: Jpn. J. Appl. Phys. 26 (1987) L1565.
- 2) H. Oyanagi, H. Ihara, T. Matsubara, T. Matsushita, T. Matsushita, M. Hirabayashi, M. Tokumoto, K. Murata, N. Terada, T. Yao, H. Iwasaki and Y. Kimura: Jpn. J. Appl. Phys. 26 (1987) L1561.

Molecular Arrangement of Langmuir-Blodgett Monolayers Studied by Surface-Sensitive X-Ray Absorption Spectroscopy

Hiroyuki Oyanagi, Mitsuru Yoneyama*, Keiichi Ikegami,
Michio Sugi, Shin-ichi Kuroda, Takehiko Ishiguro and
Tadashi Matsushita**

Electrotechnical Laboratory, Sakuramura, Ibaraki 305

**Mitsubishi Chemical Industries Ltd., Yokohama 227*

***National Laboratory for High Energy Physics, Tsukubagun Ibaraki 305*

Introduction

Metal-containing porphyrins are a simple model system of functional proteins, e.g., oxygen-binding hemoproteins such as hemoglobin (Hb) or myoglobin (Mb). Porphyrins exhibit interesting photoelectrical properties as a stable π -electron system. In functional studies of porphyrins, the use of Langmuir-Blodgett (LB) technique which provides well-defined molecular assembly is useful. In this project, the orientation of asymmetric copper phthalocyanine (asy-CuPc) mono- and multi-layers were studied by polarized near-edge spectra¹.

Experimental and Results

Asy-CuPc samples mono- and multi-layers were prepared by vertical dipping method onto flat quartz substrates. The first application of X-ray absorption spectroscopy to LB films² utilized fluorescence-detection technique. In this experiment, surface-sensitivity has been improved by a total reflection geometry and a high energy resolution detector. Figure 1 shows the schematic of experimental setup. In a total reflection regime, X-ray evanescent waves cannot penetrate beyond *ca.* 50 Å.

Fig. 1

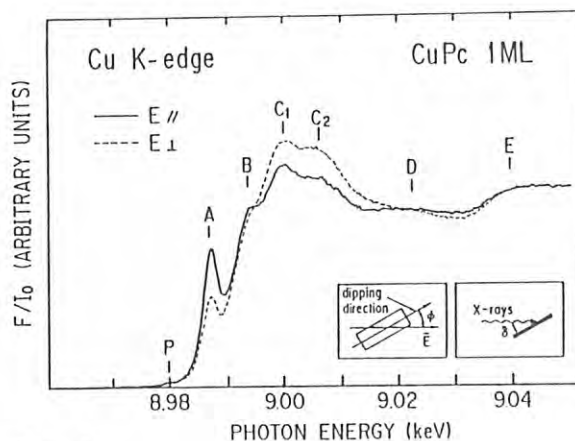
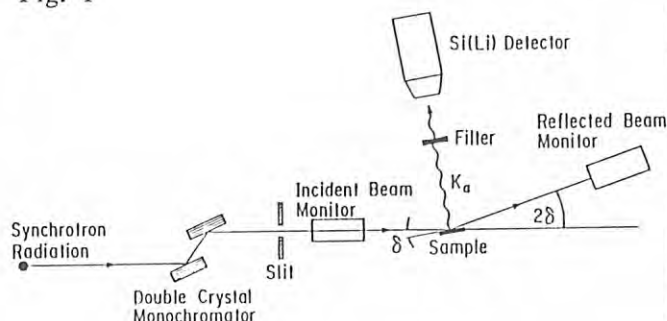


Fig. 2

In Fig. 2, the near-edge region (<50 eV) for 1 ML asy-CuPc is shown. Peaks A and B are ascribed to the transition from 1s to $4p\pi$ states. The two split peaks arise from the interaction between $4p_z$ orbitals and ligand π^* orbitals. These transitions are emphasized when E is *parallel* to porphyrin normal. Peaks C₁ and C₂ are assigned to the transition from 1s to $4p\sigma$ states, which splits into two peaks due to the interaction between $4p_{x,y}$ orbitals and ligand σ states. These peaks are emphasized for E *perpendicular* to the porphyrin normal. The observed polarization dependence rules out a possible orientation of asy-CuPc with its porphyrin plane parallel to the substrate. The results suggest that porphyrin plane is faced with the dipping direction with a tilted normal axis.

References

1. H. Oyanagi, M. Yoneyama, K. Ikegami, S. Kuroda, M. Sugi, T. Ishiguro and T. Matsushita: Proc. of 3rd Int. Conf. on Langmuir-Blodgett Films, Gottingen, 1987.
2. H. Oyanagi, M. Sugi, S. Kuroda, S. Iizima, T. Ishiguro and T. Matsushita: Thin Solid Films 133 (1985) 181.

Si/Ge/Si Monolayer Heterostructure on Si(100) Studied by Surface-Sensitive EXAFS

Hiroyuki OYANAGI, Tsunenori SAKAMOTO, Kunihiro SAKAMOTO,
Tadashi MATSUSHITA*, Takafumi YAO and Takehiko ISHIGURO

Electrotechnical Laboratory, Sakuramura, Niiharigun., Ibaraki 305

**National Laboratory for High Energy Physics, Tsukubagun, Ibaraki 305*

Introduction

Heteroepitaxial growth of $\text{Ge}_x\text{Si}_{1-x}/\text{Si}$ strained-layer superlattice (SLS) on Si substrates attracts much attention because of interesting properties such as strain-induced new optical transitions¹⁾ or two-dimensional transport properties²⁾. Confined electron states in $\text{Ge}_x\text{Si}_{1-x}/\text{Si}$ SLS's are sensitive to internal strains, and therefore it is important to study the lattice strains from microscopic viewpoints. We report the surface-sensitive EXAFS studies on MBE grown Si/Ge/Si mono- and multi-layer heterostructures.

Experimental and Results

Si/Ge/Si monolayer heterostructures were prepared on well-oriented p-type Si(100) (4 ohm-cm) in an UHV MBE growth chamber with a base pressure of 1×10^{-9} Torr. One monolayer (ML) Ge was deposited at 400 °C monitoring RHEED intensity variation during MBE growth as previously reported³⁾. The maximum-RHEED-spot intensity is attained at a full coverage of 1 ML growth. After the Ge monolayer was grown, 22 ML's of Si (30 Å) were successively grown.

Figure 1 shows the results of the Fourier transform for Si/Ge/Si (upper curve) and c-Ge (lower curve). Dashed lines indicate the results

Fig. 1

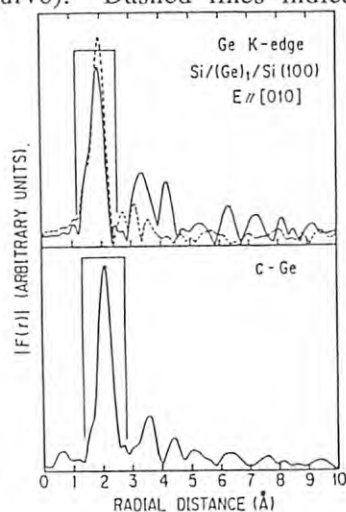
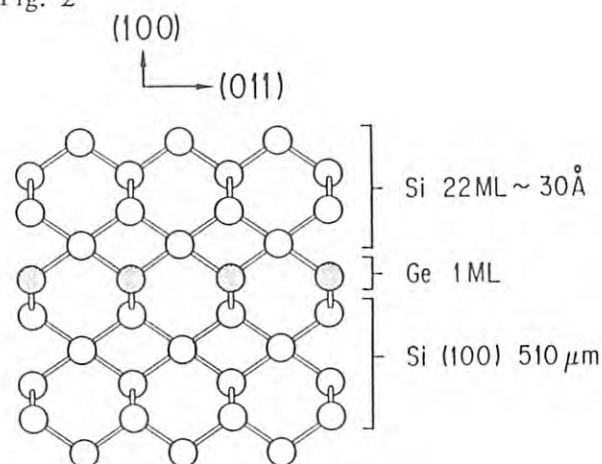


Fig. 2



of the same transform for a- $\text{Ge}_{0.05}\text{Si}_{0.95}\text{H}$. The appearance of the second and third nearest peaks clearly indicates the presence of a *long range order*. The Ge-Si distance in Si/Ge/Si heterostructure (2.38 Å) is shorter than that in a- $\text{Ge}_{0.05}\text{Si}_{0.95}\text{H}$ by 0.02 Å but rather close to the Si-Si distance in c-Si (2.35 Å).

The idealized structure of Si/Ge/Si heterointerface is shown in Fig. 2 neglecting a possible antiphase boundary. Although a lattice-mismatch between bulk Ge and Si amounts to 4.2 %, the bond length difference in Si/Ge/Si is actually less than 1.3 %, due to the observed Ge-Si bond contraction. In SLS's, a lattice-mismatch induces the in-plane strain. The present results indicate that in case of Si/Ge/Si heterostructure, bond contraction seems to effectively reduce the bending-type relaxation

References

- 1) T. P. Pearsall, J. Bevk, L.C. Feldman, J.M. Bonar, and J.P. Mannaerts: *Phys. Rev. B* **58** (1987) 729.
- 2) H.M. Manasevit, I.S. Gergis and A.B. Jones: *Appl. Phys. Lett.* **41** (1982) 464.
- 3) K. Sakamoto, T. Sakamoto, S. Nagao, G. Hashiguchi, K. Kuniyoshi and Y. Bando: *Jpn. J. Appl. Phys.* **26** (1987) 666.

Structural Studies of (Ga,In)(As,P) Alloys and $(\text{InAs})_m(\text{GaAs})_n$ Strained Layer Superlattices

Hiroyuki OYANAGI, Yoshikazu TAKEDA*, Tadashi MATSUSHITA**,
Takehiko ISHIGURO, Takafumi YAO, and Akio SASAKI*

Electrotechnical Laboratory, Sakuramura, Niiharigun, Ibaraki 305

*Department of Electrical Engineering, Kyoto University, Kyoto 606

**National Laboratory for High Energy Physics, Ohomachi, Tsukubagun, Ibaraki 305

Introduction

$(\text{Ga,In})(\text{As,P})$ alloys and $(\text{InAs})_m(\text{GaAs})_n$ strained-layer superlattice (SLS) attract much attention as a class of promising materials as optical devices. Nature of strains in these systems affects optical and electronic properties. To study the lattice relaxation, and hopefully, to distinguish layered (ordered) crystals from random alloys, we have performed EXAFS measurements¹⁾ on thin $(\text{InAs})_m(\text{GaAs})_n$ SLSs prepared by molecular beam epitaxy (MBE) technique.

Experimental and Results

$(\text{Ga,In})(\text{As,P})$ alloys lattice-matched with InP substrates were grown by LPE at 625-635 °C with the layer thickness around 5000 Å. $(\text{InAs})_m(\text{GaAs})_n$ SLSs were grown by MBE on InP substrates. The horizontally focused monochromatized X-ray beam irradiated the sample and fluorescence X-rays were recorded by a NaI scintillation detector array consisting of 9 detectors²⁾. For a dilute samples, X-ray filters were used to reduce the scattering background.

Figure 1 shows the Ga K-EXAFS oscillations for $(\text{InAs})_{6.45}(\text{GaAs})_{0.51}$ and crystalline GaAs plotted as a function of photoelectron wavenumber k . The results of Fourier transform are plotted in Fig. 2. Bold lines

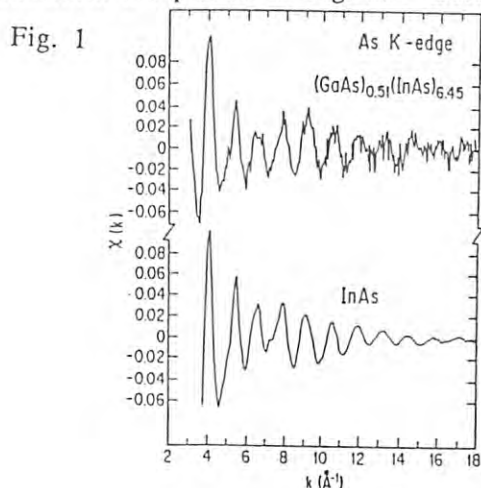
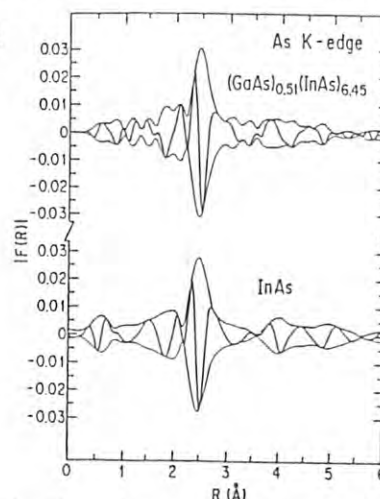


Fig. 2



indicate the imaginary part of the Fourier transform while fine lines indicate the magnitude $|F(r)|$. The Ga-As distance in $(\text{InAs})_{6.45}(\text{GaAs})_{0.51}$ is determined as 2.51 Å. The Ga-As distance in SLS is longer than that of binary crystal by 0.06 Å. Compared to the results for random alloys, this deviation (2.4 %) is much larger.

The As-In distance in SLS was determined as 2.60 Å from the Ga K-edge EXAFS data and a similar analysis. This value is shorter than that of InAs (2.62 Å) by only 0.7 %. Thus, in $(\text{InAs})_m(\text{GaAs})_n$ SLS for $m \gg n$, strains are localized in the GaAs layer as a bond length relaxation. The deviation is clearly larger than that in random alloys. At this moment it is not clear whether this comes from the long-range order or interface effects. Experiments with various m/n ratio will clarify this point.

References

- 1) H. Oyanagi, Y. Takeda, T. Matsushita, T. Ishiguro, T. Yao and Y. Sasaki: Proc. of 3rd Int. Conf. on Superlattices, Microstructures and Microdevices, Chicago, 1987.
- 2) H. Oyanagi, T. Matsushita, H. Tanoue, T. Ishiguro, and K. Kohra: Japan. J. Appl. Phys., **24** (1985) 610.
- 3) H. Oyanagi, Y. Takeda, T. Matsushita, T. Ishiguro, and A. Sasaki: Phys. Conf. Ser. No79 (1986) 295.

Bond Length Relaxation around Isoelectronic Dopants in InP Studied by Fluorescence-Detected EXAFS

Hiroyuki Oyanagi, Yoshikazu Takeda*, Tadashi Matsushita**,
Takehiko Ishiguro, Takafumi Yao and
Akio Sasaki*

Electrotechnical Laboratory, Sakuramura, Niiharigun, Ibaraki 305

*Department of Electrical Engineering, Kyoto University, Kyoto 606

**National Laboratory for High Energy Physics, Tsukubagun, Ibaraki 305

INTRODUCTION

Dislocations in bulk crystals can be reduced by In-doping in GaAs or co-doping of Ga and As in InP. The local structure around impurities is a key to understand how isoelectronic impurities are related with dislocation-free crystal growth. The local structure around doped Ga and As impurities in InP has been studied *as-grown* by fluorescence-detected EXAFS technique.

EXPERIMENTAL AND RESULTS

Ga/As-doped InP is a bulk crystal with a low dislocation density prepared by a magnetic field-applied LEC method with a small temperature gradient. The concentration of Ga and As was $1.16 \times 10^{19}/\text{cm}^3$ and $7.32 \times 10^{19}/\text{cm}^3$, respectively. Dilute (In,Ga)(As,P) alloys of InP-rich composition (Ga- and As-composition less than 0.1), lattice-matched to InP, was grown by LPE at 650 °C. X-ray filters (Zn and GeO_2) and a Si(Li) solid state detector were used.

In Fig. 1, (a) and (b) indicate the Fourier transform results of the As K-EXAFS data for Ga/As-doped InP and non-doped InAs, respectively. The magnitude (dotted line) and imaginary part (solid line) are plotted as a function of radial distance R in Å. The determined As-In distance in Ga/As-doped InP

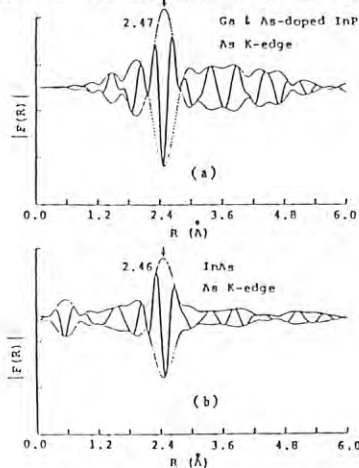


Fig. 1

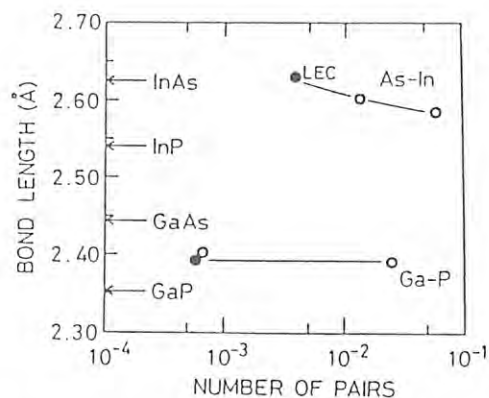


Fig. 2

(2.62 Å) is close to that in pure InAs (2.623 Å) rather than the In-P distance (2.541 Å). These results indicate that the nearest In atoms are displaced along the $\langle 111 \rangle$ direction by 0.08 Å, which amounts to 3 % *bondlength-mismatch*. The determined Ga-P distance (2.39 Å) is much shorter than the In-P distance (2.54 Å) but rather close to the Ga-P distance in pure GaP (2.360 Å). As a result, P atoms are displaced by 0.15 Å toward Ga atoms along the $\langle 111 \rangle$ direction.

Figure 2 shows the obtained bond lengths as a function of number of bond pairs. For the As-In and Ga-P distances in Ga/As-doped InP, the observed values (closed circle) are rather close to those in binary compounds than the interatomic distance of host lattice. The deviations are consistent with those observed for dilute (In,Ga)(As,P) alloys (open circles). The present result¹⁾ indicates that the *host lattice* relaxes, i.e., the nearest neighbor (host) atoms are displaced along the $\langle 111 \rangle$ direction until a bond length mismatch (3-6 %) is accommodated. This impurity-originated lattice relaxation may contribute to delocalize strains which otherwise result in dislocations, by averaging out localized strains.

REFERENCES

- 1) H. Oyanagi, Y. Takeda, T. Matsushita, T. Ishiguro, and A. Sasaki: *Proc. of 14th Int. Symp. on GaAs and Related Comp., Crete, 1987*.

CRYSTAL STRUCTURE ANALYSIS OF ω -AMINO ACID: PYRUVATE AMINOTRANSFERASE
PRELIMINARY RESULT FROM 2.3Å RESOLUTION ELECTRON DENSITY MAP

Nobuhisa Watanabe^{1,3}, Kiwako Sakabe², Noriyoshi Sakabe³, Tsuneyuki Higashi⁴,
Kyoyu Sasaki⁵, Sigeo Aibara⁶, Yuhei Morita⁶, Kazuo Yonaha⁷, Seizen Toyama⁷ and
Hirohito Fukutani¹.

1. Inst. of Physics, Univ. of Tsukuba, Ibaraki 305,
2. Dept. of Chemistry, Nagoya Univ., Nagoya 464,
3. National Lab. for High Energy Physics, Tsukuba, Ibaraki 305,
4. Dept. of Pharmaceutical Science, Kyoto Univ., Kyoto 606,
5. College of Medical Technology, Nagoya Univ., Nagoya 461,
6. The Reserch Inst. for Food Science, Kyoto Univ. Uji 611,
7. Dept. of Agricultural Chemistry, Ryukyu Univ., Naha 903, Japan.

INTRODUCTION

ω -Amino acid : pyruvate aminotransferase from *pseudomonas* SP. F-126 catalyzes the reversible transfer of an amino group from β -alanine to pyruvate. Such transamination is an essential reaction in the last stage of pyrimidine nucleotide metabolism. This enzyme is a tetramer of four identical subunits and the molecular weight is about 172,000. Each subunit consist of approximately 400 amino acid residues, and 70% of the primary sequence has been determined by K. Yonaha. One molecule of pyridoxal- 5'-phosphate and one molecule of vitamin B6 compound are found in one tetramer. The function of these coenzymes is still unsettled. The crystals are in space group I222 with the unit cell dimensions of $a=124.76\text{\AA}$, $b=137.90\text{\AA}$ and $c=61.45\text{\AA}$. Here we report on the analysis of the data and the structure model of the enzyme.

EXPERIMENTAL

Crystals were grown in a solution of 0.02 potassium phosphate buffer at pH 7.66 containing 0.5 saturated ammonium sulfate. Two heavy atom derivatives have been prepared by soaking crystals in each solution containing 2mM mersalyl and 2mM K_2PtCl_4 , respectively.

All diffraction data were collected using a Weissenberg camera (BL6A2) with an Imaging Plate and BA100. With this system, we could collect all independent data about one axis using only one crystal with an exposure time of less than one hour. The intensity data of native crystal and $PtCl_4$ derivative were collected with the rotation of the crystal about two axes (b and c). Those of mersalyl derivative were collected only about c axis. The evaluation of the intensity data is summarized in Table I.

Table I. Evaluation of Intensity Data.

Name	Resolution	λ	Data No.	R(merge)	No. of Site
Native	1.8Å	1.488Å	28900	6.7% ^a	-
mersalyl	2.3Å	1.004Å	19784	4.6%	1
			9077 ^b		
PtCl ₄ ⁻	1.8Å	1.004Å	18609	6.7%	4
			11364 ^b		

a: only about b axis data
b: No. of anomalous data

RESULTS AND DISCUSSION

The heavy atom positions were obtained from a difference Patterson and a cross Fourier's technique. The positional parameters were refined using a least-squares technique. This refinement resulted in a mean figure of merit of 0.65 with 17,953 data of 2.3Å resolution.

Figure I shows two sets of sections of the electron density map. The boundary of the tetramer is easily recognized and the contact between monomer and monomer is stronger than that

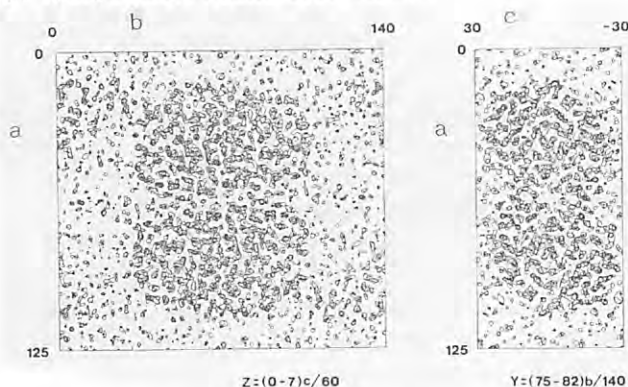


Fig. I. Composit Fourier Map of 2.3Å resolution.

of dimers. The dimensions of one subunit are $40\text{\AA} \times 45\text{\AA} \times 55\text{\AA}$.

The subunit contains twelve helixes and two beta-sheets. Many helical structures exist at the surface of the subunit. Figure II shows an element of the secondary structure and a partial arrangement of polypeptide chain in the subunit, which consists of two domains. This secondary structure is quite different from that of cytosolic aspartate aminotransferase, which primary sequence has no homology with this enzyme. The tracing of the chain is in progress using polyserine chain on 2.3Å map with FRODO on PS340.

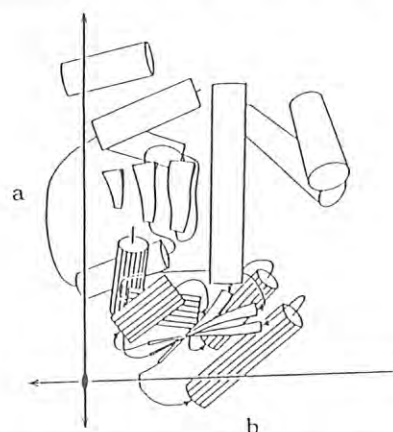


Fig. II. Model of the subunit. The Rods are helices, and the plates are β -sheets. The two domains are distinguished by stripes.

We are very thankful to Dr. K. Namba of the Hotani Project in ERATO for giving us a chance to use the BA100 system.

REFERENCE

N. Watanabe *et al.* *Acta Cris.*, A43 (1987) C-11.

HIGH RESOLUTION DATA COLLECTION OF STREPTOMYCES ERYTHRAEUS TRYPSIN USING THE IMAGING PLATE MOUNTED IN A WEISSENBERG CAMERA

Takashi YAMANE, Hideki TSUTSUI, Masanao KOBUE, Takeru TOIDA, Tamaichi ASHIDA, Yasushi KAWATA[†] and Fumio SAKIYAMA[†]

Faculty of Engineering, Nagoya University, Chikusa-ku, Nagoya 464.

[†] Institute for Protein Research, Osaka University, Yamadaoka, Suita-shi, Osaka 560.Introduction

The trypsin like serine protease (SET) secreted by *Streptomyces erythraeus* does not exhibit the property of self-autolysis at its active pH region. SET is therefore suitable to study the relationship between the function and structure. In order to determine the three-dimensional structure of SET precisely and obtain some informations for the molecular design of protease the X-ray structure analysis was undertaken.

SET crystallizes to a trigonal system, P3₂1 with the cell parameters of $a=47.0$ and $c=178.9\text{\AA}$. The structure has been determined by the heavy atom method at 3.1\AA resolution, where the X-ray data were collected using a diffractometer equipped on a rotating anode X-ray generator. The model structure of SET is shown in Fig. 1. The higher resolution data were requested to refine the model structure. The data collection less than 3.1\AA resolution is, however, difficult because of the rather long c parameter. Therefore the high resolution data up to $d=1.7\text{\AA}$ was measured using SR sources.

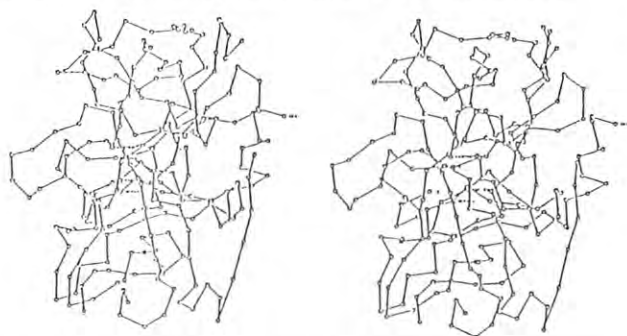


Fig. 1. Stereo view of the main chain folding of *Streptomyces erythraeus* trypsin.

Experimental

The reflection intensities were collected using Sakabe's Weissenberg camera associated with BL-6A2. Atmospheric temperature in the hatch was held at about 12°C. For the data collection the imaging plate with the dimensions of 40x20cm was mounted in the film cassette, of which radius is 28.65cm. The wave length was set to 1.488\AA. Under these conditions the data up to 1.7\AA resolution could be measured. A crystal is mounted in a glass capillary coinciding its c -axis to the camera rotation axis. The minimum separation between the l -layer lines is 3mm.

Thus the oscillation range of 6° and the ratio of oscillation angle vs. cassette moving distance of 3°/mm were selected. These resulted to the cassette movement of 2mm. To cover the independent region for oscillation, a total of 6 data sets (N31 to N36) were measured. The exposure time was 2.5min. for each data set by the use of the imaging plate, while it was about 2hr if the Kodak DEF-5 X-ray film was used.

Results

The imaging plates were digitized on a BA100 scanner using a 100μm raster step size, and processed with the use of WEIS16 which is the revised version of WEIS(1) to process the imaging plate data. The results are summarized in Tables 1 and 2. A total of 10111 independent reflections from 15015 observed ones were obtained and the merging R factor (MR) is 0.124. This data set was merged to the diffractometer data, giving 12173 reflections and MR=0.107. The refinement of the model structure is being continued using this new data set.

The authors are greatly indebted to Prof. N. Sakabe and Dr. A. Nakagawa, Photon Factory, KEK, for their kind help and suggestions in the data collection. We are also grateful to Dr. K. Nanba of Hotani project in ERATO for making available the BA100 scanner system.

Table 1. Processing results of N31

$d/\text{\AA}^3$	No. of ref.	$\langle I \rangle$	$\langle \sigma I \rangle$
17.0	12	247	15
8.5	28	418	34
5.7	78	1148	85
4.3	194	1409	119
3.4	267	1862	160
2.8	281	1579	113
2.4	322	1026	77
2.1	367	668	60
1.9	386	346	40
1.7	381	167	27

Table 2. Summary of the data processing (1.7\AA resolution)

No. of data set	Oscillation range	No. of reflections	
		rejected	accepted
N31	0° ~ 6°	722	2316
N32	5 ~ 11	802	2383
N33	10 ~ 16	420	2546
N34	15 ~ 21	658	2715
N35	20 ~ 26	523	2552
N36	25 ~ 31	701	2503

Reference

- 1) T. Higashi, J. Crystallogr. Soc. Jpn., 28 (1986) 356.

DIFFRACTION EXPERIMENTS OF HYDROGENASE AT TWO WAVELENGTHS

Yoshiki Higuchi, Kiyoshi Fujimoto, Yukio Morimoto and Noritake Yasuoka

Basic Research Laboratory, Himeji Institute of Technology,
2167 Shosha Himeji Hyogo 671-22Introduction

Hydrogenase is an enzyme which catalyzes reversible dehydrogenation of molecular hydrogen. The solubilized hydrogenase (hydrogen : ferricytochrome c_3 oxido-reductase, EC 1.12.2.1) from *Desulfovibrio vulgaris* Miyazaki F (DvMF) has 89000 of molecular weight and has two or three 4Fe-4S type clusters as the active center. It is well known that anomalous dispersion of heavy atoms in the protein molecules may give useful information to determine the location of them, and that the anomalous scattering power is depend on the wavelength of x-ray. X-ray beam from synchrotron radiation (SR) is suitable for the structure analysis using anomalous scattering because x-ray of desired wavelengths can be easily obtained. In this report, we describe the collection of intensity data from DvMF hydrogenase crystal at wavelengths of 1.388 and 1.736 Å of x-ray.

Experimental and Results

Membrane-bound hydrogenase was solubilized by trypsin digestion from the wet cells of DvMF bacterium cultured by Ajinomoto Co. The protein was isolated¹ and purified² as described before. Single crystals of freshly prepared hydrogenase were obtained by sitting-drop vapor diffusion method from 15-20% (w/w) polyethylene glycol 1000 buffer solution (25mM Tris-HCl, containing 0.05% Na₂S, pH=7.5). X-ray intensity data were collected at 5°C using a Weissenberg camera designed for macromolecular crystallography by Sakabe et al.³ (r=430.5 mm) installed in BL-6A2. The wavelengths of x-ray used were 1.736 Å (this is a wavelength near absorption edge of Fe atom and imaginary component (f'') of atomic scattering power is comparably large) and 1.388 Å (f'' component of this wavelength is not so large) from SR of National Laboratory for High Energy Physics. The diffraction patterns were recorded on Fuji Film 'Imaging Plate' (20 X 40cm), and read out by a Fuji Film BA100. The beam pass from collimator to film was filled with He gas to reduce air scattering. The hydrogenase crystals of 0.2X0.25X0.8 mm (Crystal-I) and 0.35X0.3X0.8 mm (Crystal-II) were sealed in glass tubes, and mounted on goniometer head, being one crystal axis visually parallel to the spindle axis of the camera. Then the axes of crystals were exactly aligned manually to the spindle axis considering the diffraction cones of small angle oscillation photographs recorded on Polaroid film (exposure time : 20s/film, oscillation angle : 1 degree). The collected intensity patterns on Imaging Plate were processed by program WEIS developed by Higashi et al.⁴ in order to obtain indexed F-data. For Crystal-I, 34590 of Bijvoet pair data ($h k l$ and $h k -l$)

have been collected to about 3.0Å from 7 Weissenberg photographs using 1.736 Å wavelength of x-ray. On the other hand, for Crystal-II, Bijvoet reflections data ($h k l$ and $h -k l$) have been obtained to about 3.0 Å from 7 and 12 Weissenberg photographs using x-ray of 1.736 and 1.388 Å, respectively. The details of the data collection procedure are listed in Table I. Hydrogenase crystals showed distinct decay during data collection at room temperature. Decreasing temperature down to 5°C, however, showed great improvement to reduce radiation damage of the crystals. It is expected that the difference of Bijvoet data from Crystal-I and that of intensity data from two different wavelengths of x-ray may give useful information in order to determine the positions of Fe atoms. Data processing, evaluation of Bijvoet differences and comparison with data obtained by 4-circle diffractometer using rotating anode are now in progress.

We are indebted to Prof. Noriyoshi Sakabe, Dr. Atsushi Nakagawa, Dr. Kiwako Sakabe and Dr. Tsuneyuki Higashi for their technical advice and use of computer programs. We also thank Dr. Keiichi Namba in Houtani Project, ERATO, for use of a Fuji Film BA100 system.

Table I
Experimental Condition of Data Collection by Weissenberg Camera (r=430.5mm)

Crystal	I	II	II
Wavelength(Å)	1.736	1.736	1.388
Beam current(mA)	241-230	229-221	179-173
Crystal			
rotation axis	c*	b*	b*
Oscillation			
angle(ω :deg)	15.45	16.20	8.40
Film moving			
distance(d:mm)	10.3	5.4	4.2
Ratio of ω and d	1.5	3.0	3.0
Repeat of			
oscillation	30	20	8
Rotation speed			
of ω (deg/s)	2.0	2.0	2.0
Exposure time (s)	463.5	324	67.2
Number of film	7	7	12

References

- 1) T.Yagi, K.Kimura, H.Daidoji, F.Sakai, S.Tamura and H.Inokuchi, *J. Biochem. (Tokyo)*, **79**, 661 (1976)
- 2) Y.Higuchi, N.Yasuoka, M.Kakudo, Y.Katsube, T.Yagi and H.Inokuchi, *J. Biol. Chem.*, **262**, 2823 (1987)
- 3) N.Sakabe, *J. Appl. Cryst.*, **16**, 542 (1983)
- 4) H.Higashi, N.Sakabe, *The report for a Grant-in-Aid for Scientific Research from Ministry of Education*, **52** (1984)

DEVELOPMENT OF A RAPID LAUE-DIFFRACTION TECHNIQUE FOR PROTEIN CRYSTALLOGRAPHY

Yoshinori SATOW, Yoshiyuki AMEMIYA, Tadashi MATSUSHITA and Richard Paul PHIZACKERLEY*

Photon Factory, National Laboratory for High Energy Physics,
Oho-machi, Tsukuba-gun, Ibaraki 305, Japan,

and *Stanford Synchrotron Radiation Laboratory, Stanford Linear Accelerator Center,
P.O.Box 4349, Bin 69, Stanford University, Stanford, California 94305, USA.

By combining focusing optics with an imaging plate (IP) system, we have been developing a rapid Laue-diffraction technique for protein crystallography¹⁾. This technique aims at giving a diffraction pattern with a short exposure time in order to perform time-resolved structural studies. Diffraction patterns from such protein crystals as FUT-inhibited trypsin (by courtesy of Dr. A.Itai) and hen egg white lysozyme were recorded with exposure times of few milliseconds.

The focusing optics applied here utilizes a vertically bent 1 m-long plane mirror of fused quartz, which was recently implemented into BL-6A. A synchrotron radiation beam output through beryllium windows (total thickness of 1.2 mm) was reflected by the focussing mirror set to a grazing angle of 3.3 mrad (a critical wavelength of 1 Å). X-rays irradiated to specimens at 17.1 m from the source point (Fig. 1) were about 10 times intense when compared to those of an unfocused beam, and were mostly ranged between 0.9 and 1.7 Å (an aluminium filter of 0.02 mm thick was used). Specimens were mounted on an Enraf-Nonius oscillation camera with a specimen-to-film distance of 90-100 mm and a collimator of an aperture size of 0.23 mm. Quantitative evaluation of wavelength distribution of the beam as well as its degree of polarization is under way by use of diffraction profiles from a nonoriented polyethylene plate.

The IP (prod. Fuji Photo Film Co., Ltd.) utilizes photostimulated luminescence from its phosphor surface²⁾. The most advantageous characteristic of the IP is in its high quantum efficiency. From our preliminary application of the IP to Laue diffraction, the X-ray dose required is approximately one thirtieth of that for the highly sensitive X-ray film¹⁾. The multiple film technique as is usually required for X-ray films is unnecessary for the IP to cover the full range of intensities, so that this will greatly simplify corrections for intensity response to X-rays. In the present experiments, diffraction patterns were read out by a drum-type scanner which had been newly constructed to further improve a high quantum efficiency and wide dynamic range of the IP as well as its spatial resolutions³⁾.

Diffraction patterns of good quality were obtained by 7 ms exposures for the lysozyme crystal with stored electron current of 159 mA (Fig. 2). Since the band pass of the beam was restricted by the optics, reflections including

weak ones were recorded well resolved each other on the patterns. Peak intensities for stronger reflections yielded about 12000 photons/0.01 mm². After continuous 3 s irradiation of the beam to the crystal, radiation damage on it was apparently noticed. On the other hand, when short irradiation intervals of 50-700 ms were applied, no damage was appreciable even after beam irradiation of a total of 10 s. Therefore, more than thousand exposures could be obtained from one crystal in actual data collection.

Both the 8 ms and 0.7 ms exposures for the trypsin and lysozyme crystals, respectively, were recorded well featured, but numbers of photons picked up in the patterns were insufficient for quantitative analyses. Thus we are preparing a double-focusing toroidal mirror in order to increase photon flux of the beam.

¹ Y.Satow, Y.Amemiya & T.Matsushita; PF Activity Report 1985, p 326.

² J.Miyahara, K.Takahashi, Y.Amemiya, N.Kamiya & Y.Satow; Nucl. Instr. Meth. A246 (1986), 572.

³ Y.Amemiya, T.Matsushita, A.Nakagawa, Y.Satow, J.Miyahara & J.Chikawa; to be published in Nucl. Instr. Meth.

Fig. 2

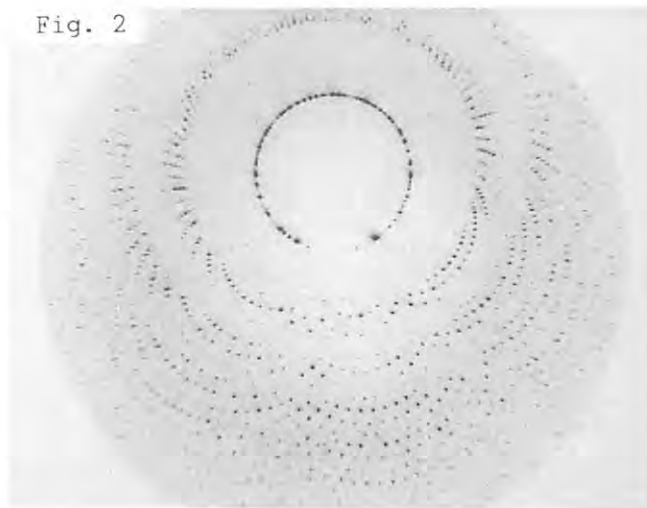
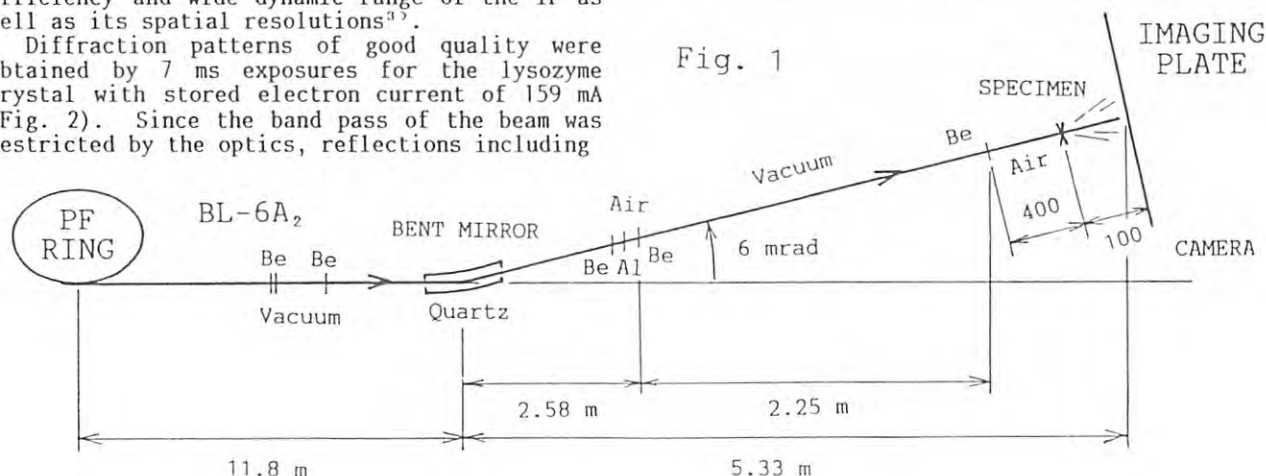


Fig. 1



HIGH PRESSURE EQUATION OF STATE OF α -Mn TO 42 GPa

Kenichi TAKEMURA¹⁾, Osamu SHIMOMURA¹⁾, Kiyoshi HASE²⁾, Yasuhiko FUJII²⁾,
Takumi KIKEGAWA³⁾, Keiichi OKUYAMA⁴⁾, Atsushi IZAWA⁵⁾,
Kaoru TAKANO⁵⁾ and Katsutoshi AOKI⁶⁾

1) National Inst. for Research in Inorganic Materials, Sakuramura, Ibaraki 305

2) Faculty of Engineering Science, Osaka University, Toyonaka, Osaka 560

3) Photon Factory, KEK, Ohomachi, Ibaraki 305

4) Applied Science for Energy, Muroran Institute of Technology, Muroran 050

5) Inst. of Materials Science, The Univ. of Tsukuba, Sakuramura, Ibaraki 305

6) National Chemical Laboratory for Industry, Yatabe, Ibaraki 305

Introduction

α -Mn, the most stable form of manganese metal under normal conditions, has an exotic crystal structure. The purpose of the present study is to investigate the stability of α -Mn structure under pressure.

Experimental and Results

The powdered specimen (99.995%, annealed) was loaded into a gasketed diamond anvil cell together with an alcohol pressure medium. The pressure was determined by the ruby fluorescence method. Diffraction patterns were obtained in energy dispersive mode at BL-6B. All measurements were done at room temperature. Typical diffraction patterns of α -Mn are shown in Fig.1. No structural phase transition has been found to 42 GPa. Intensity ratio of diffraction peaks showed no significant change with pressure, indicating that the atomic positions were almost unchanged. The pressure-volume data are fitted to the Birch equation of state. The bulk modulus and its pressure derivative at atmospheric pressure are determined as $B_0 = 131 \pm 6$ GPa and $B'_0 = 6.6 \pm 0.7$, respectively. The bulk moduli B_0 of 3d transition metals are shown in Fig.2^{1),2)}. The small bulk modulus of α -Mn results from the large local magnetic moment of Mn atom, which persists in the paramagnetic state³⁾. The pressure derivative of the bulk modulus of α -Mn ($B'_0=6.6$) is significantly larger compared to the normal 3d metals. The rapid increase of the bulk modulus of α -Mn with pressure may arise from the loss of magnetic moment of Mn atoms caused by the delocalization of 3d electrons.

References

- 1) Moruzzi V L, Janak J F and Williams A R 1978 Calculated Electronic Properties of Metals (New York : Pergamon)
- 2) Janak J F and Williams A R 1976 Phys. Rev. B14 4199
- 3) Mōri N, Takahashi M and Oomi G 1983 J. Magn. Magn. Mat. 31-34 135

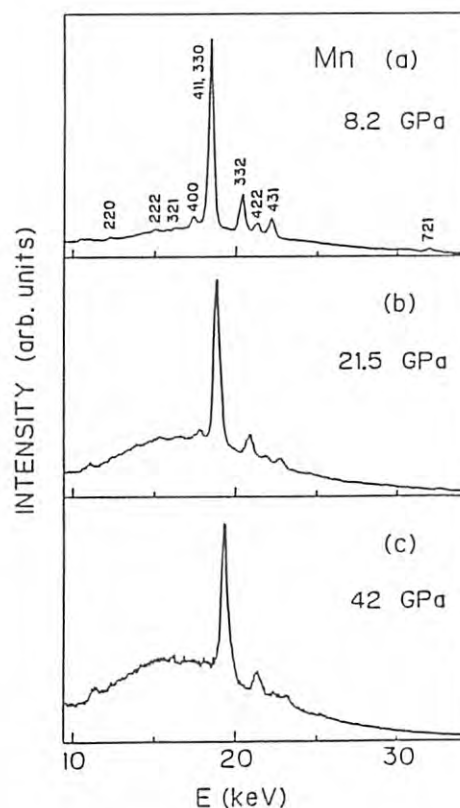


Fig.1 Energy dispersive powder X-ray diffraction patterns of α -Mn under pressure.

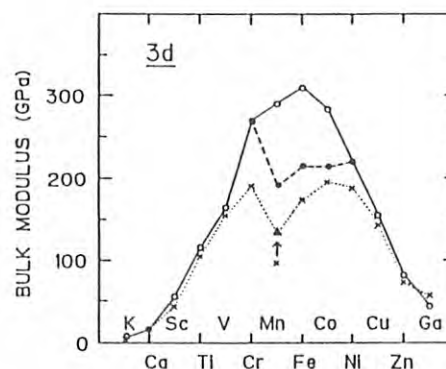


Fig.2 Bulk moduli of 3d metals.
x : obs. Δ : present result.
O : cal. (nonmagnetic, ref.1)
 \bullet : cal. (magnetic, ref.2)

PHASE TRANSITIONS OF BLACK PHOSPHORUS AND BLACK PHOSPHORUS-ARSENIC
ALLOY AT VERY LOW TEMPERATURES AND HIGH PRESSURES

Ichimin SHIROTANI, Kazuhiko TSUJI⁺, Haruki KAWAMURA⁺⁺, Osamu SHIMOMURA⁺⁺⁺,
Kazuhiko TSUBURAYA, Keiichi OKUYAMA, Shigemitsu Shiba, Osamu ENDO⁺, Takumi
KIKEGAWA⁺⁺⁺⁺, and Tetsuo NAKAJIMA⁺⁺⁺⁺

Muroran Institute of Technology, 27-1, Mizumoto, Muroran 050

⁺ Faculty of Science and Technology, Keio University, Hiyoshi, Yokohama 223

⁺⁺ Himeji Institute of Technology, 2167, Shosha, Himeji 671-22

⁺⁺⁺ National Institute for Research in Inorganic Materials, Sakura, Niihari,
Ibaraki 305

⁺⁺⁺⁺ Photon Factory, National Laboratory for High Energy Physics, Oho-machi,
Tsukuba-gun, Ibaraki 305

The superconductivity of phosphorus and phosphorus-arsenic alloy has been studied at low temperatures and high pressures^{1,2)}. This superconductivity is closely related to pressure-induced phase transitions of phosphorus. The black phosphorus (black P) transforms an orthorhombic structure to a rhombohedral structure and then further to a simple cubic form with increasing pressure at room temperature³⁾. The pressures of the phase transitions at liquid nitrogen temperature are higher than those at room temperature⁴⁾. By using synchrotron radiation, we have investigated the pressure-induced phase transitions of black P at liquid helium temperature.

A new diamond-anvil cell was developed for X-ray diffraction measurement which makes possible a continuous change in the pressure at low temperatures⁵⁾. The diffraction patterns of black P and NaCl were recorded at $2\theta = 21^\circ$. The diffraction lines of NaCl were used to determine the pressure value according to Decker's scale.

Figure 1-a and 1-b show energy dispersive X-ray diffraction profiles of the black P at about 10 K and at high pressures. A single-phase pattern of the orthorhombic form was found at 3.3 GPa. The transition to the rhombohedral structure started at around 10 GPa under 10 K. The pressure of the

transition risen from about 6 GPa at 77 K to about 10 GPa at 10 K. The element transformed from the rhombohedral structure to the simple cubic form at around 16 GPa under 10 K. This value was about 6 GPa higher than that at 77 K. The coexistence of two or three phases was observed in a wide pressure range at 10 K. As the pressure was reduced from 25 GPa to 16.8 GPa, the simple cubic phase began to be transformed into the rhombohedral one. This phase was stable on a decrease in the pressure. The diffraction lines of the orthorhombic structure at 10 K could not be observed even in the very low pressure region.

- 1) H. Kawamura, I. Shirotani and K. Tachikawa, Solid State Commun., 49, 879(1984), *ibid*, 54, 775(1985).
- 2) I. Shirotani, H. Kawamura, K. Tsuburaya and K. Tachikawa, Jpn. J. Appl. Phys., 26, supplement, 26-3, 921(1987).
- 3) J. C. Jamieson, Science, 139, 1291(1963).
- 4) I. Shirotani, H. Kawamura, K. Tsuji, K. Tsuburaya and K. Tachikawa, Bull. Chem. Soc. Japan, in press.
- 5) K. Tsuji, Solid state Physics under pressure, ed by S. Minomura (KTK Scientific Publisher, Tokyo, 1985), P. 375.

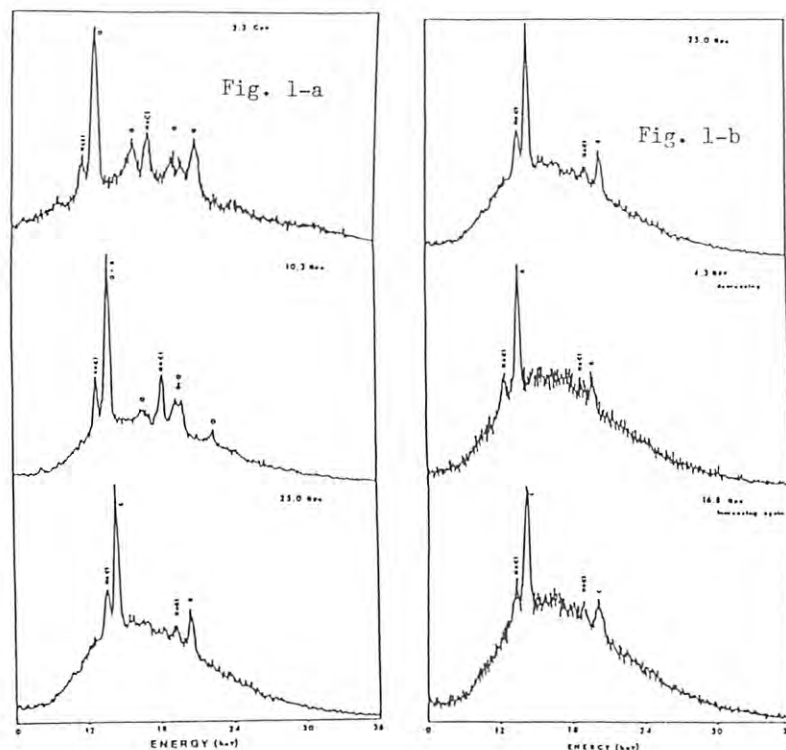


Figure 1-a. Energy dispersive X-ray diffraction profiles of black phosphorus at about 10 K and at high pressures.

Figure 1-b. Energy dispersive X-ray diffraction patterns at about 10 K under decreasing pressure.

O: orthorhombic
R: rhombohedral
C: simple cubic

X-RAY DIFFRACTION STUDY UNDER PRESSURE USING AN IMAGING PLATE

O. Shimomura^{1,4}, K. Takemura¹, T. Fujimura², K. Hase³, T. Kikegawa², Y. Ohishi³,
K. Okuyama⁴, S. Shiba⁴, Y. Fujii³, T. Matsushita² and Y. Amemiya²

¹NIRIM, Sakura-mura, Ibaraki 305, Japan

²KEK-PF, Oho-machi, Ibaraki 305, Japan

³Osaka Univ., Machikaneyama, Toyonaka 560, Japan

⁴Muroran Inst. Tech., Mizumoto, Muroran 050, Japan

Introduction

Synchrotron Radiation (SR) has been proved to be a powerful tool for X-ray study under pressure. So far, an energy dispersive method has been used because the intensity of monochromatized beam is not so strong for the very small sample under pressure even when SR is used. In order to perform an angle dispersive method under pressure, we need to use one or two dimensional detector. Recently, a photo-stimulable phosphor film named an imaging plate (IP) has been successfully used as an X-ray detector at the Photon Factory. We tried to combine a diamond anvil cell, SR and IP.

Experiment

Experiments were performed at BL6B. X-ray was monochromatized by a portable type monochromator with double crystal setting of Si(111). The beam was impinged to a sample in a diamond anvil cell through a single pinhole collimator (0.2mm). The collimator and the cell were separately set on adjusting tables. Distance between the sample and an IP was 10 to 15 cm.

Results

A diffraction pattern of Ag in the diamond anvil cell was recorded on IP with exposure time of 10 min (Fig. 1). Figure 2 shows the treated profile of the pattern together with a densitometer trace of a photograph taken with the same condition as the IP. Enlarged sections in the center part show the fluctuation of the background. The middle of fig. 2 is a one pixel trace along the horizontal line through the center. The quality is slightly better than that of the densitometer trace (bottom). This means that the sensitivity is about 50 times better in case of the IP.

By utilizing the merit of digitally two dimensional data, a profile was obtained by integrating the intensity along the ring (Fig. 2 top). There are more than 200 points along the ring, so that the standard deviation is reduced by a factor of 15, as is clearly seen by comparing the top and middle profiles.

The full widths at half maximum of the strongest peak are 0.26mm for both IP and X-ray photograph.

Fig. 3 shows the diffraction profile of InSb with X-ray energy of 27.933 keV which is lower by 5eV than the K absorption edge of In. The relative intensity of 200 reflection is practically null because it is proportional to square of the difference of scattering factor of In and Sb. But it becomes 0.005 by using an anomalous scattering. This very weak peak is evidently seen in fig 3.



Figure 1. A diffraction pattern of Ag on IP.

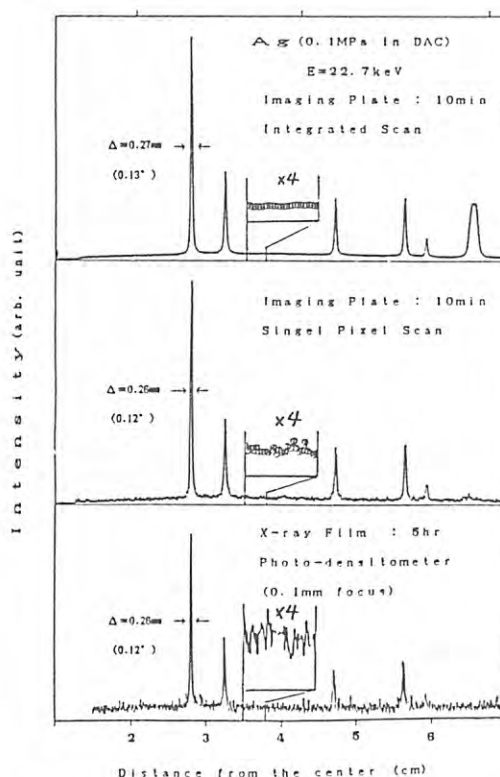


Figure 2. Treated profiles of Ag (see text).

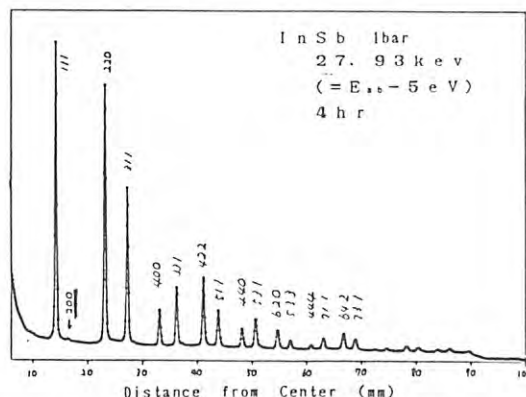


Figure 3. A diffraction pattern of InSb.

PRELIMINARY STUDY OF CHARGE DENSITY WAVE IN CHROMIUM

Masahiro MORI, Yorihiro TSUNODA⁺, Tetsuo NAKAJIMA⁺⁺, Ken-ichi OHSHIMA*, Masami YOSHIKAWA** and Tomoe FUKAMACHI**

Department of Physics, College of General Education, Nagoya University, Chikusa-ku, Nagoya 464

+ Department of Physics, Faculty of Science, Osaka University, Toyonaka, Osaka 560

++ Photon Factory, National Laboratory for High Energy Physics, Oho, Ibaraki 305

* Institute of Applied Physics, University of Tsukuba, Sakura, Ibaraki 305

** Saitama Institute of Technology, Okabe, Ohsato, Saitama 369-02

Introduction

Chromium is well known to have a spin density wave (SDW) state below 310K, in which the spin density varies sinusoidally in space. The period of the SDW is incommensurate with the lattice periodicity. Satellite reflections were observed with X-ray diffraction method¹⁾, whose period is one half of that of SDW. Main origin of these reflections is neither caused by the freezing of the transverse phonon mode modulation nor caused by the pure charge density modulation. Real main origin is the strain wave (SW) caused by the longitudinal lattice modulation. Two theoretical propositions are considered as the cause of this SW. One is the exchange striction model by Teraoka and Kanamori²⁾. The others is the two band nesting model developed by Nakajima and Kurihara³⁾ and Kotani⁴⁾. Charge density wave (CDW) is the leading role in the latter case. Therefore, this experimental aim is not the observation of SW but the observation of CDW hidden by the very large contribution of SW.

Experimental and Results

It has been 1.5 years before the completion of four circle diffractometer on 6C-BL. We had only one chance for an experiment. It could not be observed that CDW's contribution is included in the intensity of satellite reflections. Because the counting system had high background noise due to the unfinished diffractometer. The preliminary experiments have been done with the usual two-axis diffractometer, using on Cu-K x-ray radiation monochromated by PG. In order to reduce the strong fluorescent radiation, a sharp collimation system and an aluminium filter of

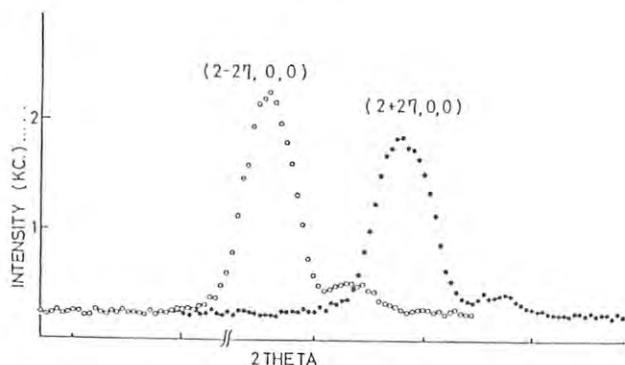


Fig.1. The comparison of both satellite reflections around 200 reflection at 150K.

suitable thickness were used. The specimen was a single crystal grown from the vapor of chromium iodide.

Fig.1 shows the scattered intensity of both satellite reflections observed around 200 reflection at 150K. This pattern was obtained by θ - 2θ scanning.

In the case of coexisting of SW and CDW, the atomic position with SW and the charge density is written as

$$r_c = r_c^0 + A \sin 2\eta \cdot \eta z^0 \quad (1)$$

$$\rho_c(r) = \rho_0(r) + \sigma(r) \cos 2\eta \cdot \eta z^0 \quad (2)$$

where $\rho_0(r)$ is the averaged electron density without CDW and $\sigma(r)$ is the CDW amplitude. Substituting (1) and (2) to the expression of the structure factor

$$F(k) = \sum \rho_c(r) e^{i k \cdot r} \\ = \sum (\rho_0(r) + \sigma(r) \cos 2\eta \cdot \eta z^0) \\ \times \exp\{i k \cdot (r_c^0 + A \sin 2\eta \cdot \eta z^0)\},$$

as the result of interference between both waves we obtain

$$|F(k)|^2 \approx |\rho_0(k)|^2 \delta(k - G) \\ + \frac{1}{2} \{ \rho_0(k) k \cdot A + \sigma(k) \}^2 \delta(k + 2\eta - G) \\ + \frac{1}{2} \{ \rho_0(k) k \cdot A - \sigma(k) \}^2 \delta(k - 2\eta - G).$$

The intensity ratio of the $(2-2\eta, 0, 0)$ and $(2+2\eta, 0, 0)$ peaks is written as

$$R = \frac{I(2+2\eta, 0, 0)}{I(2-2\eta, 0, 0)} = \left(\frac{\rho_0(k) k \cdot A - \sigma(k)}{\rho_0(k) k \cdot A + \sigma(k)} \right)^2$$

Assuming $\sigma(k) = 0$ and $|A| = 0.002a$, the intensity ratio of two peaks R is estimated to be 0.933 under the consideration of atomic form factor, Lorentz-polarization factor and Debye-Waller factor. Observed intensity ratio is 0.908. $\sigma(k=0)$ is estimated to be 0.008 electrons/atom from this experimental value, where we assumed the form factor of 3d-electrons for $\sigma(k)$. However, we should be more careful about the absolute value of CDW amplitude because the estimation of depends sensitively on the correction factors. This study needs more experiments in order to determine the CDW's amplitude and the contribution for this phase transition.

References

- 1) T. Tsunoda, M. Mori, N. Kunitomi, Y. Teraoka and J. Kanamori: Solid State Commun. **14**(1974)287
- 2) Y. Teraoka and J. Kanamori: Physica **86-88B** (1977)321; *ibid.* **91B**(1977)199
- 3) S. Nakajima and Y. Kurihara: J. Phys. Soc. Jpn. **38**(1975)330
- 4) A. Kotani: J. Phys. Soc. Jpn. **38**(1975)974

LOW TEMPERATURE AND HIGH PRESSURE X-RAY STUDY
ON THE PRESSURE-INDUCED PHASE TRANSITION OF AMORPHOUS SEMICONDUCTORS

Kazuhiko TSUJI, Motoharu IMAI, Osamu ENDO and Kenichi YAOITA

Department of Physics, Faculty of Science and Technology,
Keio University, Hiyoshi, Kohoku-ku, Yokohama 223

Introduction

Amorphous silicon and germanium prepared by vacuum evaporation (a-Si and a-Ge) have been found to show a pressure-induced semiconductor to metal transition accompanying a sharp resistance drop by six orders of magnitude.¹⁻²⁾ Their transition pressures are 10 GPa for a-Si and 6 GPa for a-Ge. These transitions are accompanied by a change of structure which is heterogeneous with a mixture of two metastable phases. The high pressure phase of a-Si below 15 GPa is reversible to the amorphous state after compression. On the other hand, the high pressure phases of a-Ge is irreversible to the amorphous state after compression. It transforms to the BC-8 structure, but in a few days it shows a further transformation to hexagonal 6H structure.²⁻³⁾

As potential barrier between two phases is usually high in covalent materials, there are many metastable forms of amorphous semiconductors under pressure. The purpose of the present study is to determine the temperature dependence of these pressure-induced phase transition.

At the first stage, we have performed the x-ray diffraction measurements for hydrogenated amorphous silicon (a-Si:H) under pressure at room temperature.

Experimental

A diamond-anvil cell was used for x-ray diffraction measurements which make possible a continuous change in the pressure at low temperatures.⁴⁻⁵⁾ Film of a-Si:H was prepared by glow discharge decomposition of silane.⁶⁻⁷⁾ At first a-Si:H was deposited on a aluminium substrate, and then the substrate was dissolved with acid. The mixture of a-Si:H and NaCl, which was used as a pressure marker, was put in a hole of gasket. Methanol and ethanol mixture was used as a pressure-transmitting medium.

Results and discussion

In the pressure range of 0-6 GPa, diffraction intensity shows a broad pattern which corresponds to the amorphous state. At 7.5 GPa, there appear peaks which correspond to the white-tin structure and the intensity increases rapidly above 10 GPa. In the Fig. 1, the intensity of (200) peak of white-tin structure is shown as a function of pressure. After compression at 10 GPa, diffraction intensity recovered to broad pattern, which is similar to evaporated a-Si:H. At 2 GPa after releasing pressure of 15 GPa, new peaks were observed which correspond to metastable form. In this case, tetragonal form, which ap-

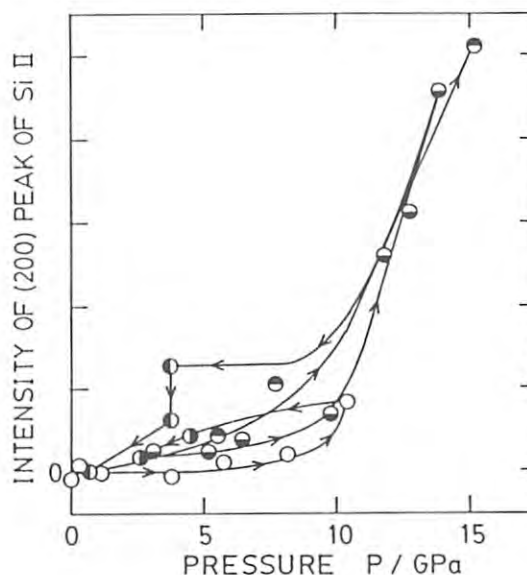


Fig. 1

peared after compression of a-Si:H at 18 GPa by using a opposed anvil device with solid pressure-transmitting medium, was not observed. This suggests the phase transition is sensitive to the degree of hydrostaticity of the liquid- and solid-pressure transmitting media. At 20 GPa, primitive hexagonal form was observed similar to c-Si.⁸⁾

References

- 1) K. Tamura, J. Fukushima, H. Endo, S. Minomura, O. Shimomura and K. Asaumi: J. Phys. Soc. Jpn. 36 (1974) 558.
- 2) O. Shimomura, S. Minomura, N. Sakai, K. Asaumi, K. Tamura, J. Fukushima and H. Endo: Philos. Mag. 29 (1974) 547.
- 3) S. Minomura: J. de Physique 42 (1981) C4-181.
- 4) N. Sakai, T. Kajiura, K. Tsuji and S. Minomura: Rev. Sci. Instrum. 53 (1982) 499.
- 5) K. Tsuji: Solid State Physics under Pressure, ed. S. Minomura (KTK, Tokyo, 1985) p.375.
- 6) S. Minomura and K. Tsuji: J. Non-Cryst. Solids 35&36 (1980) 513.
- 7) K. Tsuji and S. Minomura: J. de Physique 42 (1981) C4-233.
- 8) J. Z. Hu and I. L. Spain: Solid State Commun. 51 (1984) 263.

INTENSITY OF X-RAY (222) LINE IN InSb UNDER HIGH PRESSURE

Bin OKAI, Kaoru J. TAKANO*, Jiichiro YOSHIMOTO, Hiroki TAKAHASHI**,
Atsushi IZAWA* and Kazuhiko TSUJI***

*National Institute for Research in Inorganic Materials, Tsukuba, Ibaraki 305

**Institute of Materials Science, University of Tsukuba, Tsukuba, Ibaraki 305

***Institute for Solid State Physics, University of Tokyo, Roppongi, Tokyo 106

Department of Physics, Faculty of Science and Technology, Keio University, Hiyoshi, Yokohama 223

In general, no forerunners are observed prior to the phase transition of the first order. Thus, a noticeable change just before the semiconductor-to-metal transition, as reported by Yoder-Short et al. with Si and InSb¹⁾, seemed to be a promising candidate. By applying pressures on these materials, they found that near the transition to the metallic structure, the x-ray scattering of (222) sharply decreased. In Si, the (222) line is a forbidden reflection and in InSb, it is very weak. However, if there are anisotropic bonding charges between atoms in diamond structures, the intensity of (222), $I(222)$, increases with the pileup of interatomic charges. Thus, it was natural that Yoder-Short et al. ascribed the sharp decrease of $I(222)$ either to a smearing of the bonding charges or to an enhancement of phonon anharmonicity.

The aim of the present study is to examine the view of Yoder-Short et al. experimentally. If the intensity of (222) reflection, $I(222)$, of InSb and Si is suddenly decreased at a critical pressure, p_c (ca. 3 GPa for InSb), just before the transition for the reason as mentioned by Yoder-Short et al., the specimen will continue to show the decreased $I(222)$ above p_c as long as it retains the original diamond structure. The pressure range of diamond structure is extended by cooling the specimen. For this reason, the $I(222)$ of InSb was measured in the present study at liquid nitrogen temperature up to the transition pressure, 4.5 GPa.

The samples were single crystals cut parallel to (112). A diamond-anvil device was used. The [110] direction of the specimens was oriented vertically so that the (111) plane became the reflection plane to horizontally incident x-rays. The angle of reflection was set to $6\sim 7^\circ$ so that the (222) Bragg reflection coincided with the maximum of the SR spectra within the cell. Details of the apparatus are described elsewhere.²⁾

In Figs. 1 and 2 are shown the ratios $I(222)/I(111)$ and $I(222)/I(333)$, respectively. The open circles are measurements at room temperature and the closed ones are at 77K. The abrupt decrease at p_c as reported by Yoder-Short et al. was not observed in the present study; at liquid nitrogen temperature, neither sharp decrease nor sudden change in the gradient was detected at p_c . The variation of $I(222)$ with pressure was monotonous and continuous, as seen from Figs. 1 and 2. Therefore, we can conclude that the sharp decrease, as reported by Yoder-Short et al., was not due to a sudden smearing of the bonding charges nor abrupt change of the Dawson and Willis anharmonic force-constant³⁾; the sharp decrease of Yoder-Short et al. is not a forerunner of the transition. In the present study too, $I(222)$ decreased just before the transition at 77K. This is probably related to dynamics of the transition, e.g., partial transition or some misfits accompanied with it.

References

- 1) D. R. Yoder-Short, R. Colella and B. A. Weinstein: Phys. Rev. Letters **49**(1982) 1438.
- 2) K. Tsuji: Solid State Physics under Pressure, edited by S. Minomura, KTK and Reidel(1984) p.375.
- 3) D. Keating, A. Nunes, B. Batterman and J. Hastings: Phys. Rev. **B4**(1971) 2472.

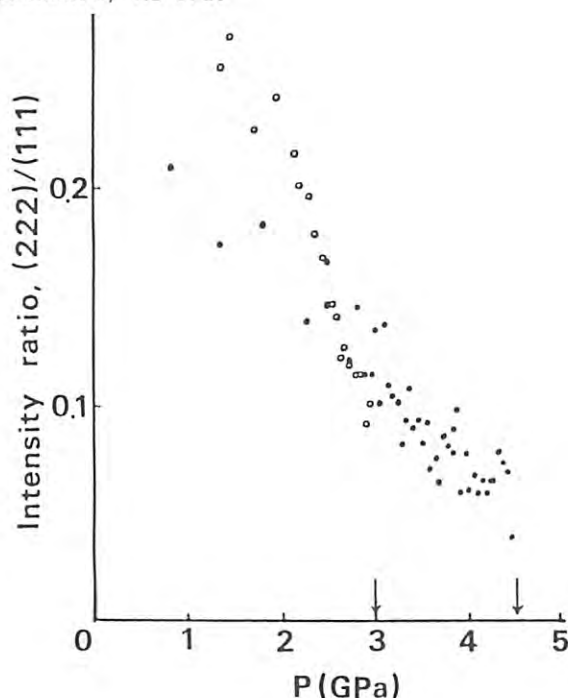


Fig.1

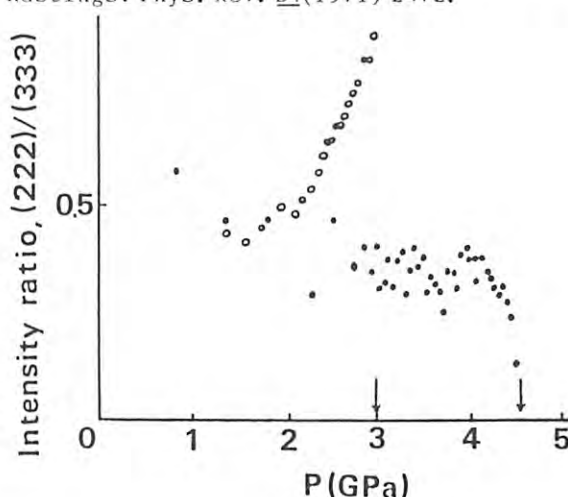


Fig.2

A New Kind of Interference Fringe Induced by X-ray Resonant Scattering

Masami YOSHIKAWA, Takaaki KAWAMURA⁺, Tomoe FUKAMACHI, Tetsuo NAKAJIMA⁺⁺,
Kenji EHARA, Fumito NISHI, Hitosi SUGAWARA

Saitama Institute of Technology, Okabe, Ohsato, Saitama 369-02

⁺Department of Physics, Yamanashi University, Kofu, Yamanashi 400

⁺⁺Photon Factory, National Laboratory for High Energy Physics, Oho, Ibaraki 305

X-ray resonant scattering causes characteristic changes in the x-ray diffraction intensities very near the absorption edge of the constituent atom of the crystal. This resonant scattering has a wide variety of applications in structure analysis of condensed matters such as the polarity of a polar crystal, the absolute structure and the phase problem. Studies of the resonant scattering especially very near the absorption edge are, however, not enough for these applications.

The thickness fringe (Pendellösung fringe) is caused by the interference between the incident and the diffracted x-rays in a perfect crystal. It has been observed by changing the thickness of the crystal continuously for a wedge-shaped crystal. The thickness fringe is used to determine the crystal structure factor precisely.¹⁾ The Pendellösung fringe has also been observed by changing the x-ray wavelength, which is applied to accurate determination²⁾ of structure factors for many crystals.

In this paper, we have observed a new kind of Pendellösung fringe which is induced by x-ray resonant scattering. The real part of anomalous scattering factor f' varies very much just below the absorption edge due to the resonant scattering, which results in oscillatory behaviors in the integrated reflection intensities as a function of x-ray energy. The samples were GaAs(100) single crystal³ which contained about 2×10^{20} atom/cm³ In as a dopant (denoted as Ga(In)As). The perfection of the samples was extremely good and almost free from lattice defects. The 200 diffracted intensities were measured as a function of x-ray energy across the Ga K-absorption edge. The measuring system was described elsewhere.³⁾

An example of the measured integrated intensities is shown in Fig. 1. The sample thickness is 150 μm . The large fluctuations of measured intensity seem to be caused by movement of the focussed points of x-ray source. We normalized the 200 reflection intensities (\circ) by the 400 intensities (\bullet) for eliminating the fluctuation of the x-ray source. The result is shown in Fig. 2 (a). Peaks are observed at 4 and 50 eV below the absorption edge. The solid line is the calculated intensities and the broken line is the calculated ones without the oscillating part. In Fig. 2 (b), the intensity curve for a sample of 90 μm thick is shown. The two peaks in Fig. 2 (a) and one peak in (b) are caused by the Pendellösung fringe due to x-ray resonant scattering. From the measurement of energy position of peaks and dips in the intensities, we can determine the real part of the anomalous scattering factor f' . We conclude that this new kind of Pendellösung fringe is useful to determine the anomalous scattering factor precisely near the absorption edge, especially below the edge.

The authors thank to Mr. Nagasawa of Iwaki Handoutai Corporation for supplying the GaAs sample.

References

- 1) T. Saka and N. Kato: Acta Cryst. A42, (1986) 469
- 2) T. Takama, M. Iwasaki and S. Sato: Acta Cryst. A36 (1980) 1025
- 3) M. Yoshizawa, T. Kawamura, K. Ehara, H. Sugawara, T. Nakajima, T. Fukamachi and K. Hayakawa: P. F. Activity Report 4 (1986) 161

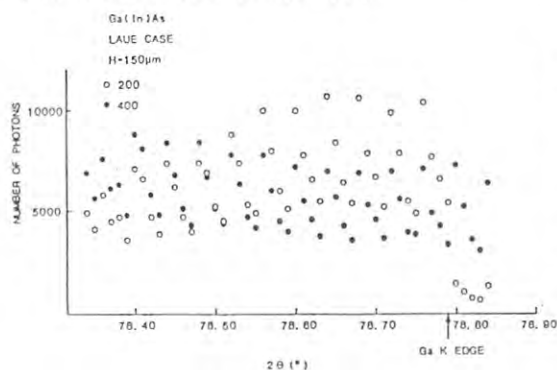


Fig. 1

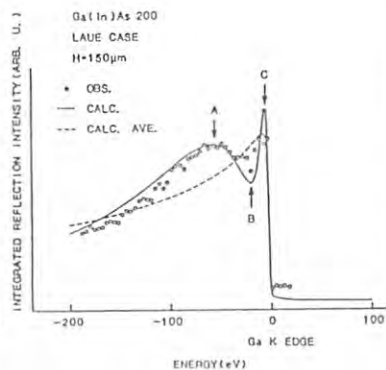


Fig. 2 (a)

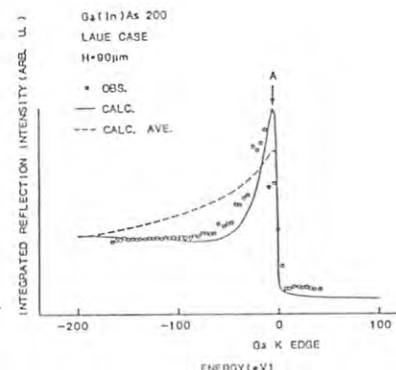


Fig. 2 (b)

ABSOLUTE LATTICE PARAMETER MEASUREMENT OF GaAs CRYSTALS USING MONOCHROMATIC SYNCHROTRON RADIATION

Koji USUDA, Shigeru YASUAMI, Yasuo HIGASHI*, Hiroshi KAWATA* and Masami ANDO*

Research and Development Center, Toshiba Corporation
1, Komukai Toshiba-cho, Saiwai-ku, Kawasaki 210, Japan
* Photon Factory, National Laboratory for High Energy Physics
Ohomachi, Tsukuba-shi, Ibaraki 305, Japan

Introduction

There are several inconsistent reports¹⁻³⁾ on variations in GaAs lattice parameter ($\Delta d/d \sim 10^{-5}$) with non-stoichiometry and with defects. When the measurement is carried out by Bond's method⁴⁾, the accuracy is limited by the angular divergence ($\sim 10^{-3}$ rad) and wavelength dispersion ($\Delta\lambda/\lambda \sim 10^{-4}$ order) of incident X-ray beams. We constructed a high-resolution diffractometer with 3-crystal arrangement using monochromatic synchrotron radiation, and hence the lattice parameter variation can be discussed with 10^{-6} accuracy.

Experimental

Figure 1 shows a plan view of the present diffractometer set-up at BL-6C₂. The 1st crystal is a (111) channel-cut Si crystal. The 2nd crystal is a monolithic monochromator, which has two reflection planes (335, $\bar{5}3\bar{5}$). A Si crystal was used as a reference sample to calibrate the system resolution regarding its lattice parameter as being $d = 5.4310652$ Å, as derived by Deslattes et al⁵⁾. As a result, an X-ray beam with 1.3536 Å for the wavelength, $\Delta\lambda/\lambda = 3.2 \times 10^{-6}$ for the dispersion, and $\Delta\theta = 5.0 \times 10^{-6}$ rad for the angular divergence, respectively, were obtained. Hence, the lattice parameter was determined with an accuracy better than $\Delta d/d \sim 2.6 \times 10^{-6}$. The angular positions of the 2nd and 3rd goniometers were monitored by rotary-encoders which read $1/10000$ degree of arc. This diffractometer was in a room in which temperature fluctuations were kept within $\pm 0.05^\circ\text{C}$ during a measurement of one sample.

Results and Discussion

In Fig. 2, we compare the lattice

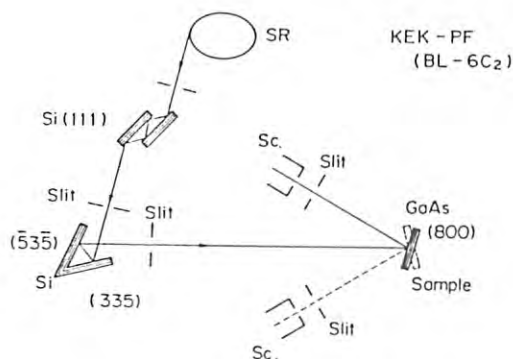


Fig. 1 Experimental arrangement for lattice parameter measurement.

parameters obtained for undoped, 3 inch diameter MLEC crystals with varied raw material compositions. The same magnetic field was applied to samples A, B and C, but not to sample D. For crystals grown under the same magnetic field, the lattice parameter seems to increase as the As fraction increases. However, the lattice parameter difference among the crystals with the same material composition (B and D) is larger than that among sample A, B and C. Incidentally, the topographs taken at peak positions of the rocking curves for sample A \sim D clearly show that sample A \sim C contain a higher density of dislocations than sample D. We hence conclude that further investigation is required for extracting meaningful results on effects of composition on the lattice parameter.

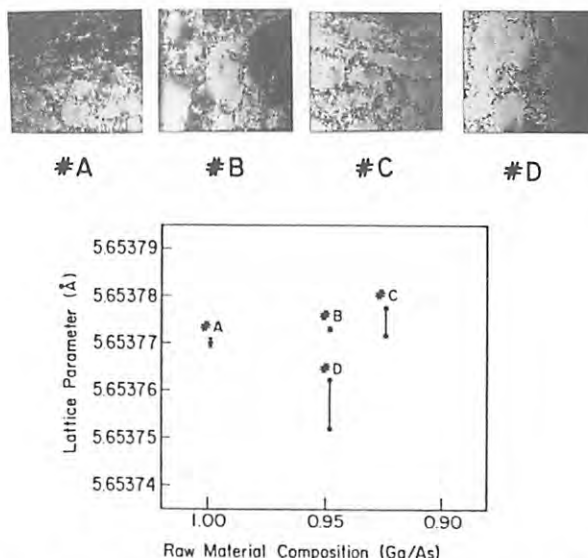


Fig. 2 Lattice parameter variation obtained for crystals grown from varied raw composition. Each topograph was taken at one of peaks of respective rocking curves.

References

- 1) Y. Okada, Y. Kadota and Y. Tokumaru: Appl. Phys. Lett. **48** 975 (1986).
- 2) M. Nakajima, T. Sato, T. Inada, T. Fukuda and K. Ishida: Appl. Phys. Lett. **49** 1251 (1986).
- 3) H. Kuwamoto and D.E. Holmes: J. Appl. Phys. **59** 656 (1986).
- 4) W.L. Bond: Acta. Crystallogr. **13** 814 (1960).
- 5) R.D. Deslattes and A. Henins: Phys. Rev. Lett. **31** 972 (1973).

Hidetoshi NAMBA, Hiroshi DAIMON¹⁾, Kosuke UYAMA²⁾, Yoji IDEI, Masaki TANIGUCHI³⁾, Shigemasa SUGA³⁾, Yoshitada MURATA³⁾, Tsuneaki MIYAHARA⁴⁾ and Haruo KURODA.

Research Centre for Spectrochemistry and Department of Chemistry, Faculty of Science, The University of Tokyo, Hongo, Bunkyo-ku, Tokyo 113, Japan

1)Department of Physics, Faculty of Science, The University of Tokyo, Hongo, Bunkyo-ku, Tokyo 113, Japan

2)Kuroda Solid Surface Project, Research Development Cooperation of Japan, Toyosato, Tsukuba-gun, Ibaragi-ken 300-26, Japan

3)The Institute of Solid State Physics, The University of Tokyo, Roppongi, Minato-ku, Tokyo 106, Japan

4)Photon Factory, The National Laboratory for High Energy Physics, Oho-machi, Tsukuba-gun, Ibaragi-ken 305, Japan

A soft X-ray beam line whose energy range is from 20 to 1000 eV has been designed for surface studies and constructed at BL-7A in Photon Factory. It was planned that the photon intensity and the energy resolution at 500 eV of the excitation energy were more than 10^{11} photons/s.100mA and less than 1 eV, respectively.

The beam line is, now, available for experiments of photoelectron spectroscopy and surface EXAFS after many cycles of performance test and improvements. We report some characteristics of the beam line.

Outline of the beam line

The beam line is composed from a prefocusing mirror apparatus and a plane grating monochromator. The schematics of the optics and their parameters are shown in Fig.1. A bent toroidal mirror installed at 14 m from the source point reshapes the incident radiation as approximately parallel rays in vertical which is the direction of the grating dispersion. One of the five plane mirrors with different incident angles is inserted on the optical axis. Each plane mirror acts as a low pass filter against white light of synchrotron radiation. Dispersed radiation is focused on the exit slit by two spherical mirrors. The parameters of the spherical mirrors could be canceled each together. Diverging monochromatized light is focused by the postfocusing mirror on a sample put at 26 m from the source point. Details of the beam line will be published elsewhere.

Experimental and Results

We note a remark on stability of the grating surface under irradiation. A replica grating on a quartz substrate(Hitachi, 1200 l/mm) was used in the experiment. Spectra were degraded in short time, because the grating surface was damaged by intense synchrotron radiation. So we installed a cooling mechanism for reducing heat of the grating and used SiC as the grating substrate. Stability of the grating surface is significantly improved.

Spectral characteristics of the beam line were examined by measuring the known absorption of N_2 , Ar, Kr and Xe. We also measured the photocurrent flowed out of the postfocusing mirror surface under irradiation. The photocurrent measured as a function of the incident energy is shown in Fig. 2. The maximum intensity is found to be from 300 to 400 eV. The dip around 280 eV is due to absorption by carbon contamination stuck on the

optics surfaces. The photocurrent measured on PM5 is too low because of damage of PM5 mirror surface. The full width at half maximum(FWHM) of N 1s absorption peak at 400 eV is 1.5 eV.

We examined photoelectron intensity and contribution of higher order light by angle resolved photoelectron spectroscopy. Samples used in the experiments were clean Au and Ni(100). The photoelectron intensity and the FWHM of Au 4f peak excited by 250 eV of the photon energy is about 1.5 kc/s.100mA and 1.5 eV, respectively.

In summary, the results mentioned above roughly agree with the design characteristics. However the energy resolution should be more improved and the absolute photon intensity is to be measured.

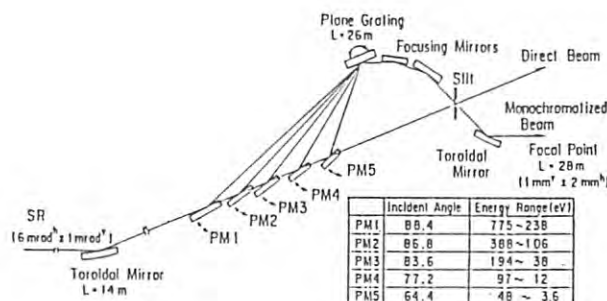


Fig.1 Layout of the optical system of BL-7A.

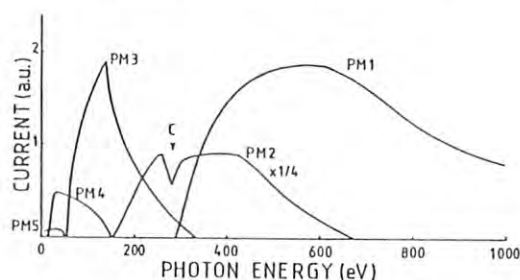


Fig.2 Spectral characteristics measured by mirror current

Research Centre for Spectrochemistry and Department of Chemistry, Faculty of Science, The University of Tokyo, Hongo, Bunkyo-ku, Tokyo 113, Japan

Introduction

Metal atoms adsorbed on one dimensional atomic array of the substrate surface has shown one dimensional metallic character¹⁾. It has been suggested that clean surfaces of diamond(111) and (100) have given such atomic arrays²⁾. So it is expected that metal atoms adsorbed on clean diamond surfaces show characteristics of low dimensional metal. However surface characterization of diamond is not enough clear yet.

We studied 2x1 reconstructed surface of diamond(111) by ultraviolet photoelectron spectroscopy(UPS) and electron energy loss spectroscopy(EELS). We report the experimental results and discuss the electronic structure of the reconstructed surface.

Experimental and Results

A clean and 2x1 reconstructed sample examined by low energy electron diffraction(LEED) was obtained by heating the sample to about 900C. The LEED pattern irreversibly transforms from 2x1 to 1x1 by hydrogen adsorption as the result that hydrogen atom occupy one dangling bond of surface diamond atom.

The UPS results are shown in Fig.1. The position of the Fermi level indicated in the figure was determined by the simultaneous UPS measurements on a clean Au. On the 2x1 surface, a surface state peak whose position is almost independent of the photon energy appears just below the Fermi level. It is confirmed that by analysing the difference spectra between 2x1 and 1x1 surfaces, the surface state peak has two maxima at -1.2 and -2.6 eV, respectively.

The difference spectrum of EELS between 2x1 and 1x1 surfaces is shown in Fig. 2. A clear peak and a broad weak peak detected at 2 and 6.5 eV, respectively. These energy loss peaks and the surface state peak detected in UPS are surface sensitive, because those peaks simultaneously disappear by hydrogen adsorption.

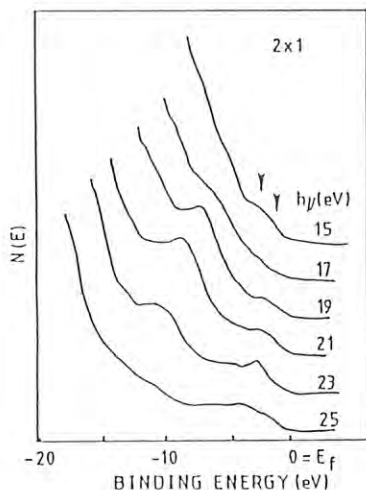


Fig.1 UPS spectra measured on the 2x1 surface by different photon energy.

Discussion

We put a remark on the fact that The energy losses and the emission peak from the surface states simultaneously appear with the formation of a 2x1 LEED pattern and disappear by hydrogen adsorption. The results suggest that the initial states are common for both in UPS and EELS. Based on the interpretation, we assigned the energy losses as shown in the upper part of Fig.3. The energy loss of 2 eV is due to the excitation from the occupied surface states around -1.2 eV to the unoccupied states at 0.8 eV. The energy loss of 6.5 eV is explained as the excitation from the occupied states at -2.6 eV to the unoccupied states at 3.9 eV. The present results can be fitted to the band structure based on a dimerized-chain model³⁾ as shown in Fig. 3. The band gap around J-point of the calculated band structure adjusted to 2 eV which corresponded to the energy loss. The energy loss of 6.5 eV is interpreted as the interband excitation in the surface states along J-point to the origin.

References

- 1) H. Tochiyama and Y. Murata: J. Phys. Soc. Japan 51(1982)2920.
- 2) P.G. Lurie and J.M. Wilson: Surface Sci. 65(1977)453.
- 3) J.F. Morar, F.J. Himpsel, G. Hollinger, J.L. Jordan, G. Hughes and F.R. McFeely: Phys. Rev. B33(1986)1346.

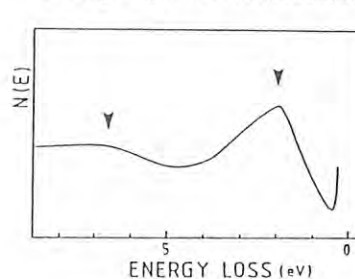


Fig.2 A difference spectrum of EELS. The primary energy is 120eV.

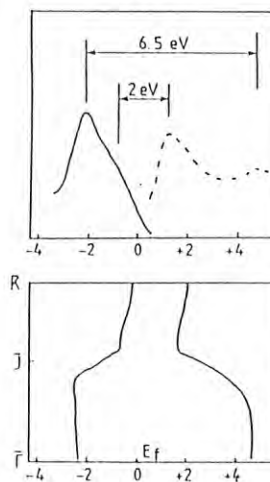


Fig.3 Comparison of the present results in UPS and EELS (upper figure) with the band structure based on a dimerized-chain model (lower figure)

Hidetoshi NAMBA, Toshiaki OHTA^{*}, Masataka MASUDA and Haruo KURODA

Research Centre for Spectrochemistry and Department of Chemistry, Faculty of Science, The University of Tokyo, Hongo, Bunkyo-ku, Tokyo 113, Japan

^{*}Department of Physics, Faculty of Science, The University of Hiroshima, Higashisenda-cho, Naka-ku, Hiroshima 730, Japan

A VUV beam line whose energy range is from 5 to 45 eV has been designed and constructed at BL-7B in Photon Factory. The design principle was to obtain high photon intensity in the order of 10^{12} photons/s.100mA with moderate energy resolution. The beam line is almost completed. We report a brief summary of the characteristics of the beam line.

Outline of the beam line

The optical system is illustrated in Fig.1. The synchrotron radiation(SR) is deflected to the vertical direction by two prefocusing mirrors. One is a cylindrical mirror made by pure copper and another is a spherical one made by quartz. SR is focused on the entrance slit of 1 m Seya-Namioka monochromator. Three gratings were set in the monochromator. The blazed wavelength of each grating is 38, 96, 150 nm, respectively. Depending on energy range which is preferable in each experiment, one of them can be selected from outside of the vacuum. Monochromatized radiation is focused on a sample by the postfocusing toroidal mirror. The monochromator was installed on the second floor, and so, the space for experimental apparatus was limited. Details of the beam line will be published elsewhere.

Experimental and Results

In early times of the experiments, the first copper mirror was cooled by only thermal conduction through the support of the mirror. The beam position on the entrance slit of the monochromator moved as a function of the irradiation time and of the ring current. A water cooling system was adopted to the mirror support, and so, the beam shift was greatly reduced.

Spectral profile was monitored by measuring the photocurrent flowed out of the postfocusing mirror under irradiation. The profiles for three gratings are shown in Fig. 2. Each curve shown in the figure corresponds to one of three gratings with different blazed angles. Each curve shows a maximum at the energy corresponding to the blazed wavelength. We also measured luminescence of sodium salicylate by a photomultiplier in the energy range below 10 eV of the excitation energy.

The energy resolution and the absolute photon intensity were estimated in the absorption measurements by the double ion chamber technique. The energy resolution is less than 15 meV at the best around 15 eV of the excitation energy in the case that 2400 l/mm of grating has been used. More than 1×10^{12} photons/s.100mA at maximum can be obtained but the slit has to be much opened.

We examined photoelectron intensity and contribution of higher order light by angle resolved photoelectron spectroscopy. Sample was clean Au. The peak intensity of Au 5d is about 5 kc/s.100mA,

In conclusion, the results mentioned above satisfy the specification of the beam line design. The first experiment of photoelectron spectroscopy has been already finished and a preliminary experiment of photochemical decomposition of adsorbed species has been started. However further test of I₀ monitor and improvement of surface roughness of the copper mirror are necessary.

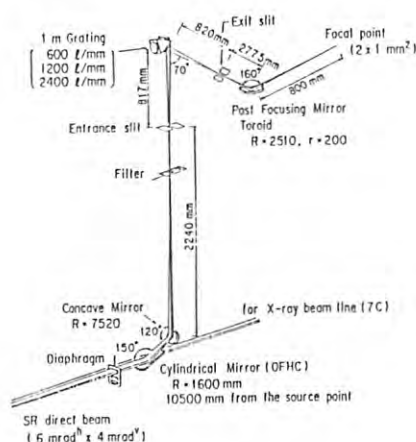


Fig.1 Layout of the optical system of BL-7B.

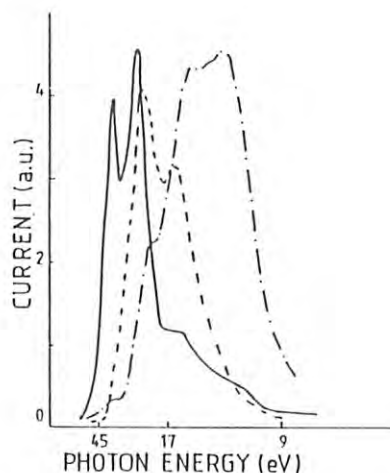


Fig.2 Spectral characteristics above 10eV measured by mirror current.

Ce L₁₁₁ EXAFS STUDY OF CeO₂-STABILIZED TETRAGONAL ZrO₂

Fumiyuki MARUMO, Hideki MORIKAWA, Yutaka SHIMIZUGAWA, Hiroyuki IKAWA*,
Kazuyori URABE* and Masaharu NOMURA**

Research Laboratory of Engineering Materials, Tokyo Institute of
Technology, Nagatsuta, Yokohama 227

* Department of Inorganic Materials, Tokyo Institute of Technology,
Ookayama, Tokyo 152

** Photon Factory, National Laboratory for High Energy Physics,
Oho-machi, Ibaraki 305

Introduction

Monoclinic ZrO₂ which is stable at room temperature undergoes phase transitions at 1150 C° to tetragonal ZrO₂ and at 2370 C° to cubic ZrO₂. The high temperature phases can be stabilized at room temperature by the addition of impurities such as Y₂O₃ and CeO₂. Since a high fracture toughness was obtained for sintered bodies containing tetragonal ZrO₂ polycrystals, CeO₂-stabilized tetragonal ZrO₂ is considered a candidate materials for toughened zirconia ceramics. In the present study, local structures around Ce atoms in CeO₂-stabilized tetragonal ZrO₂ are investigated by Ce L₁₁₁ EXAFS analysis to clarify the role of Ce ions in stabilizing tetragonal phase.

Experimental and Results

The CE10 sample (86ZrO₂.10CeO₂.4YO_{1.5}) was synthesized by coprecipitation at pH=9 from a mixed solution of Zr(SO₄)₂, dissolved Y₂O₃ in H₂SO₄ and dissolved CeO₂ in H₂SO₄ using (NH₄)OH followed by calcination at 900 C°. The CE4 sample (93ZrO₂.4CeO₂.3GdO_{1.5}) was similarly synthesized from a aqueous solution of ZrOCl₂, CeCl₄ and GdCl₃. The samples were subsequently heated at 1500 C° for 1.5 h and then powdered. After annealing at 1200 C° for 1.5 h, the samples were quenched to room temperature and used for EXAFS measurements.

EXAFS spectra of the samples in the neighborhood of the Ce L₁₁₁ absorption edge(5.723 keV) were measured by the normal absorption mode with a two crystals Si(111) monochromator. CeO₂ crystals (Ce-O=2.34 Å, eight-fold coordination) were used for a reference sample (CE100). The EXAFS oscillation curves $\chi(k)$ were obtained after subtraction of the smooth X-ray absorption backgrounds and normalization and the transformed magnitudes $|F(r)|$ were calculated. By comparing

the first peaks on the curves of the samples with that of the reference sample, real atomic distances of Ce-O pairs for tetragonal ZrO₂ were estimated. Atomic distances of the second coordination shell in the samples were analyzed by the curve-fitting method. Results obtained were listed in Table 1 together with cell dimensions and average Zr-Zr distance calculated from the cell dimensions.

The Ce-O distance of 2.32 Å in tetragonal ZrO₂ is slightly shorter than that in CeO₂ crystals (Ce-O=2.34 Å) however, longer than that in pure tetragonal crystals (Zr-O=2.22 Å). When ZrO₂ changes from tetragonal into monoclinic phase with decreasing of temperature, cell volume increases by about 4%. Since the ionic radius of Ce ion is larger than that of Zr ion, the introduction of CeO₂ into ZrO₂ causes the increase of cell volume, which prevents the stabilized ZrO₂ transforming into monoclinic phase.

The Ce-Zr distances are close to the average Zr-Zr distances, indicating that the addition of CeO₂ does not deform the atomic arrangement in the ZrO₂ crystals to a great extent.

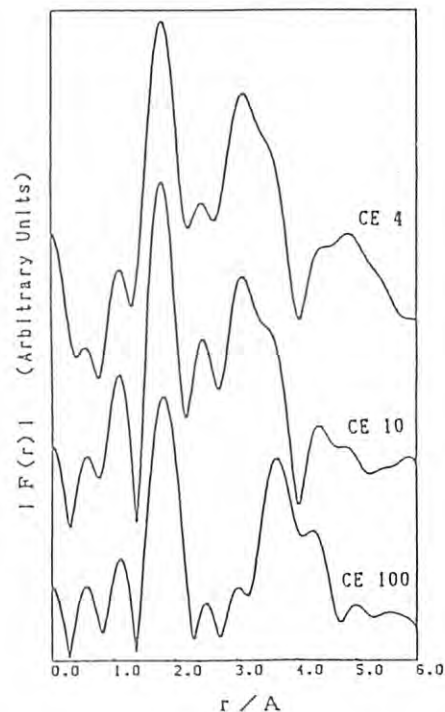


Fig.1 Magnitude of Fourier transform. CE4 and CE10: CeO₂-stabilized tetragonal ZrO₂, CE100: CeO₂ crystals

Table 1 Results of EXAFS analysis for stabilized ZrO₂ crystals.

Sample	Atomic Distance M-O - M-Zr, Å	Cell Dimensions, Å	Average Zr-Zr Distance, Å	Remarks
CE10	2.32 3.62 (Ce-O)	a=3.625 c=5.204	3.64	Ce EXAFS Tetragonal
CE4	2.32 3.61 (Ce-O)	a=3.611 c=5.197	3.63	Ce EXAFS Tetragonal
Y19*	2.28 3.59 (Y-O)	a=5.145	3.64	Y EXAFS Cubic
ZR81*	2.11 3.55 (Zr-O)	a=5.145	3.64	Zr EXAFS Cubic

* Callow et al., J. Amer. Ceram. Soc., 69, 272(1986)

EXAFS STUDY OF RELAXATION OF A Cu^+ IMPURITY IN ALKALI HALIDES

Takatoshi MURATA, Shuichi EMURA*, Hiroyuki ITO*, and Hironobu MAEDA**

Department of Physics, Kyoto University of Education, Fushimi-ku, Kyoto 612
 *Institute of Scientific and Industrial Research Osaka University-Suita Campus,
 8-1 Mihogaoka, Ibaraki, Osaka 565
 **Department of Chemistry, Faculty of Science, Okayama University, Okayama 700

Introduction

On the lattice relaxation at an impurity ion site in a crystal, several alkali halides containing Cu^+ ions are known to be in the situation that the substitutional Cu^+ ion is not located at a normal lattice site, but at an off-center position. Several experimental¹⁾ and theoretical²⁾ works have been done to reveal the off-center distance and its direction. No definite results, however, have been obtained so far. EXAFS is the most suitable method for observing the amount of the ionic relaxation in the lattice. Preliminary results have been reported recently for $\text{NaCl}:\text{Cu}^+$.³⁾ We report here the extended studies of the previous work.

Experimental

Samples investigated were $\text{NaBr}:\text{Cu}^+$ and $\text{KBr}:\text{Cu}^+$. CuBr was used as a reference material. Methods of the sample preparations were described in the previous report.³⁾ EXAFS measurements on Cu K-edge in a fluorescence mode at room and at about 50 K were made at EXAFS station installed at BL-7C using a fluorescence detector developed by Lytle et al.⁴⁾

Results and Discussions

In Figs. 1 and 2 are shown the spectra of magnitude of Fourier transform of the EXAFS for two samples. The best fit values of the 1st and 2nd shell distances obtained from inverse Fourier transformed EXAFS spectra are shown in Table 1.

Table 1

Sample	Cu-Br Distance/Å	
$\text{NaBr}:\text{Cu}^+$ (50 K)	2.54 ± 0.02	3.51 ± 0.02
$\text{KBr}:\text{Cu}^+$ (300 K)	2.36 ± 0.35	4.54 ± 0.02
	2.51 ± 0.34	4.78 ± 0.02

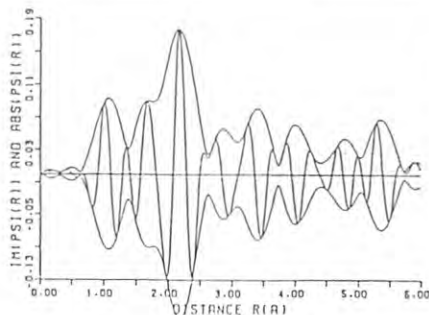


Fig. 1

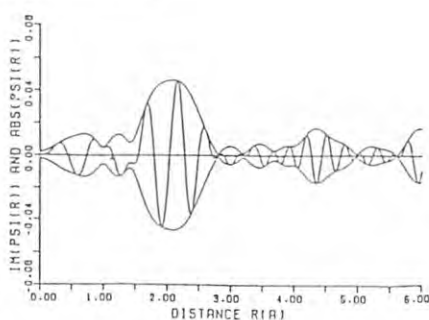


Fig. 2

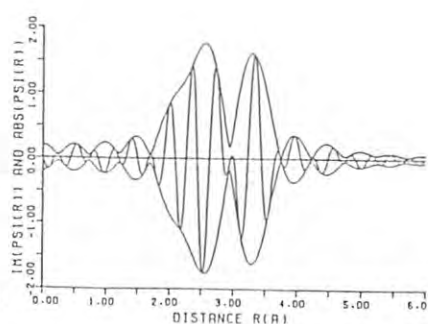


Fig. 3

These values are very different from the values of the 1st shell distances of host matrices, i.e. 2.98 and 3.30 Å for NaBr and for KBr, respectively. They are rather similar with the value of CuBr , 2.46 Å. This fact means that the deformation around a Cu^+ ion in the host is very large.

We performed a simulation in the case of $\text{NaBr}:\text{Cu}^+$ by calculating the EXAFS spectrum with assuming a displacement of the impurity ion toward various direction in the NaCl matrix putting the off-center distance as 0.55 Å. A plausible result was obtained in the case of $\langle 111 \rangle$ displacement. The Fourier spectrum of the simulation is shown in Fig. 3. Only in this case are obtained the double peaks in Fourier spectrum; in other cases of the displacement towards $\langle 100 \rangle$ or $\langle 110 \rangle$ direction, no clear cut doublet was obtained. The different positions of the Fourier peaks from the experimental results are due to the situation that in the simulation a perfect lattice of the host was assumed. We believe that this is the first work of obtaining a direct evidence of the off-center relaxation of an impurity ion.

Further analysis is in progress in order to explain the result of the $\text{KBr}:\text{Cu}^+$ with a reasonable model.

References

- 1) S. Emura and M. Ishiguro: J. Phys. Soc. Jpn. **45**, 1425 (1978).
- 2) S. Nagasaka: J. Phys. Soc. Jpn. **50**, 1570 (1981); *ibid.* **51**, 898 (1982).
- 3) T. Murata and S. Emura: J. Phys. (France) **47**, C8-795 (1986).
- 4) F. W. Lytle, R. B. Gregor, D. R. Sandstrom, E. C. Marques, J. Wong, C. L. Spiro, G. P. Huffman and F. E. Huggis: Nucl. Instr. Meth. **226**, 542 (1984).

LOCAL STRUCTURE AROUND Br ATOMS IN AgBr-Ag O-GeO GLASSES

Hideki MORIKAWA, Yutaka SHIMIZUGAWA, Yasunori TABIRA, Kiichi KIMURA, Fumiyuki MARUMO
and Masayuki YAMANE*

Research Laboratory of Engineering Materials, Tokyo Institute of Technology, Nagatsuta, Yokohama 227

* Department of Inorganic Materials, Tokyo Institute of Technology, Ookayama, Tokyo 152

Introduction

Glasses with high ionic conductivity have been prepared in the systems based on silver halides.¹⁾ Local structures around Ge and Ag atoms of the glasses in the system AgI-Ag₂O-GeO₂ were investigated by the EXAFS method. Ge atoms²⁾ mainly occupy tetrahedral sites. On the other hand, Ag atoms³⁾ are surrounded by two or more O atoms with Ag-O=2.15-2.22 Å or by four I atoms with Ag-I=2.74-2.87 Å. The present report describes an EXAFS study of AgBr-Ag₂O-GeO₂ glass carried out to examine the local structure around Br atoms.

Experimental

Mixtures of AgBr, Ag₂O and GeO₂ were melted in a silica crucible and the melt was poured onto a copper plate to obtain glasses. Table 1 listed the nominal compositions of the glasses prepared.

Table 1 Chemical composition and Br-Ag atomic distance estimated by the EXAFS analysis.

Sample	Chemical composition(mol%)			O/Ge ratio	Br-Ag distance(Å)
	GeO ₂	Ag ₂ O	AgBr		
G20	20	40	40	4.0	2.76
G30	30	30	40	3.0	2.76
G40	40	24	36	2.6	2.77
AgBr	-	-	100	-	2.88

EXAFS spectra of the glasses in the neighborhood of the Br K absorption edge(13.470 keV) were measured by the normal absorption mode using a two-crystal Si(111) monochromator. Absorption spectrum of AgBr crystals were also measured as a reference sample. Powder sample was mixed with polyethylene powder and then pressed to a disc with a diameter of 12 mm, which was used for EXAFS measurements.

Results and Discussions

Fig. 1 showed X-ray absorption spectra for the glass sample(G30) together with the reference sample from 12.970 to 14.570 keV. The $k^3\chi(k)$ in the range $2.2 \leq k \leq 10.0$ was Fourier transformed to get $|F(r)|$ curve. Atomic distance of the first coordination shell was analyzed by the curve-fitting method using phase shifts and back-scattering amplitudes reported by Teo and Lee.⁴⁾ Least squares curve-fitting was carried out in the range $4.0 \leq k \leq 7.0$. AgBr crystals(Br-Ag=2.88 Å, six-fold coordination) were used to determine the inner potential energy of 4.011 eV and the mean free path for photoelectron of 2.79 Å.

The Br-Ag distance is 2.88 Å and the coordination number is 6 for AgBr crystals which do not show ionic conductivity, while the I-Ag distance is 2.82 Å and the coordination number is 4 for AgI crystals which show ionic conductivity. Average Br-Ag distances for three kinds of glasses were estimated by the present EXAFS analysis to be 2.76-2.77 Å and coordination numbers to be

approximately 4. One of the reasons for ionic conductivity of the AgBr-Ag₂O-GeO₂ glass may result from the structural similarity around halogen atoms between AgI crystal and AgBr-Ag₂O-GeO₂ glass.

References

- 1) T.Minami, J.Non-Cryst.Solids, **56**, 15(1983)
- 2) C.D.Yin, T.Osuka, H.Morikawa, F.Marumo and H.Oyanagi, J.Non-Cryst.Solids, **74**, 237(1985)
- 3) H.Morikawa, T.Osuka, C.D.Yin, M.Okuno and F.Marumo, J.Ceram.Soc.Japan, **95**, 551(1987) (in Japanese)
- 4) B.K.Teo and P.A.Lee, J.Amer.Chem.Soc. **101**, 2815 (1979)

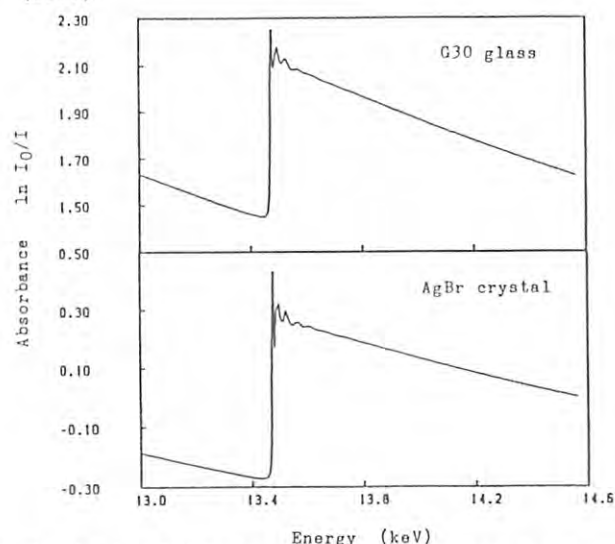


Fig.1 K edge EXAFS spectra of Br for AgBr-Ag O-GeO glass and AgBr.

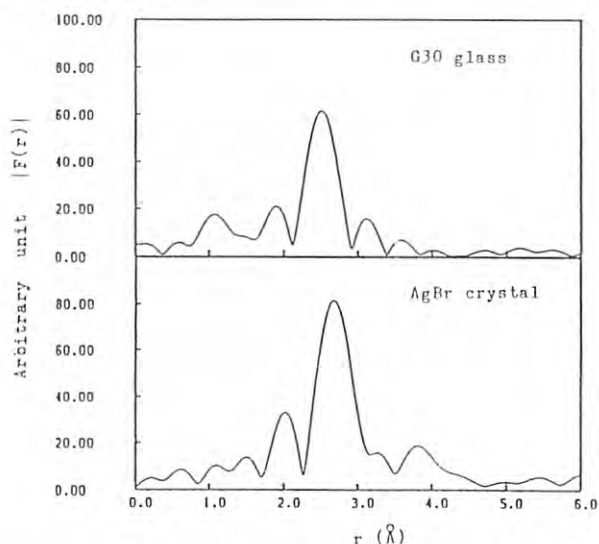


Fig.2 Fourier transform magnitude of Br K EXAFS data in Fig.1. No corrections for phase shift and inner potential energy were applied.

THE MECHANISM OF SOLUTION STRENGTHENING BY C AND N IN AUSTENITIC STEEL

NOBUHIKO KONDOH, KOJI SHIBATA, KATSURO ODA, KOUZOU FUJITA*1, AND MASAHARU NOMURA*2

*1 Department of Metallurgy and Material Science, Faculty of Engineering,
University of Tokyo, Hongo, Bunkyo-ku, Tokyo 113*2 Photon Factory, National Laboratory for High Energy Physics
Oho-machi, Tsukuba-gun, Ibaraki 305Introduction

Austenitic steel strengthened by nitrogen and carbon are remarkably softened during low cyclic deformation, and the softening tendency is more marked in the case of nitrogen than of carbon. These softening phenomena can be explained quantitatively by presuming a existence of the short range ordering of substitutional and interstitial atoms (I-S complex), and its breakdown during cyclic deformation¹⁾. However, any direct evidence of the I-S complexes has never been shown yet. On the other hand, XANES²⁾ gives local information about electronic structure and bond state around alloying atoms. In this study, in order to have some evidences of the existence of I-S complexes XANES observation of austenitic stainless steels was made with a high and a very low content of nitrogen or carbon before and after the low cyclic deformation.

Experimental procedures

Table 1 shows the chemical compositions of the steels. The steels were prepared by melting high purity materials in vacuum, and were forged and rolled to plates. After the solution treatment at 1573K for 1.5h the plates were water quenched and machined to round specimens of 8mm diameter by 10mm gage length for cyclic deformation which was conducted with an Instron-type machine at ambient temperature. Thin plates were cut from as-solution treated and cyclically deformed specimens, and were polished mechanically and then electrolytically in a 5% solution of oxalic acid to foils of 20 to 40 μm in thickness for XANES observations. XANES observations were carried out at room temperature by using synchrotron radiation at 7C beam line of the Photon Factory in the National Laboratory for High Energy Physics at Tsukuba.

Results

Fig.1 shows the change of stress amplitude of the steels subjected to XANES observations with the cyclic deformation. The steel B containing nitrogen exhibits large softening after the initial work hardening, while the low nitrogen steel A shows the hardening with a saturated stage. The similar tendency was observed in the steels C and D. Fig.2 shows absorption spectra at K-edge of Cr. Shoulder peaks which indicate the excitation of electrons to the Fermi level are observed in the center of all the spectra. However, the shapes of peaks varied with the addition of interstitial atoms. The shoulder peaks that observed in steels B and D containing nitrogen and carbon, respectively, are more clear than in steels A, C containing very few interstitial atoms. Fig.2 shows the effect of cyclic deformation on the peak of the steel B. The shapes of the peaks are very similar before and after the deformation.

Conclusion

The XANES of the austenitic stainless steels were observed. It was found that the existence of interstitial atoms around Cr atoms changes the shape of the shoulder peak in absorption spectra of Cr K-edge. The effect of cyclic deformation on XANES may be very small, so a more precise observation is necessary.

References

- 1) K. Shibata et al.: Fatigue at Low Temperatures, ASTM STP 857(1985), Philadelphia, p.31.
- 2) P. A. Lee: Rev. Mod. Phys., 53(1981), p.769.

Table 1. Chemical compositions (wt%).

steels	C	Si	Mn	Al	P	S	Cr	Ni	N
A	0.006	0.037	0.006	0.073	0.007	0.003	20.1	14.9	0.0098
B	0.008	0.11	0.031	0.052	0.007	0.003	20.3	15.3	0.18
C	0.01	0.77	1.00	0.020	0.0033	0.0073	19.8	15.2	0.006
D	0.29	0.80	1.50	0.010	0.0032	0.0074	19.5	15.4	0.005

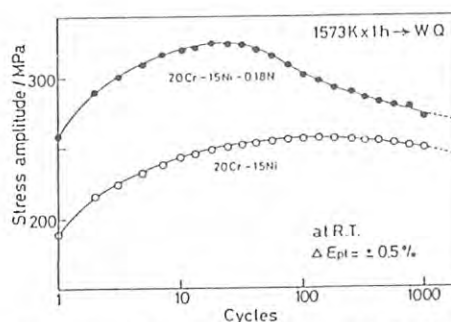


Fig.1. Stress amplitude responses of steels A and B for constant plastic strain amplitude tests at room temperature.

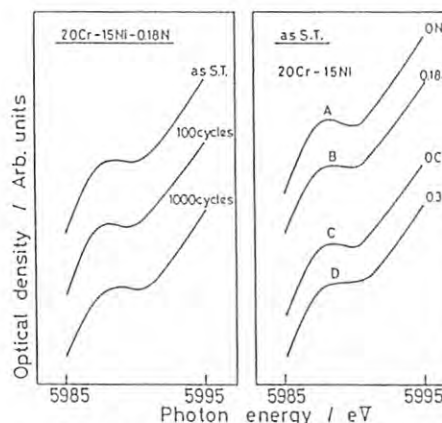


Fig.2. Effect of interstitial atoms and cyclic deformation on Cr K-edge absorption spectra.

HIGH PRESSURE-INDUCED POLYMORPHISM IN VANADIUM OXIDES

Ayako TOKIWA, Keiji KUSABA, Nobuyuki SHIMODA,
Masae KIKUCHI, Yasuhiko SYONO, Izumi NAKAI*,
Ichiro NOMACHI* and Katsuhiro IMAI*

Institute for Materials Research, Tohoku University
Katahira, Sendai 980

*Department of Chemistry, University of Tsukuba
Sakura-mura, Ibaragi-ken 305

Introduction

V_2O_5 is known to have a layered structure with an orthorhombic symmetry, in which V^{5+} ions occupy square pyramidal five-coordinated sites. A high pressure phase has been reported above about 3 GPa, although the crystal structure was not determined yet. Under high pressure, we may expect an increase in coordination number and more averaged bond length, and XANES and EXAFS studies are most appropriate to obtain information of the short range structure around vanadium ions.

Experimental and Results

The high pressure phase of V_2O_5 was synthesized at high pressure and high temperature condition of 3-7 GPa and 450-750°C, using a 250 ton cubic anvil press. $4N$ V_2O_5 powders were encased in a platinum capsule, which served as a heater by applying a large current. High pressure phase was obtained by quenching from high pressure and high temperature condition, and examined by x-ray powder diffraction and electron diffraction analyses (Fig. 1). The unit cell dimensions of the high pressure phase were tentatively determined to be $a = 7.16\text{\AA}$, $b = 7.00\text{\AA}$ and $c = 6.31\text{\AA}$, by assuming an orthorhombic symmetry. XANES and EXAFS measurements were carried out by utilizing intense x-ray source from synchrotron radiation at BL-7C port of the Photon Factory, KEK. Powder specimens were spread on thin plastic films, and appropriate absorption was obtained by changing the number of specimen films.

Figure 2 (a) and (b) show XANES spectra of the ambient and high pressure phase of V_2O_5 respectively. Rather resembled features were observed in both spectra, suggesting that short-range structure around vanadium ions were not much altered by the pressure-induced phase transition. Energy position of observed XANES spectra of various vanadium oxides are summarized in Table I. Peak positions of the high pressure phase can be interpreted on the way from square-

pyramid to regular octahedron. Detailed analysis of EXAFS spectra is now being made. Experimental results of $LiVO_3$ will also be reported shortly.

References

- 1) J. Wong, F. W. Lytle, R. P. Messmer and D. H. Maylotte, Phys. Rev. B30 (1984) 5596.

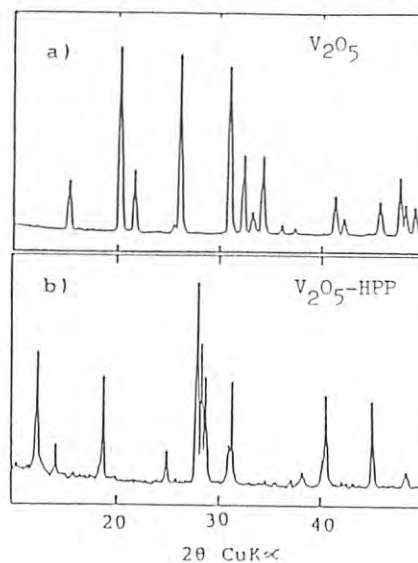


Fig. 1

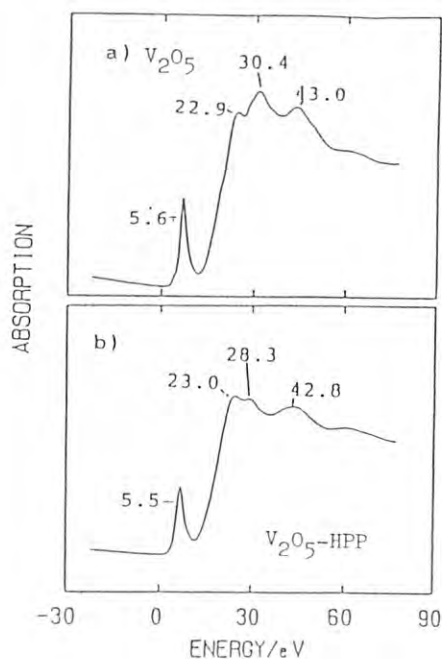


Fig. 2

Table I Energy position of various spectral features in XANES spectra of vanadium oxides¹⁾

Compound	Threshold (eV)	Pre-edge peak	1s-4p transition	Cage geometry
V_2O_3	1.9	3.4	23.5	Distorted
V_2O_4	3.5	4.5	26.6	octahedron
V_2O_5	4.8	5.6	30.1	Distorted
$V_2O_5^*$	4.6	5.6	30.4	square-
$V_2O_5\text{-HPP}^*$	4.7	5.5	28.3	pyramid

*This work

Zn EXAFS MEASUREMENTS UNDER HIGH PRESSURE CONDITIONS USING A DIAMOND ANVIL CELL

Shigeo SUENO

Institute of Geoscience, University of Tsukuba, Ibaraki 305.

Izumi NAKAI

Department of Chemistry, University of Tsukuba, Ibaraki 305.

Kazumasa OHSUMI and Masaharu NOMURA

Photon Factory, National Laboratory for High Energy Physics, Ibaraki 305.

Hideki MORIKAWA, Yasunori TABIRA and Katsuhisa ITOH

Research Laboratory of Engineering Materials, Tokyo Institute of Technology, Yokohama 227.

Tokuhei TAGAI

Mineralogical Institute, University of Tokyo, Tokyo 113.

Introduction

A combination of the EXAFS method with the diamond anvil cell technique is useful for structural studies under high pressures. However, conceivable problems for adopting the diamond anvil to generate high pressure are diffraction and absorption by the diamonds. For eliminating the effect of disturbing diffraction peaks, adjustment of the orientation of the cell by changing a tilt angle of the goniometer arc prior to the measurement is effective when the number of diffraction is small. Absorption is more important for atoms such as Cr and Mn with a lower energy absorption edge. Previous studies reported that EXAFS spectra for Cr, Mn, Fe, Co and Ni K-edges were successfully measured by using a specially designed apparatus. This study examined the possibility to obtain an analyzable EXAFS spectrum on Zn atom, under high pressures.

Experimental and Results

The measurements of absorption spectra for Zn K-edge were carried out at the 7C beam line in the Pf at an energy of 2.5 GeV.

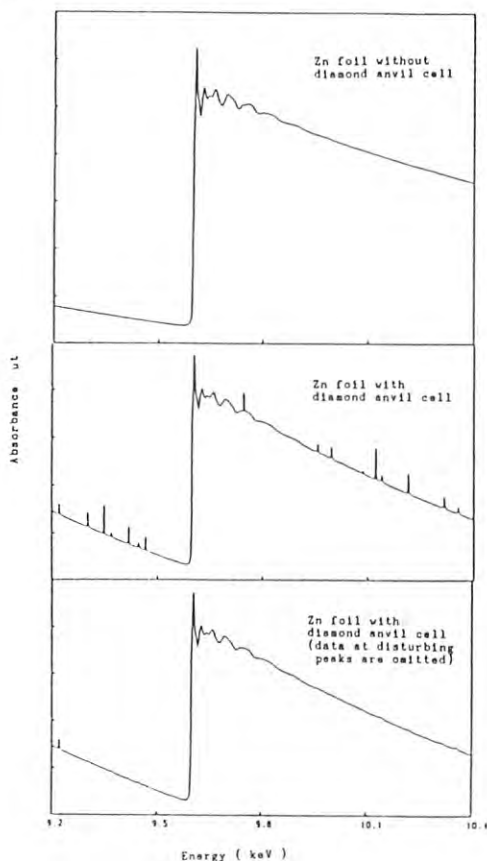


Fig.1 Zn K-edge X-ray absorption spectra of Zn foil

Normal 1/8 carats anvils (3.5 mm in total thickness) were used. A Zn foil was placed outside of the cell and therefore the pressure was not charged to the foil in the present study. X-ray absorption spectra were measured from 9.161 to 10.661 keV with a constant step interval of 2.5 eV. The measuring time is 10 s for each step. The disturbing diffraction peaks were not serious around the absorption edge, however, 17 peaks were observed on the spectrum shown in Fig.1. The disturbing peaks are very sharp and consist of one or two datum points. Therefore, the data points distributed by diffraction are easily distinguishable from others. The lower spectrum in Fig.1 is obtained by omitting the data disturbed by diffraction due to diamond. The Fourier transforms $|F(r)|$ of $k^3\chi(k)$ were calculated, using the data from 3.0 to 13.0 in k and shown in Fig.2. The $\chi(k)$ in the range includes three disturbing diffraction peaks. The phase shifts were not taken into accounts in the Fourier transforms. The strong peaks around 2.30 Å corresponding to the nearest neighbor Zn-Zn pairs were observed on $|F(r)|$ curves of both with and without diamond anvil cell.

The present study clarified that Zn K-edge EXAFS analysis can be performed under high pressures using the diamond anvil cell.

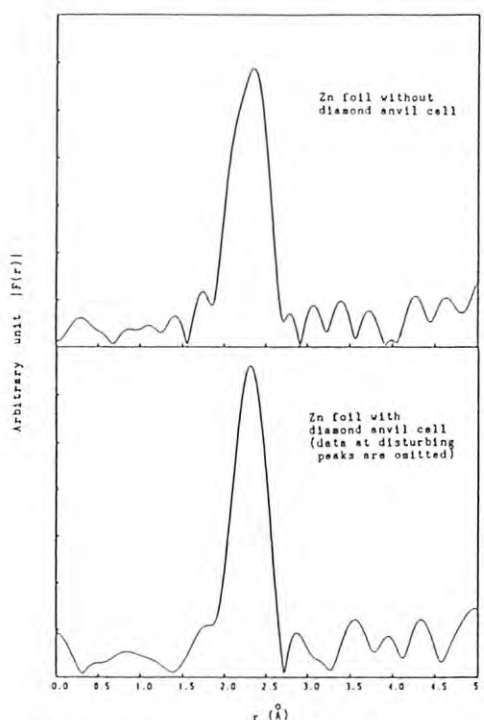


Fig.2 The fourier transforms of Zn K-edge for Zn foil

EXAFS AND XANES STUDIES OF COBALT(III)-EDTA COMPLEX

Hideto SAKANE, Takafumi MIYANAGA, Iwao WATANABE, Shigero IKEDA

Department of Chemistry, Faculty of Science, Osaka University,
Toyonaka, Osaka 560Introduction

Ethylenediaminetetraacetic acid (EDTA) is used for quantitative analysis of many kinds of metal ions in water. The metal-EDTA complexes take various forms in solution, because for some metal ions the EDTA is not large enough as a six-coordinate ligand.

We report the difference of structures of Co(III)-EDTA complexes in solids, aqueous solutions, and dimethylformamide (DMF) solution by EXAFS and XANES.

Experimental

X-ray absorption spectra measurements were performed at BL-7C using Si(111) double crystal monochromator.

Solid samples, $\text{NH}_4[\text{Co}(\text{edta})] \cdot 2\text{H}_2\text{O}$ and $\text{Na}[\text{Co}(\text{edta})] \cdot 4\text{H}_2\text{O}$, were prepared in usual way. Aqueous solutions were prepared from sodium salt, and HNO_3 or NaOH were used to adjust their pH to 3, 5, 7, or 9. DMF solution was prepared from potassium salt which was synthesized by conventional method. 18-crown-6-ether was also added to get sufficient solubility.

Results and Discussion

No dependence on pH was observed in both EXAFS and XANES spectra of aqueous solutions. Therefore, $[\text{Co}(\text{edta})]^-$ has a very stable structure in the aqueous solution of pH 3 to 9.

Fig.1 shows XANES spectra of two powder samples, and aqueous and DMF solutions. These spectra are slightly different from each other. The spectrum of aqueous solution is similar to that of Na salt.

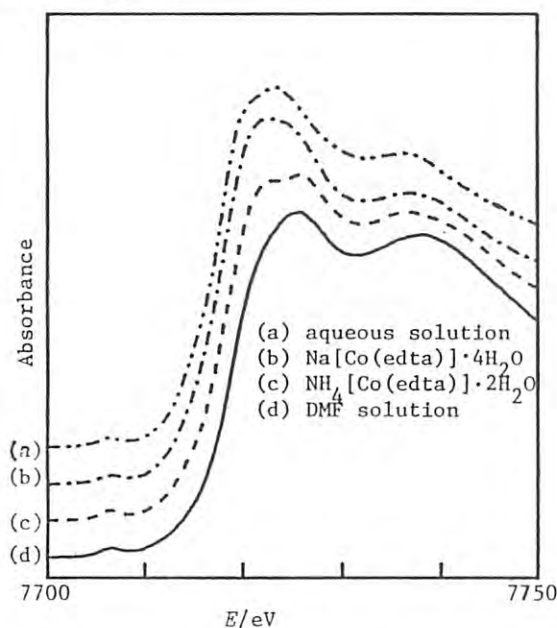


Fig.1 XANES spectra of Co K-edge for Co(III)-EDTA complexes

Fourier transforms of EXAFS for these samples are shown in Fig.2. Three peaks are observed in all of them. By referring to the crystallographic data of NH_4 salt¹⁾, these peaks are assigned to the bond distances between Co and coordinating O_1 and N (1.9Å), all of C (2.75Å), and O_2 (3.8Å) of not coordinating in the carboxyl groups of EDTA. In spite of the small number of O_2 in the third shell and its long distance, third peaks for NH_4 salt and DMF solution are anomalously strong. This must be the result of multiple scattering effect since the angles of $\text{Co}-\text{C}_1-\text{O}_2$ are about 170° .

Peak heights are quite different, i.e., $\text{Na salt} \approx \text{aqueous solution} < \text{NH}_4 \text{ salt} < \text{DMF solution}$. For Na salt and aqueous solution, the first peaks consisting of the bonds of $\text{Co}-\text{O}_1$ and $\text{Co}-\text{N}$ appear at shorter distance than that¹ for NH_4 salt. Infrared and Raman spectra for the complexes show quite different behavior in the region of the carboxyl group vibrations, but very similar frequencies for $\text{Co}-\text{N}$ vibration. Thus, we conclude that the length of $\text{Co}-\text{N}$ are similar among the samples, while that of $\text{Co}-\text{O}_1$ are shorter for Na salt and aqueous solution.

It seems that the distributions of the $\text{Co}-\text{O}_1$ bond distances are different from sample to sample because the peak heights widely differs. One of the origins of such large distribution of the distance must be the hydrogen bond between carboxyl group and water molecules.

Reference

- 1) H.A.Weakliem and J.L.Hoard, J. Am. Chem. Soc., 549 (1959)

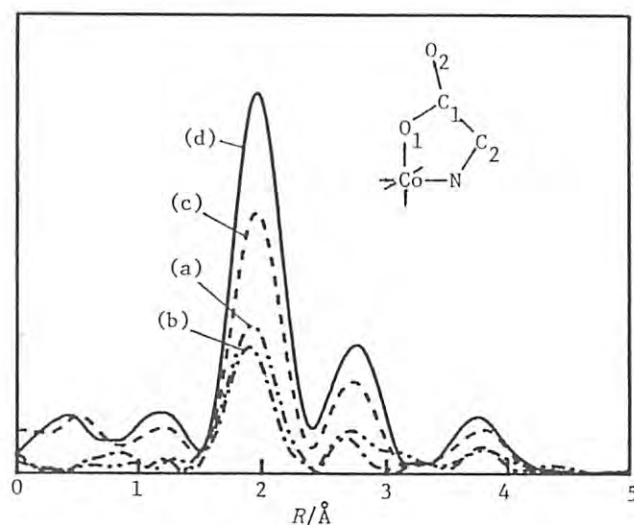


Fig.2 Fourier transforms of EXAFS

COORDINATION OF Fe IN GARNETS BY EXAFS SPECTROSCOPY

Yasunori TABIRA, Kiyooki TANAKA, Hideki MORIKAWA and Fumiyuki MARUMO

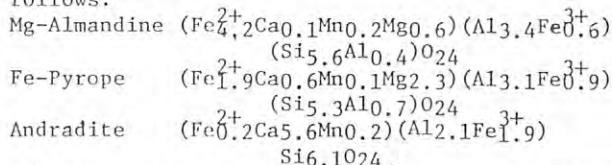
Research Laboratory of Engineering Materials, Tokyo Institute of Technology, Nagatsuta, Yokohama 227

Introduction

Garnet group minerals commonly occur in metamorphic rocks, but are also found in igneous rocks. They have a wide range of chemical composition $X_3Y_2Z_3O_{12}$ ($X=Ca, Mg, Fe^{2+}, Mn^{2+}$; $Y=Al, Fe^{3+}, Cr^{3+}, Ti^{4+}$; $Z=Si, Al$) with X in dodecahedral sites, Y in octahedral sites and Z in tetrahedral sites. It has been known that there is a strong correlation between the chemical compositions and the condition under which metamorphic rocks were formed to produce garnets. Some investigations with X-ray diffraction technique showed that differences in growth conditions and chemical compositions cause a kind of cations to occupy different sites in the garnet structure. It is, however, difficult to determine the cation distributions over these sites by X-ray diffraction experiments when several kinds of cations are contained in the structure. Local structures around Fe atoms were investigated by EXAFS spectroscopy with the intention to obtain detailed knowledges on the relation between distribution of Fe atoms and occurrence of the minerals.

Experimental and results

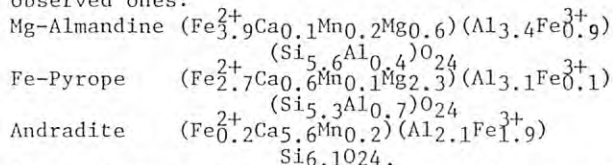
Experimental formulae were obtained from results of chemical analyses carried out by the ICP method for the garnet samples on the basis of ordinary site assignment for cations as follows:



Alkali metals were analysed by the atomic absorption spectroscopy but only the traces of them were found. All the samples are confirmed to consist only of garnets with X-ray powder diffractometry. EXAFS spectra of powdered samples were collected at room temperature with monochromatized X-ray by Si(111) double crystals over the energy range from 6.67 KeV to 7.91 KeV at BL7C.

X-ray absorption spectra near Fe K-edge of garnet samples are shown in Fig. 1 together with Fe foil and α -Fe₂O₃ for comparison. Magnitudes $|F(r)|$'s of the Fourier transforms of $k^2\chi(k)$'s are depicted in Fig. 2 for all samples and reference material α -Fe₂O₃ without taking account of phase shifts. The first peak of each $|F(r)|$ curve, which is due to the nearest neighbor Fe-O pairs, is backtransformed into the k space, and then analysed by the curve-fitting method to obtain the mean Fe-O distance, using the theoretical phase shifts and backscattering amplitudes⁽¹⁾. The results are given in the column "observed" in Table 1. The expected Fe²⁺-O distance for 8-fold coordinations and Fe³⁺-O distance for 6-fold coordinations were calculated as the sums of the effective ionic radii⁽²⁾ to be 2.30Å and 2.03Å, respectively. Using these values average Fe-O distances expected for samples were evaluated on the basis of the ratios of dodecahedral Fe²⁺ to octahedral Fe³⁺ in experimental formulae, and given in the column "predicted" in Table 1. As seen in Table 1 there are significant

discrepancies between the observed and expected bond distances, in particular Fe-Pyropo. If we assume that the total numbers of Fe²⁺ and Fe³⁺ ions per formula unit were equal to those given in the chemical formulae determined by the chemical analyses, and that Fe²⁺ and Fe³⁺ ions occupy the dodecahedral and octahedral sites, respectively, the ratios of Fe²⁺ to Fe³⁺ should be changed as shown in the following formulae to make the expected Fe-O distances equal to the observed ones:



Although there exist no significant differences between these formulae and those from chemical analyses in Mg-Almandine and Andradite, a large difference is observed in Fe-Pyropo. The observed distance indicates that almost all iron atoms should be in the divalent state in this garnet. Considerable amounts of vacancies are suggested to exist in dodecahedral sites in Mg-Almandine and in octahedral sites in Fe-Pyropo from the above formulae, but we need more accurate chemical analysis to give definite conclusion.

References

- (1) R.D.Shannon, Acta Cryst., A32, 751(1976)
- (2) B.K.Teo and P.A.Lee, J.Amer.Chem.Soc., 101, 2815(1979)

Table 1 Fe-O distances

	observed(Å)	predicted(Å)
Mg-Almandine	2.26	2.27
Fe-Pyropo	2.29	2.23
Andradite	2.03	2.06

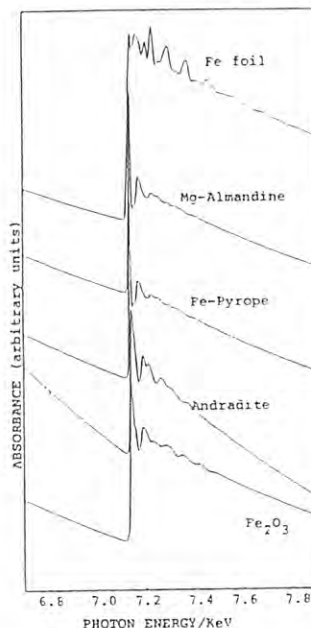


Fig.1 Fe K-edge EXAFS spectra.

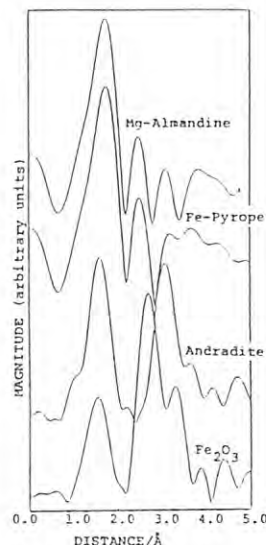


Fig.2 Fourier transform.

THE LOCAL STRUCTURE OF A VANADATE IN SUPPORTED VANADIUM OXIDE CATALYSTS. II.

Tsunehiro TANAKA, Hiroshi MIZUTANI, Yasuo NISHIMURA, Risa TSUCHITANI,
 Takuzo FUNABIKI and Satohiro YOSHIDA
*Department of Hydrocarbon Chemistry and Division of Molecular Engineering,
 Kyoto University, Sakyo-ku, Kyoto 606.*

We have previously reported the structures of vanadium oxide supported on silica and alumina using EXAFS/XANES¹ and concluded that vanadium oxide on alumina has an isolated tetrahedral structure while the oxide on silica is present mainly as a two-dimensional array of VO₆ octahedra. The conclusion is inconsistent with that deduced from ESR studies.² So far, isolated tetrahedra on silica have been thought to be the active species in photocatalysis³ and the ESR results have justified the hypothesis.

The result of our EXAFS/XANES is inconsistent with not only ESR results but also those from other techniques; UV/VIS, Raman, IR, etc. This may be related to the mode of measurements. Since our experiments were carried out *ex situ*, it is possible that the catalyst adsorbed water molecules resulting in an increase in the coordination number. In order to avoid such effects, the measurements were carried out under the Ar-purged condition in the present study.

Experimental

The catalyst samples (VS,VA: vanadium oxide supported on silica and alumina, respectively.) were the same as reported previously.¹ Dried samples (VSD, VAD) were treated *in vacuo* at 673 K and pressed into discs in the argon atmosphere. Hydrated samples (VSH, VAH) were pressed into discs under the ambient condition. The disc was sealed with polypropylene film. X-Ray absorption experiments were carried out using an Si(111) two-crystal monochromator on the beam line 7-c at KEK-PF.

Results and Discussion

Silica-supported vanadium oxide. Normalized XANES spectra of VSH and VSD are shown in fig. 1 (a) and (b), respectively. A characteristic pre-edge peak in the vicinity of 0 eV changed in height by hydration. In the case of VSD, the pre-edge peak is higher than that of VSH. This suggests that a vanadium ion of the catalyst is present in a dried state as a coordinatively unsaturated ion and the coordination number increases after hydration because of adsorption of water molecules. Fig. 1 (a') and (b') show the Fourier transforms (FTs) of EXAFS of VSH and VSD. The FTs are very different from each other. The most striking feature is that a peak is well recognized at $R = 2.5$ Å due to a V-V pair in VSH, but not in VSD. Structural parameters obtained from a curve-fitting procedure are summarized in Table 1.

These results show that isolated VO₄ species exist on a dried catalyst surface, while an adsorbed H₂O molecules bridges two VO₄ species resulting in fixing an adjacent vanadium ion.

Alumina-supported vanadium oxide. In marked contrast with the VS system, both XANES and EXAFS of a VA catalyst do not change by hydration. This

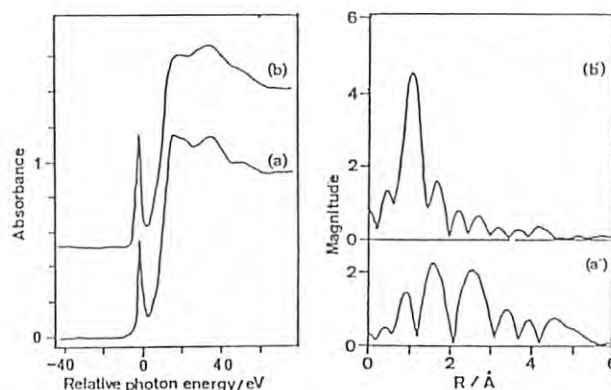


Figure 1 XANES of A-VSH(a) and A-VSD(b) and Fourier transforms of EXAFS of A-VSH(a') and A-VSD(b'). Energy offset of XANES is taken to be 5470.0 eV.

Table 1 Structural parameters for V-O shells

catalyst	dry		hydrated	
	CN	R	CN	R
A-VS	1.0	1.62	0.9	1.61
	1.0	1.78	1.5	1.81
	2.0	1.92	1.8	1.98
A-VA	1.0	1.63	1.3	1.67
	2.9	1.78	2.6	1.77

CN: coordination number
 R: bond length in Å

implies that water molecules are not adsorbed on a vanadium ion directly although a vanadium ion on alumina is located in the center of an oxygen-tetrahedron as reported previously. However, the short bond, corresponding to a V=O bond, elongates after hydration as shown in Table 1. This shows that adsorbed water molecules interact with a vanadium oxide cluster. The similar phenomenon was observed in a Raman spectroscopic study.⁴

References

- 1) T. Tanaka, H. Yamashita, R. Tsuchitani, T. Funabiki and S. Yoshida, *Photon Factory Activity Report*, 1986, #4, 198. T. Tanaka, H. Yamashita, R. Tsuchitani, T. Funabiki and S. Yoshida, *J. Chem. Soc., Faraday Trans. 1*, submitted.
- 2) S. Yoshida, T. Iguchi, S. Ishida and K. Tarama, *Bull. Chem. Soc. Jpn.*, **45**, 376 (1972).
- 3) T. Tanaka, Y. Nishimura, S. Kawasaki, T. Funabiki and S. Yoshida, *J. Chem. Soc., Chem. Commun.*, 1987, 506.
- 4) S. S. Chan, I. E. Wachs, L. L. Murrell, L. Wang and W. K. Hall, *J. Phys. Chem.*, **88**, 5831(1984).

STRUCTURE OF ULTRAFINE IRON OXIDES ON ACTIVATED CARBON FIBER

Katsumi KANEKO, Akihiko Matsumoto, Takaomi Suzuki,
Nobuhiro KOSUGI[†], and Haruo KURODA

[‡] Department of Chemistry, Faculty of Science, Chiba University
[†] Department of Chemistry, Faculty of Science, University of Tokyo

Introduction

Activated carbon fiber (ACF) has uniform micropores. The ACF modified with iron oxides can adsorb NO molecules up to 300 mg/g-adsorbent at 30 °C, although the critical temperature of NO is -93 °C. One of these authors proposed the mechanism of the chemisorption-assisted micropore filling for the anomalous NO adsorptivity (1). The structure of iron oxides on the ACF should be characterized in order to understand the role of iron oxides in the NO micropore filling. We characterized iron oxides formed on the ACF with the aid of X-ray absorption spectroscopy.

Experimental and Results

The cellulose-based ACF was mainly used. α -FeOOH was dispersed on the ACF preoxidized in 6 M HNO₃ (α -ox-ACF₃). α -ox-ACF was heated at 300-500 °C under 10⁻³ Torr for 15 h; h-ox-ACF-t was obtained by heating α -ox-ACF at t °C in vacuo. Also the ACF modified with Cu oxides was prepared for comparison.

We measured Fe K-edge XANES and EXAFS spectra of α -FeOOH, β -FeOOH, γ -FeOOH, α -Fe₂O₃, γ -Fe₂O₃, Fe₃O₄, α -ox-ACF, and h-ox-ACF by use of the EXAFS facilities at BL7C of Photon Factory in the National Laboratory for High Energy Physics. The XANES and EXAFS spectra of Cu(OH)₂, CuO, and Cu oxide-ACF were measured, too.

Figure 1 shows Fourier transforms of the k³-weighted EXAFS spectra for α -ox-ACF, h-ox-ACF-500, α -FeOOH, and α -Fe₂O₃. Each spectrum has two main peaks at near 1.4 and 2.8 Å; the 1.4 and 2.8 Å peaks can be assigned to the Fe-O and Fe-Fe distances, respectively. The spectrum of α -FeOOH has a different feature of that of α -Fe₂O₃.

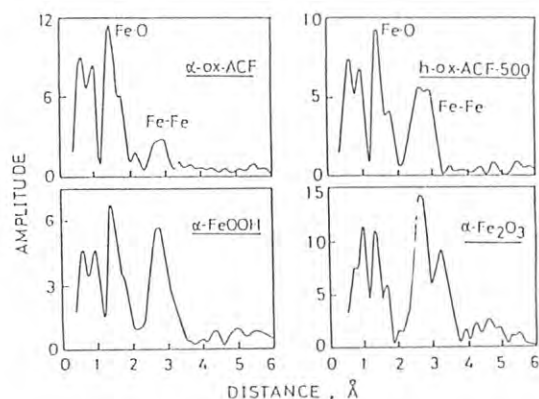


Figure 1

The predominant features of α -ox-ACF and h-ox-ACF-500 resemble to those of α -FeOOH and α -Fe₂O₃, respectively. The amplitudes of the Fe-Fe peak for α -ox-ACF and h-ox-ACF-500 are much less than those for bulk α -FeOOH and α -Fe₂O₃, respectively, suggesting that ultrafine α -FeOOH substance is on α -ox-ACF and transforms into α -Fe₂O₃-like one on heating α -ox-ACF at 500 °C. The XANES spectra of α -FeOOH, α -Fe₂O₃, α -ox-ACF, and h-ox-ACF-500 are shown in Figure 2. The spectra of α -FeOOH, α -ox-ACF, and h-ox-ACF resemble closely each other; each spectrum has a weak 1s-3d absorption and a strong 1s-4p absorption with a shoulder. Only α -Fe₂O₃ has different features; the α -Fe₂O₃-like substance on h-ox-ACF-500 suggested by the EXAFS spectra may have a slightly different structure from bulk α -Fe₂O₃. Also h-ox-ACF-300 and -400 gave the similar results to h-ox-ACF-500 (2).

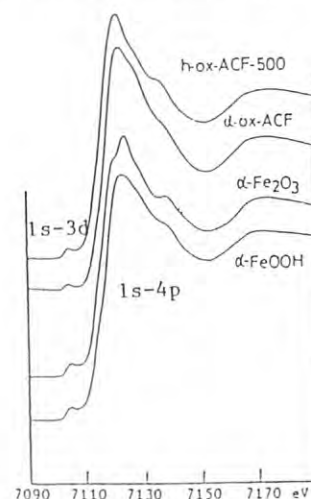
The ultrafine α -Fe₂O₃-like crystallites assume to take a role of pillars between the slit-shaped micropores of the ACF, strengthening the adsorption field against NO(3).

The EXAFS and XANES spectra of Cu(OH)₂, CuO, and Cu oxide-ACF showed that ultrafine Cu(OH)₂ or CuO is produced on the ACF in the case of Cu oxides. Also Cu oxides on the ACF enhance the NO adsorptivity as well as the iron oxides on the ACF(4).

References

- 1) K. Kaneko: Langmuir 3 (1987) 357.
- 2) K. Kaneko, A. Matsumoto, T. Suzuki, N. Kosugi, and H. Kuroda: submitted to Langmuir.
- 3) K. Kaneko: Characterization of porous solids, Elsevier, Amsterdam, 1987, in press.
- 4) K. Kaneko, T. Ohta, K. Kakei, S. Ozeki, N. Kosugi, and H. Kuroda: submitted to Appl. Surf. Sci.

Figure 2



THE STRUCTURE CHANGE OF $P_2O_5-V_2O_5$ DURING THE C_4H_8 OXIDATION REACTION

Kiyotaka ASAKURA, Hideaki YOSHITAKE, Yasuhiro IWASAWA, and Haruo KURODA

Department of Chemistry, Faculty of Science, the University of Tokyo, Hongo, Tokyo 113.

Introduction

The Al_2O_3 -supported $P_2O_5-V_2O_5$ catalysis is known for the synthesis of maleic anhydride from the 1-butene¹⁾. We studied the structure change of Al_2O_3 -supported $P_2O_5-V_2O_5$ catalysis during the 1-butene oxidation reaction by means of EXAFS spectroscopy.

Experimental

The Al_2O_3 -supported $P_2O_5-V_2O_5$ catalyst was prepared in the previous reported way¹⁾. The EXAFS measurements were carried out at BL-7C.

Results and Discussion.

Fig.1 shows the Fourier transforms of V K-edge EXAFS spectra of $P_2O_5-V_2O_5$ catalysts during the oxidation reaction. Fig.1a shows the $P_2O_5-V_2O_5$ catalysts calcined at 673 K. The first peak is due to V-O coordination. After the reaction of C_4H_8 at 750 K, the Fourier transform as shown in Fig.1b was obtained. The peak corresponding to V-O shifted to the longer side compared to that shown in Fig.1a. The interatomic distance reflects the valency of the central atom and coordination number. As the valency increases and the coordination number decreases, the interatomic distance decreases. The EXAFS analysis shows no change in the oxygen coordination number before and after the reaction. Thus the longer distance of V-O as shown in Fig.1b means that the V^{5+} is reduced to V^{4+} in the reaction with C_4H_8 . The sample was subsequently treated with O_2 at 673 K, the V-O distance was shortened again. Thus the V was reoxidised to V^{5+} . Thus the Valency of V varied between 4+ to 5+ during the reaction.

1)Mistubishi Kasei, Japan. Pat., 40-7888.

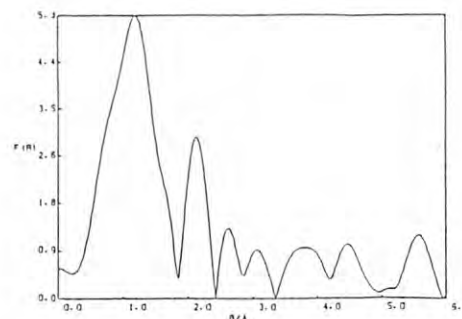


Fig.1 Fourier transform of $VOPO_4/Al_2O_3$

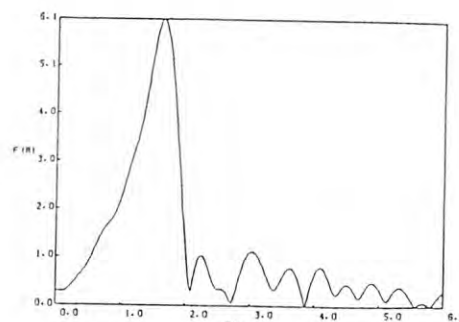


Fig.2 Fourier transform of the sample after the C_4H_8 reaction.

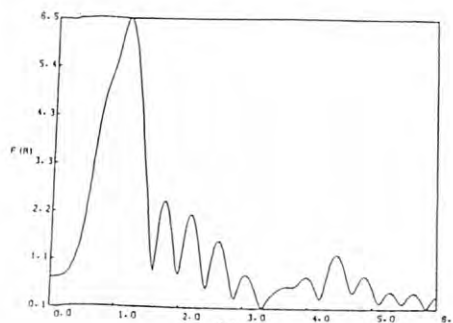


Fig.3 Fourier transform of the sample after the re-oxidation.

AN EXAFS STUDY OF Co-Mn/SiO₂ BIMETALLIC SOLVATED METAL ATOM DISPERSED CATALYSTS

Hiro Yoshi KANAI, Tsunehiro TANAKA, Satoshi YOSHIDA,
Beng Jit TAN*, and Kenneth J. KLABUNDE*

Department of Hydrocarbon Chemistry, Faculty of Engineering,
Kyoto University, Sakyo-ku, Kyoto 606

*Department of Chemistry, Kansas State University, Manhattan
Kansas 66506, U.S.A.

We have reported the synthesis and activities of unusual catalysts prepared by the solvated metal atom dispersion (SMAD) method.¹⁾ Metal atoms are solvated at low temperatures in some appropriate solvents, and upon warming metal atom clustering begins. The growing clusters incorporate carbonaceous fragments which stabilize them as amorphous "organometallic" powders and provide good means of attachment of the metal particles to support surfaces. Bimetallic catalysts are formed by the cocondensation of two metals. The addition of an equimolar amount of Mn to Co/SiO₂ SMAD catalysts increased the catalytic activity for hydrogenation of olefins by 100 fold.^{1a)} This prompted us to use EXAFS spectroscopy to obtain informations on the local structure surrounding the Co and Mn atoms.

Experimental

The Co-Mn/SiO₂ catalysts which were prepared by the SMAD method¹⁾ were pressed under N₂ into disks of 20 mm diameter using polyethylene powder as a filler. The SiO₂-supported catalysts include the following: 3.67%Co, 8.32%Co-1.57%Mn, 5.6%Co-1.47%Mn, and 3.24%Co-3.98%Mn/SiO₂. These catalysts and some Co and Mn reference compounds were measured at r.t. using the EXAFS spectrometer at BL-7C.

Results and Discussion

The Fourier transforms of Co K-edge EXAFS for SMAD Co-Mn/SiO₂ bimetallic catalysts are shown in Fig. 1. Most of the cobalt in 3.67%-Co/SiO₂ is oxidized. However, the addition of Mn (Mn/Co = 0.2 mole ratio) inhibits the formation of cobalt oxides. When the ratio of Mn/Co reaches a value of 1.32, the Fourier transform of the 3.24%Co-3.98%Mn catalyst indicates that there are a large number of metallic Co-Co bonds. Interestingly, the most active Co-Mn/SiO₂ catalyst has a Mn:Co of ca. 1. Most of cobalt clusters should be very small (ultra-fine particles) since the contributions from the higher coordination shells are small. The best result in the curve

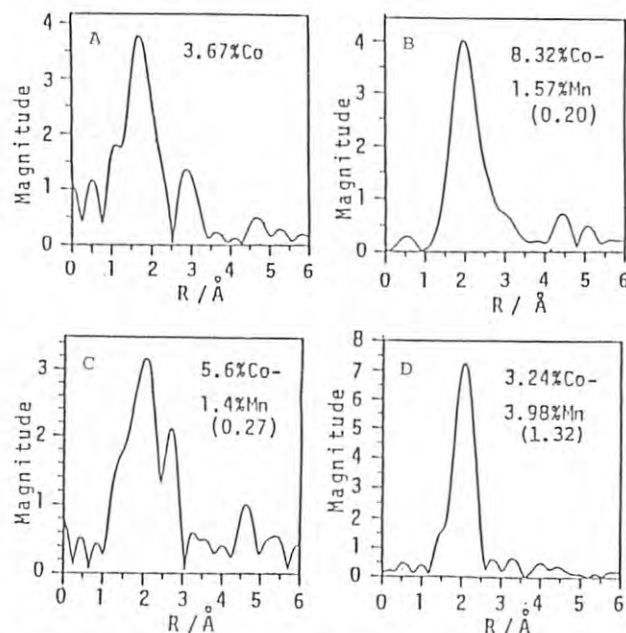


Fig. 1. Fourier transforms of Co K-edge EXAFS for Co-Mn/SiO₂ bimetallic catalysts. (): Mn/Co

fitting analysis (Table 1) was obtained only when the contribution of C atoms was taken into account. There seems to be at least some coordination between carbonaceous fragments and Co atoms.

The Fourier transform of Mn K-edge EXAFS of 3.24%Co-3.98%Mn shows that Mn species are in the oxidized state. The SiO₂ surface can provide significant but limited amount of oxygen. The more oxophilic Mn scavenges the oxygen allowing Co to remain in the metallic state. The enhancement of reactions by the addition of Mn is due to the large amount of reactive metallic Co species whose electrons are partially withdrawn by the oxidized Mn species.

References

- 1a) K.J.Klabunde and Y.Imizu, J. Am. Chem. Soc., 106, 2721 (1984);b) H.Kanai, B.J.Tan and K.J.Klabunde, Langmuir, 2, 760 (1986) and references cited therein.

Table 1 Structural parameters for Co-Mn/SiO₂ bimetallic catalysts^{a)}

Catalyst (Mn/Co)	Co-Co		Co-Mn		Co-C		Co-O	
	CN	R	CN	R	CN	R	CN	R
3.67%Co	0.27	2.48			0.13	1.89	1.42	2.01
8.32%Co-1.57%Mn (0.20)	2.95	2.47	0.51	2.67	0.25	1.96	0.25	2.01
5.60%Co-1.40%Mn (0.27)	2.30	2.47	0.24	2.72	0.33	1.92	0.51	2.04
3.24%Co-3.98%Mn (1.32)	3.29	2.46	1.25	2.67	0.32	1.91	0.10	2.03

^{a)} CN: Coordination number, R: bond length (Å)

EXAFS STUDIES ON THE Se-Nb CATALYST OBTAINED BY USE OF THE TWO-STEP FIXATION REACTION

Kiyotaka ASAKURA, Yasuo IZUMI, Rika KUWABARA, Hideaki YOSHITAKE, Junji INUKAI, Yasuhiro IWASAWA, and Haruo KURODA.

Department of Chemistry, Faculty of Science, the University of Tokyo, Hongo, Tokyo 113,

The synthesis of a new type of catalytically active species on the solid surface is one of the intriguing problem in surface science. The stepwise fixation reaction has possibility to produce the bimetallic catalyst with a well-defined structure.

We intended to prepare the SiO_2 attached Nb-Se catalyst by using the two-step fixation reaction between the $\text{Se}(\text{CH}_3)_2$ and the $\text{Nb}(\text{C}_3\text{H}_5)_3(\text{O})_x^-$ already attached on SiO_2 with the reaction of $\text{Nb}(\text{C}_3\text{H}_5)_4$ and OH groups of the SiO_2 . We studied the structure of the thus-obtained surface species by means of EXAFS to examine the existence of the Nb-Se bonding.

Experimental

The $\text{Se}(\text{CH}_3)_2$ purchased from the Toyo-Stopher Chemical Co. was used without any purification. The SiO_2 -attached allyl Nb complex was prepared in a previously reported way¹⁾. The attached allyl Nb was pretreated at 323 K under H_2 atmosphere. The 13 Torr of $\text{Se}(\text{CH}_3)_2$ was introduced into the glass system and reacted with the SiO_2 -attached Nb complex at 323 K. The amount of introduced Se was twice as large as that of Nb complex. The sample was then transferred to the EXAFS measurement cell. EXAFS spectra were taken at BL-10B.

Results and discussion

Fig. 1 shows the normalized EXAFS oscillation and Fourier transform of $\text{Se}(\text{CH}_3)_2$ in the gas phase. The Se-C bonding was observed. The normalized EXAFS oscillation and Fourier transform after the deposition of $\text{Se}(\text{CH}_3)_2$ on the SiO_2 -attached allyl Nb was shown in Fig. 2. The first peak was attributed to the bonding between the light element such as Se-O or Se-C. It possibly arises from the methyl ligand of Se. The peak at 0.24 nm was well reproduced in the several independent measurements. In Fig.3 the comparison of the Fourier-filtered EXAFS oscillation of the peak at 0.24 nm and the calculated EXAFS oscillation based on the Se-Nb bonding. The distance between Se-Nb was 0.267 nm, well corresponding to that of Se-Nb in the bulk NbSe_2 . We concluded that Se-Nb was attached selectively on Nb site. This work gives the direct evidence for the possibility to produce a desired structure on the surface if one uses the stepwise fixation process.

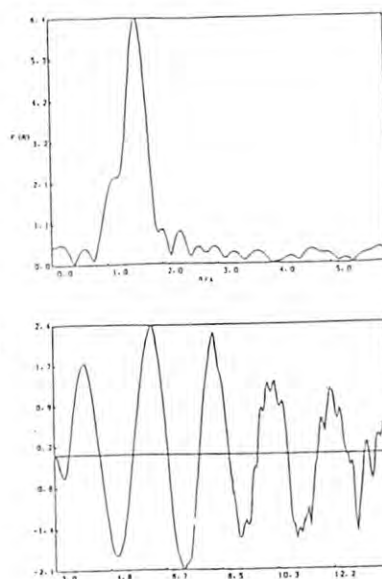


Fig.1 EXAFS oscillation and its Fourier transform of $\text{Se}(\text{CH}_3)_2$

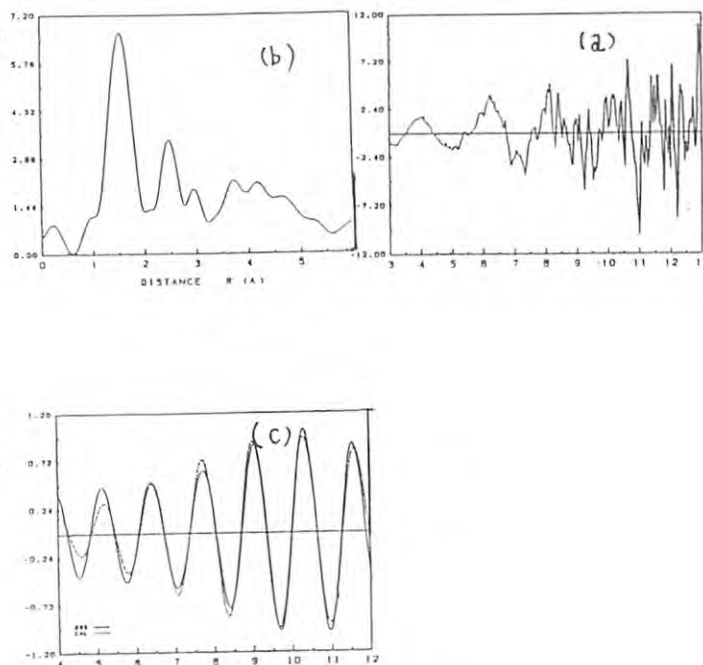


Fig.2 EXAFS oscillation and its Fourier transform of the surface Nb-Se complex (a,b). Theoretical fit of the data inversely Fourier filtered over 0.2-0.3 nm. (c)

1) M.Nishimura, K.Asakura, and Y.Iwasawa, Chem. Lett., 1986, 1457.

DETERMINATION OF THE ENVIRONMENTAL STRUCTURE AROUND A SPECIFIC ATOM IN
DISORDERED MATERIALS BY THE ANOMALOUS X-RAY SCATTERING

Yoshio WASEDA, Eiichiro MATSUBARA, Kazumasa SUGIYAMA, Kazuhiro HARADA and Shin'ichi TAKEDA⁺

Research Institute of Mineral Dressing and Metallurgy (SENKEN),
Tohoku University, Sendai 980

⁺ College of Bio-Medical Technology, Niigata University, Niigata 951

The local chemical environments around a specific element is strongly required for describing the fine structure in multi-component disordered materials. For this purpose, the Anomalous X-ray Scattering (AXS) by applying the anomalous dispersion effect near an absorption edge of a constituent element has recently received much attention coupled with the availability of synchrotron radiation source. The main purposes of this proposal is to develop the AXS technique itself and to characterize the structure of disordered materials by this relatively new technique.

Fig.1 shows the schematic diagram for the experimental set-up of the present AXS measurements at BL-7C beam line. This facility involves the ω -2 θ goniometer designed by Ishikawa et al and the associated electronics prepared by Nomura², although some modification were required for the present purpose.

The present interest for the AXS measurements focuses on the lower energy side of the absorption edge where only monotonic energy dependence of the real part of f' is observed and the imaginary part of f'' is almost constant and small. It contrasts to the energy region of the EXAFS. The energy dependence of the real part part of the anomalous dispersion, f' , was experimentally determined at several photon energies by measuring the intensity of the Bragg reflection from several polycrystalline powder samples. For the purpose of normalizing the intensity, the value of f' at energy by about 500 eV away from the edge was assumed to be the theoretical value. Fig.2 shows the energy dependence of f' obtained in this work with Cu and Ge powders as an example and agreement appears to be satisfactory. Thus, the incident energies could be selected accurately for further AXS measurements.

Recent works on the Al-Mn based alloys clearly indicate the formation of the certain

chemical short range order (SRO) in these alloys and then the formation of a similar SRO is strongly suggested in these alloys in the amorphous and liquid states. Such point may be strongly related to the formation of the quasi-periodicity found in these alloys. The variation of the intensity of amorphous $\text{Al}_{60}\text{Ge}_{30}\text{Mn}_{10}$ alloy was measured at several energies close to the absorption of Ge-K edge and the part of the results is given in Fig.3. Some distinct structural features such as three headed first peak and the second peak with shoulder are detected. As shown in Fig.3, the intensity is also significantly dependent upon energy and such variation corresponds to the local chemical environment around a Ge atom in amorphous $\text{Al}_{60}\text{Ge}_{30}\text{Mn}_{10}$ alloy, although the detailed information is not obtained yet.

1.T.Ishikawa,J.Matsui and T.Kitano: Nucl. Instr. Meth., A246(1986)613.

2. M.Nomura: KEK Report Inter. No.87-1(1987).

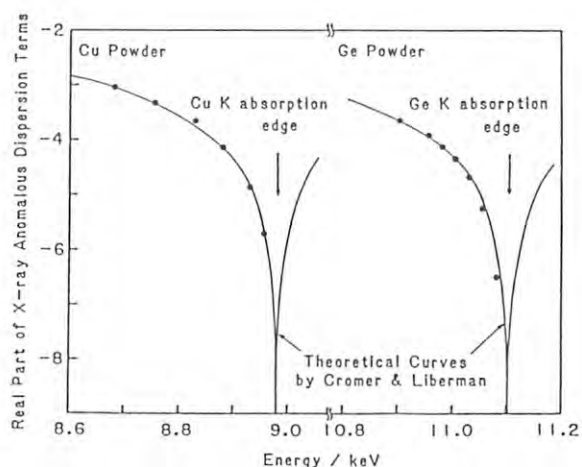


Fig.2 Energy dependence of f' for Cu and Ge.

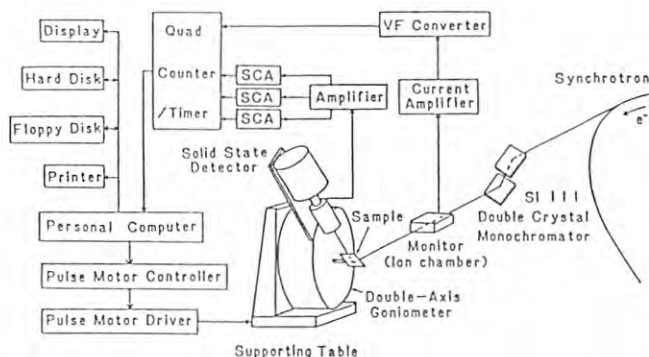


Fig.1 Schematic diagram for AXS measurements.

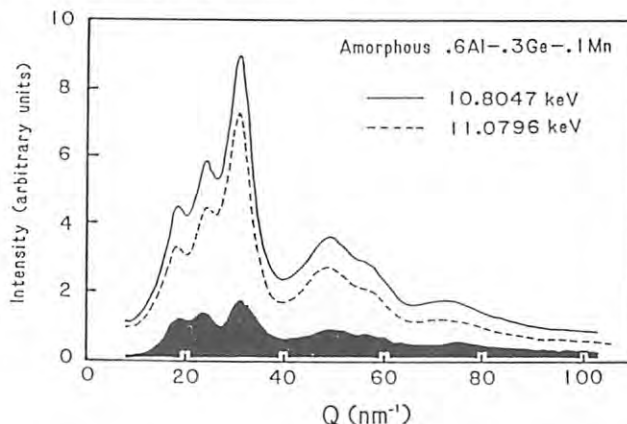


Fig.3 Energy dependence of the intensity pattern of amorphous Al-Ge-Mn alloy.

VANADIUM K-EDGE X-RAY ABSORPTION SPECTROSCOPY OF THE REDUCED AND THIONINE-OXIDISED FORMS OF THE VFe PROTEIN OF THE VANADIUM NITROGENASE FROM *AZOTOBACTER CHROOCOCCUM*

Judith M. Arber, Barry R. Dobson*, Robert R. Eady**, S. Samar Hasnain*, C. David Garner, Tadashi Matsushita[†], Masaharu Nomura[†] and Barry E. Smith**

Department of Chemistry, University of Manchester, Manchester M13 9PL, UK

*SERC Daresbury Laboratory, Warrington WA4 4AD, UK

**AFRC Unit of Nitrogen Fixation, University of Sussex, Brighton BN1 9RQ, UK

[†]Photon Factory, National Laboratory for High Energy Physics, Oho-machi, Tsukuba-gun, Ibaraki 305

Introduction

The free-living nitrogen-fixing bacterium *Azotobacter chroococcum* has recently been shown to contain two nitrogenase systems. One of these is the well-characterised molybdenum-containing enzyme and the other, which is encoded by different genes, contains vanadium^{1,2}. Our initial EXAFS study has shown that the V environment contains O, S and Fe and has a striking similarity to the environment of Mo in FeMoco, thus suggesting the presence of a vanadium-containing cofactor³.

Vanadium K-edge X-ray absorption spectra have been collected for samples of thionine-oxidised, super-reduced (during enzyme turnover) and dithionite-reduced vanadium-iron protein of the vanadium nitrogenase from *Azotobacter chroococcum* (Acl*)^{1,2}. Both the extended X-ray absorption fine structure (EXAFS) and the X-ray absorption near-edge structure (XANES) are consistent with previous data for the dithionite-reduced protein³, implying that the vanadium is present as part of a VFeS cluster and that the environment of the vanadium is not significantly altered in different oxidation states of the protein.

Experimental and Results

X-ray absorption spectra were recorded in fluorescence mode on EXAFS station 7C at the Photon Factory; ca. ten scans were recorded and averaged for each sample. A sagittal focusing, double crystal Si(111) monochromator was used together with a 200 mm long fused quartz mirror placed at an angle of ca. 8 mrad to reduce harmonic contamination. Incident intensity was measured using a windowless ionisation chamber whilst a Lytle cell, filled with 100% argon and masked with a titanium foil, monitored fluorescent intensity. An average sample temperature of 80 K was maintained during data collection by use of a liquid nitrogen cryostat. Data analysis was accomplished via the single-scattering spherical-wave method for EXAFS calculation and phaseshifts were derived from *ab initio* calculations as described previously⁴⁻⁶.

Vanadium K-absorption edge and XANES data are shown in Fig. 1 for both the thionine-oxidised and dithionite reduced forms of Acl*, together with a single scan for the protein during enzyme turnover. The structure of the edge and XANES are similar for all samples, namely a weak pre-edge feature and edge inflection, and a 'doublet' in the XANES, and also resemble those previously observed for the dithionite-reduced protein³. This overall

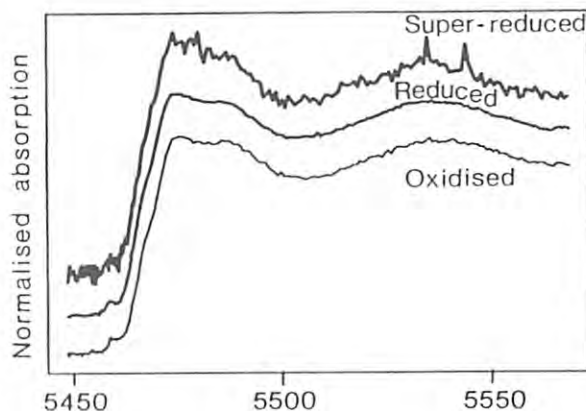


Fig. 1

similarity implies that no major changes are occurring in the local environment of the vanadium. The intensity of the pre-edge feature implies distorted octahedral coordination of the vanadium in all the systems studied⁷. The position of the edge and pre-edge feature relative to vanadium metal indicate an oxidation state of between V(II) and V(IV).

Fig. 2 shows the vanadium K-edge EXAFS data for dithionite-reduced and thionine-oxidised Acl* ((a) and (b) respectively) together with their Fourier transforms and simulations employing the parameters given in the Figure. The two sets of data resemble each other closely and are also like the previously published data for the dithionite-reduced protein³. In both cases the data were best simulated with backscattering from 3 ± 1 oxygen, 3 ± 1 sulphur and 3 ± 1 iron atoms, assuming octahedral coordination at vanadium, as deduced from the edge data.

Thus the edge, XANES and EXAFS data presented here are consistent with vanadium in the reduced and oxidised forms of Acl* being coordinated in a similar environment to the cluster compound $[\text{NMe}_4][\text{VFe}_3\text{S}_4\text{Cl}_3(\text{DMF})_3]$ ⁸. This situation is analogous to that of the MoFe protein of nitrogenases where X-ray absorption studies of reduced and oxidised samples showed that molybdenum is present as part of a MoFeS cluster and that there are no appreciable differences in the molybdenum K-edge EXAFS upon a change in the oxidation level⁹. In the case of molybdenum this has been attributed to delocalisation effects and similar effects are probably operable for vanadium in the VFe protein.

....

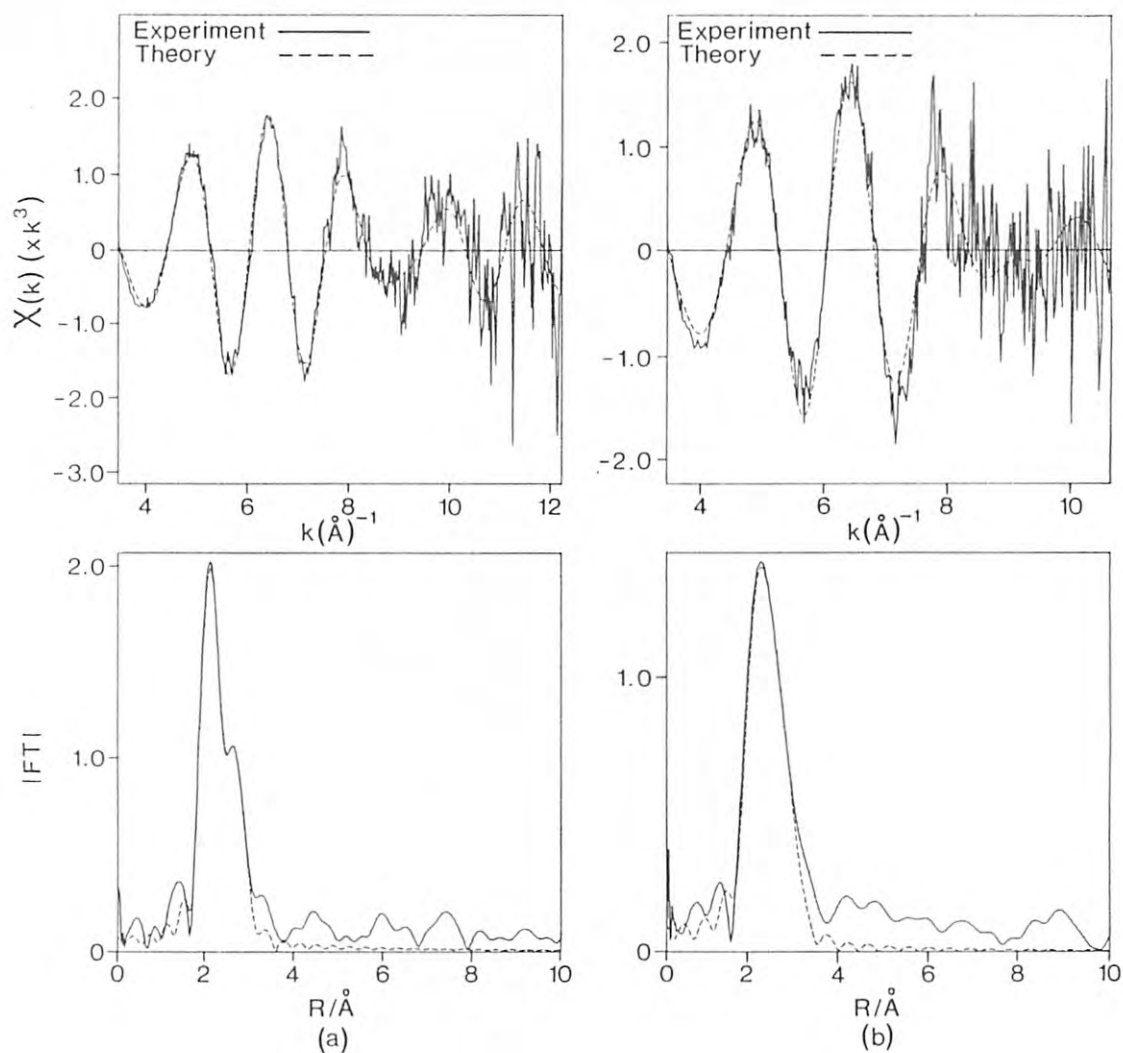


Fig. 2. Theoretical simulations using (a) three oxygen at 2.13 Å, three sulphur at 2.35 Å and three iron at 2.71 Å, and (b) three oxygen at 2.13 Å, three sulphur at 2.35 Å and three iron at 2.70 Å.

References

- 1) R.L. Robson, R.R. Eady, T.H. Richardson, R.W. Miller, M. Hawkins and J.R. Postgate: Nature 322 (1986) 388.
- 2) R.R. Eady, R.L. Robson, T.H. Richardson, R.W. Miller and M. Hawkins: Biochem. J. 244 (1987) 197.
- 3) J.M. Arber, B.R. Dobson, R.R. Eady, P. Stevens, S.S. Hasnain, C.D. Garner and B.E. Smith: Nature 325 (1987) 372.
- 4) P.A. Lee and J.B. Pendry: Phys. Rev. B11 (1975) 2795.
- 5) M.F. Perutz, S.S. Hasnain, P.J. Duke, J.L. Sessler and J.E. Hahn: Nature 295 (1982) 535.
- 6) S.J. Gurman, N. Binsted and I. Ross: J. Phys. C17 (1984) 143.
- 7) J. Wong, F.W. Lytle, R.P. Messmer and D.H. Maylotte: Phys. Rev. B 30 (1984) 5596.
- 8) J.A. Kovacs and R.H. Holm: J. Amer. Chem. Soc. 108 (1986) 340.
- 9) S.P. Cramer, K.O. Hodgson, W.O. Gillum and L.E. Mortenson: J. Amer. Chem. Soc. 100 (1978) 3398.

A HIGH-SPEED DIGITAL SUBTRACTION ANGIOGRAPHY SYSTEM FOR PHANTOM AND SMALL ANIMAL STUDIES

Ken UEDA, Keiji UMETANI, Ryuichi SUZUKI and Hisatake YOKOUCHI

Central Research Laboratory, Hitachi Ltd.
Kokubunji, Tokyo 185

Introduction

Until now, selective coronary angiography requires invasive procedure. Study on new method with less-invasive transvenous injection of contrast materials is being carried out in several facilities using synchrotron radiation! This study aims to develop a high-speed, high-resolution imaging system. A proto-type system has been constructed for phantom and small animal studies.

Experiment

The present system is shown in Fig. 1. Synchrotron radiation 60 mm in width was obtained at Hitachi beam line (BL-8C) of Photon

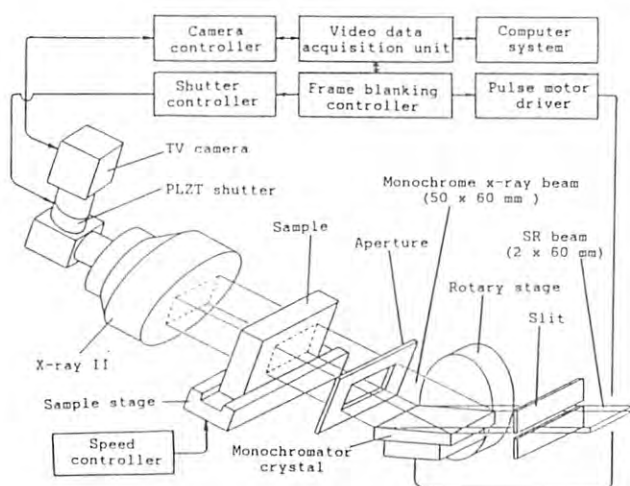


Fig. 1. System configuration

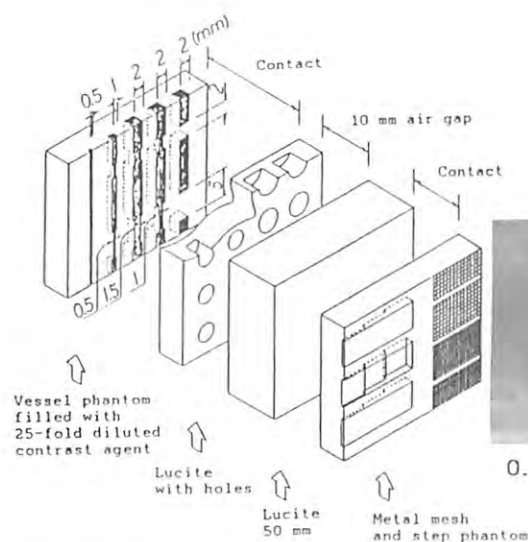


Fig. 2. Iodine K-edge subtraction image

Factory. A 450 mm x 70 mm silicon monocrystal is used for monochromator. Asymmetric reflections at silicon (111) planes expand beam size 25 times and offer a 50 mm x 60 mm monochromatic x-ray beam, whose intensity is 400 mR/s at electron current of 200 mA. Change of x-ray photon energy is performed by stepping motor controlled rotation of the crystal. Time required to change energy between above and below iodine K-edge is less than 16 ms for 500 eV change. The TV camera incorporates high-resolution Saticon tube, and is operated 1125 lines for precise mode. It can be operated either 525 or 262 lines for dynamic mode. Frame scanning time is 33.3 ms and 16.7 ms respectively. 8 images are acquired continuously in 2M byte frame memory. Further developments are being planned.

Results

For 2 mm vessel phantom filled with 25-fold diluted agent (14 mg/ml iodine) in composite phantom, 44 percent contraction was clearly visualized (Fig. 2). Detection limit of the diluted agent was 0.5 mm. For a phantom consisted of Lucite, pig ribs, and a coronary artery filled with denser contrast material, 0.3 mm vessels were visualized free from obstruction of the rib image (Fig. 3). Energy subtraction with each exposure time of 16.7 ms and time interval of 16.7 ms was achieved, and 1 mm vessel phantom moving at 30 mm/s was clearly seen.

This work has been performed under the approval of National Laboratory for High Energy Physics (Acceptance No. 86-018).

References

- 1) A. Akisada, M. Ando, K. Hyodo, S. Hasegawa, K. Konishi, K. Nishimura, A. Maruhashi, F. Toyohuku, A. Suwa and K. Kohra, Nucl. Instrum. and Meth. in Phys. Res. A246 (1986) 713-718.

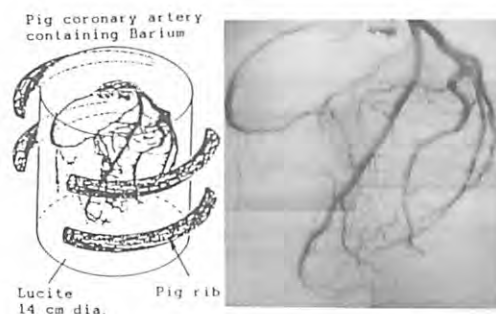


Fig. 3. Barium K-edge subtraction image (synthesis from 6 sub-images)

HIGH RESOLUTION TOMOGRAPHY EMPLOYING AN X-RAY SENSING PICKUP TUBE

Tatsumi HIRANO, Katsuhisa USAMI, Koozoo SAKAMOTO, Yoshio SUZUKI*

Hitachi Research Laboratory, Hitachi Ltd., Hitachi Ibaraki

*Advanced Research Laboratory, Hitachi Ltd., Kokubunji Tokyo

Introduction

Recently, X-ray computed tomography(CT) using synchrotron radiation(SR) has been applied in nonmedical fields such as industrial materials research. CT using SR is able to observe the distribution of a specific element and to provide CT images with high spatial resolution.¹⁾²⁾ In order to get high quality CT images with high resolution, it is necessary to use not only monochromatized X-ray beam from a point-like X-ray source, but also an X-ray image detector with high spatial resolution. This report describes high resolution CT images detected by an X-ray sensing pickup tube.

Experimental and Results

The CT instruments are installed on BL-8C connected to KEK Photon Factory storage ring. SR having a white spectrum is monochromatized by an Si(400) channel cut monochromator. It is collimated into a width of 30mm and a height of 0.05-2mm by the entrance slit. The beam is applied to the sample, before being led to the image detector. A test sample which is SiC fiber reinforced Si₃N₄ ceramics is used to confirm high spatial resolution of the CT image. The SiC fiber (140 $\mu\text{m}\phi$) consists of a carbon core(30 $\mu\text{m}\phi$) and SiC which is deposited around the core by CVD(see Fig.1).

Firstly, A photo diode array detector(PDA) which has 1024ch and 25 μm width x 2.5mm height is used. The projection image of the sample is magnified by asymmetric Bragg diffraction because the spatial resolution of the PDA is about 120 μm .³⁾ As shown in Fig.2, the CT image of the sample is obtained with an exposure time of 30s per one projection, using nine fold magnification, at 24keV photon energy. The carbon fiber core and SiC fiber are found as individual components. It is not, however,

enough only to distinguish the boundaries between carbon fiber core, SiC fiber and Si₃N₄ ceramics.

Secondly, the projection image of the sample is detected with an X-ray direct-sensing pickup tube whose spatial resolution is about 8 μm , as estimated with a radial pattern test chart.⁴⁾ Channel size of this pickup tube is 7.5 μm wide x 6.0 μm high for the present scanning size of 7.7x6.1mm². In Fig.3 the CT image of the sample is shown with an exposure time of 1.2s at 24keV photon energy. No magnification is used. The boundaries between carbon fiber core, SiC fiber and Si₃N₄ ceramics are clearly seen. The X-ray direct-sensing pickup tube is able to obtain higher resolution CT images than those measured by PDA with several fold magnification.

This work has been performed under the approval of the Photon Factory Program Advisory Committee (Proposal No.86-018)

References

- 1) Yu.I.Borodin et al., Nucl. Instr. and Meth. A246 (1986) 649.
- 2) A.C.Thompson et al., Nucl. Instr. and Meth. 222 (1984) 319.
- 3) K.Sakamoto et al. in preparation
- 4) Y.Suzuki et al. in preparation

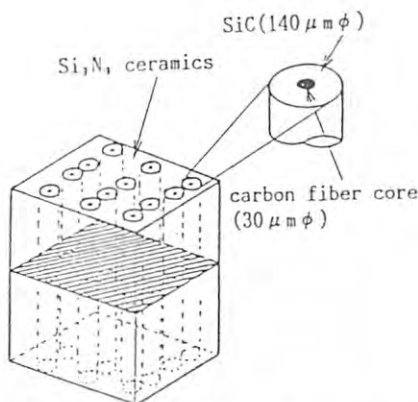


Fig1. An illustration of the SiC fiber Si₃N₄ ceramics composite.

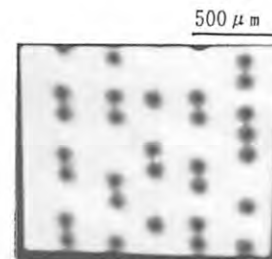


Fig2. A CT image with nine fold magnification of the sample measured by PDA. Slice width is 1.0mm.

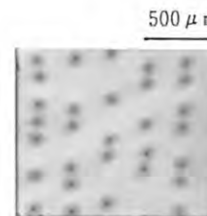


Fig3. A CT image of the sample measured by the X-ray sensing pickup tube with no magnification. Slice width is 0.9mm.

X-RAY SENSING PICKUP TUBE

Yoshio Suzuki, Kazunobu Hayakawa, Katsuhisa Usami*,
Tatsumi Hirano*, Tooru Endo** and Yoshinori Okamura**

*Advanced Research Laboratory, Hitachi Ltd., Kokubunji Tokyo
*Hitachi Research Laboratory, Hitachi Ltd., Hitachi Ibaraki
**Hitachi Denshi Ltd., Kobuchizawa Yamanashi

Introduction

The X-ray two-dimensional image sensor is one of the most important components in X-ray microscopy and X-ray topography. Chikawa et al [1] have recently developed a high resolution (6 μm) X-ray sensing pickup tube. The X-ray direct-sensing pickup tube has a beryllium faceplate. The faceplate adversely affects image quality of the pickup tube: white defects appear in the scanning area. Since it is very difficult to make smooth beryllium surfaces, small pits remain. These small pits on the faceplate are believed to cause the white defects. This report describes an X-ray direct-sensing pickup tube with a new faceplate structure free of white defects.

Experiments and Results

Tube structure is shown in Fig. 1. The faceplate consists of two parts. The atmosphere side is 500 μm thick beryllium. The vacuum side is a 25 μm glass plate. The transparent electrode and photoconductive layer are deposited on this glass plate. Using this faceplate, both high X-ray transmittance and smooth surface are obtained, since glass polishes much easily than beryllium. The glass plate is so thin that transmittance is sufficiently high. The photoconductive layer is identical to that of Chikawa. Amorphous Se/As alloy of 20 μm thick is used. A diode electron gun [2] of high-definition pickup tube (H4186, Mobara Works, Hitachi Ltd.) provides narrow scanning electron beam.

The pickup tube's characteristics has been evaluated at BL-8C. Measured spectral response is shown in Fig. 2. This pickup tube functions in wide X-ray energy range from 7 to 40 keV. Sensitivity takes a maximum (6×10^{-17} A/(photons/s)) at 20 keV. Measured square wave amplitude response is shown in Fig. 3. A lead test chart whose finest pattern is 10 line pairs/mm is reduced to 20% by asymmetric Bragg diffraction. The measured amplitude response at 50 line pairs/mm is about 9%. Limiting resolution is estimated to be about 8 μm .

Preliminary study for monochromatic X-ray microradiography has also been performed as shown in Fig. 4. Projection images of a test sample are

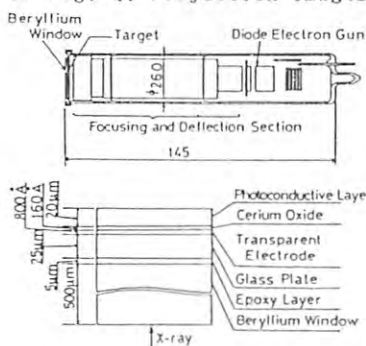


Fig.1
Pickup tube
and
faceplate

taken at different X-ray energies above and below the Mo K-absorption edge. Elemental mapping of the sample can be observed by difference between two images. No defects such as white spots are observed in the scanning area.

The authors would like to thank Dr.T.Kawamura of NHK Science and Technical Research Laboratories for valuable discussions on developing the pickup tube and appreciate the staff of KEK-PF for useful advice for use of synchrotron radiation. This study has been performed under the approval of National Laboratory for High Energy Physics (Accepted No.86-014)

References

- [1] J.Chikawa, F.Sato, T.Kawamura, T.Kuriyama, T.Yamashita and N.Goto X-ray Instrumentation for the Photon Factory: Dynamic Analysis of Micro Structure in Matter pp145 (1986) KTK Scientific Publishers, Tokyo
- [2] Y.Isozaki, J.Kumada, S.Okude, C.Ogusu and N.Goto IEEE Trans. ED28(1981)1500

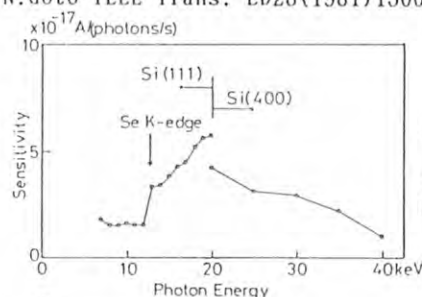


Fig.2
Spectral response
of
the X-ray sensing
pickup tube

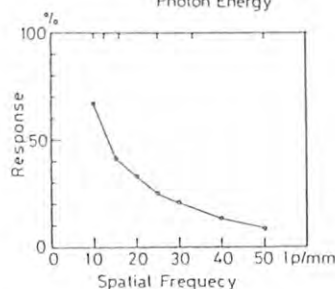


Fig.3
Amplitude response
of
the X-ray sensing
pickup tube

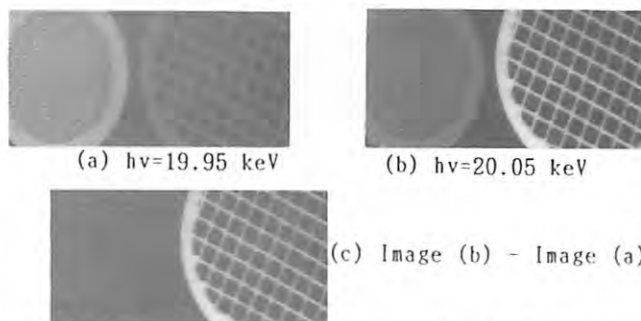


Fig.4 Energy differential image of a test sample.
Right is 400-mesh 3 mm-diameter copper screen.
Left is 100-mesh 4 mm-diameter molybdenum screen.

INVESTIGATION OF SYSTEM RELIABILITY ON THE BL-9A SR LITHOGRAPHY BEAMLINE

Koichi OKADA, Kiyoshi FUJII, Yutaka KAWASE⁺,
Masaharu NAGANO⁺ and Hidehiko KURODA⁺

Microelectronics Research Laboratories, ⁺R&D Planning and
Technical Service Division, NEC Corporation, 1-1, Miyazaki
4-chome, Miyamae-ku, Kawasaki 213

Introduction

Synchrotron radiation (SR) lithography is a promising technology for replacing photolithography in future dimensions below 0.5 μ m. The high intensity and good collimation achievable by using SR appear to realize high throughput and highest resolution. Recently, we have developed an SR lithography beamline using the BL-9A branch line.¹⁾

During the present work, system reliability has been investigated in terms of vacuum breakdown protection.

FCV and ADL

The BL-9A SR lithography beamline, one of 3 branch lines split from a basic beamline, is a 10^{-7} Pa UHV system with an oscillating mirror. In addition to a 40 msec closing-time fast closing valve (FCV) and an acoustic delay line (ADL), installed in the basic beamline,²⁾ we have set up a <15 msec closing-time FCV and 40 msec delay-time ADL in the branch beamline, thus organizing a double vacuum protection system. Particularly, the FCV and ADL are placed far upstream of the oscillating mirror, to cope with unforeseen occurrences, such as gas leakage caused by the oscillating mechanism and gas release from the mirror irradiated by SR. A vacuum breakdown test was undertaken to confirm the performance of the FCV and ADL installed in the branch beamline. The variation in pressure with time lapse is demonstrated in Fig. 1. The results showed that the pressure, measured at a cold-cathode gauge set up just upstream of the FCV, was increased from 1×10^{-4} Pa to 5×10^{-3} Pa, when 10^5 Pa air was introduced downstream of the ADL. The 10^5 Pa air introduction leads to an abrupt increase in pressure, measured at a

Bayard-Alpert pressure gauge placed downstream of the ADL. After the FCV operated, the pressure at the cold-cathode pressure gauge was kept at 5×10^{-3} Pa. As a result, it was found that the FCV and ADL provided appreciably good performance and operated successfully for the present purpose.

Double-structured bellows

The oscillating mirror is driven through a bellows by a combination of DC servomotor and a cam mechanism. The bellows expands and contracts with a vibrating shaft motion. Therefore, it could happen that a small but sudden leakage in the bellows would lead to a vacuum breakdown. In order to provide against such a gas leakage, a double-structured bellows has been contrived, as shown in Fig. 2. Low vacuum evacuation is made in the space between the two bellows. Even if a gas leakage were to take place in the outer bellows, the system would not be damaged. In the case of a gas leakage in the inner bellows, the increase in pressure at the mirror chamber results in the operation of an interlock function, followed by shutting all gate valves in the beamline.

References

- 1) K. Okada, K. Fujii, Y. Kawase and M. Nagano: J. Vac. Sci. Technol. (to be published).
- 2) S. Sato, T. Koide, Y. Morioka, T. Ishii, H. Sugawara and I. Nagakura: Nucl. Instr. and Meth. **208**, 31 (1983), and N. Kanaya, S. Sato, K. Nakajima and S. Hayashi: IEEE Trans. Nucl. Sci. **NS-33**, 1071 (1986).

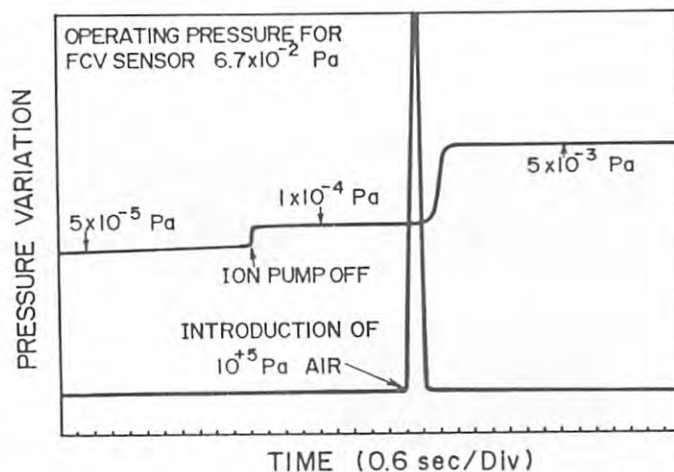


Fig. 1. Vacuum breakdown test, using the present FCV and ADL.

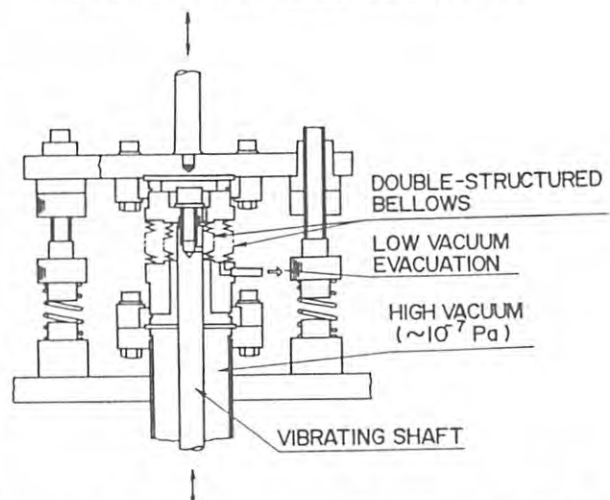


Fig. 2. Double-structured bellows. The tip of a vibrating shaft is connected to the mirror edge.

INTERFACIAL SUPERSTRUCTURE OF a-Si/Si(111)-7x7 AND a-Si/Ge_{0.2}Si_{0.8}(111)-5x5 STUDIED BY GRAZING INCIDENCE X-RAY DIFFRACTION

Koichi AKIMOTO, Jun'ichiro MIZUKI, Ichiro HIROSAWA, Toru TATSUMI, Hiroyuki HIRAYAMA, Naoaki AIZAKI and Junji MATSUI

Fundamental Research Laboratories, NEC Corporation
1-1 Miyazaki 4-chome, Miyamae-ku, Kawasaki, Kanagawa 213, Japan

Introduction

Heterojunctions are widely used in semiconductor devices. In these systems, the interfaces often play an important role in the determination of physical characteristics. Although a reconstructed structure on a clean solid surface is well studied by many techniques, it has not been clear so far that a reconstructed structure or a superstructure does exist at an interface between two solid layers.

Recently, a 7x7 interfacial superstructure was observed at an a-Si/Si(111) interface by the TED technique 1). In this report, we will show the experimental results of the structural studies on a-Si/Si(111)-7x7 and a-Si/Ge_{0.2}Si_{0.8}(111)-5x5 interfacial superstructures. And we will discuss these structures in the real space according to the DAS model 2).

Experimental

The sample preparation procedure is as follows. Ge_{0.2}Si_{0.8}(111) alloy layers were grown by an MBE technique 3). After a Si(111)-7x7 or a Ge_{0.2}Si_{0.8}(111)-5x5 RHEED pattern was obtained, an amorphous Si layer of 100 Å in thickness was deposited at room temperature.

X-Ray Bragg peaks from interfacial superstructure of a-Si/Si(111)-7x7 and a-Si/Ge_{0.2}Si_{0.8}(111)-5x5 were observed by the grazing incidence X-ray diffraction technique. The experimental configuration in detail was described in the previous report 3).

Results and Discussion

The observed 7x7 intensity diagram is shown in Fig. 1. Areas of the solid circles are

proportional to intensities. The open circles show that at the corresponding reciprocal lattice points, no diffraction peaks were observed. The star marks show the fundamental lattice points. The observed 5x5 intensity diagram is shown in Fig. 2.

It was found that the intense peaks lay around fundamental lattice points (10), (01), (11) etc.) and on the line connecting fundamental lattice points in both samples.

In the Patterson maps constructed from the observed intensities of fractional-order reflections, Patterson peaks concerned with adatoms in the DAS model disappear or intensity of those peaks is weak. This implies that the deposition of a-Si results in destroying the periodic order of adatoms in the DAS model.

The diagram illustrating the observed intensity distribution has a resemblance to that calculated from the stacking-fault structure in the DAS model. This may suggest that the ordering of amorphous layers occurs on top of the stacking-fault layer and the interface structure results in emphasizing stacking-fault layers.

The intensity diagram in which two stacking-fault layers and one dimer layer are taken into account, agrees fairly well with the observed intensity diagram.

References

- 1) J.M.Gibson, H.-J.Gossmann, J.C.Bean, R.T.Tung and L.C.Feldman: Phys. Rev. Lett. 56 (1986) 355.
- 2) K.Takayanagi, Y.Tanishiro, M.Takahashi and S.Takahashi: J. Vac. Sci. Technol. A3 (1985) 1502.
- 3) K.Akimoto, J.Mizuki, T.Tatsumi, N.Aizaki and J.Matsui: Surf. Sci. 183 (1987) L297.

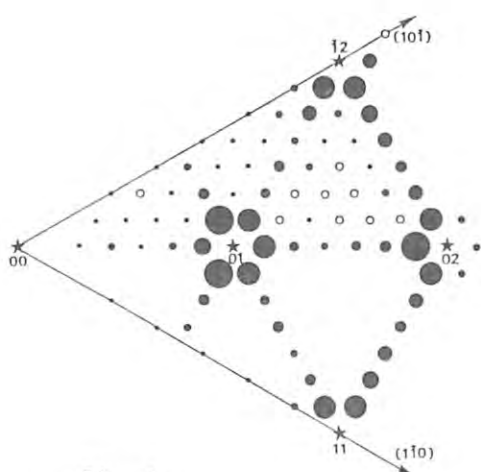


Fig. 1

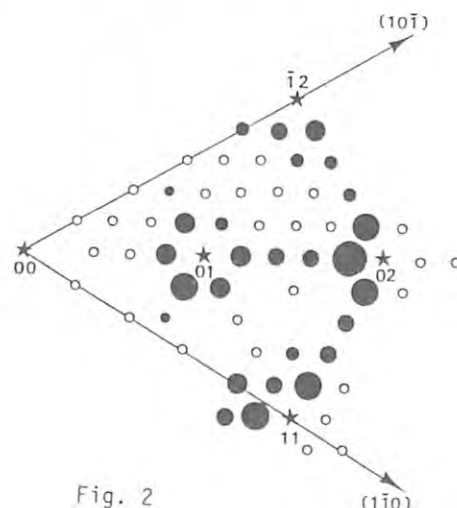


Fig. 2

INTERFACIAL SUPERSTRUCTURE BETWEEN AN EPITAXIAL Si(111) LAYER AND A B($\sqrt{3}\times\sqrt{3}$)/Si(111) SUBSTRATE STUDIED BY GRAZING INCIDENCE X-RAY DIFFRACTION

Koichi AKIMOTO, Jun'ichiro MIZUKI, Ichiro HIROSAWA, Toru TATSUMI,
Hiroyuki HIRAYAMA, Naoaki AIZAKI and Junji MATSUI

Fundamental Research Laboratories, NEC Corporation
1-1 Miyazaki 4-chome, Miyamae-ku, Kawasaki, Kanagawa 213, Japan

Introduction

Heterojunctions are widely used in semiconductor devices. In these systems, the interfaces often play an important role in the determination of physical characteristics. Although a reconstructed structure on a clean solid surface is well studied by many techniques, an atomic structure at the interface has not been clear so far.

In this report, we will show that the superstructure exists at the interface between epitaxial layers 1).

Experimental

The sample preparation procedure is as follows. A Si(111)-7x7 RHEED pattern was obtained by the surface cleaning technique. A pure Si(111) buffer layer of 300 Å in thickness was grown on the cleaned Si(111) surface, whose temperature was 750°C. Boron from an H₂O₂ crucible cell was deposited on the substrate at 750°C. The ($\sqrt{3}\times\sqrt{3}$)R30° RHEED pattern was observed at the coverage of 1/3 ML of boron. Finally, a Si(111) epitaxial layer of 100 Å in thickness was grown on this ($\sqrt{3}\times\sqrt{3}$)R30°-B ($\theta = 1/3$ ML) surface structure at the substrate temperature of 600°C. The surface structure of this Si(111) epitaxial overlayer was 7x7 reconstructed structure. The structure of this sample is shown in Fig. 1(a).

As another sample, an amorphous Si layer of 100 Å in thickness was deposited on the ($\sqrt{3}\times\sqrt{3}$)R30°-B ($\theta = 1/3$ ML) surface structure processed by the same procedure. The sample structure is shown in Fig. 1(b).

A grazing incidence X-ray diffraction technique was employed to study the interfacial superstructure. The X-rays with a wavelength of

1.5 Å struck the sample at the grazing incident angle of 0.2°. The experimental configuration in detail was described in the previous report 2).

Results and Discussion

The diffraction profiles from the sample of Si(111)/B($\sqrt{3}\times\sqrt{3}$)/Si(111) are shown in Fig. 2. The diffraction profiles are taken with θ -scans at the (2/3, 2/3) and the (-2/3, 4/3) fractional lattice points in the two-dimensional reciprocal lattice space. These profiles show existence of ($\sqrt{3}\times\sqrt{3}$)R30° superstructure.

The diffraction profiles from the sample of a-Si/B($\sqrt{3}\times\sqrt{3}$)/Si(111) are shown in Fig. 3. The diffraction peaks were observed at the (-2/3, 4/3) and the (-1/3, 5/3) fractional lattice points. Intensity of these peaks is higher than that of the diffraction peaks from the interfacial superstructure between epitaxial layers. This is because the interfacial superstructure between epitaxial layers may be partially destroyed, relative to that between an amorphous layer and a substrate.

Using this interfacial superstructure, a three-dimensional superstructure can be formed. And a two-dimensional monolayer doping can be realized.

References

- 1) K.Akimoto, J.Mizuki, I.Hirosawa, T.Tatsumi, H.Hirayama, N.Aizaki and J.Matsui: Extended Abstracts of the 19th conference on Solid State Devices and Materials, Tokyo, 1987, pp. 463-466.
- 2) K.Akimoto, J.Mizuki, T.Tatsumi, N.Aizaki and J.Matsui: Surf. Sci. 183 (1987) L297.

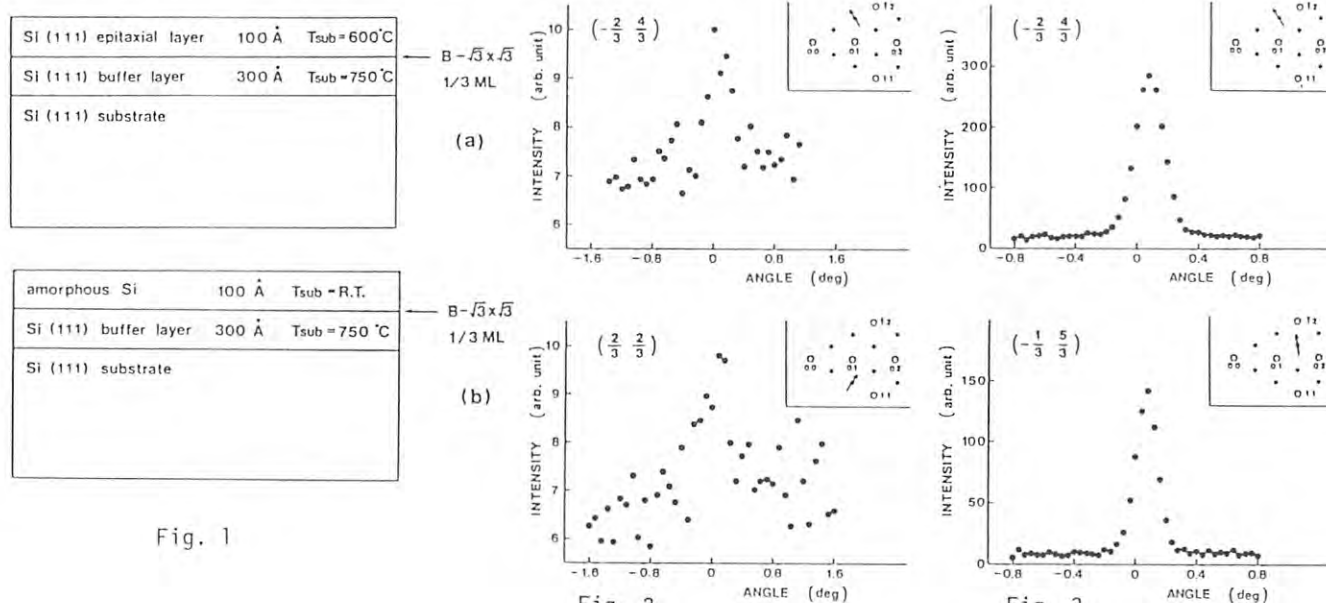


Fig. 1

Fig. 2

Fig. 3

INVESTIGATION OF THE INTERFACE STRUCTURE BETWEEN Al AND GaAs(001) BY GRAZING INCIDENCE X-RAY DIFFRACTION

Jun ichiro Mizuki, Koichi Akimoto, Ichiro Hirosawa,
Kazuyuki Hirose, Takashi Mizutani and Junji Matsui

Fundamental Research Laboratories, NEC Corporation
1-1 Miyazaki Yonchome, Miyamae-ku, Kawasaki, Kanagawa, 213

Introduction

Our understanding of the metal-semiconductor contact has been relatively poor so far in spite of extensive studies nearly a half century. An Al on GaAs surfaces, for instance, is of some interest as the system, which can be used as an example in both experimental and theoretical investigations of Schottky barriers and adsorption phenomena. Since the atomic structure at the interface, which must be important to understand the Schottky barrier height, has not been clear so far, no single model can explain all the experimental data for the formation of Schottky barrier height. In this report, we will show the existence of the super-structure at the interface between Al and GaAs(001) by grazing incidence X-ray diffraction¹⁾.

Experimental and Results

The sample structure studied in the present experiment consists of a 90-150 Å-thick Al top layer and 1 μm-thick Si-doped GaAs epitaxial layer. The Al layer was deposited at 30°C in the MBE-grown chamber after the desired surface structure on GaAs (001) was formed. The two kinds of samples were prepared for the present studies; one is that the (2×4)-reconstructed structure, which is As-stabilized surface structure, was formed before the deposition of Al layer (labeled Sample A), and the other is the (4×6)-reconstructed structure, which is Ga-stabilized surface structure (labeled Sample B). The present experiment was performed at BL-9C. The X-rays of 1.5 Å in wavelength were selected by two (111)Si monochromators and was impinged on the sample under the condition of 0.3 grazing incident angle. The experimental configuration in detail was described in the previous report²⁾. The typical scattering patterns with Sample B are shown in Figure 1. They were taken by rocking the sample. The direction and the center of the scan in the reciprocal lattice

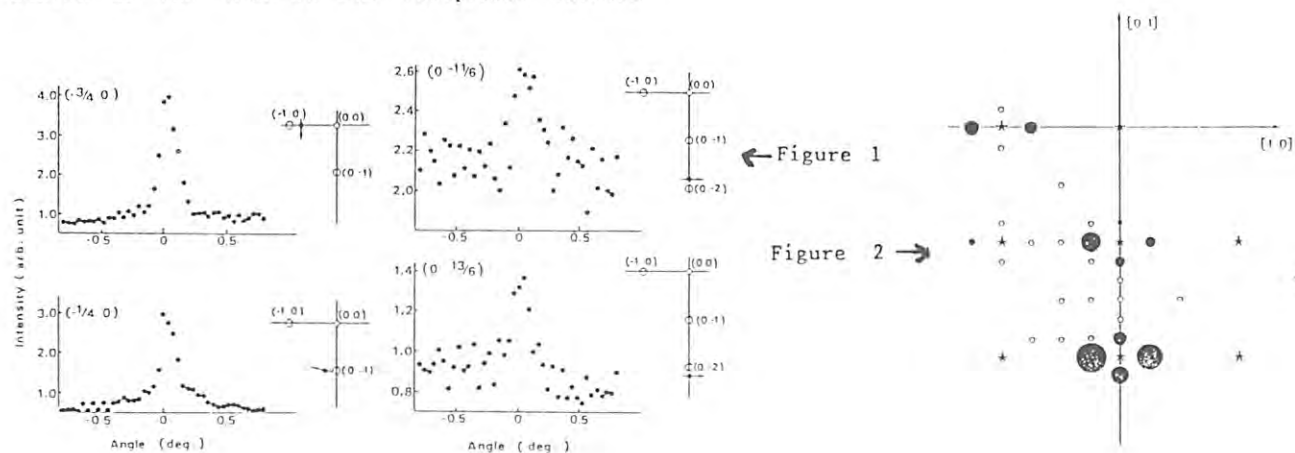
space are indicated in the right hand side of the figure. On the other hand, the scattered X-ray profile with Sample A did not show the peaks at any fractional ordered points which correspond with the (2×4)-reconstructed structure. Figure 2 shows the observed structure factor with the correction for the polarization, Lorentz factor and the variation of the active sample area. The radius of the circles is proportional to the observed structure factor.

Discussion

G. Landgren et al.⁴⁾ studied the dependence of the degrees of the interface reactivity on the surface reconstruction for the Al deposition. They investigated the interaction of Al with C(2×8)-GaAs(001), which is As-stabilized, and with (4×6)-GaAs(001), which is Ga-stabilized. They concluded that an exchange reaction was observed at room temperature for the (4×6)-GaAs (001) surface, but not for the C(2×8). From the present results with considering theirs, one may assume that the (4×6)-reconstructed structure must be constructed by at least two layers accompanied with stacking faults and vacancies. On the other hand, the (2×4)-reconstruction might be stabilized by, for instance, the As-dimers which are destroyed easily by an Al deposition because of the construction of the stable covalent Al-As bonds. To clarify these, more experiments for investigating the atomic structure not only at the interface, but also on the clean surface are required.

References

- 1) W. C. Marra, P. Einsenberger and A. Y. Cho: J. Appl. Phys. **50** (1970) 6927.
- 2) K. Akimoto, J. Mizuki, T. Tatsumi, N. Aizaki and J. Matsui: Surf. Sci. Lett. **183** (1987) L297
- 3) G. Landgren, S. P. Svensson. and T. C. Andersson: Surf. Sci. **122** (1985) 55.



X-Ray Topography of 6 inch Diameter Si Crystal

Tomohisa KITANO, Tetsuya ISHIKAWA*, Junji MATSUI, Koichi AKIMOTO, Jun'ichiro MIZUKI and Yutaka KAWASE

Fundamental Research Laboratories, ** R&D Planning and Technical Service Division, NEC Corporation, 4-1-1 Miyazaki, Miyamae-ku, Kawasaki 213
Photon Factory, National Laboratory for High Energy Physics, Oho-machi, Tsukuba-gun, Ibaraki 305

Introduction

Si wafers with large diameters of, for example, more than 4 inches are now required to cope with low cost LSI. Also, quality Si crystals are necessary for the high performance of an integrated circuit. We detected small change of lattice distortion under the condition of plane wave X-ray topography and took the surface sensitive X-ray topographs under the condition of specular reflection for 6 inch Si crystal.

Experimental

The experimental arrangement for the X-ray topography is as follows. Plane wave X-ray was obtained by the double crystal monochromator of (+,+) setting. The first and second crystals were (111) 6 inch Si wafers grown by CZ method. The first crystal was aligned as a monochromator to give 111 symmetric reflection and the second one as a collimator to give 008 asymmetric reflection. A (001) CZ Si wafer was aligned at the third crystal and 008 symmetric reflection was used. (+,-) non-dispersive setting was constructed between the second and third crystal. Selected wavelength was 0.1111 nm and the asymmetric factor of the second crystal was estimated to be 0.0043. Surface sensitive topographs of the second crystal was taken by adjusting glancing angle to the second crystal changing the X-ray wavelength from the first crystal. Experiments were performed at beam line 9C with a wide horizontal beam divergence of 5 mrad to cover the beam width of 150 mm at the 30 m position from the source point of the storage ring. Employing asymmetric reflection, X-ray topographs of 6 inch Si wafer can be taken without sample scanning.

Results and Discussion

Figure 1 shows a series of plane wave X-ray topographs of the third crystal which was taken around the Bragg peak by the (+,+,-) triple crystal arrangement. The swirl pattern was observed and the change in image contrast was clearly observed at intervals of 0.2 arc second. The swirl pattern was not so fine because penetration depth was so great that the spatial resolution became poor. Figure 2 shows a topograph of the second crystal with a glancing angle of 0.1°. The intensity of diffracted beam was very weak on this condition. Calculated penetration depth taking only the incident wave into account is several nm as shown by arrow (a) in Fig.3. This topograph is sensitive enough to the surface that defects such as scratch or damage layer by mechanochemical polishing can be detected. Penetration depth is so small that a fine swirl pattern can be detected in the wafer, even though the fluctuation of solid-liquid interface perpendicular to the pulling axis is very small in the CZ Si crystal. When the glancing angle becomes larger than the critical angle, however, the penetration depth increases

abruptly (arrow (b) in Fig.3), so that the topograph is not so sensitive to the surface as shown in Fig.2 (b).

References

1) T. Ishikawa, T. Kitano and J. Matsui: Jpn. J. Appl. Phys. 24 (1985) L968.

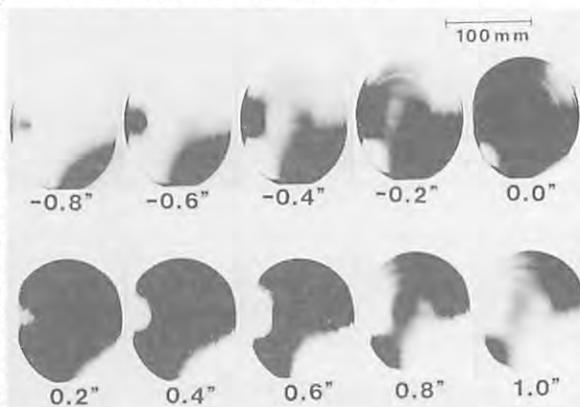


Fig.1

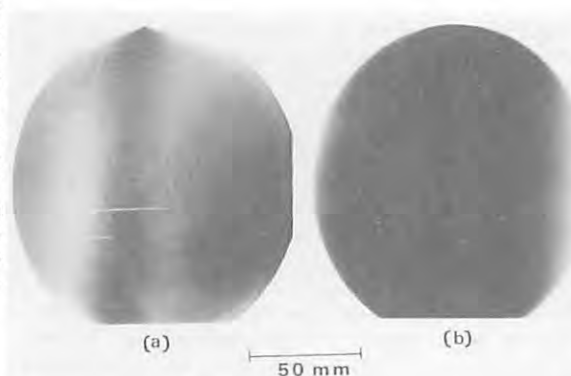


Fig.2

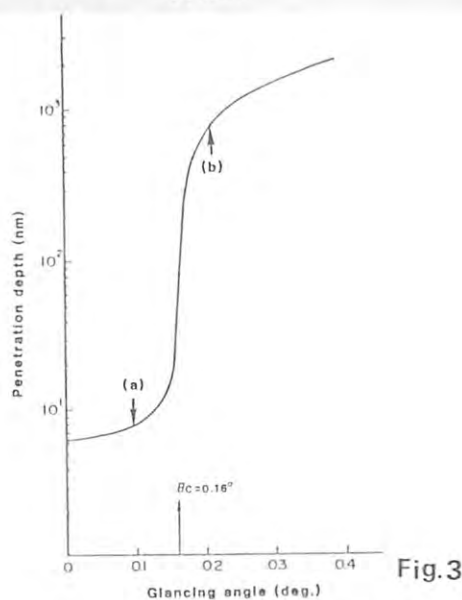


Fig.3

Fluorescence EXAFS Study of AlGaAs Doped with Se Donor Impurities

Tomohisa KITANO, Masashi MIZUTA and Junji MATSUI

Fundamental Research Laboratories, NEC Corporation, 4-1-1
Miyazaki, Miyamae-ku, Kawasaki 213, Japan

Introduction

The native defects in III-V semiconductor crystals are often electrically active and form the deep level such as EL2 and DX center. The configuration-coordinate model together with the lattice relaxation has been widely proposed to explain the capture and recombination of carriers at the deep level(1). However, the abscissa of the configuration-coordinate model has remained ambiguous. In the present work we investigated the lattice relaxation in AlGaAs doped with Se donor impurities by measuring the local structure of Se by means of fluorescence EXAFS.

Experimental

Sample was $\text{Al}_{0.38}\text{Ga}_{0.62}\text{As}:\text{Se}(1 \times 10^{19} \text{ atom/cm}^3)$ on (001) GaAs grown by MOCVD. EXAFS measurements were performed for the same sample under the two condition (a) the sample was placed in the dark space at the temperature of 70 K. (b) the sample was irradiated by a halogen lamp at the temperature of 8 K. Under the condition (a) carrier concentration was $1 \times 10^{16} \text{ atom/cm}^3$, in this case, electrons were localized at the Se and nearly all the Se were in the deep DX state. Under the condition (b) PPC was realized and electrons localized at the deep DX state were changed into the shallow DX state. According to the configuration-coordinate model together with the lattice relaxation, the large lattice relaxation was generated under the condition (a) and was not generated under the condition (b). We investigated the lattice relaxation with respect to displacement by comparison between the conditions (a) and (b).

Results and Discussion

Figure 1 shows the oscillation of the Se K fluorescence yield as a function of incident X-ray energy above threshold under the conditions (a) and (b). Figure 2 shows the imaginary part $\text{Im } F(r)$ and the magnitude $|F(r)|$ of the Fourier transform without phase shift correction for the EXAFS oscillation displayed in Fig.1. E_0 has been taken to coincide with the maximum of the derivative at the absorption edge. The difference of chemical bonding between the conditions (a) and (b) can be roughly considered as the difference of activation energy by C-V measurements. These value were (a) 119 meV and (b) 16 meV, respectively and the effect of E_0 on the displacement determination was considered to be the same between the conditions (a) and (b). Furthermore, considering the transferability, we can discuss the displacement of the nearest neighbor atoms around Se between the conditions (a) and (b) by comparing the first peak positions in Fig.2 directly. From Fig.2 it was said that since the first peak positions coincided between the conditions (a) and (b), although the first peak was attributed by the two elements Al and Ga, no large lattice relaxation as large as 0.4 Å reported by Morgan(2) was observed even though the deep DX state existed.

References

- (1) D.V.Lang and R.A.Logan: Phys. Rev. Lett. 39 (1977) 635.
- (2) T.N.Morgan: Phys. Rev. B34 (1986) 2664.

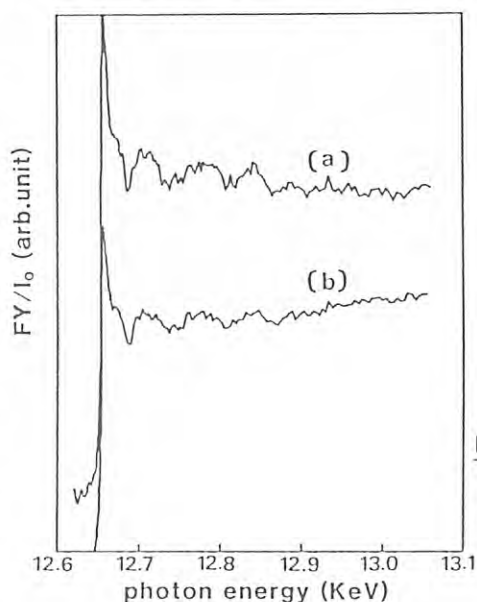


Fig.1
Fluorescence
yield of Se
for AlGaAs:Se

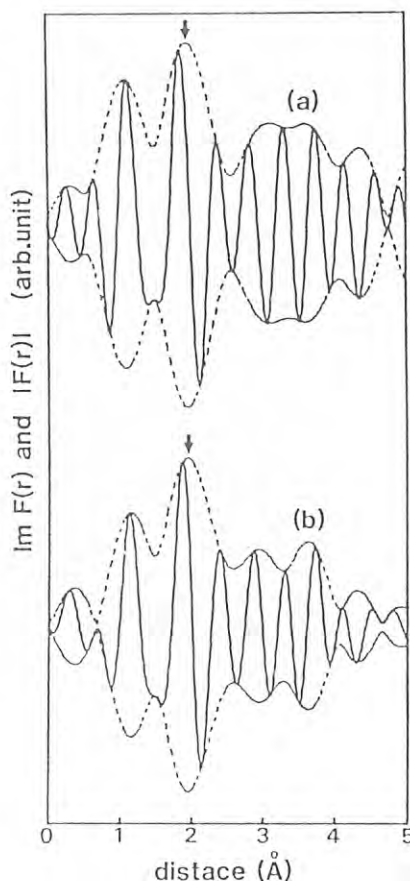


Fig.2
Fourier
transform
of $kX(k)$

Fluorescence EXAFS Study of Zn Doped LEC InP Crystal

Tomohisa KITANO, Hisao WATANABE and Junji MATSUI

Fundamental Research Laboratories, NEC Corporation, 4-1-1
Miyazaki, Miyamae-ku, Kawasaki 213, JapanIntroduction

Doping with certain kinds of impurities is effective in reducing the dislocation density in III-V semiconductor crystals grown by LEC method. Various models of interaction between the impurity atom and dislocation have been proposed¹⁻²⁾, but atomic structure of the impurity atom was not necessarily clarified. In the present work we studied the interatomic distance between the impurity atom and the host atom in Zn doped LEC InP crystal, in which system dislocation density was effectively reduced³⁾, by means of EXAFS by monitoring of the Zn $K\alpha$ fluorescence yield.

Experimental

Sample was LEC InP:Zn crystal. Polycrystalline InP was placed in a silica crucible and them covered with a dried B_2O_3 to form a encapsulant on top of the melt. Zn impurity was added into the crucible as element form. The concentration of Zn atom was estimated to be 8×10^{18} atoms/cm³. Crystal was pulled in a $\langle 111 \rangle$ In direction. X-ray from SR was monochromatized by Si(111) double crystals and Zn $K\alpha$ fluorescence yield was detected using a pure Ge SSD.

Results and Discussion

Figure 1 shows the oscillation of the Zn K fluorescence yield as a function of incident X-ray energy above threshold. Figure 2 shows the imaginary part $\text{Im } F(r)$ and the magnitude $F(r)$ of the Fourier transform using the phase shift and the⁴⁾ backscattering amplitude given by Teo and Lee⁴⁾. By comparing the Zn K absorption spectra between InP:Zn and ZnP_2 with respect to the damping and period of the oscillation, it was considered that Zn atom was surrounded by P atom as nearest neighbors. Zn-P interatomic distance was determined to be 2.41 Å. This value does not coincided the value calculated from VCA but the value calculated from Pauling's tetrahedral radii for zinc blende structure⁵⁾. In the case of LEC InP:Zn crystal where the impurity doping was simultaneously performed during crystal growth, Zn-P bond might be preferentially formed in liquid state and was succeeded to solid state. Since Zn-P interatomic distance was remarkably different from that of InP host crystal, lattice distortion might be easy to be generated around the impurity atom, which was shown in XANES spectra. This local structure was assumed to contribute to suppress the dislocation motion (slip and/or climbing) and to reduce the dislocation density.

References

- 1) S.A.Erofeeva and Yu.A.Osip'yan: Sov. Phys. -Solid State 15 (1973) 538.
- 2) V.B.Osvenskii, L.P.Kholodnyi and M.G.Mil'vidskii :Sov. Phys. -Solid State 15 (1973) 661.

- 3) Y.Seki, H.Watanabe and J.Matsui: J. Appl. Phys. 49 (1978) 822.
- 4) B.-K.Teo and P.A.Lee: J. Am. Chem. Soc. 101 (1979) 2815.
- 5) L.Pauling: The Nature of the Chemical Bond.

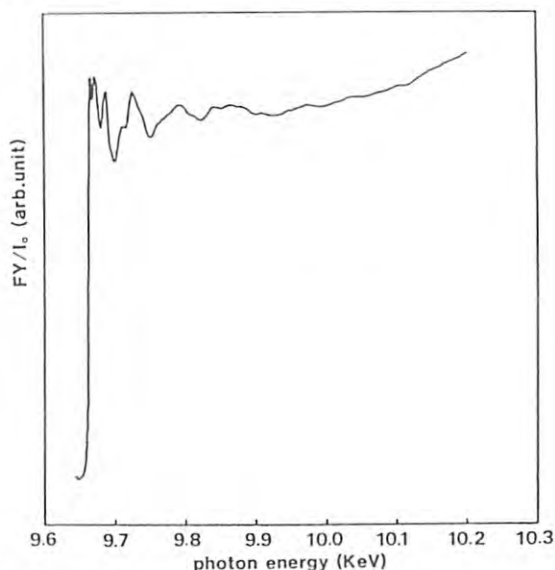


Fig.1
Fluorescence yield as a function of incident X-ray for Zn in a LEC InP:Zn Crystal.

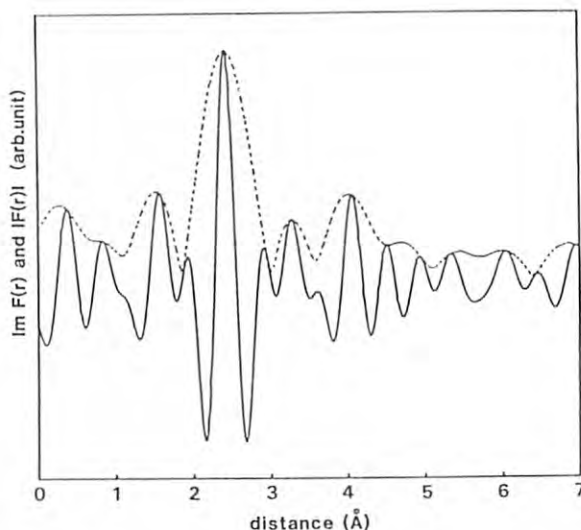


Fig.2
Magnitude value $F(r)$ (dashed lines) and imaginary part $\text{Im } F(r)$ (solid lines) of Fourier transform of the EXAFS oscillation.

DETERMINATION OF FE AND NI ORDERING IN TETRATAENITE FROM SAINT SEVERIN
METEORITE USING SYNCHROTRON RADIATION

Tokuhei Tagai, Hiroshi Takeda, Masayasu Tokonami
Mineralogical Institute, University of Tokyo, Hongo, Bunkyo-ku, Tokyo 113
Satosi Sasaki
Photon Factory, National Laboratory for High Energy Physics
Oho-machi, Tsukuba-gun, Ibaraki 305
Jacques Dannon
Centro Brasileiro, de Pesquisas Fisicas, Rio de Janeiro, Brazil

Introduction

Taenite is one of the Fe-Ni minerals which is commonly found in meteorites. The crystal structure of taenite is simply described as face-centered cubic structure, where all the atomic positions are occupied by Fe and Ni with equal probability. Its space group symmetry is $Fm\bar{3}m$.

Tetrataenite is found only in the extremely slow-cooled meteorite (cooling rate of some degrees per million years for the temperature interval of 700-350°C). The structure of tetrataenite can be derived from taenite structure by ordering of Fe and Ni atoms and it is, therefore, described to be C-centered tetragonal and reduced to primitive tetragonal with; $\bar{a} = 1/2\bar{a}_c + 1/2\bar{b}_c$, $\bar{b}_p = 1/2\bar{a}_c - 1/2\bar{b}_c$ and $\bar{c}_p = \bar{c}_c$ (p: primitive lattice and c: C-centered lattice). The space group symmetry has been described $P4/mmm$ by Clarke and Scott (1980). The existence of the ordered tetragonal phase has been confirmed by optical observation and Moessbauer experiments. But the structure analysis of tetrataenite has not been carried out because of the difficulties to find good single crystal and to distinguish Fe and Ni with usual X-ray sources.

In this study, we report the results of the single crystal experiments on tetrataenite using synchrotron radiation, which is characterized by its strong intensity and the tunable wave length.

Experimental and results

A single crystal of tetrataenite of 50 μm in diameter could be separated from the Saint-Severin meteorite (type-LL6). The chemical composition was determined to be FeNi by means of the electron microprobe analysis. Lattice constants were determined by the four-circle diffractometer using $Mok\alpha$ radiation are :

$a = 3.577(2)$, $b = 3.576(3)$, $c = 3.569(2)$ Å,
 $\alpha = \beta = \gamma = 90$ (same orientation with FCC-lattice).

The crystal was then mounted on a four-circle diffractometer of vertical type on BL-10a in Photon Factory, Laboratory for High Energy Physics, Tsukuba. The diffraction data was collected with the ring current of 135-85 mA.

The X-ray of $\lambda = 1.746$ Å was used to the experiment by Si(111) monochromator. The correction parameters for anomalous scattering are:

for Fe atom; $f' = -6.299$, $f'' = 0.469$ and

for Ni atom; $f' = -1.740$, $f'' = 0.638$

(Sasaki, 1984).

The large difference in f' and the small difference in f'' are very adequate to determine the site occupancies in the structure. A total of

56 reflections were collected with $10 < 2\theta < 100^\circ$.

The standard reflections measured at intervals of five reflections were used to the correction for decreasing intensity of the primary X-ray. All the reflections which contradict with the extinction rule of the C-centered lattice symmetry were observed. Tetrataenite has P-lattice with lattice constants of $a = b = 3.577$ and $c = 3.569$ Å. The structure determination was carried out using least squares program. On the first stage of the structure determination, the space group symmetry of $P4mm$ was assumed, in which only occupational parameters, z-coordinates and temperature factors (anisotropic) of the atoms can be refined. R-factor was 12%. Then, the space group symmetry of Pm was assumed, where x-coordinates can additionally be refined. The final R-factor is 7%. The results of the refinements shows ;

1) Fe and Ni atoms are almost perfectly ordered and construct a layer-like structure.

2) Fe and Ni atoms move of about 0.04-0.07 Å from the positions of the disordered structure.

Discussion

Tetrataenite was first found by its optical anisotropy, which indicates that it has a lower symmetry than cubic one. Then the lattice constants were measured and it was concluded that tetrataenite was tetragonal. According to the present results, tetrataenite is only metrically tetragonal and its structure has monoclinic symmetry. The lower symmetry was attained by the ordering of Fe and Ni and their slight shifts from the averaged positions.

Clark RS & Scott ERD (1980) Am Min 65, 624-630.
Sasaki S (1984) KEK Rep KEK 83-22.

CRYSTAL STRUCTURE OF KBSi_3O_8 MICROCRYSTAL

Mitsuyoshi KIMATA and Satoshi SASAKI*

Institute of Geoscience, The University of Tsukuba,
Ibaraki 305, Japan.* Photon Factory, National Laboratory for High-Energy
Physics, Oho-machi, Ibaraki 305, Japan.Introduction

A four-circle diffractometer combined with synchrotron radiation has a great advantage to determine the crystal structures of microcrystals. The BL-10A station is supplied with strong photon flux because of its shorter distance from the SR source and the horizontal focussing system using an asymmetric curved crystal.

We successfully analyzed the crystal structure of a single crystal of KBSi_3O_8 smaller than 40 micron in length.

Experimentals

The specimen investigated was a new potassium borosilicate, KBSi_3O_8 , synthesized hydrothermally under the condition of 430°C, 430kg/cm² and 90 days. Table 1 contains the crystal and diffraction data for KBSi_3O_8 . The wavelength was determined by calibration with the already-known cell parameters of this sample. Dimensions of the sample were accurate in SEM measurement. Data were collected by step-scanning at 0.01° intervals with collection time of 1s per point.

Structure solution and refinement

The solution of the structure was begun using direct methods [the MULTAN 80 package¹⁾] and the structure of danburite²⁾ as a guide. Statistics produced by MULTAN indicated the structure to be centrosymmetric, thus fixing the space group as Pnam, which is also the symmetry of danburite. The refinement calculations are carried out with the program RFINEZ³⁾.

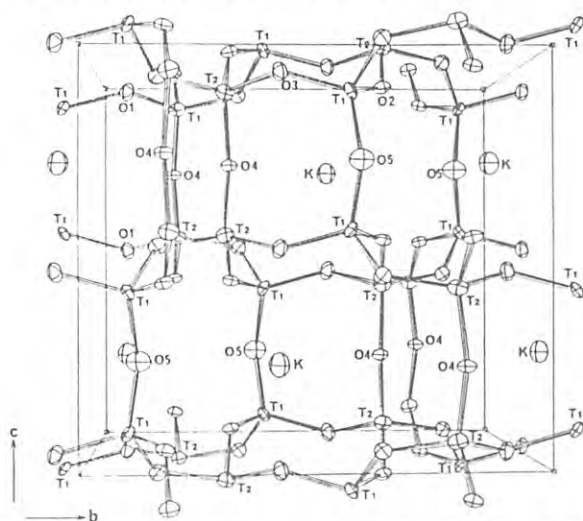


Fig. 1. A projection onto (100) of the KBSi_3O_8 structure.

Structure description and discussion

The KBSi_3O_8 crystal determined is different from feedmergerite NaBSi_3O_8 with the low albite structure, and isostructural with danburite $\text{CaB}_2\text{Si}_2\text{O}_8$. The chemical relationship between this sample and danburite is the coupled substitution $\text{K}^+ + \text{Si}^{4+} = \text{Ca}^{2+} + \text{B}^{3+}$ in the extraframework and tetrahedral sites. However, in both frameworks there is complete ordering of tetrahedral cations, i.e., (B,Si), for the latter and the present analysis revealed partial disordering of the B and Si atoms which jointly reside in two kinds of general equivalent points, T(1) and T(2) sites. Thus the expanded crystal-chemical formula can be written in the form $\text{K}(\text{B}_{0.44}\text{Si}_{0.56})_2(\text{B}_{0.06}\text{Si}_{0.94})_2\text{O}_8$, which is the first report on the borosilicate with B/Si disordering.

References

- 1) Main, P. : MULTAN80. University of Cambridge, England (1980)
- 2) Phillips, M. W., Gibbs, G. V. and Ribbe, P. H. : Am. Mineral. 59 (1974) 79.
- 3) Finger, I. W. and Prince, E. : Nat. Bur. Stand. U.S. Tech. Note 854 (1975).

Table 1. Crystal and diffraction data for KBSi_3O_8 .

K-danburite	
Formula	KBSi_3O_8
Molar wt.	262.16
Symmetry	orthorhombic
S.G.	Pnam
a	8.683(1) Å
b	9.253(1) Å
c	8.272(1) Å
V	664.4(1) Å ³
Z	4
Crystal size	20×29×37 μm
D	2.620g/cm ³
F(000)	420
Radiation	synchrotron
Wavelength	0.7055 Å
Monochromator	flat Si(111)
μ	13.34cm ⁻¹
2θ range	<90°
Observed reflections	761
(with F>3σF)	
R(unweighted)	6.7
R _w (weighted)	3.0

STRUCTURE STUDY ON THE SINGLE CRYSTAL OF CU-AL-NI τ_1' MARTENSITE PHASE

J. Ye, M. Tokonami, H. Horiuchi, S. Sasaki*
H. Sawada, N. Haga, T. Ozawa, S. Kuranaka, M. Tanaka

Mineralogical Institute, Univ. of Tokyo, Bunkyo-ku, Tokyo 113
* Nat. Lab. High Energy Phys., Oho-machi, Tsukuba-gun, Ibaraki 305

Introduction

$|F|^2 = K_a K_s I$

Since the discovery of pseudoelasticity and shape memory effect of the Cu-Al-Ni alloy, crystallographical studies on such alloy receive a wide interest because of its unique mechanical behavior and related application expected as a kind of excellent functional material. It is now considered that both shape memory effect and pseudoelasticity have a close relationship to the thermoelastic martensitic transformation between the parent and martensite phase [1]. Therefore, the detailed structural information concerning the τ_1' martensite phase is undoubtedly very important for better understanding of the mechanisms. Unfortunately, because of the great difficulty both in obtaining a single crystal of the martensite and keeping it stable during experiments, and the fact that Cu follows Ni in atomic number in the periodic table makes the site occupancies difficult to be determined, the detailed structure information of the martensite has not yet been reported.

In the present work, we have used four different wave lengths close to Cu and Ni K-absorption edges in order to determine the Cu/Ni distribution in the structure by applying anomalous dispersion effects. And the structure refinement was based on the model established by Otsuka and Shimizu [2].

Experimental and results

A Cu-27.14at%Al-3.64at%Ni τ_1' single crystal (0.23x0.29x0.37mm in size) synthesized using modified Bridgman method [3], has been selected for the reflection intensity data collection. In order to prevent from reverse transformation of the martensite phase ($A_s=32^\circ\text{C}$), the specimen was kept under 27°C during the experiment process. The data have been collected using four different wave lengths on the vertical type four-circle diffractometer at BL-10A station. A ω - 2θ step scan mode ($\Delta\omega = 0.01^\circ$, scan range $=1.0^\circ$) was employed for the careful examination of the reflection profiles. Four attenuators were used, and the standard reflection 113 was measured at an interval of ten reflections so as to check the declining of source intensity with time. Among the four different wave lengths used, two of them (1.3850Å and 1.4065Å) are close to Cu K-absorption edge ($\lambda_K=1.380\text{\AA}$), another one (1.4966Å), close to Ni K-absorption edge ($\lambda_K=1.488\text{\AA}$), and the last one, very short (0.5622Å) for the sake of small linear absorption coefficient. As a result, within the range of $2\theta<120^\circ$, 504 reflections (145 independent) have been obtained using the wave lengths of 1.3850Å and 1.4066Å; 373 reflections (100 independent) for the wave length of 1.4966Å.

After having subtracted backgrounds, we integrated the diffraction intensity over all steps which were rectified by Lorentz factor. And from which the structure factors (F) have been calculated according to the following function:

here K_a , the attenuator factor; K_s , the normalization factor derived from the intensity of standard reflection; I , integrated intensity. The structure refinement has been carried out using the program RFINE 2. The anomalous dispersion factors were taken from the list of Sasaki (1984) that are calculated with the method presented by Cromer & Liberman (1970). Varying the parameters, such as scale factor, positional parameters, site occupancies, anisotropic temperature factors and the isotropic extinction factor in the refinement cycles, we obtained the R factor about 3.9% using the data collected with the wave 1.4966Å in length. The results of refinement are shown in Table 1, and the shifting of atoms from ideal 2H structure are schematically illustrated in Fig.1.

The further study on the structure using other data sets is being processed

Table 1 The structural parameters of τ_1' martensite

Atom	X	Y	Z
Al1	1/6+0.0182(3)	3/4	3/4
Cu1	1/6+0.0171(2)	1/4	3/4
Cu2	1/3-0.0154(2)	0-0.00052(8)	1/4
Site	Symbol	Composition	
I	Al	Al	
II	Cu1	Cu0.914 Al0.086	
III	Cu2	Cu0.927 Ni0.073	

References

[1] W. A. Rachinger: Brit. J. Appl. Phys. 9(1958), 250.
[2] K. Otsuka and K. Shimizu: Trans. JIM., 15(1974), 103.
[3] K. Otsuka, C.M. Wayman, K. Nakai, H. Sakamoto and K. Shimizu: Acta Metall. 24(1976), 207.

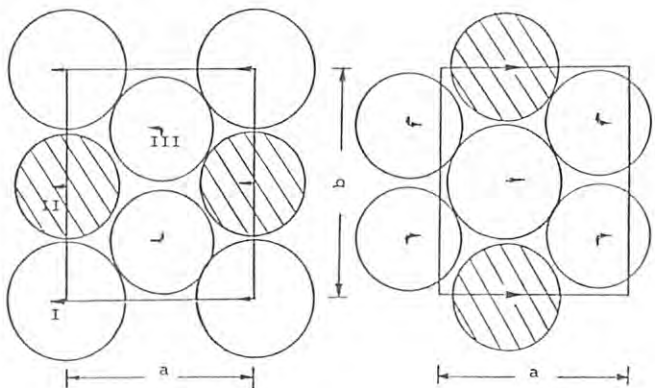


Fig.1 First (left) and second layer (right) along c axis of τ_1' martensite. Arrows showing the sense of atoms shifting; I: Al; II: Cu, Al; III: Cu, Ni.

DYNAMICAL DIFFRACTION AND ANOMALOUS TRANSMISSION OF THERMALLY SCATTERED X-RAYS IN A PERFECT GERMANIUM CRYSTAL

Yasuji KASHIWASE, Masahiro MORI, Motokazu KOGISO, Masayuki MINOURA and Satoshi SASAKI*

Department of Physics, College of General Education, Nagoya University, Nagoya 464

*National Laboratory for High Energy Physics, Tsukuba, Ibaraki 305

Introduction

Excess lines were observed across thermal diffuse spots in X-ray diffraction patterns of perfect crystals of germanium and silicon. Their origin was assigned to dynamical diffraction and anomalous transmission of thermally scattered X-rays.^{1,2)} The present report is made on a further investigation of such lines for germanium crystals. Diffractometry as well as photographic observation was carried out.

Experimental

The experiment was performed at BL-10A using synchrotron radiation monochromatized by the Si-111 reflection. Diffraction lines due to thermal diffuse scattering (TDS) from germanium crystals were observed across the 220 TDS spot and near the incident spot in the Laue case. Observation was made under various conditions of X-ray wavelength, crystal thickness and crystal orientation.

The wavelengths were 1.5405 Å and 1.15 Å. Thin plates of thickness 0.1 ~ 0.2 mm were used as specimens. Their surfaces were parallel to the (111) plane. The rocking curves of the 111 Bragg reflection from the crystals had full widths at half maximum about 25", which were close to that of an ideally perfect crystal. Orientations of crystals were varied in the range $-0.6^\circ \sim 0.6^\circ$ of the angular deviation from the 220 Bragg position $\Delta\theta = \theta - \theta_{220}$. The cross section of the incident beam collimated with slits was 0.25 mm x 2.5 mm. Diffraction photographs were taken on cosmic ray films and medical X-ray films. Line profiles were also measured by 2θ diffractometry with the scintillation counter, where the receiving slit width was about 0.1 mm.

Result and Discussion

As was previously reported, an excess line was observed across the 220 TDS spot.^{1,2)} Besides an excess-defect line was found as shown in Fig. 1(a).³⁾ This depends on X-ray wavelength λ and crystal thickness D . When $\lambda = 1.5405$ Å, an excess line was observed for $D \sim 0.2$ mm, and an excess-defect line for $D \sim 0.1$ mm. When $\lambda = 1.15$ Å, however, an excess-defect line was observed for $D \sim 0.2$ mm. The excess part of the excess-defect line was always on the side of the incident spot. The line profiles were not so affected by crystal orientation $\Delta\theta$. Near the incident spot, an excess line was found in Fig. 1(b). This is the pair of the line across the 220 TDS spot and moves with $\Delta\theta$ in the same manner. The line is produced by the 220 Bragg reflection of the 220 TDS waves.

Profiles in diffractometry of excess-defect and excess lines across the 220 TDS spot are shown in Fig. 2 (a) and (b). The line width is determined mainly by the incident beam size.

The experimental results can be interpreted reasonably within the framework of the dynamical theory of X-ray diffraction for absorbing perfect

crystals. The wavelength and thickness dependence of line profiles follows from absorption of TDS waves propagating dynamically to the observation point. The lines observed above are distinct from defect lines in the case of mosaic crystals dealt with by the kinematical theory.¹⁾

References

- 1) Y. Kashiwase, M. Mori, M. Kogiso, Y. Oya, M. Minoura, S. Sasaki and T. Ishikawa: Photon Factory Activity Report 1986, p.166.
- 2) Y. Kashiwase, M. Mori, M. Kogiso, M. Minoura, S. Sasaki and T. Ishikawa: J. Phys. Soc. Jpn. 55 (1986) 4172.
- 3) Y. Kashiwase, M. Mori, M. Kogiso, M. Minoura and S. Sasaki: Proc. 14th Int. Cong. Crystallography, IUCr, Perth, 1987, C-221.

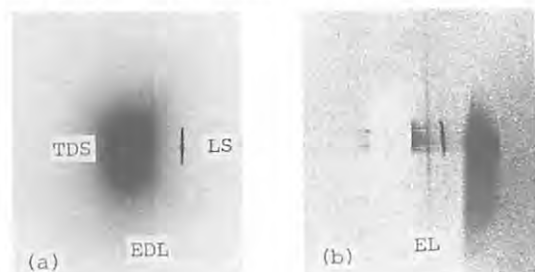


Fig. 1. Diffraction photographs of the lines at $\lambda = 1.5405$ Å and $\Delta\theta = 0.4^\circ$. (a) Excess-defect line (EDL) across the 220 TDS spot for $D \sim 0.1$ mm where LS indicates a Laue spot. (b) Excess line (EL) near the incident spot for $D \sim 0.2$ mm.

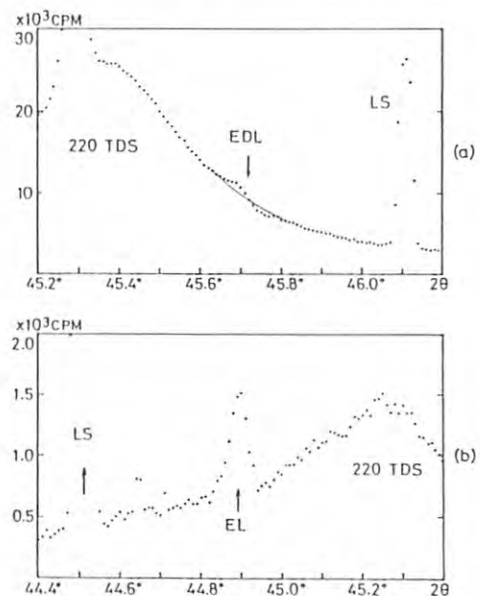


Fig. 2. Line profiles in 2θ diffractometry at $\lambda = 1.5405$ Å. (a) Excess-defect line for $D \sim 0.1$ mm and $\Delta\theta = 0.4^\circ$. (b) Excess line for $D \sim 0.2$ mm and $\Delta\theta = -0.4^\circ$.

PHOTON COUNTING IN X-RAY DIFFRACTION

Kazutoshi GOUHARA, Kazuhiko OMOTE*, Makoto SAKATA**, Satoshi SASAKI***, Norio KATO****

Department of electronics, Faculty of Engineering, Nagoya University,
Furocho, Chikusa-ku, Nagoya, Japan 464

*Rigaku Denki Kogyo Co., Ltd, Asoji-cho, Takatuki, Japan, 564,

**Department of Applied Physics, Faculty of Engineering, Nagoya University,
Furocho, Chikusa-ku, Nagoya, Japan 464***Photon Factory, National Laboratory for High Energy Physics,
Oho-machi, Tsukuba-gun, Ibaraki 305****Department of Physics, Meijo University,
Tempakuku, Nagoya, Japan 464Introduction

It is well known in light optics that the photon counting distribution and the time correlation are useful measures for characterizing light beams. No equivalent work, however, has been reported in any extent of details in X-ray optics.

The motivation of our research is to see how far the photon counting method is useful in a region of Å X-rays. For this purpose, the following subjects must be worked but step by step.

- (a) Instrumental innovations and the theoretical understanding.
- (b) The characterization of X-ray sources.
- (c) The application to any time-dependent diffraction phenomena.

In this report, the first two will be presented.

Experimentals and Results

(a): For the photon counting method, a new digital memory system was developed. This enables us to count photon numbers in a fixed time interval from $1 \mu\text{s}$ to $99 \mu\text{s}$ sequentially up to 10^6 times without interruption. All data are stored in a floppy disc for the later analysis. Usually, such data are collected within a few seconds or less, so that cares on physical environments are much easier than ordinary experiments. This is a potential advantage in the subject (c).

(b): We applied this method to characterizing the beam source of the Photon Factory (BL-10A station). Fig.1 shows the photon distribution (black columns) and the theoretical Poisson distribution (white). The discrepancy was well inter-

preted in terms of the dead time, if one assumes $0.27 \mu\text{s}$ in this case. The correction can be performed by the theory of Omote^{1),2)}.

Fig.2 indicates the normalized correlation of the photon numbers at two different times against the time interval. The same data were used as those of Fig.1. It is clear that the source was oscillating with two frequencies, 5.6 ms and 20 ms . It must be pointed out, however, that the experiment was performed by using a periphery of the beam. If the central part was used, no appreciable fluctuation was detected.

From the analysis of our data, it is possible to measure the normal correlation with an accuracy of 10^{-3} in the order of magnitude.

We hope to apply the method to any physical phenomena in near future.

Reference

- 1) N.Kato, N.Suzuki and K.Omote,
The report of UHIXDL, No.7(1985)20,
Nagoya University, Japan
- 2) K.Omote, The collected abstracts of
the meeting of Phys. Soc.Jap.,
Autumn(1985)437

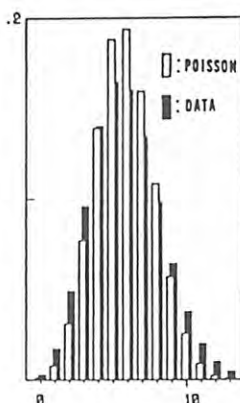


Fig.1

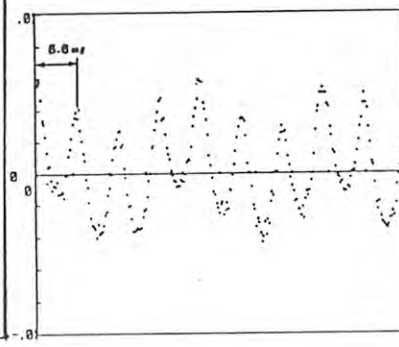


Fig.2

EXAFS Study on Local Structure Changes of Amorphous Alloy

Toshio NASU, Masaki SAKURAI*, Toshiharu FUKUNAGA*, Fumitake ITOH*
and Kenji SUZUKI*

Faculty of Education, Yamagata University,
Kojirakawa, Yamagata 990

*Institute for Materials Research, Tohoku University,
Katahira, Sendai 980

Introduction

One of the most outstanding properties of amorphous alloy is the mechanical property. For example amorphous alloys exhibit very high fracture strength, toughness and very small strain-hardening¹⁾. Amorphous alloys are not perfectly elastic, but possess anelasticity. The stress-strain curves show a hysteresis loop on loading and unloading process. In this report, the atomic scale process of mechanical deformation of Pd₈₃Si₁₇ amorphous alloy has been studied using EXAFS measurement.

Experimental

Amorphous samples were in shape of ribbon (2.7 mm width and 0.03 mm thickness) prepared by single-roller quenching method. The composition used here was Pd₈₃Si₁₇. EXAFS spectra of Pd₈₃Si₁₇ amorphous alloy were measured in situ under some degrees of tensile strain. The amount of tensile strain were 0.0, 0.3, 0.6 and 0.8 %. Extended X-ray absorption fine structure (EXAFS) measurement from Pd K-edge up to about 1 keV above the edge energy were carried out for Pd₈₃Si₁₇ amorphous alloy with synchrotron radiation at the beam line 10B of the Photon Factory of KEK. The structure parameters, coordination number N, interatomic distance R and Debye-Waller type factor σ , were derived by curve

fitting²⁾ after the EXAFS measurement.

Results

The structure parameters derived by the curve fitting procedure, which are the refined coordination number N and interatomic distance R, are shown in Fig. 1 (A) and (B). The Pd-Si atomic distance increases with increasing the strain, but the coordination number change is rather small. The Pd-Pd atomic distance, however, decreases with increasing the strain, accompanied with large change in the coordination number. This may be an indication that there exist a strong chemical bonding between Pd-Si (metal-metalloid) atomic pair. It is to be noticed that both the atomic distance and the coordination number in Pd-Si and Pd-Pd pairs do not return to their initial values after the loading-unloading process. The present EXAFS measurement confirmed that the anelasticity can occur in the atomic scale by the irreversible rearrangement of atoms.

References

- 1) T. Masumoto and R. Maddin: Mater. Sci. Eng. 19 (1975) 1.
- 2) N. Kosugi and H. Kuroda: Program EXAFS1, Research Center for Spectrochemistry, the University of Tokyo (1985).

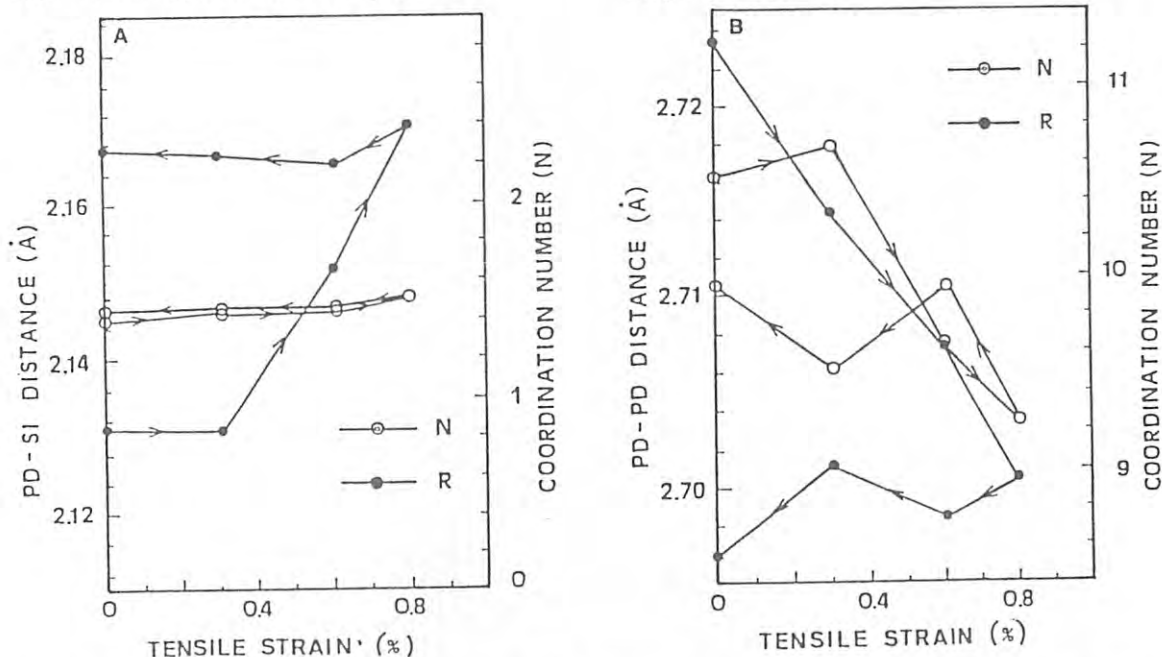


Fig. 1 (A) (B) Strain dependence of interatomic distance (closed circle) and coordination number (open circle) for Pd₈₃Si₁₇ amorphous alloy derived by parameter fitting. (A) for Pd-Si atomic pair and (B) for Pd-Pd atomic pair.

EXAFS AND XANES STUDY OF THE $\text{Bi}_2\text{O}_3\text{-Gd}_2\text{O}_3$ SOLID SOLUTION

Richiro KOTO, Hiroyuki ITO, Akira YOSHIASA, and Shuichi EMURA

The Institute of Scientific and Industrial Research, Osaka University,
Mihoga-oka, Ibaraki, Osaka, 567, Japan

Introduction

The fluorite-type high oxide ion conductors of Bi_2O_3 can be stabilized by adding certain metal oxides at low temperatures but the conductivity decreases with increasing the content of doped oxides 1).

The displacement of oxide ions from the normal tetrahedral site in the fluorite-type structure decreases with increasing Gd_2O_3 content and is zero value at about 32 mol% Gd_2O_3 2), 3). Although there exist the different configurations of oxide ions around Bi in the electron density map 2), no appreciable difference is observed in profile and distance of Bi for the compounds with 10 and 30 mol% Gd_2O_3 3).

Local structures of the compounds for various compositions of the $\text{Bi}_2\text{O}_3\text{-Gd}_2\text{O}_3$ system were studied by EXAFS and XANES.

Experimental

The compounds were synthesized by using $\alpha\text{-Bi}_2\text{O}_3$ (99.99%) and Gd_2O_3 (99.9%) in powder form as starting materials. Appropriate amounts of well-blended mixture of Bi_2O_3 and Gd_2O_3 were calcined at 850-1040 °C for 14 hours in platinum crucible and quenched into cold water. The samples for EXAFS study were prepared by dusting the powder uniformly onto both sides of cellophane tape. Several layers of tape were used to make a complete sample. X-ray absorption measurements near Bi L3 and Gd L3 edges were made for the samples with 10, 15, 20, 25, 27, 30, 33, 35, 37 and 40 mol% Gd_2O_3 contents at room temperature in transmission with synchrotron radiation on the Beam Line 10-B at Photon Factory.

In obtaining the EXAFS function $\chi(k)$, the background level was subtracted from the observed absorption coefficient by using Victoreen fit and the absorption coefficient for the isolated atom was obtained by the cubic spline technique. Bond distances were refined by the curve-fitting method. The results are shown in Fig. 1.

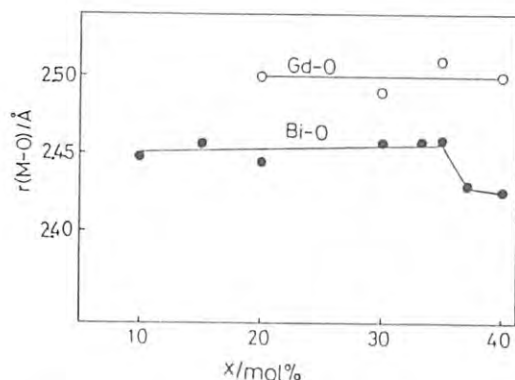


Fig. 1 Distances of M-O (M=Gd, Bi) refined by the curve-fitting method in the $(1-x)\text{Bi}_2\text{O}_3\cdot x\text{Gd}_2\text{O}_3$ system.

Results

The Gd-O distances are longer than those of the Bi-O by 0.4-0.7 Å in the composition range studied. The Gd-O distances remain constant but the Bi-O distances decrease by about 0.3 Å at the composition of 33 mol% Gd_2O_3 content.

The features of primary differential by energy of XANES of Gd L3 (Fig. 2) remain unchanged, but one of the changes in the features of Bi L3 is sharpening of the shoulder after the main peak (+18eV) at 33 mol% Gd_2O_3 content which is the same composition at which the Bi-O distance decreases (Fig. 3). The results obtained by EXAFS and XANES explain the dependence of displacement from the normal site on composition by X-ray diffraction 2).

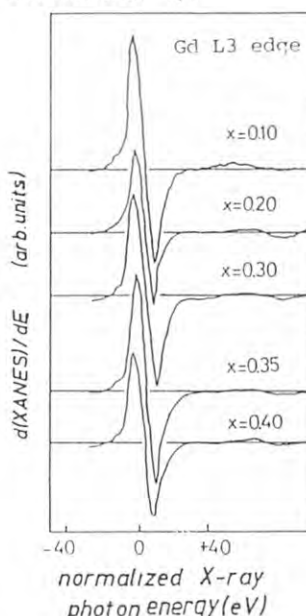


Fig. 2 Primary differential of XANES of Gd L3 in the $(1-x)\text{Bi}_2\text{O}_3\cdot x\text{Gd}_2\text{O}_3$ system.

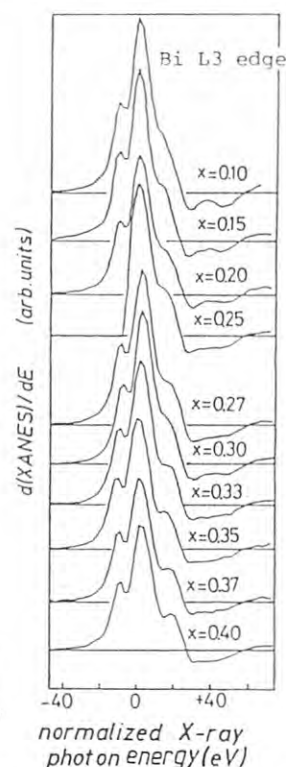


Fig. 3 Primary differential of XANES of Bi L3 in the $(1-x)\text{Bi}_2\text{O}_3\cdot x\text{Gd}_2\text{O}_3$ system.

The authors are indebted to Dr. H. Maeda, Okayama Univ., for providing us the programs of EXAFS analysis. Thanks are also to Drs. S. Nomura and A. Koyama, KEK, for their help and useful advices in the experiments.

References

- 1) T. Takahashi and H. Iwahara, Mater. Res. Bull., **13** (1978) 1447.
- 2) K. Koto, H. Mori and Y. Ito, Solid State Ionics, **18/19** (1986) 720.
- 3) K. Koto, S. Emura, Y. Ito, H. Mori and H. Ito, KEK, Act. Rep., (1986/1987) 187.

CHAIN STRUCTURE OF LIQUID SELENIUM SYSTEMS (II)

Hirohisa ENDO, Makoto YAO, Masanori INUI and Yoshinori KATAYAMA
Department of Physics, Faculty of Science, Kyoto University, Kyoto 606
Kozaburo TAMURA

Faculty of Integrated Arts and Sciences, Hiroshima University, Hiroshima 730
Hideoki HOSHINO

Faculty of Education, Hirosaki University, Hirosaki 036

Hiroyuki OYANAGI

Electrotechnical Laboratory, Sakura-mura, Niihari-gun, Ibaraki 305

Masaharu NOMURA

National Laboratory for High Energy Physics, Oho-machi, Tsukuba-gun, Ibaraki 305

Introduction

Liquid selenium (l-Se) with 2-fold coordinated chain structure is a semiconductor with optical gap of 1.8 eV. On the other hand liquid tellurium (l-Te) is a metal and has 3-fold coordinated network structure. In liquid Se-Te mixed system a semiconductor to metal transition is known to occur with increasing temperature or increasing Te concentration.^{1),2)} It is interesting to study how the chain structure of Se is changed on this transition. EXAFS measurement on the Se K-edge is expected to give information on local environment around a central Se atom. In this paper we report results of the first observation of EXAFS for liquid Se and Se-Te mixtures up to 750°C.

Experimental

We have made a special polycrystalline sapphire cell in order to measure EXAFS of a liquid sample up to 1100°C. In the cell a liquid sample fills the space with 50 μm thickness between sapphire X-ray windows. EXAFS spectra of l-Se₅₀Te₅₀ were obtained up to 750°C using this cell. A graphite cell in which a sample is sandwiched between grafoil was also used for measurements up to 650°C. The X-ray absorption spectra were obtained by using the EXAFS facilities installed at BL-10B.

Results and discussion

Figure 1 shows the Se K-edge EXAFS oscillation $\chi(k)$ of (a) l-Se at 250°C, (b) l-

Se₈₀Te₂₀ at 300°C, (c) l-Se₅₀Te₅₀ at 400°C and (d) l-Se₃₀Te₇₀ at 425°C. With increasing Te content, the amplitude in small k region becomes large owing to strong backward scattering from Te. Figure 2 shows $\chi(k)$ of l-Se₅₀Te₅₀ at various temperatures up to 750°C. With increasing temperature, EXAFS oscillation becomes attenuated because of thermal disorder. It should be noticed that in this system the oscillation remains even at high temperatures near the boiling point. Figure 3 shows the magnitude of Fourier transform $|F(r)|$ of k times $\chi(k)$ for the data shown in Fig. 1. The first peak is clearly observed in l-Se, which represents intrachain nearest neighbor distance. A shoulder is seen for l-Se₈₀Te₂₀ on the small- r side of the peak. In l-Se₅₀Te₅₀ and l-Se₃₀Te₇₀, there is a peak at 1.8 Å besides a main peak at 2.4 Å. The distance of 1.8 Å is too short to be assigned as a real bond length even if the phase shift effect is taken into account. A preliminary analysis shows that the split of the first peak could originate from the interference between the backward scattering from Te and Se. Figure 4 shows $|F(r)|$ of l-Se₅₀Te₅₀ in the temperature range covering the semiconductor-metal transition region. Detailed analysis of EXAFS spectra in this temperature range is now in progress.

1) J.C.Perron, Adv. Phys. **16** (1967) 657

2) H.Endo, J.Non-Cryst. Solids **59-60** (1983) 1047

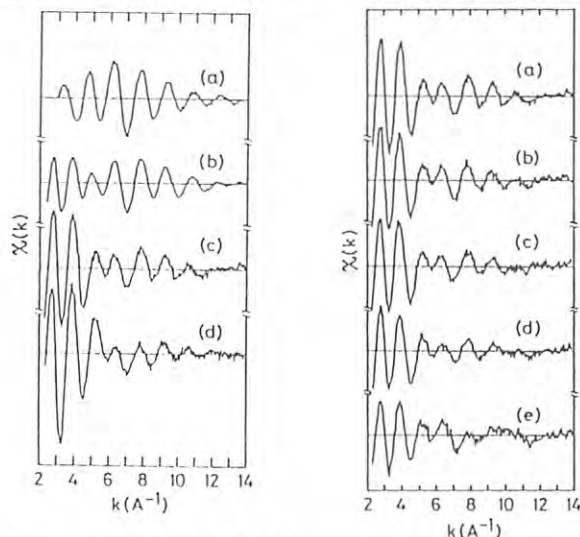


Fig.1. The Se K-edge EXAFS oscillation $\chi(k)$ of (a) l-Se at 250°C, (b) l-Se₈₀Te₂₀ at 300°C, (c) l-Se₅₀Te₅₀ at 400°C and (d) l-Se₃₀Te₇₀ at 425°C.

Fig.2. The $\chi(k)$ of l-Se₅₀Te₅₀ at (a) 400°C, (b) 500°C, (c) 600°C, (d) 700°C and (e) 750°C.

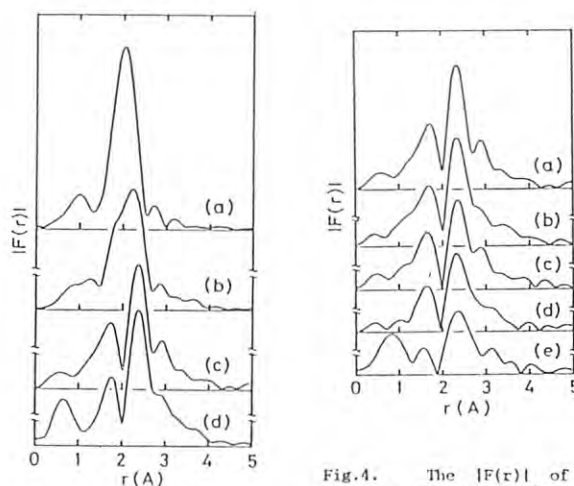


Fig.3. The magnitude of Fourier transform $|F(r)|$ of (a) l-Se, (b) l-Se₈₀Te₂₀, (c) l-Se₅₀Te₅₀ and (d) l-Se₃₀Te₇₀.

Fig.4. The $|F(r)|$ of l-Se₅₀Te₅₀ at (a) 400°C, (b) 500°C, (c) 600°C, (d) 700°C and (e) 750°C.

AN EXAFS STUDY OF NICKEL(II) COMPLEXES CONTAINING CARBOHYDRATES;
A NOVEL C-2 EPIMERIZATION OF ALDOSES PROMOTED BY NICKEL(II) DIAMINE COMPLEXES
INVOLVING A STEREOSPECIFIC REARRANGEMENT OF CARBON SKELETON

Tomoaki Tanase, Fumihiko Shimizu, Hiroyuki Matsusaka, Koshiro Toriumi, and Shigenobu Yano*
Department of Synthetic Chemistry, Faculty of Engineering, the University of Tokyo,
Hongo, Bunkyo-ku, Tokyo 113, Japan

Introduction

It is receiving increasing attention to develop the methods whereby metals promote transformation of sugars in bioinorganic chemistry. We have recently found the novel C-2 epimerization of aldoses promoted by nickel(II) diamine complexes (diamine = N,N,N',N'-trimethylethylenediamine (N,N,N',N'-Me₃en), and N,N,N',N'-tetramethylethylenediamine (N,N,N',N'-Me₄en)), which has much potential for the synthesis of naturally rare aldoses as well as theoretical importance. In this report, the reaction mechanism was investigated in detail especially by EXAFS analyses for the intermediate nickel(II) complex containing sugar moieties.

Experimental

X-ray absorption measurements near Ni-K edge were made at room temperature in transmission mode with synchrotron radiation (PF) using the EXAFS facilities installed on the Beam Line 10B. EXAFS analyses were carried out by the use of theoretical least-squares curve-fitting techniques for Fourier filtered waves with the program EXAFS1.²⁾

Results and Discussions

First of all, the EXAFS spectra of [Ni(en)₃](NO₃)₂ (1), [Ni₂Cl₂(en)₂]Cl₂ (2), [Ni(N-(L-Rha)-tn)₂]²⁺ (3), and μ -(D-Man)-[Ni₂(CH₂OH)(N-(D-Man)-N,N'-Me₂en)(N,N'-(D-Man)₂-N,N'-Me₂en)]²⁺ (4) were measured as reference compounds to examine the reliability of our EXAFS analyses for nickel(II) complexes containing diamines and sugars, and the results derived from EXAFS are in good agreement with those from X-ray crystallography (Table I).

The Fourier transform of the methanolic solution of NiCl₂·6H₂O (0.1M) and N,N,N',N'-Me₄en (0.2M), (the starting complex) is shown in Figure 1a, which is very similar to that of dimeric (2). Four peaks around 1.6, 2.1, 2.6-2.7, and 3.4 Å are attributable to the N or O atoms in the first shell, the bridging Cl atoms, the C atoms in the outer shell, respectively. Further, the coordination numbers of N (or O), Cl, C, and Ni suggest the dimeric structure of nickel with the six-coordinated octahedral geometry (Table I). In contrast, the Fourier transform of the methanolic solution of NiCl₂·6H₂O (0.1M), N,N,N',N'-Me₄en (0.2M), and D-glucose (0.1M), which contains mainly the stable intermediate nickel(II) complex, dramatically changes from that of the starting solution (Figure 1b); the Ni-Cl and Ni-Ni peaks disappear and the remaining two peaks at about 1.6 and 2.5 Å are attributable to the N or O atoms in the first sphere (N = 5.8) and the C atoms in the outer shell, directly

indicating that the stable intermediate complex supposed from AB and CD spectral data is a mononuclear nickel(II) complex having the six-coordinated octahedral structure (Table I).

In this EXAFS study, it was revealed that the present C-2 epimerization of aldoses proceeds via a mononuclear intermediate nickel(II) complex where the stereospecific rearrangement of carbon skeleton smoothly takes place.

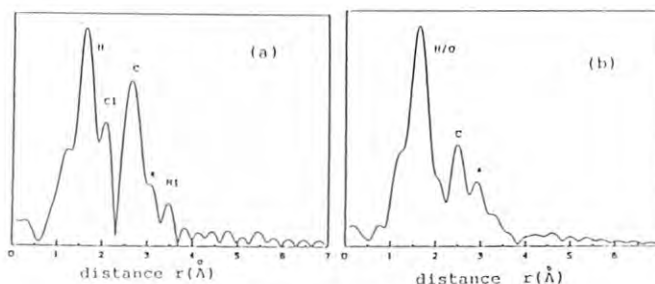


Figure 1. Fourier transforms

Table I. Atomic Parameters Determined by Curve Fitting Analysis

no	complex	EXAFS				X-ray Cryst.	
		A-B ^a	r(Å) ^b	N	σ	r(Å)	N
1	[Ni(en) ₃](NO ₃) ₂ (1) (powder)	Ni-H	2.10	6.0 ^c	0.036	2.12(1)	6
		Ni-C	2.89	6.0 ^c	0.077		
		Ni-Ni	3.70	1.0 ^d	0.094		
2	[Ni ₂ (en) ₂ Cl ₂]Cl ₂ (2) (powder)	Ni-H	2.05	3.9	0.043	2.10(1)	4
		Ni-Cl	2.50	2.0 ^d	0.051		
		Ni-C	2.96	2.6	0.030		
3	[Ni(H-(L-Rha)-tn) ₂] ²⁺ (powder) (2)	Ni-H/O ^e	2.08	6.9	0.052	2.12(4)	6
		Ni-C	3.11	5.1	0.057		
		Ni-N/O ^e	2.06	6.8	0.039		
4	μ -(D-Man)-[Ni ₂ (CH ₂ OH)(N-(D-Man)-N,N'-Me ₂ en)(N,N'-(D-Man) ₂ -N,N'-Me ₂ en)] ²⁺ (powder) (4)	Ni-C	3.13	3.8	0.029	2.10(6)	6
		Ni-Ni	3.56	1.4	0.096		
		Ni-H	2.05	2.8	0.032	unknown	
5	[Ni(N,N,N',N'-Me ₄ en)Cl ₂] (powder) (5)	Ni-Cl	2.45	1.6	0.050		
		Ni-C	2.94	4.6	0.037		
		Ni-Ni	3.64	1.0	0.095		
6	NiCl ₂ ·6H ₂ O + 2 N,N,N',N'-Me ₄ en (in methanol)	Ni-H	2.07	3.5	0.038	unknown	
		Ni-Cl	2.45	2.0	0.054		
		Ni-C	3.02	8.2	0.049		
7	NiCl ₂ ·6H ₂ O + 2 N,N,N',N'-Me ₄ en + D-Glc (in methanol)	Ni-N/O ^e	2.08	5.8	0.049	unknown	
		Ni-C	2.89	3.5	0.040		
		Ni-H	2.05	2.8	0.032		

a) A is the absorber (Ni) and B is back scattering atom.

b) Estimated errors are ± 0.03 Å for inner-shell and ± 0.04 Å for outer-shell.

c,d) The numbers of neighbor atoms (Ni-N/O, Ni-C) referenced to the complex (1) and those (Ni-Cl, Ni-Ni) referenced to the complex (2).

e) All back scattering atoms in the first sphere are calculated as nitrogen.

References

- 1) T. Tanase, F. Shimizu, S. Yano, and S. Yoshikawa, J. Chem. Soc., Chem. Commun., 1986, 1001; T. Tanase, F. Shimizu, M. Kuse, S. Yano, M. Midai, and S. Yoshikawa, *ibid.*, 1987, 659.
- 2) N. Kosugi and H. Kuroda, EXAFS1, Research Center for Spectrochemistry, the University of Tokyo (1985).

EXAFS AND XANES STUDIES ON MARTENSITIC TRANSFORMATION IN IRON BASE ALLOYS

late Osamu YAMADA, Hitoshi YAMAZAKI, Hironobu Maeda,* Hiroshi MARUYAMA,
Naruhiko BAMBA, Koichi SATO and Tomoki FUKAGAWA.

Department of Physics, Faculty of Science, Okayama University,

* Department of Chemistry, Faculty of Science, Okayama University,
3-1-1 Tsushima-Naka, Okayama 700.

Introduction

Since the martensitic transformation is a typical first-order phase transition, an interface between the matrix and the transformation product properly exists. In the vicinity of the starting temperature M_s of the transformation, however, several features of second-order transition characterized by a continuous change have been observed. Therefore, a nucleation process comes into question. Although several theoretical models on the nucleation and growth of martensite have been proposed^{1,2)}, there is very little direct observation of local-structure change with the martensitic transformation. It is clear that information of the local-structure change is essential to an understanding of the mechanism of martensitic nucleation. For this purpose, we have carried out EXAFS and XANES studies on iron base alloys.

Experimental

Fe-Ni, Fe-Pd and Fe-Pt alloys were prepared by induction melting. The concentration was determined by chemical analysis. After grinding the ingots, the powdered samples were annealed

for 2 hours at 800°C under vacuum and subsequently given a suitable thermal treatment to obtain the ordered or disordered alloy. In order to determine the lattice parameter and the M_s -temperature, X-ray diffraction measurements were carried out. X-ray absorption measurements near the K-edge of Fe and the L₃-edge of Pd and Pt were made by use of the EXAFS facility installed at beam line 10-B in KEK-PF. Data analysis was made by the conventional procedure³⁾.

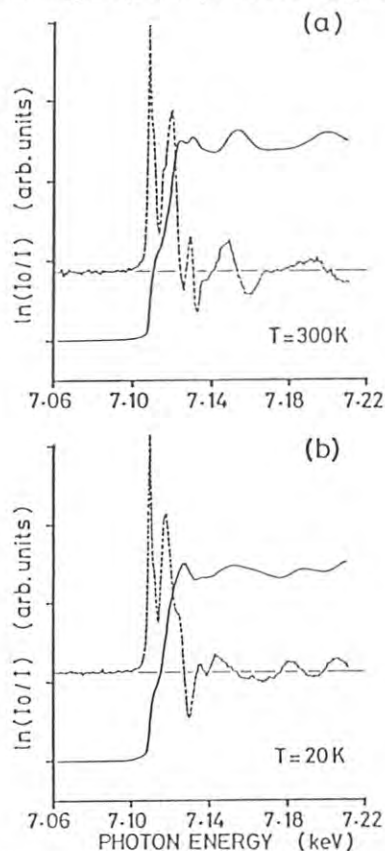


Fig.1. XANES spectrum (solid line) and the first derivative (broken line) of Fe K-edge on the disordered 25.0at%Pt-Fe.

Results and Discussion

As a typical example, we will report the results of the disordered 25.0at%Pt-Fe alloy, which undergoes the martensitic transformation from FCC into BCC at the M_s -temperature previously determined to be 260K by X-ray diffraction. Figure 1(a) shows the XANES spectrum for Fe K-edge and the first derivative of that on the disordered 25.0at%Pt-Fe alloy at room temperature. They at low temperatures ($T < M_s$) are shown in Fig.1(b). From these figures, it is easily found out that the XANES of Fe K-edge transforms clearly from double peak in FCC at R.T. into single peak in BCC at low temperatures. However, no chemical shift has appeared in the X-ray absorption threshold energy within the resolution of 0.5eV. These features insist that the martensitic transformation has strongly influenced the electronic state of the Fe atoms resulting from the structural change from the FCC to the BCC phase, but has not influenced the Fermi energy. On the other hand, no change has been recognized in the XANES of Pt and Pd (L₃-edge).

Figure 2 shows radial structure function (RSF) obtained by the Fourier transform of the EXAFS of Fe K-edge on the disordered 26.4at%Ni-Fe alloy. RSF at 300K indicates the pattern arising from FCC structure; on the other hand, RSF at 20K transforms entirely to that originating in BCC structure. It is caused by the martensitic transformation. Unfortunately, a determination of the local-structure parameters has not yet succeeded. It may be ascribed to a complicated state of the low temperature-phase; that is, the sample becomes a mixture of the FCC matrix and the BCC transformation product; and the local-structure near the interface is largely distorted. More detailed analysis of EXAFS on the disordered Fe-Pd and Fe-Pt alloys is also in progress.

References

- 1) G. Guenin and P.F.Gobin: J. de Phys. **43** (1982) C4-57.
- 2) Y.Yamada: Proc. Int. Conf. on Martensitic Transformations. (1986) p.89.
- 3) H. Maeda: J. Phys. Soc. Jpn. **56** (1987) 2779.

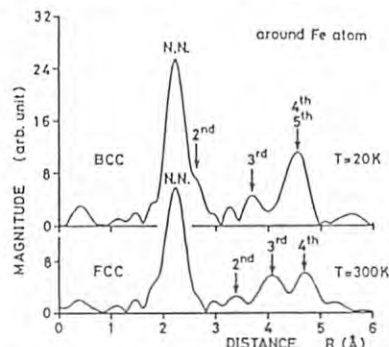


Fig.2. Radial structure function of Fe K-edge on the disordered 26.4at%Ni-Fe.

DISORDERED EFFECT IN PENTANARY ALLOY SEMICONDUCTOR AlGaInPAs

Shun-ichi GONDA, Shuichi EMURA, Kichiro KOTO, Akira YOSHIASA,
Hiroyuki ITO, Fumiyuki KIHARA, and Seiji MUKAI

Institute of Scientific and Industrial Research, Osaka University
Mihogaoka 8-1, Ibaraki, Osaka 567, Japan

* Electrotechnical Laboratory, Sakuramura, Niiharigun,
Ibaraki 305, Japan

Introduction

Pentanary alloy semiconductor $(\text{AlGa}_{1-x})_{1-z}\text{PAs}_{1-y}$ is an interesting material from the view point of material design, because in the alloy three compositional parameters can be varied independently. Hence, three of various physical parameters such as the lattice constant, band gap energy, refractive index, and thermal expansion coefficient can be selected independently. On the other hand, the translational symmetry will be broken out in the crystal of multinary alloy. These disordered effects appear on above physical parameters. Here, the disordered effects will be investigated by EXAFS, discussing mean free path of photo-electron.

Experimental

The pentanary alloy samples $(\text{AlGa}_{1-x})_{1-z}\text{PAs}_{1-y}$ studied here were grown on the GaAs substrates by liquid phase epitaxy. The compositions of the grown layers were examined with electron microprobe analysis. For EXAFS measurement, the epitaxial layers of about $4 \times 3 \text{ mm}^2$ are cleaved on the glass of 0.18 mm in thickness and the GaAs substrate is removed by the selective etching. The x-ray absorption spectra were observed near Ga and As K-edges at the Beam Line 10-B at Photon Factory.

In obtaining the EXAFS function $\chi(k)$, the background level was subtracted from the observed spectrum by using Victoreem fit. The absorption spectrum corresponding to a isolated atom was obtained by the cubic spline technique.

Results and Discussion

Figures 1(a) and 1(b) show the spectra of $\chi(k)k^2$ at Ga K-edge of bulk GaAs and $(\text{AlGa}_{1-x})_{1-z}\text{PAs}_{1-y}$ ($x=0.322$, $y=0.035$, $z=0.012$), respectively. The intensity of EXAFS $\chi(k)$ depends on a Debye-Waller factor and a mean-free-path of photo-electron $\lambda=k/\eta$, where k is wave vector of photo-electron and η constant determining the length of mean-free-path. The $\chi(k)$ of AlGaInPAs is more attenuated in comparison with the $\chi(k)$ of GaAs in the region of shorter wave vector. It indicates that the mean-free-path in pentanary alloy semiconductor AlGaInPAs is shorter than in compound GaAs (see Figs. 3.8(a) and (b) in Ref. 1). The randomness of the potential

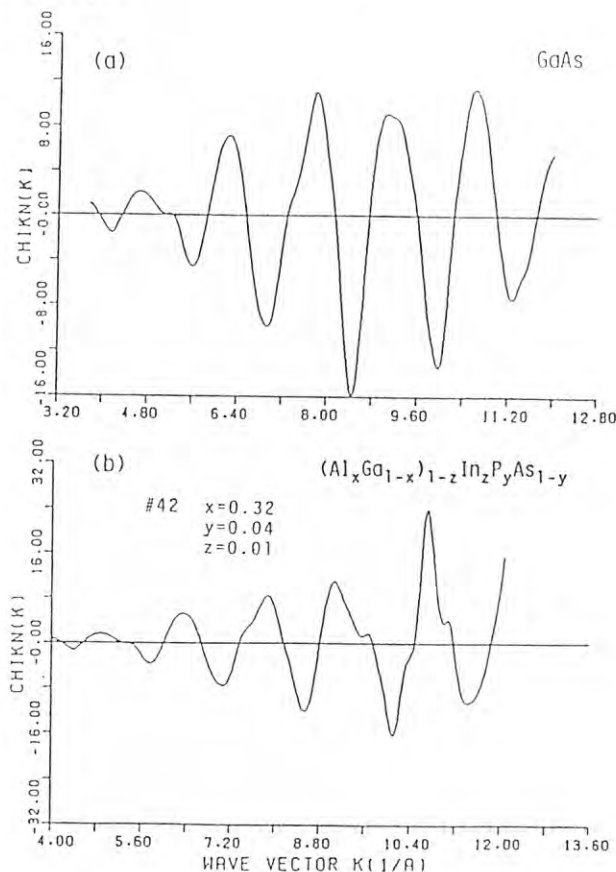


Fig. 1. EXAFS oscillations at Ga K-edge, (a) for GaAs, (b) for pentanary alloy AlGaInPAs.

which an electron feels is greater in alloy than in compound. The photo-electron will strongly scattered by this random potential and this is reflected in the attenuation of the EXAFS oscillation at the region of shorter wave vector.

The authors are indebted to Dr. H. Maeda (Okayama Univ.) for providing us the programs of EXAFS analysis, and are grateful to Drs. S. Nomura and A. Koyama, KEK, for their help and useful advices in the experiments.

Reference

- 1) B.K.Teo, EXAFS: Basic Principles and Data Analysis (Springer-Verlag, Berlin, 1986) p.34.

X-RAY ABSORPTION STUDY OF LINEAR-CHAIN SEMICONDUCTOR $(\text{NbSe}_4)_3\text{I}$

Mitsuru IZUMI, Toshiaki IWAZUMI[†], Hiroyuki OYANAGI^{*}, Ryoza YOSHIZAKI[§]
and Etsuyuki MATSUURA

Department of Physics, Tokyo University of Mercantile Marine,
Koto-Ku, Tokyo 135, Japan.

[†]Institute of Physics, University of Tsukuba, Sakura-mura, Ibaraki 305, Japan

^{*}Electrotechnical Laboratory, Sakura-mura, Ibaraki 305, Japan

[§]Institute of Applied Physics, University of Tsukuba, Sakura-mura, Ibaraki 305, Japan

INTRODUCTION

$(\text{NbSe}_4)_3\text{I}$ undergoes to the successive structural phase transition below room temperature. To clarify the mechanism of the phase transitions from the point of the local-crystal structure, the EXAFS and near-edge spectra were measured on the Nb K-shell absorption below room temperatures.

Experimental and Results

The Fourier transformation of the EXAFS function induced from the Nb K-edge spectra of $(\text{NbSe}_4)_3\text{I}$ at room temperature is shown in Fig. 1. The correction of the phase shift by scattering has not been done. The most intensified peak corresponds to the distance between Nb atoms at two symmetry sites and Se atoms at four symmetry sites in the unit cell of the crystal structure [1]. The peak which corresponds to the bond distance in-between Nb atoms has relatively small intensity around 2.8 Å. In this material the second-order displacive type of the phase transitions occur around 274 and 90 K. Existence of a softening of the mode at $q=0$ has been observed by means of X-ray diffuse scattering studies around 274 K [2-4] and atomic displacement pattern has been characterised by a freezing of the soft B_{1u} phonon mode [5]. We attempted the study of the temperature dependence of the Debye-Waller-like factors in EXAFS spectra in the vicinity of the critical transition temperature 274 K. The Debye-Waller-like factor of EXAFS is the average of the square of the fluctuation of the distance between the central atom and a scatterer. A theoretical approach has been done on the EXAFS near second order phase transition [6]. It was shown that thermal damping of the

EXAFS is caused by bond-length fluctuations and is predicted to show a weak change in temperature derivative at transition temperature [6]. EXAFS and near-edge spectra were obtained at temperatures between 280 and 260 K with temperature interval of 2 K. Curve fitting [7] were performed under the assumption of six kinds of Nb-Se bond length for each EXAFS oscillation spectra between 5 and 15 Å⁻¹. The obtained Debye-Waller-like factors are plotted as a function of temperature in Fig. 2. It seems to be some kind of anomaly in the temperature dependence of the value of the obtained Debye-Waller-like parameters around 270 K. Further analysis including XANES spectra is now under progress.

REFERENCES

- 1) P. Gressier, L. Guemas and A. Meerschaut: *Mat. Res. Bull.*, 20 539 (1985).
- 2) M. Izumi, T. Iwazumi, K. Uchinokura, R. Yoshizaki and E. Matsuura: *Solid State Commun.* 52 379-383 (1984).
- 3) M. Izumi, T. Iwazumi, K. Uchinokura, R. Yoshizaki and E. Matsuura: *Mol. Cryst. Liq. Cryst.* 121 15-18 (1985).
- 4) T. Iwazumi, M. Izumi, F. Sasaki, R. Yoshizaki and E. Matsuura: *Physica* 143B, 261-263 (1986).
- 5) M. Izumi, T. Iwazumi, T. Seino, K. Uchinokura, R. Yoshizaki, T. Sekine and E. Matsuura: *Synthetic Metals*, 19 863-868 (1987).
- 6) P.B. Allen: *Solid State Commun.*, 54 929 (1985).
- 7) N. Kosugi and H. Kuroda: *Progrm EXAFS1*, Research Center for Spectrochemistry, The University of Tokyo (1985).

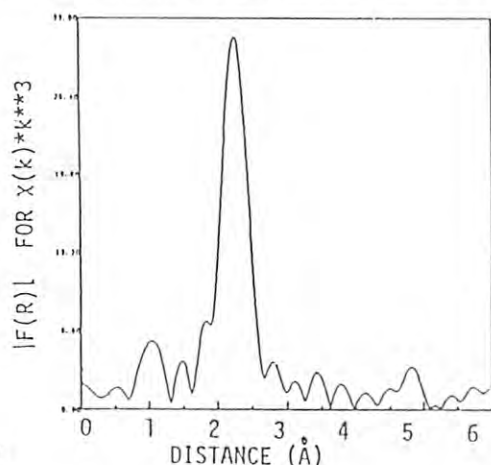


Fig. 1

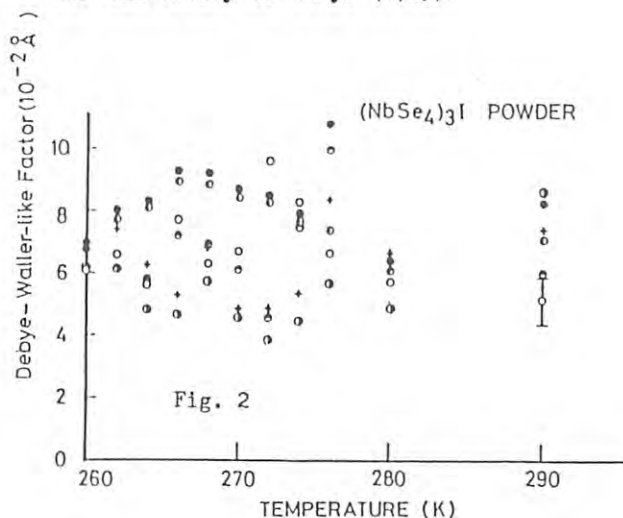


Fig. 2

X-RAY ABSORPTION STUDY OF QUASI-ONE DIMENSIONAL CONDUCTOR NbS_x ($x \approx 3$)

Toshiaki IWAZUMI, Mitsuru IZUMI⁺, Hiroyuki OYANAGI^{*}, Ryoze YOSHIKAZI[§]
and Etsuyuki MATSUURA

Institute of Physics, University of Tsukuba, Sakura-mura, Ibaraki 305, Japan

⁺Department of Physics, Tokyo University of Mercantile Marine,
Koto-Ku, Tokyo 135, Japan.

^{*}Electrotechnical Laboratory, Sakura-mura, Ibaraki 305, Japan

[§]Institute of Applied Physics, University of Tsukuba, Sakura-mura, Ibaraki 305, Japan

INTRODUCTION

The EXAFS spectra were measured on the Nb K-shell absorption semiconducting NbS_3 and metallic NbS_x ($x \approx 3$). The motivation of the present study was to clarify the difference of the crystal structure between semiconductor NbS_3 and metallic NbS_x from the point of microscopic view of the local structure.

Experimental and Results

The radial distribution function of the semiconductor NbS_3 at room temperature is shown in Fig. 1. The correction of the phase shift by scattering has not been done. The most intensified peak corresponds to the distance between Nb and S. The two peaks which are indicated by arrows correspond to the two different distances between Nb atoms along the chain direction. Thus the results of the Fourier transform of the EXAFS data show that each metal atom forms Nb-Nb pair [1]. Figure 2 shows the Fourier transformation of the EXAFS of metallic NbS_x at room temperature. The main difference between Figs. 1 and 2 is the appearance of the second largest peak around 3.0 Å. The position of the most prominent peak in Fig. 2 is nearly equal to the most intensified peak of semiconducting NbS_3 . Then the most prominent peak in Fig. 2 corresponds to the distance between Nb and S. The position of the peak around 3.0 Å is just in the middle of two arrows which indicate the two different distances between Nb atoms of semiconductor NbS_3 as shown in Fig. 1. In metallic NbS_x the obtained results exhibits that the Nb-Nb pair is deformed and the Nb chain is undistorted as shown in Fig. 2.

The difference of the radial distribution function of metallic NbS_x from that of semiconducting NbS_3 should be strongly related to the origin of the difference of the electrical transport properties between both type of crystals [2-4]. Two small peaks are present around the positions indicated by arrows in Fig. 2. If these two peaks are due to the distorted Nb

chain, the crystal of metallic NbS_x must be the mixture of the crystals of semiconductor and metallic phases and/or intermediate phase between undistorted and distorted phases. From this hypothesis, the crystal of semiconducting NbS_3 must be also the mixture or intermediate phase because the small shoulder is present in the middle of two arrows in Fig. 1. The obtained results lead that the main difference between the structures of semiconducting NbS_3 and metallic NbS_x is the existence ratio of the distorted to the undistorted Nb chains in the crystal.

Present study clearly shows the microscopic evidence of the difference of the structure of Nb chain between semiconducting and metallic crystals. The existence of the undistorted chains is deeply related to the transport properties, since the semiconducting properties of NbS_3 has been interpreted to come from the formation of Nb-Nb pair. The analysis of the EXAFS data was carried out by using the program by Kosugi and Kuroda [5].

REFERENCES

- 1) J. Rijnsdorp and F. Jellinek: *J. Solid State Chem.* **25**(1987) 325.
- 2) M. Izumi, T. Nakayama, K. Uchinokura, T. Iwazumi, T. Seino, R. Yoshizaki and E. Matsuura: *Proc. Int. Symposium on Nonlinear Transport and Related Phenomena in Quasi-One Dimensional Inorganic Conductors*, ed. T. Sambongi and Y. Abe (Sapporo, Japan, 1983), p. 301.
- 3) M. Izumi, T. Nakayama, K. Uchinokura, R. Yoshizaki and E. Matsuura: *Mol. Cryst. & Liq. Cryst.* **121**(1985) 79.
- 4) T. Iwazumi, M. Izumi, K. Uchinokura, R. Yoshizaki and E. Matsuura: *Physica* **143B**(1986) 255; T. Iwazumi, M. Izumi, H. Oyanagi, R. Yoshizaki and E. Matsuura: *Jpn. J. Appl. Phys., Suppl.* **26-3** 971 (1987).
- 5) N. Kosugi and H. Kuroda: *Program EXAFS 1*, Research Center for Spectrochemistry, The University of Tokyo (1985).

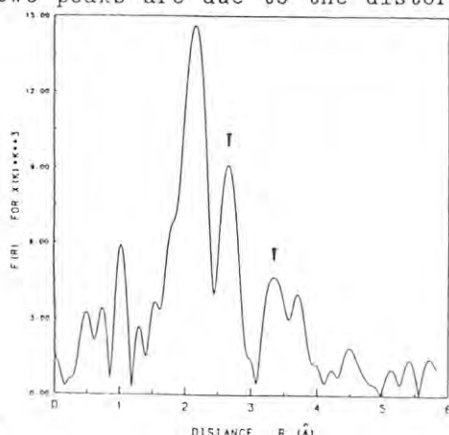


Fig. 1

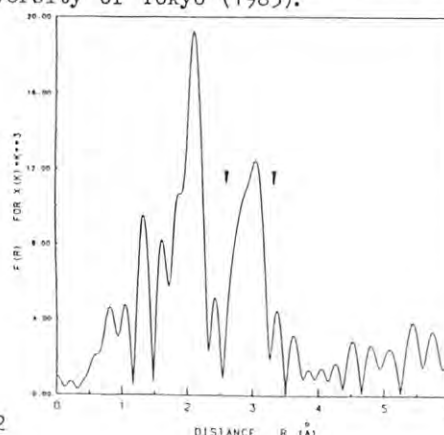


Fig. 2

SHORT-RANGE ORDER INVESTIGATION IN $a\text{-Ge}_{1-x}\text{Sn}_x\text{O}$ BY EXAFS

Hiroaki MYOREN, Keiji TSUNETOMO, Hiroyuki NASU, Takeshi IMURA and Yukio OSAKA

Department of Electrical Engineering, Faculty of Engineering,
Hiroshima University, Saijo, Higashi-Hiroshima 724Introduction

The structural change of Ge-Sn and Ge-Sn-O alloy by compositional change has been investigated. The optical properties of these films can be applied in the field of optical record media. Because $\text{Ge}_{1-x}\text{Sn}_x$ and $\text{Ge}_{1-x}\text{Sn}_x\text{O}$ ($x < 0.6$) is amorphous as deposited, the structural studies is actually difficult by X-ray and electron diffraction.¹⁾

In this report, we have undertaken an investigation of the local structure around Ge of $a\text{-Ge}_{1-x}\text{Sn}_x\text{O}$ by EXAFS at the Ge K-edge.

Experimental and Results

The samples of $a\text{-Ge}_{1-x}\text{Sn}_x\text{O}$ films were prepared on Kapton films by the conventional rf sputtering of a crystalline Ge target in mixed gases of Ar and O_2 . Tin was introduced in the films by placing small pieces of Sn on the Ge target in radial array. The Sn content in the films was controlled by varying pieces of Sn on the target. The oxygen content in the films was altered by oxygen partial pressure (0 and 2.67×10^{-2} Pa) under the constant total pressure (0.67 Pa). Usually, the rf power and substrate temperature were 30 W and 20 °C (water-cooled), respectively. The film thickness was ~ 20 μm .

The composition of the films was determined by the relative photo-ionization yields and the intensity ratio of the photoelectrons from Ge_{4d} and Sn_{4d} core levels in X-ray photoelectron spectroscopy.

X-ray absorption measurements were carried out with Synchrotron orbital radiation (SOR) at the Photon Factory in National Laboratory for High Energy Physics on 10-b beam line.

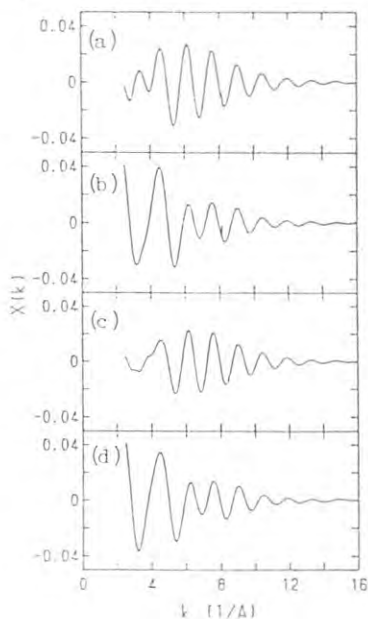


Fig. 1

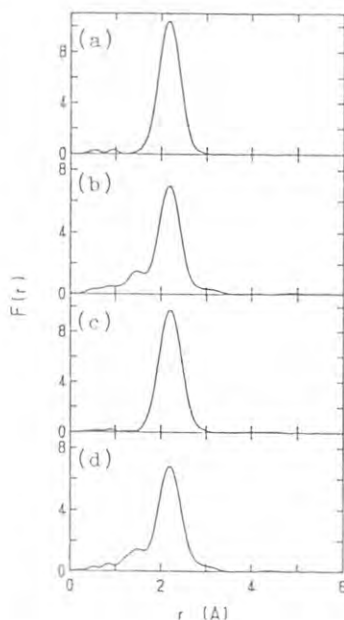


Fig. 2

Figure 1 shows normalized EXAFS oscillation of the Ge-K absorption edge for (a) $a\text{-Ge}$, (b) $a\text{-GeO}$, (c) $a\text{-Ge}_{0.83}\text{Sn}_{0.17}$ and (d) $a\text{-Ge}_{0.83}\text{Sn}_{0.17}\text{O}$ films as a function of photoelectron wave number k . Figure 2 shows the Fourier transform $|F(r)|$ of the EXAFS oscillation of the Ge-K absorption edge for the same samples as shown in Fig. 1. The peaks in this figure are influenced by the phase shift effect. The dependence of the phase shift δ_j on k (wave number) can be approximated by the simple equation $\delta_j(k) = -\alpha_j + \beta_j k$.²⁾ Then, the peak position is represented as $R_1 - \alpha_1$, where R_1 is the nearest neighbor atom distance around Ge.

Figure 3 shows $R_1 - \alpha_1$ as a function of Sn content in the alloy films. The nearest neighbor distance of Ge-Ge is linearly increasing with the Sn content. Considering the appearance of microcrystalline GeSn by annealing at 100 °C¹⁾, this result shows $a\text{-Ge}_{1-x}\text{Sn}_x$ alloy films consist of uniform mixture of Ge and Sn atoms. On the other hands, in the films containing oxygen, both of the nearest neighbor distances in Ge-Ge and Ge-O are linearly increasing with the increase of Sn content in the films. The nearest neighbor distance of Ge-Ge in $a\text{-Ge}_{1-x}\text{Sn}_x\text{O}$ is smaller than that of Ge-Ge in $a\text{-Ge}_{1-x}\text{Sn}_x$ at each Sn content and the proportional constant is smaller too. This result suggests the existence of GeO_x and SnO_x which restricts the degree of freedom on the bonding between Ge and Sn atom.

References

- 1) H. Fukumoto, H. Myoren, T. Nakashita, T. Imura and Y. Osaka ; Jpn. J. Appl. Phys. 25 (1986) 1312.
- 2) F. W. Lytle, D. E. Sayers and E. A. Stern ; Phys. Rev. B 11 (1975) 4825.

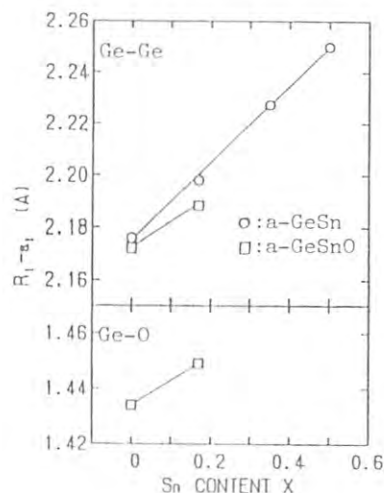


Fig. 3

EXAFS STUDY ON THE STRUCTURE CHANGES OF GeTe₂ FILMS

Keiji TSUNETOMO, Hiroaki MYOREN, Hiroyuki NASU, Takeshi IMURA and Yukio OSAKA

Department of Electrical Engineering, Faculty of Engineering,
Hiroshima University, Higashi Hiroshima 724Introduction

The GeTe₂ films prepared by sputtering technique are amorphous when they are formed on substrates at room temperature. Amorphous(a-) GeTe₂ films with the thickness less than 1 μm transform into crystalline(c-) GeTe₂, a new phase recently found by our group, at T_a (annealing temperature)=200 °C.¹⁾ X-ray diffraction measurements show the structure of c-GeTe₂ seems to be cubic and isomorphic to that of β -cristobalite SiO₂.¹⁾ Furthermore, the stability of c-GeTe₂ is related to the film thickness and existence of substrates.²⁾

The purpose of this study is to clarify the local structure around Ge atom in a-GeTe₂ that is converted into c-GeTe₂ at T_a =200 °C.

Experimental and Results

All samples were prepared onto 0.8 μm thick Kapton substrates by sputtering a Ge target upon which Te chips were placed. The film thicknesses of the samples are about 1 μm . About 20 layers of the film were stacked to attain a μx of about 2.5 for EXAFS measurements. EXAFS spectra of Ge-K edge were measured at room temperature in the air.

Our measurements were carried out at the Photon Factory in National Laboratory for High Energy Physics on 10-b beam line. The details of the theory and the measurements of EXAFS are described in references 3)-5).

In Fig. 1, normalized EXAFS oscillations of the Ge-K absorption edge for GeTe₂ films are plotted as a function of the photoelectron wave number k .

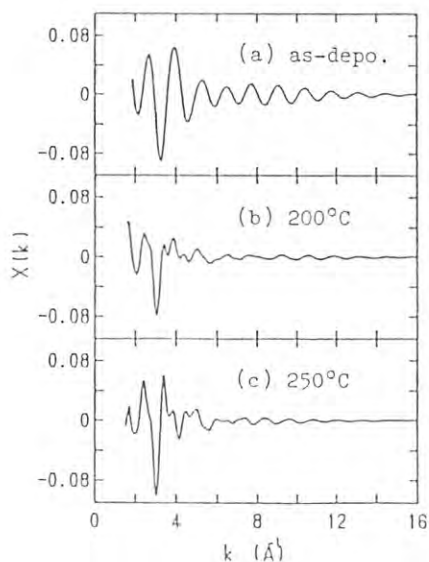


Fig. 1

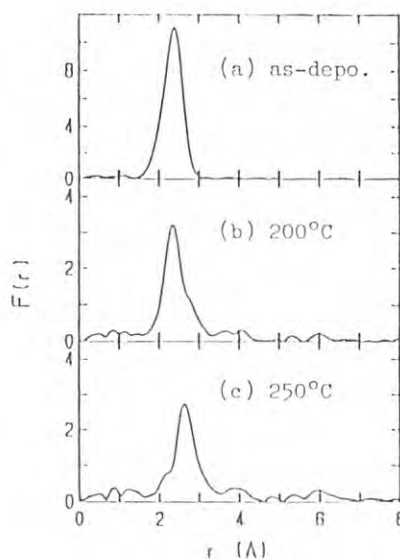


Fig. 2

Figure 2 shows the Fourier transform of the EXAFS oscillations shown in Fig. 1. The peaks in this figure are shifted toward smaller radial distance r due to the phase shift effects. The first nearest neighbor is observed, but another peaks are not clear. We consider that the reason for this phenomena is the influence of the measurements temperature for S/N ratio on the EXAFS spectra.

In Table 1, $r-\alpha$ of each samples are listed. The phase shifts factor (α) is constant in all samples. Hence, the bond length of Ge-Te atoms in amorphous is 0.04 Å larger than that of crystalline GeTe₂. From a comparison with the experimental bond length of c-GeTe and the peak position of the nearest neighbor in Fig. 2 (c), the phase shift factor is ~ 0.21 Å.

We can estimate the coordination number of Ge atoms by comparing with the EXAFS of a reference, in which the coordination number of Ge atom is known. Now, we are planning the next measurements of EXAFS. The coordination number of Ge atoms in GeTe₂ films, and EXAFS measurements of Te edge will be reported in next report.

References

- 1) H. Fukumoto, K. Tsunetomo, T. Imura and Y. Osaka; J. Phys. Soc. Jpn. 56 (1987) 158.
- 2) K. Tsunetomo, T. Sugishima, T. Imura and Y. Osaka; J. Phys. Soc. Jpn. 56 (1987) in press.
- 3) E. A. Stern; Phys. Rev. B10 (1974) 3027.
- 4) P. A. Lee, P. H. Citrin, P. Eisenberger and B. M. Kincaid; Rev. Mod. Phys. 53 (4) part 1 (1981) 769.
- 5) H. Oyanagi, T. Matsushita H. Tanoue, T. Ishiguro and K. Kohra; Jpn. j. Appl. Phys. 24 (1985) 610.

Table 1

Sample	$r-\alpha$ (Å)
(a) as-depo.	2.39
(b) 200°C	2.35
(c) 250°C	2.63

EXAFS STUDY ON PREMARTENSITIC PHASE IN A-15 COMPOUNDS

Kazuya KAMON, Hirofumi SAKASHITA*, Hikaru TERAUCHI, Nagao KAMIJO**,
Hironobu MAEDA†, Naoki TOYOTA++ and Tetsuo FUKASE++

Department of Physics, Kwansei-Gakuin University, Nishinomiya 662.

*Center of Advanced Instrumental Analysis, Kyushu University, Kasuga 816.

**Government Industrial Research Institute Osaka, Ikeda, 563.

†Department of Chemistry, Okayama University, Okayama, 770.

++The Research Institute for Iron, Steel and Other Metals, Tohoku University, Sendai, 980.

Introduction

A-15 compounds undergo a cubic-to-tetragonal phase transition, a martensitic transformation, at T_m . In Nb_3Sn and V_3Si , precursor phenomena such as an anisotropic dilatation^{1,2} and an appearance of the forbidden reflection³ have been observed above T_m . The precursor region is referred to premartensitic phase. It is not clear whether the precursor is the critical phenomenon of martensitic transformation or is caused by a static origin such as a local strain¹⁻⁴. We report on EXAFS study in Nb_3Sn and V_3Si to clarify the local structure.

Experiments

EXAFS measurements of Nb_3Sn and V_3Si were carried out at BL-10B (Si(311) channel cut crystal) and BL-7C (Si(111) double crystal monochromator), respectively. The procedure of sample preparations and methods of the spectral analysis are reported elsewhere⁵.

Results and Discussions

The temperature dependence of the interatomic distances of Nb_3Sn is shown in Fig.1. It is clear that the interatomic distance between the 1st-neighbor Nb-Nb atoms (o) splits into three kinds above T_m . The distances in the premartensitic phase are nearly equal to those at 20K ($<T_m$). The fact suggests that there is a region with the local tetragonal structure in the premartensitic phase, because the cubic structure is confirmed⁶. The interatomic distances (●) estimated from the lattice constant⁷ are shown in Fig.1. The estimated difference between 1st and 3rd neighbor distances at 20K is 0.07Å, while that determined by EXAFS is 0.09Å.

A similar behaviour is seen in V_3Si as shown in Fig.2. The splitting of the distances starts at 60K. In addition, an anomalous increase of the interatomic distance between V-Si (Δ) was observed below 60K. These facts indicate that the local distortion in the premartensitic phase is characterized by the martensitic structure. The internal displacement parameter δ estimated from the EXAFS analysis is 2.19×10^{-3} at 9K; its magnitude is comparable to that of Nb_3Sn ($\delta = 3.2 \times 10^{-3}$).

The local tetragonal distortion exists above T_m because of the existence of the tetragonal structure in cubic matrix. The distortion may be due to an embryo of the martensitic phase distributed randomly in the crystal. It is not evident, however, that the formation of the embryo originates from a critical fluctuation of the tetragonal distortion or lattice imperfection such as defects or impurities. In the former case, the precursor is the critical phenomenon, i.e. the premartensitic phase is not a thermodynamical phase. In the latter case, the precursor is a static phenomenon if defects or impurities pin embryos and the embryo have a very long life time compared with a time scale of the measurement. Therefore, the premartensitic phase is defined as the thermodynamical phase.

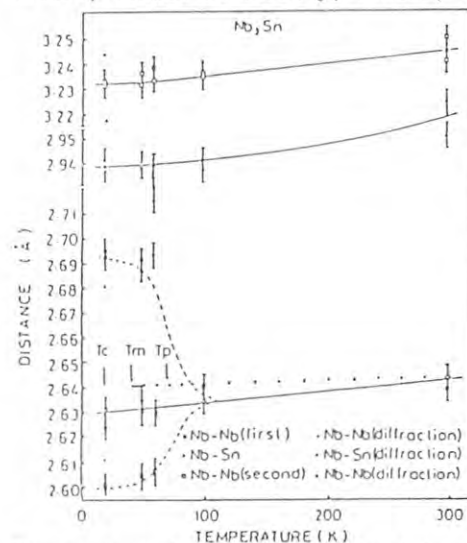


Fig.1. Temperature dependence of the interatomic distances between the 1st neighbor Nb-Nb (o), the 2nd neighbor Nb-Nb (□) and the Nb-Sn (Δ). (●), (■) and (▲) represent interatomic distances estimated from the diffraction.

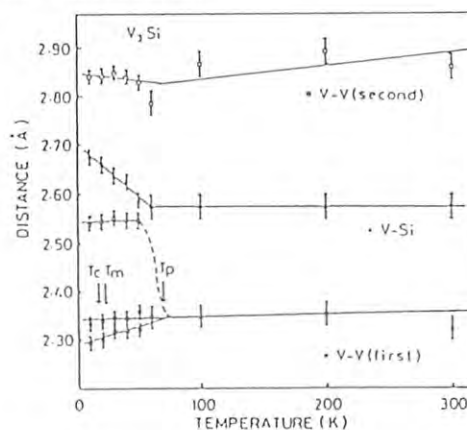


Fig.2. Temperature dependence of the interatomic distances between the 1st neighbor V-V (o), the 2nd neighbor V-V (□) and the V-Si (Δ) in V_3Si .

References

- 1) T.Kobayashi, T.Fukase, N.Toyota and Y.Muto: *Physica* **107-110B+C** (1981) 261.
- 2) H.Watanabe: M.S.Thesis. Tohoku University.
- 3) J.B.Hastings, G.Shirane and S.J.Williamson: *Phys. Rev. Lett.* **43** (1979) 1249.
- 4) J.B.Hastings, Y.Fujii, G.Shirane and S.J.Williamson: *Phys. Rev.* **B28** (1983) 322.
- 5) H.Sakashita, K.Kamon, H.Terauchi, N.Kamijo, H.Maeda and N.Toyota: *J. Phys. Soc. Jpn.* (to be appeared).
- 6) K.Kamigaki, H.Sakashita, H.Terauchi, H.Maeda and N.Toyota: *Proceedings of ICOMAT-86* 138.
- 7) G.Shirane and J.D.Axe: *Phys. Rev.* **B4** (1971) 2957.

LOCAL STRUCTURE OF THE α -AgI_{1-x}Br_x SOLID-SOLUTIONAkira YOSHIIASA, Fumiyuki KIHARA, Shuichi EMURA, Fumikazu KANAMARU,
and Kichiro KOTOThe Institute of Scientific and Industrial Research, Osaka University,
Mihoga-oka, Ibaraki, Osaka 567, Japan

Introduction

The α -phase silver iodide is the typical superionic conductor of Ag ions. Covalent character in the AgI-AgBr system is increasing from AgBr to AgI. Under ambient conditions AgI is stable in the tetrahedrally-coordinated wurtzite type structure, while AgBr is in the octahedrally-coordinated rock-salt type. α -AgI_{1-x}Br_x solid solution is stable in the cubic system^x (space group Im3m) over a wide range of composition and temperature. In the α -AgI_{1-x}Br_x solid-solution having a statistically disordered distribution of Ag ions, it is expected that the local environments of the Br ions differ from those of the I ions though the chemical composition and basic structure are simple. EXAFS spectroscopy is a useful probe of the local environment around a particular absorbing atom in the random solid-solution.

Experimental

AgI and AgBr were mixed together in appropriate proportions. The mixture was melted under the iodine atmosphere (about 100 mmHg) at 973K for 20 hours in silica tube and then quenched. The sample was ground to a fine powder and annealed at 623K for two hours before measurements. The formation of single phase α -AgI_{1-x}Br_x solid-solution ($0 \leq x \leq 0.4$) was confirmed by X-ray powder diffraction technique at 573K. For high temperature X-ray absorption measurements, the fine powder samples were mixed with boron nitride and pressed into pellets. Our fabricated furnace for X-ray absorption measurements maintained the samples at 623K and 573K with a stability of ± 1 K.

The X-ray absorption measurements near the Br K- and Ag K-edges were made with synchrotron radiation (PF) by use of the EXAFS facilities installed at the beam line 10B. The Fourier transforms for Ag K-edge are shown in Fig. 1. Using a curve-fitting analysis of EXAFS, the structure parameters (coordination number, interatomic distance and Debye-Waller factor) of the α -AgI_{1-x}Br_x solid-solution are determined by the least-squares parameter fitting. The amplitude and phase shift parameters are obtained from the reference samples (pure β -AgI and AgBr at room temperature). Data processing and analysis applied to the absorption spectra were described in detail in our previous work²⁾.

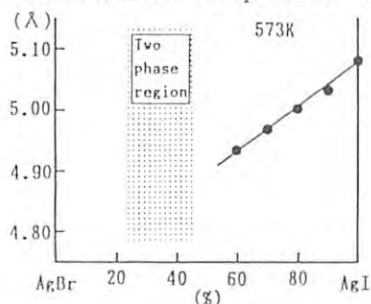


Fig. 2. Relationship between cell parameter and composition of α -AgI_{1-x}Br_x solid solution at 573K.

Results and Discussion

The cell dimensions (Fig. 2) decrease linearly with increasing AgBr content because of the substitution of smaller ion Br⁻ for I⁻ and it follows Vegard's law. The peak in each radial structure function around the Ag ion of the solid-solution at 573K (Fig. 1) gradually develops a shoulder at shorter distance with increasing AgBr content. Through the solid-solution range, the Ag-I and Ag-Br distances are constant and 2.76(2)Å and 2.70(2)Å, respectively. The experimental Ag K-edge XANES spectra are shown in Fig. 3 with the reference samples. It is suggested from the EXAFS results that only tetrahedral sites are appreciably occupied at equilibrium in the solid-solution.

We are grateful to Dr. H. Maeda, Okayama Univ., for providing us the programs and to Drs. S. Nomura and A. Koyama, KEK, for their assistance on the EXAFS measurement.

- 1) A. Yoshiasa et al., Acta Cryst. in press
- 2) A. Yoshiasa et al., J. Phys. Colloq. **47** (1986) C-8 803

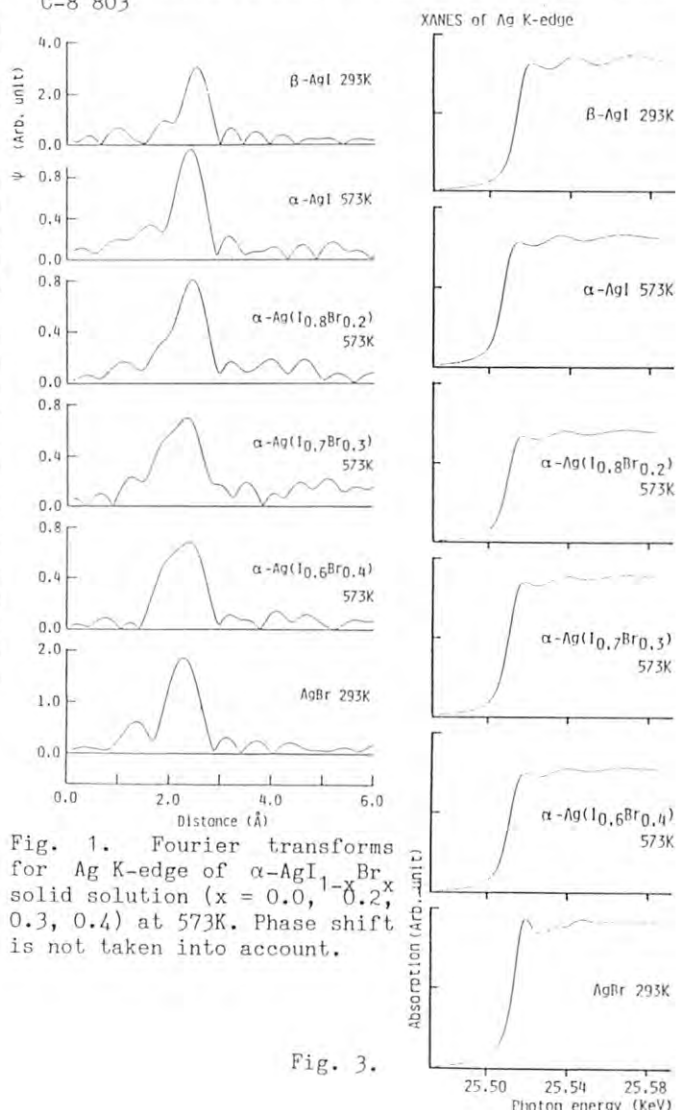


Fig. 1. Fourier transforms for Ag K-edge of α -AgI_{1-x}Br_x solid solution ($x = 0.0, 0.2, 0.3, 0.4$) at 573K. Phase shift is not taken into account.

Fig. 3.

EXAFS AND XANES STUDIES ON $\text{Na}_2\text{O}-\text{B}_2\text{O}_3$ GLASSES CONTAINING COPPER ION

Qiang XU, Takashi MAEKAWA, Hideki MAEKAWA, Katsuyuki KAWAMURA, Toshio YOKOKAWA, Hiroyuki OYANAGI*, Masayuki OKUNO** and Fumiyuki MARUMO***

Department of Chemistry, Faculty of Science, Hokkaido University, Sapporo 060

*Electrotechnical Laboratory, Sakuramura, Niiharigun, Ibaraki 305

**Department of Geology, Faculty of Science, Kanazawa University, Kanazawa 920

***Research Laboratory of Engineering Materials, Tokyo Institute of Technology, Nagatsuta, Yokohama 227

Introduction

There have been reported many EXAFS and XANES studies on the oxide glasses containing transition metals in order to clarify the electronic states and the coordination situation of these ions in oxide glasses. Among them the local structure and the oxidation state of iron and titanium in oxide glasses have been investigated by combining with the other analytical methods. However, there have not been reported the EXAFS and XANES investigations of oxide glasses containing copper ion, though their physical and optical properties were studied. In the present study, EXAFS and XANES experiments were carried out in order to determine the distance of copper-oxygen bond as well as the coordination number of copper ion in the sodium borate glasses.

Experimental

$x\text{Na}_2\text{O} \cdot (1-x)\text{B}_2\text{O}_3$ oxide glasses, where x are 0.05, 0.1, 0.15, 0.2, 0.25, 0.3, 0.4 and 0.7, were prepared from CuO , Na_2CO_3 and H_3BO_3 by the usual melt quenching method. The powder samples of 150 meshes on Scotch tape were used for the measurements, except for a glass of $x=0.7$ (in a plate) because the glass is very hygroscopic.

The X-ray absorption measurements near Cu-K edge were carried out at BL-10B of the Photon Factory in the National Laboratory for High Energy Physics (KEK).

Results and Discussion

The XANES spectra of $\text{Na}_2\text{O}-\text{B}_2\text{O}_3$ oxide glasses containing 1mol% CuO , CuO and Cu_2O powders are shown in Fig.1. The pre-edge peak at 8977~8978eV, assigned to a transition from 1s to 3d state, are very weak due to the forbidden transition. This pre-edge peak in oxide glasses appeared at 1eV lower than that of CuO powder sample and did not change among glasses investigated. Though the peak near 8982~8983eV in oxide glasses does not shift, the change of intensity is extensive. It is considered that

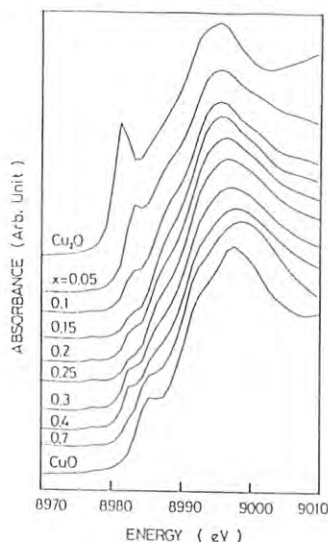


Fig.1 XANES of Cu-K edge for sodium borate glasses containing 1mol% CuO , CuO and Cu_2O powders.

the peak at 8985~8988eV in oxide glasses corresponds to that of CuO . The peak position shifts to lower energy side with an increase of Na_2O content. On the other hand, it is found that the apparent peak at 8992~8999eV, which may be due to a transition from 1s to 4p state, separates into two peaks with an increase of Na_2O content.

Fig.2 presents the result of Fourier transform of Cu-K edge EXAFS for oxide glass of $x=0.2$. It has a peak in the region of 1~2Å, which is attributable to Cu-O bond. The results of curve-fitting analyses are shown in Table 1.

Table 1. Results of curve-fitting analyses for $x\text{Na}_2\text{O} \cdot (1-x)\text{B}_2\text{O}_3$ glasses containing 1mol% CuO .

x	$R(\text{\AA})$	N_1	σ
0.05	1.936	3.70	0.117
0.10	1.940	4.10	0.116
0.15	1.934	4.29	0.116
0.20	1.922	4.00	0.117
0.25	1.912	3.79	0.115
0.30	1.908	3.65	0.116
0.40	1.913	3.74	0.117
0.70	1.936	3.98	0.113
error	± 0.003	± 0.25	± 0.002

It is indicated that the nearest Cu-O distance decreases systematically when the Na_2O content, x , changes from 0.05 to 0.4. The value for a glass of $x=0.7$ shows a similar one to that of low content glass. Debye-Waller factor σ keeps mostly a constant value. It is also shown that the copper ions coordinated with 4 nearest oxide ions, although some change can be found with an increase of Na_2O content. It means that the bond distance of nearest Cu-O is much influenced, whereas coordination number does not change with an increase of the basicity in the sodium borate glasses.

It is reported by ESR studies that oxygen coordination around copper ion has an elongated octahedral structure. At present, it is not certain whether the peak appeared at about 2.7Å in Fig.2 corresponds to the oxide ions in the longer axis of octahedron reported or not.

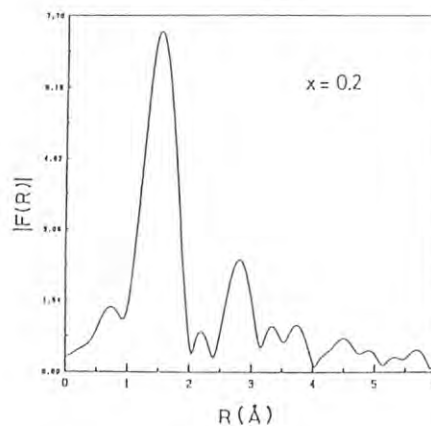


Fig.2 Fourier transform of Cu-K edge EXAFS for $\text{Na}_2\text{O} \cdot 4\text{B}_2\text{O}_3$ glass.

STUDY OF THE ELECTRONIC STRUCTURES OF HIGHLY CONDUCTIVE
PHTHALOCYANINATO NICKEL COMPLEXES BY POLARIZED XANES SPECTRA

Haruo KURODA, Kyuya YAKUSHI, Nobuhiro KOSUGI and Isao HAMADA

Department of Chemistry and Research Center for Spectrochemistry,
Faculty of Science, The University of Tokyo, Hongo, Tokyo 113Introduction

We found in the ESR experiment¹⁾ that the conduction electrons are located not only on the ligand but also on the metal in bis(phthalocyaninato)nickel hexafluoroantimonate $(\text{NiPc})_2\text{SbF}_6$ in contrast of phthalocyaninato nickel iodide NiPcI . That is, the ligand and Ni 3d orbitals of NiPc are partially oxidized by SbF_6 while only the ligand orbital of NiPc is oxidized by I_3 . The structure of the molecular column of $(\text{NiPc})_2\text{SbF}_6$ is almost the same as that of NiPcI , except slight shortening of the Ni-Ni distance of $(\text{NiPc})_2\text{SbF}_6$ from 3.244 Å to 3.230 Å. The crucial difference is the degree of oxidation from 1/3 for $\text{NiPc} \cdot (\text{I}_3^-)_{1/3}$ to 1/2 for $\text{NiPc} \cdot (\text{SbF}_6^-)_{1/2}$. The increase in the degree of oxidation pushes down the Fermi energy and generates some 3d vacancy. The $3d_{x^2-y^2}$ orbital is sufficiently separated from the other 3d orbitals and is already unoccupied in NiPc^0 . It is, however, difficult to predict which orbital of the closely located $3d_{z^2}$, $3d_{xy}$, $3d_{xz}$ and $3d_{yz}$ orbitals is involved in the conduction band.

In the present work, we measured Ni K-edge XANES spectra of the $(\text{NiPc})_2\text{SbF}_6$ single crystal in order to characterize the symmetry of the vacant 3d orbitals by observing the polarization dependence of 1s-3d electric quadrupole transition.

Experimental

The single crystal of the dimension $0.15^2 \times 2$ mm³ was fixed with vacuum grease onto the round mask which was made from stainless steel with the thickness of 0.1 mm and had a diaphragm of 0.1×1 mm². Polarized Ni K-edge XANES spectra were measured at Beam Line 10B in Photon Factory with the X-ray polarization plane (the plane of vibration of electric field) parallel, 45° and perpendicular to the stacking axis of the crystal, in which NiPc molecules are stacking along the c axis and perpendicular to the stacking axis.

Results and Discussion

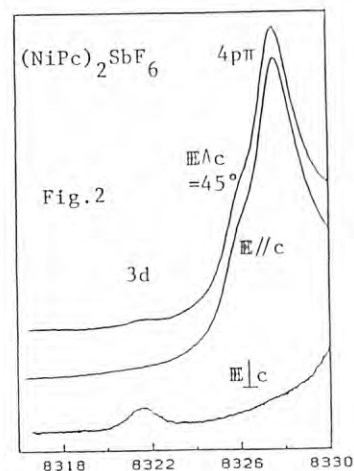
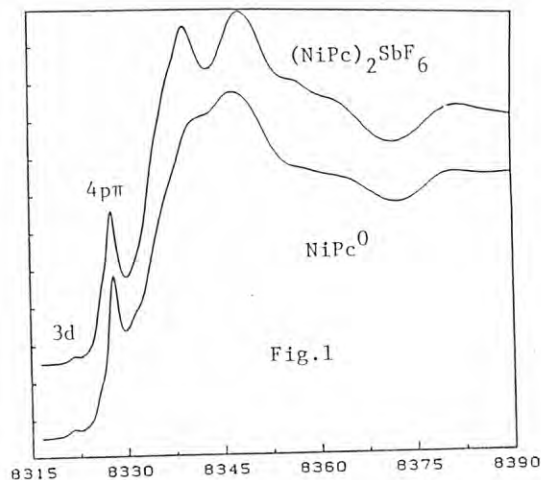
Fig.1 shows the X-ray absorption spectra of the powdered sample of NiPc and $(\text{NiPc})_2\text{SbF}_6$. The weak absorption band at about 8321.5 eV is quadrupole-allowed 1s-3d transition. Fig.2 shows the polarization dependence of the 1s-3d transition of the single crystal of $(\text{NiPc})_2\text{SbF}_6$. Since XANES of CoPc and FePc exhibited only a single 1s-3d band within the resolution of the monochromator used, we can expect that the 1s-3d band of $(\text{NiPc})_2\text{SbF}_6$ observed is attributable to the superposition of the $3d_{x^2-y^2}$ and the other 3d transitions. The candidate of the oxidized orbital is $3d_{z^2}$ or $3d_{xy}$ from the quadrupole selection rule shown in Table 1. The $3d_{z^2}$ orbital is expected to become higher in energy in the solid state due to the electrostatic effect between the neighboring Ni atoms. Furthermore, the slight shortening of the Ni-Ni distance from 3.244 Å to 3.230 Å contributes to

make more holes in the d band through the expansion of the band width and the unstabilization of the $3d_{z^2}$ orbital. In conclusion, it is the most probable that the origin of the d character of the unpaired electron is $3d_{z^2}$.

1) K.Yakushi et al., Chem.Lett. (1986) 1161 ;
Synthetic Metals 19 (1987) 769.

Table 1. Selection rule of quadrupole transition. It is impossible to distinguish d_{xz} from d_{yz} and $d_{x^2-y^2}$ from d_{xy} experimentally because the NiPc ligands are alternately twisted by about 40° along the stacking c-axis in $(\text{NiPc})_2\text{SbF}_6$.

	$d_{x^2-y^2}, d_{xy}$	d_{z^2}	d_{xz}, d_{yz}	exptl.
$\text{E} \perp c$	o	x	x	OBS
$\text{E} // c$	x	x	o	NOT OBS
$\text{E} \wedge c = 45^\circ$	o	o	x	OBS



CRYSTALLIZATION OF Gd_2O_3 STABILIZED ZIRCONIA FROM GEL BY EXAFS

Kichiro KOTO, Daidou KOUMYOUJI, Akira YOSHITASA, Fumikazu KANAMARU
and Shuichi EMURA

The Institute of Scientific and Industrial Research, Osaka University,
Mihoga-oka, Ibaraki, Osaka 567, Japan

Introduction

Stabilized zirconias, oxide ion conductors, are generally synthesized by calcining and sintering gel obtained by wet chemical method. In the process of calcining and sintering, the peak profile in the X-ray diffraction pattern changes from halo pattern for gel to sharp peak for the well sintered compound, indicating crystallization from amorphous state to the well ordered arrangement of atoms¹⁾.

The crystallization process of the Gd_2O_3 stabilized zirconia with the pyrochlore composition from gel was studied by EXAFS and XANES.

Experimental and Results

The precipitated zirconium and gadolinium hydroxide gel with the composition of $\text{Zr}/\text{Gd}=1$ was obtained by coprecipitation method using $\text{ZrOCl}_2 \cdot 8\text{H}_2\text{O}$ (99%) and $\text{GdCl}_3 \cdot 6\text{H}_2\text{O}$ (99.9%) in powder form (Wako) as starting materials. The samples were heated at 30°, 110°, 450°, 950° and 1370 °C for one day. TG-DTA curve from room temperature to 500°C was obtained by using the sample dried at 30°C. X-ray diffraction patterns were obtained for all the samples.

Chemical compositions were analyzed by analytical electron microscopy to confirm the homogeneity of the samples.

The mixture of the sample and BN powder was pressed to make a pellet with 10 mm ϕ and was used for EXAFS study. X-ray absorption measurements near Zr-K and Gd-L1 edges were made at room temperature in transmission with synchrotron radiation on the Beam Line 10-B at Photon Factory. The data analysis was made using the program written by H. Maeda. The results were shown in Fig.1 and listed in Table 1.

The distance of the first shell of Zr remains constant whereas those of the second shell of Zr and the first shell of Gd become large with increasing crystallization. The changes of the features of XANES(Fig.2) agree with those of the distances in the Fourier transform. These suggest increasing interaction between polyhedra of metal atoms in the process of crystallization.

The authors thank to Dr. H. Maeda, Okayama Univ., for providing us the program of EXAFS analysis. Thanks are also to Drs. S. Nomura and A. Koyama, KEK, for useful advices in the experiments.

Reference

- 1) T. Uehara, K. Koto, F. Kanamaru and H. Horiuchi: Solid State Ionics **23** (1987) 137.

Table 1. Distances (\AA) in the Fourier transform. No phase shift corrections were made.

Heated Temp.(°C)	X-ray diffraction	Zr 1st-shell	Zr 2nd-shell	Gd 1st-shell
30	H	1.65	3.14	1.62
110	H	1.66	3.12	1.64
450	H	1.62	3.17	1.75
950	F(B)	1.64	3.23	1.76
1370	F(S)	1.66	3.22	1.83

H: Halo pattern, F(B): Broad fluorite-type peak, F(S): Sharp fluorite-type peak

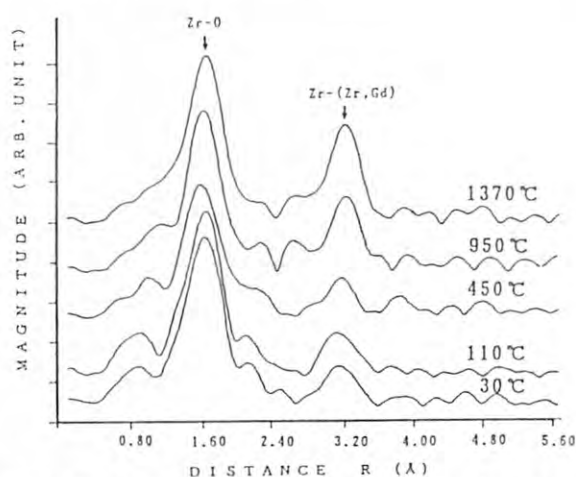


Fig.1 The Fourier transform for Zr-K edge of the $\text{Zr}_2\text{Gd}_2\text{O}_7$. No phase shift corrections were made.

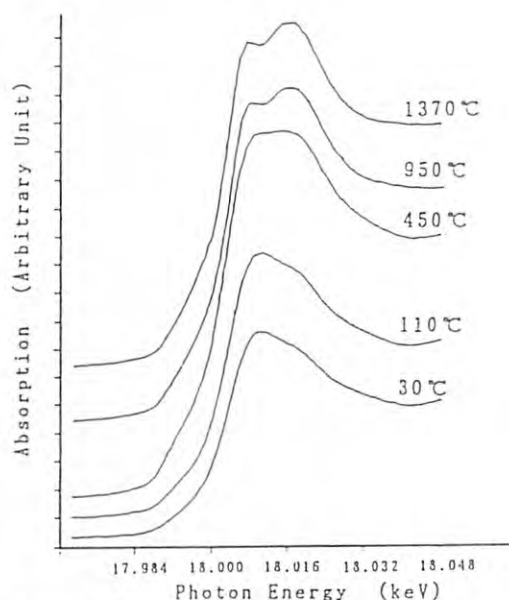


Fig.2 Experimental XANES spectra of the compounds with $\text{Zr}_2\text{Gd}_2\text{O}_7$ composition for Zr K-edge.

EXAFS STUDY OF THE PEROVSKITE TYPE $\text{SrCo}_{1-x}\text{Mn}_x\text{O}_3$ SOLID SOLUTIONAkira YOSHIIASA, Yukari INOUE, Fumikazu KANAMARU
and Kichiro KOTOThe Institute of Scientific and Industrial Research, Osaka University,
Mihogaoka, Ibaraki, Osaka 567, JapanIntroduction

Functional properties such as superconductivity and catalytic activity for oxidation of CO have been found in the perovskite and its related compounds.

The system $\text{SrCo}_{1-x}\text{Mn}_x\text{O}_3$ forms a continuous solid solution with the perovskite type structure. Both Mn^{4+} and Co^{4+} ions occupy the octahedral site randomly. The octahedra that constitute the framework of the structure share corners each other. It has been reported that the spin state of Co^{4+} ion changes from low ($[d\epsilon]^0 [d\gamma]^0$) to high ($[d\epsilon]^3 [d\gamma]^2$) at about $x=0.33$ in connection with the peculiar variation of the lattice constant. In this study the local structure of the solid solution has been studied to elucidate the characteristic features of the lattice constant and the spin state of Co^{4+} ion.

Experimental

The mixture of SrCO_3 , MnCO_3 , and CoCO_3 powder in the desired ratio was fired under the appropriate conditions according to the previous study. As the compounds obtained in this way were oxygen-deficient, they were annealed under oxygen pressure of 1300 atm at 300 °C. The formation of single phase solid solution was confirmed by X-ray diffractometry. The lattice constants are shown in Fig. 1. The X-ray absorption measurements near the Mn K- and Co K-edges were made for the samples formed to pellets with BN powder with synchrotron radiation on the Beam Line 10B at Photon Factory. Each Fourier transform of k^3 -weighted Mn K-edge EXAFS for the solid solutions is shown in Fig. 2. Using a curve fitting analysis of EXAFS, the structure parameters of the solid solution were determined by the least-squares parameter fitting. The amplitude and phase shift parameters are obtained from the reference samples (both end-members).

Results and Discussion

It is revealed that the Mn-O distance from EXAFS analysis decreases with increase of Co^{4+} ion content, nevertheless the mean (Mn,Co)-O distance, one half of the lattice constant, becomes large (Fig. 3). This trend is considered due to the shift of O^{2-} ion toward Mn^{4+} ion in the Mn-O-Co combination.

The variation of the lattice constant in the range $0.0 \leq x \leq 0.33$ is explained from the formation of Mn-O-Co combinations by partial increase of Co-O distances. It is expected that the strength

of the ligand field for Co^{4+} ion becomes weak gradually with increase of Mn^{4+} ion content. Since four of six Co-O bonds in a CoO_6 octahedron are lengthened at the composition of $x=0.33$, the strength of the ligand field decreases so that the spin state of Co^{4+} ion is changed from low to high. Similarly it can be understood why Co^{4+} ion in the high spin state, which has a larger ionic radius, becomes more stable than that in the low spin state in the range $0.33 < x < 1.0$ though the solid solutions have smaller unit cell volumes.

The features of Co K-edge XANES spectra (Fig. 4) change discontinuously at $x=0.33$ accompanying with the change of the spin state of Co^{4+} ion. On the other hand, such a behavior is not observed in the Mn K-edge XANES spectra.

We are grateful to Dr. H. Maeda, Okayama Univ., for providing us the programs and to Drs. S. Nomura and A. Koyama, KEK, for their assistance on the EXAFS measurement.

1) Taguchi et al., J. Solid State Chem., 35 (1980) 246.

2) Inoue et al., Mineral. Soc. Japan, 1987 Ann. Meet. Abst. (1987) 103.

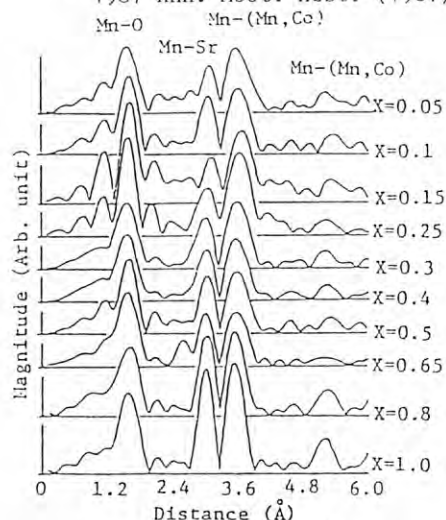


Fig. 2. Fourier transforms of the k^3 -weighted Mn K-edge spectra. Phase shift is not taken into account.

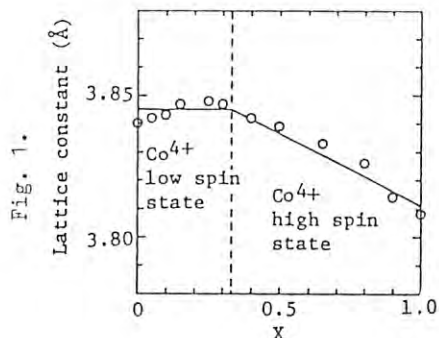


Fig. 1.

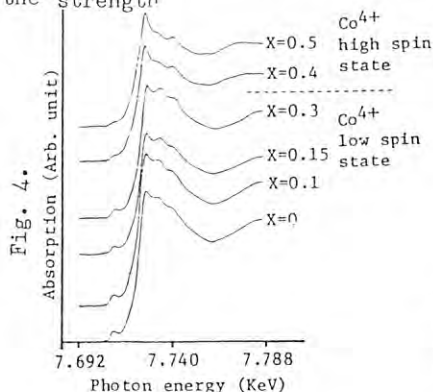


Fig. 4.

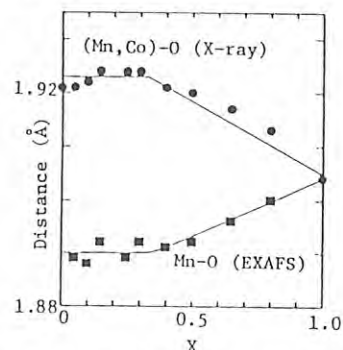


Fig. 3. The Mn-O distance measured by EXAFS vs composition (X). Solid circles denote the mean (Mn,Co)-O distances obtained from diffraction experiment.

LOCAL CRYSTAL STRUCTURE OF EXCHANGED IONS IN ZEOLITE

Yasushige KURODA, Hironobu MAEDA, Hisaki MORIWAKI, Akira MORIYA, Naruhiko BANBA,* and Tetsuo MORIMOTO

Department of Chemistry, Faculty of Science, Okayama University, Okayama 700, Japan

*Department of Physics, Faculty of Science, Okayama University, Okayama 700, Japan.

Introduction

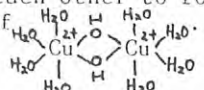
Zeolites are crystalline aluminosilicates containing three dimensional arrays of SiO_4 and AlO_4 tetrahedra. Because of the presence of aluminum atoms in the zeolite lattice, there is a net charge in the lattice, and the compensating cations, typically sodium, are required to balance the anionic framework charge. Other kinds of cations are relatively easily exchangeable. It is well-known that the catalytic properties of zeolites are influenced by the variety, amount, and distribution of the exchanged cations.¹⁾ It was found in our laboratory that the Cu-exchanged mordenites can contain an excess amount of Cu ions compared with that expected from the stoichiometry. It is interesting to investigate the local structure of the Cu ions. The Fourier transform method of the EXAFS spectrum is one of the powerful techniques for the investigation of the structure of the exchanged zeolites. In this work, we report the result of the EXAFS study on the local structure of Cu-exchanged mordenites.

Experimental

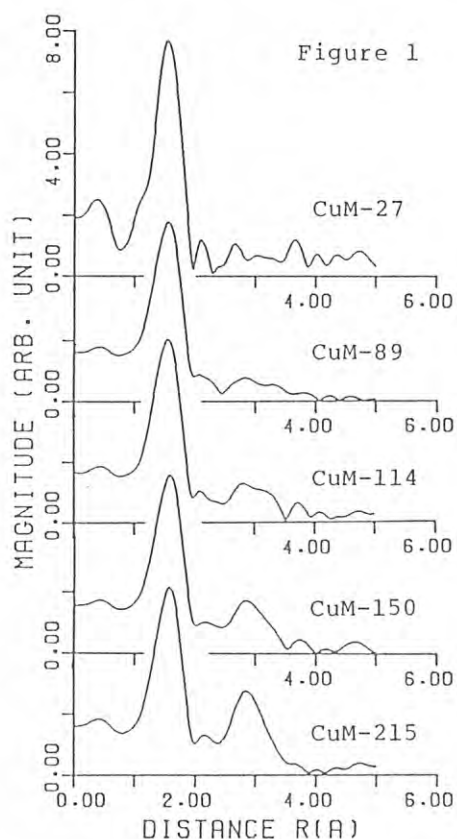
Cu-exchanged mordenites with different amounts of Cu ions were prepared from Na-mordenite by the usual method.²⁾ The extent of ion exchange, determined by chelatometric titration, were found to be 27, 89, 114, 150, and 215 for Cu(II) ions (CuM-27 etc.). The X-ray absorption measurement was performed by using the synchrotron radiation from the Photon Factory (PF) at the National Laboratory of High Energy Physics (KEK, Tsukuba). The Cu K-edge EXAFS spectra of the CuM samples and the reference sample Cu(II)O were taken with the transmission mode, using a beam line BL-10B with channel-cut silicon (311) crystal monochromator under a ring operating conditions of 2.5 GeV and 200 mA maximal current. The energy resolution is 0.5 eV for near-edge scan and 2.0~3.0 eV for EXAFS scan. The Photon energy, E, was calibrated with respect to a Cu foil by assigning 8.9788 keV to the pre-edge peak on the absorption edge. Details of the performance for both EXAFS spectrometers and data processing procedure have been described in refs. 3 and 4.

Results and Discussion

The Fourier transform of the EXAFS function of CuM-27, -89, -114, -150, and -215 at room temperature is shown in Fig. 1. Using

CuO and CuCl_2 solution as the reference substances, we attributed the first major peak centered at 1.54 Å (no phase-shift correction) to the backscattering from the nearest neighbor oxygen atoms. It is seen from Fig. 1 that the second major peak appears when the extent of exchange exceeds 100 %, and the intensity of this peak increases with increasing extent of exchange. From this fact, we attributed the second major peak at 2.85 Å (no phase-shift correction) to the backscattering from the second nearest Cu ions. These results suggest that Cu ions are bound to each other to form dimers, i.e., in the form of . Detail analysis of EXAFS is now in progress.

- 1) L. Kevan, Acc. Chem. Res., **20**, 1, 1987.
- 2) J. R. Rearce, W. J. Mortier, J. B. Uytterhoeven, and J. H. Lunsford, J. Chem. Soc. Faraday **1**, **77**, 937, 1981.
- 3) H. Oyanagi, T. matsushita, M. Ito and H. Kuroda, KEK Report, **83-30**, 1984.
- 4) H. Maeda, J. Phys. Soc. Jpn., **56**, 2777, 1987.



STRUCTURE STUDIES OF NIOBIUM AND TANTALUM OXIDES BY EXAFS

Takashi USHIKUBO, Toshio AKAI, Yasuo KOIKE, Keisuke WADA and Satoshi OGURA

Research Center, Mitsubishi Chemical Industries Ltd.,
1000 Kamoshida-cho, Midori-ku, Yokohama 227Introduction

The hydrated niobium and tantalum oxides, or the niobic and tantalic acids, show strong acid properties and they are expected to be applicable as industrial catalysts.¹⁻²⁾ In their active forms, they are amorphous in state below about 580 and 730 °C for niobic and tantalic acids, respectively. Thus, there has been little knowledge about the structures of these solid acids. B. K. Sen et al. postulated that the structure of niobic acid was an isopoly acid of composition of $H_8Nb_6O_{19}$.³⁻⁵⁾ But their postulate has not been confirmed spectroscopically, yet. So we tried to study the structures of niobic and tantalic acids by using EXAFS.

Experimental and Results

The Nb K-edge and Ta L_{III}-edge EXAFS data of these oxides were obtained at EXAFS apparatus(BL-10B). Fig. 1 shows the results of Fourier transformations of the EXAFS data for (a), (b) niobic acid (heat-treated at 120 and 300 °C, respectively) (c) T-Nb₂O₅, which was formed by heating of niobic acid at 700 °C and (d) niobium isopoly acid potassium salt ($K_8Nb_6O_{19}$), in momentum (k) space, (left side) over the finite k range about 2.5 - 13 Å⁻¹, in order to determine their Nb-O bonds, and (right side) over the finite k range about 7-14 Å⁻¹, in order to determine their Nb-Nb bonds. Although the dehydration of niobic acid occurred by heat-treatment at about 300 °C, the Nb-Nb bond length of niobic acid did not change, thus, suggesting the retention of the skeleton of niobic acid during the heat-treatment. The Nb-Nb distance of niobic acid is intermediate between those of

T-Nb₂O₅ and $K_8Nb_6O_{19}$. It might be due to difference of the share of O-atom in NbO₆ octahedra among these oxides.

Furthermore, it was found that Nb-O distances were significantly different from each other among niobic acid, T-Nb₂O₅ and $K_8Nb_6O_{19}$. The existence of at least two types of Nb-O bonds was suggested for niobic acid. Confirming these results by Raman spectroscopy is under investigation.

In the similar studies on tantalum oxides, Fig. 2 shows the Fourier transformations of the EXAFS data for (e) tantalic acid, (f) Ta₂O₅ and (g) $K_8Ta_6O_{19}$. The more detailed studies will be reported in another places.

References

- 1) T. Iizuka, K. Ogasawara and K. Tanabe, Bull. Chem. Soc., Jpn. **56**, 2927 (1983).
- 2) T. Ushikubo, Y. Koike, K. Wada and S. Ogura, Proceeding of Japan-France Seminar on Catalysis with Metal Compounds, 111 (1987).
- 3) B. K. Sen et al., Mat. Res. Bull., **16**, 923 (1981).
- 4) B. K. Sen et al., ibid., **17**, 161 (1982).
- 5) B. K. Sen et al., ibid., **17**, 611 (1982).

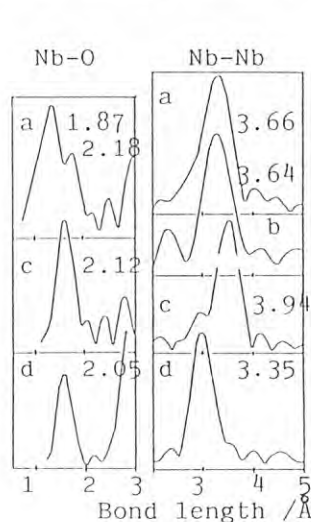


Fig. 1

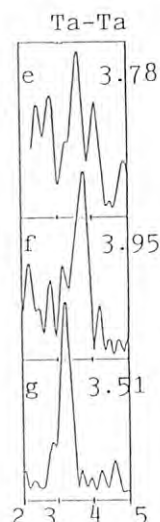


Fig. 2

XANES AND EXAFS OF HIGH T_c SUPERCONDUCTIVE CERAMICSHaruo KURODA¹, Nobuhiro KOSUGI¹ and Hiroyuki TAJIMA²

- 1) Dept. of Chemistry, Fac. of Science, The University of Tokyo, Hongo, Bunkyo, Tokyo 113
 2) J. R. D. C., 5-9-4 Tokodai, Toyosato, Ibaragi 300-26

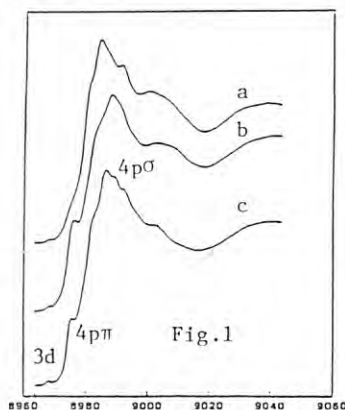
The 3d valence state of Cu in high- T_c superconductors $\text{La}_{2-x}\text{Sr}_x\text{CuO}_4$ ($x \sim 0.15$) and $\text{YBa}_2\text{Cu}_3\text{O}_{7-y}$ ($y \sim 0.1$) can be clarified by observing 1s-3d absorption. We measured highly-resolved Cu K-edge XANES spectra at Beam Line 10B in Photon Factory in order to determine the valency of Cu ions in the high- T_c superconductors and related compounds.

Figs.1 and 2 show Cu K-edge XANES for $\text{La}_{2-x}\text{Sr}_x\text{CuO}_4$ ($x \sim 0.15$) and $\text{YBa}_2\text{Cu}_3\text{O}_{7-y}$ ($y \sim 0.1, \sim 0.6, \sim 0.9$), respectively, together with some cupric and cuprous compounds. We obtained $\text{YBa}_2\text{Cu}_3\text{O}_{6.9}$ by cooling slowly in O_2 , $\text{YBa}_2\text{Cu}_3\text{O}_{6.4}$ by quenching in air, and $\text{YBa}_2\text{Cu}_3\text{O}_{6.1}$ by quenching in N_2 . Powder X-ray diffraction showed that the $y \sim 0.1$ and ~ 0.6 species have orthorhombic structure and the $y \sim 0.9$ tetragonal one. T_c of $\text{La}_{1.85}\text{Sr}_{0.15}\text{CuO}_4$, $\text{YBa}_2\text{Cu}_3\text{O}_{6.9}$ and $\text{YBa}_2\text{Cu}_3\text{O}_{6.4}$ were about 40K, 90K and 50K, respectively. Tetragonal $\text{YBa}_2\text{Cu}_3\text{O}_{6.1}$ showed no superconductivity.

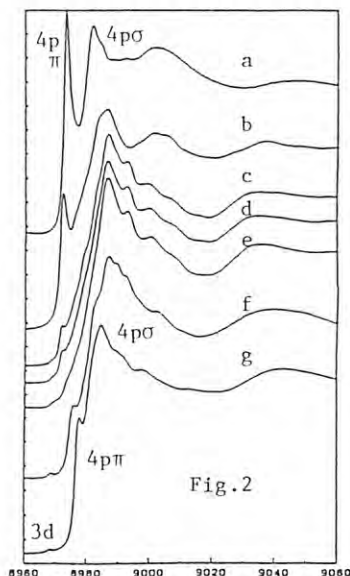
In Fig.1, Cu 1s-3d transitions are distinctly observed in the pre-edge region of XANES. This observation shows that Cu ions in $\text{La}_{1.85}\text{Sr}_{0.15}\text{CuO}_4$ are mainly in a divalent d^9 state. Although it is possible to estimate the number of 3d holes from the intensity of 1s-3d transition, it is difficult within the framework of experiments for powder samples. For example, the Cu 1s-3d transition in $\text{Y}_2\text{Cu}_2\text{O}_5$ has larger intensity than that of CuO though they are both "purely" cupric d^9 compounds and have four oxygen atoms coordinated around Cu. Information about the coordination symmetry (nearly square-planar (D_{4h}) in CuO ; distorted like T_d in $\text{Y}_2\text{Cu}_2\text{O}_5$) is necessary to explain the difference in intensity. Distortion like T_d from D_{4h} induces hybridization of 3d with a $\ell=1$ component; therefore, the 1s-3d transition can borrow the intensity from dipole-allowed 1s-p transition. On the other hand, sub-peaks about half-way up to the main absorption give another information about the oxygen coordination. The sub-peak is a 1s-4p π transition and the main absorption 1s-4p σ . In octahedrally coordinated compounds like $\text{La}_{1.85}\text{Sr}_{0.15}\text{CuO}_4$, there is no sub-peak because of no 4p π orbitals.

In Fig.2, no 1s-3d pre-edge structure is observed for the cuprous d^{10} compounds, and weak pre-edge structure for the $\text{YBa}_2\text{Cu}_3\text{O}_{7-y}$ compounds. Fig.3 shows spectra magnified around the 1s-3d and 1s-4p π energy region. A weak 1s-3d absorption is observed for the $y=0.6$ and 0.9 species and a broad 1s-3d band for the $y=0.1$. The former shows existence of divalent d^9 Cu atoms. Interpretation of the latter is difficult under the present stage of study. There are some candidates: contribution of trivalent Cu, band broadening induced by strong covalency between Cu and O, and so on. In the $y=0.6$ and 0.9 species, distinct contribution of 1s-4p π is observed. The energy (and intensity) of 1s-4p π transition is dependent on the coordination number, the coordination bond length and the bonding character (covalency or ionicity), but not dependent on the

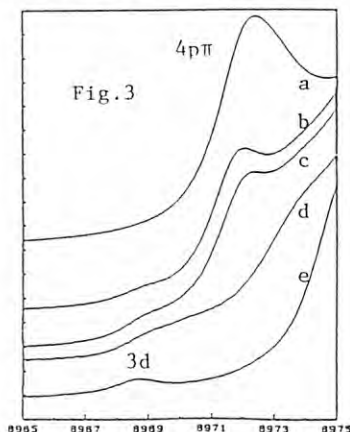
valence state of Cu atom. The Cu compound and complex, Cu_2O and CuCl_2^- (with BEDT-TTF), are coordinated by two ligand atoms; therefore, the observation shows existence of Cu ions coordinated by two oxygen atoms in the $y=0.6$ and 0.9 species considering the energy position of the 1s-4p π absorption.



- a) $\text{La}_{2-x}\text{Sr}_x\text{CuO}_4$
 $x \sim 0.15$
 b) CuO
 c) $\text{Y}_2\text{Cu}_2\text{O}_5$



- a) CuCl_2^-
 b) Cu_2O
 c) $\text{YBa}_2\text{Cu}_3\text{O}_{7-y}$
 $y \sim 0.9$
 d) $\text{YBa}_2\text{Cu}_3\text{O}_{7-y}$
 $y \sim 0.6$
 e) $\text{YBa}_2\text{Cu}_3\text{O}_{7-y}$
 $y \sim 0.1$
 f) $\text{Y}_2\text{Cu}_2\text{O}_5$
 g) $\text{CuCl}_2 \cdot 2\text{H}_2\text{O}$



- a) Cu_2O
 b) $\text{YBa}_2\text{Cu}_3\text{O}_{6.1}$
 c) $\text{YBa}_2\text{Cu}_3\text{O}_{6.4}$
 d) $\text{YBa}_2\text{Cu}_3\text{O}_{6.9}$
 e) $\text{CuCl}_2 \cdot 2\text{H}_2\text{O}$

EXAFS OBSERVATION OF VAPOR QUENCHED Fe-Ag AND Fe-Ti ALLOYS

Yoji NAKAMURA, Kenji SUMIYAMA, Hideyuki YASUDA
and Koichi TAKEMURA

Department of Metal Science and Technology, Kyoto University
Kyoto 606, Japan

Introduction

In vapor quenching methods such as sputtering and thermal evaporation, a high energy vapor solution is condensed onto a cold substrate so as to exhibit nonequilibrium alloys^{1,2}. The typical examples are Fe-Ag solid solutions and Fe-Ti amorphous alloys^{2,3}, where Fe and Ag are immiscible in each other even in the equilibrium liquid state at 2300 K and no amorphous single phase has been obtained by liquid quenching. This report mentions the experimental results of the X-ray diffraction and the extended X-ray absorption fine structure (EXAFS) on amorphous Fe-Ti alloys.

Experimental

Fe-Ti alloy specimens with thickness from 5 μm to 50 μm were prepared by a facing target type DC sputtering on polyimide and silicon wafer substrates whose temperatures were about 50°C during sputter-deposition. The electron probe microanalysis was made for the determination of chemical compositions of these sputter-deposited alloys. X-ray diffraction patterns at 290 K were observed using Mo-K α radiations and a graphite monochromator. EXAFS study was done by using EX-12 in Photon Factory, National Laboratory for High Energy Physics.

Results

Figure 1 shows the radial distribution function of an amorphous Fe-34at%Ti alloy with thickness of about 50 μm . The first, second and third peaks correspond to the first, second and third coordination shells within the spiral

polytetrahedral cluster model of an amorphous structure^{3,4}, which consists of a monotonic and dense stacking of tetrahedra^{4,5}. The splitting of second and third peaks becomes vague with increasing Ti concentration. The average coordination number is estimated to be about 11.5 and independent of the alloy concentration. In the amorphous Fe-Ti alloys, the Mössbauer spectra have also showed that their local atomic structures are resemble to topologically close packed intermetallics constructed from the stacking of tetrahedra and insensitive to the alloy concentration^{5,6}.

Figure 2 shows the Fourier transform of EXAFS oscillation, $k^3\chi(k)$, at the Fe-K α edge for an α -Fe metal and an amorphous Fe-34at%Ti alloy with thickness of about 5 μm ^{5,6}. In the amorphous Fe-34at%Ti alloy, the number of nearest neighbor pairs of Fe-Fe and Fe-Ti are about 7 and 4, being roughly consistent with the analysis of the X-ray diffraction spectra. EXAFS data on other amorphous Fe-Ti alloys and crystalline Fe-Ag alloys are now under analysis.

References

- 1) S.Mader: J.Vac.Sci.Tech. **2** (1965) 35.
- 2) K.Sumiyama: Bull. Japan Inst. Metals **25** (1986) 615.
- 3) H.Yasuda, K.Sumiyama, Y.Nakamura: in preparation.
- 4) S.Takeuchi and S.Kobayashi: Phys.Stat.Sol. (a) **65** (1981) 315.
- 5) K.Sumiyama, H.Ezawa and Y.Nakamura: Phys. Stat. Sol. (a) **93** (1986) 81.
- 6) H.Yasuda, K.Sumiyama, Y.Nakamura, T.Tanaka, H.Mizutani and S.Yoshida: in preparation.

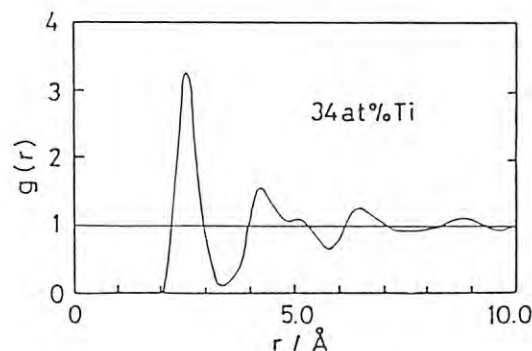
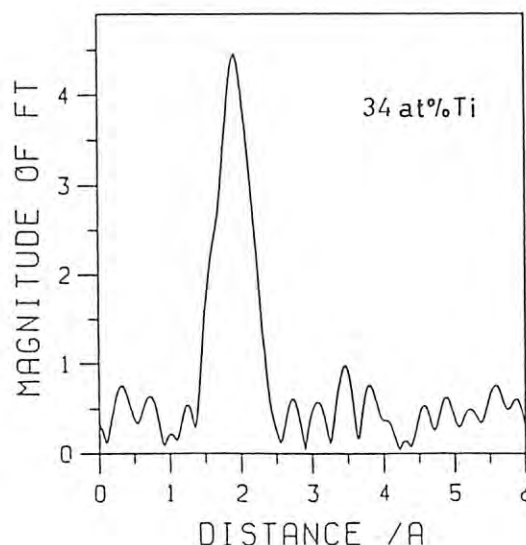


Fig.1
Fig.2



LOCAL STRUCTURE IN THE PRE-MARTENSITIC STATE OF AuCd ALLOY

Yukio NODA, Kazuya KAMON⁺, Hironobu MAEDA⁺⁺ and Hikaru TERAUCHI⁺

Faculty of Engineering Science, Osaka University, Toyonaka 560

⁺Department of Physics, Kwansei-Gakuin University, Nishinomiya 662⁺⁺Department of Chemistry, Okayama University, Okayama 700Introduction

Premartensitic phenomena in thermoelastic martensite transformations are one of the renewed interest in connection with the mechanism of the phase transition, particularly from a bcc or a CsCl type β -phase to an R-type martensite phase. As precursor phenomena, tweed patterns in electron microscopies, anomalous incommensurability in diffraction patterns, soft phonon modes, etc. are reported. Based on the analysis of X-ray diffraction experiments of a NiTi(Fe) alloy¹ and a AuCd alloy², the modulated lattice relaxations (MLR's) model was proposed³, in which an embryo dressed by MLR's within the β -matrix plays an important role. The idea of the model is that the embryo created by thermal excitations introduces the modulated strain field in the matrix lattice within the period of its life time. The structure of the MLR's might be very similar to that of the embryo and also of the martensite itself because the characteristics of the soft phonon mode are responsible to the phase transition as well as the formation of the quasi-static lattice modulation in the β -phase.

The purpose of the present investigation is to carry out the local structure analysis of the AuCd alloy by EXAFS techniques to verify the existence of the modulated lattice in the β -phase.

Experimental and Results

Powder samples of the AuCd alloy are prepared from a single crystal which was previously used in the X-ray diffraction experiment². Conventional EXAFS experiments on the 10B beam line as well as a preliminary fluorescence EXAFS experiment on the 7C beam line were carried out at the temperature from 200K up to 450K. The M_s point of this powder sample is confirmed by an

X-ray diffraction experiment to be about 300K.

Following the standard procedure, $\kappa^3\chi(\kappa)$'s are obtained. We assumed that the structure of the sample at 200K is that of the martensite phase so that the first nearest neighbor distance (8 atoms around the probed atom) in the β -phase splits to three shells; inner shell(2), intermediate shell(4) and outer shell(2). By comparing the $\kappa^3\chi(\kappa)$ at 200K with the above model, we obtained the energy shift E_0 , the parameter of the phase shift as well as the atomic distances and the temperature factor. For the further analyses, two parameters, E_0 and the phase shift are fixed with the values given at 200K. Atomic distances, coordination numbers and the temperature factor are the fitting parameters. Results are summarized in Fig. 1. Even though the data points are scattered, the coordination numbers and the atomic distances above the M_s point show still the characteristics of the martensite phase. When the temperature is raised up far above the M_s point, the tendency of the deviation from the martensite structure is seen in the figure.

Discussions

When we consider the existence of the martensite-like region in the β -phase, it is straightforward to calculate the probability of the volume of each region from Fig. 1b). Results are given in Fig. 2. Remarkable point is that the probability of the volume of the martensite-like region is still high in the β -phase from the view point of the local structure. This conclusion is qualitatively consistent with the previous X-ray diffraction experiment², and it should be emphasized that the local structure in the premartensitic state is directly analyzed on the present EXAFS experiments.

In connection with the existence of embryos in a metal alloy, the local structure of the ω -phase are also investigated and the data analysis is now undergoing.

References

- 1) S.M.Shapiro, Y.Noda, Y.Fujii and Y.Yamada: Phys. Rev. B30(1984)4314.
- 2) Y.Noda, M.Takimoto, T.Nakagawa and Y.Yamada: Metal. Trans. in press.
- 3) Y.Yamada, Y.Noda and M.Takimoto: Solid State Commun. 55(1985)1003.

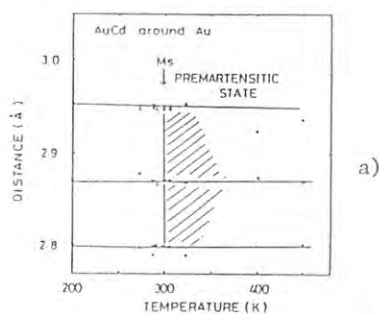


Fig. 1

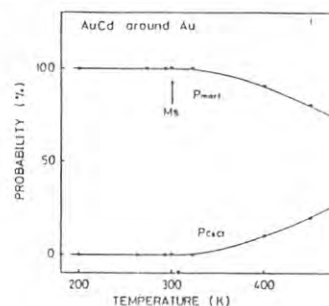
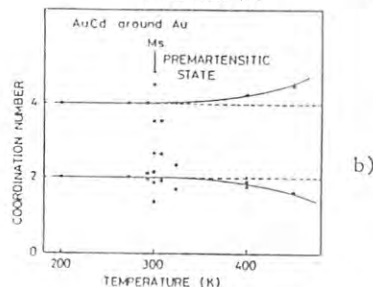


Fig. 2

Fe K-EDGE XANES STUDY OF THE METAMICT STATE IN OXIDE MINERALS

Junji AKIMOTO, Masayuki IMAFUKU, Yoshinori SUGITANI and Izumi NAKAI
Department of Chemistry, The University of Tsukuba, Sakura-mura, Ibaraki 305

Introduction

We have previously demonstrated that EXAFS and XANES are powerful techniques in the study of metamict minerals-natural amorphous substances caused by radiation damage¹⁾. To study alterations in these minerals during the metamictization process, it is useful to obtain the chemical and structural information around Fe, because Fe is easily affected by redox atmosphere. Fe K-edge XANES spectra give much information on details of the oxidation state and the coordination environment²⁾, though it seems desirable to use other spectroscopic technique simultaneously. The present report describes Fe K-edge XANES study of metamict gadolinite and samarskite, and the results are compared with those of the Mössbauer analysis.

Experimental

X-ray absorption measurement near Fe K-edge was made at room temperature using the EXAFS facilities installed at BL-10B in PF. Mössbauer measurement was made at Tandem Accelerator Center, the University of Tsukuba (UTTAC) using ⁵⁷Co as a source. Samples used were metamict and annealed gadolinite $Y_2FeBe_2Si_2O_{10}$, samarskite $(Y,U,Ca)(Nb,Ta,Fe)_2O_6$, and some synthetic compounds.

Results and Discussion

The pre-edge absorption, which is due to electronic transitions from inner *ls* state to empty *d*, *s* or *p* states, is often observed in Fe K-edge XANES spectra. The energy shift of this absorption due to valence change is mainly an electrostatic effect due to the increased binding energy of the *ls* electron as the formal valence increases.

The pre-edge absorption spectra of four reference compounds are shown in Fig. 1(a). These spectra indicate that the doublet pre-edge peaks (I and II) in the ferric compounds ($YFeO_3$ and $\alpha-Fe_2O_3$), are shifted to higher energy side by 1.0–2.0 eV compared with those in the ferrous compounds (Fe_2SiO_4 and $FeCO_3$). This tendency is in good agreement with the results in previous reports^{2),3)}. Fig. 1(b) shows the pre-edge absorption spectra of the gadolinite group samples. The spectra of metamict, annealed and crystalline samples have the pre-edge absorptions at approximately equal energy (7112 eV), which can be assigned to the divalent Fe. These data are consistent with the results of Mössbauer analysis.

It is known that the intensity of the pre-edge absorption varies according to the degree of distortion from centrosymmetry in octahedral Fe compounds³⁾. The tendency observed in our reference compounds (Fig. 1(a)) is consistent with their crystallographic data.

In Fig. 1(b), the intensity of the pre-edge absorption of metamict gadolinite is about three

times as high as that of the crystalline gadolinites. This suggests that the octahedral Fe-O coordination symmetry in the metamict gadolinite is significantly lower than that in the crystalline gadolinite. These results are consistent with the results of Mössbauer analysis: that is, the QS values of crystalline gadolinites (av:1.7 mm/sec) are much smaller than that of the metamict sample (2.0 mm/sec) indicating lower coordination symmetry in the latter structure, and whereas the IS values of all the samples are about 1.0 mm/sec.

It is reported that the role of Fe in the construction of gadolinite structure is not important and the Fe site tends to have vacancy⁴⁾. This may indicate that the Fe-O bonds are weaker than the other metal-oxygen bonds in gadolinite. Therefore, it is expected that the Fe-O coordination geometry would suffer serious radiation damage. The results of XANES and Mössbauer analyses indicate that metamict gadolinite has a very distorted octahedral Fe-O coordination compared with crystalline gadolinite. In contrast to Fe, EXAFS analysis of Y K-edge indicated that there was no significant difference in the Y-O coordination geometry between metamict and crystalline gadolinites¹⁾. Accordingly, Fe may be one of the key elements of metamict minerals to reveal "why a mineral occurs in the amorphous state?".

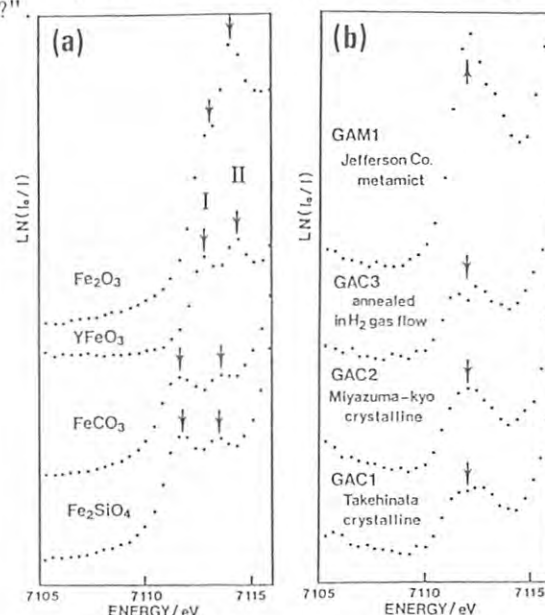


Fig. 1. The pre-edge absorption spectra in the Fe K-edge XANES of (a) reference compounds and (b) gadolinite group samples. All spectra have been normalized with respect to edge-crest absorption intensity.

- 1) I. Nakai et al., Phys. Chem. Minerals (1987) in press.
- 2) G. Calas et al., Phys. Chem. Minerals **11**, 17 (1984).
- 3) G. A. Waychunas et al., Phys. Chem. Minerals **10**, 1 (1983).
- 4) R. Miyawaki et al., Am. Mineral. **69**, 948 (1984).

EXAFS/XANES ANALYSIS OF SELENIUM COMPOUNDS

Takuji KAWASHIMA, Ichiro NOMACHI, Tadashi HIRANO, Izumi NAKAI

Department of Chemistry, The University of Tsukuba, Ibaraki, 305

Introduction

Aromatic o-diamines (o-phenylenediamine and its derivatives, 4-methyl-, 4-chloro-, 4,5-dichloro- and 4-nitro-o-phenylenediamine) and Bismuthiol II (3-phenyl-5-mercapto-1,3,4-thiadiazole-2-thione) have been used as reagents for the determination of Se(IV). These reagents react with Se(IV) in acidic solution to form piaselelenols and an Se-Bismuthiol II complex, which can be extracted into organic solvents. However, the structures of these compounds formed are still ambiguous: the structures and chemical formulas of the products a) ~ d) have been proposed (Fig. 1).

In the present study we aimed at determining the structures and the oxidation state of selenium for these products in crystals and nitrobenzene solutions by EXAFS/XANES technique. The electronic effects of substituents are also discussed in connection with the structures of piaselelenols.

Experimental

The piaselelenols and the Se-Bismuthiol II complex^{1),2)} were prepared as described previously^{1),2)} with a slight modification.

Powder samples of piaselelenols and its methyl-, chloro-, dichloro-, nitro-derivatives and the Se-Bismuthiol II complex were measured by dusting onto Scotch tapes. Commercially available Na_2SeO_3 , Na_2SeO_4 and $(\text{C}_6\text{H}_5)_2\text{Se}_2$ were used as standard materials for XANES spectra. Nitrobenzene solutions containing piaselelenols except NO_2 - derivative and the Se-Bismuthiol II complex were also measured. Se-K absorption spectra were measured by using a Si(311) channel-cut crystal monochromator on the EXAFS facilities installed at BL-10B at PF.

Results and Discussion

XANES spectra of Se-K edge of piaselelenol, Se-Bismuthiol II complex, $(\text{C}_6\text{H}_5)_2\text{Se}_2$, Na_2SeO_3 and Na_2SeO_4 are shown in Fig. 2. Fourier transforms of $k^2 \chi(k)$ of EXAFS for the substituted piaselelenols are given in Fig. 3. From the comparison of the XANES spectra of the piaselelenols with those of Se(VI) (Na_2SeO_4), Se(IV) (Na_2SeO_3) and Se(II) ($(\text{C}_6\text{H}_5)_2\text{Se}_2$), it can be concluded that oxidation state of Se in piaselelenol is not quadrivalent but divalent. Thus the structure shown in Fig. 1-a) is recommended. Similarly, oxidation state of Se for the Bismuthiol II complex is found to be divalent and the complex takes the formula given in Fig. 1-c).

The first strongest peaks in Fig. 3 correspond to the Se-N bond distance. The Se-N bond distances of the substituted piaselelenols were compared with that of the non-substituted compound. It was observed that the Se-N bond distances for NO_2 - and

dichloro substituted piaselelenols are 0.109 Å and 0.007 Å shorter than that of the non-substituted piaselelenols, whereas those for CH_3 - and monochloro substituted ones are 0.010 Å and 0.004 Å longer than the non-substituted compounds, respectively. The results are explained on the basis of the Hammett rule.³⁾ The resonance effect of CH_3 and NO_2 groups can transmit their electronic effects over long conjugated systems, but resonance effect of CH_3 groups is weaker than that of NO_2 groups. Further, the resonance effect of CH_3 and NO_2 groups affect the Se-N bond distance in an opposite manner, because CH_3 and NO_2 are electron donating and electrophilic substituents. On the other hand, the inductive effects of Cl groups decrease rapidly with the increase in the distance between interacting groups. Therefore, no apparent effect on the Se-N distance has been observed for monochloro and dichloro substituted compounds.

The second peaks in Fig. 3 correspond to the Se-C nonbonding distance. It is observed that the Se-C distances of NO_2 -, CH_3 - and monochloro substituted piaselelenols are 0.012 Å, 0.003 Å and 0.040 Å longer than that of the non-substituted one, respectively. The Se-C distance of dichloro derivative are 0.017 Å shorter than that of the non-substituted one. These results suggest that the changes in the Se-C distances may result from the decrease in the C-N distance or changes in bond angles, etc. It is noteworthy that the effect of substituent groups on the Se-N distances of piaselelenols were not observed in the nitrobenzene solutions. A further study will be necessary to clarify the solvent effect on the structures of piaselelenols.

References

- 1) H. Yoshida, M. Taga and S. Hikime, Japan Analyst, **14**, 1109, (1963).
- 2) M. Tanaka and T. Kawashima, Talanta, **12**, 211, (1964).
- 3) L. P. Hammett, Physical Organic Chemistry McGraw-Hill, 184, (1940).

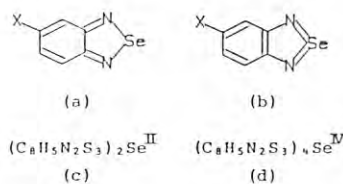


Fig.1 Proposed formulae for the selenium compounds

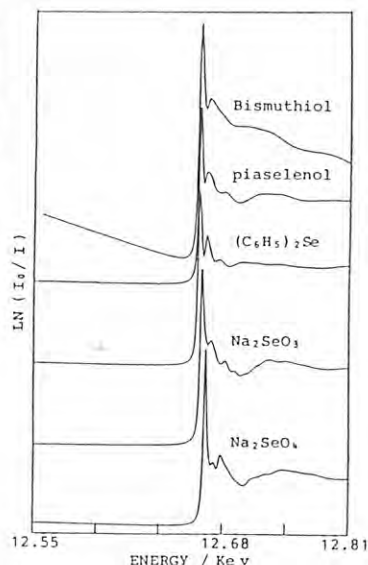


Fig.2 XANES spectra of Se-K edge

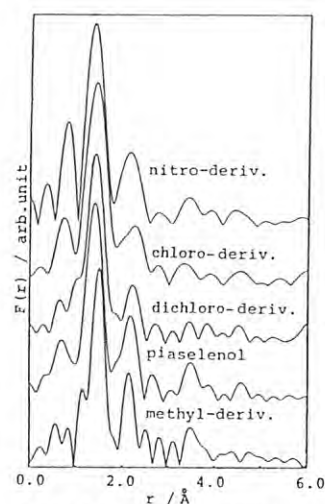


Fig.3 Fourier transforms of Se-K edge of piaselelenol and its derivatives

EXAFS STUDY ON THE LOCAL STRUCTURAL REARRANGEMENT OF AMORPHOUS CU-ZR ALLOY DURING THE CRYSTALLIZATION PROCESS

Hiromi YAMASHITA, Tsunehiro TANAKA, Hiroshi MIZUTANI, Takuzo FUNABIKI and Satoshi YOSHIDA
Department of Hydrocarbon Chemistry and Division of Molecular Engineering, Faculty of Engineering,
Kyoto University, Kyoto, 606, Japan.

Introduction

Several EXAFS studies have been carried out to investigate the local structure of as-prepared amorphous alloys¹, but the EXAFS studies on the change in the local structure of amorphous alloy during the crystallization process have only recently studied by A. Sadoc et al.². In this study, short range structural changes of amorphous Cu₆₀Zr₄₀ alloy during the crystallization process have been investigated by EXAFS at both the Cu and Zr K-absorption edges.

Experimental

The Cu₆₀Zr₄₀ amorphous alloy in a form of ribbon was prepared by the rapid quenching method using a single steel roll³ and heated at various temperatures in the range 473–773 K under vacuum for 30 min. EXAFS data were obtained at room temperature by employing the EXAFS facilities at BL-10B of KEK-PF.

Results and Discussion

Cu K-edge. The EXAFS spectra (a-e) and their Fourier transforms (A-E) in the alloys heated at various temperatures are shown in Fig. 1. The EXAFS oscillations in the as-quenched amorphous alloy (a) became negligible beyond 10 Å⁻¹. However, the EXAFS oscillations in the alloys heated at 573 and 623 K (b,c) could be observed clearly over a wide range of energies and the amplitude of the oscillations were larger than those of the as-quenched amorphous alloy. The FT in the as-quenched amorphous alloy (A) exhibited the main peak with 3.15 peak height (PH). The intensity of this main peak increased with the heating temperature up to 623 K (PH=4.65 (573 K); 5.10 (623 K)) (B,C). These results suggest that the disordered structure of the as-quenched amorphous alloy induced the quenching of EXAFS oscillations⁴ and the structure of the amorphous alloy became less-disordered by the heating at

573 and 623 K. On the other hand, the EXAFS oscillations in the alloy heated at 773 K (e) became negligible beyond 9 Å⁻¹. This might be due to the formation of multi-phases, because Cu₃Zr₂ phase is not stable at room temperature.

The Cu K-edge EXAFS spectra were reconstructed well by using combinations of four subshells. The results of the curve-fitting suggested that a weak increase of the Cu K-edge EXAFS spectrum observed in the alloy heated at 623 K is due to the increase of the amount of neighboring atoms in the 3rd and 4th shells. The short range structural rearrangement might occur remarkably in the atoms which exist at a distance from the central Cu atom, such as the atoms in the 3rd or 4th shells, but in the nearest neighboring atoms.

Zr K-edge. The EXAFS oscillations in the alloy heated at 623 K could be observed clearly over the wider range of energies than those in the as-quenched amorphous alloy and the alloys heated at 773 K. This result indicates that the structure of amorphous alloy became less-disordered by heating at 623 K, as well as the results observed in the case of the Cu K-edge EXAFS oscillations. However, the maximum intensity of the main FT peak was observed in the alloy heated at 773 K, while the decrease in the intensity of the main peak was observed in the FT of Cu K-edge EXAFS. These results indicate that the aggregation of zirconium atoms occurs by heating at 773 K and induces the formation of the multi-phases which is suggested from the results in the Cu K-edge EXAFS analyses.

References

- 1) J.Wong et al., Phys.Rev.B, 29 (1984) 651.
- 2) A.Sadoc et al., J.Non-Crys.Solids, 65 (1984) 109.
- 3) H.Yamashita et al., J.Chem.Soc., Faraday Trans.I, 82 (1986) 1771.
- 4) D.E.Sayers et al., Phys.Rev.Lett., 27 (1971) 1204.

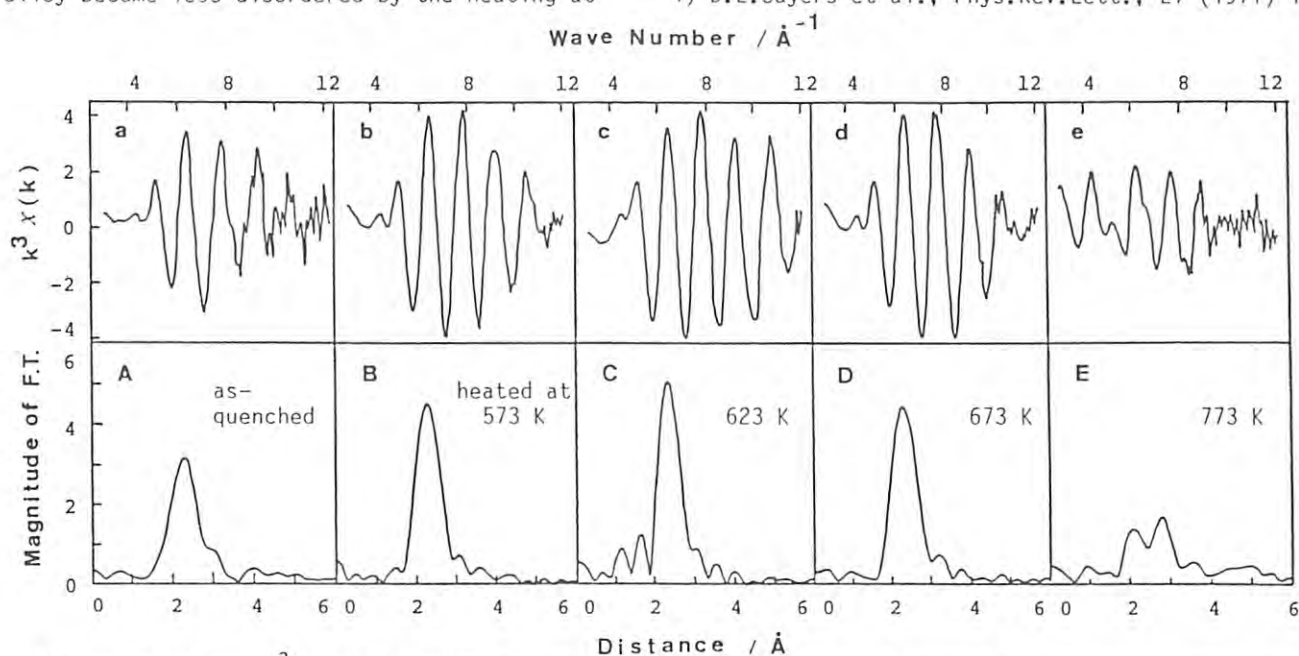


Fig. 1 Cu K-edge k^3 -weighted EXAFS spectra (a-e) and magnitudes of their Fourier transforms (A-E).

STUDIES ON THE STRUCTURE OF MOLYBDENUM(V) SPECIES IN AQUEOUS ACIDIC SOLUTION BY EXAFS

Kunihiko YOKOI, Takafumi MIYANAGA*, Nobuyuki MATSUBAYASHI**, Iwao WATANABE*, and Shigero IKEDA*
 Department of Chemistry, Osaka Kyoiku University, Ikeda, Osaka 563
 * Department of Chemistry, Faculty of Science, Osaka University, Toyonaka, Osaka 560
 ** National Chemical Laboratory for Industry, Yatabe, Ibaraki 305

Introduction

Mixed-valence molybdenum complexes (Mo-MIX) produced from pentavalent and hexavalent molybdenum have been known as molybdenum blue, however, few study concerning to the structure and properties of Mo-MIX has been reported. Our previous investigation¹⁾ about the Mo-MIX in weakly acidic solution (pH 2.5) indicated that Mo-Mo distance for Mo-MIX is somewhat longer than that for Mo(VI) polyanion, MoO_4^{2-} . In the present work we found a new Mo-MIX in 9 M H_2SO_4 (also blue solution) and analyzed its XANES and EXAFS.

Experimental

Mo(VI) solutions were prepared from sodium molybdate ($\text{Na}_2\text{MoO}_4 \cdot 2\text{H}_2\text{O}$). Mo(V) in HCl was prepared by reducing Mo(VI) in 2-3 M HCl solution with mercury. For Mo(V) in H_2SO_4 , Mo(V) in less than 1 M HCl, $\text{Mo}_2\text{O}_4^{2+}$, was collected on a cation exchange column (Dowex 50W-X8) and eluted by 2 M H_2SO_4 . Mo-MIX solutions were prepared by mixing adequate quantities of Mo(VI) and Mo(V) solutions. Mo(V) and Mo-MIX solutions were deoxygenated by bubbling pure nitrogen. The X-ray absorption measurements were carried out with the EXAFS apparatus at BL 10B. Photon energy was calibrated by using the pre-edge peak of $\text{Na}_2\text{MoO}_4 \cdot 2\text{H}_2\text{O}$ at 20007.0 eV. Other experimental conditions are in the same as those reported previously.²⁾

Results and Discussion

Figure 1 shows the XANES spectra for Mo(VI), Mo-MIX and Mo(V) in pH 2.5 (pH of the solution was adjusted by using H_2SO_4 and NaOH) and in 9 M H_2SO_4 solutions. In both cases pre-edge peaks assigned to be 1s-4d transition³⁾ are observed. The intensity of this peak has correlation with the number of the Mo=O bond per molybdenum atom,^{2,3)} therefore, for Mo(VI), Mo-MIX and Mo(V) the number gradually decreases in this series. This phenomenon was also observed for pH 2.5 solution which contained chloride ion.²⁾

EXAFS Fourier transforms (FT) of molybdenum samples are shown in Fig. 2. In pH 2.5 solution, for Mo(VI), MoO_4^{2-} , peaks at 1.70 Å and 3.24 Å correspond to Mo=O and Mo-Mo, respectively. For Mo-MIX, peaks for Mo=O and Mo-Mo are observed at 1.68 Å and 3.31 Å. The Mo=O distance for Mo-MIX is almost the same as that for Mo(VI), while the Mo-Mo distance for Mo-MIX is somewhat longer than that for Mo(VI). For Mo(V), $\text{Mo}_2\text{O}_4^{2+}$, the peak for Mo-Mo is observed at 2.59 Å. Similar results were obtained for pH 2.5 solution in the presence of chloride ion.²⁾

In 9 M H_2SO_4 solution, for Mo(VI), the peak for Mo=O is observed at 1.72 Å while no peak corresponding to Mo-Mo is observed, indicating that no polymerized species exists. For Mo(V), peaks at 1.79 Å and 2.53 Å correspond to Mo=O and Mo-Mo, respectively, and the small peak at

3.82 Å may also correspond to Mo-Mo indicating that the polymerized species exists. For Mo-MIX, also polymerized species, two peaks at 3.24 Å and 3.78 Å are considered to correspond to Mo-Mo, however, the structural difference between Mo(V) and Mo-MIX remains to be established.

References

- 1) K.Yokoi et al., Photon Factory Activity Report, 1986, 191.
- 2) K.Yokoi et al., Chem. Lett., 1987, 1453.
- 3) S.P.Cramer et al., J. Am. Chem. Soc., 100, 3398 (1978).

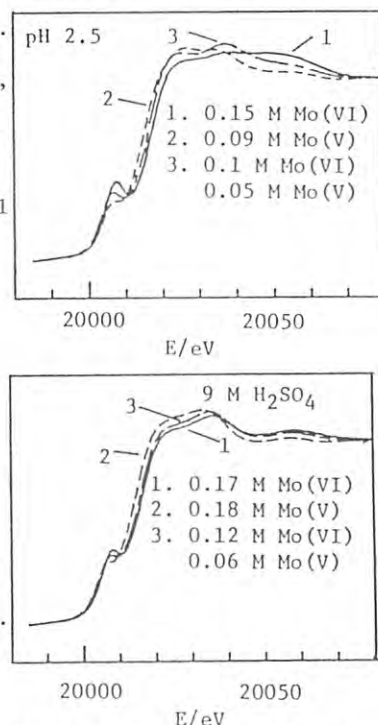


Fig.1. XANES spectra for Mo samples.

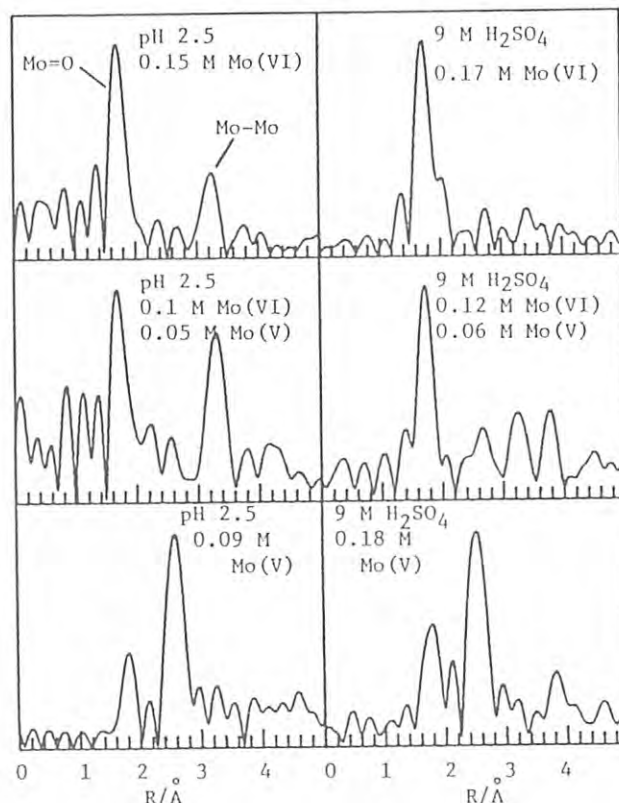


Fig.2. EXAFS FT for Mo samples.

SOLUTE STRUCTURE OF COPPER(II)PERCHLORATE AQUEOUS SOLUTION IN LIQUID AND GLASSY STATES: ITS CONCENTRATION DEPENDENCE

Masaharu NOMURA and Toshio YAMAGUCHI*

Photon Factory, National Laboratory for High Energy Physics, 305
* Department of Chemistry, Faculty of Science, Fukuoka university,
Nanakuma, Jonan-ku, Fukuoka 814-01

Copper(II) perchlorate is well known to take distorted octahedral structure of $[\text{Cu}(\text{OH}_2)_6]^{2+}$ in its aqueous solution owing to Jahn-Teller effect. However, there found significant distribution on the axial Cu-O bond-length (2.28-2.60Å) among reported structural parameters.¹⁻⁵⁾ The reason of this distribution may be large Debye-Waller factor (σ_{ax}) and concentration dependence of the bond length. Determination of complex structure at low temperature is one of the most reliable way to determine structural parameters on such weak bonds. A solution at low temperature will be represented by a glassy state solution. However, there is no EXAFS study on the solute structure in glassy solutions except our report on copper(II) acetate solutions.⁶⁾

We report here the solute structure of copper(II) perchlorate aqueous solutions in glassy state compared with that in liquid state.

Experimental

Weighed amounts of copper(II) perchlorate was dissolved in distilled water(A) or equivalent mixture of water and glycerol(AG). The copper content was determined by direct titration with a standard EDTA solution. Sample solutions were sealed in cells or treated as liquid films, then immersed in liquid nitrogen. After vitrification, they were kept at this or lower temperature. The vitrification of solutions was visually checked that they were optically transparent, which is good index according to our experiences.⁶⁾ XANES was also used as an indicator of a structural change during vitrification, because it is sensitive to the change of electronic state and the symmetry around the X-ray absorbing atom.⁶⁾ X-Ray absorption spectra were measured at BL10B using a Si(311) channel-cut monochromator in transmission mode.

Results and Discussion

XANES spectra of glassy solutions are shown in Fig.1. The structures B and D in glassy state became more enhanced than those in liquid state, when solutions were vitrified. These structures became clearer with increasing solute concentration. Other structures did not change with vitrification nor increasing concentration. It is confirmed that hydrolysis and addition of glycerol is not the reason of the concentration dependence of XANES. As perchlorate ion has very low coordination ability in aqueous solutions, this concentration dependence should be due to the outer-sphere coordination of perchlorate ions.

The number ratio of short and long Cu-O bonds were assumed to be 4:2 during the analysis of EXAFS. Equatorial Cu-O bond-length and Debye Waller factor does not change with concentration; 1.96Å and 0.06Å², respectively. Axial Debye Waller factor, however, increases with

increasing concentration from 0.10Å² at 0.3 mol/dm³ to 0.14 Å² at 3.4 mol/dm³ though the axial bond length does not change significantly(2.3Å).

In summary, XANES and axial Debye-Waller factor changes with the concentration in copper(II) perchlorate aqueous solution. Crystalline sample shows different XANES spectrum from solution, which may be also due to the medium range order around an X-ray absorbing atom. So the outer-sphere contribution must be included in calculating XANES spectra.

References

- 1) H.Ohtaki and M.Maeda, *Bull. Chem. Soc. Jpn.*, **47**, 2197 (1974).
- 2) H.Ohtaki, T.Yamaguchi, and M.Maeda, *Bull. Chem. Soc. Jpn.*, **49**, 701 (1976).
- 3) M.Magini, *Inorg. Chem.*, **21**, 1535 (1982).
- 4) T.K.Sham, J.B.Hastings, and M.L.Pearlman, *Chem. Phys. Lett.*, **83**, 391 (1981).
- 5) Y.Tajiri and H.Wakita, *Bull. Chem. Soc. Jpn.*, **59**, 2285 (1986).
- 6) M.Nomura and T.Yamaguchi, *J. Phys(Paris)*, **C8**, 619 (1986).

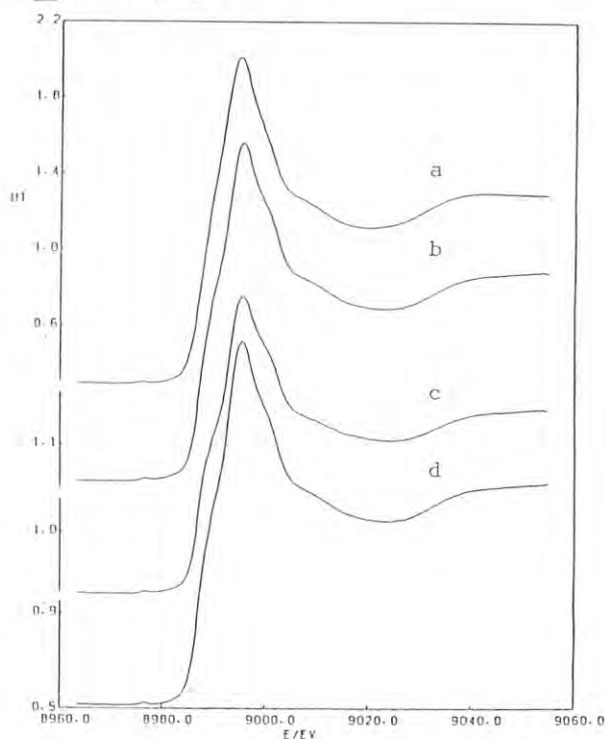


Fig.1 XANES spectra of $\text{Cu}(\text{ClO}_4)_2$ aqueous solutions of glassy state.

- a: 0.3 mol dm⁻³ (AG)*.
b: 2.5 mol dm⁻³ (A)*.
c: 3.4 mol dm⁻³ (A)*.
d: slowly cooled 0.3 mol dm⁻³ (A)*.

* see text.

SOLVATION STRUCTURE OF Cu(II) IN LIQUID AMMONIA

Toshio YAMAGUCHI, Hisanobu WAKITA and Masaharu NOMURA†

Department of Chemistry, Faculty of Science, Fukuoka University,
Nanakuma, Jonan-ku, Fukuoka 814-01, Japan

†Photon Factory, National Laboratory for High Energy Physics,
Oho-machi, Tsukuba-gun, Ibaraki 305, Japan

Introduction

The *blue shift* of the pentaammine Cu(II) complex in aqueous solution has been known for a long time, but its structure in the solid state has recently been revealed to have a square pyramid with four ammonia molecules in the equatorial plane and the fifth one in the axial site.¹⁾ No atom occupies another axial site of Cu(II). In aqueous solution the structure of the pentaammine Cu(II) has also been investigated by the X-ray diffraction²⁾ and EXAFS³⁾ methods. However, their conclusions are not consistent with each other. In the present study we have examined the solvation structure of Cu(II) in liquid ammonia, in which all coordination sites of the Cu(II) have to be occupied by ammonia molecules.

Experimental and Results

Tetraammine Cu(II) nitrate was prepared in a standard manner, dissolved in liquid ammonia filling a high pressure cell made from a stainless steel. The cell was opened just before EXAFS measurements. EXAFS spectra were measured at 223 K using a cryostat cooled with a mixture of alcohol and dry ice at the BL10B station of the Photon Factory. A structure standard used was crystalline $[\text{Cu}(\text{en})_2]\text{Cl}_2 \cdot 2\text{H}_2\text{O}$. The analysis

of the spectra was performed in a usual manner. The values of the phase shift and backscattering amplitude were taken from the Teo and Lee table.

The XANES spectrum of the liquid ammonia solution is shown in Fig. 1. Its feature is very similar to that found in a highly concentrated ammoniacal solution of copper(II) sulfate.³⁾ It should be noted that an absorption spectrum of copper(II) in liquid ammonia does not differ significantly from that of the pentaammine Cu(II) complex in aqueous solution except for about 10 % higher intensity in liquid ammonia. The Fourier transform of the sample is shown in Fig. 2. The first peak is due to the Cu-N bonds within solvated Cu(II). The structure parameter was obtained by a least-squares fitting procedure applied to the Fourier filtered data of the first peak. Preliminary results showed that Cu(II) was surrounded by 4.5 ammonia molecules at 2.03 Å. Further refinements are now in progress.

References

- 1) M. Duggan, N. Ray, B. Hathaway, G. Tomlinson, P. Brint, and K. Pelin, J. Chem. Soc. Dalton Trans., (1980) 1342; L. Alagna, T. Prosperi, and A. A. G. Tomlinson, *ibid.*, (1983) 645.
- 2) T. Yamaguchi and H. Ohtaki, Bull. Chem. Soc. Jpn., 52 (1979) 415.
- 3) M. Sano, T. Maruo, Y. Masuda, and H. Yamatera, Inorg. Chem., 23 (4466) 1984.

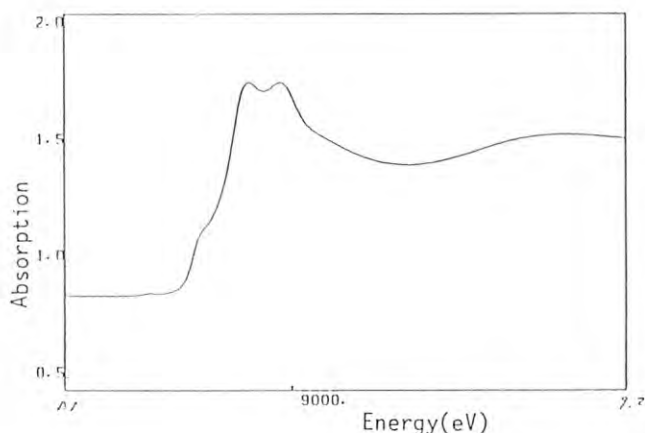


Fig. 1 XANES of CuK-edge of Cu(II) in liq.NH₃

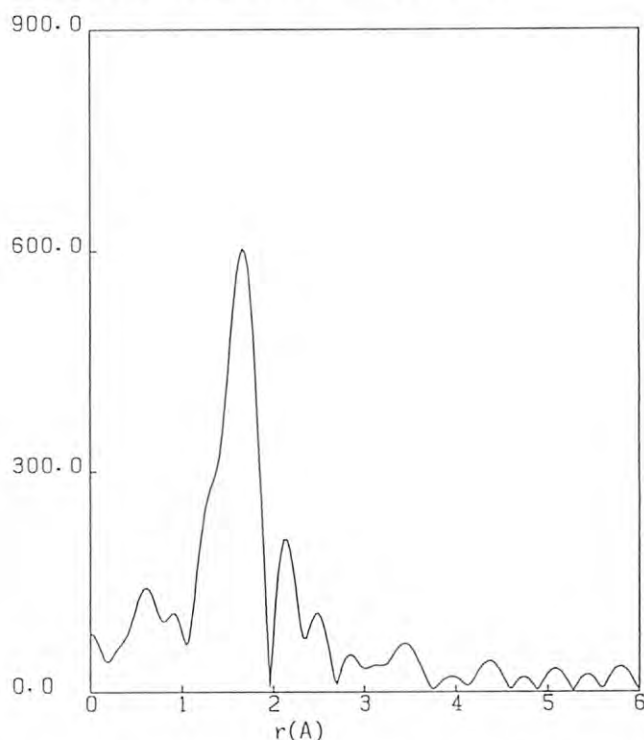


Fig. 2 Fourier transform of Cu(II) in liq. NH₃

SOLVATION OF Ag(I) IN SOME N-DONOR SOLVENTS

Toshio YAMAGUCHI, Hisanobu WAKITA and Masaharu NOMURA†

Department of Chemistry, Faculty of Science, Fukuoka University,
Nanakuma, Jonan-ku, Fukuoka 814-01, Japan†Photon Factory, National Laboratory for High Energy Physics,
Oho-machi, Tsukuba-gun, Ibaraki 305, JapanIntroduction

Solvation structure of Ag(I) in liquid ammonia has been an open question. From Raman spectroscopic measurements of liquid ammonia solutions of silver nitrate, Gans et al.¹⁾ proposed four ammonia molecules bound to Ag(I), while Tobias et al.²⁾ suggested that solvated Ag(I) complex had a distorted octahedron with two short and four long Ag-N bonds. In connection with the liquid ammonia system, solvation of Ag(I) in pyridine and acetonitrile (AN) with different donicity is also of interest. The EXAFS spectroscopy has been applied to determine the structure of Ag(I) solvates in these non-aqueous solvents.

Experimental and Results

Silver nitrate and perchlorate were dried in vacuo over 12 hours and solvents were dried in the usual way. The concentration of sample solutions was ca. 0.2 mol/dm³. EXAFS spectra near the AgK edge were measured at the BL10B station of the Photon Factory. A liquid ammonia solution was measured at 223 K using a cryostat containing a mixture of alcohol and dry ice. The absorption spectra were corrected for background expressed by an equation $a+bE$, where E is the energy. The values of the phase shift and backscattering amplitude were taken from the Teo and Lee table.

The Fourier transforms of the sample solutions are given in Fig. 1. The first peak is assignable to Ag-N bonds in solvated Ag(I) complexes. In acetonitrile and pyridine there also appear peaks corresponding to the interactions between Ag(I) and other atoms in coordinated solvent molecules. Structure parameters were extracted from a least-squares fitting procedure applied to Fourier filtered

modulations of the first peak. The final results are given in Table 1. The values of Ag(I) hydration is also included for comparison. In liquid ammonia Ag(I) is coordinated by four ammonia molecules with Ag-N distance of 2.31 Å. The Tobias model could not reproduce the experimental data. In pyridine the solvation number of Ag(I) is also four, and the Ag-N bond length is close to that in the solid state. In poor donating acetonitrile the Ag-N distance is 2.24 Å, significantly shorter than those found in the solvents of stronger donicity. In the crystal of [Ag(AN)₄]ClO₄ the Ag-N distances vary in the range 2.18-2.33 Å, their average value being 2.26 Å. The various Ag-N bond lengths in the crystal may be due to weak acetonitrile coordination to Ag(I). In the solution, however, the σ value is similar to those for the other solvents, indicating regular tetrahedral coordination of acetonitrile molecules to Ag(I). The Ag-N distance in the solvents may depend on a electronic state of N atoms in coordinating molecules, not on the solvent donicity.

References

- 1) P. Gans and J. B. Gill, J. Chem. Soc. Dalton Trans., (1976) 779.
- 2) J. W. Lundeen and R. S. Tobias, J. Chem. Phys., 63 (1975) 924.

Table 1. Structure parameters of solvated Ag(I)
The values in parentheses are X-ray data.

Solvent	r(Å)	N	σ (Å)	DN
NH ₃	2.31	3.7	0.100	59
Pyridine	2.39 (2.32)	3.9	0.091	33.1
Acetonitrile	2.24 (2.26)	3.7	0.089	14.1
H ₂ O	2.37 (2.40)	3.9		18.1

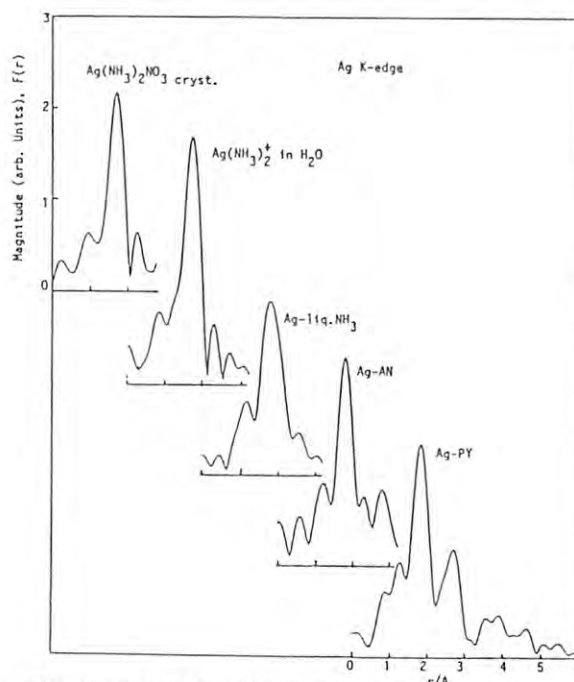


Fig. 1. Fourier transforms of Ag K-edge EXAFS spectra of the samples

STRUCTURE OF BIS(2,3-ALKANEDIONE DIOXIMATO)NICKEL(II) IN
SOLID AND PYRIDINE SOLUTION BY THE EXAFS METHOD

Seiichi YAMASHITA, Yoshio YANASE, Toshio YAMAGUCHI and Hisanobu WAKITA

Department of Chemistry, Faculty of Science, Fukuoka University
Nanakuma, Jonan-ku, Fukuoka 814-01 (JAPAN)

Introduction

Bis(2,3-alkanedione dioximato)nickel(II) complexes, $Ni(R,R'-dioxH)_2$, shows red color and their crystal structures (A, B and C in Table 1) are built up by square planar $Ni(II)$ complexes overlapping each other along the axial Ni-Ni direction¹⁾⁻²⁾. Pyridine solutions of these complexes also shows reddish orange color, which indicates the presence of similar structure in the solutions. Absorption spectra of pyridine solutions of the complexes, however, suggested that each square planar complex existed as a monomer with no pyridine molecule solvated at axial sites in the solution⁴⁾. In this study, we aimed at determining structures of a series of $Ni(R,R'-dioxH)_2$ complexes (Table 1) both in crystals and in pyridine solution by EXAFS spectroscopy.

Experimental and Results

Ni K-edge spectra were measured at KEK-PF (BL-10R) for crystalline powder and pyridine solutions of $Ni(R,R'-dioxH)_2$ complexes. The concentration of the $Ni(II)$ complexes in the pyridine solutions were 0.042, 0.343, 0.347 and 0.342 mol dm⁻³ for complexes C, D, E and F, respectively. A reference compound used was complex A since its crystal structure has been reported¹⁾.

Figure 2 shows the radial distribution curves, $|F(r)|$, of the solid and pyridine solution of complexes C ~ F. In each radial distribution curve the prominent peak found

about 1.5 Å corresponds to Ni-N interactions within $Ni(II)$ complex. Peaks in the range of 2~3 Å may be due to Ni--C and Ni--O interactions. In Fig.3 are plotted the Ni-N interatomic distances determined for the $Ni(II)$ complexes in solid and pyridine solutions. From these results, we can conclude as follows; (1) two different Ni-N interatomic distances are shorter in pyridine solution than in solid, (2) the difference between the two Ni-N bond lengths is larger in pyridine solution than in solid, and (3) no pyridine molecule is coordinated at the apical positions of $Ni(II)$. From (1)~(3) it is suggested that $Ni(II)$ complex is more distorted in pyridine solution than in the solid state. In connection with the present study, we have also measured melts of the above complexes.

References

1) M.Calleri and G.Ferraris, Acta Cryst., 22 (1967) 468.
2) L.E.Godycki and R.E.Rundle, Acta Cryst., 6 (1953) 487.
3) E.Frasson and C.Panattoni, Acta Cryst., 13 (1960) 893.
4) S.Shinra, "KAGAKU" 19 (1963) 939.

Table 1. Composition of $Ni(R,R'-dioxH)_2$.

Sample	-R	-R'
A	$Ni(gH)_2$	H
B	$Ni(dagH)_2$	CH ₃
C	$Ni(eagH)_2$	CH ₃
D	$Ni(pzagH)_2$	CH ₃
E	$Ni(bagH)_2$	CH ₃
F	$Ni(hzagH)_2$	CH ₃

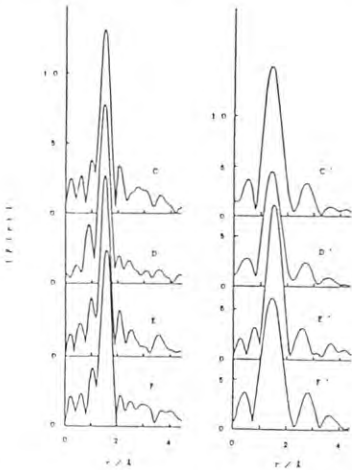


Fig.1. The radial distribution curves $|F(r)|$ of complexes C~F.
C, D, E, F: for powder
C', D', E', F': for pyridine solution

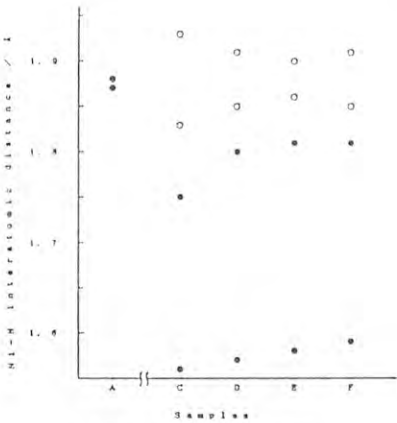


Fig.2. The interatomic distances of Ni-N interactions.
O: powder
◐: pyridine solution
*: single crystal

STRUCTURE OF ZINC BROMIDE COMPLEXES IN GLASSY AQUEOUS SOLUTIONS

Toshio YAMAGUCHI, Osamu YATA, Hisanobu WAKITA and Masaharu NOMURA †

Department of Chemistry, Faculty of Science, Fukuoka University,
Nanakuma, Jonan-ku, Fukuoka 814-01, Japan†Photon Factory, National Laboratory for High Energy Physics,
Oho-machi, Tsukuba-gun, Ibaraki 305, JapanIntroduction

The structure of metal complexes in glassy ionic solutions has been of great interest in Mössbauer, ESR and Raman spectroscopic measurements in connection with structural investigations of the corresponding liquid state. We have developed a cryostat and a cell suitable for EXAFS measurements of glassy ionic solutions.¹⁾ In the present study we have determined the structure of zinc(II) bromide complexes in both liquid and glassy states by the EXAFS spectroscopy.

Experimental and Results

Sample solutions were prepared by dissolving commercial zinc(II) bromide of reagent grade in water. The samples measured were $\text{ZnBr}_2 \cdot R\text{H}_2\text{O}$ ($R=4, 10, 30, 60$) and $\text{ZnBr}_2 \cdot 3\text{LiBr} \cdot 15\text{H}_2\text{O}$. Structure standards used were crystalline ZnBr_2 and $\text{ZnSO}_4 \cdot 7\text{H}_2\text{O}$. EXAFS spectra near the ZnK- and BrK edges were measured at the BL10B station of the Photon Factory. Glassy samples were prepared by quickly immersing the liquid solutions into liquid nitrogen just before EXAFS measurements. The analysis of the EXAFS data were performed in a usual manner with the phase shifts and backscattering amplitudes taken from the Teo and Lee table.

Figure 1 shows the Fourier transforms of

the sample solutions. The peaks for glassy samples are more enhanced than those for liquid solutions, indicating less active thermal motion of species in the glassy state. The first peak seen for $\text{ZnSO}_4 \cdot 7\text{H}_2\text{O}$ is ascribed to Zn-OH₂ bonds within octahedral Zn(II) hydrates. In the ZnBr_2 solutions a new peak appears at the longer distance and increases with increasing solute concentration. This peak corresponds to Zn-Br bonds within zinc(II) bromide complex [formed in the solutions. These peaks were extracted by a Fourier filtering technique and structure parameters of an average species were determined by a least-squares method. The Zn-Br distance determined from both edges is 2.38 Å, independent on the solute concentration. For a solution with the same composition the coordination number of the Zn-Br pairs is significantly smaller in the glassy state than in the liquid state. This may indicate that complex formation is less favourable in the glassy state. The coordination number of Br atom in the $\text{ZnBr}_2 \cdot 4\text{H}_2\text{O}$ solution was found to be close to two, indicating polymerization of the complexes in the solution. In the corresponding glassy state, however, such aggregate was not evidenced.

References

- 1) T. Yamaguchi, H. Ohtaki and M. Nomura, PF-Activity Report, p. 194 (1986).

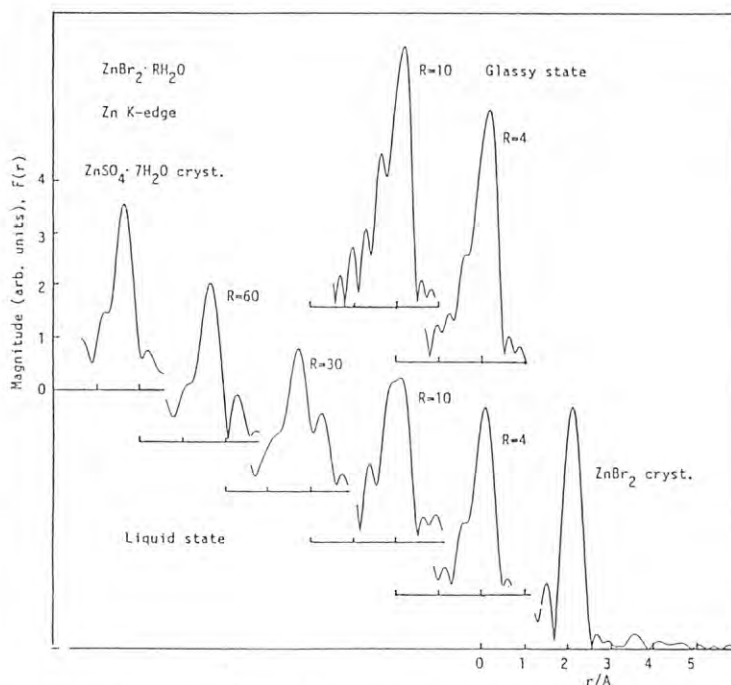


Fig. 1. Fourier transforms of Zn K-edge EXAFS spectra for the samples.

EXAFS Studies on Mo, Co-Mo, and Ni-Mo Supported Catalysts for Hydrotreating of Petroleum
II. The Deactivation Behavior of Molybdenum Catalysts Used for Hydrotreating Coal-Derived LiquidNobuyuki MATSUBAYASHI, Hiromichi SHIMADA, Nobuhiro KOSUGI[†], Haruo KURODA[†]
Yuji YOSHIMURA, Toshio SATO, and Akio NISHIJIMA[†] National Chemical Laboratory for Industry, Yatabe, Ibaraki 305[†] Department of Chemistry, Faculty of Science, The University of Tokyo,
Hongo, Bunkyo, Tokyo 113Introduction

It has been considered that supported molybdenum sulfide catalysts are deactivated not only by deposition of carbonaceous materials and metallic foulants onto the catalysts, but also by changes in the structure or properties of the catalyst species during the hydrotreating process. Many studies concerning the deactivation of molybdenum catalysts by the depositions have been published, but little information has been obtained on the local environment around Mo because of the lack of an effective technique to study them. Recently, EXAFS has been used in the determination of the structure of supported catalysts¹⁾. In the present report, EXAFS method was applied to the investigation of the changes in the local environment around Mo in the catalyst caused by hydrotreating coal-derived liquids.

Experimental

The catalysts studied in this report were NiO(3.3wt%)-MoO₃(12.5wt%)/Al₂O₃ catalysts (surface area: 176m²/g, pore volume: 0.499ml/g) used for hydrotreating coal-derived liquids obtained from Australian brown coal. The reaction was run for 1500 hours in a fixed bed reactor (reaction temperature: 350-400°C, hydrogen pressure: 14.7 MPa). After the reaction, the catalyst was removed from three different locations in the reactor (inlet, middle, and outlet). The deactivation of the catalyst was in the order of inlet middle outlet, which was obtained by the model test reactions for hydrogenation and hydrocracking activities. Before EXAFS measurements, the used catalysts were washed by ultrasonic cleaner with tetrahydrofuran (THF) for 5 minutes to remove coal-derived liquids from the catalysts, and then powdered and pressed into pellets under a nitrogen atmosphere. The Mo K-absorption EXAFS spectra were measured at BL10B of the Photon Factory.

Results and Discussion

The results from the EXAFS for molybdenum on the used catalyst are shown in Table 1. The distance, R, from absorbing atom was corrected by using standard samples MoS₂ and Na₂MoO₄·2H₂O. The average number of coordinating atoms, N, was calculated from the intensity of the peak. Table 1 clearly shows the differences between the average number of coordinating S atoms, N(S), and the nearest Mo atoms, N(Mo), around Mo in the fresh and used catalysts. The decrease in N(S) observed for the inlet catalyst causes the change in valence structure of Mo, which was observed by XPS²⁾. Two plausible causes can be considered for this phenomenon. One is the dissociation of coordinating S under low H₂S concentration. The other

Table 1. Results of analysis of EXAFS for used catalysts.

catalyst	S		Mo		N(Mo)
	R/Å	N	R/Å	N	N(S)
MoS ₂	2.39	6	3.17	6	1
FRESH/S	2.40	4.5	3.16	2.0	0.44
INLET	2.40	4.2	3.17	2.2	0.52
MIDDLE	2.40	4.7	3.17	2.6	0.55
OUTLET	2.39	5.0	3.17	2.9	0.58

is oxidation of MoS₂ by oxygen containing compounds. Both of these causes are reasonable since coal-derived liquids contain a small amount of sulfur and a large amount of oxygen. It appears that the change in the oxidation state of Mo on the catalysts is one of the reasons for the large deactivation at the inlet. In fact, after sulfiding the used catalysts the catalytic activity can be recovered to some extent.

Another change observed in the used catalysts is the increase in N(Mo). It is believed that this increase is caused by the agglomeration and growth of crystalline MoS₂. The ratio N(Mo)/N(S) serves as a good index for the agglomeration of Mo. The agglomeration of MoS₂ proceeded in the order of outlet middle inlet. It is suggested that the higher temperature at the outlet part of the reactor compared to the inlet, which is caused by the exothermal reaction, accelerated the agglomeration process. Though the agglomeration of Mo will lead to some changes in the catalytic function, the deactivation of the catalyst caused by MoS₂ agglomeration seems to be smaller than that caused by deposition of carbonaceous materials and metals. More detailed studies on the relationship between the structure and activity of the catalyst are now progressing.

The authors wish to thank Drs. Tadashi Matsushita and Masaharu Nomura of the National Laboratory for High Energy Physics (KEK) for their help with the X-ray absorption measurements.

References

- 1) T.Yokoyama, K.Yamazaki, N.Kosugi, H.Kuroda, M.Ichikawa, and T.Fukushima, J. Chem. Soc. Chem. Commun., **15**, 962 (1984).
- 2) H.Shimada, T.Sato, Y.Yoshimura, A.Nishijima, S.Kashiwaya, and K.Ogino, Advances in X-ray Chem. Anal. Jpn., **18**, 213 (1987).

EXAFS STUDIES ON THE METAL-SUPPORT INTERACTION IN THE Pd-SUPPORTED Nb SYSTEM.

Kiyotaka ASAKURA, Yasuhiro IWASAWA, and Haruo KURODA

Department of Chemistry, Faculty of Science, the University of Tokyo, Hongo, Bunkyo-ku, Tokyo 113.

Introduction

The support is used not only to disperse the metal particle on it but also to alter the catalytic properties through the chemical and physical interaction.

When Pt and Rh are deposited on the TiO_2 and Nb_2O_5 and reduced at high temperature, the hydrogen chemisorption properties of the metals are lost¹. This phenomenon is called as SMSI. The SMSI is thought to be caused by the coverage of the partially reduced TiO_x and NbO_x on the Metal particles. But the real mechanism has not yet been completely explained on the molecular level. In this work we used Pd fine particle (crystalline size = 10 nm) with the Nb_2O_5 deposited on it as a model system for the SMSI catalyst. The structures of this Pd-supported Nb_2O_5 after the H_2 reduction treatments at the high temperature and at low temperature were studied by means of EXAFS.

EXPERIMENTAL

The Pd-supported Nb_2O_5 system was prepared by the impregnation of Pd fine particle with NbCl_5 ethanol solution. The sample was calcined at 773 K for 2 h. The Nb K-edge EXAFS measurement was carried out at BL-10B of Photon Factory.

RESULTS AND DISCUSSION

Figure 1 shows the Fourier transforms of the EXAFS oscillation. After the 473 K reduction the Nb existed in the form of Nb_2O_5 in comparison to the Fourier transform of the Nb_2O_5 powder. After the 773 K reduction, the peak corresponding to the Nb-Pd appeared as shown by the arrow in the figure. When the sample was then oxidized at 673 K and reduced at 473 K, the Nb-Pd peak became smaller. This means that the Nb-Pd bond on the surface was cleaved after the 673 K oxidation but was not reformed after the 473 K reduction. The remaining peak corresponding to the Nb-Pd may be due to the bulk Nb-Pd bonding. When the sample was reduced at 773 K again, all the Nb dissolved into the NbPd alloy and no peaks were observed due to the Nb_2O_5 as shown in Fig.1d. The structure models were summarized in Fig.2.

The results of the chemisorption of hydrogen shows that the the Pd fine particle with the Nb_2O_5 deposited on it lost its H_2 chemisorption property after 773 K H_2 reduction and it recovers the H_2 chemisorption property subsequently treated with O_2 at 673 K and with H_2 at

473 K. Combining the EXAFS results with the chemisorption, the H_2 chemisorption property is lost when the surface Nb-Pd bond is observed. Thus the surface Nb-Pd bond must be the cause for the SMSI phenomenon.

1) R.T.K.Baker, S.J.Tauster and J.A.Dumesic ed., "Strong Metal-Support Interaction", ACS Symposium Series 298, (1986).

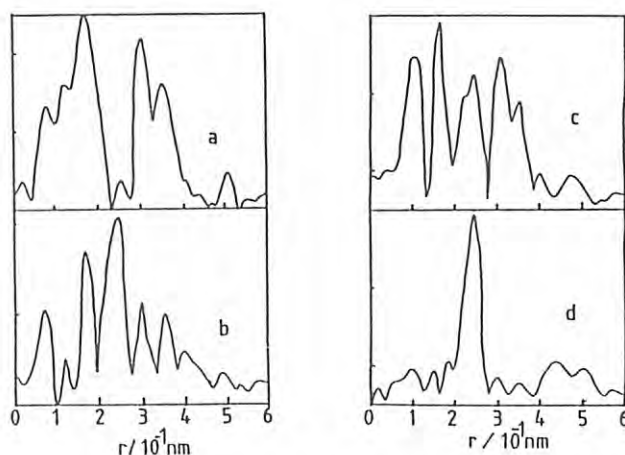


Fig.1 Fourier transforms of (a) 773 K calcination, followed by 473 K reduction. (b) subsequently reduced at 773 K. (c) subsequently oxidized at 673 K and reduced at 773 K. (d) subsequently reduced at 773 K

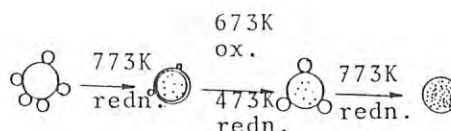


Fig.2 The structure change of Nb on the Pd particle.

EXAFS STUDIES OF SILICA-SUPPORTED METAL CATALYST

I. EFFECT OF ADDITIVES SUCH AS Ti, Nb AND Ta ON THE SURFACE STRUCTURE OF SUPPORTED METAL

Takakazu FUKUSHIMA, Sadao OGASAWARA, Toshihiko YOKOYAMA[†], Nobuhiro KOSUGI[†] and Haruo KURODA[†]

Department of Materials Science and Chemical Engineering, Faculty of Engineering,
Yokohama National University, 156 Tokiwadai, Hodogaya-ku, Yokohama 240

[†] Department of Chemistry, Faculty of Science, University of Tokyo, Hongo, Bunkyo-ku, Tokyo 113

Introduction

The supported metal catalysts operated in chemical industry contain not only active metals but also several additives. It has been shown by XRD technique that the particle size of Rh on SiO_2 is decreased by the addition of Ti¹⁾. No more structural information of the surface particle was available, because of the limitation of XRD technique as the particle size becomes smaller. Thus we decided to study the morphological effects of additives on the surface metal particle by EXAFS.

Experimental

Catalysts were prepared by co-impregnating the solutions of both metal chlorides with silica (Aerosil-300). The preparatives were dried in vacuum, reduced in flowing H_2 at 400 °C for 6 hr and then passivated at r.t. The sample powder was pressed into wafer and mounted in a specially designed glass sample cell. After in situ re-reduction the x-ray absorption measurements were carried out in H_2 atmosphere at r.t. by use of the EXAFS spectrometer at the Beam Line 10B.

Results and Discussion

EXAFS parameters, first coordination number (N) and Debye-Waller factor ($\Delta\sigma^2$), for non-promoted Rh catalysts supported on silica are tabulated in Table 1. Since no noticeable changes in coordination distance (R) from the bulk were observed for all samples measured in this study, the values of R are omitted on this Table and the following ones. As can be speculated, N becomes smaller and $\Delta\sigma^2$ larger with the

Table 1 Curvefitting results for Rh/ SiO_2

wt%	N	$\Delta\sigma^2 \times 10^3$
foil	12	0.0
4	10.5	0.43
2	8.6	1.73
1	7.3	1.89
0.5	5.9	2.22

Table 2 Curvefitting results for promoted Rh/ SiO_2

Rh	Additive ^a	N	$\Delta\sigma^2 \times 10^3$
4wt%	-	10.5	0.43
	Al	7.2	1.79
	Ti	7.9	1.32
	Ta	8.7	2.40
	Nb	8.7	3.65
	Mn	10.0	0.65
	Mo	9.5	3.22

a: Rh/Additive=1/1

decrease of Rh loadings. $\Delta\sigma^2$ is plotted against N, in Fig. 2, for the non-promoted samples listed in Table 1 and a linear relation between $\Delta\sigma^2$ and N is clearly shown. This finding shows that the thermal disorder becomes larger as the Rh loading decreases without changing Rh-Rh distances.

The effects of additives to 4wt% Rh/ SiO_2 on EXAFS parameters are listed in Table 2 and the values of $\Delta\sigma^2$ and N are plotted on Fig. 1. The points for Al-, Ti- and Mn-promoted catalysts lie on the line taken for the non-promoted systems, but for Nb-, Mo- and Ta-promoted ones the deviations from the line increase with the following order; Nb>Mo>>Ta. These results indicate that the structures of Rh particle for the latter three catalysts are different from the former three ones possibly by the strong interactions between these additives and Rh particles.

The promoting effects of Ti on other noble metals than Rh are shown in Table 3. The trends of changes in EXAFS parameters are the same as Rh catalyst except Ir catalyst. This indicates that the particle size does not decrease by the addition of Ti only for Ir case. The reason of this is not known right now.

The x-ray absorptions were measured for promoted Rh catalysts on the Nb and Ta edges and the only oxygen peak was detected as a nearest neighbors for both systems. Because the amount of these promoters is much less than that of surface Si, the promoter metal may be dispersed almost atomically as an oxide. It has been already shown that the additive metal such as Zr to Rh keeps high valency as an oxide ion even after reduction at high temperature²⁾.

References

- 1) H. Arakawa, T. Fukushima, M. Ichikawa, S. Matsushita, K. Takeuchi, T. Matsuzaki and Y. Sugi: Chem. Lett. (1985) 881.
- 2) M. Ichikawa, K. Sekizawa, K. Shikakura and M. Kawai, J. Mol. Catal. 11(1981) 167.

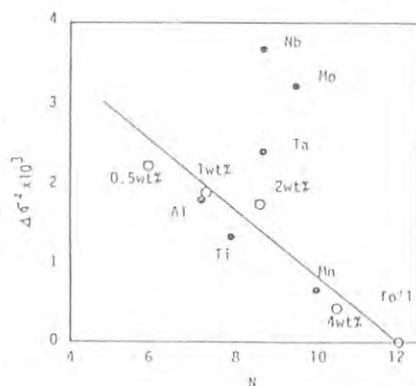


Fig. 1 $\Delta\sigma^2$ as a function of N.

Table 3 Curvefitting results for metal-Ti/ SiO_2

Catalyst ^a	wt%	N	$\Delta\sigma^2 \times 10^3$
Pt	4	9.5	0.62
Pt-Ti	4	7.3	2.67
Pd	2	10.0	2.81
Pd-Ti	2	8.3	3.40
Ru	2	9.4	2.66
Ru-Ti	2	7.8	3.07
Ir	2	10.4	2.00
Ir-Ti	2	10.5	1.90

a: Metal/Ti=1/1

THERMAL EXPANSION AND DEBYE TEMPERATURE OF FCC METALS

Toshihiko YOKOYAMA¹ and Haruo KURODA²

- 1) Department of Materials Science, Faculty of Science, Hiroshima University, 1-1-89 Higashisenda-machi, Naka-ku, Hiroshima 730
 2) Department of Chemistry, Faculty of Science, the University of Tokyo, 7-3-1 Hongo, Bunkyo-ku, Tokyo 113

Temperature dependence of EXAFS spectra is of great importance for investigating thermal motion and structural disorder, and also for improved understanding of EXAFS spectroscopy itself. It is necessary to clarify the quantitative accuracy of temperature dependent EXAFS by analyzing the well-defined model systems before applying this technique to poorly-understood but interesting materials such as (supported) small metal particles. In the present report we show the Debye temperature and the thermal expansion of several FCC metals determined by the temperature-dependent EXAFS measurements.

EXAFS spectra of Cu, Rh, Pd, Ag, Pt and Au foils were taken by use of the EXAFS spectrometer of BL10B at various temperatures, and were analyzed with the ratio method based on the third-order cumulant-expansion technique(1). It should be noticed that the conventional analysis in which the radial structure function is assumed to be a symmetric Gaussian cannot explain the thermal expansion because it is caused by the intrinsic asymmetry of the interatomic potentials. The interatomic distances of the first nearest neighbors of Au and Ag determined by the third-cumulant (C3) analysis are tabulated in table 1, together with the results by the conventional method (C3=0).

The Debye temperature can be evaluated by the correlated Debye model(2). Difference of the mean square relative displacements which are obtained experimentally leads to the determination of the Debye temperature. The final results are given in table 2; all the values agree quite well with the data determined by the calorimetric measurements. This exemplifies that the Debye temperature can be estimated with quantitative accuracy by the EXAFS spectroscopy.

As shown in table 1, the Ag-Ag interatomic distance at 295K obtained through the optimization of the third-cumulant moments is 2.891 Å which is in excellent agreement with the given data (2.889 Å), whereas the conventional analysis erroneously leads to the significant contraction which is evidently unreasonable since the interatomic distance at 295K should not be smaller than the value at 30K. At higher temperature discrepancy becomes more serious; for 362K data the cumulant technique yields 2.896 Å while the conventional method provides 2.855 Å which is 0.04 Å shorter. A similar extent of asymmetric correction is required to describe the Au-Au interatomic distance properly.

It can be concluded that the cumulant-expansion analysis allows us to obtain the interatomic distance with excellent accuracy (the estimated error being less than 0.005 Å), and to detect such small difference as thermal expansion. On the other hand it may be quite dangerous to employ the conventional analysis to determine the bond distance correctly. The deviation seems to be much more serious than usually expected.

We will apply the temperature-dependent EXAFS technique to the supported metal particles in order to understand their thermal properties and their structural disorders which are supposed to be dissimilar with the bulk metals.

References

- (1) G. Banker, Nucl. Instr. Meth., 207 (1983) 437.
 (2) G. Beni and P. M. Platzman, Phys. Rev., B14 (1976) 1514.

Table 1. Results of EXAFS analysis for Ag and Au metals

metal	temp.	EXAFS	thermal	C ₃ (Å ³)
Ag	30K	(2.877)	2.877	(0.0)
	184K	2.868	2.883	(0.0)
		2.884		1.16x10 ⁻⁴
		2.862		(0.0)
	295K	2.891	2.889	2.80x10 ⁻⁴
Au	362K	2.855	2.893	(0.0)
		2.896		4.63x10 ⁻⁴
	80K	(2.876)	2.876	(0.0)
Au	295K	2.851	2.884	(0.0)
		2.880		1.87x10 ⁻⁴

*Interatomic distances are given in Å unit. The values in parentheses are the fixed parameters in the fitting procedures. The upper values correspond to the results given by the conventional analysis and the lower to those by the third-cumulant expansion technique.

Table 2. Debye temperature of FCC metals

metal	EXAFS	calorimetry*
Cu	328 K	310 K
Rh	362 K	350 K
Pd	282 K	275 K
Ag	228 K	228 K
Pt	232 K	225 K
Au	172 K	165 K

*around room temperature

HIGH PRESSURE IN-SITU EXAFS STUDIES ON THE CATALYTIC REACTION MECHANISM THE OXIDATION OF CO ON THE Co(II) OXIDE CLUSTER.

Kiyotaka Asakura, Yasuhiro IWASAWA, Hideaki YOSHITAKE, and Haruo KURODA

Department of Chemistry, Faculty of Science,
University of Tokyo, Hongo, Tokyo 113.

INTRODUCTION

To determine the reaction mechanism including the structure change of the catalyst is important to understand the nature of the catalysis and to design a highly functionalized and highly active catalyst. Al_2O_3 -supported Co(II) oxide cluster catalyst derived from the $\text{Co}_2(\text{CO})_8$ shows high activity toward CO oxidation reaction¹. We will report in this paper the mechanism of this high active CO oxidation reaction determined by means of high-pressure in-situ EXAFS spectroscopy.

EXPERIMENTAL

The catalyst was prepared by the dry-mixing method of $\text{Co}_2(\text{CO})_8$. The sample was then exposed to O_2 at 273 K. The sample was pressed to a disk, mounted on the in-situ EXAFS high-pressure cell and evacuated up to 512 K. The preparation scheme was shown in Fig.1.

RESULTS and DISCUSSION

Figure 2 shows the Fourier transforms of the Co oxide cluster catalyst. The sample 1 which was obtained by being exposed to O_2 at 273 K shows two prominent peaks. The first one is attributed to Co-O and the second one is attributed to Co-Co as shown by curve fitting analysis. The sample 2 obtained subsequently heating the sample 1 to 512 K under vacuum exists in the form of Co oxide monomer because no peak corresponding to Co-Co. Even if the sample was cooled to liquid nitrogen temperature, the Co-Co peak did not appear. When sample 2 was exposed to 1 atm O_2 , the peak appeared around 0.280 nm, and it was enhanced under the 10 atm O_2 atmosphere. The curve fitting analysis shows that it was due to the Co-Co bonding. This peak was lost after CO treatment. These results could be explained as follows. In the sample 2, the Co ions are close together without any links between the Co-Co ions. Because there is a wide distribution in the Co-Co distances, one cannot obtain the peak attributable to Co-Co bonding even at Liquid Nitrogen temperature. After the introduction of O_2 , the two Co atoms are fixed around a certain distance and the Co-Co peak appeared. The O_2 was dissociatively adsorbed on the Co pair because isotope exchange reaction took place between $^{18}\text{O}_2$ and $^{16}\text{O}_2$ under the same reaction conditions. The bridging Oxygen is activated and it is readily attacked by the CO, leaving the unlinked Co pairs. Thus the Co-Co

bond disappeared again after the reaction with CO. The reaction mechanism was summarized as shown in Fig.3.

1) Y.Iwasawa, M.Yamada, Y.Sato, and H.Kuroda, *J.Mol.Catal.*, **23**, 95(1984); M.Yamada, and Y.Iwasawa, *Nikkashi*, 1042(1984).

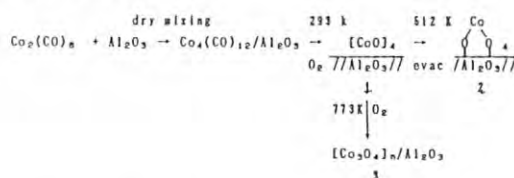


Fig.1 The preparation of the Al_2O_3 -supported Co oxide catalyst.

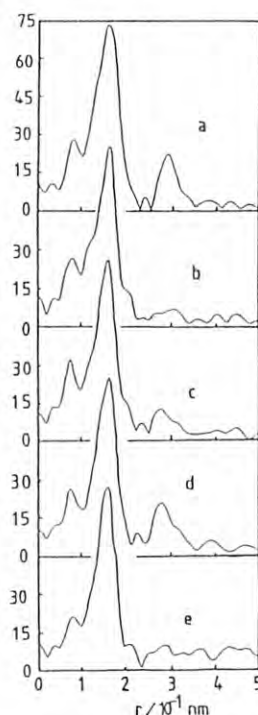


Fig.2 Fourier transforms of (a) $(\text{CoO})_4$; (b) (2); (c) exposure to 1 atm O_2 ; (d) exposure to 10 atm O_2 ; (e) subsequent exposure to CO.

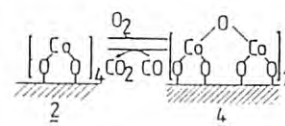


Fig.3 Reaction model for CO oxidation.

EXAFS CHARACTERIZATION OF ZEOLITE-ENCAPSULATED RH AND
BIMETALLIC RHFE CARBONYL CLUSTER CATALYSTS.Masaru ICHIKAWA, Atsushi FUKUOKA, Takuma KIMURA, Rao LING-FEN,
Nobuhiro KOSUGI[†], and Haruo KURODA[‡]Research Institute for Catalysis, Hokkaido University,
Kita-11 Nishi-10, Kita-ku, Sapporo 060[†]Department of Chemistry, Faculty of Science,
The University of Tokyo, Hongo, Bunkyo-ku, Tokyo 113Introduction

Lack of control of product selectivity has been a principal problem in a CO+H₂ reaction catalyzed on transition metals. The metal particle size and the geometric situation associated with metal-support interaction govern the product distribution. We have studied the novel preparation of well-defined Rh and bimetallic RhFe clusters derived from the carbonyl cluster compounds synthesized in NaY zeolite supercage. Their structural properties were studied by Rh K-edge and Fe K-edge EXAFS spectroscopy.

Experimental

Rh³⁺/NaY zeolite (Rh, 2 wt%) was heated under CO (600 Torr) and H₂O (10 Torr) at 343K, resulting in a formation of Rh₆(CO)₁₆ inside NaY supercage: Rh₆(CO)₁₆/NaY. Reduced Rh₆ cluster in NaY, Rh₆/NaY, was obtained by oxidation of Rh₆(CO)₁₆ in O₂ at 473 K after removal of H₂O, followed with H₂ reduction at 473 K and 673 K with carefully eliminating residual H₂O at each stage of the treatment. The bimetallic RhFe carbonyl cluster was synthesized by the reaction of [HFe₃(CO)₁₁]⁻/NaY with Rh₄(CO)₁₂ at 343 K in vacuo, while [HFe₃(CO)₁₁]⁻ in NaY was prepared from Fe₂(CO)₉ and H₂O at 343 K.³⁾ EXAFS measurements were carried out at the BL 10B in the Photon Factory of the National Laboratory for High Energy Physics (KEK-PF).

Results and Discussion

Figure 1 shows the Fourier transform of Rh K-edge EXAFS $k^3\chi(k)$ of Rh₆(CO)₁₆/NaY, and Table 1 summarizes the curve-fitting analyses for Rh and Fe clusters in NaY. The Rh-Rh coordination

number of Rh₆(CO)₁₆/NaY is 3.1 and the Rh-Rh distance is 2.74 Å, which are almost the same as those obtained for the powder of original carbonyl Rh₆(CO)₁₆. These results indicate that the original octahedral Rh₆ framework of the clusters is retained, but with a small contribution of Rh-O bonding with oxide wall (Rh-O: C.N.=1.9, R=2.06 Å) in the NaY supercage. After oxidation of Rh₆(CO)₁₆/NaY at 473 K to eliminate CO, followed with H₂ reduction at 473 K and 673 K, the reduced samples Rh₆/NaY were also found to keep Rh cluster units (Rh-Rh: C.N.=4.6, R=2.70 Å), having a small Rh-O bonding (Rh-O: C.N.=0.7, R=2.09 Å). It seems that Rh₆ carbonyl species (Rh-Rh: C.N.=3.2, R=2.72 Å), which is partially attached with zeolite oxygent framework (Rh-O: C.N.=0.8, R=2.03 Å), is generated even after CO chemisorption on Rh₆/NaY (CO/Rh=2.0, H/Rh=0.6).

[HFe₃(CO)₁₁]⁻ entrapped in NaY supercage gave the EXAFS data: Fe-Fe; C.N.=1.8, R=2.2 Å. Bimetallic RhFe/NaY synthesized in NaY shows the characteristic IR carbonyl bands, and their Rh K-edge and Fe K-edge EXAFS structural evaluations are now in progress.

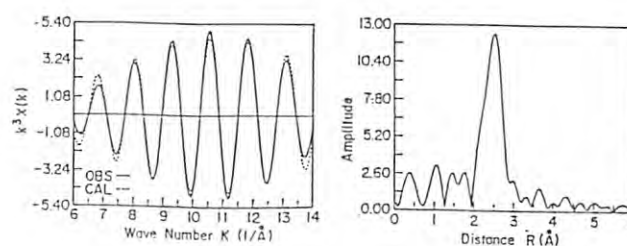


Figure 1. Rh K-edge EXAFS oscillation $k^3\chi(k)$ and its Fourier transform of Rh₆(CO)₁₆/NaY.

Table 1. Results of the Curve-Fitting Analyses of EXAFS Data for Rh and Fe Clusters in NaY.

Sample	Rh-CO(terminal)		Rh-CO(bridge)		Rh-O(support)		Rh-Rh	
	C.N.	R(Å)	C.N.	R(Å)	C.N.	R(Å)	C.N.	R(Å)
Rh ₆ (CO) ₁₆ /NaY	1.5	1.88	1.6	2.15	1.9	2.06	3.1	2.74
Rh ₆ /NaY (473 K red.)	-	-	-	-	0.7	2.10	4.6	2.70
Rh ₆ /NaY (673 K red.)	-	-	-	-	0.7	2.09	4.6	2.70
Rh ₆ /NaY + CO	1.4	1.85	1.4	2.15	0.8	2.03	3.2	2.72
Rh ₆ (CO) ₁₆	2.1	1.87	2.0	2.17	-	-	4.0	2.76

Sample	Fe-CO(terminal)		Fe-O(support)		Fe-Fe	
	C.N.	R(Å)	C.N.	R(Å)	C.N.	R(Å)
[HFe ₃ (CO) ₁₁] ⁻ /NaY	0.8	1.81	1.6	2.09	1.8	2.58
[HFe ₃ (CO) ₁₁] ⁻	2.3	1.81	-	-	2.2	2.62

AN XANES AND EXAFS STUDY OF GOLD CATALYSTS

Hiroyuki KAGEYAMA*, Nagao KAMIJO*, Hironobu MAEDA**, Tetsuhiko KOBAYASHI*, and Masatake HARUTA*

*Government Industrial Research Institute, Osaka

Midorigaoka 1-8-31, Ikeda 563, Japan

**Department of Chemistry, Faculty of Science, Okayama University

Tsushima-Naka 3-1-1, Okayama 700, Japan

Introduction

Recently Haruta *et al.* discovered that the novel gold catalysts Au/ α -Fe₂O₃ prepared by coprecipitation from an aqueous solution of chloroauric acid and iron(III) nitrate and subsequent calcination at the temperatures from 200°C to 500°C, have highly active catalysis for CO oxidation even at -70°C, where the activity is at a maximum for the catalyst calcined at 300°C¹⁾. Our edge and EXAFS study about the catalyst precursors and the calcined catalysts were begun in attempts to investigate the variation of the valence states of the Au and Fe atoms during the preparation steps, and the relationship between the locale structures of the Au atoms with the catalytic activities. We will describe here some results from XANES and EXAFS study of Au L₃-edge.

Experimental and Results

The X-ray absorption spectra about Au L₃-edge of the catalyst precursors dried in vacuum and dried at 80°C, and the catalysts calcined at

200°C, 300°C, 400°C and 500°C, and those of Au₂O₃ and Au foil were measured by use of the EXAFS facilities at the beam line 10B. Data analysis was made according to Maeda *et al.*²⁾.

The XANES spectra of the precursors and the catalysts are shown in Fig. 1. The "White line" peaks peculiar to the Au³⁺ species (designated by an arrow in the figure) are reduced for the catalyst calcined at 300°C and not observed for the catalysts calcined at 400°C and 500°C of which XANES spectra are almost similar to that of Au foil. The radial structure functions (RSF) of the samples shown in Fig. 2 indicate that the Au-O peaks are still observed for the precursors and the catalyst calcined at 200°C, and for that calcined at 300°C (together with the Au-Au peak), while only the Au-Au peaks are found in the RSF's of the catalysts calcined at 400°C and 500°C. From the results it is elucidated that the formation of Au metal occurs at the temperatures 300°C and upward of 300°C. The curve-fitting analysis of the Au-Au peaks in Fig. 2 gives the result that the coordination numbers of the Au atoms in the catalysts calcined at 300°C, 400°C and 500°C are 6, 8 and 12, respectively, where their interatomic distances are equal to that of Au foil within 0.01 Å. More detailed curve-fitting analysis about the precursors and the catalysts are in progress.

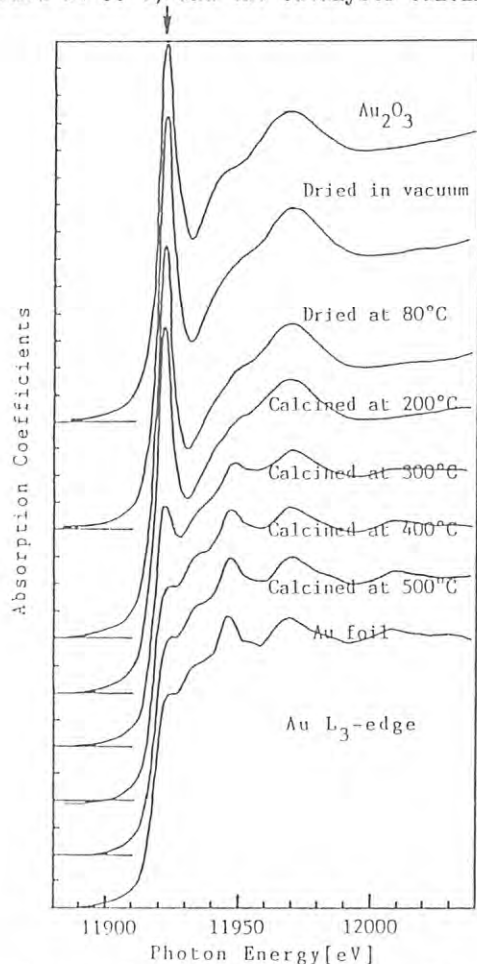


Fig. 1. The XANES spectra of Au L₃-edge of six samples measured at 60 K with those of Au₂O₃ and Au foil measured at 300 K, respectively.

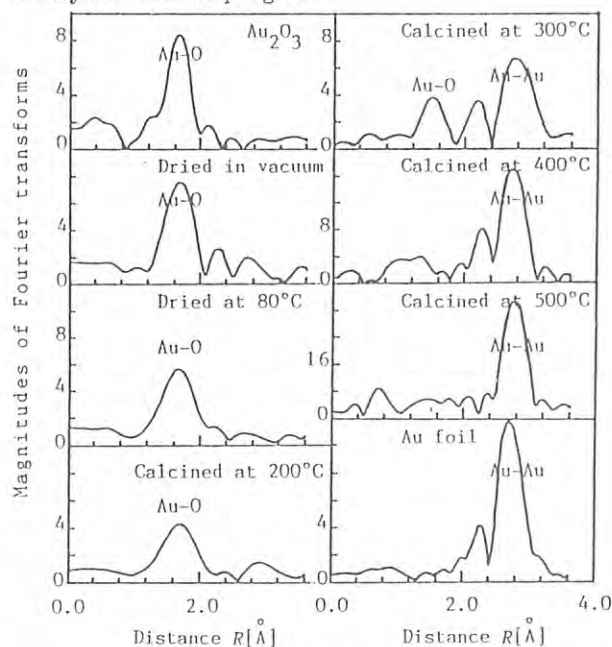


Fig. 2. Fourier transforms of k^3 -weighted EXAFS oscillation about Au L₃-edge of six samples measured at 60 K, and those of Au₂O₃ and Au foil measured at 300 K, respectively.

References

- 1) M. Haruta *et al.*, Chem. Lett., 1987, 405(1987).
- 2) H. Maeda *et al.*, Jpn.J.Appl.Phys., 31, 1342(1982).

EXAFS STUDY ON THE STRUCTURE OF CATALYSTS FOR PHOTODECOMPOSITION OF WATER

Akihiko KUDO, Joji YOSHIMURA, Kazunari DOMEN, Takaharu ONISHI, Kiyotaka ASAKURA,⁺ and Haruo KURODA⁺

Research Laboratory of Resources Utilization, Tokyo Institute of Technology, Nagatsuta 4259, Midori-ku, Yokohama 227; ⁺ Faculty of Science, The University of Tokyo, Hongo, Bunkyo-ku, Tokyo 113.

Introduction

The photodecomposition of water into H_2 and O_2 proceeds efficiently over the pretreated $NiO-K_4Nb_6O_{17}$ catalyst.¹⁾ It has a layer structure; two types of interlayers exist and potassium ion between niobium oxide layers can be replaced with many other cations.²⁾ On the other hand, the nickel in a $NiO-K_4Nb_6O_{17}$ catalyst prepared by the impregnation method exists in the interlayers from the measurements of X-ray photoelectron spectroscopy and scanning electron microscopy. However, the structure of the nickel in the interlayers was not clear. In this report, the state of nickel in the $NiO-K_4Nb_6O_{17}$ photocatalyst after some pretreatments was studied by EXAFS measurement.

Experimental and Results

$NiO(1 \text{ wt}\%)-K_4Nb_6O_{17}$ was prepared by the impregnation method as described in previous paper.¹⁾ EXAFS measurements were carried out in air as disks (20 ϕ) of a mixture of polyethylene or BN, and $NiO-K_4Nb_6O_{17}$ after the pretreatments.

The results of the Fourier transforms of EXAFS functions $K^2x(K)$ of Ni K shell absorption of the $NiO(1 \text{ wt}\%)-K_4Nb_6O_{17}$ photocatalysts after various pretreatments are shown in Fig. 1. The peaks of Ni-Ni ($R=2.98$, $N=5$) and Ni-O of oxide were observed on the untreated catalyst although the peak ratio of Ni-O/Ni-Ni of it was larger than that of NiO as shown in Fig. 1(a). It seems to indicate that the particle size of the nickel oxide in the untreated catalyst is very small. The untreated catalyst showed the low activity (H_2 ; 3 $\mu\text{mol/h}$, O_2 ; 1 $\mu\text{mol/h}$) for the photodecomposition of water. After the untreated catalyst was reduced by H_2 at 773 K for 2 h the nickel was metallic ($R=2.48$ Å, $N=6$) as shown in Fig. 1(b). The particle size of the nickel metal was estimated to be ca. 7 Å from the average coordination number.³⁾ This catalyst evolved both H_2 and O_2 in the stoichiometric ratio (H_2 ; 19 $\mu\text{mol/h}$, O_2 ; 9 $\mu\text{mol/h}$) under the band gap irradiation while the $NiO-SrTiO_3$ photocatalyst after the same pretreatment did not. Although the catalyst reduced at 773 K was reoxidized by O_2 at 473 K for 1 h the nickel metal ($R=2.47$ Å, $N=7$) was hardly oxidized as shown in Fig. 1(c). In this state, the highest activity was obtained (H_2 ; 66 $\mu\text{mol/h}$, O_2 38 $\mu\text{mol/h}$). On the other hand, a part of the nickel metal ($R=2.53$ Å, $N=2$) remained even after the reoxidation at 773 K for 1 h, and the peaks of Ni-Ni ($R=3.02$ Å, $N=5$) and Ni-O were also observed as shown in Fig. 1(d). The activity over this catalyst is low (H_2 ; 10 $\mu\text{mol/h}$, O_2 ; 3 $\mu\text{mol/h}$). The same results mentioned above were obtained by ESR measurements. To the contrary, the nickel in the $NiO-SrTiO_3$ photocatalyst previously reported⁵⁾ was oxidized partially by O_2 at 473 K and completely at 773 K. Thus, the

nickel metal produced by the reduction in the interlayer of $K_4Nb_6O_{17}$ is not oxidized easily because the diffusion rate of O_2 into the interlayer is probably very slow.

From these results, the photodecomposition of water into H_2 and O_2 occurs in the interlayer under the band gap irradiation as shown in Fig. 2. H_2 evolves on the nickel in the interlayer and O_2 on the niobium oxide layer.

References

- 1) K. Domen, A. Kudo, A. Shinozaki, A. Tanaka, K. Maruya and T. Onishi, J. Chem. Soc., Chem. Commun., 356 (1986).
- 2) M. Gasperin and M. T. Le Bihan, J. Solid State Chem., 33, 83 (1980); G. Lagaly and K. Beneke, J. Inorg. Nucl. Chem., 38, 1513 (1976).
- 3) R. B. Gregor and F. W. Lytle, J. Catal., 63, 476 (1980).
- 4) K. Domen, A. Kudo and T. Onishi, J. Catal., 102, 92 (1986).
- 5) K. Domen, A. Kudo, T. Onishi, N. Kosugi and H. Kuroda, J. Phys. Chem., 90, 292 (1986).

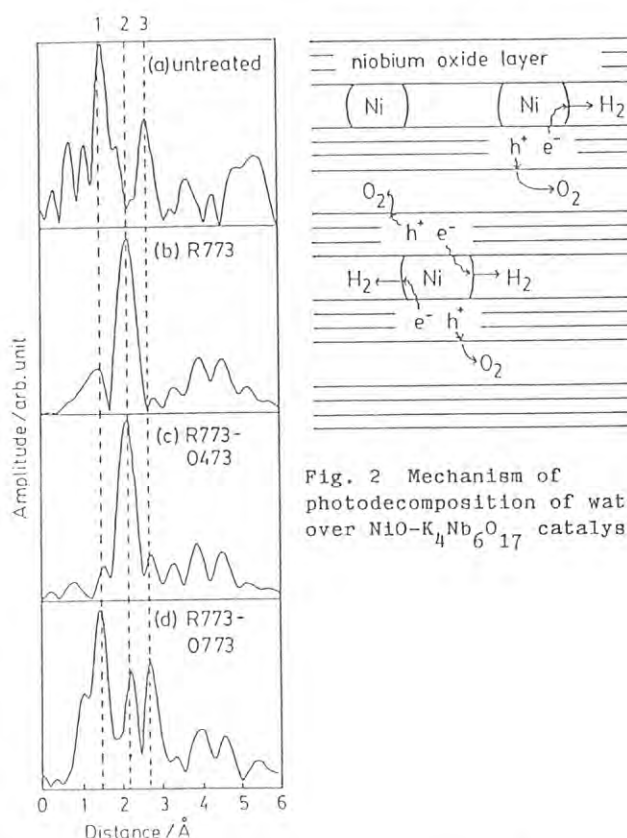


Fig. 1 Fourier transforms of EXAFS of Ni in $NiO-K_4Nb_6O_{17}$ catalyst
1; Ni-O of oxide, 2; Ni-Ni of metal, 3; Ni-Ni of oxide.

Fig. 2 Mechanism of photodecomposition of water over $NiO-K_4Nb_6O_{17}$ catalyst

EXAFS STUDY ON THE STRUCTURE OF THE ZSM-5-ATTACHED ONE ATOMIC ZrO_2 CATALYST

Kiyotaka ASAKURA, Hideaki YOSHITAKE, Yasuhiro IWASAWA, and Haruo KURODA

Department of Chemistry, Faculty of Science, the University of Tokyo, Hongo, Tokyo 113.

INTRODUCTION

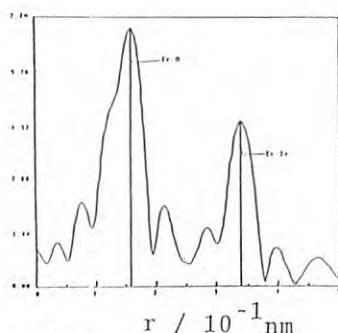
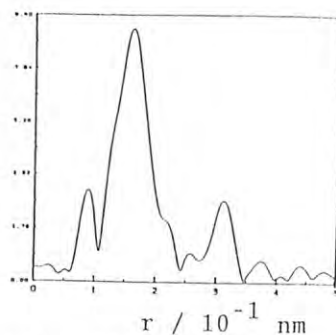
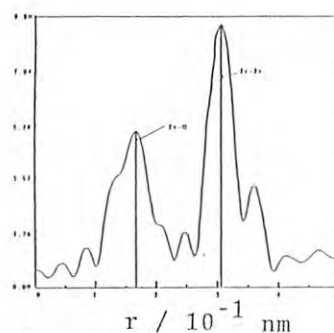
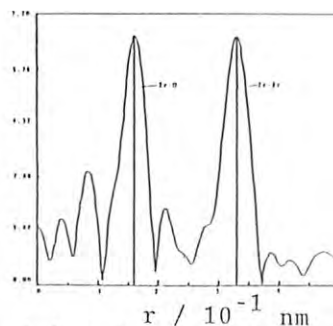
When ZrO_2 was attached on the external surface of the ZSM-5 in the one-atomic layer structure, it selectively produces the C_5 -hydrocarbon (more than 80 %) from methanol. On the other hand the SiO_2 -attached one-atomic layer ZrO_2 catalysts showed no such selectivity in the same reaction. In this paper we studied the structure of the one-atomic layer ZrO_2 catalysts by means of EXAFS to understand the difference in the catalyses between the two catalysts.

EXPERIMENTAL

The one-atomic layer ZrO_2 catalyst was prepared using the reaction between the ZSM-5 and the vapor of $\text{Zr}(\text{OC}_2\text{H}_5)_4$ at 503 K, followed by the calcination at 773K. The sample was examined by X-ray diffraction to confirm no formation of the crystalline ZrO_2 . The EXAFS was measured at BL-10B.

RESULTS AND DISCUSSION

Figure 1 shows the Fourier transforms of ZSM-5-attached and SiO_2 -attached one atomic layer ZrO_2 catalyst, monoclinic ZrO_2 and tetragonal ZrO_2 . The first peaks were attributed to the Zr-O bonding. The second ones were to the Zr-Zr. The Zr-Si bondings were observed at 0.278 nm for both ZSM-5-attached and SiO_2 -attached one atomic layer catalysts in the curve fitting analysis. The Zr-Zr distance of ZSM-5 attached ZrO_2 (0.367 nm) was longer than that of SiO_2 -attached ZrO_2 (0.350 nm) and was close to that of the monoclinic ZrO_2 (0.362 nm). Such structural difference causes the different catalytic property.

Fig.1 Fourier transform of ZSM-5-attached one-atomic layer ZrO_2 .Fig.2 Fourier transform of SiO_2 -attached one-atomic layer ZrO_2 .Fig.3 Fourier transform of ZrO_2 (tetragonal)Fig.4 Fourier transform of ZrO_2 (monoclinic).

AN EXAFS STUDY OF THE LOCAL STRUCTURE OF IRON-TIN COMPOSITE OXIDES

Satohiro YOSHIDA, Hiroshi MIZUTANI, Tsunehiro TANAKA and Takuzo FUNABIKI
 Department of Hydrocarbon Chemistry and Division of Molecular Engineering,
 Kyoto University, Sakyo-ku, Kyoto 606.
 And Mikio TAKANO
 Institute for Chemical Research, Kyoto University, Uji

A composite oxide composed of iron and tin is known as an useful material of sensors for reducing gases such as methane and hydrogen. The sensitivity depends on the composition and the highest sensitivity is attained at about 15 mol% of SnO_2 . The structure of the composite oxide is believed to be one of the main factors affecting the sensitivity. In the present study, the local structures of iron-tin composite oxides with various compositions have been investigated by measurements of the EXAFS at both Fe and Sn K-edge.

Experimental

Fe-Sn composite oxides were prepared by calcination of precipitates at 600°C , which were obtained by adding aqueous ammonia to solutions of SnCl_4 and FeSO_4 of a given concentration. EXAFS of the oxides were recorded in a transmission mode on a beam line BL-10B at KEK-PF at room temperature using a Si(311) channel cut monochromator.

Results and Discussion

Fe K-edge EXAFS. Figure.1 shows the Fourier transforms (F.T.s) (phase shift uncorrected) of Fe K-edge EXAFS of $\alpha\text{-Fe}_2\text{O}_3$ (corundum structure) and Fe-Sn composite oxides. A significant change in the F.T.s is observed in a range of $R=2\sim4\text{ \AA}$ by the change of SnO_2 content. The peaks in the range result from Fe-Fe and Fe-Sn atom pairs. The structural parameters were obtained by a curve fitting procedure described elsewhere¹⁾. The results indicate that a part of iron ions were replaced by tin ions forming a solid solution phase of corundum structure until 15 mol% of SnO_2 . When the content of SnO_2 exceeded 15 mol%, a separate phase of SnO_2 was formed.

Sn K-edge EXAFS. Figure.2 shows the F.T.s (phase shift uncorrected) of Sn K-edge EXAFS of SnO_2 and the composite oxides. The main peak at $R=1\sim2\text{ \AA}$ is attributed to Sn-O pairs. The peak decreased in the height and broadened with decrease in SnO_2 content. Peaks in the range of $R=3\sim5\text{ \AA}$ result from mainly the fine structures due to Sn-Sn pairs. The peaks were also reduced with decrease in SnO_2 content and reached to a noise level at 50 mol% of SnO_2 . The decrease of peaks can result both from interference of the fine structures due to Sn-Sn pairs with those due to Sn-Fe pairs and from the increase in disorder in SnO_2 phase. As the quality of EXAFS was not good enough to carry out the curve fitting procedure, we can not judge which is the main factor at present. For oxides containing SnO_2 less than 50 mol%, new peaks appeared in a range of $R=2.5\sim3\text{ \AA}$, indicating the existence of Sn-Fe pairs.

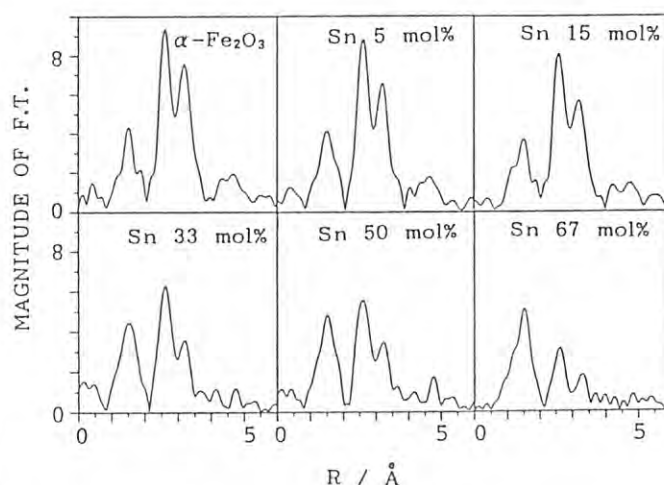


Fig.1 Fourier transform at Fe K-edge

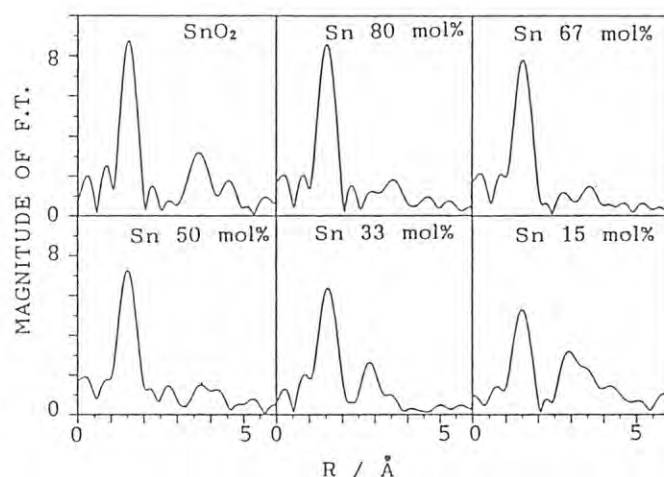


Fig.2 Fourier transform at Sn K-edge

It is noteworthy that in the sample of SnO_2 33 mol%, no peaks due to Sn-Sn pairs was observed in spite of larger back scattering amplitude of a Sn atom than that of a Fe atom. Although EXAFS due to Sn-Sn pairs could become dim by interference with the fine structure of Sn-Fe pairs, the observation of peaks due to Sn-Fe pairs indicate a minor effect of the interference to the F.T. Thus, the SnO_2 phase in the sample possibly covers the corundum structure phase as a thin layer with significant disorder.

Reference

1. T.Tanaka, H.Yamashita, R.Tsuchitani, T.Funabiki and S.Yoshida, *J.C.S., Faraday Trans.1*, in press.

CHARACTERIZATION OF SUPPORTED RHFE AND PTFE BIMETALLIC CARBONYL CLUSTERS AND THEIR CATALYTIC FUNCTIONS

Masaru ICHIKAWA, Atsushi FUKUOKA, Takauma KIMURA, Rao LING-FEN,
Nobuhiro KOSUGI[†], and Haruo KURODA[†]

Research Institute for Catalysis, Hokkaido University,
Kita-11 Nishi-10, Kita-ku, Sapporo 060

[†]Department of Chemistry, Faculty of Science,
The University of Tokyo, Hongo, Bunkyo-ku, Tokyo 113

Introduction

Surface organometallic chemistry, particularly involving metal cluster compounds, has been a subject of recent interest,¹⁾ because supported clusters make possible the molecular-level elucidation of heterogeneous catalysis in terms of organometallic chemistry. In the catalytic CO+H₂ reaction, the conventional Rh-Fe and Pt-Fe catalysts exhibit a unique activity for producing alcohols. We have employed RhFe and PtFe bimetallic carbonyl clusters as molecular precursors for preparation of RhFe and PtFe bimetallic catalysts. In this study, we have conducted in situ EXAFS investigations on RhFe/SiO₂ and PtFe/SiO₂ catalysts to elucidate the surface structure and location of bimetallic clusters.

Experimental

The carbonyl clusters were supported on SiO₂ from the adequate organic solution. The catalysts were reduced with H₂ at 673 K. EXAFS measurements were carried out at BL 10B.

Results and Discussion

Figure 1 shows the Fourier transform of $k^3\chi(k)$ of the Fe K-edge EXAFS obtained for RhFe/SiO₂ catalyst prepared from [NMe₃CH₂Ph]₂[Fe₂Rh₄(CO)₁₆]. A relatively strong peak at about 2.4 Å can be attributed to the Fe-Rh bond, and the peak at about 1.9 Å is the one arising from the splitting of the Fe-Rh peak by the nonlinearity of the Fe-Rh phase-shift function. The curve-fitting analysis of the Fe-Rh peak gave the Fe-Rh coordination number of 1.8 and the interatomic distance of 2.54 Å. The shoulder peak at 1.5 Å is attributable to Fe-O (C.N.=3.0, R=1.99 Å). This is derived from the bonding with the O atoms of SiO₂ support. There is little contribution of Fe-Fe bonding.

The Fourier transform of Rh K-edge EXAFS of the same catalyst is shown in Figure 2. According to the curve-fitting analysis, the Rh-Rh coordination number is 7.2 and the Rh-Rh distance is 2.65 Å. These results suggest that bimetallic RhFe particles are highly dispersed in the range of 10 Å size. From Mossbauer study, the oxidation states of Fe atoms are Fe and Fe³⁺, and 73 % of Fe atoms are in the state of Fe³⁺.

Compared with the previous EXAFS²⁾ and Mossbauer³⁾ studies on the conventional Rh-Fe/SiO₂ (Fe/Rh atomic ratio=0.5) catalyst, we can derive the following structural model for

the cluster derived RhFe/SiO₂ catalyst. Fe atoms which are mostly in the state of Fe³⁺ are located in the metal-support interface forming chemical bonds with the oxygen atoms of SiO₂. Since the contribution of Fe-Fe is negligible, Fe atoms should be highly dispersed without aggregation. Thus, Fe³⁺ ions forming Fe-O bonding in the metal-support interface have the role to anchor Rh particles onto the support. The bimetallic Rh-Fe³⁺ species derived from SiO₂-supported RhFe carbonyl clusters are highly active for migratory CO insertion as judged by the rates of the hydroformylation of olefins which are dramatically enhanced.⁴⁾

The Pt L-edge and Fe K-edge EXAFS study of the bimetallic cluster derived PtFe/SiO₂ catalyst is now in progress.

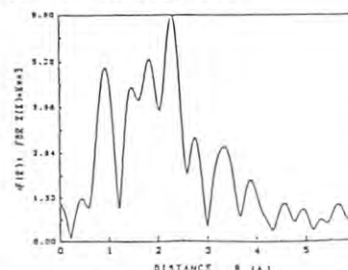


Figure 1. Fourier transform of the Fe K-edge EXAFS $k^3\chi(k)$ of SiO₂-supported [Fe₂Rh₄(CO)₁₆]²⁻ derived catalyst.

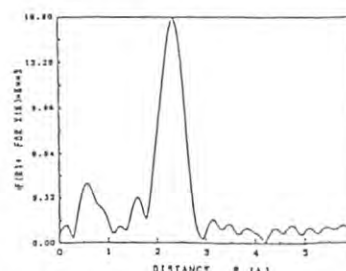


Figure 2. Fourier transform of the Rh K-edge EXAFS $k^3\chi(k)$ of SiO₂-supported [Fe₂Rh₄(CO)₁₆]²⁻ derived catalyst.

References

- 1) M. Ichikawa, Tailored Metal Catalysts (D. Reidel Pub., Dordrecht, 1986) p.183.
- 2) M. Ichikawa, T. Fukushima, T. Yokoyama, N. Kosugi, and H. Kuroda, J. Phys. Chem., **90**, 1222 (1986)
- 3) Y. Minai, T. Fukushima, M. Ichikawa, T. Tominaga, J. Radioanal. Nucl. Chem., **87**, 189 (1984)
- 4) A. Fukuoka, M. Ichikawa, J. A. Hriljac, and D. F. Shriver, Inorg. Chem., in press

EXAFS STUDIES OF SUPPORTED ULTRA FINE METAL PARTICLES

I. EFFECT OF ADDITIVES AND SUPPORTS ON THE MORPHOLOGY OF Rh

Takakazu FUKUSHIMA, Sadao OGASAWARA, Toshihiko YOKOYAMA⁺ and Haruo KURODA⁺

Department of Materials Science and Chemical Engineering, Faculty of Engineering,
Yokohama National University, 156 Tokiwadai, Hodogaya-ku, Yokohama 240

⁺Department of Chemistry, Faculty of Science, University of Tokyo, Hongo, Bunkyo-ku, Tokyo 113

Introduction

It has been shown in the former study that the additives such as Ti and Al decrease the particle size of Rh/SiO₂ and that Debye-Waller factor ($\Delta\sigma^2$) increases as the particle size decreases. In that study the promoters were added to 4wt% Rh/SiO₂. The particle size of 4wt% Rh/SiO₂ calculated by H₂ chemisorption is 20 Å and the dispersion (ratio of surface to total metals) is 0.58. In this study, the effect of additives to ultra fine particles, which have the dispersion of about 1, on the EXAFS parameters are investigated.

Experimental

The catalysts were prepared and reduced by the method described elsewhere. The sample powder was pressed into wafer and mounted in a glass cell. After in situ re-reduction the x-ray absorption measurements were carried out in H₂ atmosphere at r.t. by use of the EXAFS spectrometer at the Beam Line 10B.

Results and Discussion

EXAFS parameters, first coordination number and Debye-Waller factor ($\Delta\sigma^2$), for supported Rh catalysts are tabulated in Table 1 and plotted in Fig. 1. As found in the former study, Rh-Rh first coordination distance does not change even N decreased to about 5 from the bulk value of 12. The linear line depicted in Fig. 1 shows the relation between $\Delta\sigma^2$ and N obtained in the former study with using various non-promoted Rh/SiO₂ samples.

Table 1 Curvefitting results for Rh catalyst

wt%	Support	Additive ^a	N	$\Delta\sigma^2 \times 10^3$
2	SiO ₂	-	8.6	1.73
		Al	5.9	2.41
		Zr	5.2	2.80
		Ti	5.4	3.27
1	SiO ₂	-	7.3	1.89
1	Al ₂ O ₃	-	6.7	2.74

a: Rh/Additive=1/1

It can be seen clearly that the points of Rh-Zr/SiO₂ and Rh-Al/SiO₂ samples are both on the line and that the points of Rh-Ti/SiO₂ and Rh/Al₂O₃ samples locate on a upper region. It is noticeable that the deviations from the line are small compared with the data points of 4wt% Rh-Nb/SiO₂ and Rh-Mo/SiO₂. It was speculated in the former study that the static disorder of the surface particles increased by the strong interactions between Rh and additives such as Nb and Mo. It is important to know whether this deviation from the linear line, especially in a small coordination number region (5-6), has any meaning for the morphology change in the fine particle or not.

To understand this, we need more experimental evidences taken at low temperatures. But catalytically, there obtained a great difference between Rh-Ti/SiO₂ and Rh-Al/SiO₂. The dispersions taken by H₂ chemisorption is 0.92, 0.67 and 1.30 for non-promoted Rh, Rh-Ti and Rh-Al, respectively. It is reasonable that a small particle has a larger dispersion and this is the case for the Rh-Al/SiO₂. But for the case of Rh-Ti/SiO₂, the value of H/Rh decreases, despite the decrease of coordination number. Because the value of CO/Rh increases slightly, this phenomenon is not derived from SMSI¹⁾. We think this loss of H₂ adsorption ability is one of the clues to invoke the nature of the morphology of fine metal particles in the promoted catalyst systems.

Reference

- 1) S.J. Tauster, S.C. Fung, R.T.K. Baker and J.A. Horsley, Science 211(1981)1121.

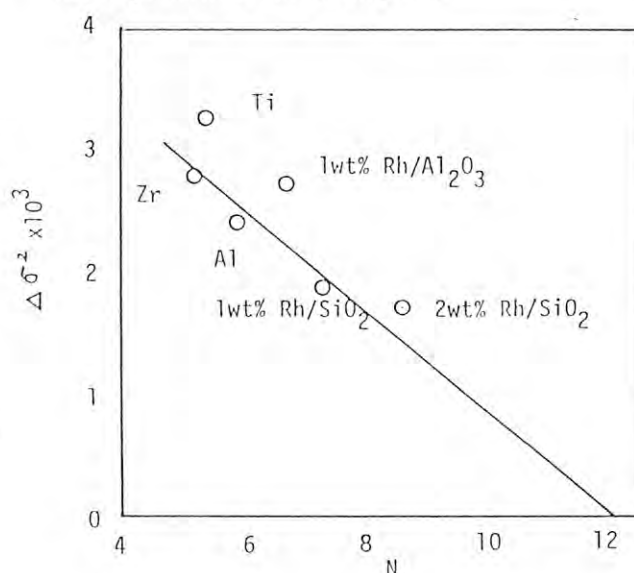


Fig. 1 $\Delta\sigma^2$ as a function of N.

EXAFS STUDIES ON THE STRUCTURE OF THE ATTACHED Rh DIMER CARBENE COMPLEX.

Kiyotaka ASAKURA, Kyouko BANDO, Yasuhiro IWASAWA and Haruo KURODA

Department of Chemistry, Faculty of Science, the University of Tokyo, Hongo, Tokyo 113.

INTRODUCTION

The carbene species($=CH_2$) is considered to be one of the most important intermediate in the CO hydrogenation reaction. But it is not in question how the carbene operates in the reaction. The Attached carbene complexes can be considered as a good model system to answer question. We have prepared SiO_2 -attached $(C_5Me_5)_2Rh_2(\mu-CH_2)_2(CH_3)_2$. In this paper we examined the incipient structure of the Rh complex on the surface of SiO_2 by means of EXAFS.

Experimental

The SiO_2 was impregnated with the $[(C_5Me_5)_2Rh_2(CH_2)_2Me_2]$ pentane solution, followed by drying the catalyst in the He flow. The sample was then transferred to the EXAFS measurement cell without exposure to air. The EXAFS was measured at BL-10B.

Results and discussion.

From the analysis of the gas phase during the deposition process, we find the formation of a methane per Rh atom. Thus the Rh_2 complex was on the surface O by the reaction with OH as in eq.1.

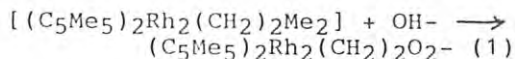


Figure 1 shows the Fourier transform of the SiO_2 -supported Rh_2 complex. The first main peak is attributed to the light atoms like C and O and the second one is to the Rh-Rh bond. In Fig. 2 the comparison was made between the observed EXAFS oscillation Fourier-filtered around the second peak and calculated EXAFS on the basis of the Rh-Rh bonding. The Rh-Rh bond length obtained from the curve fitting analysis was 0.267 nm a little longer than that in the original $[(C_5Me_5)_2Rh_2(CH_2)_2Me_2]$ which was 0.261 nm as a result of EXAFS analysis. Thus the Rh-Rh bonding was retained after the deposition of the complex on the SiO_2 surface, somewhat loosened by the coordination of the surface OH groups.

Acknowledgment

The authors express their thanks to Prof.K.Isobe, (Institute for Molecular Science) for the synthesis of the Rh dimer complex and to Dr.Y.Arakawa (National Chemical Laboratory for Industry) for the preparation of the attached Rh dimer complex catalyst.

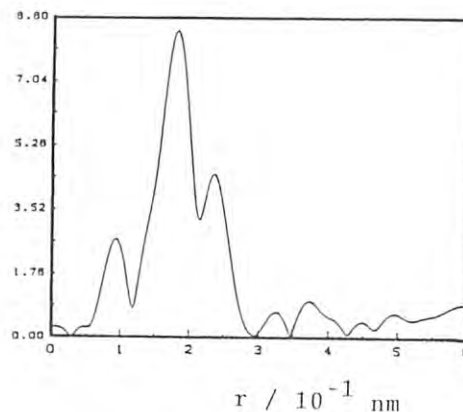


Fig.1 Fourier transform of SiO_2 -supported Rh_2 complex.

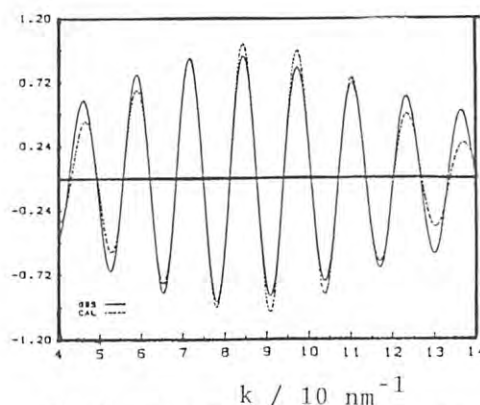


Fig.2 comparison between the observed EXAFS oscillation inversely Fourier filtered over the range of $r=0.22-0.28$ nm and the calculated one on the basis of the Rh-Rh phase shift and amplitude functions.

THE STRUCTURE STUDIES ON THE TiO_2 ONE-ATOMIC LAYER BY MEANS OF EXAFS

Kiyotaka ASAKURA, Junji INUKAI, Hideaki YOSHITAKE, Yasuo IZUMI, Rika KUWABARA, Yasuhiro IWASAWA, and Haruo KURODA

Department of Chemistry, Faculty of Science, the University of Tokyo, Hongo, Tokyo 113.

The thin layer oxide shows unique catalyses as well as unique support nature¹⁾. We have prepared Nb_2O_5 , ZrO_2 , La_2O_3 one-atomic layer catalysts. They show quite different properties as a support from the corresponding bulk oxides. Although the bulk Nb_2O_5 shows a SMSI character, the SiO_2 -supported Nb_2O_5 one-atomic layer do not. We attributed this reason to the strong Nb-O-Si bond. TiO_2 is known as an SMSI support. It is expected that TiO_2 one-atomic layer shows no SMSI behavior. We investigated the property of TiO_2 one-atomic layer as well as its structure by means of EXAFS. In this paper we report the EXAFS results on the structure of TiO_2 one-atomic layer.

Experimental

The TiO_2 one-atomic layer catalyst was prepared by use of the reaction between $\text{Ti}(\text{OC}_3\text{H}_7)_4$ vapor and surface silanols of SiO_2 at 473 K, followed by evacuation of the sample at 473 K to remove the unreacted $\text{Ti}(\text{OC}_3\text{H}_7)_4$. Thus obtained sample corresponds to 0.5 atomic-layer oxide. To obtain one-atomic layer catalyst, we repeated the above mentioned process once more. Pt was deposited by the impregnation of the TiO_2 one-atomic layer with the H_2PtCl_6 aqueous solution. EXAFS spectra were taken at BL 7C.

Results and Discussion.

Fig.1 shows the Fourier transforms of one-atomic layer catalysts. Fig.2 shows the Fourier transforms of TiO_2 with the Rutile and anatase crystal structures. The Fourier transform of one-atomic layer catalyst is similar to that of anatase-type TiO_2 . Therefore one-atomic layer TiO_2 takes an anatase-like structure. The structure of TiO_2 one-atomic layer with Pt supported on it and reduced at 773 K shows no remarkable change from that of the unsupported TiO_2 one-atomic layer. Thus the one-atomic layer support is stable after the high temperature reduction. 1) K.Asakura and Y.Iwasawa Chem. Lett., 511(1986); K.Asakura and Y.Iwasawa, to be published.

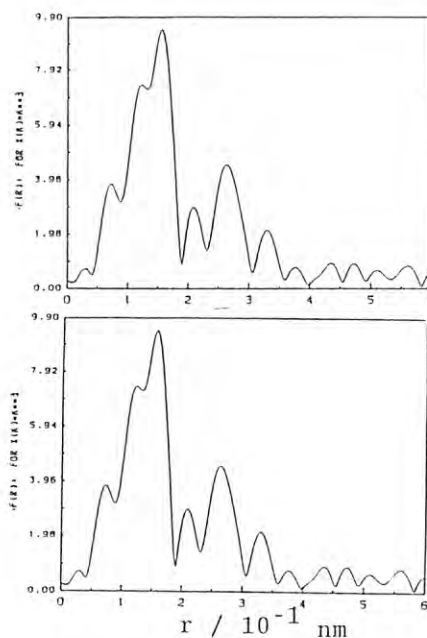


Fig.1 The Fourier transforms of (a) 1ML $\text{TiO}_2/\text{SiO}_2$ and (b) $\text{Pt}/\text{TiO}_2/\text{SiO}_2$ with 773 K reduction.

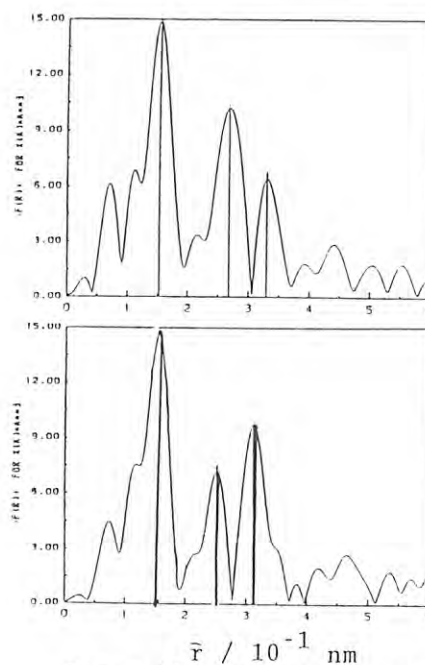


Fig.2 The Fourier transforms of (a) Anatase and (b) Rutile.

THE STRUCTURE OF $\text{Mo}(\text{CO})_6$ SUPPORTED IN THE ZEOLITE NaY.

Kiyotaka ASAKURA, Hideaki YOSHITAKE, Yasuo IZUMI, Junji INUKAI, Rika KUWABARA,
Yasuhiro IWASAWA, Haruo KURODA and Russel F. Howe*

Department of Chemistry, Faculty of Science, the University of Tokyo,
Hongo, Tokyo 113.

Chemistry Department, University of Auckland, Private Bay, Auckland, New Zealand

INTRODUCTION

Zeolites are a well-known class of aluminosilicate support characterized by the regular well-defined pore structures and intensely high degree of crystallinity. The zeolite Y has the largest pores called as supercages. When the $\text{Mo}(\text{CO})_6$ introduced in the supercage of zeolite NaY and thermally decomposed, Mo cluster $(\text{Mo})_n$ was formed which was stable against aggregation to a larger metal particle. The stability of the Mo cluster is considered to be attained due to the existence of Na^+ which becomes a nuclear of the Mo cluster. We studied the structure of Mo cluster in the zeolite NaY system prepared from the $\text{Mo}(\text{CO})_6$ by means of EXAFS.

EXPERIMENTAL

The sample was prepared by the deposition of gaseous $\text{Mo}(\text{CO})_6$ on the NaY zeolite in vacuum. It was then heated to 673 K. The EXAFS spectrum was measured at BL10B of Photon Factory.

Results and Discussion

Fig.1 shows the Fourier transforms of $\text{Mo}(\text{CO})_6$ deposited on NaY subsequently treated at 673 K. Two peaks are attributed to Mo-O and Mo-Mo, respectively. The curve fitting analysis was carried out by use of the theoretical amplitude function and phase shift. In Fig.2 the Fourier filtered EXAFS oscillation was compared with the calculated spectra on the basis of the two shell model Mo-O+ Mo-Mo. We could not obtain the better fitting result in the three shell model Mo-O+Mo-Mo+Mo-Na. This means the Na atom involved in the cluster is too small comparing to the Mo atom. Mo-Mo bonding was 0.282 nm longer than Mo-Mo distance in Mo metal. This value is comparable to the Mo-Mo distance of the SiO_2 -attached $\text{Mo}(\text{II})$ (0.280 nm)¹⁾. Therefore we concluded that $\text{Mo}(\text{CO})_6$ was thermally decomposed and fixed on the internal surface of the supercage of the zeolite through the Mo-O-bonding as shown in Fig.3.

1) Y.Iwasawa, K.Asakura, H.Ishii, and H.Kuroda, Z.Phys.Chem., NF. 144, 105(1985).

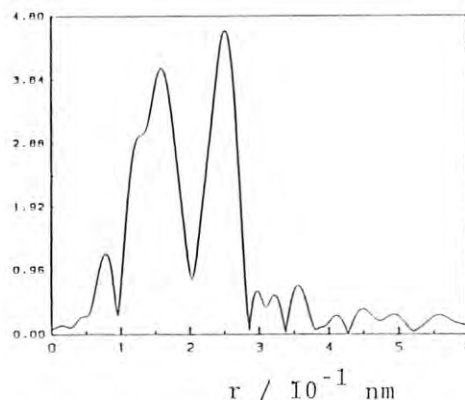


Fig.1 Fourier transform of $\text{Mo}(\text{CO})_6/\text{NaY}$ treated at 673 K.

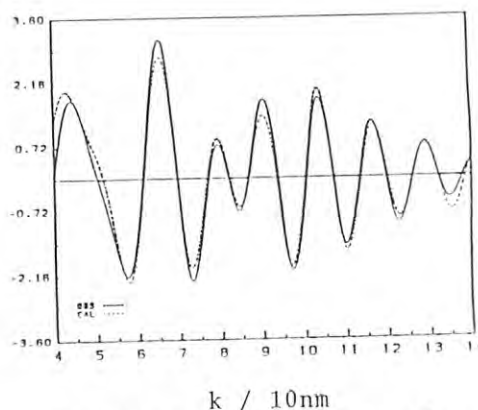


Fig.2 Curve fitting result.

obs: —
calc: ----

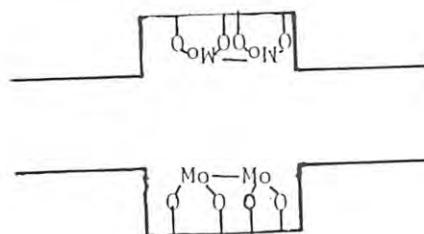


Fig.3 Model for $(\text{Mo})_n/\text{NaY}$ derived from $\text{Mo}(\text{CO})_6$

STUDIES ON THE STRUCTURE OF BIMETALLIC COLLOIDAL CATALYSTS

Naoki Toshima, Tadahito Takahashi, Youichi Sagawa, Tetsu Yonezawa,
and *Kiyotaka Asakura, *Yasuhiro Iwasawa

Department of Industrial Chemistry, Faculty of Engineering,
and *Department of Chemistry, Faculty of Science,
The University of Tokyo, Hongo, Bunkyo-ku, Tokyo, 113.

Introduction

Colloidal metals not only act as catalysts having high activity and selectivity, but also afford a relatively simple system, in which the structure of the metal particles is able to be discussed regardless of the interaction with the support.^{1,2)} The present authors have successfully prepared the homogeneous colloidal noble metals protected by water-soluble polymers by reducing noble metal salts in the presence of polymers, and have applied them to the catalyst for hydrogenation, for example.

We have recently disclosed that Pd-Pt bimetallic colloids are produced by refluxing the mixed solution of palladium chloride and hexachloroplatinic acid in alcohol in the presence of poly(vinyl pyrrolidone) (PVP).³⁾ When these colloids were used for the catalyst for selective partial hydrogenation of 1,3-cyclooctadiene⁴⁾, they showed higher activity than colloidal Pd, colloidal Pt or the mixture of them. The formation of the bimetallic colloid has been suggested by UV and TEM observations.⁸⁾ This cooperative research has been going on since this spring to examine the structure of these colloids. The results of the first measurement using a BL-10B PF-EXAFS station are reported here.

Experimental and Results

The bimetallic colloids at the ratios of Pt:Pd=4:1, 1:1, and 1:4 (molar ratio) were prepared by refluxing in the water-ethanol mixed solution under nitrogen atmosphere. These colloidal dispersions were concentrated by evaporation of the solvent under reduced pressure, and the concentrated solutions were sealed in the 50 mm (for Pd), and 10 mm (for Pt) cells under nitrogen atmosphere. K edge of Pd and L₃ edge of Pt of the sample were measured by the BL-10B station. The results were analysed

by Program EXAFS1 (Research Center for Spectrochemistry, the University of Tokyo).^{5,6)}

The measurement of the Pt:Pd=4:1 colloid went on well. The Pt in this sample was measured by L₃ edge and the phase-unadjusted Fourier-transformed EXAFS spectrum is shown in Fig. 1. It is assumed that the high peak at the center represents a Pt-Pt bond, and a Pt-Pd bond is shown by the peak at the left. Figure 2 shows the phase-unadjusted Fourier-transformed EXAFS spectrum of the same sample measured by K edge of Pd. Compared with other EXAFS data, the second highest peak at the center is thought to be a Pd-Pd bond, and a Pd-Pt bond is thought to be shown by the peak at the left. Concerning these results, the fact that this colloid is bimetallic having Pt-Pd bonds has been assured. More detailed studies are in progress. The structure including the location of Pt and Pd, the change in the structure with the change in Pt/Pd ratio, and the relationship between the structure and the catalytic activity of these bimetallic colloids will be examined.

References

- 1) N. Toshima and H. Hirai, "Photoenergy Conversion" ed. by A. Yamada, N. Toshima, and M. Kaneko, Japan Scientific Societies Press, Tokyo, 1983, pp.133-168.
- 2) H. Hirai and N. Toshima, "Tailored Metal Catalysts", ed. by Y. Iwasawa, D. Reidel Publishing Co., 1986, pp.89-140.
- 3) N. Toshima, K. Kushihashi, and H. Hirai, Preprints of 54th Spring Meeting of the Chemical Society of Japan, p.720 (1987).
- 4) H. Hirai, H. Chawanya and N. Toshima, *Reactive Polymers*, **3**, 127 (1985).
- 5) K. Asakura and Y. Iwasawa, *Petrotech*, **8**(12), 41 (1985).
- 6) K. Asakura, N. Kosugi, H. Kuroda and Y. Iwasawa, *Catalyst*, **26**(5), 390 (1984).

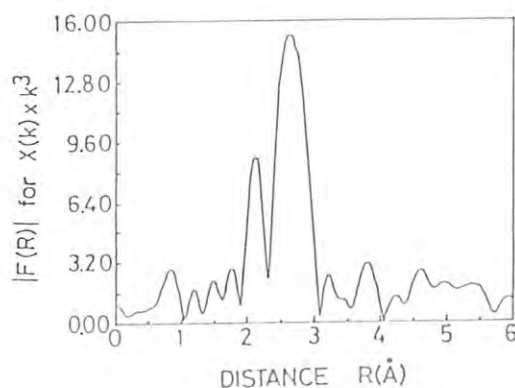


Fig. 1. EXAFS Spectrum of Pt/Pd (4/1) Bimetallic Colloid at L₃ Edge of Pt

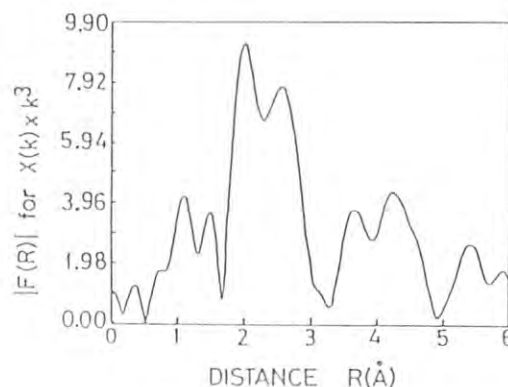


Fig. 2. EXAFS Spectrum of Pt/Pd (4/1) Bimetallic Colloid at K Edge of Pd

EXAFS Study on Local Structures of Active Site on Mo Supported Catalysts for Hydrocracking and Hydrogenation Activities I. The Effect of Presulfiding Condition

Nobuyuki MATSUBAYASHI, Hiromichi SHIMADA, Nobuhiro KOSUGI[†], Haruo KURODA[†], Yuji YOSHIMURA, Toshio SATO, and Akio NISHIJIMA

National Chemical Laboratory for Industry, Yatabe, Ibaraki 305

[†]Department of Chemistry, Faculty of Science, The University of Tokyo, Hongo, Bunkyo, Tokyo 113

Introduction

Supported molybdenum sulfide catalysts are used for hydrotreating of heavy oil. The structure of active site for the reaction has not been known well yet. In the present report, EXAFS method was applied to the investigation of the changes in the local environment around Mo in the catalyst by changing presulfiding conditions such as temperature and time.

Experimental

10 and 20wt% MoO₃ catalysts (Cat.A and Cat.B) supported on the γ -Al₂O₃ were prepared by an impregnation method with a solution of ammonium paramolybdate. The catalysts were presulfided in a stream of 5 vol% of H₂S/H₂ at 200–600°C for 0–16h. Mo K absorption EXAFS spectra were measured at BL10B of the Photon Factory.

Results and Discussion

Figure 1 shows the Fourier transforms of the EXAFS for the Cat.B presulfided at 200, 400, and 600°C for 1h. The peak at 1.7 Å observed in the Fourier transform of the catalyst presulfided at 200°C is corresponding to the Mo–O, which indicates that the catalyst is not sulfided completely at 200°C. The peaks at 2.4 Å and 3.2 Å are corresponding to the Mo–S and Mo–Mo in the crystal of the MoS₂, respectively. In the Fourier transforms of the catalyst presulfided at 400 and 600°C, the Mo–O peak does not appear and the Mo–S and Mo–Mo peaks are larger than that at 200°C.

The average numbers of coordinating S atoms (N(S)) and nearest Mo atoms (N(Mo)) around Mo were calculated from the intensities of the Mo–S and Mo–Mo peaks referring to the structure of MoS₂ crystal. Figures 2 and 3 show the changes in N(S) and N(Mo) of the Cat.A and Cat.B presulfided at different temperatures and reaction times, respectively. In Fig. 2, the time of presulfiding was fixed at 1h. In Fig. 3, the temperature of presulfiding was fixed at 400°C. In the same conditions of presulfiding, the N(S) and N(Mo) of Cat.B are larger than that of Cat.A indicating a correlation between the concentration of Mo and the degree of the growth of the MoS₂ crystal like structure. Figure 2 shows that the N(S) and N(Mo) of catalysts become larger with increasing of temperature of presulfiding showing more growth of the MoS₂ crystal like structure. Figure 3 shows the sulfiding of the catalysts progresses rapidly in the first one hour and after that does not progress more.

The ratio N(Mo)/N(S) will be a good indicator for agglomeration of MoS₂. Tables 1 and 2 show the ratios N(Mo)/N(S) when reaction time and temperature of presulfiding were changed, respectively. These ratios of Cat.B are larger than

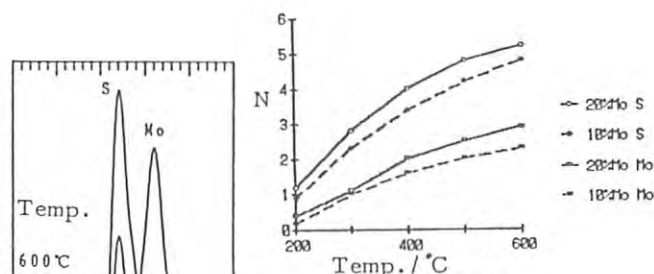


Fig.1. Fourier transforms of EXAFS.

Fig.2. Effect of temp.

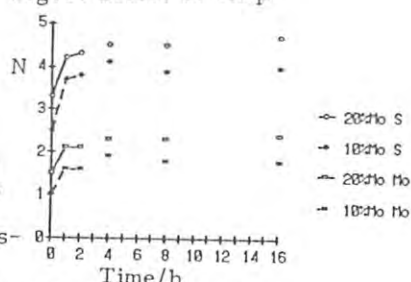


Fig.3. Effect of time.

Table 1. N(Mo)/N(S) of various time of sulfiding at 400 °C.

	0h	1h	2h	4h	8h	16h
10wt%MoO ₃ /Al ₂ O ₃	0.40	0.43	0.42	0.46	0.46	0.45
20wt%MoO ₃ /Al ₂ O ₃	0.46	0.49	0.47	0.50	0.51	0.50

Table 2. N(Mo)/N(S) of various temperature of sulfiding for 1h.

	200 °C	300 °C	400 °C	500 °C	600 °C
10wt%MoO ₃ /Al ₂ O ₃	0.22	0.43	0.47	0.48	0.48
20wt%MoO ₃ /Al ₂ O ₃	0.28	0.39	0.49	0.52	0.55

those of Cat.A. This is due to a difference in percentage of Mo atoms which have less interaction with supports. In the case of presulfiding at 400°C, the ratios of N(Mo)/N(S) rapidly increase early in the reaction, and then gradually increase. This shows that an agglomeration of MoS₂ occurs immediately at high temperature. In the case of presulfiding at 200°C, N(Mo)/N(S) is relatively small. This indicates that Mo is kept highly dispersive at 200°C. The value of N(Mo)/N(S) becomes larger as the temperature of presulfiding is higher. The value of N(Mo)/N(S) of presulfiding at 600°C for 1h is larger than that at 400°C for 16h. These results suggest that each Mo has different interaction with the support and Mo can migrate on the surface of the catalyst at high temperature when the interaction between Mo and the support is strong.

More detailed studies on the relationship between the structures and the activities of the catalysts are now progressing.

EXAFS STUDY OF SELENOCYSTEINE STRUCTURE

Yuzuru HIRAGI,¹⁾ Hironobu MAEDA,²⁾ Takatoshi MURATA,³⁾ Kanji KAJIWARA,¹⁾
 Hiromu SAKURAI,⁴⁾ Nobuyoshi ESAKI,¹⁾ Hidehiko TANAKA,¹⁾ and Kenji SODA¹⁾

¹⁾Institute for Chemical Research, Kyoto University, Uji, Kyoto-Fu 611, ²⁾Department of Chemistry, Okayama University, Okayama 700, ³⁾Department of Physics, Kyoto University of Education, ⁴⁾Department of Pharmaceutical Sciences, Tokushima University, Tokushima 770

Introduction

Various selenium amino acids occur in nature, and most are physiologically important. Several mammalian and microbial proteins, in particular enzymes, contain selenium amino acid as a prosthetic group. The selenium moiety of bacterial glycine reductase, bacterial formate dehydrogenase, and mammalian glutathione peroxidase has been identified as selenocysteine. The three-dimensional structure of glutathione peroxidase of bovine erythrocytes has been analyzed at 2.0 Å, but little is known about the fine environment around the catalytically essential selenocysteine residue. We here report the results of an EXAFS study of selenocysteine in aqueous solution.

Results and Discussion

L-Selenocysteine was synthesized from 3-chloro-L-alanine and elemental selenium as described by Tanaka and Soda. EXAFS measurements were carried out for aqueous solutions of selenocysteine and selenocysteine, and for selenocysteine powder solidified with polyethylene. The following aqueous solutions were prepared to be analyzed: 10 mM L-selenocysteine in 0.2 M 2-(N-cyclohexylamino)ethanesulfonic acid (CHES) buffer (pH 9.5); 40 mM L-selenocysteine in 0.2 M CHES buffer (pH 9.5) (selenol group of selenocysteine is dissociated under the conditions (pKa of SeH is 5.0)); 40 mM L-selenocysteine in 0.5 N HCl (selenol is not dissociated under the conditions).

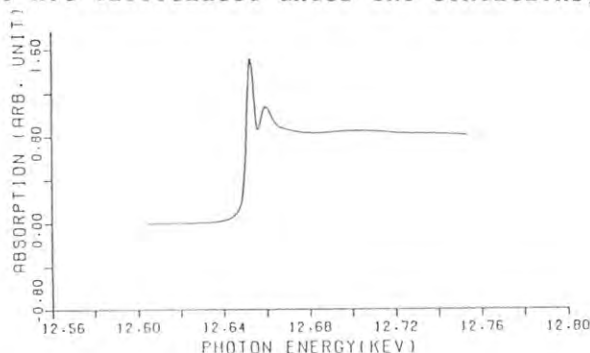
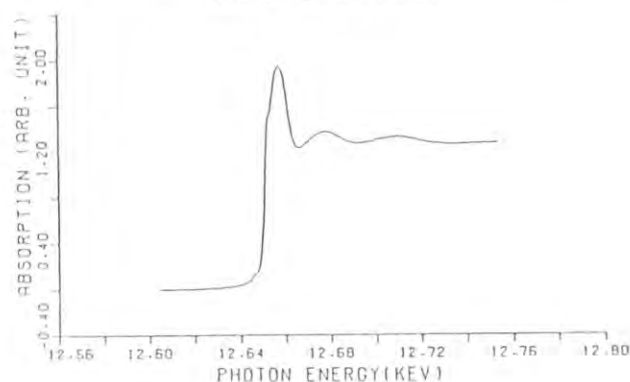
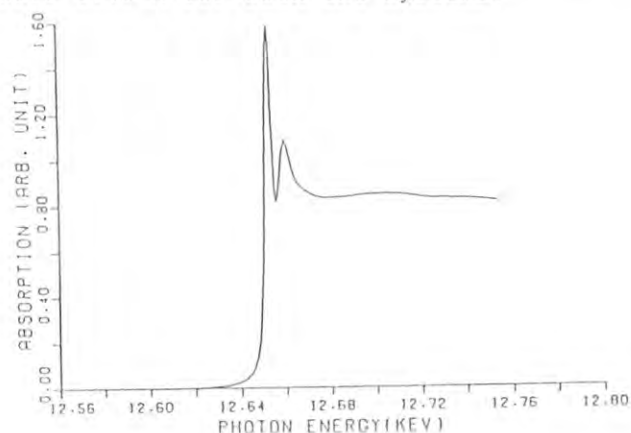


Figure 1 (upper) Se K-edge absorption spectrum of L-selenocysteine, L-selenocysteine under acidic conditions (Figure 2, right upper), and under alkaline conditions (Figure 3, right bottom).

X-ray absorption spectra were recorded over the energy range corresponding to the selenium K-edge. Data were collected at room temperature at an energy of 2.5 GeV with an average current of 193 mA. The X-ray absorption data were converted to EXAFS modulation spectra with a cubic spline fit background subtraction.

Figure 1 shows the X-ray absorption spectrum in the region of the Se K-edge for aqueous solution of L-selenocysteine. Essentially identical spectrum was obtained for L-selenocysteine powder solidified with polyethylene. The bond lengths were determined as follows: C-Se, 1.88 Å; and Se-Se, 2.32 Å. When L-selenocysteine was dissolved in 0.1 N HCl and analyzed, the same EXAFS was observed. Therefore, these bond lengths were not influenced by dissociation of COOH and NH₂. Figure 2 illustrates the X-ray absorption spectrum for aqueous acidic solution of selenocysteine whose selenol group is not dissociated, while Figure 3 shows the spectrum for the alkaline selenocysteine solution in which selenol of selenocysteine is dissociated. The C-Se bond length length determined were 1.96 Å for both the systems.



X-RAY ABSORPTION STUDY ON THE TYPE II COPPER-DEPLETED
CUCUMBER ASCORBATE OXIDASETakeshi SAKURAI, Shinnichiro SUZUKI and Mitsuru SANO[†]Institute of Chemistry, College of General Education, Osaka University,
Toyonaka, Osaka 560[†]Chemical Laboratory, College of General Education, Nagoya University,
Nagoya 464Introduction

Ascorbate oxidase (EC 1.10.3.3) is a multi-copper oxidase together with ceruloplasmin and laccase. There are three type I Cu²⁺, one type II Cu²⁺ and two pairs of type III Cu²⁺ in the enzyme. Selective depletion of type II copper has been successfully performed for laccase and ascorbate oxidase as a strategy to shed light on the active site and reaction mechanism of these enzymes. However, there has been controversial discussion about the oxidation state of the type III coppers in the type II copper-depleted laccase. Reinhammar et al.¹⁾ obtained absorption spectrum where the shoulder band at 330 nm which has been believed to be concerned with the coupled type III Cu(II)'s was intact as that of native laccase. Contrary, other groups²⁻⁴⁾ reported that the band disappears or is greatly reduced in its intensity because of the reduction of type III coppers. Although similar discussion has never arose on ascorbate oxidase, our recent study about type II copper-depleted cucumber ascorbate oxidase⁵⁾ indirectly suggested that type III coppers are reduced during the process to deplete type II copper. Here we show the direct evidence for the reduction of type III coppers from X-ray absorption edge spectroscopy.

Experimental and Results

X-ray absorption Cu K-edge spectra were measured on the storage ring of Photon Factory at KEK, running at 2.5 GeV with the beam current of 230-260 mA.

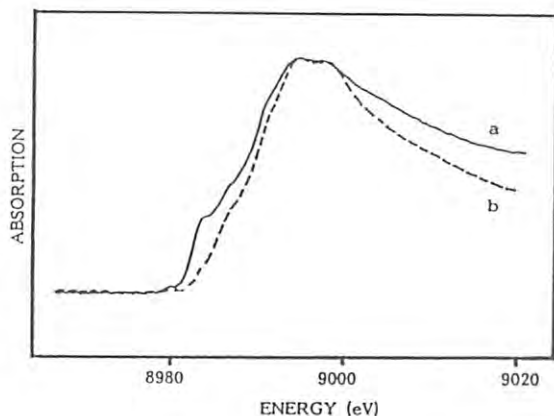


Fig. 1

Fig. 1 shows the absorption Cu K-edge spectra of type II copper-depleted cucumber ascorbate oxidase (a) and its H₂O₂ (x28)-treated derivative (b). Since the low energy shoulder at about 8983 eV is characteristic of cuprous ion, the former spectrum (a) is apparently that of a mixture of cupric and cuprous ions. In the spectrum (a), the cupric species are three type I coppers because the strong blue color due to type I Cu²⁺ did not bleach at all even after irradiation of strong X-ray. Therefore the cuprous species must be type III coppers which were in the cupric state in native enzyme. On the other hand, cuprous species are not observed in the spectrum (b), because type III coppers were oxidized by H₂O₂. The present X-ray absorption spectra indicate, even though qualitatively but unequivocally, that type III coppers are reduced during the procedure to deplete type II copper and are stable in the cuprous state in the absence of type II copper under air. In addition, the absorption band at 330 nm is ascertained to be concerned directly with the coupled type III copper(II)'s.

References

- 1) B. Reinhammar and Y. Oda: *J. Inorg. Biochem.* 11 (1979) 115.
- 2) L. Mourpurgo, M. T. Graziani, A. Finazzi-Agro, G. Rotilio and B. Mondovi: *Biochem. J.* 187 (1980) 361.
- 3) J. E. Penner-Harn, B. Hedman, K. O. Hodgson, D. J. Spira and E. I. Solomon: *Biochim. Biophys. Res. Commun.* 119 (1984) 567.
- 4) F. Frank, O. Farver and I. Pecht: *J. Biol. Chem.* 258 (1983) 11112.
- 5) T. Sakurai, S. Sawada, S. Suzuki and A. Nakahara: *Biochim. Biophys. Acta*, in press.

EXAFS AND XANES OF THE METALLIC COMPONENTS IN PLANT LEAVES

Masayasu KURAHASHI, Isao KOJIMA, Yoshinori KOBAYASHI,
Kazumasa HONDA, Natsuo FUKUMOTO, and Hisao WATANABE*

National Chemical Laboratory for Industry, Yatabe-machi, Tsukuba-gun, Ibaraki 305

*Tropical Agriculture Research Center, Yatabe-machi, Tsukuba-gun, Ibaraki 305

Introduction

Manganese is one of the indispensable elements to the growth of plants and its behavior is attracted much attention in the field of plant nutrition study. Our recent work using X-ray fluorescence element mapping spectrometry¹⁾ revealed that the enrichment of manganese takes place at the injured part of plant leaf under an external stresses such as X-ray irradiation, mechanical damage, or insect damage. However, the mechanism of the movement of manganese is still unrevealed. In order to obtain some informations about this problem, especially about the chemical state of manganese in a plant leaf, an EXAFS and XANES study has been performed.

Experimental

X-ray absorption of Mn K-edge for rice leaf and several standard samples (powder and solution) was measured by using the EXAFS facilities at BL-10B. A bundle of 50 leaves was used for the measurement of the rice leaf. $\text{MnSO}_4(2+)$, Chlorotetraphenylporphinatomanganese (TPPMnCl; $3+$), $\text{MnO}_2(4+)$, $\text{KMnO}_4(7+)$ were used as standard samples.

Results and Discussion

The X-ray absorption spectra for rice leaf and standard samples are shown in Fig. 1, and the shifts of the absorption edge and prepeak are summarized in Table 1. Both the absorption edge and prepeak shift toward higher energy with the increase of the charge of manganese. The energy positions of the edge and prepeak for rice leaf are similar to those of MnSO_4 , indicating that the charge of the manganese in rice leaf is mostly $+2$. This is further confirmed by the comparison of the amplitude of the prepeak which is known to be sensitive to the charge of the metal. Figure 2 shows the Fourier transform of the EXAFS function $X(k)$ multiplied by k^3 . The radial distance of the maximum peak for rice leaf ($d=2.15$ Å) is in good agreement with the Mn-O distances in $\text{Mn}(\text{OH})_2^{2+}$ cluster observed for $\text{MnSO}_4\text{aq.}$ ($d=2.25$ Å) and MnCl_2 ($d=2.17$ Å)²⁾. The peaks of $R>3$ Å for rice leaf are in similar positions to those for TPPMnCl. However, measurement with higher accuracy is needed for the interpretation of the peaks.

In this preliminary experiment we confirmed that the information about the chemical state of metal such as manganese in 'living' plant, where the concentration is as low as 0.1 %, is obtainable by EXAFS and XANES analysis.

The authors thank Dr. T. Higuchi of University of Tokyo for providing TPPMnCl.

References

- 1) N. Fukumoto, Y. Kobayashi, H. Watanabe, A. Uchiumi, M. Kurahashi, A. Kawase, Adv. X-Ray Chem. Anal. Jpn., **18**, 233 (1987).

- 2) G. Licheri and G. Finna, "EXAFS and Near Edge Structure", Vol.27 of Springer Series in Chemical Physics, edited by A. Bianconi, L. Incoccia, and S. Stipcich, Springer, Berlin (1983) pp.240.

Table 1. Observed shifts* of the edge and prepeak feature.

Compound	Edge shift	Prepeak shift
	/eV	/eV
$\text{MnSO}_4 \cdot 4\text{H}_2\text{O}$, powder	-10.6	-2.8
MnSO_4 , aq (pH4.0)	-9.7	-2.8
TPPMnCl, powder	-7.8	-2.4
MnO_2 , powder	-6.7	-1.0
KMnO_4 , powder	-1.3	-0.1
KMnO_4 , aq (0.1N KOH)	0.0	0.0
Rice leaf	-9.9	-2.8

*Values are relative to $\text{KMnO}_4\text{aq.}$

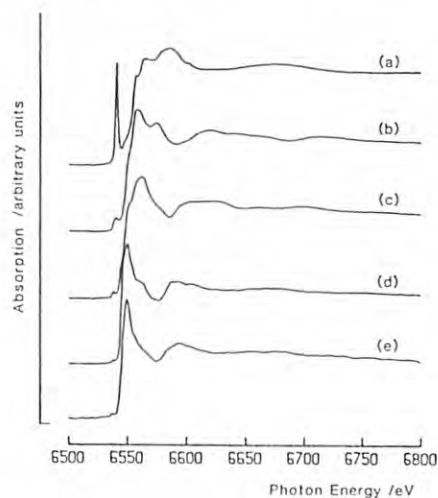


Figure 1. X-ray absorption spectra of standard samples (powder) and rice leaf; (a) KMnO_4 , (b) MnO_2 , (c) TPPMnCl, (d) MnSO_4 , and (e) rice leaf.

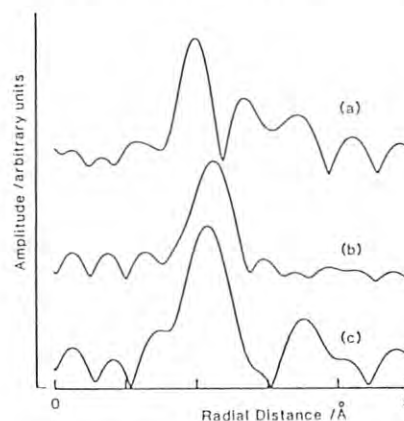


Figure 2. Fourier transform of the k^3 -multiplied EXAFS data of (a) TPPMnCl, (b) $\text{MnSO}_4\text{aq.}$, and (c) rice leaf.

SMALL-ANGLE SCATTERING FROM POLYMER SOLUTIONS USING SYNCHROTRON RADIATION

Hiroyuki Tagawa¹, Hiroshi Aoki¹, Takashi Ichimura¹, Kimio Kurita¹, Tatsuzo Ueki², Yuzuru Hiragi³, Yoshinobu Izumi⁴, Mikio Kataoka⁵, Yoshio Muroga⁶ and Yoshiyuki Amemiya⁷

- 1.College of Science and Technology,Nihon University Chiyoda-ku,Tokyo 101,Japan
- 2.Faculty of Engineering Science,Osaka University,Toyonaka,Osaka 560,Japan
- 3.Institute for Chemical Research,Kyoto University,Uji,Kyoto 611,Japan
- 4.Faculty of Science,Hokkaido University,Sapporo,Hokkaido,060,Japan
- 5.Faculty of Engineering,Nagoya University,Nagoya,Aichi 464,Japan
- 6.Faculty of Science,Tohoku University,Sendai,Miyagi 980,Japan
- 7.Photon Factory,National Laboratory for High Energy Physics,Oho-machi,Ibaraki 305

INTRODUCTION

In small-angle neutron scattering (SANS) and X-ray scattering (SAXS) from semi-dilute solutions, the angular dependence of the scattered intensity $I(q)$, q being the scattering vector, is given by the following Lorentzian form:

$$I(q)^{-1} = I(0)^{-1} (1 + \xi^2 q^2) \quad (1)$$

where $q = 4\pi/\lambda \sin(\theta/2)$, λ =wavelength, θ =scattering angle, ξ =correlation length. This scattering function applies for the range of scattering vector $R_g^{-1} < q < b^{-1}$, where R_g is the radius of gyration and b is the segment length.

It is reported by Kinugasa et al.¹⁾ that linear variations in a modified Zimm representation are obtained in SANS measurements but excess scattering at about $q < 5 \times 10^{-2} \text{ \AA}^{-1}$ has been observed leading to deviation from the equation (1) in SAXS measurements. The SANS data were obtained by use of the point collimating system, but on the other hand, the SAXS data were obtained by use of the line-slit collimating system and desmeared.

In this report, in order to reexamine the origin of the excess scattering in SAXS measurements with line-slit collimating system, the SAXS experiments were carried out on a point focusing optics.

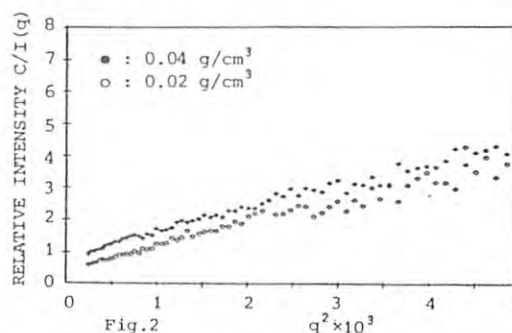
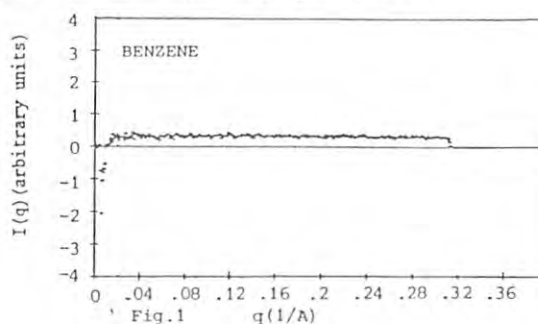
EXPERIMENTAL

The SAXS measurements were performed with the SAXES²⁾ installed in BL-10C at 30°C. Counting times of 500 and 1000 sec were used for each measurement of the solvent and solution, respectively. The entrance slit height of 1.5 mm was placed in front of the sample and the specimen-to-detector distance was about 1880 mm. The sample studied was the monodisperse polystyrene ($M_w = 2.0 \times 10^6$, $M_w/M_n < 1.3$) in benzene. Measurements were performed on two solutions of polystyrene in benzene, 0.02 and 0.04 g/cm³ concentration.

RESULTS AND DISCUSSIONS

Fig.1 shows the scattered intensities $I(q)$ for benzene as a function of the scattering vector $q \text{ \AA}^{-1}$. It was confirmed that a small-angle resolution of $q = 0.015 \text{ \AA}^{-1}$ useful for our purpose has been obtained in the figure.

The data of $C/I(q)$ for $C = 0.02$ and 0.04 g/cm^3 are shown in Fig.2. A departure from the Lorentzian scattering behaviour is not clearly found out in the figure. From the slope of the figure below $q = 5.5 \times 10^{-2} \text{ \AA}^{-1}$, the correlation lengths of 45 and 30 \AA were obtained for 0.02 and 0.04 g/cm³, respectively. These values agree closely with the data obtained by M.Daoud³⁾.



REFERENCES

- 1) S.Kinugasa, H.Hayashi, F.Hamada, A.Nakajima, K.Kurita, S.Nakajima, M.Furusaka and Y.Ishikawa, Polymer Communications, 27, (1986) 47
- 2) T.Ueki, Y.Hiragi, Y.Izumi, H.Tagawa, M.Kataoka, Y.Muroga, T.Matsushita and Y.Amemiya, KEK Report (1985) in the press.
- 3) M.Daoud, J.P.Cotton, B.Farnoux, G.Jannink, G.Sarma, H.Benoit, R.Duplessix, C.Picot, and P.G.de Gennes, Macromolecules, 8, (1975) 804

STUDY ON THE SIZE AND SHAPE OF FINE PARTICLES OF SEMICONDUCTORS BY
MEANS OF X-RAY SMALL-ANGLE SCATTERINGTadashi ITOH, Mikio KATAOKA, Yasuo IWABUCHI, Tatzuo UEKI*
and Yoshiyuki AMEMIYA**

Faculty of Science, Tohoku University, Sendai, Miyagi 980

*Faculty of Engineering Science, Osaka University, Toyonaka, Osaka 560

**Photon Factory, National Laboratory for High Energy Physics, Ohō-machi, Ibaraki 305

Introduction

In NaCl crystals heavily doped with Cu⁺ ions, CuCl microcrystals are known to be formed by coagulation of Cu⁺ ions. Exciton states in such microcrystals are considered to be influenced by quantum size effects, in other words, the finiteness of crystal lattices, because they are broadened and shifted to the higher energy side by several tens of meV compared with those of the bulk exciton.¹⁾ The purpose of this work is to know the size and the shape of the microcrystals with use of small-angle X-ray scattering (SAXS) and to make sure of the correlation between the microcrystal size and the blue shift of the exciton luminescence energy.

Experimentals

Single crystals of NaCl doped with CuCl by 1 mol% were grown in an ordinary transverse Bridgman furnace. As-grown crystals were cleaved into several pieces, with which various heat treatments were performed in vacuum as are listed in Table 1. Methods for the measurements of luminescence spectra and SAXS are the same as reported before.²⁾

Results and Discussion

Guinier plots of the SAXS intensities for various samples were examined. Each plot is found to be approximated with a single straight line except for #01. The radii of gyration R_g of the CuCl microcrystals are summarized in Table 1. In rapid cooling R_g becomes smaller for longer annealing. Luminescence spectra for various samples are also measured at 77K. Each spectrum has a broad peak on the higher energy side of the bulk Z₃ exciton peak. A close correlation is found between R_g and the peak energy E_{ex} of the exciton luminescence; the smaller the radius, the more the blue shift of the luminescence peak.

Firstly, it is assumed for simplicity that all the microcrystals are spherical in shape and have the same size. In Fig.1 the mean peak energies of the exciton luminescence E_{ex} versus

sample number	annealing (°C), (hour)	cooling (hour)	R_g (nm)
#01	as grown		>3.95
#02	630 47	Slow 39	4.40
#03	630 0.33	Rapid	3.82
#04	630 12	Rapid	2.59
#05	630 47	Rapid	2.08±0.03
#12	600 96	Slow 12	3.58
#13	600 96	Rapid	1.74±0.06
#22	730 18.5	Rapid	2.76
#23	730 18.5 and 530 21	Repid	2.41

Table 1

the reciprocals of the square radii a^{-2} of CuCl microcrystals are plotted by open circles for the different samples. The length of a vertical bar on each data point indicates the amount of change in the peak energy caused by the X-ray irradiation. The solid curves 1 and 2(2') represent theoretical ones for the electron-hole confinement and for the exciton confinement (with exciton dead layer of $0.5a_{ex}$), respectively.³⁾ The curve 3 represents the result of the variational calculation in spherical particles. It is obvious that the experimental points are well fitted with the curve 2', which means that the exciton translational motion is quantized.

Secondly, further informations about the shape of the microcrystals are obtained both from the volume of the microcrystals and from the detailed curve fittings with the SAXS profiles. The result shows that oblate ellipsoids are better for the fitting with the experimental data, and the shape of the microcrystals is approximated to be a thin platelet except for extremely small size of less than 2 nm, where the number of spherical microcrystals reaches to a considerable amount compared with that of the platelet ones. The result of the variational calculation for thin slab is drawn by a curve 4, but the exciton confinement model (curve 2') is found to be still valid for microcrystals of non-spherical shape.

References

- 1) T. Itoh and T. Kirihaara, J. Luminescence 31/32 120 (1984).
- 2) T. Itoh et al. PF Activity Report #4, 223 (1986).
- 3) T. Itoh and Y. Iwabuchi, to be published in J. Luminescence (1988).

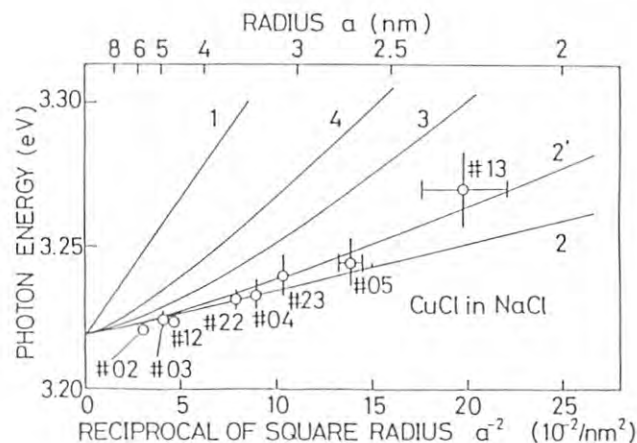


Fig.1

* a_{ex} is an exciton effective Bohr radius and is about 0.7 nm in CuCl.

AGGREGATION PROCESS OF β -CASEIN

Kanji KAJIWARA,^{a)} Ryoya NIKI,^{b)} Hiroshi URAKAWA,^{c)}
Yuzuru HIRAGI,^{a)} Nobuo DONKAI,^{a)} Masanobu NAGURA^{d)}

- ^{a)} Institute for Chemical Research, Kyoto University, Uji, Kyoto-fu, 611 Japan
^{b)} Faculty of Agriculture, Hokkaido University, Kita-ku, Sapporo, 060 Japan
^{c)} Faculty of Engineering and Design, Kyoto Institute of Technology,
Matsugasaki, Sakyo-ku, Kyoto, 606 Japan
^{d)} Faculty of Textile Research, Shinshu University, Ueda, Nagano-ken, 386 Japan

INTRODUCTION

β casein monomer consists of 209 aminoacids and its molecular weight is calculated as 24000. β casein possesses 40 successive polar units in one chain end and 74 non-polar units in the other end, so that a β -casein molecule is regarded as an approximate amphiphile. Though β casein exhibits no secondary structure, the light scattering from β -casein solutions shows the formation of micelles with increasing temperature and/or concentration where the molecular weight increases without expanding its micellar dimension. Various models were proposed for the structure of micelles, though no direct proof was available for these proposed micellar structures. The present work is aimed to examine the structural change of β -casein micelles as a function of temperature by means of the small-angle X ray scattering.

EXPERIMENTAL

β caseins were prepared by urea fractionation according to von Hippel, and dissolved in 0.2M phosphate buffer adjusted to pH 6.7. The concentration of each solution was estimated by applying the Kjeldhal method after sufficient dialysis against buffer. The SAXS measurements were performed on these solutions at 15°C, 20°C and 25°C with a SAXES focusing optics installed at the BL-10C.

RESULTS AND DISCUSSION

β casein self-associates in solution with increasing temperature, and its micelle consists of approximately 50 monomers at 20°C in the spherical form of ca. 100Å in diameter. A hard sphere with radiating long arms is suggested as a possible model of β -casein micelle¹⁾ though this model fails to describe the process of the molecular weight increase of the micelle with temperature while maintaining its original dimension.

The scattered intensities were Fourier-transformed to yield the distance distribution function $p(r)$ and the $f(r)$ function defined by $f(r) \equiv p(r)/r$, which exhibited the characteristics of oblate ellipsoids (see Fig.1). The scattered intensities were simulated as demonstrated in Fig.2 with a model ellipsoid by applying the non-linear least-square method SALS, giving the dimension at each temperature as

semi-axes	5°C	15°C	25°C
$a(\text{\AA})$	108.0	107.6	97.8
$b(\text{\AA})$	112.7	114.7	140.4
$c(\text{\AA})$	19.1	43.8	62.1
$R_G(\text{\AA})$	70.3	73.0	81.4

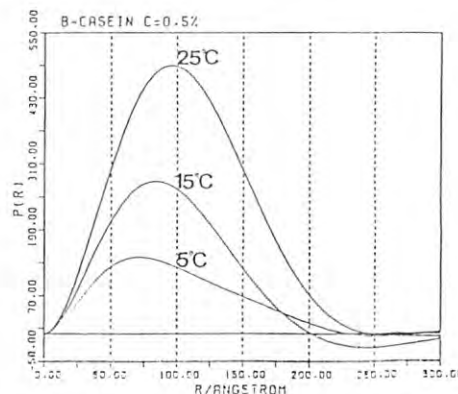


Fig.1: The distance distribution function of β -casein (0.5% in PB) at various temperatures.

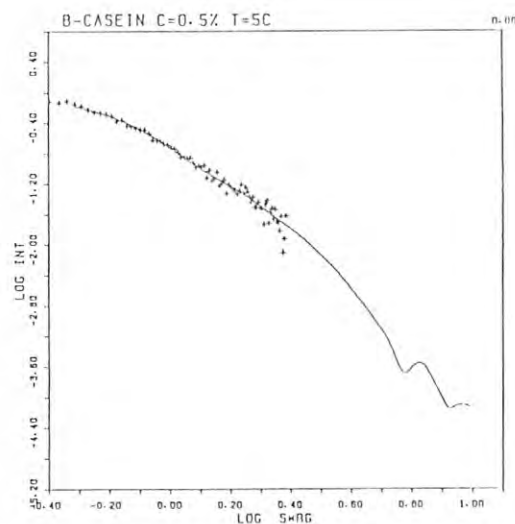


Fig.2: An example of the observed and simulated scattered intensities where the dimension of the model oblate ellipsoid is given in the table in the text.

The semi-axis c increases with temperature and the shape of the β -casein micelle approaches to a sphere while other dimensions of semi-axes a and b hardly change, so that the increase of R_G is not appreciable. Thus the β -casein molecules seem to form a micelle of the shape of a flat oblate ellipsoid which grows in the c -axis direction only with increasing temperature.

REFERENCES

- 1) A. Thurn, *Ph.D. Thesis*, Freiburg University, 1986

SMALL-ANGLE X-RAY SCATTERING STUDY ON HIGHER-ORDER STRUCTURES OF CHROMATIN IN SOLUTION

Yoji INOKO, Satoru FUJIWARA, Masaki INADA, Tatzuo Ueki, Yuzuru HIRAGI⁺
Mikio KATAOKA⁺⁺ and Yoshiyuki AMEMIYA^{*}

Department of Biophysical Engineering, Faculty of Engineering Science,
Osaka University, Toyonaka, Osaka 560

⁺Institute for Chemical Research, Kyoto University, Gokasho Uji, Kyoto 611

⁺⁺Department of Physics, Faculty of Science, Tohoku University, Sendai, Miyagi 980

^{*}Photon Factory, National Laboratory for High Energy Physics, Oho-machi,
Tsukuba-gun, Ibaraki 305

Introduction

It is generally accepted that condensed 30-nm chromatin fibers observed at high ionic strength are generated by higher-order folding of poly-nucleosome chains observed as 10-nm fibers at low ionic strength. In what manner are the 10-nm fibers folded into the 30-nm fibers? What is the higher-order structure of chromatin like? There are now several types of models for chromatin structures¹⁻³⁾ proposed from studies by the use of a variety of techniques. However, the detailed subunit structure of chromatin in a condensed state has not been established yet.

We investigated the effect of monovalent cation on both the structures of chromatin fragment and nucleosome core particle by means of X-ray solution scattering. This report describes results of the scattering experiments mainly on chromatin solutions.

Experimental and Results

Chromatin fragments consisting 20-50 nucleosomes were prepared by a brief micrococcal nuclease digestion of rat thymus nuclei and core particles with a length of 140-150 base pairs of DNA by a further digestion of the fragments. Both samples were used in 1mM Tris-HCl, 0.2mM EDTA, pH7.5 with 0-75mM NaCl.

Scattering patterns were collected on a double-focusing X-ray camera⁴⁾ for solution at BL-10C, using 0.148 nm wavelength.

Fig.1 illustrates the X-ray scattering patterns, in plots of $\log(sI(s))$ vs. s , from dilute solutions of chromatin fragments (3mg/ml) at different NaCl concentrations. A prominent feature is that the scattered intensity near

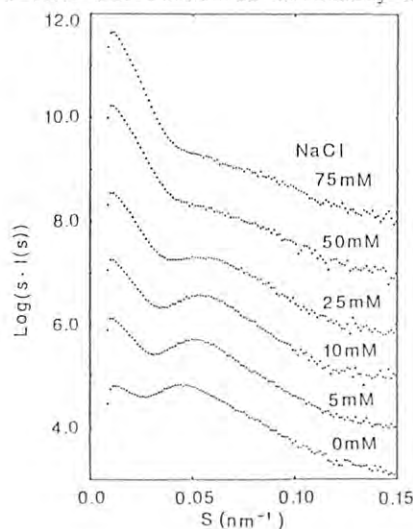


Fig.1

zero angle abruptly increases with raising the NaCl concentration. A cross sectional Guinier-plot ($\log(sI(s))$ vs. s^2 plot) was done for the data in the small angle region of $s < 0.025 \text{ nm}^{-1}$. This plot could give radius of gyration, R_g , and relative mass per unit length, $\sqrt{I(0)}$, of chromatin fragment when regarded as a rod-like particle. Fig.2 shows the changes in values for R_g and $\sqrt{I(0)}$ as functions of NaCl.

Each curve shown in Fig.1 is also characterized by a maximum around 0.05 nm^{-1} and a minimum around 0.03 nm^{-1} , originating from the shape and/or internal structure of chromatin. These maximum and minimum are shifted to higher angle with the increasing NaCl concentration, with a disappearance of the maximum beyond 50mM NaCl. According to a solenoid model, the spacings of the maximum and minimum are related to the dimensions of helical diameter and pitch. Their shifts to higher angle can be interpreted as the compaction of helical structure. Our observations indicate that the condensation of chromatin fibers is initiated at very low salt concentration (e.g. <5mM NaCl) even in the case of monovalent cation.

From the results of small-angle X-ray scattering measurements on core particles in solution, it was found that the radius of gyration of the particle is nearly constant from $4.29 \pm 0.01 \text{ nm}$ at 0mM NaCl to $4.24 \pm 0.02 \text{ nm}$ at 25mM NaCl.

References

- 1) J. I. Finch and A. Klug: Proc. Natl. Acad. Sci. USA. 73 (1976) 1897.
- 2) J. Bordas, L. Perez-Grau, M.H.J. Koch, M. C. Vega and C. Nave: Eur. Biophys. J. 13 (1986) 157 and 13 (1986) 175.
- 3) K. O. Greulich, E. Wachtel, J. Ausio, D. Seger and H. Eisenberg: J. Mol. Biol. 193 (1987) 709.
- 4) T. Ueki, Y. Hiragi, M. Kataoka, Y. Inoko, Y. Amemiya, Y. Izumi, H. Tagawa and Y. Muroga: Biophys. Chem. 23 (1985) 115.

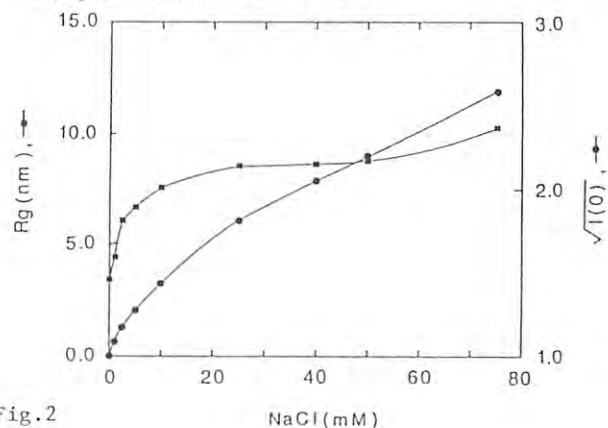


Fig.2

X-RAY SOLUTION SCATTERING STUDIES ON SOLUBILIZED BACTERIORHODOPSIN II.

Mikio KATAOKA¹, Masayoshi NAKASAKO¹, Fumio TOKUNAGA¹
Tatzuo UEKI², Yuzuru HIRAGI³ and Yoshiyuki AMEMIYA⁴

1. Faculty of Science, Tohoku University, Sendai, Miyagi 980
2. Faculty of Engineering Science, Osaka University, Toyonaka, Osaka 560
3. Institute for Chemical Research, Kyoto University, Uji, Kyoto 611
4. Photon Factory, National Laboratory for High Energy Physics, Oho-machi, Tsukuba-gun, Ibaraki 305

INTRODUCTION

Bacteriorhodopsin (bR) is a sole protein of purple membrane and acts as a light-driven proton pump. In order to obtain the structure information during the photocycle, we studied solubilized bR as well as purple membrane. The structure of solubilized bR was studied by small-angle X-ray scattering (SAXS) techniques with contrast variation method. It is suggested that bR exists as a trimeric form in the solubilized bR.¹ Moreover, with the combination of contrast variation and heavy atom labeling, we obtained important informations on solubilized bR.

EXPERIMENTAL

Preparation of solubilized bR was described in previous issue.¹ For heavy atom labeling, purple membranes were iodinated before solubilization. In our condition, 6 or 7 iodine atoms bound to one bR molecule in solubilized I-bR.

SAXS experiments were performed with SAXES. Sucrose was used for varying the solvent electron density. Scattering profiles were recorded at following eight sucrose concentrations; 0, 2.5, 5, 7.5, 10, 12.5, 30, 40% (w/w). Final protein concentration was adjusted to 3mg/ml.

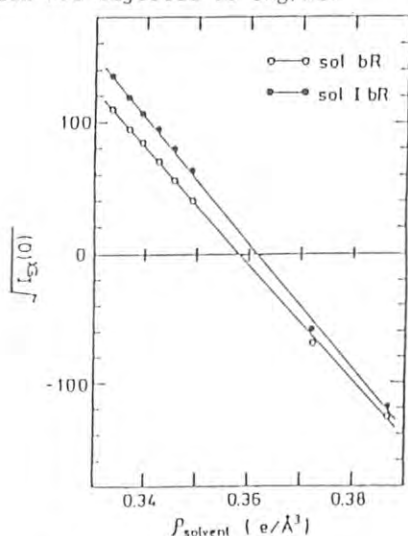


Fig. 1 The dependence of zero angle scattering amplitude on solvent electron density.

Structure parameter	sol bR	sol I-bR
$\bar{\rho}$ ($e/\text{\AA}^3$)	0.3586	0.3617
R_c (\AA^2)	36.8	37.3
α ($e/\text{\AA}$)	0.1	1.0
β ($e^2/\text{\AA}^4$)	0.03	0.03

Table I Structure parameters of sol bR and I-bR

RESULTS

The radius of gyration and zero angle scattering intensity at each sucrose concentration were obtained with ordinary Guinier analysis. From Fig.1, average electron density ($\bar{\rho}$) of solubilized bR and I-bR were determined and listed in Table I. The increment of $\bar{\rho}$ in solubilized I-bR clearly reflects iodine atoms binding. With this increment and the volume of solubilized bR estimated from shape scattering function, the number of binding iodine atoms was determined to 22±1. This fact strongly suggests that there are three bR molecules in solubilized bR.

Structure parameters concerning with the internal structure and the shape were determined from Fig.2 with the following relation (Table I).

$$R_g^2 = R_c^2 + \alpha/\Delta\rho - \beta/(\Delta\rho)^2$$

By comparing the structure parameters of solubilized I-bR with those of solubilized bR, following informations were obtained. 1) The shape of solubilized bR and I-bR are identical (from R_c). 2) Mean square distance of iodine atom position is found to be 1600\AA^2 (with the difference of α). This value can be realized only in the case of trimeric bR. 3) Iodine atoms distribute symmetrically about the centre of solubilized I-bR (from β).

These informations obtained with the combination method sufficiently confirm the previous suggestion.

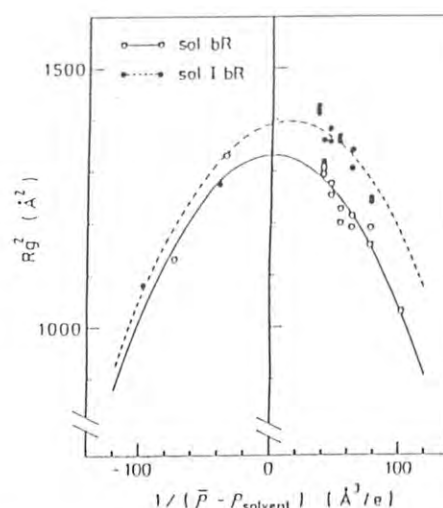


Fig. 2 Stuhmann plot (Radius of gyration, R_g , against inverse of contrast)

REFERENCES

1. M. Kataoka et.al. PF Activity Report #4, 213 (1986)

MICROSEGREGATED STRUCTURE IN THE SILK FIBROIN FROM BOMBYX MORI

Masanobu NAGURA^{a)}, Yuzuru HIRAGI^{b)}, Kanji KAJIWARA^{b)}, Hiroyuki TAGAWA^{c)}, Masuhiro TSUKADA^{d)}^{a)} Faculty of Textile Science and Technology, Shinshu University, Ueda, Nagano-ken, 386 Japan^{b)} Institute for Chemical Research, Kyoto University, Uji, Kyoto-fu, 611 Japan^{c)} Faculty of Science and Technology, Nihon University, Chiyoda-Ku, Tokyo, 100 Japan^{d)} Sericultural Experiment Station, Yatabe-chou, Tsukuba-gun, 305 Japan

INTRODUCTION

Recently, it has been found that the silk fibroin from *Bombyx mori* is very useful for binding enzymes¹⁾, which is probably due to the existence of an amorphous region, but no one has elucidated the fine structure such as the dispersed state in the silk fibroin.

In this report, investigations were made on the fine structure of the silk gland dried for various time by using small angle X-ray scattering (SAXS).

EXPERIMENTALS

Silk glands from *Bombyx mori* dried for various time at 50° C were used for SAXS measurements.

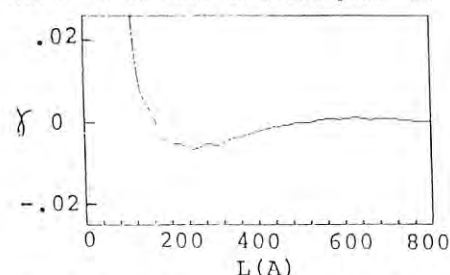
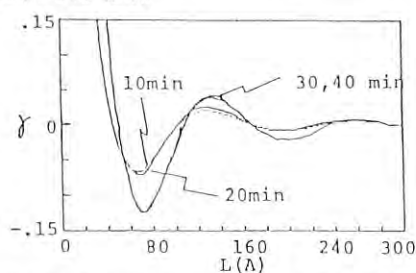
The SAXS experiments were performed with point-focusing optics installed at the BL-10C.

Electron micrographs were obtained by using a Nihon Denshi JEM 100 CX-11 transmission electron microscope. The sample used was stained by methods previously described²⁾. Ultrathin sections were cut perpendicular to silk gland with a glass knife, and stained for 30 min in 70 % ethanol saturated with uranyl acetate.

RESULTS AND DISCUSSION

Fig. 1 shows the dependence of correlation length (L) on three dimensional electron density correlation function $\gamma(L)$. First peak is not clear. This indicates that the silk gland of about 30 wt% aqueous solution of silk fibroin is almost homogeneous aqueous solution.

Fig. 2 shows the dependence of L on $\gamma(L)$ for the silk gland dried for various time at 50° C. There is an obvious first peak at about 130 Å in

Fig. 1 Dependence of L on $\gamma(L)$ of the undried silk gland.Fig. 2 Dependence of L on $\gamma(L)$ of the dried silk gland.

every sample. This indicates a domain structure, namely a microsegregated structure, in the dried silk gland with a mean distance between the centers of neighbouring domains is about 130 Å. This domain structure is formed at early step, and becomes clearly by drying above 30 min, at which density increased abruptly³⁾. According to Lucas et al.⁴⁾ the silk fibroin molecule is a block co polymer consisting of two blocks; one block is a chain of very simple amino acids such as alanine and glycine forming only crystalline region, and the other is a chain having the polar and bulky amino acids forming only amorphous regions. Therefore it is suggested that the bundles consist of only the crystalline regions separate clearly from the amorphous region in the dried silk gland.

Fig. 3 is an electron micrograph with the electron beam normal to the ultrathin section. A bundle structure is observed. The mean long period perpendicular to the direction of the axis of the bundles is about 120 Å, corresponding to the mean distance between the centers of neighboring domains.

REFERENCES

- 1) A. Kuzuhara, T. Asakura, R. Tomoda and S. Matsunaga, *R.P.P.P.J.*, **XXIX**, 725 (1986)
- 2) H. Akai and K. Kataoka, *J. Sericult. Sci. Japan*, **47**, 273 (1978).
- 3) M. Nagura, M. Tsukada and H. Ishikawa, *Sen i Gakkaishi*, **43**, 92 (1987).
- 4) F. Lucas, J. T. B. Shaw, and S. G. Smith, *Biochem. J.*, **66**, 468 (1957)

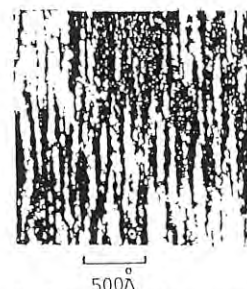


Fig. 3 Electron micrograph of the dried silk gland.

STRUCTURAL STUDIES ON ALDOLASE BY MEANS OF TIME-RESOLVED X-RAY SCATTERING

Mamoru SATO, Youichi KATO, Nobuo TANAKA, Yukiteru KATSURU, Tatzuo UEKI^{*1},
Mikio KATAOKA^{*2}, Yuzuru HIRAGI^{*3}, and Yoshiyuki AMEMIYA^{*4}

Institute for Protein Research, Osaka University, Suita, Osaka 565

^{*1}) Faculty of Engineering Science, Osaka University, Toyonaka, Osaka 560

^{*2}) Faculty of Science, Tohoku University, Sendai, Miyagi 980

^{*3}) Institute for Chemical Research, Kyoto University, Uji, Kyoto 611

^{*4}) Photon Factory, National Laboratory for High Energy Physics,
Tsukuba, Ibaragi 305

Introduction

Rabbit muscle aldolase is an enzyme which splits fructose 1,6-diphosphate and yields in glyceraldehyde 3-phosphate and dihydroxyacetone phosphate in the second stage of glycolysis. The enzyme is a tetramer composed of four identical subunits with the molecular weight of 40,000. Ohga et al¹⁾ have subjected this enzyme to a stopped-flow light scattering and fluorescence, and suggested that the tetrameric enzyme was dissociated into a monomer form with the decrease of pH value to 2.7. To elucidate the structure-function relationship of the enzyme by scrutinizing this structural change, time-resolved X-ray scattering experiment was undertaken using a stopped-flow mixing device.

Experimental

Sample preparation ----- Rabbit muscle aldolase was purchased from Boehringer mannheim as a crystalline suspension in 3.2M ammonium sulfate at pH6. After centrifugation of the suspension, the enzyme solution was dialyzed against 0.01M sodium citrate buffer, pH5.4 for two days. Protein concentration was determined by UV absorption at 280nm using $E_{1\%}^{1\text{cm}} = 9.1$. Buffer solution of pH2.7 used for stopped-flow experiment was prepared from 0.2M sodium citrate and 0.2N HCl solutions.

X-ray Experiments ----- An X-ray measurement was undertaken on a small-angle X-ray scattering apparatus at the beam-line BL-10C which installs a semipoint-focussing X-ray optics. The scattered X-rays were recorded on a one-dimensional position-sensitive proportional counter (receiving slit of 2.0mm). The sample-to-detector distance was 790mm and the wavelength used was 1.488Å. A stopped-flow mixing device was constructed by Unisoku Co. Ltd.. Equal volumes of the enzyme and buffer (pH2.7) solutions were immediately mixed and transferred into a sample chamber (4 x 6mm) with an X-ray path of 1mm. The concentration of the enzyme was 1% in the reaction mixture. To clarify the initial and final stages of a reaction, static measurements of scattering intensities were carried out in 1% enzyme solutions at pH5.4 and 2.7. The respective accumulations of scattered X-rays were 900s. At the time-resolved measurement, scattered X-rays were recorded in 30 time-frames after mixing in the stopped-flow device without any time-gaps. In each frame, scattered X-rays were accumulated for either 2 or 60s. As for the experiment of accumulation time with 2s, ten cycles of these measurements were performed to obtain sufficiently intense scattered X-rays.

Results and Discussion

Radius of gyration, R_g and zero-angle intensity, $I(0)$ were estimated from Guinier plot of scattering intensities by a least-squares method. The time courses of the R_g and the $I(0)$ are depicted in Fig.1. From this figure, it was found that both of the parameters were appreciably decreasing with time until 50s after mixing, indicating the dissociation of the enzyme. In addition, since the static measurement at pH2.7 gave $R_g = 24.2\text{Å}$, it was followed that the reaction reached equilibrium at 50s after mixing, and the tetrameric enzyme was completely dissociative to a monomer at this stage. On the other hand, the R_g of the tetramer was estimated to 36.8Å from the static measurement at pH5.4, and was significantly different from that of the first frame of the time-resolved experiment (accumulation time is 2s per frame). This discrepancy may be attributable to the result in fast dissociation-reaction just after mixing. To assess this fast reaction, it is necessary to measure the scattered X-rays at the time interval shorter than that of the present study, which is thought to be subsequent experiment of this project.

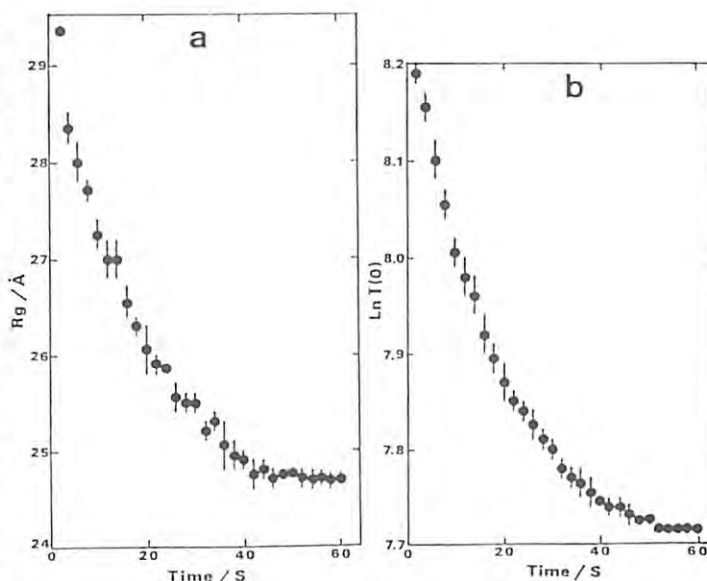


Fig.1. Time courses of (a) radius of gyration, R_g and (b) zero-angle scattering intensity, $I(0)$. The time-resolved measurement was done in the accumulation time of 2s per frame. The errors are expressed by vertical lines in the data points.

Reference

- 1) Y. Ohga, M. Nakanishi, and M. Tsuboi, *Bull. Chem. Soc. Jpn.*, **57**, 692-695 (1984).

LYOTROPIC MESOPHASE OF IMOGOLITE OBSERVED BY SMALL-ANGLE X-RAY SCATTERING

Kanji KAJIWARA,^{a)} Nobuo DONKAI,^{a)} Hiroshi URAKAWA,^{b)}
Yuzuru HIRAGI,^{a)} Akiyoshi KAWAGUCHI,^{a)} Masanobu NAGURA^{c)}

^{a)} Institute for Chemical Research, Kyoto University, Uji, Kyoto-fu, 611 Japan

^{b)} Faculty of Engineering and Design, Kyoto Institute of Technology,
Matsugasaki, Sakyo ku, Kyoto, 606 Japan

^{c)} Faculty of Textile Research, Shinshu University, Ueda, Nagano-ken, 386 Japan

INTRODUCTION

Imogolite is a hydrated aluminium silicate of a rod like shape, found in the clay fraction of Japanese soil derived from glassy volcanic ash or in weathered pumice beds. As expected from its shape, imogolite forms lyotropic mesophase when the imogolite concentration exceeds a certain point defined as an A point.¹⁾ The raft-like imogolite sheet floating in the mesophase has been observed by electron microscope from the solution above the A point,²⁾ though the onset of the fragmental imogolite sheet is expected at much lower concentrations. The exact dimension of imogolite was evaluated from its dilute solution properties³⁾ as a hollow cylinder of a few thousands Å in length with an outer diameter 25.2Å and an inner diameter 15.5Å. We observe the process of forming the mesophase with the small-angle X-ray scattering (SAXS) from the solutions of these cylindrical molecules in this work.

EXPERIMENTAL

Two fractionated imogolite (Imogolite a and Imogolite c) of different molecular weights were used for SAXS measurements. These samples were characterized by static and dynamic light scattering as follows:

Imogolite	$M_w \cdot 10^{-6}$	$\langle S^2 \rangle^{1/2} (\text{Å})$	$R_H (\text{Å})$
a	0.980	438	180
c	2.43	1053	386

The A and B points (lower and upper phase boundary concentrations) were estimated as 0.0355% and 0.0577% for Imogolite a, and 0.0175% and 0.0333% for Imogolite c, respectively, in terms of imogolite weight fraction. The SAXS measurements were performed with a SAXES focusing optics installed at the BL-10C.

RESULTS AND DISCUSSION

The distance distribution functions (defined as the Fourier transform of the scattered intensities) are shown in Fig.1 (Imogolite a) and Fig.2 (Imogolite c) where the imogolite concentrations are indicated in the figures. The first double peaks (appeared around 18 ~ 45Å) reflect the rod cross-section of two imogolite molecules aligned in parallel. The Guinier plot for cross-section yielded the radii of gyration as 10.5Å and 13.8Å, respectively, for the cross-section of a single imogolite molecule and a bimolecular aggregate.²⁾ The second peak characteristic to the mesophase appears around 170Å above the A point (see Figs.1 and 2). The third peak appears around 270Å when the imogolite concentration approaches the B point, though a remaining background scattering due to the X-ray

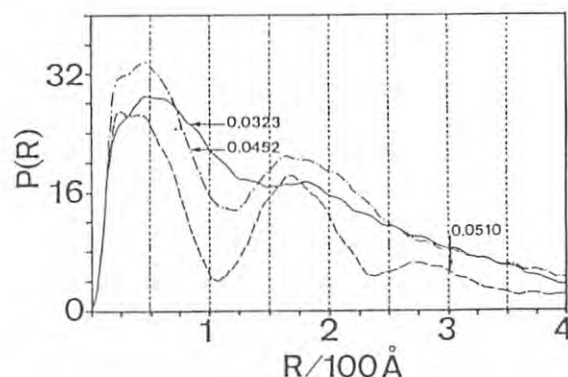


Fig.1: Distance distribution function of Imogolite a in solution

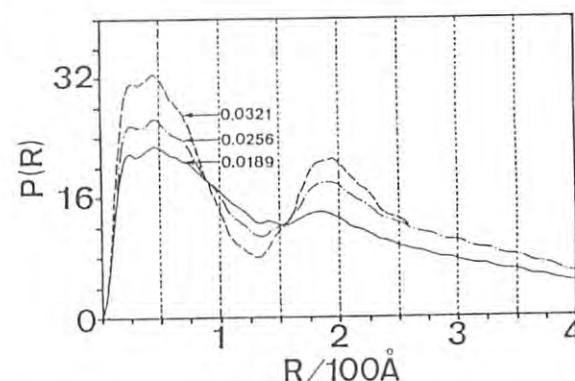


Fig.2: Distance distribution function of Imogolite c in solution

absorption in high imogolite concentrations causes Fourier ripples smearing the distance distribution curves. The molecular arrangement of imogolite in mesophase was speculated from various periodic structures observed by electron microscope.⁴⁾ The ordering of imogolite molecules proceeds in such a way that imogolite molecules align loosely in parallel at first and form raft-like sheet clusters exhibiting various periodicities. The mesophase model consistent with the present observation is being considered.

REFERENCES

- 1) K. Kajiwara, N. Donkai, Y. Hiragi, H. Inagaki, *Macromol. Chem.*, **187**, 2883 (1986)
- 2) K. Kajiwara, N. Donkai, Y. Fujiyoshi, Y. Hiragi, H. Urakawa, H. Inagaki, *Bull. Inst. Chem. Res., Kyoto Univ.*, **63**, 320 (1985)
- 3) N. Donkai, H. Inagaki, K. Kajiwara, H. Urakawa, M. Schmidt, *Macromol. Chem.*, **186**, 2623 (1985)
- 4) K. Kajiwara, N. Donkai, Y. Fujiyoshi, H. Inagaki, *Macromol. Chem.*, **187**, 2895 (1986)

EFFECTS OF IONIC STRENGTH, TEMPERATURE AND THE COENZYME ON THE QUATERNARY STRUCTURE AND ACTIVITY OF TRYPTOPHANASE

Yuzuru HIRAGI¹, Tsuneo ODA², Masanobu TOKUSHIGE², Kanji KAJIWARA¹, Yoh SANO³, Euiho KIM¹, Tazuo UEKI⁴ and Mikio KATAOKA⁵

- 1) Institute for Chemical Research, Kyoto University, Uji, Kyoto 611
- 2) Faculty of Science, Kyoto University, Sakyo-ku, Kyoto, 606
- 3) National Institute of Agrobiological Resources, Yatabe, Ibaraki 305
- 4) Faculty of Engineering Science, Osaka University, Toyonaka, Osaka 560
- 5) Faculty of Science, Tohoku University, Sendai, Miyagi 980

Introduction

Tryptophanase from *Escherichia coli* B/117-A is a pyridoxal phosphate dependent enzyme that catalyses α , β -elimination and β -replacement reactions in addition to the decomposition of L-tryptophan and requires monovalent cations for activity. The enzyme has a molecular weight of 220,000 and is composed of four identical subunits. Each subunit has one binding site for the coenzyme, pyridoxal phosphate. In the presence of 100 mM KCl, apoenzyme, which of course has no enzymatic activity, undergoes dissociation to dimers at 5°C whereas holoenzyme does not. At 20°C sedimentation velocity of holoenzyme is larger than that of apoenzyme. It is recently found that the holoenzyme has the activity even in the more dilute monovalent cation concentration of 30mM KCl.

Results and Discussion

Results of the small-angle X-ray scattering experiments with SAXES at BL-10C with KCl concentration of 30mM if added are shown in Table 1. Radii of gyration of the apoenzyme at 5°C are as same large as that of 20°C, suggesting the apoenzyme conserves tetramer structure in this ionic strength even at lower temperature. Throughout the whole scattering experiments under the condition given in Table 1, the radii of gyration fall into $38.5 \pm 1.0 \text{ \AA}$ irrespective of the solvent condition. Considering of the experimental error, it seems that the change of the structure or size of the enzyme was very slight or did not changed.

In spite of the conservation of the R_g value under different conditions, scattering curves at very small angle, the profile of which reflects the inter-particular interaction owing to the change in the state of surface of the enzyme (for example electrostatic charge), differs each other. Addition of KCl weakens the inter-particular interaction. This can be explained by the screening effect of the potassium and chloride ions attaching the small ions to the surface of the charged amino acid residues to cancel the surface charge. The attachment of the pyridoxal phosphate increased the interaction. Namely the holoenzyme molecules more strongly interact each other than the apoenzyme. Considering from the charge of the coenzyme, it is difficult to explain the results by screening effect. Rather it is more plausible to interpret that the subunits are slightly rearranged by the addition of the

coenzyme to change the state of the surface more interactive than that of the apoenzyme.

The above discussion is valid only for the solution of 30mM KCl concentration. When KCl concentration is increased to 100mM, radii of gyration of apoenzyme at 5°C decreased considerably whereas that of holoenzyme did not, suggesting that the apoenzyme split into dimer as is known from sedimentation and HPLC experiments.

From the present experimental results we may infer the role of the potassium ion to the activity is in the first place to adjust the electrostatic charge at the coenzyme binding site or active site. And suitable distribution of the charge at the site render the enzyme to catalyze the reaction.

Temp °C	Prot. Conc.	Coenz. & K ⁺	R _g (Å)
5.1	45.1 mg/mL	Holo, +K	38.0
		Apo, +K	38.4
		Holo, -K	39.1
		Apo, -K	38.9
	10.0 mg/mL	Holo, +K	38.9
		Apo, +K	37.8
		Holo, -K	39.3
		Apo, -K	38.0
20.2	45.1 mg/mL	Holo, +K	38.7 (38.9)
		Apo, +K	37.5 (37.0)
		Holo, -K	38.7 (38.8)
		Apo, -K	39.2 (37.7)
	10.0 mg/mL	Holo, +K	38.2
		Apo, +K	38.6
		Holo, -K	39.1
		Apo, -K	39.3
	5.0 mg/mL	Holo, +K	38.6
		Apo, +K	38.9
		Holo, -K	39.1
		Apo, -K	38.9
	45.1 mg/mL	Holo, +K	38.2
		Apo, +K	38.6
		Holo, -K	39.1
		Apo, -K	39.3
	10.0 mg/mL	Holo, +K	38.6
		Apo, +K	38.9
		Holo, -K	39.1
		Apo, -K	38.9
	5.0 mg/mL	Holo, +K	39.4 (39.0)
		Apo, +K	39.1 (39.6)
		Holo, -K	39.2 (39.1)
		Apo, -K	38.8 (39.4)

Table.1 Radii of gyration (R_g) of tryptophanase in 30mM KCl and at various solvent conditions and temperatures. R_g 's are obtained from the Guiner plots in the S^2 range of 2.0 to $4.0 \times 10^{-3} \text{ \AA}^{-2}$, ($S = 4\pi \sin \theta / \lambda$ being 2θ scattering angle and λ wavelength). R_g values in the parentheses are from S^2 range of 1.0 to $5.0 \times 10^{-3} \text{ \AA}^{-2}$.

THE STRUCTURE OF P2 MYELIN PROTEIN IN THE SOLUTION

Michio Kimura¹, Norio Masaki², Keiichi Uemura³, Yuzuru Hiragi⁴, Kanji Kajiwar⁵,
and Hiroshi Urakawa⁶

¹Niigata College of Pharmacy, 5829 Kamishin'ei-cho, Niigata 950-21, Japan

²Faculty of Pharmaceutical Sciences, Kyoto University, Yoshida, Sakyo-ku, Kyoto 606, Japan

³Department of Physiology, Saitama Medical School, Iruma-gun, Saitama, 350-04, Japan

⁴Laboratory of Physical Chemistry of Enzyme, Institute for Chemical Research, Kyoto-fu, 611, Japan

⁵Laboratory of Molecular Design for Physiological Functions, Institute for Chemical Research, Kyoto University, Uji, Kyoto-fu, 611, Japan

⁶Faculty of Polytechnic Sciences, Kyoto Institute of Technology, Kyoto, Japan

Introduction

The P2 protein is a basic protein localized in peripheral nerve myelin. K. Uyemura et.al. have developed purification procedures of the bovine P2 protein and characterized some of its properties. They had determined the complete amino acid sequence of bovine P2 protein (1, 2). The P2 protein is considered to be important as the most likely candidate of neuritogenic protein to induce experimental allergic neuritis(EAN).

The structure of the bovine P2 protein in 0.03 M HCl buffer was examined by means of the small-angle X-ray scattering(SAXS).

is developing now. The simple model analysis is developing with a non-linear least-squares fitting in terms of two simple triaxial bodies; an elliptic cylinder, and an ellipsoid.

References

- 1) K. Uemura, C. Tobar and S. Hirano, *Biochim. Biophys. Acta* **214**, 190 (1970).
- 2) K. Kitamura, M. Suzuki, A. Suzuki, and K. Uyemura *FEBS LETTERS*, **115**, 27.
- 3) K. Uyemura, T. Yamanaka, and K. Uyemura *Biochim. Biophys. Acta* **375**, 582(1975)
- 4) T. Ueki et. al. *Biophysical Chemistry*, **23**, 115(1985)

Experimental and Results

The P2 protein was extracted by the method of K. Uemura et. al.(3) Experiments were carried out by using the small-angle scattering equipment designed by T. Ueki and Y. Hiragi et. al. (4), set up at the Photon Factory in the National Laboratory for High-Energy Physics, Tsuba. The solutions for small-angle X-ray scattering were prepared by dissolving P2 protein in 0.03 M HCl (pH=1.30). Three solutions of P2 protein were used in the concentration range of 1.5, 1.0, and 0.5% respectively. The detail analyses were achieved by using 1.5 % solution because other lower concentration solutions caused the strong back ground. The original scattering curve is shown in Fig. 1 for 1.5 % solution. The Guinier plot (Fig. 2) using the data yields 16.45 Å for the radius of gyration R_g of P2 protein. The scattering data were extrapolated to the larger h region to compute the distance distribution function (Fig. 3). These two independently estimated values of R_g were considered to be good agreement. The further examinations regarding the conformation of P2 protein

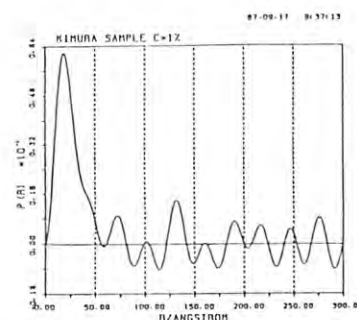
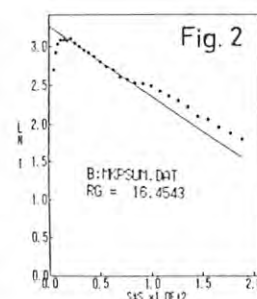
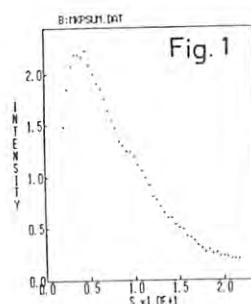


Fig. 3

X-RAY SOLUTION SCATTERING STUDIES ON PHYTOCHROME PHOTOTRANSFORMATION

Satoru TOKUTOMI¹, Mikio KATAOKA², Jun SAKAI^{1,3,4}, Masayoshi NAKASAKO²,
Fumio TOKUNAGA², Mitsuo TASUMI⁴ and Masaki FURUYA^{1,3}

¹Division of Biological Regulation, National Institute for
Basic Biology, Okazaki, 444

²Department of Physics, Faculty of Science, Tohoku University,
Aobayama, Sendai, 980

³Frontier Research Program, RIKEN, Wako, Saitama, 351-01

⁴Department of Chemistry, Faculty of Science, University of
Tokyo, Hongo, Bunkyo-ku, Tokyo 113

Introduction

Phytochrome, a noble photoreceptor protein in green plants for a variety of photomorphogenic responses, undergoes photoreversible transformation between red-light-absorbing form (P_r) and far-red-light-absorbing form (P_{fr}). We are trying to figure out the conformational change of phytochrome by small angle X-ray scattering (SAXS) to understand the molecular basis of the phytochrome-mediated responses. We have obtained, so far, the informations regarding the macromolecular structure of the pea 121-kDa phytochrome and its 114-kDa chromopeptide in P_r .

Experimental and Results

SAXS was measured on a focusing optics, Small-Angle X-ray Scattering Equipment for Solution at BL-10C¹, where the wavelength of X-ray was 1.49 Å. The obtained data were analyzed by Guinier plot². The plot can be approximated by a straight line in the $S^2 \times 10^6$ region from 20 to 60 at the concentrations below 0.5% (w/v) with

both the phytochrome and the chromopeptide (see the Figure). R_g (radius of gyration) and $I(0)$ (scattering intensity at zero angle) were determined from the slope and the intercept with y axis, respectively.

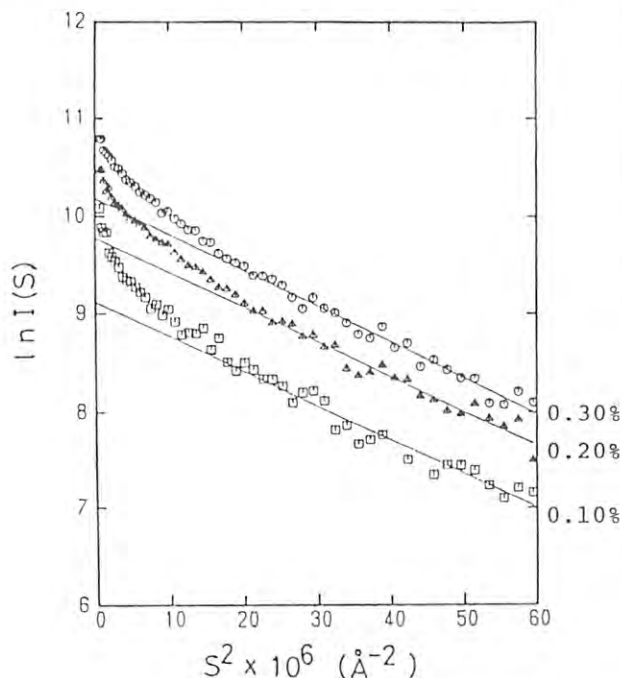
The molecular mass of the 114-kDa chromopeptide was determined as 228 kDa from comparison of the slope of the $I(0)$ vs concentration curves³ for the chromopeptide and for BSA (66 kDa), indicating that the chromopeptide is a dimer. R_g of the phytochrome and the chromopeptide were determined as 54.0 and 53.8 Å respectively, suggesting the 7-kDa N-terminal polypeptide contributes only slightly to the molecular dimension.

If the overall shape of the molecule is assumed to be a sphere, the molecular mass of the sphere with R_g of 53.8 Å is calculated as 1140 kDa using the partial specific volume of 0.74, which is far greater than the obtained molecular mass of 228 kDa. The discrepancy comes from the deviation of the molecular shape from a sphere and (or) the dense distribution of electrons in the marginal area of the molecule.

The apparent molecular mass of the chromopeptide was determined as 314-318 kDa from the steric exclusion column chromatography suggesting the nonglobular shape of the molecule. Assuming the shape is an ellipsoid, a prolate ($a=24$, $b=115$ Å) and an oblate one ($a=85$, $b=9$ Å) are calculated to have the R_g of 53.8 Å and the molecular mass of 228 kDa, where a and b are the equatorial diameter and the half axial length, respectively. The maximum distance of the electron pair in the 114-kDa chromopeptide was estimated as 140 Å from the distance distribution function³, which is comparable with the equatorial diameter of the oblate ellipsoid.

References

- 1) Ueki, T., Y. Hiragi, M. Kataoka, Y. Inoko, Y. Amemiya, Y. Izumi, H. Tagawa and Y. Muroga: *Biophys. Chem.* 23 (1985) 115.
- 2) Guinier, A. and G. Fournet: "Small Angle Scattering of X-Rays" (1955) John Wiley and Sons, New York.
- 3) Glatter, O. in "Small Angle X-Ray Scattering" (Glatter, O. and O. Kratky eds.) (1983) pp.119-166, Academic Press, London.



Guinier plot for 114 kDa-chromopeptide of pea phytochrome in P_r .

SMALL-ANGLE X-RAY SCATTERING STUDY OF AGGREGATION PROCESS OF CUCUMBER GREEN MOTTLE MOSAIC VIRUS PROTEIN

Yoh SANO¹, Hideo INOUE¹, Yuzuru HIRAGI², Kanji KAJIWARA², Hiroshi URAKAWA³, Tatsuo UEKI⁴, and Mikio KATAOKA⁵¹ National Institute of Agrobiological Resources, Yatabe, Ibaraki 305² Institute for Chemical Research, Kyoto University, Uji, Kyoto 611³ Kyoto Institute of Technology, Kyoto 606⁴ Faculty of Engineering Science, Osaka University, Toyonaka, Osaka 560⁵ Faculty of Science, Tohoku University, Sendai, Miyagi 980Introduction

Cucumber green mottle mosaic virus (CGMMV) is a rod-shaped virus and is morphologically similar to tobacco mosaic virus (TMV). The biophysical and biochemical properties of CGMMV are also similar to those of TMV. The homology of the amino acid sequence of both proteins is also very high.

It has been known from sedimentation velocity runs, standard light scattering, and small-angle X-ray solution scattering (SAXS) using synchrotron radiation that the coat protein of TMV self-associates to form several kinds of aggregates depending upon pH, temperature, ionic strength and the protein concentrations. However, few studies have been made on the self-association process of CGMMV protein. We have studied temperature dependence of the aggregate structure by small-angle scattering in order to compare the scheme of aggregation process of CGMMV protein with that of TMV protein.

Results and Discussion

Experiments were performed with the Enzyme Diffractometer BL-10C using different solutions in ionic strength (5, 50, 100 mM phosphate buffer (PB)), protein concentration (5 and 12 mg/ml) and temperature (5 to 25 °C). Fig. 1 shows an example of plot, where logarithms of scattered intensities $I(h)$ were plotted against squares of the scattering vector h ($=4\pi\sin\theta/\lambda$). As the CGMMV protein solution contains several degree of aggregates, the scattering data obtained are the sum of the scattered intensities of each constituent particle. In the present

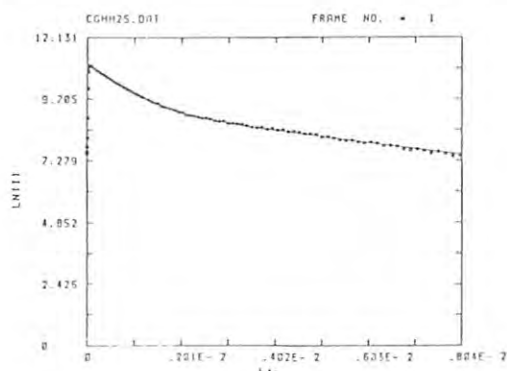


Fig. 1. Plot of logarithm of the scattered intensities from CGMMV protein (12 mg/ml) in 100 mM PB at 25°C. A solid curve was calculated from two exponential component equation.

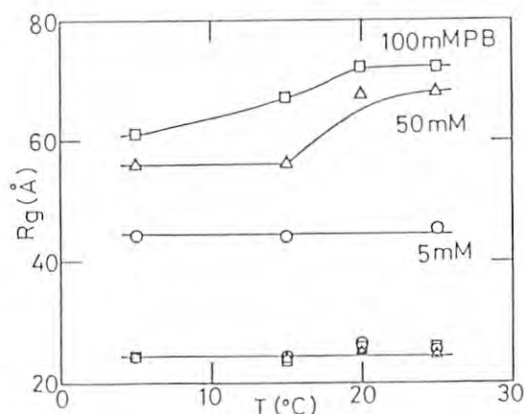


Fig. 2. The radius of gyration of CGMMV protein aggregates as a function of temperature and ionic strength.

case protein solutions are mixtures of 4S (Λ -protein), 8S, 20S disk and intermediate particles, although their existing ratio varies by the condition of the solution. In the most cases the above plots could be approximated by two components over the wide range of h . Therefore, a radius of gyration R_g of the particle and a scattered intensity at $h=0$, $I(0)$, are calculated from Simplex curve fitting method.

Fig. 2 shows the variation of R_g of the protein aggregates as a function of temperature and ionic strength. The content of Λ -protein having R_g of 2.5 nm reached 70% in 5 mM PB and did not show an appreciable temperature dependence. However, the content of Λ -protein, which is 45% and 35% in the presence of 50 mM and 100 mM PB, respectively, decreased with increasing the temperature and, at 25°C it reached up to 20% and 10%, respectively. The remainder in 5 mM PB has R_g of about 4.5 nm, whose content did not change with the increase of temperature. These components may act as a precursor of 20S disk components. The remainder in the presence of 50 mM and 100 mM PB, however, has R_g of 5.5-7.0 nm, whose content and the R_g increased with increasing the temperature. These components are equivalent to the radius of gyration of the disk components existing at 15-25°C in the case of TMV protein.

STRUCTURAL BEHAVIOR OF TROPONIN-C UPON CALCIUM ION BINDING

Tetsuro Fujisawa, Tatzuo Ueki, Inoko Yoji, Mikio Kataoka⁺, Katsumi Kobayashi⁺⁺

Faculty of Engineering Science, Osaka University, Toyonaka, Osaka 560

⁺Faculty of Science, Tohoku University, Sendai, Miyagi 980⁺⁺KEK, National Laboratory for High Energy Physics, Oho-machi, Tsukuba-gun, Ibaraki 305Introduction

Troponin-C (Tn-C) is one of intracellular calcium binding proteins and its distinctive structural change upon calcium binding were reported by various methods (1). Up to now our small-angle X-ray scattering (SAXS) studies on Tn-C solution have shown that its SAXS is distorted by interparticle interference (2). In order to eliminate that effect, we made a concentration series of experiments and obtained the extrapolated structural parameters to zero protein concentration.

Experimental

The experiments were performed at BL-10C by the SAXS equipment for 1.5 Å. The specimen to detector distance was 80 cm. Three calcium concentrations, that is, 0, 2, 4 molar equivalents of calcium to Tn-C were prepared. We made a concentration series of experiments at 2, 3, 4, 6, 8, 10 mg/ml for each calcium concentration. Sample temperature was maintained at about 5 °C during the exposure. The exposure time was at most 20 min.

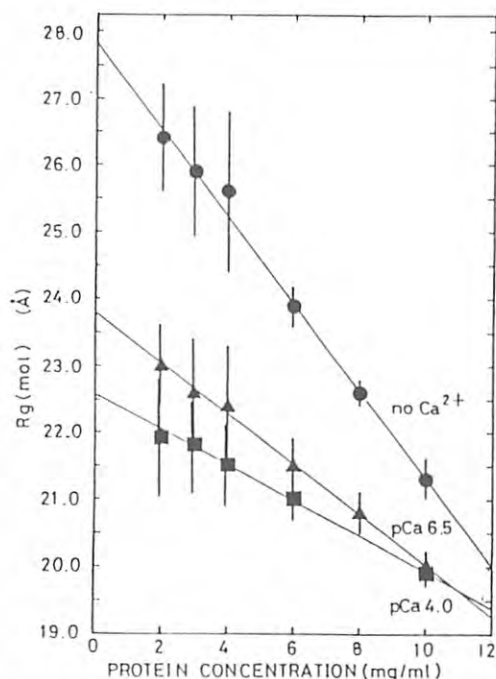
Results and Discussion

Fig. 1

Fig. 1 shows the protein concentration dependency of radius of gyration of Tn-C (Rg or Rg(mol)). These Rg(mol) were obtained from the S^2 region of between 2×10^{-5} and 12×10^{-5} in the Guinier plot. No Ca⁺⁺, pCa 6.5 and pCa 4.0 corresponds 0, 2, 4 molar equivalents of calcium respectively. Each error bar represents one sigma. Main feature of Fig. 1 is that the protein concentration dependency of Rg(mol) is very different in three calcium concentrations. This feature is presumably derived from the variations in surface nature of Tn-C upon calcium binding.

Extrapolated values of Rg(mol) to zero concentration are 27.8 Å, 23.8 Å and 22.6 Å for no Ca⁺⁺, pCa 6.5, pCa 4.0, respectively.

Fig. 2 shows the protein concentration dependency of average radius gyration of domains (Rg(dom)), which is derived from S^2 region of between 5 and 9×10^{-4} in $S^2 - \ln[I(S)/S]$ plot (3). Extrapolated values of Rg(dom) to zero protein concentration are 15.1 Å, 14.8 Å and 14.6 Å for no Ca⁺⁺, pCa 6.5 and pCa 4.0 respectively.

We also measured molecular weight of Tn-C from SAXS but reliable data has not been obtained so far. Further SAXS experiments on Tn-C solution should be continued to obtain definitive structural parameters.

References

- 1) Leavis et al. (1984) CRC Crit. Rev. Biochem., **16**, 235.
- 2) Pilz et al. (1980) Eur. J. Biochem., **105**, 539.
- 3) Fujisawa et al. (1987) In press, J. Appl. Cryst..

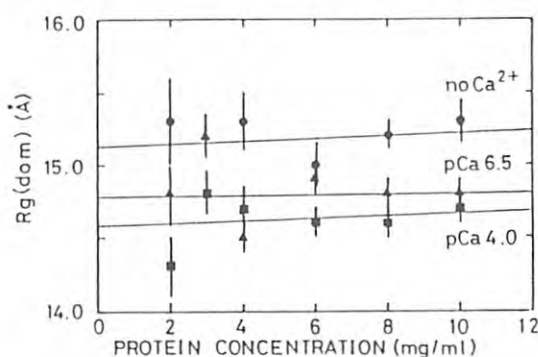


Fig. 2

MICELLE STRUCTURE OF POLYETHYLENE GLYCOL MONOETHER LIQUID CRYSTAL

Hiroshi URAKAWA,¹⁾ Kanji KAJIWARA,²⁾ Yuzuru HIRAGI,²⁾ Nobuo DONKAI,²⁾
 Walter RICHTERING,³⁾ Walther BURCHARD³⁾

- 1) Faculty of Engineering and Design, Kyoto Institute of Technology, Matsugasaki, Sakyo-ku, Kyoto, 606 Japan.
 2) Institute for Chemical Research, Kyoto University, Uji, Kyoto-fu, 611 Japan.
 3) Institut für Makromolekulare Chemie, der Universität, D-7800 Freiburg i.Br., Stefan-Meier-Strasse, 31, W. Germany.

INTRODUCTION

An amphiphile consists of two parts: a hydrophobic group at an end and a hydrophilic group at the other. An amphiphile shows several singular behaviors in the presence of water due to the high solubility of its hydrophilic group conciliated with the insolubility of the rest of the molecule. To analyze the properties of the amphiphile-water system, it is necessary to examine its phase diagram. E.Jahns¹⁾ succeeded in drawing the temperature-concentration diagram of octaethylene glycol monotetradecyl ether $\text{CH}_3(\text{CH}_2)_{13}(\text{OCH}_2\text{CH}_2)_8\text{OH}(\text{C}_{14}\text{E}_8)$ -water system through the observations by a polarizing microscope, although the micellar structure of each phase was not revealed. We investigate the form of micelle and the liquid crystal structure of the phases in the diagram with the small-angle X-ray scattering (SAXS) experiments.

RESULTS AND DISCUSSION

Fig.1 shows the temperature-concentration diagram, obtained by E.Jahns, of C_{14}E_8 -water system. The domains indicated by L_1 and Water-L_1 in the diagram are corresponding to the isotropic solution and the two phase state, respectively. In the other domains C_{14}E_8 constructs the liquid crystals having different structures. V.Luzzati described the several models of liquid crystalline phases of ionic amphiphile-water system based on the SAXS experiments.²⁾ We have carried out SAXS measurements of C_{14}E_8 -water mixtures of varying ratio from 0.05 to 1

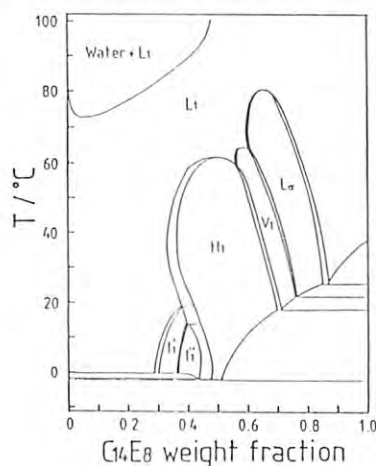


Fig.1 The phase diagram of C_{14}E_8 -water system.

(pure amphiphile) at the temperatures of 5, 20, 40 and 60°C using a SAXES focusing optics installed at the BL-10C. The variations of scattering patterns in the range of scattering vector, Q , below 0.34\AA^{-1} are shown as a function of temperature and weight fraction of C_{14}E_8 in Fig.2. These scattering intensities on a log scale are not made any corrections, so that the sharp raising at low Q range is due to the parasitic scattering from slit edges. The scattering patterns from isotropic solutions have one or two broad maxima which may originate in the nearest-neighbor correlation between micelles or ordering of micelles. In the liquid crystalline state, several sharp diffraction peaks are observed, which position and intensity vary with each domain in the phase diagram (Fig.1). It is proved that the changes of scattering patterns agree well with the phase diagram.

REFERENCES

- 1) E.Jahns : Diplomarbeit, Freiburg 1985
 2) V.Luzzati, H.Mustacchi, A.Skoulis and F.Husson : Acta Cryst., **13**, 660(1960)

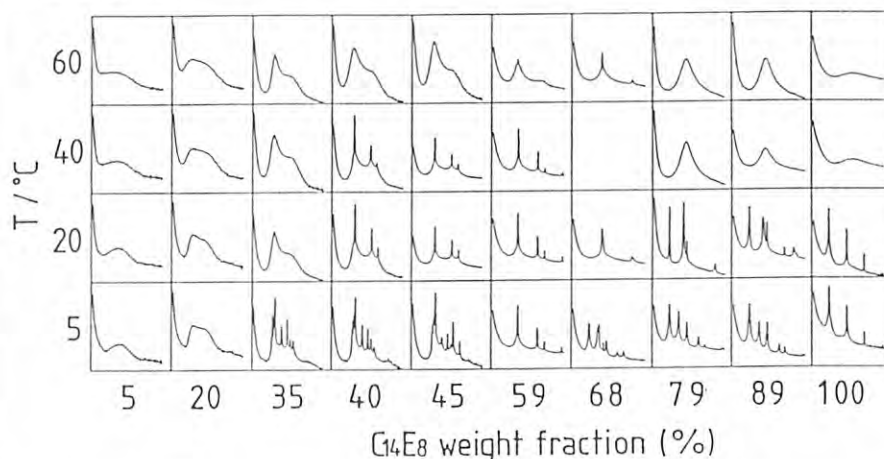


Fig.2 The variations of scattering patterns from C_{14}E_8 -water mixtures as a function of temperature and weight fraction of C_{14}E_8 .

MULTIPLY CHARGED Xe IONS PRODUCED IN 4.1 - 8.0 keV X-RAYS

T.TONUMA,¹ A.YAGISHITA,² H.SHIBATA,³ T.KOIZUMI,⁴ T.MATSUO,⁵ K.SHIMA,⁶ T.MUKOYAMA,⁷ and H.TAWARA⁸¹ Institute of Physical and Chemical Research, Wako-shi, Saitam 351-01² Photon Factory, National Laboratory for High Energy Physics, Tsukuba, Ibaraki 305³ Research Center for Nuclear Science and Technology, University of Tokyo, Tokai, Ibaraki 319-11⁴ Department of Physics, Rikkyo University, Tokyo 171⁵ Department of Pathology, Medical Research Institute, Tokyo Medical and Dental University, Tokyo 113⁶ Institute of Applied Physics and Tandem Accelerator Center, University of Tsukuba, Ibaraki 305⁷ Institute for Chemical Research, Kyoto University, Kyoto 606⁸ Institute of Plasma Physics, Nagoya University, Nagoya 464

We have already reported a preliminary analysis of our measurement of the charge distribution and mean charge of Xe ions produced by 4.1 - 8.0 keV X-ray impact from KEK Photon Factory¹⁾. In X-ray impact, the principal mechanism of production of multiply charged ions is known to be due to the vacancy cascade, that is, a vacancy produced in an innershell is continuously transferred into outer shells. Therefore, the structures of the atoms should be reflected in their charge distributions when they are ionized by X-rays. Indeed, these structures have been observed when the X-ray energy changes from the threshold energy of L₃ subshell to that of L₂ subshell and then to that of L₁ subshell in Xe atoms¹⁾.

In the present work we try to reproduce these observed results theoretically based upon Monte Carlo simulation technique where the successive Auger and radiative processes for an initial vacancy produced in a particular innershell and the electron shake-off effect are taken into account. The detailed method of the present Monte Carlo procedures has been described elsewhere²⁾. In brief the procedure is as follows: i) the initial innershell vacancy distributions are estimated from photo-electric effect. ii) the vacancy filling is decided by the fluorescence yields: when X-rays are emitted, the vacancy transfer is determined using the partial radiative transition probabilities, whereas two new vacancies are determined by the partial Auger rates when Auger electrons are emitted. iii) this procedure is repeated until all the vacancies are transferred up to the outermost-shells and then no more transition is possible. The necessary data are taken from a series of references³⁻⁷⁾.

Thus the final vacancy distributions and the mean charge of ions are calculated as a function of the X-ray energy. The calculated results are shown in Table 1, together with the previously reported experimental results¹⁾ for the X-ray energies below and above the subshell threshold energies. The agreement is found to be surprisingly good for all the energies investigated.

Figure 1 shows the observed results, together with other measurements. Clearly the present data differ from those by Carlson et al.⁸⁾ This might be due to the fact that X-rays used by Carlson et al. were not pure but included significant fractions of low energy X-rays which have high probabilities for production of low charge ions.

More systematic measurements are under way in order to understand the mechanisms involved in multiply charged ion productions by X-rays.

References

- 1) T.Tonuma, A.Yagishita, H.Shibata, T.Koizumi, T.Matsuo, K.Shima and H.Tawara, Photon Factory Activity Report #4 (1986) p.218.

2) T.Mukoyama, Bull. Inst. Chem. Res., Kyoto Univ. 63, 373 (1985)

3) J.H.Scofield, At. Data & Nucl. Data Tables 14, 121 (1974)

4) T.Mukoyama, J.Phys. Soc. Japan 55, 3054 (1986)

5) M.H.Chen, B.Crasemann and H.Mark, At. Data & Nucl. Data Tables 24, 13 (1979)

6) E.J.McGuire, Phys. Rev. A 5, 52 (1972)

7) E.J.McGuire, Phys. Rev. A 9, 1840 (1974)

8) T.A.Carlson, W.Hund and M.O. Kause, Phys. Rev. 151, 41 (1966)

9) T.Hayaishi, Y.Morioka, Y.Kageyama, I.H.Suzuki, A.Mikuni, G.Isoyama, S.Asaoka and M.Nakamura, J.Phys. B 17, 3511 (1984)

Table 1

A comparison of the calculated and observed mean charge of Xe ions produced by X-rays

E _X (keV)	Measured <q>	calculated <q>
4.50	6.01	6.12
4.90	7.30	7.39
5.10	7.45	7.40
5.30	7.55	7.62
5.45	7.65	7.63
5.80	7.74	7.85
6.80	7.84	7.90
8.00	7.97	7.95

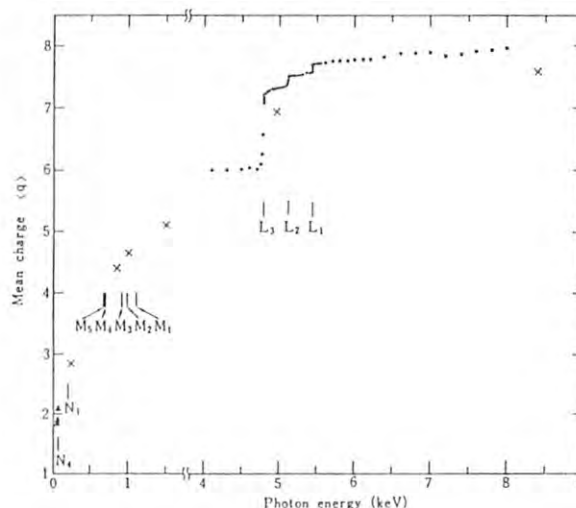


Figure 1 The mean charge of Xe ions as a function of X-ray energy. •: present result. x: Carlson et al. ▲: Hayaishi et al.⁹⁾

X-RAY RAMAN SCATTERING AS A TOOL FOR STRUCTURE DETERMINATION

Kazuyuki TOHJI and Yasuo UDAGAWA

Institute for Molecular Science, Myodaiji, Okazaki, Aichi 444

Introduction

For noncrystalline materials EXAFS (Extended X-ray Absorption Fine Structure) is now used as an established tool for the determination of local structure around a central atom. An application of EXAFS to the elements with low atomic number is, however, limited because K-absorption edges lie in the soft x-ray region where the experiment is not feasible in air and adequate window materials are not available. Inelastic x-ray scattering using hard x-ray may supply the same information as the absorption. The relationship between x-ray Raman scattering and x-ray absorption was first revealed by Mizuno and Ohmura¹⁾ and immediately confirmed by Suzuki about beryllium²⁾. Since then x-ray Raman scattering has been studied by several workers, but the detailed features have never been observed; extreme weakness of the scattering intensity did not allow one to have a spectrum with sufficient resolution and signal-to-noise ratio. Here we present the first observation of EXAFS-like oscillation in the x-ray Raman scattering from graphite.

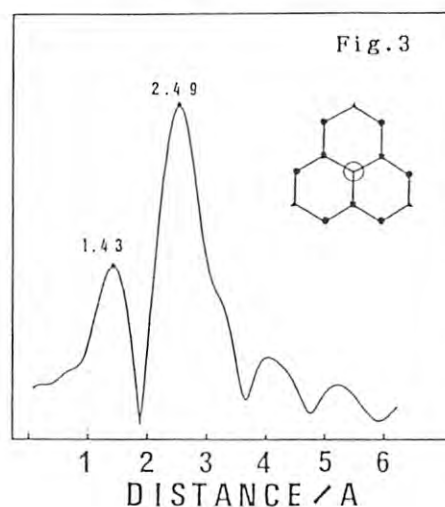
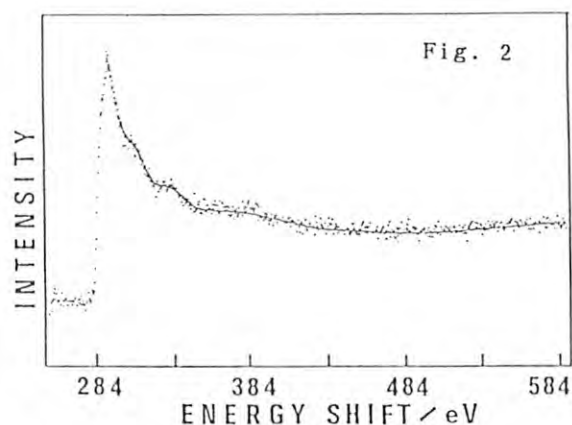
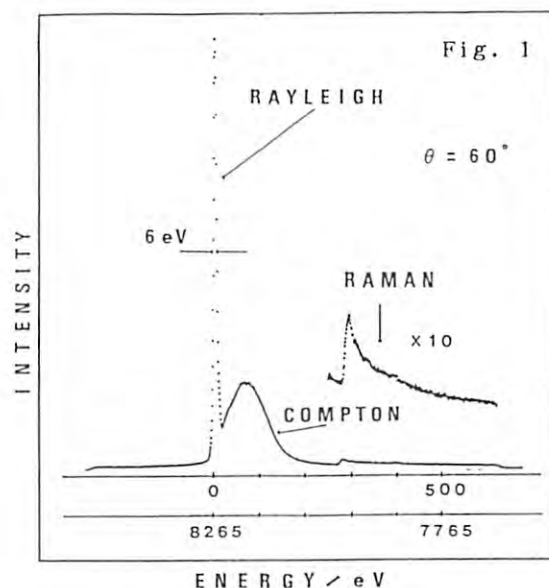
Experimental and Results

The experiment was carried out at BL-10C with the apparatus. A typical example of the x-ray scattering spectrum collected in 24 hours at the scattering angle of 60 degree is shown in Fig. 1. A sharp peak at the energy of 8265 eV is the Rayleigh scattering whose width (6 eV at FWHM) represents the energy resolution of this experimental condition. A broad peak shifted by 70 eV from Rayleigh scattering is the well known Compton scattering. Besides, x-ray Raman scattering is observed beyond 284 eV, which coincides the binding energy of K-electron in carbon atom. Fig.2 shows the Raman part in an expanded scale. Fig. 3 shows the associated radial structure function obtained by the Fourier transformation using the theoretical amplitude and phase factor. Two peaks are clearly observed at distances 1.43 and 2.48 Å, which nicely coincide with the known C-C distances of graphite (1.42 and 2.46 Å).

This work clearly shows that x-ray Raman scattering can be used to determine the local structure around a central absorbing atom with low atomic number.

References

- 1) Y.Mizuno and Y.Ohmura: J.Phys.Soc.Jpn. 22, 445 (1967).
- 2) T.Suzuki: J.Phys.Soc.Jpn. 22, 1139 (1967).



SURFACE STRUCTURE ANALYSIS OF $\text{Si}(111)\sqrt{3}\times\sqrt{3}\text{-Bi}$ BY X-RAY DIFFRACTIONToshio TAKAHASHI, Shinichiro NAKATANI, Tetsuya ISHIKAWA⁺ and Seishi KIKUTA⁺⁺Institute for Solid State Physics, University of Tokyo,
Roppongi, Minato-ku, Tokyo 106⁺Photon Factory, National Laboratory for High Energy Physics,
Oho-machi, Tsukuba-gun, Ibaraki 305⁺⁺Department of Applied Physics, Faculty of Engineering,
University of Tokyo, Hongo, Bunkyo-ku, Tokyo 113Introduction

We have shown in a previous work that X-ray diffraction is useful to analyze the system in which heavy atoms are adsorbed on the clean Si surface and determined the structure of the adsorbed layer of $\sqrt{3}\times\sqrt{3}\text{-Bi}$ on the $\text{Si}(111)$ surface¹⁾. Although we have considered only the X-rays scattered by Bi atoms, it is necessary to consider the contributions from Si atoms for more detail analysis. In this work, we measured four intensity versus energy (I-E) curves along (00), (10), (10) and (02) rods and determined the 3-dimensional structure of $\sqrt{3}\times\sqrt{3}\text{-Bi}$ on the $\text{Si}(111)$ surface in consideration of the interference effect between the X-rays scattered by the adsorbed layer and by the substrate.

Experimental and Results

The experimental conditions were the same as previous one except that, in this work, a position sensitive proportional counter was used as the detector so that the diffraction spots could be found out easily among the backgrounds.

The intensities of diffracted X-rays are proportional to the square of the absolute value of the structure factor F_{tot} , which is written as

$$F_{\text{tot}} = F_{\text{Bi}} + F_{\text{Si}}^{\text{surf}} + F_{\text{Si}}^{\text{bulk}} \quad (1)$$

Here F_{Bi} , $F_{\text{Si}}^{\text{surf}}$ and $F_{\text{Si}}^{\text{bulk}}$ are the structure factors for Si an adsorbed layer of Bi, reconstructed or displaced layers of Si, and a semi infinite Si crystal, respectively. The positions of Bi atoms with respect to the substrate can be determined by the interference effect of the first and third terms of (1), and once it is determined, the position of reconstructed or displaced Si atoms with respect to Bi atoms can be determined by the interference effect of the second and first terms of (1). Fig.1 shows two of the I-E curves. In other curves calculations fit to measurements to the same extent. From the best choice of fitting parameters we deduced next conclusions. (see also Fig.2 and Fig.3)

1. Bi atoms, forming trimers whose interatomic distances are 3.08 ± 0.08 Å, locate nearly right above the first layer Si atoms and bond with the dangling bonds.

2. The spacing distance between the Bi adsorbed layer and the ideal first Si layer is 2.68 ± 0.02 Å.

3. The first and second layer substrate Si atoms are displaced from their ideal positions less than 0.15 Å.

4. It is preferable that the centers of Bi trimers locate above the second layer Si atoms to

that they locate above the forth layer Si atoms.

5. The agreements between measurements and calculations are improved provided a Si adatom layer, forming honeycomb structures, 0.8 ± 0.2 Å above Bi adsorbed layer is introduced.

Reference

- 1) T.Takahashi, K.Izumt, T.Ishikawa and S.Kikuta: Surf.Sci. 183 (1987) L302

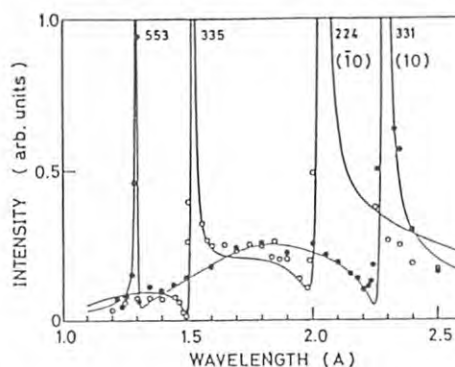


Fig.1 I-E curves measured along (10) rod (solid circles) and (10) rod (open circles). Solid lines are calculated curves.

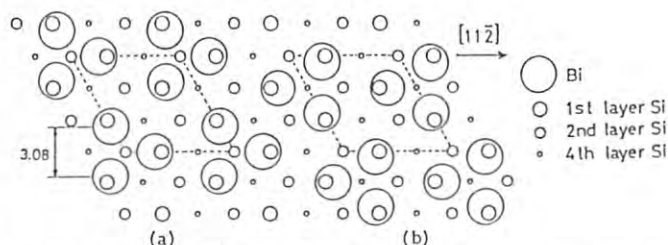


Fig.2 Two $\sqrt{3}\times\sqrt{3}\text{-Bi}$ structure models. The rhombi drawn by dashed lines are unit cells. Model (a) is more likely to agree with calculations than model (b).

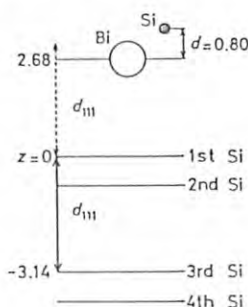


Fig.3 The illustration of positions of the adsorbed Bi and a Si adatom in z-direction.

MULTIPLE-PHOTOIONIZATION OF Cs AND Ba ATOMS DUE TO CREATION OF 4d-HOLE STATES

T.Nagata,¹ Y.Itikawa,² T.Hayaishi,³ Y.Itoh,⁴ T.Koizumi,⁵ T.Matsuo,⁶ Y.Sato,⁷ E.Shigemasa,⁸ K.Ueda,⁷ A.Yagishita,⁹ M.Yoshino⁹ and Li Guoping¹⁰

Photon Factory, National Lab. High Ener. Phys., Oho, Ibaraki 305. ¹Dept. Sci. Tech., Meisei Univ., Hodokubo, Hino, Tokyo 191. ²Inst. of Space Sci., Komaba, Tokyo 153. ³Univ. of Tsuba, Sakuramura, Ibaraki 305. ⁴Fac. of Sci., Josai Univ., Sakado, Saitama 350-52. ⁵Dept. Phys., Rikkyo Univ., Toshima, Tokyo 171. ⁶Med. Res. Inst., Tokyo Med. Den. Univ., Bunkyo, Tokyo 113. ⁷Res. Inst. of Sci. Meas., Tohoku Univ., Sendai, Miyagi 980. ⁸Fac. of Engine. Sci., Osaka Univ., Toyonaka 560. ⁹Shibaura Inst. of Tech., Omiya, Saitama 330. ¹⁰Dept. of Phys., Sophia Univ., Chiyoda, Tokyo 102.

As a part of a series of multiple photoionization experiments of metal atoms, we report here the results on 4d-shell photoionization of Cs and Ba atoms. Yields of M^{q+} (M =Cs or Ba, $q=1-4$) have been measured as a function of photon energy. From these results combined with reported photoabsorption and photoelectron data, we expect to obtain detailed knowledge of decay processes after creation of 4d-hole states.

The experiment was carried out by the use of a 2-meter Grasshopper monochromator at BL-11A. A metal-atom beam from an oven was crossed with the monochromated VUV radiation, and resulting photoions were mass analyzed with time-of-flight technique. Intensities of different ions M^{q+} were simultaneously recorded with wavelength scanning.¹⁾

Figure 1 shows the ion yield spectra obtained for Cs. Peak structure is seen in the lower energy side, and this region has been examined more precisely, as shown in Fig.2. The entire spectrum is characterized by resonant peaks corresponding to the transition to the $4d^{-1}nl$ Rydberg states below the 4d ionization threshold and a broad shape resonance peaking around 115 eV. It is immediately apparent that main products are doubly- and triply-charged ions. Their intensity ratio Cs^{3+}/Cs^{2+} varies increasingly from 1 around the 4d ionization threshold to 2.1 around the 4p ionization threshold, indicating the existence of shake-up and/or shake-off processes in the stage of photoabsorption. We can see a non-negligible amount of Cs^{4+} ions in the higher energy region. The yield curve of these Cs^{4+} ions indicates clearly the existence of two thresholds at about 110 and 140 eV, the latter lying near the 4p ionization threshold. The result obtained for Ba is shown in Fig.3. Dominant products in this case are again doubly- and triply-charged ions. However, the ratio Ba^{3+}/Ba^{2+} amounts to about 3 in the higher energy region, considerably larger than that in Cs case. Non-negligible amount of Ba^{4+} ions begin to be produced around the structure attributed to shake-up process.

Ejected-electron spectra available in the literature^{2,3)} are very helpful to understand the present results. The energy and relative intensities of Auger lines as well as the assumption of multi-step processes allow us to estimate relative intensities of M^{q+} . Such estimations are in qualitative agreement with the present results. However, quantitatively satisfactory explanation needs inclusion of shake processes in the stage of relaxation as well.

References

- 1) Y.Sato et al.: J. Phys B **18** 225 (1985).
- 2) H.Aksela and S.Aksela: Phys. Rev. **28** 2851 (1983).
- 3) Th.Prescher et al.: J. Phys. B **19** 1645 (1986).

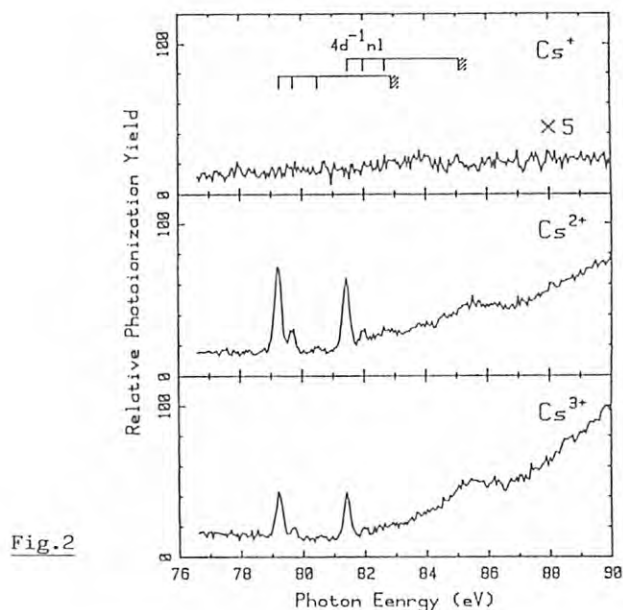
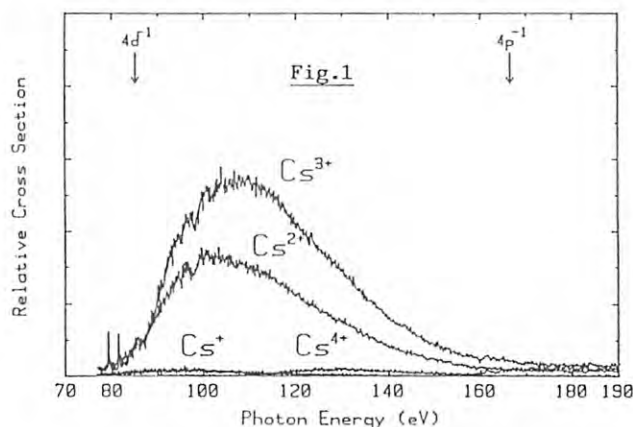


Fig.2

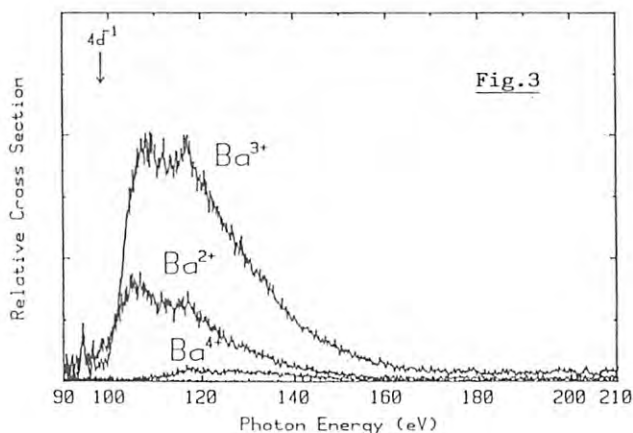


Fig.3

2p-SHELL PHOTOIONIZATION OF K AND Ca ATOMS

T.Matsuo,¹ T.Hayaishi², Y.Itikawa,³ Y.Itoh,⁴ T.Koizumi,⁵ T.Nagata,⁶ Y.Satoh,⁷ E.Shigemasa,⁸ A.Yagishiata⁹ and M.Yoshino.¹⁰

¹Med. Res. Inst., Tokyo Med. Den. Univ., Bunkyo, Tokyo 113. ²Univ. of Tsukuba, Sakuramura, Ibaraki 305.

³Inst. of Space Sci., Komaba, Tokyo 153. ⁴Fac. of Sci., Josai Univ., Sakado, Saitama 350-52.

⁵Rikkyo Univ., Toshima, Tokyo 171. ⁶Meisei Univ., Hino-shi, Tokyo 191.

⁷Res. Inst. of Sci. Meas., Tohoku Univ., Sendai, Miyagi 980. ⁸Osaka Univ., Toyonaka, Osaka 560.

⁹Photon Factory, KEK, Ohomachi, Ibaraki 305. ¹⁰Shibaura Inst. of Technol., Omiya, Saitama 330.

Introduction

This study is one of a series of our experimental investigations concerning inner-shell photoionization of metal atoms using synchrotron radiation. Production of inner-hole states, in most cases, results in formation of multiply-charged ions. We present here the ion yield spectra for K and Ca atoms as a result of 2p-shell photoionization.

Experimental

The synchrotron radiation emitted from 2.5 GeV storage ring in the Photon Factory was dispersed with a 2 meter Grasshopper monochromator, and crossed with a beam of target atoms from a furnace. The resultant photoions were mass-selected with a time-of-flight spectrometer. The details of the experimental apparatus has been described elsewhere.¹⁾ The intensities of secondary ions M^{q+} ($M=K$ and Ca , $q=1-4$) were measured as a function of photon energy in the region around 2p-ionization threshold of each target.

Results and Discussion

Figures 1 and 2 show the partial yield spectra for ions with different charge states ($q=1-3$).

As can be seen, the yield spectra have two prominent peaks below the 2p-shell ionization threshold in the case of K^{3+} , K^{2+} and also K^+ . The positions of these peaks in this work (297 and 299 eV) agree well with those in the photo-absorption spectra by Mansfield, who assigned these peaks to the excitation of 2p electron to the 3d level.²⁾ The intensity of doubly-charged K^{2+} ions predominates in the total ion yield in the present measurement range (290-400 eV). The relative yield of K^{3+} to K^{2+} ions is markedly altered below and above the 2p ionization threshold; the intensity ratio K^{3+}/K^{2+} increases from 1/9 at the resonance to 1/3 above the threshold. A slight increase of K^{4+} yield was observed at 2s-ionization threshold.

In the case of Ca, there also appeared prominent 2p-3d resonance peaks, at 349 and 352.5 eV, in Ca^{3+} and Ca^{2+} yield spectra, but no such enhancement of the yield observed for Ca^+ . The intensity of Ca^{3+} is remarkably strong in comparison with that in the K target. The most abundant product below the 2p-ionization threshold is again Ca^{2+} ions, whereas it is replaced by Ca^{3+} ions above the threshold; the intensity ratio Ca^{3+}/Ca^{2+} is 1/3 at the resonance and 3/1 above the 2p-threshold. The intensity of Ca^{4+} ions was found to increase slightly at the 2s-ionization threshold.

According to the normal Auger spectra from

2p-shell vacancy state of K and Ca atoms and the relevant energy level diagram of the ions, it was concluded that the photoexcitation followed by successive Auger process can well explain the observed yield spectra for both K and Ca targets. For example, the yield ratio Ca^{3+}/Ca^{2+} is estimated to be about 1/3.2 at the resonance, which shows reasonable agreement with the experimental value 1/3. Further analysis of the result is in progress.

References

- 1) Y. Satoh et al., J. Phys. B **18** 225 (1985).
- 2) M.W.B. Mansfield, Proc. R. Soc. Lond. A **346** (1975).

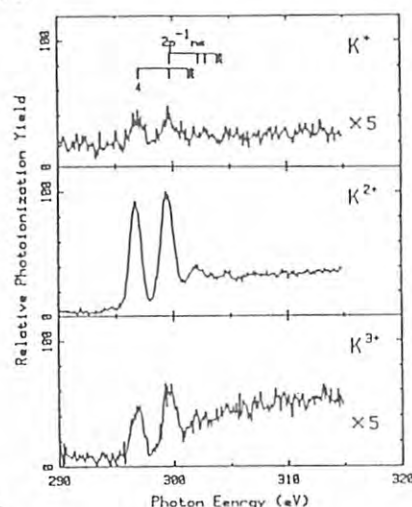


Fig. 1

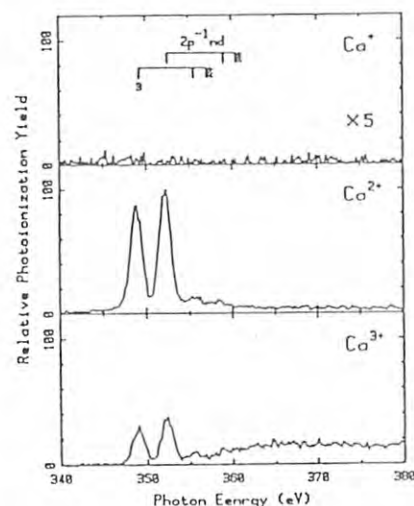


Fig. 2

THRESHOLD PHOTOIONIZATION OF Kr 3d SUBSHELL

Tatsuji HAYAISHI¹, Eigorou MURAKAMI², Akira YAGISHITA³, Yumio MORIOKA⁴,
Guo Ping LI⁵, Eiji SHIGEMASA⁶ and Taizo SASAKI⁶

¹Institute of Applied Physics, University of Tsukuba, Sakura, Ibaraki 305 Japan

²Chiba Institute of Technology, Narashino, Chiba 275 Japan

³National Laboratory for High Energy Physics, Oho, Ibaraki 305 Japan

⁴Institute of Physics, University of Tsukuba, Sakura, Ibaraki 305 Japan

⁵Department of Physics, Sophia University, Kioicho, Chiyoda-ku, Tokyo 102 Japan

⁶Faculty of Engineering Science, Osaka University, Toyonaka-shi, Osaka 560 Japan

Introduction

Threshold electrons, having zero kinetic energies, can be ejected from atoms when the photon energy of irradiation is of the same level as the ionization energy of a shell. The measurement of threshold electrons gives us about information on the ionization process of only the shell. In this article we report the measurement of multiply charged ions in coincidence with threshold electrons near the 3d ionization threshold of Kr.

Experiment

Experiments were carried out using a 2m grasshopper monochromator at BL-11A. The monochromator was equipped with a 2400 lines/mm grating. The spectral resolution was about 0.17 Å (0.12 eV at 95 eV) with 80µm slit widths. The mass spectrometer used was of time-of-flight type accompanied with a threshold-electron energy analyzer¹). The resolution of the electron energy analyzer is roughly estimated to be about 0.03 eV on the basis of the FWHM measured at the Kr 4p ionization threshold.

Results and Discussion

Figure 1 shows the yield spectra of Kr²⁺ and Kr³⁺ ions in coincidence with threshold electrons in the 89-99 eV photon energy region. For comparison, the yield spectrum of total ions is shown in the lower part of figure 1.

Two dominant peaks which appear just above the 3d ionization threshold are due to the 3d photoelectron. The photoelectron is really the threshold electron, in itself. The profiles show the effect of post-collision interaction, namely, shifts of peak positions and asymmetric shapes²).

Many structures below the 3d ionization threshold correspond to the Rydberg states, 3d⁻¹np. It signifies that threshold electrons are ejected through decay on these resonance states. The decay channels expected can be considered as follows. The one is due to shake-off in double or triple Auger processes. In these events, one of two or three electrons ejected may have very low-kinetic energy. The other is due to two-step ionization. When intermediate states locate at the same potential energies as the final ionic states, threshold electrons can be ejected via the intermediate states. It is likely that two-step ionization plays a main role in decay processes on the resonance states because the Auger event is more prominent than the double or triple Auger event.

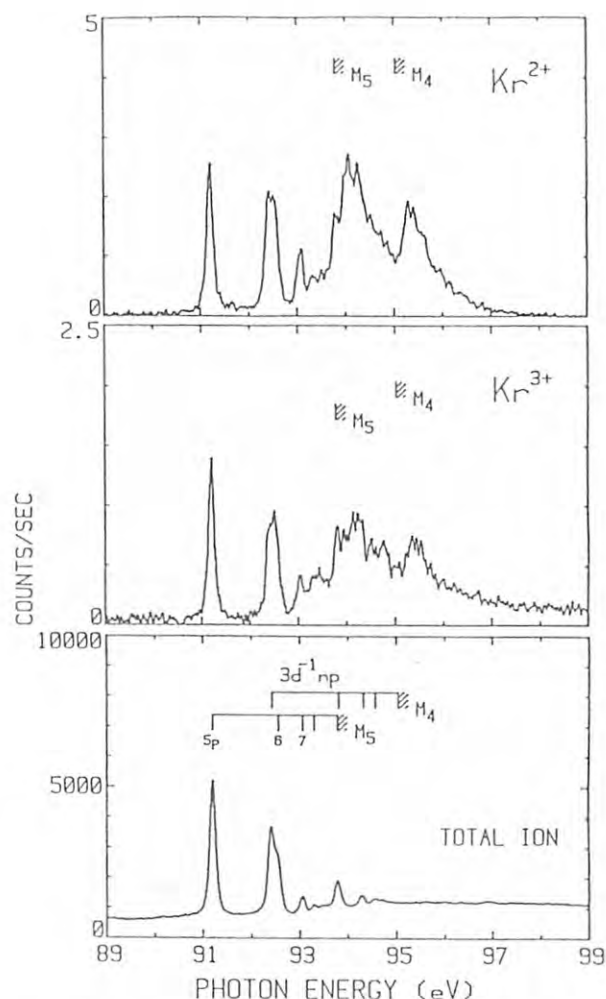


Figure 1. Yield spectra for Kr²⁺ and Kr³⁺ ions obtained in coincidence with threshold electrons as a function of photon energy. For comparison, the yield spectrum of total ions is shown in the lower part. The photon energy scale was calibrated on the Kr3d⁻¹5p peak at 91.2 eV³).

References

- 1) Y. Morioka, T. Akahori, T. Hayaishi, T. Namioka, T. Sasaki and M. Nakamura, J. Phys. **B19**, 1075 (1986)
- 2) A. Niehaus, J. Phys. **B10**, 1845 (1977)
- 3) G. C. King, M. Tronc, F. H. Read and R. C. Bradford, J. Phys. **B10**, 2479 (1977)

INVESTIGATION OF FRAGMENTATION PROCESSES FOLLOWING INNER-CORE LEVEL EXCITATION OF $\text{Pb}(\text{CH}_3)_4$ AND $\text{Sn}(\text{CH}_3)_4$ IN THE VAPOR PHASE

Shin-ichi NAGAOKA¹, Kiyoshi UEDA², Inosuke KOYANO¹, Tatsuya SATO²
Yukinori SATO², Eiji SHIGEMASA³, Kenichiro TANAKA⁴, Tetsuo NAGATA⁵
and Tatsuji HAYAISHI⁶

¹Institute for Molecular Science, Myodaiji, Okazaki 444

²Research Institute for Scientific Measurements, Tohoku University, Katahira,
Sendai 980

³Faculty of Engineering Science, Osaka University, Machikaneyama, Toyonaka 560
⁴Photon Factory, National Laboratory for High Energy Physics, Oho-machi,
Ibaraki 305

⁵Department of Science and Technology, Meisei University, Hodokubo, Hino 191

⁶Institute of Applied Physics, University of Tsukuba, Sakuramura, Ibaraki 305

Introduction

In contrast to the cases of valence electrons delocalized over the molecule, core electrons in a molecule are localized near the atom to which they belonged originally. As a result, the photoionization from the core level is expected to produce dissociation pathways quite different from those following the valence photoionization. We have studied the fragmentation of organometallic molecules and silanes following the core level excitation so far^{1,2)}. In the present work, we have investigated the dynamic processes of $\text{Pb}(\text{CH}_3)_4$ (TML) and $\text{Sn}(\text{CH}_3)_4$ (TMT) following the excitation of the inner-core levels located in the region 100–600 eV.

Experimental

Experiments were carried out at BL-11A using a 2m Grasshopper monochromator equipped with a 2400 lines/mm grating. Fragment ions generated by the absorption of monochromatized soft X-ray in a molecule were mass-analyzed by means of the time-of-flight method and were detected by a microchannel plates detector. Photoion-photoion coincidence (PIPICO) measurements were also performed using a single ion detector. 99.99 % TML (Rare Metallic) and extra-pure grade TMT (Nakarai) were used without further purification.

Results and Discussion

The $4f_{7/2} \rightarrow \sigma^*$ and $4f_{5/2} \rightarrow \sigma^*$ transitions of TML are assigned as indicated in Fig. 1 on the basis of the absorption spectrum of Pb atom³⁾. The most plausible explanation of the dynamic process following the $4f \rightarrow \sigma^*$ excitation can be given by an Auger process producing a doubly-charged ion and the subsequent fragmentation into $\text{CH}_n^+ - \text{Pb}^+$ ion-pairs.

The PIPICO spectrum of TML (Fig. 2) considerably changes in the relative intensity of various ion-pairs near the $4f$, $5s$ and $5p$ edges of TML. At higher energies than that corresponding to each core edge, doubly-charged ions are produced mainly by newly-opened Auger processes. A part of these doubly-charged ions seems to dissociate efficiently owing to the hole in the $\sigma_{\text{C-H}}$ orbital. As a result, the relative intensities of $\text{H}^+ - \text{Pb}^+$ and $\text{H}^+ - \text{PbCH}_n^+$ ion-pairs are likely to increase above each edge. A similar change in PIPICO spectrum is also observed by excitation near the $4s$, $4p$ and $3d$ edges of TMT.

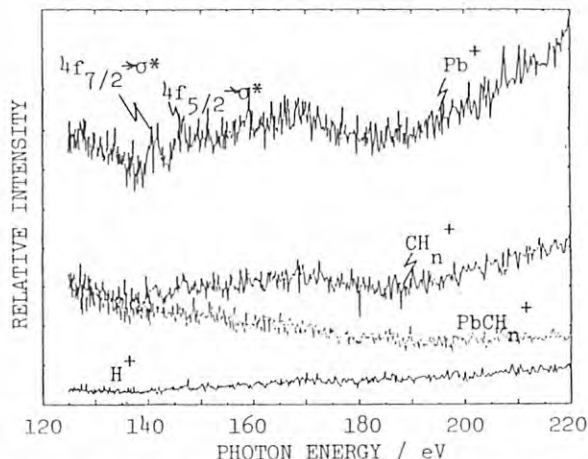


Fig. 1 Photoionization efficiency curves of $\text{Pb}(\text{CH}_3)_4$

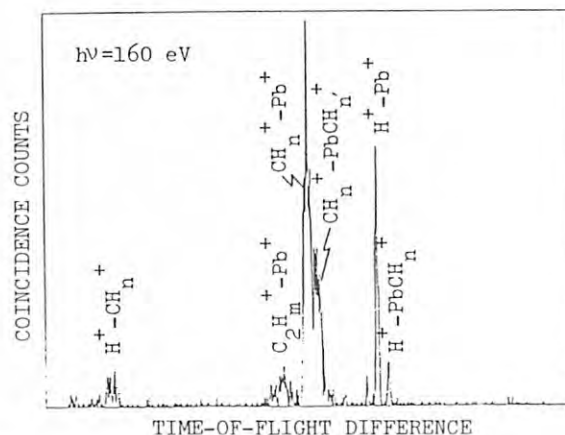


Fig. 2 PIPICO spectrum of $\text{Pb}(\text{CH}_3)_4$

References

- 1) S. Nagaoka, S. Suzuki and I. Koyano, Phys. Rev. Lett., **58**, 1524 (1987); Nucl. Instrum. Methods, in press.
- 2) Y. Sato, A. Yagishita, T. Nagata, T. Hayaishi, M. Yoshino, T. Koizumi, Y. Itoh, T. Sasaki and A. A. MacDowell, in preparation.
- 3) J. P. Connerade, B. Drerup and M. W. D. Mansfield, Proc. Royal Soc. London, **A348**, 235 (1976).

S K AND $L_{2,3}$ ABSORPTION SPECTRA OF $Ni(mnt)_2$

Koichi KIKUCHI, Nobuhiro KOSUGI[†], Tatsuji SANO, Kazuya SAITO,
Toshiaki OHTA,^{††} and Isao IKEMOTO

Department of Chemistry, Faculty of Science, Tokyo Metropolitan University,
Fukazawa, Setagaya-ku, Tokyo 158

[†] Department of Chemistry, Faculty of Science, The University of Tokyo,
Hongo, Bunkyo-ku, Tokyo 113

^{††} Department of Materials Science, Faculty of Science, Hiroshima University,
Higashisenda-cho, Naka-ku, Hiroshima 730

Introduction

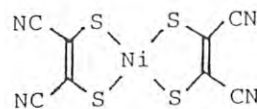
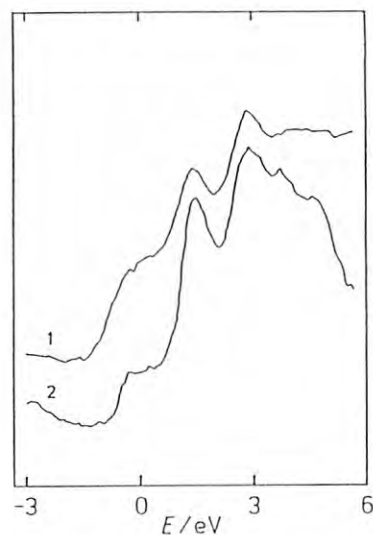
$Ni(mnt)_2$ (mnt = maleonitriledithiolene) (Fig. 1) is one of the acceptors which consist of a metal atom and organic chelates, and its oxidation number can change between 0 and -2. The previous studies have revealed that the electronic state of Ni changed little with the variation of oxidation number of $Ni(mnt)_2$. In the present work, we measured S₁K and $L_{2,3}$ absorption spectra of $Ni(mnt)_2$ and $Ni(mnt)_2^{1-}$ in order to clarify the change in the electronic state of the organic chelate, mnt, with the change in the oxidation number of $Ni(mnt)_2$.

Experimental

The samples for the measurements were powder of $(TBN)[Ni(mnt)_2]$ and $(TBN)_2[Ni(mnt)_2]$ (TBN = tetrabutylammonium). The experiments were performed at BL-11A (2 m Grasshopper) and BL-11B (Soft X-ray Double Crystal) in Photon Factory. The SK and $L_{2,3}$ absorption spectra of each sample were obtained by monitoring the total electron yield.

Results and Discussion

Figures 2 and 3 show the S₁K and $L_{2,3}$ absorption spectra, respectively. While the $L_{2,3}$ spectra of $Ni(mnt)_2$ and $Ni(mnt)_2^{1-}$ are similar in the low energy region, the K spectra are largely different from each other. In the case of $Ni(mnt)_2^{1-}$, the HOMO is half occupied and the transition to it is expected to be observable at low energy. On the other hand, the corresponding transition is impossible in $Ni(mnt)_2$ because the HOMO is fully occupied. Therefore, the difference in the K spectra at the lowest peak is attributed to the presence of the transition to the HOMO in $Ni(mnt)_2^{1-}$. In the $L_{2,3}$ spectra, no apparent difference is recognized at low energy. Since a transition to a d-orbital is forbidden in the K transition but allowed in the $L_{2,3}$ transition, the absence of the HOMO component in the lowest peak in the $L_{2,3}$ spectra suggests that the 3d-orbitals of sulfur atoms contribute negligibly to the construction of the HOMO of $Ni(mnt)_2$. It is noteworthy that the apparent chemical shift of the second peak in the K spectra is opposing to the normal behavior. The detailed investigation is in progress.

Fig. 1. $Ni(mnt)_2$.Fig. 2. K spectra of $Ni(mnt)_2$.Fig. 3. $L_{2,3}$ spectra of $Ni(mnt)_2$.

POLARIZED S K AND $L_{2,3}$ ABSORPTION SPECTRA OF $(TMTTF)_2ClO_4$

Koichi KIKUCHI, Nobuhiro KOSUGI,[†] Tatsuji SANO, Kazuya SAITO, Kenichiro TANAKA,^{††}
Toshiaki OHTA,^{†††} and Isao IKEMOTO

Department of Chemistry, Faculty of Science, Tokyo Metropolitan University,
Fukazawa, Setagaya-ku, Tokyo 158

[†] Department of Chemistry, Faculty of Science, The University of Tokyo,
Hongo, Bunkyo-ku, Tokyo 113

^{††} Photon Factory, National Laboratory for High Energy Physics,
Oho-machi, Tsukuba-gun, Ibaraki 305

^{†††} Department of Materials Science, Faculty of Science, Hiroshima University,
Higashisenda-cho, Naka-ku, Hiroshima 730

Introduction

Tetrathiafulvalene (TTF) and the derivative donors have provided organic conductors, in which these donors are mainly contributed to the electrical conduction. These donors have chalcogen atoms. Chalcogen atoms have empty d orbital at lower energy than the atoms in second row in periodic tables, so empty d orbital can be also contributed to the electrical conduction. In the present work, we measured polarized S K and $L_{2,3}$ absorption spectra of $(TMTTF)_2ClO_4$ in order to investigate the contribution of 3d orbital to the electrical conduction.

Experimental

The crystals for measurement were prepared by the electrochemical method. The crystals were arranged using the adhesive tape of aluminum. The X-ray absorption measurements were performed at BL11A (2m Grasshopper) and BL11B (Soft X-ray Double Crystal) by monitoring the total electron yield. The polarized spectra were obtained for the x-ray polarizations parallel (//) and perpendicular (⊥) to the growing axis, which is the conducting axis and nearly perpendicular to TMTTF molecular plane.

Results and Discussion

Figures 1 and 2 show the polarized S K and $L_{2,3}$ -edge spectra, respectively. The lowest energy peak of $L_{2,3}$ spectra is observed for ⊥ polarization. On the other hand that of K spectra is observed for the // polarization. The transition to the HOMO orbital (b_{1u}) is observable at lowest energy and allowed for the // polarization. Therefore we can assign the peaks A and B of K spectra to $1s \rightarrow b_{1u}$ (HOMO) and a_g (LUMO), respectively. The peak A of spectra g may be also assigned $2p \rightarrow a_g$ (LUMO). The difference in energy between HOMO and LUMO is found to be about 1.8 eV. The contribution of 3d orbital to HOMO is also found to be small because we can not observed the peak due to the transition to HOMO.

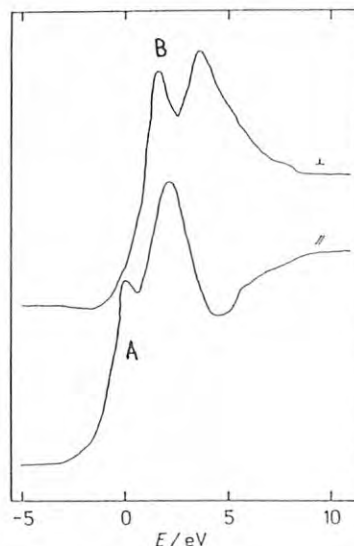


Fig. 1. K spectra of $(TMTTF)_2ClO_4$.

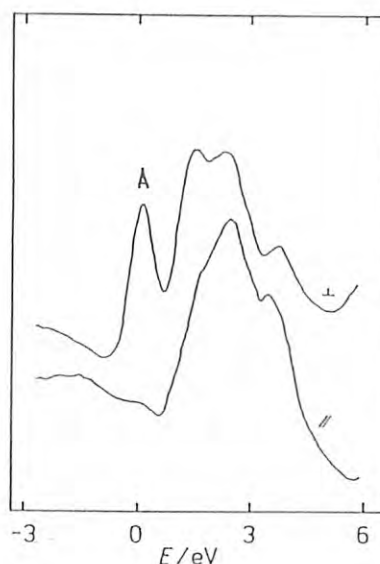


Fig. 2. $L_{2,3}$ spectra of $(TMTTF)_2ClO_4$.

OPTICAL CONSTANTS OF SiC IN THE SOFT X-RAY REGION; DETERMINED FROM EIGHT SAMPLES

Mihiro YANAGIHARA, Tsuneharu KOIDE,* and Shigeru SATO*

Research Institute for Scientific Measurements, Tohoku University,
Katahira, Sendai 980*Photon Factory, National Laboratory for High Energy Physics,
Oho-machi, Tsukuba-gun, Ibaraki 305Introduction

As synchrotron radiation mirrors SiC is a useful material for its optical and thermal properties. We have previously determined the optical constants of CVD-SiC in an energy range of 80-1000 eV using the reflectance method.¹⁾ In this method light scattering due to surface roughness is inevitable. It should be checked up whether the scattering model correctly explains the reflections of the soft X-rays or not. In this work we determine the optical constants for eight SiC mirrors²⁾ having various crystallizations and surface roughnesses using the same method, and observe the sample dependence of the optical constants.

Measurements

The crystallization of the samples was observed using an X-ray diffractometer. The rms roughness of the surface was measured using two WYKO profilometers (4-20 Å). Between the devices the rms values in the individual sample agree within 20 % except for a very rough sample. The reflectance was measured at BL-11A from 200 to 1000 eV using a high-precision reflectometer. The optical constants were determined by the least-squares fitting for curves of reflectance vs angle of incidence in terms of a scalar diffractive scattering model.

Results

The refractive indices n of eight samples determined in this method agree well to each other within 5 %, while the extinction coefficients k show a little more disagreement. But the deviation of the estimated constants is not found to significantly depend on the individual crystalline character. Figure 1 shows the optical constants of SiC in straight lines determined by averaging over the eight samples. For comparison our previous data are also plotted in circles and crosses. They coincide with the lines quite well. From the matched line we obtain an exponential formula for the relationship between δ and E (eV);

$$\delta = 1 - n = 4.17 \times 10^2 E^{-1.92} \quad (300 < E < 1000 \text{ eV}) \quad (1)$$

and similarly for k and E

$$k = 1.65 \times 10^7 E^{-3.84} \quad (2)$$

The exponent of E in eq.1, however, deviates from -2, it agrees within an experimental error.

To briefly summarize, the scalar scattering model explains the reflections of the soft X-rays. But the estimated rms roughness during the curve fitting is in general greater than those measured with profilometers. More extensive

investigation using an STM, for example, is now necessary.

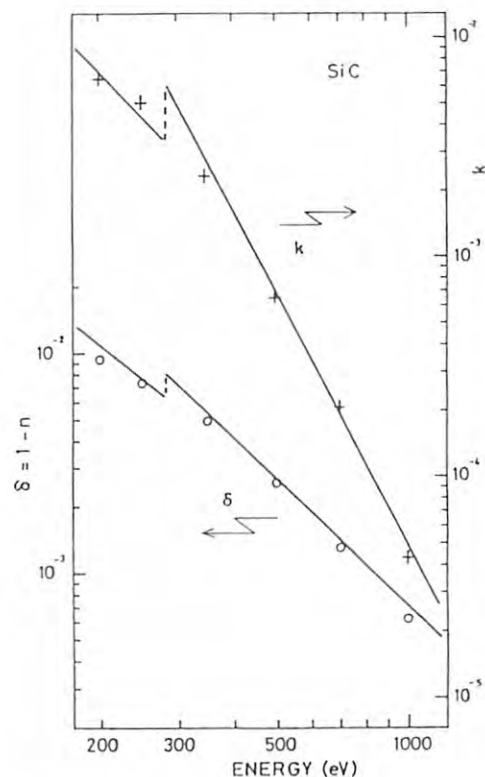


Fig.1

References

- 1) M. Yanagihara, M. Niwano, T. Koide, S. Sato, T. Miyahara, Y. Iguchi, S. Yamaguchi, and T. Sasaki: Appl. Opt. 25 (1986) 4586.
- 2) We owe these samples to Toshiba Ceramics Co. for preparing the blanks, and to Canon Co. for polishing them and measuring their surface roughness.

Introduction

For optics design in the soft X-ray region, it is very important to get accurate optical constants of various materials, especially those which have absorption edges in this region. Soft X-ray multilayer mirrors, which consist of materials with absorption edges between 1nm ~ 4nm, are under development in our project.

Henke et al.¹⁾ have calculated atomic scattering factors by means of dispersion relations and absorption measurements. However those factors are fundamentally not reliable near the absorption edges.

We measured angle dependent reflection curves and obtained optical constants of V, Ni, Si and glass (BK7), for soft x-rays between 1nm ~ 4nm. In this report, we will present the obtained optical constants and discuss the accuracy of those constants.

Experimental

The reflectance measurement was carried out at beam line 11A with S-polarized radiation, using a grazing incident reflectometer. The measurement parameters are the same as those Yanagihara and Koide²⁾ have already reported. Total resolution of the system is 0.2Å for the wavelength and 0.1° for the rotation angle of the sample and detector. As for optical filters, we used Al-foil 5μ-thick:λ=1 to 1.7nm, Cu-film 0.25μ-thick:λ=1.5 to 3.2nm and Ag-film 0.35μ-thick:λ=3 to 4nm respectively.

Our measurement procedure was: we first measured wavelength dependent curves at selected incident angles from 89.4° to the angle where the reflectance is less than 0.001, and then we analyzed the data and obtained angle dependent reflectance curves.

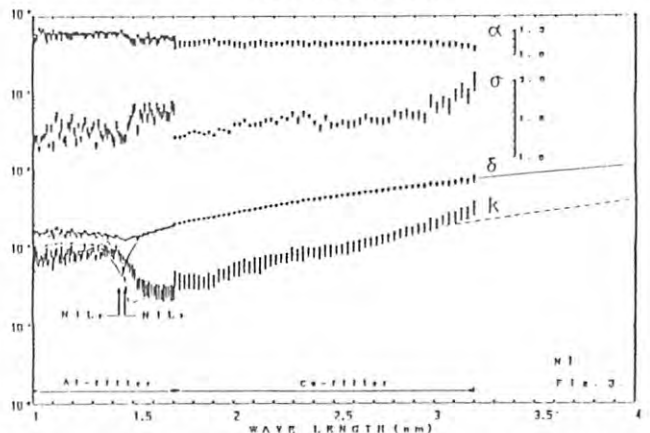
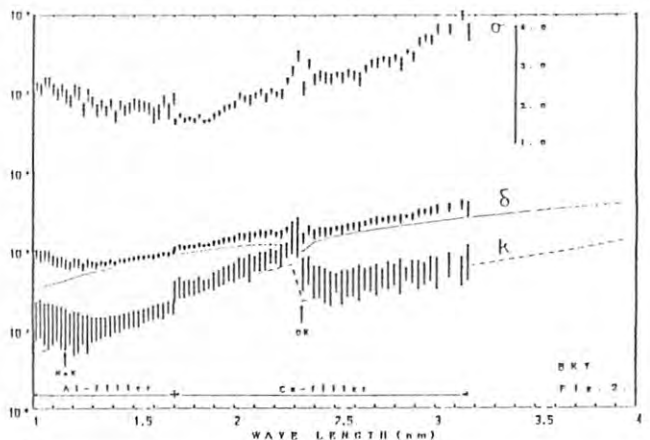
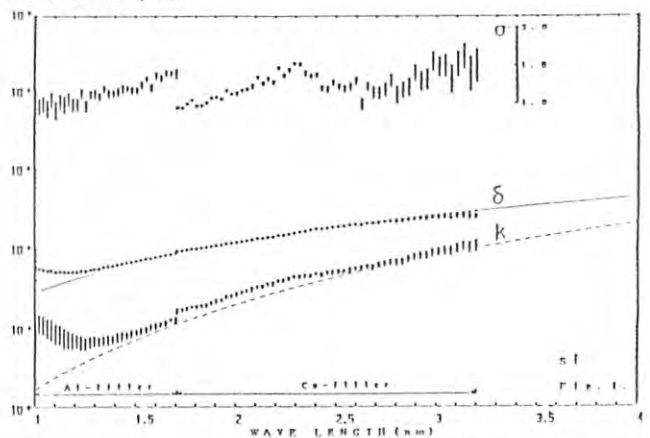
The measurement samples were silicon (111) surface, glass (BK7), sintered Nickel, all prepared by mechanical lapping and two pieces of Vanadium films, (0.2μ-thick and 0.83μ-thick) prepared by magnetron sputtering.

To estimate optical constants and surface roughness, we employed the least-squares method. For fitting curves, we used the Fresnel formula and the Bennel function. For Nickel, we adopted the micro facet model in addition to the former two models.

Results and Discussion

In Fig 1 and 2, obtained optical constants ($\delta=1-n$:circle, k :triangle) and surface roughness (σ :rectangle) are presented (Fig 1 for Si, Fig 2 for glass and Fig 3 for Nickel). In Fig 3, multiplication factors (α : bar) are also presented. Each figure is synthesized from the data using all filters. In these figures, solid and dotted lines show the optical constants calculated by using the Henke's atomic scattering factors. Also, the standard deviation of each fitting parameter is indicated by an error bar. The Oxygen K-edge, Sodium K-edge and Nickel L-edge are indicated by arrows in Fig 2. For Si the accuracies of fitting parameters are within an error of 8% for δ , 25% for k and 15% for σ , over the entire wavelength region. For glass, these are within an error of 20% for δ , 50% for k and 10% for σ . For Nickel, these are within an error of 10% for δ , 25% for k , 6% for σ and 7%

for α . The gradual increase of the fitting optical parameters, as goes from about 1.3nm to 1nm, is the result of the existence of higher order components of diffracted light which can not be cut by the Al-filter. The difference between the accuracies of the three figures depends mainly on the difference between the accuracies of the measurements. The analyses for Vanadium and the Ag-filter region of all samples have not been done yet.



1) B. Henke et al., At. Nucl. Data Tables 27, No. 1 ('82)
2) M. Yanagihara et al., Appl. Opt. 25 (1986) 4586

REFLECTIVITY OF MULTILAYER REFLECTORS IN 0.1-1KEV REGION

Koujun YAMASHITA, Hiroshi TSUNEMI, Shunji KITAMOTO, Akira MIYAKE, Isamu HATSUKADE and Yoshihiro UENO
Department of Physics, Faculty of Science, Osaka University,
Machikaneyama-cho 1-1, Toyonaka, Osaka 560

Introduction

The development of multilayer reflectors is aimed at applying to the grazing and normal incidence X-ray telescope for the cosmic X-ray observations. For this purpose multilayers of molybdenum-carbon(Mo/C) and nickel-carbon(Ni/C) were fabricated by electron beam evaporation method in ultra-high vacuum. The X-ray properties of these sample were evaluated by measuring the reflectivity, wavelength resolution and Bragg angle with characteristic X-rays of Cu-K α , Si-K α and C-K α in our laboratory.

We present here reflectivities of Mo/C and Ni/C observed with the monochromatized synchrotron radiation in 0.1-1keV region.

Results and Discussion

Multilayer reflectors thus fabricated are Ni/C(2d=72 \AA , N=20), Ni/C(2d=90 \AA , N=10), Ni/C(2d=114 \AA , N=10) and Mo/C(2d=160 \AA , N=10), which were deposited on float glass. The method of the measurement are mentioned in ref. 1. Peak reflectivities of 1st order Bragg reflection for each sample are shown in Fig. 1 and Fig. 2, compared with the calculated values based on optical constants. Mo/C shows high reflectivity in the energy range between the absorption edge C-K(0.28keV) and Mo-M(0.23keV), which is 8% just below C-K edge and 70% of the calculated value. On the other hand peak reflectivities of Ni/C are degraded depending on the layer thickness. This fact would be explained by taking into account the constant interfacial roughness which is 8-10 \AA (rms) in this case. The interfacial roughness is derived from the relation,

$$R=R_0 \exp[-(2\pi n \Delta z/d)^2],$$
where R_0 is the ideal peak reflectivity, n is the order of reflection and Δz is the rms roughness. The surface roughness of the substrate and the top layer of the deposited film is evaluated by the measuring the scattering wing to the total reflection with Si-K α ²⁾, which is derived to be 3 \AA (rms). This means that the interfacial roughness would be due to the thickness of the mixing region between adjacent layers. This effect has been noticed for Mo/Si multilayers³⁾.

References

1) K. Yamashita, H. Tsunemi, S. Kitamoto, and A. Miyake, Photon Factory Activity Report 1986, p. 233.
2) H. Kunieda, S. Hayakawa, T. Hirano, T. Kii, F. Nagase, N. Sato, Y. Tawara, F. Makino, and K. Yamashita, Jpn J. Appl. Phys., **25**, 1292(1986).
3) A. K. Petford-Long, M. B. Stearns, C. -H. Chang S. R. Nutt, D. G. Stearns, N. M. Ceglio, and A. M. Hawryluk, J. Appl. Phys., **61**, 1422(1987).

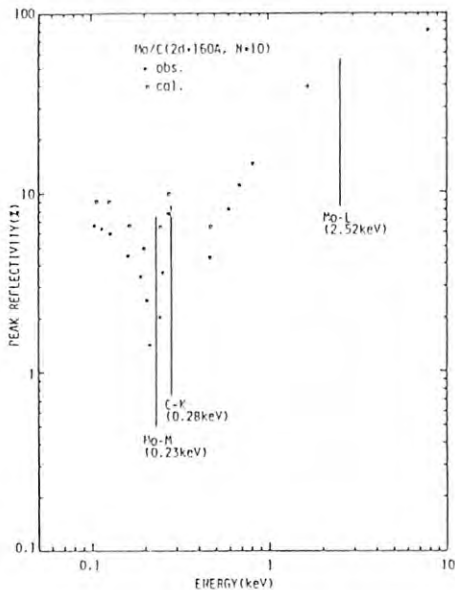


Fig. 1 Peak reflectivity of Mo/C

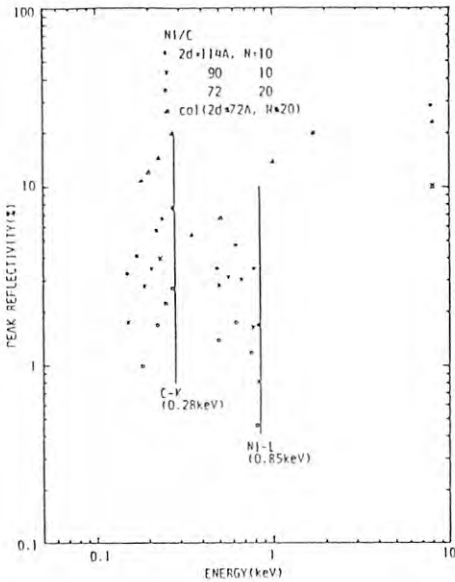


Fig. 2 Peak reflectivity of Ni/C

OPTICAL CONSTANTS OF HIGHLY REFLECTIVE MATERIALS FOR SOFT X-RAY MULTILAYER MIRRORS

Masaki YAMAMOTO, Akira ARAI, Jianlin CAO, Shigeru NAKAYAMA, Mihiro YANAGIHARA and Takeshi NAMIOKA
Research Institute for Scientific Measurements, Tohoku University, 2-1-1 Katahira, Sendai, 980

Introduction

Soft x-ray multilayer mirrors¹⁾ are key optical elements to develop x-ray optics such as a microscope, a telescope, a laser, and so on. The subjects of this study are to measure reflectance of the multilayer mirrors to evaluate the performance, and of single layers fabricated under the same condition as multilayers to investigate optical constants of the thin films of various materials²⁾. Highly reflective materials as candidates for the elements of multilayers and for reflective coating around 100 eV photon-energy are currently focused on.

Rh, Ru, and Mo are such materials selected by a new³⁾ rule applied to available optical constants³⁾. Measured reflectance of multilayer mirrors and evaluated optical constants of Mo have been reported previously²⁾.

Experimental results on a Rh single layer and a Ru single layer are shown in this report.

Reflectometer

The soft x-ray reflectometer of PF was improved on its chamber to be equipped with a sample container holding 5 samples and a feedthrough of linear and rotary motion to transport the sample from the container to a sample holder. The feedthrough can be used to select a point of measurement on a sample surface by moving the sample in the sample holder along a line of intersection with a plane of incidence, thus enables to measure at several points of the sample surface. This was particularly useful for the optical constants measurements of thin film samples in which a layer deposited in a way that at least two areas of two different thicknesses were formed on one substrate. Reflectances of these areas of optically equal condition, but their layer thicknesses, make a useful set in the accurate analysis of the optical constants of materials in thin film form.

The reflectometer was also improved on the driving systems of sample and detector rotation by employing stepping motors controlled by a personal computer (NEC PC9801-VM21). Softwares for reflectance measurements were written by the BASIC language. Automatic routines such as reflectance vs angle of incidence measurements with functions of peak search by the scans of detector or sample positions can be selected on a menu on a computer display.

Reflectance between 110eV to 55eV

Figures 1 and 2 show reflectance of Rh and Ru, respectively, measured for various angles of incidence at 110-55eV photon energy with a Be filter. It is evident that reflectances of these materials are higher than that of Au frequently used to increase reflectance in this wavelength region. High reflectance is further demonstrated in Fig.3 showing reflectance vs angle of incidence of Ru measured at 100eV and 150eV. These data are now analyzed to investigate the optical constants and roughness.

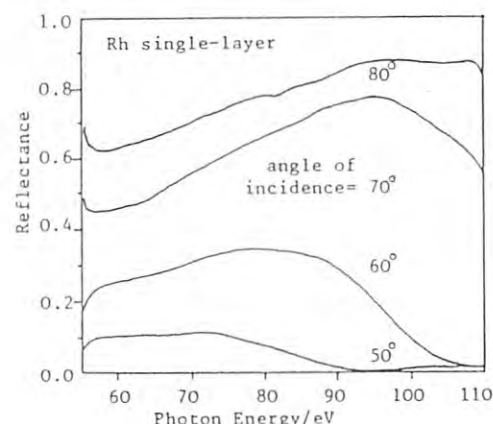


Fig.1

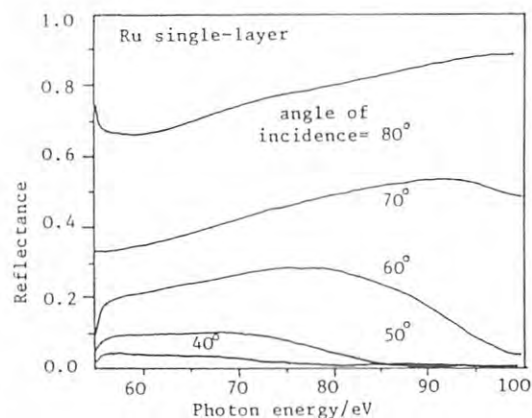


Fig.2

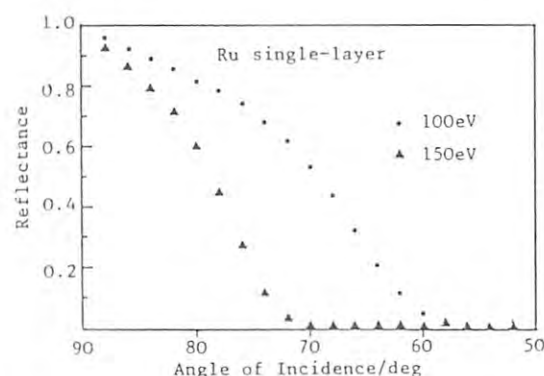


Fig.3

References

- 1) M. Yamamoto, A. Arai, M. Watanabe and T. Namioka, Proc. SPIE, 688, (1986) 99
- 2) M. Yamamoto, A. Arai, M. Watanabe, T. Namioka and M. Yanagihara, Photon Factory Activity Report, #4 (1986) 231
- 3) The optical constants were calculated by using data of atomic scattering factors after B. L. Henke, P. Lee, T. J. Tanaka, R. L. Shimabukuro and B. K. Fujikawa, Atomic Data and Nuclear Data Tables 27 No.1 (1982)

RESUSCITATION OF CARBON-CONTAMINATED MIRRORS AND GRATINGS BY OXYGEN-DISCHARGE CLEANING.

Tsuneharu KOIDE, Tetsuo SHIDARA, Mihiro YANAGIHARA*, and Shigeru SATO

Photon Factory, National Laboratory for High Energy Physics, Oho, Tsukuba-shi, Ibaraki 305

* Research Institute for Scientific Measurements, Tohoku University, Sendai, Miyagi 980

Carbon K-edge absorption spectroscopy has been greatly hindered by the carbon contamination of optical elements. In order to solve the contamination problem, we have studied the capability of dc oxygen-discharge cleaning to resuscitate their efficiencies over the 100-1000-eV energy range¹⁾. A reflectometer equipped with a discharge electrode was employed to make in situ optical measurements before and after cleanings. Cleaning was performed under the conditions determined to be the best previously²⁾. Measurements were made using a grasshopper monochromator (BL-11A).

Figure 1 shows the process of a reflectance recovery of a Pt-coated mirror. The mirror exhibited marked visible contamination. The overall spectral shape before cleaning was similar to that of carbon; near the carbon K edge the reflectance drops off precipitously, while a high reflectance can be seen in the lower energies ($h\nu \leq 250$ eV). The spectrum showed a wavy pattern above ~ 500 eV and a sharp dip, A, on the low-energy side of the K-edge dip. The energy position of A was dependent on the angle of incidence (~ 270 eV at 86° and ~ 280 eV at 88°). We made a model calculation, and the result showed that dip, A, was naturally derived and its energy position was dependent on the angle of incidence, in agreement with the observed behavior. The calculation also closely reproduced the wavy pattern above ~ 500 eV. These good agreement led to the conclusion that dip A, as well as the high-energy features, originates from an interference effect in the carbon layer. The mirror was first cleaned at a power of ~ 39 W for 20 min. The contaminant films were considerably removed, though visible contamination could still be seen. The K-edge dip remained while feature A disappeared, and

the period of oscillation above ~ 500 eV became larger. The second cleaning was made at ~ 39 W for 30 min, resulting in a complete disappearance of visible contamination. A comparison of Fig. 1 and the spectrum of a clean mirror showed an almost complete recovery of the reflectance of the mirror. The residual small dip at the K edge is evidently a spectral artifact ascribable to optical-elements contamination in BL-11A, since its depth is almost the same as that observed for a clean mirror.

Figure 2 shows the efficiency spectra of the inside first order of an Au-coated, 2400 λ/mm grating before and after cleaning¹⁾. This grating had been used at an average pressure of $\sim 3 \times 10^{-9}$ Torr for about two years. The contamination level of the grating was very low as a result of this good vacuum. However the spectrum before cleaning exhibited a noticeable degradation at the carbon K edge. The grating was given the first cleaning at a low power (~ 23 W) for a short time (3 min). The K-edge dip became shallower after the cleaning, and a considerable efficiency increase was attained above the K edge as well. The second cleaning was performed at ~ 20 W for 5 min. The spectrum after the cleaning exhibited only a very shallow dip at the K edge. The zeroth-order spectrum after the cleaning (not shown here) exhibited a K-edge dip, which was almost the same in depth as that observed for a clean mirror. This indicates that the grating efficiency has been restored even at the carbon K edge.

References

- 1) T. Koide et al., Appl. Opt. (Submitted).
- 2) T. Koide et al., Appl. Opt. **26**, 3884 (1987).

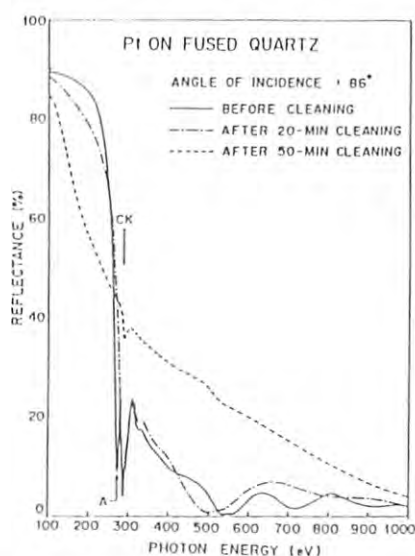


Fig. 1 Reflectance spectra of a Pt-coated mirror before and after two cleanings, measured at an 86° angle of incidence.

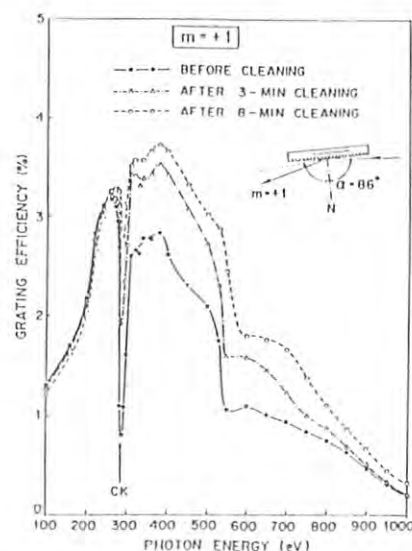


Fig. 2 Efficiency spectra of the inside first order of a 2400 λ/mm grating before and after two cleanings, measured at an 86° angle of incidence.

STE LUMINESCENCE EXCITATION SPECTRA NEAR THE K AND CL 1S EDGES IN KCl AND KBr

Mihiro YANAGIHARA, Yasuhiro KONDO,^{*} Takaaki HANYU,[†] and Shigeo YAMAGUCHI[‡]Research Institute for Scientific Measurements, Tohoku University,
Katahira, Sendai 980^{*} Department of Applied Physics, Faculty of Engineering, Tohoku University,
Aramaki, Sendai 980[†] Department of Physics, Faculty of Science, Tokyo Metropolitan University,
Fukasawa, Setagaya-ku, Tokyo 158Introduction

The intrinsic luminescence in ionic crystals has been assigned to recombination of self-trapped excitons (STE).¹⁾ Luminescence excitation spectra of the crystals give information about the intermediate relaxation processes before the recombinations. Previously we have measured the STE luminescence excitation spectra for KCl, KBr, NaCl, NaBr, and AgCl in a 5-30-eV energy range,²⁾ where $K M_{2,3}$ core holes are excited. The shallow core holes were found to relax almost through Auger processes. As a next step we are much interested in how the 1s core holes decay in these ionic crystals. In this paper we report the STE luminescence excitation spectra for KCl and KBr near the excitation energies of the 1s core levels in K (3610 eV) and Cl atoms (2825 eV).

Experimental

The cleaved KCl and KBr single crystals of about 1-mm thick were mounted on a cold finger of a helium cryostat. The samples were irradiated with monochromatized soft X-rays from a double crystal monochromator (BL-11B). The luminescence light was focused using a quartz lens to the entrance slit of a second monochromator installed outside the vacuum chamber. The band-passed photons from the second monochromator were detected with a photomultiplier R585 followed by a photon-counting system. The time dependence of the incidence light intensity was monitored with a gold mesh; the luminescence yield was always normalized to the photoelectric yield of gold.

Results

Figure 1 shows the excitation spectra of π -

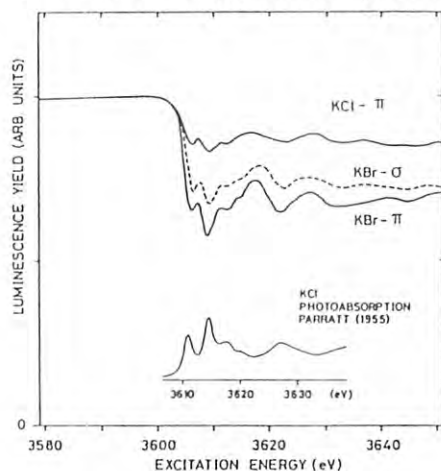


Fig.1

emission in KCl and π - and σ -emissions in KBr near the K 1s absorption edge. In each spectrum the luminescence yield is normalized to one just below the 1s edge. As is shown, above the 1s edge the luminescence yield largely lowers by amount of 40 % in π -emission of KBr, for example, and spectral dips are dominant here. In the insert is shown an X-ray absorption spectrum of KCl.³⁾ It is noticed that the dip structure in the excitation spectrum has an inverse relationship with the absorption spectrum. Figure 2 shows the excitation spectrum of π -emission in KCl near the Cl 1s absorption edge. Similarly the decrease in the yield amounts to 50 %, and the spectral structure is in inverse correlation with the X-ray absorption spectrum.

As an origin of the dips in the luminescence yield X-ray fluorescence decay is very probable. But, in terms of an atomic model the great decrease in the luminescence yield can not be explained at all ($< 8\%$). As other origins radiative recombination of 1s core excitons and that of the valence-band electrons with the 1s holes should be considered⁴⁾ (solid state effects). More extensive investigations on the soft X-ray radiative decays are hereafter necessary.

References

- 1) M.N. Kabler and D.A. Patterson: Phys. Rev. Lett. 19 (1967) 652.
- 2) M. Yanagihara, Y. Kondo, and H. Kanzaki: J. Phys. Soc. Jpn. 52 (1983) 4397.
- 3) L.G. Parratt and E.L. Jossem: Phys. Rev. 97 (1955) 916.
- 4) K. Ichikawa, M. Kamada, O. Aita, and K. Tsutsumi: Phys. Rev. B32 (1985) 8293.

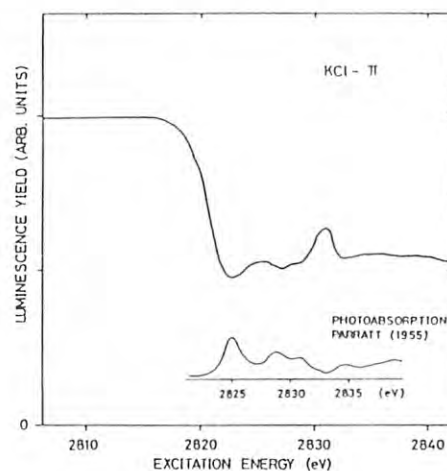


Fig.2

DIRECT OBSERVATION SYSTEM FOR TWO-DIMENSIONAL X-RAY PHOTOELECTRON DIFFRACTION (XPED) PATTERNS

Eisaku NAKAMURA, Masanori OWARI, Jun KAWAI and Yoshimasa NIHEI

Institute of Industrial Science, University of Tokyo,
Roppongi, Minato-ku, Tokyo 106

Introduction

X-ray photoelectron diffraction (XPED) has been shown to be a promising method for surface structural and chemical state analysis.¹⁾ In order to obtain an XPED pattern (angular distribution of photoelectron intensities) using a conventional deflection-type electron spectrometer, long time was required because of point-by-point collection of photoelectrons. Recently large area microchannel plates (MCP) became easily obtainable, which made it possible to detect photoelectrons projected onto large area such as a screen of LEED optics. Mizuno et al.²⁾ developed a direct observation system of XPED patterns using a retarding field type electron energy analyzer, MCP and a video camera. In this project, the authors combined the XPED direct observation system developed by Mizuno et al. with the synchrotron radiation X-ray source, and acquisition of two-dimensional XPED patterns together with consideration of data processing method were performed.

Experimental

Details of the apparatus were described elsewhere.^{2,3)} A retarding field type electron energy analyzer consisted of 4 concentric grid meshes. A sample crystal was placed on the center of the analyzer. Electrons with the energy higher than the high-pass filter potential of the analyzer were multiplied by 3-inch 2-stage MCP, and visualized by a phosphor-coated anode. Light spots were detected by a video camera, and signals were accumulated in a real-time image processor controlled by PDP-11/23 minicomputer. An image of finite energy range photoelectrons was obtained by image subtraction synchronized with modulation of high-pass filter potential.

All the experiment was performed at BL11B of Photon Factory in the National Laboratory for High Energy Physics. X-ray was monochromatized to 1764 eV by the InSb(111) double crystal monochromator. The beam was cut by two slits and irradiated a 1 mm x 2mm area of a vertically held Au(111) crystal.

Results and Discussion

Figure 1 shows the image of Au4f photoelectrons emitted into the detectable cone with the half cone angle of about 22°. Most of the contrast in the observed image was caused by moiré pattern of 4 grid meshes and other instrumental factors. In order to obtain net XPED contrast, another image was acquired from the sample which was rotated by 2° within the horizontal plane. Then the pixel-by-pixel ratio of two images was calculated so as to cancel position-dependent sensitivity factors. Figure 2 shows the ratio pattern of two images. The intensity of each point in the ratio pattern corresponds to the photoelectron intensity ratio to neighboring point. By successive multiplication of neighboring pixels from one side to another, net contrast of the XPED pattern was restored. Figure 3 shows the restored XPED pattern after the procedure described above. Resultant pattern showed reasonable agreement with the XPED pattern obtained by the angle-resolved photoelectron spectrometer.

References

- 1) Y. Nihei, M. Owari, M. Kudo and H. Kamada: Jpn. J. Appl. Phys. 20 (1981) L420.
- 2) K. Mizuno, M. Owari and Y. Nihei: Bunko Kenkyu 34 (1985) 233.
- 3) E. Nakamura, M. Owari, M. Kudo and Y. Nihei: Photon Factory Activity Report 1986, p.239.



Fig.1 Observed image of Au4f photoelectrons from Au(111).

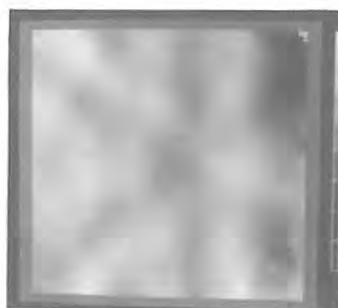


Fig.2 Ratio pattern of two observed images acquired at slightly different sample angles.

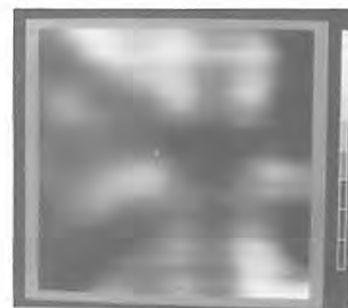


Fig.3 Restored Au4f XPED pattern from ratio pattern by numeric image processing.

POLARIZATION-DEPENDENT S K-EDGE XANES FOR SULFUR ON NICKEL

II. $(5\sqrt{3}\times 2)\text{S}/\text{Ni}(111)$ and $p(2\times 2)\text{S}/\text{Ni}(111)$

Yoshinori KITAJIMA^{1,2}, Toshihiko YOKOYAMA³, Manabu FUNABASHI⁴, Nobuhiro KOSUGI², Haruo KURODA^{2,4}, and Toshiaki OHTA³

1. Photon Factory, National Laboratory for High Energy Physics, Oho-machi, Tsukuba-gun, Ibaraki 305
2. Department of Chemistry, Faculty of Science, The University of Tokyo, Hongo, Bunkyo-ku, Tokyo 113
3. Department of Materials Science, Faculty of Science, Hiroshima University, Naka-ku, Hiroshima 730
4. J.R.D.C. 5-9-4 Tokodai, Toyosato-machi, Ibaraki 300-26

Introduction

Recently we have studied the surface local atomic structure of $(5\sqrt{3}\times 2)\text{S}/\text{Ni}(111)$ with the polarization-dependent surface EXAFS and have determined that the first layer is reconstructed to a $c(2\times 2)\text{S}/\text{Ni}(100)$ -like overlayer¹⁾. Here we report surface XANES, which is more sensitive to the local environment than EXAFS, of $(5\sqrt{3}\times 2)\text{S}/\text{Ni}(111)$ system, compared with those of $p(2\times 2)\text{S}/\text{Ni}(111)$ and $c(2\times 2)\text{S}/\text{Ni}(100)$.

Experimental

$p(2\times 2)$ LEED pattern was observed when cleaned $\text{Ni}(111)$ single crystal was dosed with 1×10^{-5} Pa H_2S for 10 s at room temperature. $(5\sqrt{3}\times 2)$ pattern was observed when dosed with 1×10^{-5} Pa H_2S for 15 s and heated to >500 K. The procedure of measurement of X-ray absorption spectra was the same as that of EXAFS experiment¹⁾. The experiment was performed at the UHV-compatible soft X-ray double crystal monochromator station (BL-11B).

Results and Discussion

The polar angle dependent surface XANES of $(5\sqrt{3}\times 2)\text{S}/\text{Ni}(111)$ and $p(2\times 2)\text{S}/\text{Ni}(111)$ are shown in Fig. 1 and Fig. 2, respectively. For the $(5\sqrt{3}\times 2)\text{S}/\text{Ni}(111)$, the peak b is enhanced at the normal incidence ($\theta=90^\circ$), while the peak c enhanced at

the grazing incidence ($\theta=15^\circ$). Therefore, the peaks b and c are assigned to S $1s - p_{x,y}$ and S $1s - p_z$ transitions, respectively, where z axis denotes $[111]$ direction. The peak a seems to be independent on the polar angle and is assigned to an isotropic $1s - 4p_{x,y,z}$ Rydberg type transition.

As these features are closely similar to other S/Ni systems²⁾, $c(2\times 2)\text{S}/\text{Ni}(100)$ and $c(2\times 2)\text{S}/\text{Ni}(110)$, we can compare these XANES spectra. The polarization dependence of XANES of $p(2\times 2)\text{S}/\text{Ni}(111)$ is distinctly different from that of $(5\sqrt{3}\times 2)\text{S}/\text{Ni}(111)$ and $c(2\times 2)\text{S}/\text{Ni}(100)$; the peak b increases at normal incidence in $(5\sqrt{3}\times 2)\text{S}/\text{Ni}(111)$ and $c(2\times 2)\text{S}/\text{Ni}(100)$ but decreases in $p(2\times 2)\text{S}/\text{Ni}(111)$. This clearly indicates that the adsorption site of S for $(5\sqrt{3}\times 2)\text{S}/\text{Ni}(111)$ is not like that for $p(2\times 2)\text{S}/\text{Ni}(111)$, which is presumed to be the 3-fold hollow site, but is similar to that for $c(2\times 2)\text{S}/\text{Ni}(100)$. The present XANES study supports the conclusion obtained by the surface EXAFS experiment¹⁾. Further analyses are now in progress with the multiple scattering calculation.

References

- 1) Y. Kitajima et al. this volume (Photon Factory Activity Report #5, 1987)
- 2) H. Kuroda et al. Photon Factory Activity Report #4, 1986, 238

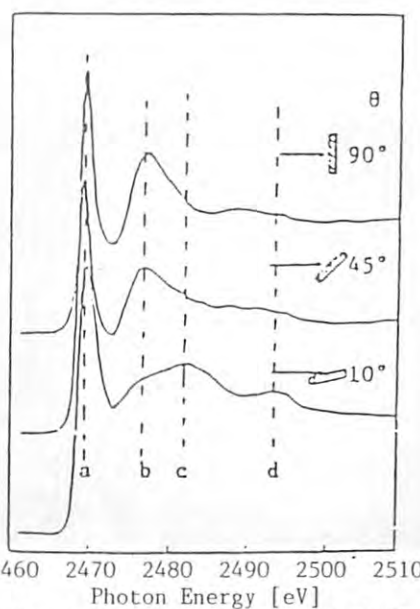
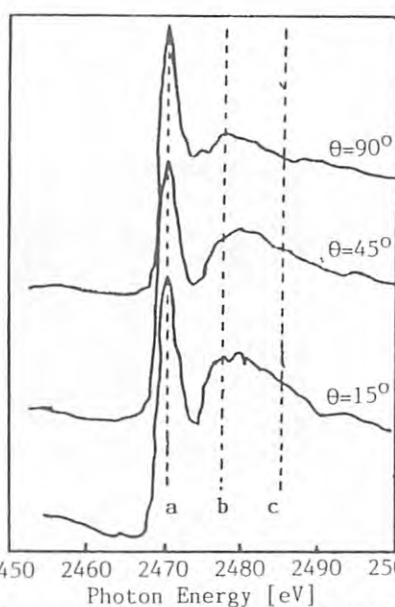
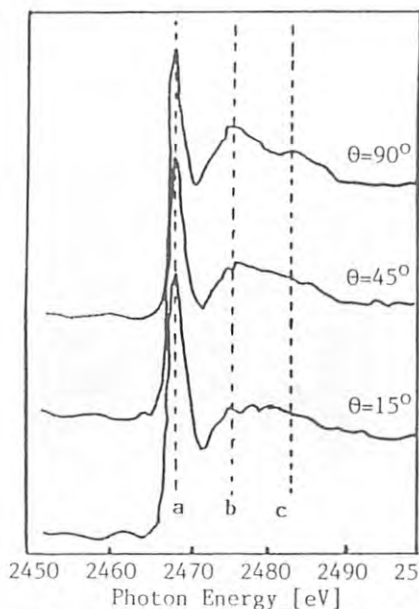


Fig. 1 XANES of $(5\sqrt{3}\times 2)\text{S}/\text{Ni}(111)$ Fig. 2 XANES of $p(2\times 2)\text{S}/\text{Ni}(111)$ Fig. 3 XANES of $c(2\times 2)\text{S}/\text{Ni}(100)$

SURFACE EXAFS OF $(5\sqrt{3}\times 2)\text{S}/\text{Ni}(111)$

Yoshinori KITAJIMA^{1,2}, Toshihiko YOKOYAMA³, Manabu FUNABASHI⁴, Nobuhiro KOSUGI², Haruo KURODA^{2,4}, and Toshiaki OHITA³

1. Photon Factory, National Laboratory for High Energy Physics, Oho-machi, Tsukuba-gun, Ibaraki 305
2. Department of Chemistry, Faculty of Science, The University of Tokyo, Hongo, Bunkyo-ku, Tokyo 113
3. Department of Materials Science, Faculty of Science, Hiroshima University, Naka-ku, Hiroshima 730
4. J.R.D.C. 5-9-4 Tokodai, Toyosato-machi, Ibaraki 300-26

Introduction

Surface EXAFS is now a powerful technique to study the local atomic structure of a solid surface-adsorbate system. Especially, the polarization dependence of EXAFS amplitude gives the information for the adsorption site of an adatom on a single crystal surface¹⁾. Here we report surface EXAFS study of $\text{S}/\text{Ni}(111)$ system with a so-called " $(5\sqrt{3}\times 2)$ " coincidence LEED pattern, which is schematically drawn in Fig. 1. This is the first application of surface EXAFS to the system with such a complicated LEED pattern.

Experimental

A $\text{Ni}(111)$ single crystal was mechanically and electrically polished and cleaned by repeated cycles of Ar^+ bombardment and annealing in a UHV chamber. Then the sample was dosed with 10^{-5} Pa H_2S for 15 s and heated to >500 K to form sharp $(5\sqrt{3}\times 2)$ pattern. X-ray absorption spectra were taken by monitoring S-KLL Auger electron yield in 2400–2900 eV range at the BL-11B soft X-ray monochromator station. Polar angles of incident X-ray chosen were 90° (normal incidence), 45° and 15° (glancing incidence). Intensity of incident beam was monitored by total electron yield from Cu mesh set before the sample.

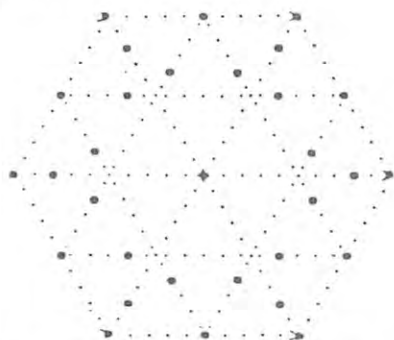


Fig. 1 Schematic view of $(5\sqrt{3}\times 2)$ LEED pattern

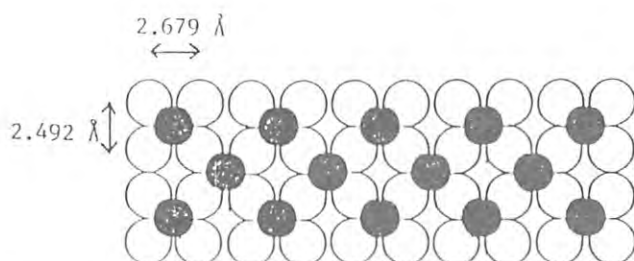


Fig. 2 The pseudo- $c(2\times 2)\text{S}/\text{Ni}(100)$ model for the $(5\sqrt{3}\times 2)\text{S}/\text{Ni}(111)$ system (● denotes S and ○ denotes Ni.)

Results and Discussion

Fourier transforms for the EXAFS modulation of the measured Auger electron yield spectra all have only one peak around 2 Å. This means that there is a short range order around the sulfur atom and that the adsorption state of S was only one type. Since it is considered that the peak corresponds to the nearest neighbor S-Ni bond, bond length R and effective coordination number N^* were obtained by the back Fourier transform curve fitting method from the peak, using EXAFS data of Ni_3S_2 ($R=2.28\text{Å}$, $N=6$) as a standard. From all the three polarization data, R is determined to be $2.22\pm 0.03\text{Å}$, that is almost the same value as the nearest neighbor S-Ni bond length of $c(2\times 2)\text{S}/\text{Ni}(100)$ system¹⁾.

In order to determine the adsorption site, polarization dependence of the experimental N^* value must be compared with that of the calculated one for several candidates for the adsorption site. In the left and center columns of Table, the experimental and calculated N^* 's for 3-fold hollow site of $\text{Ni}(111)$ are shown, respectively, which is the site presumed for $p(2\times 2)\text{S}/\text{Ni}(111)$ system, but they are quite different from each other. Therefore, it is quite unlikely that a sulfur atom of $(5\sqrt{3}\times 2)\text{S}/\text{Ni}(111)$ system is located on a 3-fold hollow site.

On the other hand, $(5\sqrt{3}\times 2)$ LEED pattern is known to correspond to a rhombic lattice in real space²⁾. In this unit mesh a is 3.67Å and α is 85.48° , which resemble those of $c(2\times 2)\text{S}/\text{Ni}(100)$ ($a=3.52\text{Å}$, $\alpha=90^\circ$). Thus we can suppose a pseudo- $c(2\times 2)\text{S}/\text{Ni}(100)$ model, shown in Fig. 2, which produces $(5\sqrt{3}\times 2)$ pattern. In the right column of Table, calculated N^* 's for this model are listed. Their polarization dependence is well agreed with that of the experimental values (left column). Therefore, we conclude that the first layer of $(5\sqrt{3}\times 2)\text{S}/\text{Ni}(111)$ surface is reconstructed to $c(2\times 2)\text{S}/\text{Ni}(100)$ -like overlayer as shown in Fig. 2.

References

- 1) S. Brennan et al, Phys. Rev. B24, 4871 (1981)
- 2) T. Edmonds et al, J. Vac. Sci. Technol. 8, 68 (1971)

Table Effective coordination number N^* for $(5\sqrt{3}\times 2)\text{S}/\text{Ni}(111)$

θ	Curve-fitted	Calculated	
		3-fold hollow of $\text{Ni}(111)$	pseudo- $c(2\times 2)\text{S}/\text{Ni}(100)$
90°	5.11	1.89	4.10
45°	4.62	3.56	3.95
15°	4.48	5.00	3.81
$90^\circ/45^\circ$	1.11	0.53	1.04
$15^\circ/45^\circ$	0.97	1.41	0.97

Ru L-edge X-ray Absorption Studies on Ru₃(CO)₁₂ Adsorption and the Formation of Ru-Cu Bimetallics on Cu(111)

T.K.Sham¹, T.Ohta², T.Yokoyama², Y.Kitajima³, M.Funahashi⁴,
Y.Takata², N.Kosugi³ and H.Kuroda^{3,4}

- 1)Dept. of Chemistry, Brookhaven National Laboratory, Upton, NY 11973, U.S.A.
- 2)Dept. of Materials Science, Hiroshima University, Naka-ku, Hiroshima 730.
- 3)Dept. of Chemistry, the University of Tokyo, Hongo, Bunkyo-ku, Tokyo 113.
- 4)J.R.D.C., 5-9-4 Tokodai, Toyosato, Ibaragi 300-26.

Electronic interaction between Ru and Cu in bimetallic Ru-Cu systems has been a subject of intense research since the experiment of Sinfelt et al(1). In the previous report(2) we showed the preliminary results on the Ru L₃-edge XANES for the Ru/Cu(111) systems prepared by the deposition of Ru₃(CO)₁₂ onto a clean Cu(111) surface. Here we present the conclusive interpretation, including the results of supplementary experiments.

The detailed procedure of sample preparation is referred to (3). About one monolayer (estimated by AES) Ru₃(CO)₁₂ was deposited onto a clean Cu(111) surface at 223K (stage (a)). The carbonyl-deposited surface was then irradiated with an electron beam, and was warmed up to room temperature (stage(b)). CO molecules were completely removed and naked clusters were deposited on the surface. The sample was subsequently annealed at 523K for 10 sec (stage(c)), followed by further annealing at 723K for 10 sec (stage(d)), and finally at 723K for 2 min (stage(e)). According to the AES intensity ratio given in table 1, little migration of Cu onto Ru clusters occurred at stage(c), while stage(d) and stage(e) exhibit the Cu-decorated surfaces. The XANES spectrum for each stage is illustrated in fig.1 together with the spectrum for Ru films prepared by evaporation of Ru onto Kapton sheets. The XANES parameters as well as the corresponding AES results are tabulated in table 1. The results for Ru/Cu(100) are essentially the same as those for Ru/Cu(111) which measured very recently and hence it is not necessary to show the latter results here.

It is well established that the L₃-

edge whiteline intensity is extremely sensitive to the d band occupation and that the edge-shift as well corresponds to the oxidation number. The chemical shift between stage(a) and Ru films clearly suggests that the d → π* back-donation is quite significant in the carbonyl compounds and the removal of CO restores a large amount of d character at the Ru site (stage(b)). The broad asymmetric whiteline and no extended structure indicate that the naked Ru clusters are in a highly disordered state. The Ru L₃ spectra of Cu-migrated Ru clusters (stage(d) and (e)) exhibit marked changes; the whiteline narrows and the intensities are noticeably smaller than that of the bare surface aggregates. These features are nearly

identical to that of the Ru film except that the Ru film has a slightly bigger area under the resonance. The three dimensional Ru clusters are formed on the Cu(111) surface. The slight decrease of the whiteline intensity indicates a decrease in unoccupied d states at the Ru site, implying the charge redistribution in the Cu-Ru interaction. (Charge transfer from Cu to Ru might occur.)

References

- (1) Sinfelt et al, J.Catal., 42 (1976) 227.
- (2) T.K.Sham et al, PF Activity Report, #4 (1986) 237.
- (3) T.K.Sham et al, submitted to J.Chem.Phys.

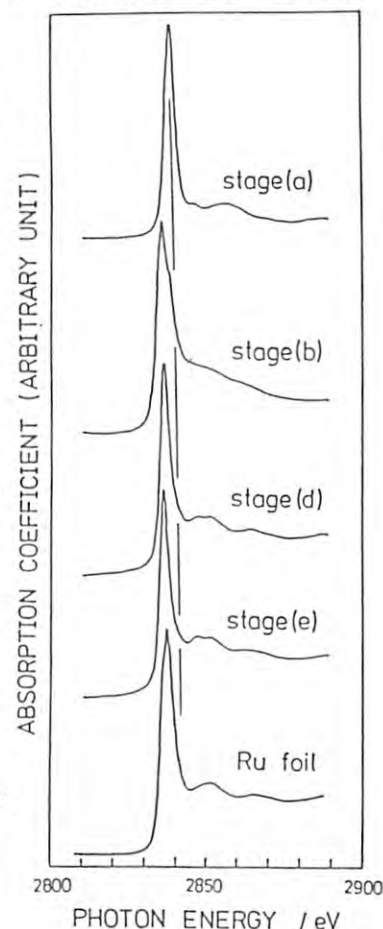


Fig.1 Ru L₃-edge
XANES spectra (AES
yield)

Table 1 AES and XANES parameters

stage	AES Ru/Cu	edge- shift(eV)	whiteline intensity
a	1.05	2.5	1.62
b	1.04	-0.4	0.82
c	1.02	—	—
d	0.26	-0.3	0.75
e	0.11	-0.3	0.71
Ru film	—	0.0	1.0

SURFACE EXAFS AND XANES OF S/Fe SYSTEMS

I. Measurement of X-ray absorption spectra of c(2x2)S/Fe(100)

Yoshinori KITAJIMA^{1,2}, Toshihiko Yokoyama³, Manabu FUNABASHI⁴, Toshiaki OHTA³, Haruo KURODA^{2,4}, Junji NAKAMURA⁵, Katsumi TANAKA⁵, and Isamu TOYOSHIMA⁵

1. Photon Factory, National Laboratory for High Energy Physics, Oho-machi, Tsukuba-gun, Ibaraki 305
2. Department of Chemistry, Faculty of Science, The University of Tokyo, Hongo, Bunkyo-ku, Tokyo 113
3. Department of Materials Science, Faculty of Science, Hiroshima University, Naka-ku, Hiroshima 730
4. J.R.D.C. 5-9-4 Tokodai, Toyosato-machi, Ibaraki 300-26
5. Research Institute for Catalysis, Hokkaido University, Kita-ku, Sapporo, Hokkaido 060

Introduction

In order to understand the adsorption mechanism of an atom or molecule onto a solid surface, it is important to perform experiments for the same adsorbate with various substrates. Though surface EXAFS is the most powerful method to determine the local atomic structure of surface, for S adsorption only S/Ni systems have been studied with this method.¹⁾⁻⁴⁾ We try to surface EXAFS and XANES of c(2x2)S/Fe(100), which is the first step to know the difference between Ni and Fe substrate.

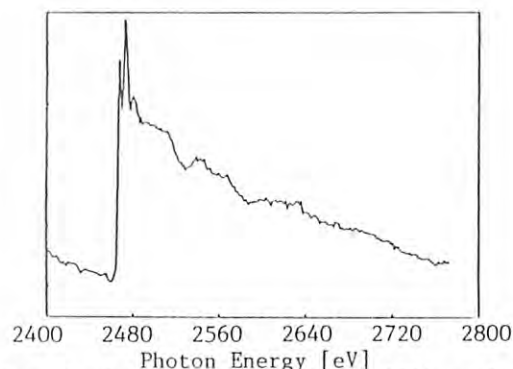
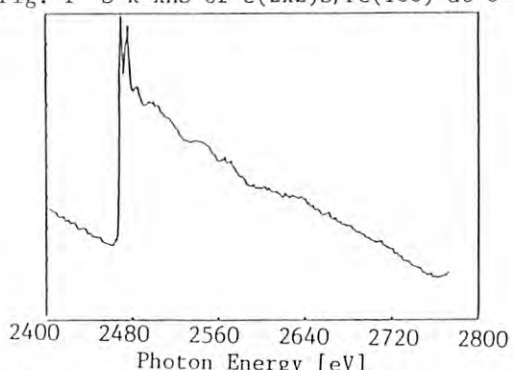
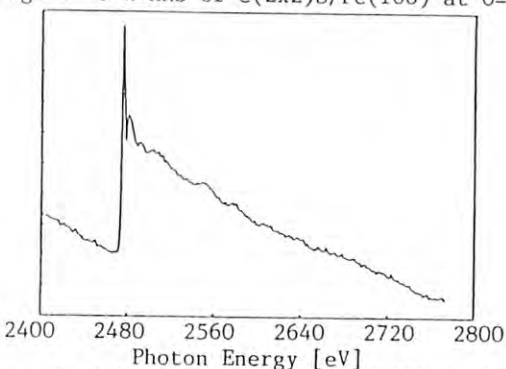
Experimental

When a Fe(100) single crystal was heated to 900 K by electron bombarding, c(2x2) LEED pattern was observed by S segregated from the bulk. Fe and S are the only two elements appearing in the Auger electron spectrum. We chose this system, c(2x2)S/Fe(100), for the first measurement. The X-ray absorption spectra were measured by monitoring S-KLL Auger electron (2110eV) yield at the soft X-ray double crystal monochromator station (BL-11B). Polarization direction θ , the angle between surface normal and \vec{E} , was changed from 90° (normal incidence) to 45° and 15°.

Results and Discussion

The measured Auger electron yield spectra are shown in Fig. 1 - Fig. 3. It is impossible to measure these spectra above 2800eV, because the Fe 2p photoelectrons enter the analyzer window of CMA at that range. We try to analyze the EXAFS modulations of the spectra in vain. This is partly because the very weak signal and small S/N ratio due to the deterioration of the monochromator and/or the detector, and partly because the interference of photoelectron of oxygen contamination adsorbed during the measurement even in the UHV condition. It is one of the different features from Ni, which is hardly contaminated by O when covered with S. Now the improvement of the monochromator and the detector and the development of a fluorescent proportional counter are in progress to measure better spectra.

In the XANES region, however, a distinct polarization dependence in the first and second peaks is observed, that is quite different from c(2x2)S/Ni(100) system. This indicates a difference between adsorption state of S/Ni and S/Fe. Further analyses are now in progress with the multiple scattering calculation.

Fig. 1 S K-XAS of c(2x2)S/Fe(100) at $\theta=90^\circ$ Fig. 2 S K-XAS of c(2x2)S/Fe(100) at $\theta=45^\circ$ Fig. 3 S K-XAS of c(2x2)S/Fe(100) at $\theta=15^\circ$ References

- 1) S. Brennan, J. Stöhr, R. Jaeger, Phys. Rev. B24, 4871 (1981)
- 2) Y. Kitajima, N. Kosugi, H. Kuroda, T. Ohta, J. Chem. Soc. Jpn., 1986, 1547 (in Japanese)
- 3) T. Ohta, H. Kuroda, N. Kosugi, Y. Kitajima, T. Yokoyama, M. Funabashi, Photon Factory Activity Report #4, 1986, 236
- 4) Y. Kitajima, T. Yokoyama, M. Funabashi, N. Kosugi, T. Ohta, H. Kuroda, this volume (Photon Factory Activity Report #5, 1987)

ENHANCED KILLING ON *E. COLI* AND BACTERIOPHAGE BY X-RAYS AT RESONANCE ENERGY OF PHOSPHORUS K-ABSORPTION EDGE.

Hiroshi Maezawa¹, Yoshiya Furusawa², Kotaro Hieda³, Katsumi Kobayashi⁴, Tomoyuki Mori¹, Kenshi Suzuki⁵ and Takashi Ito⁵.

1)Dept. Radiation Oncology, Sch. Med., Tokai Univ., Kanagawa 259-11. 2)Dept. Molecular Biol., Sch. Med., Tokai Univ., Kanagawa 259-11. 3)Biophys. Lab., Dept. Phys., Rikkyo Univ., Tokyo 171. 4)PF, National Lab. High Energy Phys., Ibaraki 305. 5)Inst. Phys., College of Sci. Art., Univ. of Tokyo, Tokyo 153.

In the previous work¹⁾, the killing enhancement based on the direct absorption of photon by phosphorous atoms in DNA has been observed in cells (*Deinococcus radiodurans*) and dried bacteriophages. We are interested in the reparability of cells for damages by K-shell photoionization in P atoms in DNA. Recently, the killing effects on *E. coli* irradiated with X-rays at resonance energy of P, K-shell absorption were investigated using the repair deficient strains.

Materials and Methods

E. coli B/r (wild type), H/r30recA (recombinational-repair deficient) and H/r30uvrA (excision-repair deficient) strains were used through experiments. Exponentially growing cells of *E. coli* out of culture were washed by centrifugation and suspended in saline. The cells were placed on a Millipore membrane filter (pore size; 0.45 μ m). The filter was then placed on a wet paper soaked in saline and mounted on a plastic dish which could be moved up and down on a sample scanning stage. After X-rays irradiation, cells were plated on the agar medium for colony formation.

Phage particles suspended in nutrient broth (0.8 %) were dropped on a polypropylene sheet and dried up in vacuum. Dried bacteriophages were irradiated with X-rays in sample chamber under vacuum in the scanning mode. After irradiation, bacteriophage particles were suspended in nutrient broth. Survivals were determined from the plaque forming unit on *E. coli* B-s-1 cells as indicator.

Beam line used were BL-11B and BL-12C. Irradiation energies were 2.146 keV, 2.153 keV (resonance energy of K-shell absorption of P atoms in DNA) and 2.160 keV.

Results and Discussion

E. coli cells Survival curves of *E. coli* B/r, H/r30recA and H/r30uvrA strains were shown in figure 1. In every cases, survival curves at

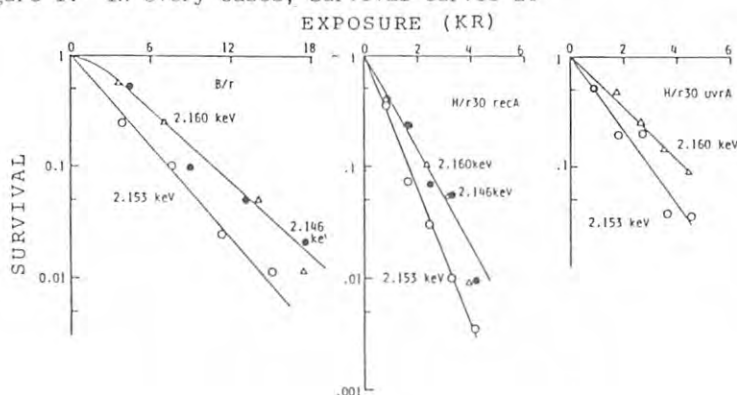


Fig. 1. Survival of *E. coli* B/r, H/r30recA and H/r30uvrA cells irradiated with monochromatic X-rays.

2.146 keV were similar to that at 2.160 keV. However, the exponential slope of survival curves of cells irradiated with 2.153 keV X-ray was steeper than that with other two X-rays. The killing sensitivity per unit exposure with 2.153 keV X-ray was 1.7 times and 1.5 times high for B/r and recA strains, as compared with 2.160 keV X-ray, respectively.

The calculated energy absorption per cell per unit exposure are not different between each X-ray energies. Therefore, it may be concluded that the killing efficiency per unit absorbed energy per cell at 2.153 keV are larger than that at 2.160 keV (or 2.146 keV). The efficient killing at K-shell resonance energy of P atoms may be able to explain by the term of the increase of localized energy absorption in the vicinity of DNA.

The number of the K-shell photoionization per one lethal hit exposure (D_{37}) can be calculated using the photoionization cross section, the number of P atoms in DNA and the photon flux per D_{37} . Assuming as the photoionization cross section at 2.153 keV is 6.22×10^{-5} barn, the number of lethal hits per K-shell resonance photoionization event in P atoms is estimated as 0.22 for B/r cells and 0.94 for H/r30recA cells. It is suggested that a part of damages produced by K-shell ionization in P atoms is repairable in the cell system.

Dried bacteriophage T1 Bacteriophage T1 irradiated with 2.153 keV X-ray was also sensitive as compared with other two X-rays. As contrast with *E. coli* cells, bacteriophage exposed to 2.160 keV X-ray was more sensitive (about 1.2 times) than that to 2.146 keV. Sensitivity at 2.153 keV was 1.7 times higher than that at 2.146 keV. If calculations are performed, the number of lethal hits per K-shell photoionization event is estimated as 0.28.

References

- 1)H.Maezawa et al., (1986) Photon Factory Activity Report -1985/1986.

STRAND BREAKS IN pBR322 DNA INDUCED BY MONOENERGETIC X-RAYS AROUND K-ABSORPTION EDGE OF PHOSPHORUS

Kotaro HIEDA, Akira AZAMI, Masao SUZUKI, Hiroshi MAEZAWA[†],
Yoshiya FURUSAWA^{††} and Katsumi KOBAYASHI[‡]

Department of Physics, Faculty of Science, Rikkyo University,
Nishi-Ikebukuro, Toshima-ku, Tokyo 171

[†]Department of Radiation Oncology and ^{††}Department of Molecular Biology,
School of Medicine, Tokai University,
Bohseidai, Isehara, Kanagawa 259-11

[‡]Photon Factory, National Institute for High Energy Physics,
Oho-machi, Tsukuba-gun, Ibaraki 305

Introduction

X-ray induced inner-shell ionization of an atom of DNA molecule is followed by Auger cascade and results in ejection of several low energy Auger electrons and production of multiply charged atom. These Auger electrons produce several nearby ionization. An inner-shell ionization, therefore, deposits energy in a highly localized fashion. These kinds of primary process might give rise to special chemical effects requiring particularly great amounts of energy or high degrees of local disturbance.

Because phosphorus is a constituent of main chain of DNA, it seems interesting to investigate if X-ray induced K-shell ionization of phosphorus produces excess single- and double-strand breaks of DNA.

Materials and Methods

DNA was plasmid pBR322 (4362 base pairs). Super helical closed circular (Form I) DNA was isolated by alkaline method and CsCl/ethidium bromide density gradient. Isolated DNA was dialyzed against TE buffer (1 mM Tris-HCl and 0.1 mM EDTA, pH 8.0) containing 0.2 M NaCl for replacement of Cs by Na, filtered by Milcut (Millipore) and dissolved in TE buffer. After buffer concentration was increased by 3 times, aliquot of 1 μ l containing 1 μ g DNA and 0.5 μ g buffer solute was spotted on polypropylene strip and dried in air. Samples in vacuum were irradiated with monoenergetic X-rays at BL-11B and 12C. Redissolved DNA was electrophoresed in agarose gel and three DNA forms (Form I, II and III) were separated. Single- and double-strand breaks were determined as a conversion from Form I to Form II and that from Form I to Form III, respectively. X-ray absorption spectrum was measured for DNA film prepared from calf thymus DNA (Na salt) dissolved in distilled water.

Results

Absorption spectrum of DNA had a resonance peak at 2.151 keV. Therefore, we used 3 monoenergetic X-rays, 2.146, 2.151 and 2.158 keV, at which relative absorptions were 1.00, 2.87 and 1.33, respectively. Exposure doses (R) giving one strand break were determined from the decrease in Form I (single-strand break) and the increase in

Form III (double-strand break). Exposure doses at 2.146 keV (below the absorption edge) were converted to absorbed doses by a conversion factor calculated from elemental composition of sample (1 μ g DNA and 0.5 μ g buffer solute) and mass-absorption coefficient tabulated by Hubbell¹⁾. The conversion factors at two higher energies were calculated on the assumption that the mass-absorption coefficient of DNA was proportional to the measured absorption spectrum of DNA film. The calculated conversion factors were 0.84, 1.86 and 1.02 cGy/R at 2.146, 2.151 and 2.158 keV, respectively. D_0 in kGy calculated by those factors were tabulated in Table 1.

For single-strand breaks, D_0 were almost same at 3 energies. Number of K-shell ionization of phosphorus per D_0 were calculated (Table 2): those were only less than 0.1. These results indicate that single-strand breaks are induced mainly by secondary electrons and K-shell ionization of phosphorus plays minor role.

For double-strand breaks, D_0 at the peak energy (2.151 keV) was somewhat lower than those at other energies. However, irradiation of D_0 induces about 2 ionizations per whole molecule at three energies but 0~1.24 ionizations of K-shell depending on X-ray energies. This may indicate that K-shell ionization of phosphorus does not effect on amount of double-strand breaks but on chemical nature of strand break.

Reference

- 1) J. H. Hubbell, Int. J. Appl. Radiat. Isot., **33**, 1269 (1982)

Table 1 Absorbed dose giving one strand break (D_0) in a pBR322 DNA molecule by monoenergetic X-rays

Energy (keV)	D_0 (kGy)	
	Single-strand break	Double-strand break
2.146	6.6	136
2.151	7.3	106
2.158	7.0	137

Table 2 Calculated number of photons absorbed by a pBR322 DNA molecule and K-shell of phosphorus of it.

Energy (keV)	Number of absorbed photons/ D_0			
	Single-strand break		Double-strand break	
	DNA	K-shell of P	DNA	K-shell of P
2.146	0.091	0	1.89	0
2.151	0.13	0.085	1.89	1.24
2.158	0.11	0.026	2.08	0.50

IRRADIATION EFFECTS OF MONOCHROMATIC SOFT X-RAYS
AROUND K-SHELL ABSORPTION EDGE OF PHOSPHORUS ON YEAST CELLS

Katsumi KOBAYASHI¹⁾, Noriko USAMI²⁾, Akinari YOKOYA²⁾, Kotaro HIEDA³⁾,
Hiroshi MAEZAWA⁴⁾, Yoshiya FURUSAWA⁴⁾ and Takashi ITO⁵⁾

- 1) Photon Factory, National Laboratory for High Energy Physics, Tsukuba 305
2) Institute of Biological Sciences, University of Tsukuba, Tsukuba 305
3) Institute of Biophysics, Rikkyo University, Tokyo 171
4) School of Medicine, Tokai University, Isehara 259-11
5) College of Arts and Sciences, University Of Tokyo, Tokyo 153

Introduction

One important application of synchrotron radiation in radiation biology, perhaps only become feasible by SR, is to see the consequences of Auger cascade in low atomic number elements located at a key position of biological molecules. At wavelength tuned to the K-absorption edge, we can irradiate selectively by taking advantage of much larger X-ray absorption cross section (absorption) than both sides of the edge. Among the elements we selected phosphorus that links adjacent deoxypentoses in DNA strands. PO_4 moiety is known to have a sharp resonance absorption near the K edge¹⁾. The inner shell absorption of phosphorus is followed by Auger cascade, leading to a multiply charged state. Irradiation of monochromatic X-rays of the K-absorption edge is expected to produce an explosion of DNA strand at phosphorus. In this preliminary note, we report an enhanced cell inactivation and induction of genetic changes in yeast irradiated with the wavelength at phosphorus K-absorption edge.

Materials and Methods

A diploid strain D7M1-1 of yeast, *Saccharomyces cerevisiae*, was used. Cells were cultured in YPD medium for 2 days and harvested in the stationary phase. After washing twice with distilled water, 1×10^6 cells were put onto 3mm x 4mm area of membrane filters. Thickness of the sample on the filter was estimated as 10 μm in average (two-cell layer), diameter of the cell being 5 μm . Irradiation was carried out with the 3 X-ray energies indicated, namely, the energy

corresponding to the resonance absorption peak (2153 eV) of phosphorus and both sides of it (2146 and 2160 eV) at beam line 11B. Since the intensity distribution in the beam area was not uniform, sample was scanned vertically during irradiation. Exposure rate was measured by an ionization chamber. Irradiated cells were resuspended in phosphate buffer and after appropriate dilution one part was plated on the synthetic complete medium for the measurement of survival and the other on the minimal medium deprived of tryptophan for the convertants.

Results

Survival curves are shown in Fig.1 with the three wavelengths of the monochromatic SR X-rays. X-rays with the energy at the absorption peak was the most effective (dose modification factor, DMF, 0.73) for lethality on the basis of exposure dose. The difference of lethality between the X-rays below (2147eV) and above (2160eV) the peak was not observed. Frequencies of mitotic gene conversion at *trp-5* locus were plotted in Fig.2. X-rays with the energy at peak absorption showed maximum efficiency of induction. These differences could be attributed to the resonance absorption of the phosphate moiety in the DNA molecule. Further experiments are well under way to investigate the consequences of Auger cascade of the phosphorus atom in DNA.

- 1) J.L. Dehmer, J. Chem. Phys., **56**, 4496-4506 (1972).

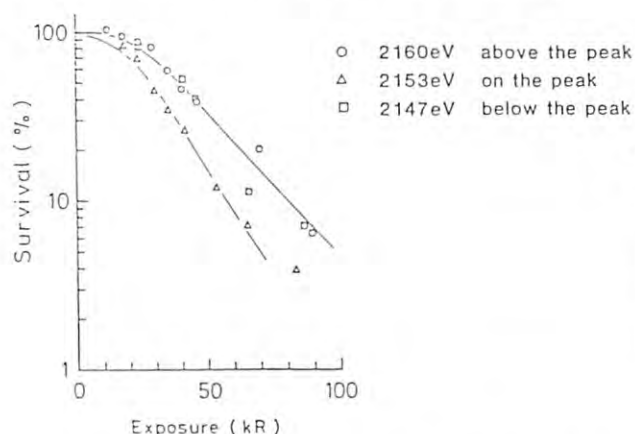


Fig. 1. Survival curves of yeast cells irradiated with three wavelengths of monochromatic soft X-rays.

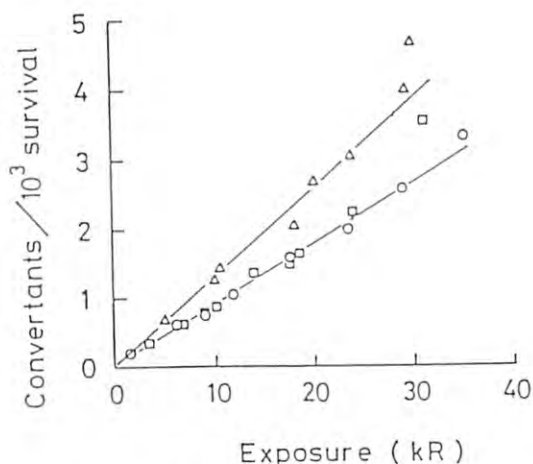


Fig. 2. Induction of genetic changes in yeast cells irradiated with monochromatic soft X-rays.

PIEZOREFLECTIVITY OF $\text{Na}^+ 2p$ CORE EXCITON IN NaCl

Masatada YURI, Katsuhiko IWASE, Kiyoshi KANISAWA, Tatsuya MARUYAMA*,
Shinobu TAKAHASHI, Masaaki KOBAYASHI, Yoshihiro AIURA+, Hirohito FUKUTANI+,
Hiroo KATO++, Tsuneharu KOIDE++ and Akira MISU

Department of Physics, Faculty of Science, Science University of Tokyo, Tokyo 162

+Institute of Physics, The University of Tsukuba, Ibaraki 305

++Photon Factory, National Laboratory for High Energy Physics, Ibaraki 305

Piezorefectivity spectra of NaCl were measured in the photon energy region from 32 to 35 eV at room temperature. In this photon energy region is located a reflectivity peak which has been attributed to a core exciton, i.e. to an electronic transition from $\text{Na}^+ 2p$ to $\text{Na}^+ 3s$ states.¹⁾ The reflectivity spectrum is very simple, because of the fact that the $\text{Na}^+ d$ state lies far above bottoms of the conduction band, and besides the peak, only a broad and weak hump is located at about 34.3 eV. The spin-orbit splitting of the $\text{Na}^+ 2p$ states is known to be 0.2 eV,²⁾ but the reflectivity peak is so broad that it shows no splitting.

Measurements were made at BL-11C by using Seya-Namioka type monochromator installed with an Au-coated 1200 grooves/mm grating of 80 nm blazing wavelength. In the piezorefectivity measurements, slits of the monochromator were made considerably wide in order to get sufficient intensity for spectra of a good S/N ratio. The band pass was approximately 0.6 eV, while it was 0.1 eV in an ordinary reflectivity spectrum measurement measured for comparison. An alternating uniaxial stress only along the [011] direction of about 10 bar was applied to single crystal samples. Linearly polarized light was incident onto a (100) cleaved surface of the samples.

Figures 1 (a) and (b) show the reflectivity spectrum and the piezorefectivity spectra, respectively. In Fig. 1 (b), a solid line shows the spectrum of light polarization parallel to the stress direction and is denoted by $(\Delta R/R)_{\parallel [011]}$ and a dashed line, $(\Delta R/R)_{\perp [011]}$, the spectrum of light polarization perpendicular to the stress direction. Positive piezorefectivity means an increase in reflectivity when the samples are elongated in the stress direction.

Structures in the piezorefectivity spectra located between 32.6 eV and 34.0 eV are associated with the reflectivity peak of core exciton located at 33.4 eV. The piezorefectivity spectra of light polarizations perpendicular and parallel to the stress direction cross the zero line at 33.3 eV. Owing to the wide band pass, location of the structures shift to low energy and width of the structures broaden with respect to the reflectivity peak. Line shapes of the piezorefectivity structures are of the positive dispersion type, and are in the same sign in both of the $(\Delta R/R)_{\parallel [011]}$ and $(\Delta R/R)_{\perp [011]}$ spectra, but the $(\Delta R/R)_{\parallel [011]}$ structure is a little larger than the $(\Delta R/R)_{\perp [011]}$ structure. The line shapes of the positive dispersion type in the both spectra mean that under a cubic expansion the reflectivity peak shifts to low energy. The direction of the shift coincides with that of the temperature shift.²⁾ This shift is larger than the shifts of reflectivity structures in the fundamental absorption region of NaCl and those of the core excitons in KCl, KBr, KI, RbCl, RbBr and RbI which we have reported in the previous papers.³⁻⁶⁾ This fact might be attributed to the very small radius of sodium ion and to the strong localization of the core excitation.

The dichroism represents that under a trigonal elongation the reflectivity peak splits so that the peak active to the light polarizations parallel to the stress direction is a high energy component and that active to the perpendicular is a low energy component. The fact that the peak

splits under the uniaxial stress is in agreement with the assignment that the peak is p to s transition. The piezorefectivity responses $(\Delta R/R)_{\parallel [011]}$ and $(\Delta R/R)_{\perp [011]}$ associated with the broad reflectivity hump are in the opposite sign. It means that this hump is of a trigonal symmetry. The hump has been assigned to an admixture of exciton and core-level to band transition²⁾ or to another core exciton.⁷⁾ The results of the piezorefectivity measurements seems to indicate that the hump is the core-level to band transition. In order to give a definite conclusion, a quantitative analysis is necessary.

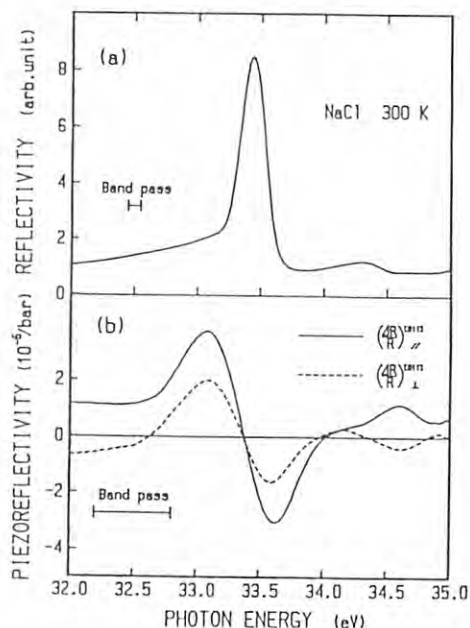


Fig. 1. Reflectivity spectrum (a) and piezorefectivity spectra (b) of NaCl at room temperature.

References

- 1) N. Kosuch, G. Wiech and A. Faessler: *Vacuum Ultraviolet Radiation Physics* (Pergamon-Vieweg, Braunschweig, 1974), p.398.
- 2) S. Nakai, T. Ishii and T. Sagawa: *J. Phys. Soc. Jpn.* **30** (1971) 428.
- 3) H. Fukutani, A. Yamada, T. Koide, A. Misu and G. Kuwabara: *J. Phys. Soc. Jpn.* **50** (1981) 1587.
- 4) A. Yamada, H. Fukutani and A. Misu: *J. Phys. Soc. Jpn.* **52** (1983) 4270.
- 5) A. Yamada, H. Fukutani, M. Miyabe, K. Yagi, H. Kato, T. Koide, T. Shidara, T. Miyahara and S. Sato: *J. Phys. Soc. Jpn.* **54** (1985) 4005.
- 6) M. Miyabe, K. Yagi, A. Yamada, Y. Aiura, T. Koide, T. Shidara, H. Kato and H. Fukutani: *J. Phys. Soc. Jpn.* **56** (1987) 378.
- 7) R. Haensel, G. Keitel, G. Peters, P. Schreiber, B. Sonntag and C. Kunz: *Phys. Rev. Lett.* **23** (1969) 530.

*Present address: Fuji-Xerox Co., Ltd.

THE OPTICAL SPECTRA OF α - Al_2O_3 SINGLE CRYSTALS IN VUV REGION

Tetsuhiko TOMIKI, Tomoyoshi FUTEMMA, Hiroo KATO*, Yoshihiro AIURA⁺, Hirohito FUKUTANI⁺
and Tsuneaki MIYAHARA*

Department of Physics, University of the Ryukyus, Nishihara, Okinawa 903-01

* Photon Factory, National Laboratory for High Energy Physics, Oho-machi, Ibaraki 305

+ Institute of Physics, University of Tsukuba, Sakura-mura, Ibaraki 305

Introduction

The spectra of the tail absorption and the reflectivity of the α -alumina were measured about 20 years ago over the energy region of 8.5 to 28.5 eV at room temperature¹⁾. Recently, the measurements were repeated for obtaining the optical functions of higher quality in the spectral range of 4.2 to 20 eV at room and liquid helium temperatures²⁾. These experiments were carried out both by use of unpolarized light in spite of the fact that α - Al_2O_3 is optically uniaxial. The main purpose of the present work is to measure these spectra of α - Al_2O_3 single crystals over the wider energy region (6 ~ 40 eV) at room and lower temperatures (78 and 10 K) with the use of the plane polarized light from BL-11C at KEK, putting attentions to its optical anisotropy.

Experimental Results and Discussion

Figure 1 shows the tail spectra (full curves) at 299, 78 and 10 K for $c \parallel \vec{E}$ and $c \perp \vec{E}$, \vec{E} being the electric field of the light waves. One may clearly note the optical anisotropy of α - Al_2O_3 . The intrinsic tails can be represented by the Urbach rule as functions of the photon energy E and temperature T with the use of the values ($\sigma_0 = 0.496$, $\hbar\omega = 30.8$ meV) for $c \parallel \vec{E}$ and ($\sigma_0 = 0.495$, $\hbar\omega = 38.8$ meV) for $c \perp \vec{E}$. The convergent points are found near the sharp peak position

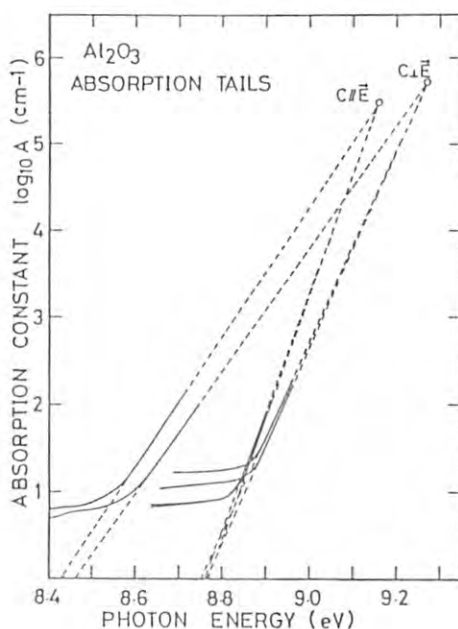


Fig. 1.

around 9 eV in the reflectivity spectra at 299 K, as shown in Fig. 2. One may thus draw the conclusion that the lowest band-gap transition is direct in the region of 299 to 10 K,³⁾ though the band-gap is calculated to be indirect³⁾.

On the reflectivity spectra, the optically anisotropic behaviour is also noticed; it is remarkable up to 25 eV and almost hardly discernible in the higher energies. On cooling the specimens to 78 K or to 10 K, the first peak at ~9 eV, which is probably due to the exciton creation associated with the interband transitions of $O^{2-} 2p^6$ valence to $Al^{3+} 3s$ conduction bands, shifts to the higher energy side with the increase in the peak height. No remarkable thermal effects are noticed on the other peaks.

One of the authors, T. T., is grateful to Dr. T. Miyata, the Matsushita Research Institute Tokyo Inc., for the informations on the etching of corundum crystals.

References

- 1) E. T. Arakawa and M. W. Williams: J. Phys. Chem. Solids **29** (1968) 735.
- 2) V. N. Abramov, M. G. Karin, A. I. Kuznesov and K. K. Sidorin: Sov. Phys.-Solid State **21** (1979) 47.
- 3) S. Ciraci and I. P. Batra: Phys. Rev. **B28** (1983) 982.

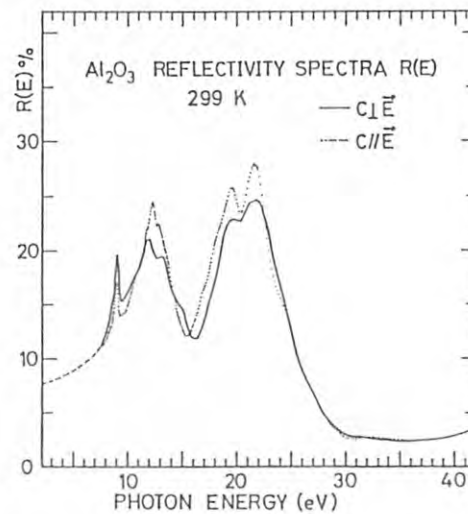


Fig. 2.

Fig. 1. The tail spectra of the corundum.

Fig. 2. The reflectivity spectra of the corundum at room temperature.

VUV SPECTRA OF CdIn_2S_4 AND $\text{Cd}_x\text{InGaS}_{x+3}$ ($x=1,2,3$) SINGLE CRYSTALS

Takeo TAKIZAWA, Hiroshi OHWADA, Kohji KAMBARA, Taizo IRIE,* Saburo ENDO,*

Hisayuki NAKANISHI,* Hiroo KATO** and Hirohito FUKUTANI***

Department of Physics, College of Humanities and Sciences, Nihon University, Setagayaku, Tokyo 156.

** Department of Electrical Engineering, Faculty of Engineering, Science University of Tokyo, Shinjuku-ku Tokyo 162.*

*** Photon Factory, National Laboratory for High Energy Physics, Oho-machi, Tsukuba-gun, Ibaraki 305.*

**** Institute of Physics, University of Tsukuba, Ibaraki 305.*

Introduction

Various compounds can be made from the pseudo-ternary system consisting of binary photosensitive chalcogenide-alloys of CdS , In_2S_3 and Ga_2S_3 with different band gaps. If we could compose of a single crystal with a given band gap from an appropriate mixing of these alloys, we would be able to control freely the characteristics of the photoelectronic devices in the future. Among many mixings, we have succeeded to make single crystals of CdIn_2S_4 , CdInGaS_4 , $\text{Cd}_2\text{InGaS}_5$ and $\text{Cd}_3\text{InGaS}_6$, and started to investigate the electronic and optical properties of these crystals in the energy range from the infrared to VUV region.

Experimental and Results

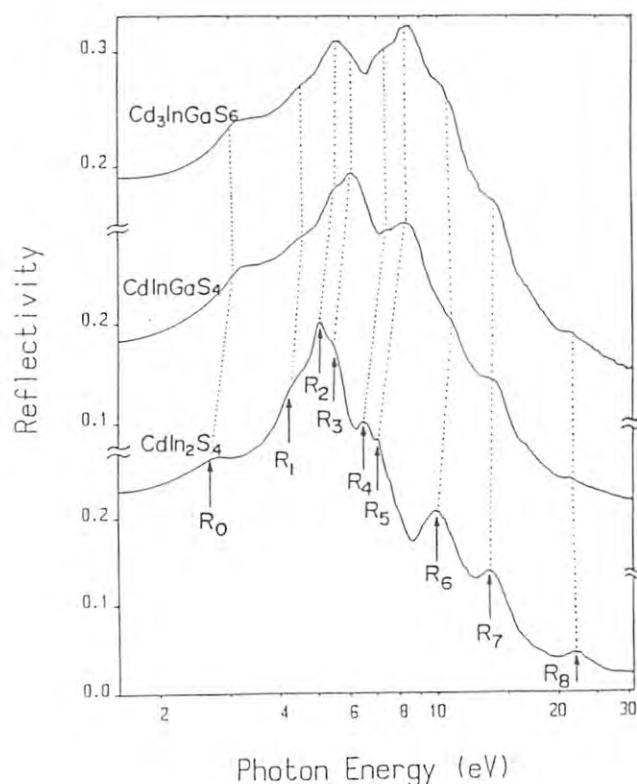
Figure 1 shows the reflection spectra of CdIn_2S_4 , CdInGaS_4 , $\text{Cd}_3\text{InGaS}_6$ in the photon energy from 2.0 to 30 eV. There observed 9 distinct structures shown as R_0 to R_8 in the reflection spectra. The energy of R_0 , the direct absorption edge of CdIn_2S_4 having the cubic spinel structure is small compared with that of the other two crystals having the hexagonal layer-structure, reflecting the strong anisotropic bonding force in the layer. The anisotropy is expected to be observed for the CdInGaS_4 and $\text{Cd}_3\text{InGaS}_6$ crystals with respect to the electric vector parallel and perpendicular to the optic axis. However, the samples of the hexagonal structure are now all in thin flakes, so that we can only measure the spectra with electric vector being in the layer.

Structures shown as R_0 to R_6 are considered on the bases of reported band schemes of CdIn_2S_4 ^{1,2)} to arise from the optical transition from valence band to conduction band. A good correspondence between the observed structures as shown by dotted lines in Fig.1 is obtained in different crystal structures, indicating that the band structure mainly determining the

critical point in reflexion spectra are made up of bondings similar to each other in those crystals. Structures shown as R_7 and R_8 appear nearly in the same energy for all crystals, and reported XPS-spectra for CdIn_2S_4 and In_2S_3 ³⁾ show that the energies of S_{3s} , Cd_{4d} and In_{4d} from the valence band edges are 12, 10, 17 eV, respectively, so that R_7 is considered to arise from the transition from the core state of $S_{3s}+\text{Cd}_{4d}$ and R_8 from that of In_{4d} to conduction bands.

References

- (1) S.Katsuki: J. Phys. Soc. Jpn 33 (1972) 1561.
- (2) E.Grilli, M.Guzzi, A.Anedda, F.Raga and A.Serpi: Solid State Commun. 27 (1978) 105.
- (3) H.Ihara, S.Endo and T.Irie: Solid State Commun. 28 (1978) 563.



YUV REFLECTION SPECTRA OF PARATELLURITE, TeO_2

Takeo TAKIZAWA, Hiroshi OHWADA, Hiroo KATO* and Hirohito FUKUTANI**

Department of Physics, College of Humanities and Sciences, Nihon University, Setagayaku, Tokyo 156.

** Photon Factory, National Laboratory for High Energy Physics, Oho-machi, Tsukuba-gun, Ibaraki 305.*

*** Institute of Physics, University of Tsukuba, Ibaraki 305.*

Introduction

The synthetic paratellurite has strong optical anisotropy and activity due to its deformed uniaxial structure and many investigations have been done about its acoustic, piezoelectric, optical and elasto-optical properties,¹⁾ leading to some good applications as an optical modulator and deflector in optical instruments. Because of the high applicability of this material, most of the investigations are so concentrated in a transparent region that overall band or electronic structures have not been fully revealed up to now. Here we report the preliminary result of the reflectivity measurement in wide energy-range with polarized light of SOR.

Experimental and Results

Figure 1 shows the reflection spectra of TeO_2 in the photon energy from 2.0 to 30 eV with the electric vector parallel and perpendicular to the optic axis.

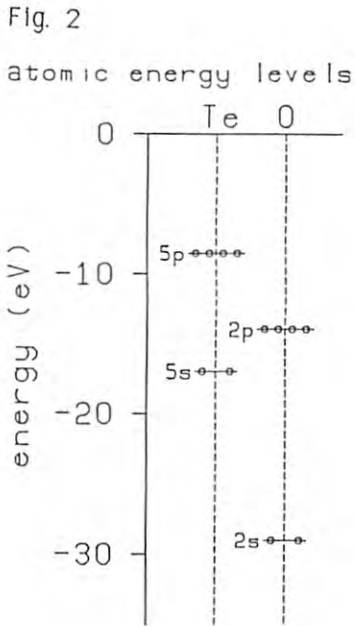
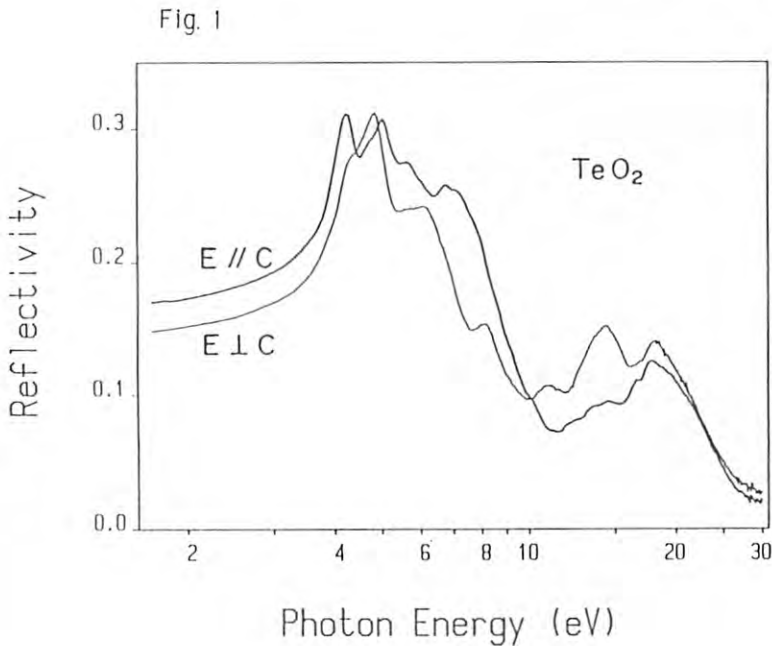
There are two reflection bands in Fig. 1; one is that from 3 to 10 eV and the other from 10 to 25 eV. From considerations based upon the energy diagram of each element as shown in Fig. 2, it is suggested that the former one is composed of transitions from valence bands consisting of mixed states of

O_{2p} and Te_{5s} to conduction bands mainly made up from Te_{5p} states. On the other hand, the latter one is due to transitions between O_{2s} -like states and the conduction bands.

Strong anisotropic effects are also observed in all energy region in good agreements with a previous result in a narrow energy range.²⁾ The dominating peaks around 4 to 6 eV and their polarization behavior can be explained with excitonic transitions between a p-like and an s-like state in a uniaxially deformed crystal field.²⁾ To explain the dispersion characteristics in the transparent region, Uchida proposed a two oscillators model;¹⁾ one of the positions of those oscillators was 4.7 and the other 9.7 eV, roughly corresponding to the reflection bands stated above. It is now possible for us to obtain more precise information for the dispersion relations as well as the band structures in terms of the dielectric functions derived through the Kramers-Kronig transformations of the reflection spectra. Such work is now in progress.

References

- (1) N. Uchida: Phys. Rev. B4 (1971) 3736, and papers cited therein.
- (2) T. Takizawa: J. Phys. Soc. Jpn. 48 (1980) 505.



ANGLE-RESOLVED PHOTOEMISSION STUDY OF OXYGEN ADSORPTION ON Ni(110) AT 300 K

Yasuo SAKISAKA, Tadahiro KOMEDA, Masaru ONCHI, Hiroo KATO⁺, Shigeru MASUDA⁺⁺ and Kazutoshi YAGI⁺⁺⁺

Department of Chemistry, Faculty of Science, Kyoto University, Kyoto 606, Japan

⁺Photon Factory, National Laboratory for High Energy Physics, Oho-machi, Ibaraki 305, Japan

⁺⁺Department of Chemistry, College of Arts and Sciences, University of Tokyo, Komaba, Tokyo 153, Japan

⁺⁺⁺Institute of Physics, University of Tsukuba, Sakura-mura, Ibaraki 305, Japan

Introduction

The dissociative adsorption of oxygen on Ni(110) at above 300 K, where (3x1), (2x1), (3x1), (9x4) and NiO(100) ordered phases are successively formed, has been of considerable interest. We report here angle-resolved photoemission study of the low-coverage (3x1), (2x1) and NiO(100) phases.

Experimental

The measurements were made on BL-11D with a spherical analyzer. The clean Ni(110) surface was prepared by repeated Ar⁺ sputtering and annealing cycles. The ordered structures were verified by LEED. The working pressure was 1×10^{-10} Torr.

Results and discussion

We measured the θ and $h\nu$ dependence of photoemission spectra of the low-coverage (3x1)-O, (2x1)-O and NiO(100) on Ni(110) to study dispersion effects on the O2p-derived levels. As an example, a set of spectra for the (2x1)-O along $\bar{\Gamma}\bar{X}'$ ($[\bar{1}10]$ Az) measured at (A) $\theta_i = 25^\circ$ and (B) $\theta_i = 60^\circ$ and at $h\nu = 30$ eV is shown in Fig.1, where the O2p-derived features are indicated by tic marks. The resulting dispersion curves for the low-coverage (3x1)-O, (2x1)-O and NiO(100) on Ni(110) are shown in Figs.2(A), 2(B) and 3, respectively. These results can be understood in terms of a simple tight-binding model.

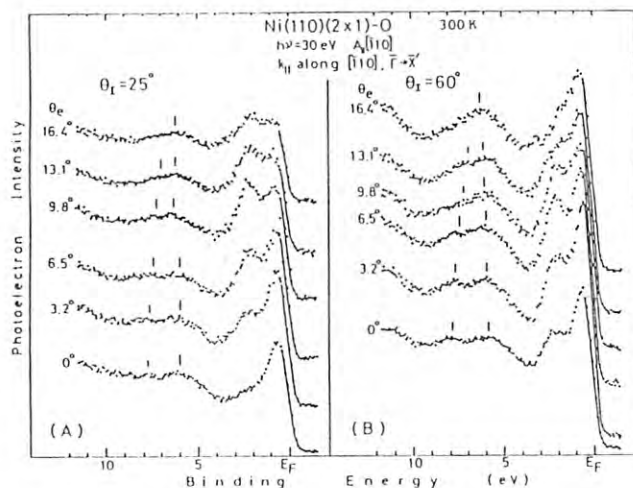


Fig. 1

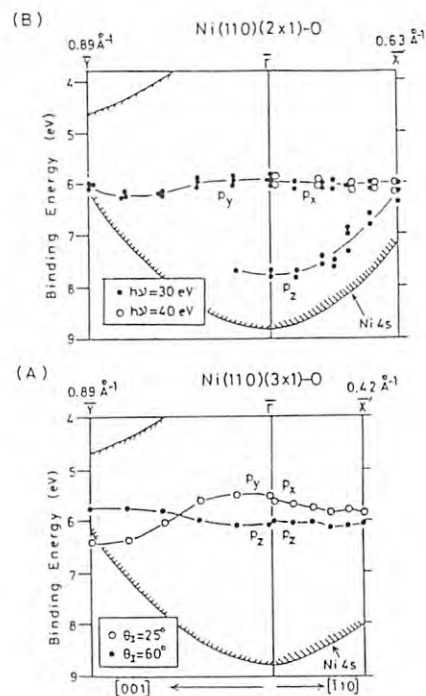


Fig. 2

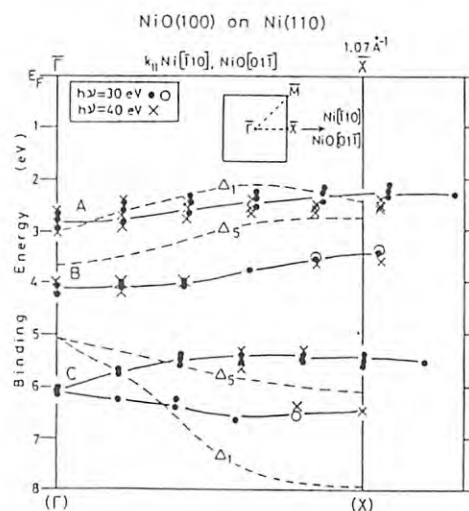


Fig. 3

ANGLE-RESOLVED PHOTOEMISSION FROM THE Ni(110)(1x2)-H SURFACE AT 80 K

Yasuo SAKISAKA, Tadahiro KOMEDA, Masaru ONCHI, Hiroo KATO⁺, Shigeru MASUDA⁺⁺ and Kazutoshi YAGI⁺⁺⁺

Department of Chemistry, Faculty of Science, Kyoto University, Kyoto 606, Japan

⁺Photon Factory, National Laboratory for High Energy Physics, Oho-machi, Ibaraki 305, Japan

⁺⁺Department of Chemistry, College of Arts and Sciences, University of Tokyo, Komaba, Tokyo 153, Japan

⁺⁺⁺Institute of Physics, University of Tsukuba, Sakura-mura, Ibaraki 305, Japan

Introduction

The dissociative adsorption of hydrogen on Ni(110) at below ~ 180 K, where a sequence of H ordered phases is formed for $\Theta \leq 1.5$ ML, has recently been studied in detail. We report here angle-resolved photoemission study of the electronic states of the Ni(110)(1x2)-H reconstructed surface for $\Theta = 1.5$ ML at 80 K.

Experimental

The measurements were made on BL-11D with a spherical analyzer. The clean Ni(110) surface was prepared by repeated Ar⁺ sputtering and annealing cycles. The (1x2)-H structure was verified by LEED. The working pressure was 1×10^{-10} Torr.

Results and discussion

Fig. 1 (left-hand side) shows angle-resolved photoemission spectra of clean Ni(110) [lines] and Ni(110)(1x2)-H [dots] along $\bar{1}\bar{1}0$ ($\bar{1}\bar{X}$) measured at $h\nu = 30$ eV and $\theta_e = 60^\circ$. The difference curves [(1x2)H-clean] corresponding to the curves on the left-hand side are shown on the right-hand side. The feature due to the H1s-Ni bonding state, split off from the Ni bulk bands, is indicated by solid circles. This split-off state moves in energy as θ_e is changed. We measured the same spectra along 001 ($\bar{1}\bar{Y}$) also. Fig. 2 shows the resulting experimental dispersions of the peaks in the photoemission spectra for (A) clean Ni(110) and (B) Ni(110)(1x2)-H along $\bar{1}\bar{X}$ and $\bar{1}\bar{Y}$. The shaded regions are the calculated projection of the Ni bulk bands onto the (110) surface. From these results, we found that (1) no features due to the intrinsic surface states are identified along $\bar{1}\bar{X}$, (2) the H1s derived bonding level split off from the bulk bands is at 9.0 eV at $\bar{1}$, (3) this split-off state shows no measurable dispersion along $\bar{1}\bar{Y}$ (001), whereas it exhibits considerable dispersion of ~ 3.1 eV along $\bar{1}\bar{X}$ ($\bar{1}\bar{1}0$), (4) these results reflect the highly anisotropic structure of the (1x2)-H, and (5) the Ni Σ_1 -symmetry 3d-like bulk bands participate in the H-Ni bonding.

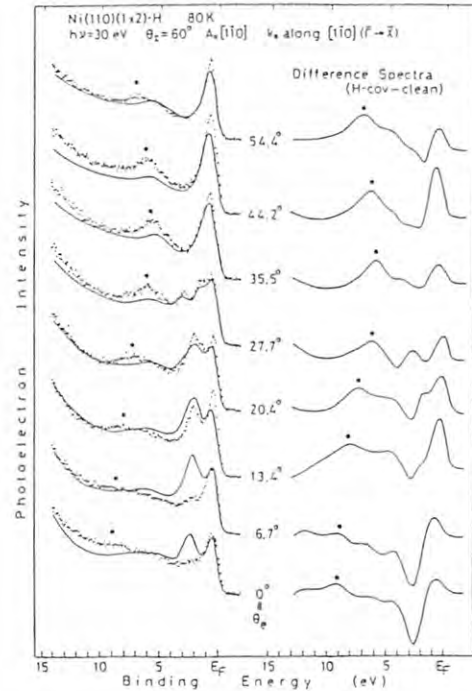


Fig. 1

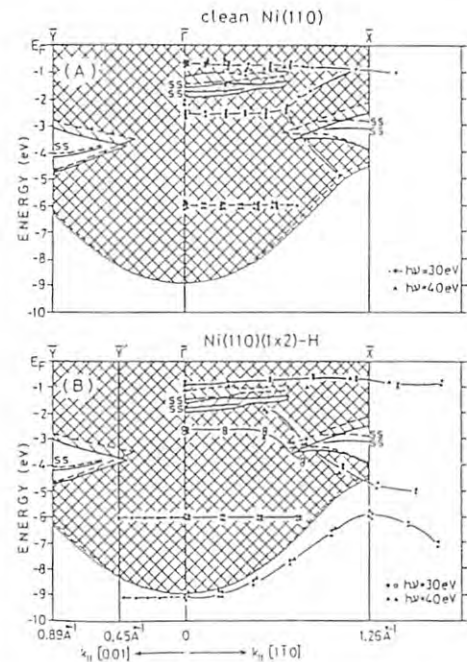


Fig. 2

ANGLE-RESOLVED PHOTOEMISSION STUDY OF OXYGEN ADSORPTION ON Ni(110) AT 80 K

Yasuo SAKISAKA, Tadahiro KOMEDA, Masaru ONCHI, Hiroo KATO⁺, Shigeru MASUDA⁺⁺ and Kazutoshi YAGI⁺⁺⁺

Department of Chemistry, Faculty of Science, Kyoto University, Kyoto 606, Japan

⁺Photon Factory, National Laboratory for High Energy Physics, Oho-machi, Ibaraki 305, Japan

⁺⁺Department of Chemistry, College of Arts and Sciences, University of Tokyo, Komaba, Tokyo 153, Japan

⁺⁺⁺Institute of Physics, University of Tsukuba, Sakura-mura, Ibaraki 305, Japan

Introduction

The dissociative adsorption of oxygen on Ni(110) at above 300 K has extensively studied in the past. The dissociative adsorption of diatomic molecules is thought to proceed via a weakly bound undissociated precursor. However, no evidence for such a short-lived, molecularly adsorbed oxygen on Ni(110) has been found. Adsorption studies at low temperatures offer a number of important advantages, e.g., surface reaction intermediates may be frozen in. We report here angle-resolved photoemission study of oxygen adsorption on Ni(110) at 80 K. We find a molecular O₂ intermediate on a NiO layer formed on Ni(110).

Experimental

The measurements were made on BL-11D with a spherical analyzer. The clean Ni(110) surface was prepared by repeated Ar⁺ sputtering and annealing cycles. With liquid-N₂ cooling, the crystal could be cooled to 80 K, which was exposed to oxygen. The base pressure was 1×10^{-10} Torr.

Results and discussion

At 80 K, LEED shows no ordered oxygen overlayer structure on Ni(110) over the exposure range up to 200 L, with an exception of a c(2x4)-O phase associated $\theta=0.25$ which occurred between 0.5 and 2.5 L. For this c(2x4) phase, no dispersion of the O2p-derived levels is observed (<0.05 eV). Our photoemission data indicate that at 80 K adsorption of O₂ on Ni(110) leads to formation of an atomic overlayer up to ~ 3 L, and above ~ 6 L a disordered NiO layer is formed on Ni(110). We found that features of molecular O₂ also are observed immediately after exposure above 50 L and pump-down.

Figs.1(a) and (b) show examples of normal-emission spectra of NiO formed on Ni(110) [all the spectra in Fig.1 were measured at 80 K, $h\nu=35$ eV and $\theta_i=60^\circ$]. Spectrum (a) [(b)] was measured after 50 L [additional 50 L (i.e., a total of 100 L)] oxygen exposure at 80 K and subsequent heating to 300 K for a few

minutes. In order to investigate molecularly adsorbed O₂ on Ni(110), we measured the time-dependent change in the spectrum from the surface prepared by a further additional oxygen exposure of 60 L at 80 K (see spectra (c),(d),(e) and (f) measured $\sim 3, 6, 9$ and 14 min, respectively, after the reexposure). In the spectrum (c), four new peaks marked by arrows are clearly seen. The binding energies of these peaks are compared to the vertical ionization potentials of molecular O₂ in the gas phase (see the bottom of Fig.1). Note that all the features in spectrum (f) increase in intensity by ~ 20 and ~ 10 % as compared with those in spectra (a) and (b), respectively. It can be concluded, therefore, that the physisorbed molecular O₂ converts into the dissociated² species on standing in vacuum leading to the growth of oxide.

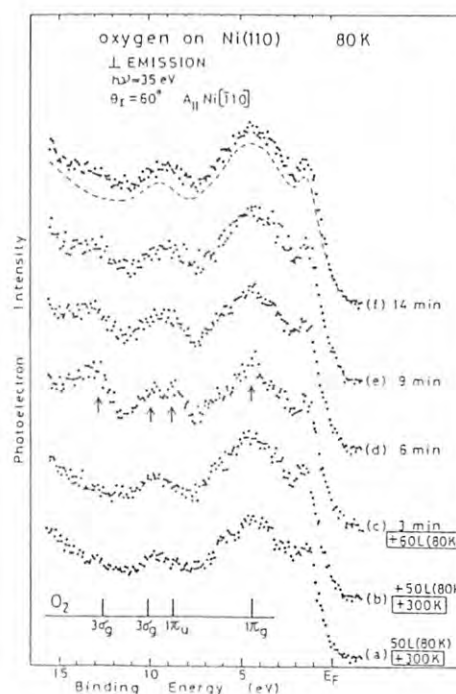


Fig. 1

4f-ELECTRON DENSITIES OF STATES IN LIGHT RARE-EARTH HALIDES STUDIED BY RESONANT PHOTOEMISSION SPECTROSCOPY

Atsushi FUJIMORI, Tsuneaki MIYAHARA,⁺ Tsuneharu KOIDE,⁺ Tetsuo SHIDARA,⁺
Hiroo KATO,⁺ Hirohito FUKUTANI,⁺⁺ Shigeru SATO⁺

National Institute for Research in Inorganic Materials

Sakura-mura, Niihari-gun, Ibaraki 305

⁺Photon Factory, National Laboratory for High Energy Physics

Oho-machi, Tsukuba-gun, Ibaraki 305

⁺⁺Institute of Physics, Tsukuba University

Sakura-mura, Niihari-gun, Ibaraki 305

Introduction

The origin of the double-peak structure in the 4f-derived photoemission spectra of Ce compounds has been the subject of controversies since its discovery,¹ as only one peak would be expected from the atomic picture ($4f^1 + h\nu \rightarrow 4f^0 + e$). So far several mechanisms have been proposed: The two peaks are attributed to (1) 4f holes screened by localized and extended Ce 5d conduction electrons;² (2) those screened by 5d conduction electron and by a 4f electron itself;³ (3) hybridized 4f-hole ($4f^0$) and ligand-hole ($4f^1L$) states;⁴ or (4) a Kondo-like resonance and a bare 4f hole.⁵

Screening of the 4f hole certainly plays an essential role in giving the double-peak structure and should be quite different between metals and insulators, but so far experimental studies have been restricted to metallic systems. We therefore studied insulating trihalides of light rare earths in order to clarify the origin of the double-peak structure.

Results and Discussion

4f-derived densities of states (DOS) were obtained as difference curves between spectra taken on- and off-resonance of the $4d \rightarrow 4f$ excitation. As shown in Fig. 1, one can clearly see two 4f peaks except for CeF_3 . The peak at higher

binding energy results from resonance enhancement of the halogen p band. As this band showed no appreciable resonance effect in La trihalides, its resonance in the Ce compounds is of the 4f origin and not due to hybridized 5d component.

The presence of the double-peak structure in the Ce trihalides is obviously inconsistent with mechanisms (1) and (2) since there are no conduction electrons in the present case. On the other hand, mechanism (3) does not necessitate conduction electrons and can explain the present mechanism (3). (4) is usually based on metallic systems, but can be extended to insulators, becoming equivalent to (3). Further, the halogen-atom dependence of the relative positions and intensities of the two 4f peaks is consistent with the $4f^0$ - $4f^1L$ hybridization mechanism: As one goes from CeF_3 to $CeCl_3$ to $CeBr_3$, the p-band energy increases and becomes closer to the bare $4f^0$ state. This increases the hybridization strength between the $4f^0$ and $4f^1L$ states, and consequently the intensity of the 4f-derived emission in the p-band region. Based on this model,⁴ we have evaluated the difference between the bare $4f^0$ and $4f^1L$ energies (ϵ_{4f} , ϵ_L) and the effective hybridization matrix elements (V) as shown in Fig. 2.

References

1. A. Franciosi, J. H. Weaver, N. Mårtensson, and M. Croft, Phys. Rev. B24, 3651 (1981).
2. S.-H. Liu and K.-M. Ho, Phys. Rev. B28, 4220 (1983).
3. M. R. Norman et al., Phys. Rev. Lett. 53, 1673 (1984).
4. A. Fujimori, Phys. Rev. B28, 4489 (1983).
5. O. Gunnarsson and K. Schönhammer, Phys. Rev. Lett. 50, 604 (1983).

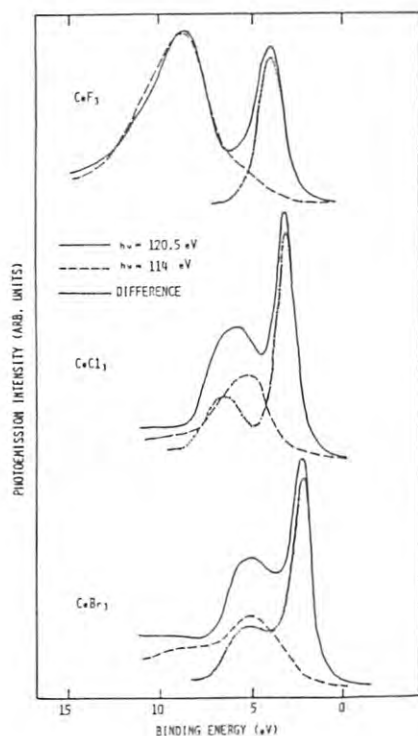


Fig. 1

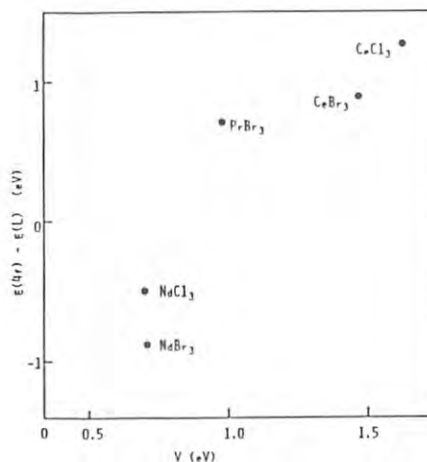


Fig. 2

PHOTOELECTRON SPECTRA OF La- AND Ce-COMPOUNDS

Takaaki HANYU, Tsuneaki MIYAHARA^{*}, Mihiro YANAGIHARA^{**}, Hiroyoshi ISHII and Hiroo KATO^{*}Department of Physics, Faculty of Science, Tokyo Metropolitan University,
Setagaya-ku, Tokyo 158^{*} Photon Factory, National Laboratory for High Energy Physics, Ibaraki, 305^{**} Research Institute for Scientific Measurements, Tohoku University,
Katahira, Sendai 980Introduction

In the systems containing rare earth the anomalous phenomena in macroscopic properties have been observed. The phenomena can not be understood only by the localization of the 4f electron. It is pointing out that the itinerancy of the 4f states must be taken into consideration simultaneously with the localization which is characteristic of the rare earths. The valence states of the 4f states in these systems have been investigated both experimentally and theoretically by various methods¹. In order to obtain the manifestation of itinerant and localized 4f electronic states, we have measured systematically the resonant photoemission spectra in the cerium-based transition metal compounds²). In this study lanthanum compounds having no 4f electrons were investigated to make the contribution of the 4f electrons clear in the valence band region.

Experimental

Photoelectron spectra were measured by double cylindrical mirror analyzer at beam line 11D. Over-all resolution of the spectra were 0.2~0.5 eV in the photon energy region between 40 and 140 eV. The measurements were carried out at a vacuum below 2×10^{-10} Torr and at room temperature. Samples were prepared from a mixture of

99.9 % rare earths and 99.99% transition metal by an argon arc melting. The cleanliness of samples was performed by filing using diamond files.

Results and Discussion

Figure 1 shows the valence-band photoelectron spectra of LaOs_2 and CeOs_2 at the excitation energy of 121 eV. In the spectra of CeOs_2 , the two prominent peaks appear at 0.2 and 1.4 eV. At the high binding energy the small structure can be observed. On the other hand the two structures can be only seen at 0.5 and 2.2 eV in the spectra of LaOs_2 .

Lanthanum has no 4f electrons in the ground states. The above two structures are due to the 5d bands of lanthanum and osmium. While in the spectra of CeOs_2 , the intensity of the peak near the Fermi level was enhanced resonantly at the excitation energy of the cerium 4d absorption edge. The intensity of the structure at 1.4 eV in CeOs_2 was also enhanced like the peak near the Fermi level. From this result the peaks at 0.2 and 1.4 eV can be considered to be due to the contribution of the 4f electrons.

The dependency of the excitation energy shows the reduction of intensity for the structure at 1.4 eV in the off-resonance energy region. This indicates that the structure at 1.4 eV is almost due to the character of 4f electrons.

From the comparison of both spectra of La- and CeOs_2 , the peak near the Fermi level is due to the d-f hybridization of the conduction band (La, Ce and Os 5d) with the Ce 4f states. The conduction bands in these compounds ought to be altered by the kind of the transition metals. In the previous note²) the dependence of the chemical environment on the valence band spectra has been presented. The sharp peak was observed apparently near the Fermi level only in the case of CeOs_2 which was mixed with 5d transition metals.

From the comparison of the Ce containing systems with La-compounds, it could be confirmed that the sharp peak was the contribution of the 4f states which hybridized strongly with the conduction band formed by Ce 5d and Os 5d electrons.

References

- 1) Valence Fluctuations in Solids, edited by L.H. Falicov, W. Hanke and M.P. Maple (North-Holland, Amsterdam, 1981).
- 2) T. Hanyu et al., Photon Factory Activity Report 1986, #4, p245.

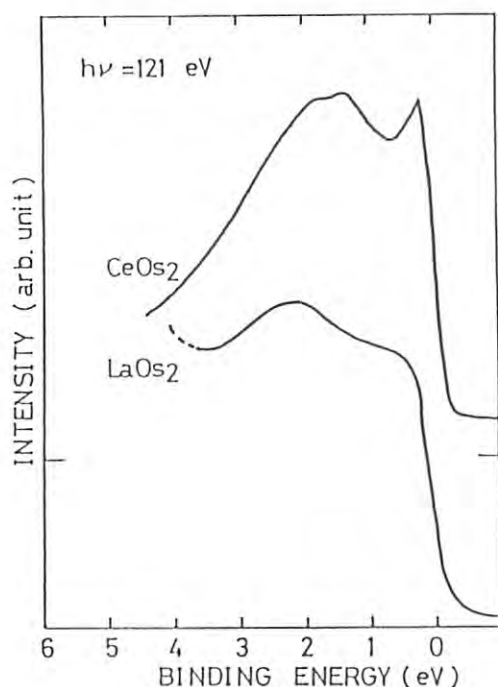


Fig.1 Photoelectron spectra of CeOs_2 and LaOs_2 .

Near Normal Reflectance Spectra of CeO_2

Tsuneaki MIYAHARA, Atsushi FUJIMORI,^{*} Tsuneharu KOIDE, Shigeru SATO, Shik SHIN^{**} and Marco ISHIGAME

^{*}Photon Factory, National Laboratory for High Energy Physics, Ibaraki 305

^{**}National Institute for Research in Inorganic Materials, Ibaraki 305

Research Institute for Scientific Measurements, Tohoku University, Sendai 980

Among the materials showing valence fluctuation CeO_2 has taken a strong attention because it has no localized magnetic moment in the ground state though the local occupation of $4f$ states has been estimated to be around 0.5 from $3d$ XAS or $3d$ XPS data.¹⁾ This disappearance of a localized magnetic moment is usually explained in terms of formation of a singlet ground state composed of a $4f$ electron and a ligand hole, where the hybridization between $4f$ and ligand (or valence) states has been described by a cluster model²⁾ or the Anderson model with filled valence band.³⁾ In these models the $4f$ wavefunction is assumed to be rigid between the initial and the final states regardless of its energy level. The models well describe and reproduce the results of $3d$ XAS and $3d$ XPS, where it should be noted that the effect of exchange interaction between a $3d$ hole and $4f$ electron is relatively small.⁴⁾ In the $4d4f$ photo-absorption spectra,⁴⁾ however, the exchange interaction between a $4f$ electron and a $4d$ hole is so large that the term dependence of the potential cannot be neglected in principle. Under those circumstances the $4f$ wavefunctions are also term-dependent and it is important to check the term dependence in the calculation of the multiplets associated with $4d$ excitation.

Single crystalline CeO_2 was made using a solar furnace and the surface was mechanically polished for reflectivity measurement.

The reflectances were measured at BL-11D of the Photon Factory, where the light was monochromatized by a constant deviation monochromator (CDM). The incident angle was 10° and the energy resolution was better than 0.1 eV.

Figure 1(a) shows the reflectance spectra of CeO_2 in the photon energy region from 90 to 140 eV, where both the giant absorption structure and the small structures due to multiplets are seen. Figure 1(b) is the enlarged view of the multiplet component at the prethreshold region. In the figure the broken line corresponds to the results for the sample partially deoxidized due to annealing at 200°C in the vacuum and the solid line shows the result for the sample oxidized in the atmosphere at 900°C and introduced into the vacuum chamber. The former clearly indicates the mixture of intrinsic CeO_2 and Ce_2O_3 .

The present data show a clear splitting of the larger component located from 107 to 108 eV. It is important to notice that the present result is not a simple superposition of the two configurations caused by a ground state hybridization between $4f$ and ligand states.

Calculations including at least the term dependence of the wavefunction seem to be necessary for the above multiplet structure to be explained theoretically.

Reference

- 1) T.Jo and A.Kotani: J.Phys.Soc.Jpn.55(1986)
- 2) A.Fujimori: Phys.Rev.B28(1986)4489.
- 3) T.Jo and A.Kotani: *Proc. 8th Int. Conf. on Vacuum Ultraviolet Radiation Physics, Lund, Sweden 1986*, also published in Phys. Scr. 35(1987)570.
- 4) T.Hanyu, T.Miyahara, T.Kamada, H.Ishii, M.Yanagihara, H.Kato, K.Naito, S.Suzuki, T.Ishii: J.Magn. & Magn.Mater.52(1985) 193.

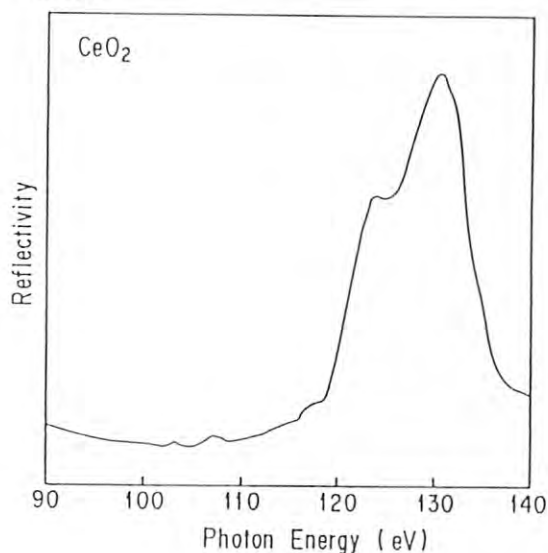


Figure 1(a)

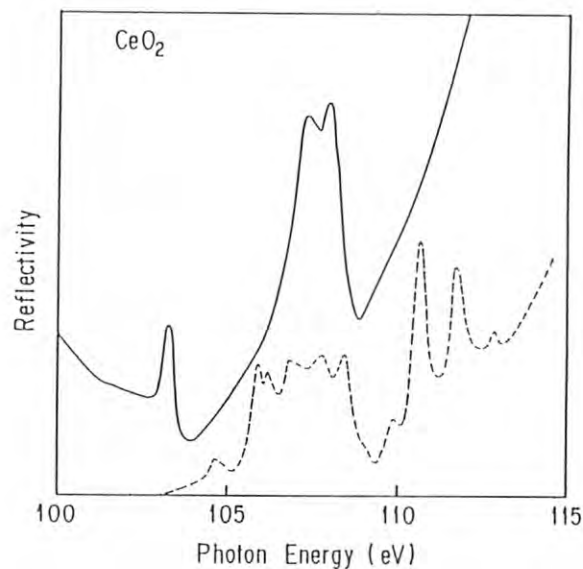


Figure 1(b)

PHOTOEMISSION STUDIES OF NEUTRON-IRRADIATED GRAPHITE

Kazutoshi YAGI, Yoshihiro AIURA, Nobuhisa WATANABE, Hirohito FUKUTANI.
 Tsuneaki MIYAHARA⁺, Hiroo KATO⁺, Tsuneharu KOIDE⁺, Tetsuo SHIDARA⁺,
 and Atsushi FUJIMORI⁺⁺

Institute of Physics, University of Tsukuba,

Sakura-mura, Niihari-gun, Ibaraki 305

⁺Photon Factory, National Laboratory for High Energy Physics

Oho-machi, Tsukuba-gun, Ibaraki 305

⁺⁺National Institute for Research in Inorganic Materials

Sakura-mura, Niihari-gun, Ibaraki 305

Graphite is an important material used in the fuel elements of the high-temperature gas-cooled nuclear reactors and also one of the candidates to be used in the fusion reactors as their walls. In such circumstances, graphite is suffered from neutron irradiation and its physical properties, mechanical, thermal and electrical, are changed because of crystal defects produced by the irradiation. The irradiation induced changes in the physical properties are studied by many researchers.

In this report, the neutron irradiation effects on the electronic states are studied by reflection and photoemission measurements.

The reflectivity spectra are shown in Fig.1 the dotted line is for un-irradiated sample and the dott-dashed line is for the 8×10^{19} neutrons/cm² irradiated sample.

The 5-eV structure is almost completely diminished by the neutron irradiation.

The peak has been assigned to an interband transition between the π bands at the M critical point. The results suggest substantial changes of the electronic states around the M point. The broad structures in the high energy region (10-30eV) are changed by irradiation. They have

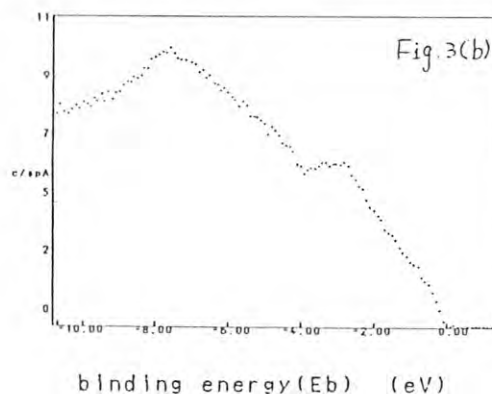
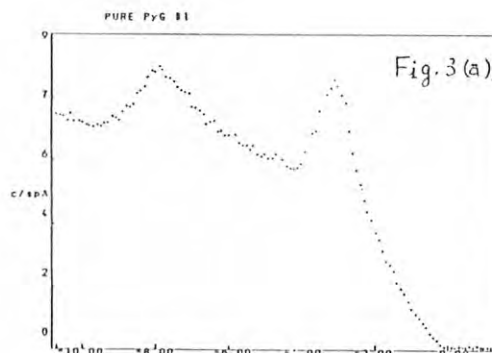
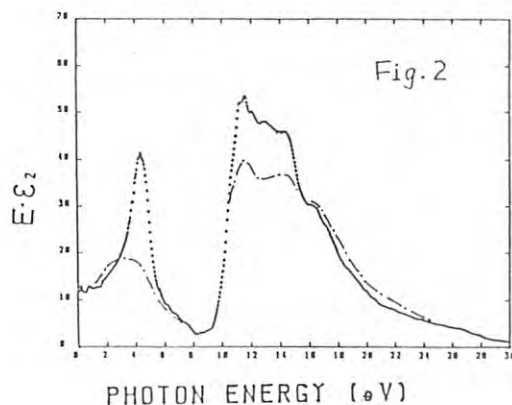
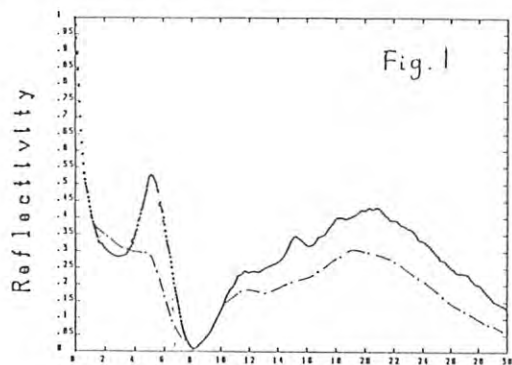
been attributed to transitions between the σ band. The changes of the electronic states around the M point is more clearly seen in Fig.2, $E\epsilon_2(E)$ curve, which is related to the joint density of states. Upon irradiation the peak position is shifted to a lower energy and its width becomes broader.

The angle-integrated photoemission spectra are shown in Fig.3, (a) is for the un-irradiated and (b) is for the irradiated sample, respectively. The peak located about 2.5 eV below the Fermi level is the state density of the occupied π band at the M point. The figures indicate the similar aspects upon irradiation as shown in Fig.1 and 2.

In conclusion, the neutron irradiation effects on the electronic states of the graphite have been revealed from the reflection and photoemission measurements.

The angle-resolved photoemission is expected to give more detailed information on the irradiation-induced changes of the electronic states of the graphite.

We are grateful to Dr.T. Iwata of Japan Atomic Energy Research Institute, Tokai Research Establishment, for supplying the samples and useful discussions.



ANGLE-RESOLVED PHOTOEMISSION STUDY OF Cr(110). ENERGY-BAND
DISPERSIONS AND MAGNETIC-PHASE TRANSITION

Yasuo SAKISAKA, Tadahiro KOMEDA, Masaru ONCHI, Hiroo KATO⁺, Shoji SUZUKI⁺⁺,
Kazuyuki EDAMOTO⁺⁺⁺ and Yoshihiro AIURA⁺⁺⁺⁺

Department of Chemistry, Faculty of Science, Kyoto University, Kyoto 606, Japan

⁺Photon Factory, National Laboratory for High Energy Physics, Oho-machi, Ibaraki 305, Japan

⁺⁺Department of Physics, Faculty of Science, Tohoku University, Sendai 980, Japan

⁺⁺⁺Department of Chemistry, Faculty of Science, Tokyo Institute of Technology, Ookayama, Tokyo 152, Japan

⁺⁺⁺⁺Institute of Physics, University of Tsukuba, Sakura-mura, Ibaraki 305, Japan

Introduction

Cr is unique among metals in displaying an itinerant antiferromagnetic (AF) state with a sc unit cell. Above T_N , Cr is paramagnetic (PM) with a bcc unit cell. We report here angle-resolved photoemission data for Cr(110).

Experimental

The measurements were made on BL-11D with a spherical analyzer. The clean Cr(110) surface was prepared by repeated Ar⁺ sputtering and annealing cycles. The working pressure was 1×10^{-10} Torr.

Results and discussion

Fig.1 shows normal-emission spectra of Cr(110) measured at 80 K and $\theta_i = 25^\circ$ ($A_{||}$ [001]). The inset are the same spectra but for $\theta_i = 60^\circ$. The prominent features between E_F and ~ 2 eV are due to emissions from the upper 3d bands. For $h\nu \geq 44$ eV, the $M_{23}VV$ Auger emission (arrows) is observed at $h\nu - 37$ eV. Two features (tic marks) around 3 and 6 eV which show small dispersion of 0.5 ± 1 eV with $h\nu$ are due to the emission from the lower Σ_1 bulk bands. The point to be stressed here is that we find no evidence for a valence-band satellite in Cr. Assuming direct transitions, we determined energy band dispersions along ΓM from the measured spectra. We found that the overall agreement with the calculated AF bands of Asano and Yamashita¹ is rather good for the upper bands, but not so good for the lower bands. As shown in Fig.2, we measured the normal-emission spectra for $\theta_i = 25^\circ$ ($A_{||}$ [001]) at below and above T_N to study the changes in the band structure caused by the magnetic-phase transition. The positions of the Σ_3 -band emission peak observed in the $T = 80$ K spectra are indicated by triangles. For $h\nu = 40$ eV, no essential difference is observed in the spectra recorded at 80 K and 470 K, since in this case ($\sim 20 < h\nu < 45$ eV) the AF Σ_3 band corresponds to the PM Σ_3 band itself. On the other hand, for $h\nu = 52.5$ and 55 eV the Σ_3 -band emission peak disappears above T_N , since for these photon energies the AF Σ_3 band corresponds to the PM G_3 band along HN.

References

- 1) S.Asano and J.Yamashita, J. Phys. Soc. Jpn. 23, 714 (1967).

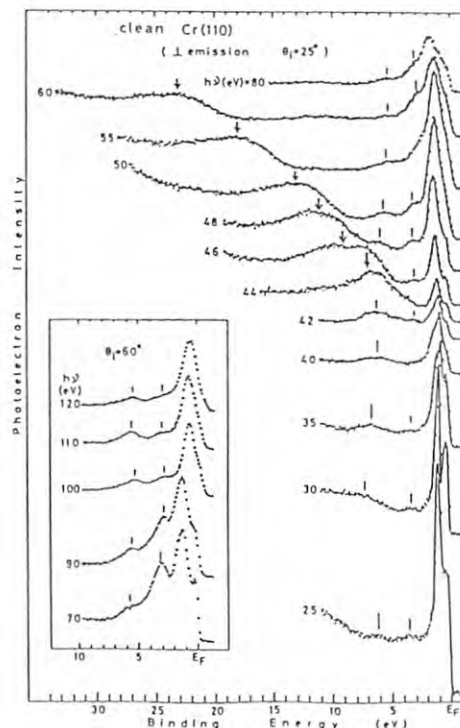


Fig. 1

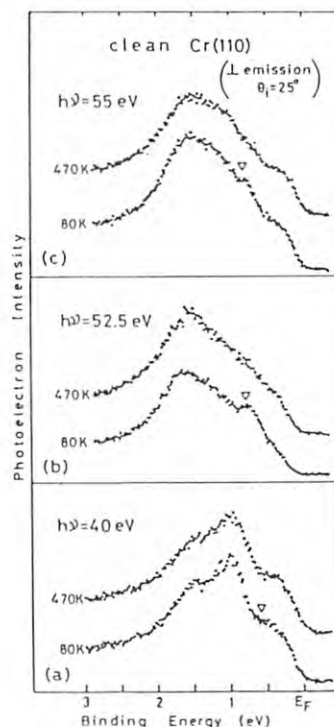


Fig. 2

ANGLE-RESOLVED PHOTOEMISSION STUDY OF NO CHEMISORPTION ON Ag(111)

Kazuyuki EDAMOTO, Seiji MAEHAMA, Eizo MIYAZAKI,
Tsuneaki MIYAHARA⁺ and Hiroo KATO⁺

Department of Chemistry, Tokyo Institute of Technology,
Ookayama, Meguro-ku, Tokyo 152, Japan

⁺ Photon Factory, National Laboratory for High Energy Physics,
Oho-machi, Tsukuba-gun, Ibaraki 305, Japan

Introduction

NO molecule possesses an unpaired electron in the antibonding 2π orbital which may play an important role in the chemisorption and surface reaction. We have reported that molecularly adsorbed NO has a bent orientation on Pd(111); the tilt angle is $20^\circ \sim 25^\circ$ from the surface-normal direction.¹ In this report, the adsorption of NO on the Ag(111) surface at 150 K is investigated using angle resolved photoemission spectroscopy. The angle resolved measurement using polarized light enables us to determine the orientation of adsorbed NO.

Results and Discussion

Fig. 1 shows normal emission spectra for the Ag(111) surface exposed to 40000 L NO at 150 K (saturation coverage). The spectra are taken at two incident angles: $\theta_i = 25^\circ$ (predominantly s-polarized) (Fig. 1a), and $\theta_i = 60^\circ$ (predominantly p-polarized) (Fig. 1b). The NO-induced peaks are observed at 2.5, 3.3 and 8.4 eV. The 8.4 eV peak is assigned as an emission from the $5\sigma + 1\pi$ level of the molecularly adsorbed NO, indicating that NO is adsorbed molecularly at 150 K.

Fig. 2 shows a plot of the photoionization cross sections for the $5\sigma + 1\pi$ emission as a function of photon energy. A remarkable maximum is observed at around 38 eV, which is attributed to the shape resonance of 5σ level.¹

The spectra shown in Fig. 1 are obtained using the photon energy of $h\nu = 35$ eV, which is included in the resonance region (Fig. 2). Thus, the 8.4 eV peak may be composed of mainly 5σ component. Fig. 1 shows that the 5σ emission is enhanced as the p-polarized light is used. Considering the symmetric selection rule,² this result indicates that adsorbed NO has the molecular axis perpendicular to the (111) surface.

Further evidence for an upright orientation comes from the observation of angular distribution of 5σ cross section at resonance. Previous theoretical study has indicated that the 5σ resonance occurs in the σ final state channel,³ indicating that the emission is peaked in the direction of NO molecular axis at resonance.⁴ Fig. 3 shows a plot of the photoionization cross sections of the $5\sigma + 1\pi$ level as a function of detection angle using the photon energy of 37 eV.

The plot shows that the emission is peaked in the surface normal direction, which also indicates that the adsorbed NO has an upright orientation. This result is contrast to that for the Pd(111)-NO system.

References

- 1 E. Miyazaki, I. Kojima, M. Orita, K. Sawa, N. Sanada, K. Edamoto, T. Miyahara and H. Kato, J. Electron Spectrosc. Relat. Phenom. in press.
- 2 E. W. Plummer and W. Eberhardt, Advan. Chem. Phys. 49 (1982) 533.
- 3 G. Loubriel, Thesis, University of Pennsylvania (1980).
- 4 F. Greuter, D. Heskett, E. W. Plummer and H. -J. Freund, Phys. Rev. B27 (1983) 7117.

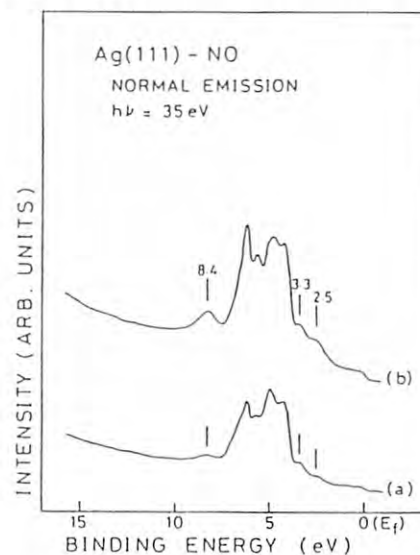


Fig. 1

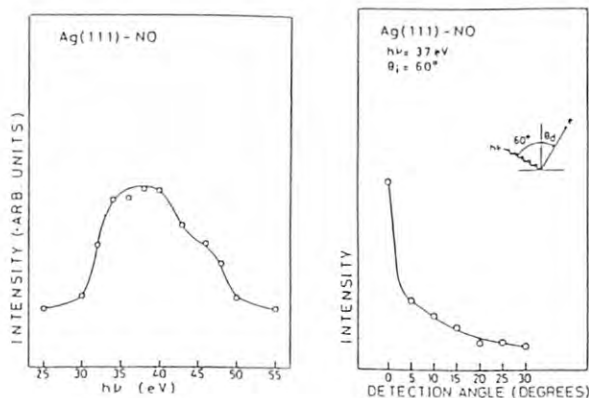


Fig. 2

Fig. 3

RESONANT PHOTOEMISSION STUDY OF HIGH- T_c SUPERCONDUCTORS

Takashi TAKAHASHI, Fumihiko MAEDA, Hiromu ARAI, Hiroshi KATAYAMA-YOSHIDA, Yutaka OKABE, Takashi SUZUKI, Shoichi HOSOYA^a, Atsushi FUJIMORI^b, Tetsuo SHIDARA^c, Tsuneharu KOIDE^c, Tsuneaki MIYAHARA^c, Masashige ONODA^d, Shinichi SHAMOTO^d and Masatoshi SATO^d

Department of Physics, Tohoku University, Sendai 980

^aResearch Institute for Materials Research, Tohoku University, Sendai 980

^bNational Institute for Research in Inorganic Materials, Tsukuba, Ibaraki 305

^cPhoton Factory, National Laboratory for High Energy Physics, Tsukuba, Ibaraki 305

^dInstitute for Molecular Science, Myodaiji, Okazaki 444

We have performed photoemission measurements for the high- T_c superconductors, $(La_{1-x}Sr_x)_2CuO_4$ ($x=0.075$) and $YBa_2Cu_3O_{6.85}$, with use of synchrotron radiation of 20–140 eV. The samples are sintered pressed pellets and show the superconducting transition temperature (T_c) of 40 and 90 K, respectively. The sample-surface was scraped with a diamond file in the spectrometer to obtain a fresh and clean surface for the measurements and the sample was kept at low temperature ($\sim 150^\circ\text{C}$) during the measurements.

Figure 1 shows the photoemission spectra of $YBa_2Cu_3O_{6.85}$ measured at various photon energies. Band A is due to the heavily hybridized states of Cu 3d and O 2p states. The origin of band B is unknown at present, probably may be ascribed to some other oxides because the intensity of band B increases with time. Since band D shows an enhancement at the Ba 4d core threshold (~ 105 eV), it is attributed to the Ba 5p doublet.

We should remark that band C appears only at a little above the Cu 3p core threshold (~ 75 eV). Band C is ascribed to the "two-hole-bound state" which is a kind of satellites of the Cu 3d main band.² The obtained experimental results are summarized as follows; (1) the density of states at the Fermi level is very small compared with the band calculation,³ (2) the valence-band photoemission spectrum is shifted as a whole toward higher-binding-energy side by ~ 2 eV relative to the calculation, (3) the copper atoms are mostly divalent (Cu^{2+}); we did not find any traces of Cu^{1+} or Cu^{3+} , and (4) the intra-atomic Coulomb energy between 3d electrons (U_{dd}) has been evaluated to be 5–6 eV, which is comparable to the valence-band width (6–7 eV). These experimental results

clearly indicate that the one-electron-band picture breaks down in these high- T_c superconductors and the strong electron correlation dominates the electronic structures of these materials.

Figure 2 shows a schematic diagram of the electronic structure of the high- T_c superconductor derived from the present photoemission study. The Cu 3d electron is almost localized due to the strong correlation as in a Mott-insulator, forming a Mott-Hubbard gap. The O 2p orbital, which may be located a little above the occupied Cu 3d level, hybridizes strongly with the Cu 3d orbital, giving the valence band with the width of 6–7 eV.

Since it has been found that copper atoms are mostly divalent, we must consider *mono-valent* oxygens which may be produced by the charge-transfer, $(Cu^{3+}O^{2-})^+ \rightarrow (Cu^{2+}O^{1-})^+$. This mono-valent oxygen leaves the 2p state at the Fermi level, which gives the metallic character of the high- T_c superconductors and also may contribute to the superconductivity.

In conclusion, the present resonant photoemission study indicates that the electron correlation in the high- T_c superconductors is very strong, dominating the electronic structure of this system and the mono-valent oxygen due to the charge-transfer may play an important role giving rise to the novel properties of the high- T_c superconductors.

¹T. Takahashi, F. Maeda, H. Arai, H. Katayama-Yoshida, Y. Okabe, T. Suzuki, S. Hosoya, A. Fujimori, T. Shidara, T. Koide, T. Miyahara, M. Onoda, S. Shamoto, and M. Sato; Phys. Rev. B36 (1987) 5686.

²T. Ishii, M. Taniguchi, A. Kakizaki, K. Naito, H. Sugawara, and I. Nagakura; Phys. Rev. B33 (1986) 5664.

³L.F. Mattheiss and D.R. Hamann, Solid State Commun. 63 (1987) 395.

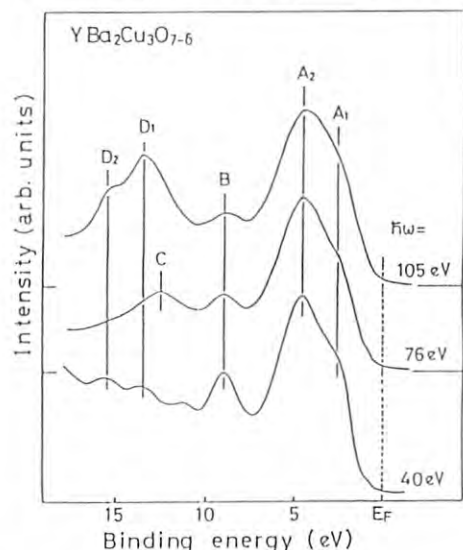


Fig. 1

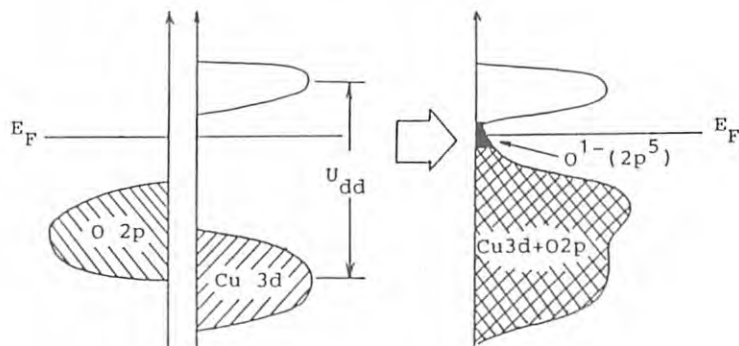


Fig. 2

PHOTODISSOCIATION OF THE DOUBLY EXCITED STATES OF H_2

Shin ARAI, Tetsu KAMOSAKI, Kyoji SHINSAKA, Masatoshi UKAI⁺, Yoshiro ITO⁺⁺,
Hitoshi KOIZUMI⁺⁺⁺, Akira YAGISHITA⁺, Kenichiro TANAKA⁺ and Yoshihiko HATANO⁺
Department of Chemistry, Tokyo Institute of Technology, Meguro-ku, Tokyo 152
+Photon Factory, National Laboratory for High Energy Physics, Oho-machi

Tsukuba-gun, Ibaraki 305

++Department of Mechanical Engineering, Technological University of Nagaoka
Nagaoka, Niigata 949-54

+++Faculty of Engineering, Hokkaido University, Sapporo 060

The photodissociation of the doubly excited molecular hydrogen has been successfully studied by observing Lyman- α radiation emitted from fragment $H(2p)$ atoms. Three thresholds have been found in the Lyman- α excitation spectrum and ascribed to the excitation to the doubly excited $Q_1^1\Sigma(1)$, $Q_1^1\Pi(1)$ and/or $Q_1^1\Sigma(2)$, and $Q_2^1\Pi(1)$ states of H_2^+ . This paper presents the angular distributions of Lyman- α radiation. A dissociation process into $H(2p) + H(2p)$ has been also observed by using the coincidence detection of two Lyman- α photons.

Lyman- α radiation was detected by a Ceratron or a microchannel plate through a MgF_2 window. Two microchannel plates were used in the coincidence detection of two Lyman- α photons.

Figure 1 shows the observed angular distributions of Lyman- α radiation. The intensity of Lyman- α radiation has a maximum at the angle of 0(deg.), i.e., the direction of the main polarization plane of incident SR photons. The observed Lyman- α radiation shows the largest anisotropy at 28.0 eV. The anisotropy of Lyman- α radiation decreases with increasing the energy. At 28.0 eV the possible optically allowed doubly excited state is only $Q_1^1\Sigma(1)$ state, while the other states with other symmetry can be excited in the higher energy region. This must be the reason for the decrease in the anisotropy of Lyman- α radiation with increasing the energy. Figure 2 shows a Lyman- α - Lyman- α coincidence spectrum measured at 33.0 eV. Similar spectra have been measured in the energy region of 29.0 - 36.0 eV. Figure 3 is the energy dependence of the intensity estimated from the coincidence peaks. The intensity of the peak has a threshold at 29.0 eV and increases with increasing the energy. The present detection of the coincidence of two Lyman- α photons corresponds to the observation of the dissociation process of the doubly excited states of H_2 into $H(2p) + H(2p)$. The main precursor of these two $H(2p)$ atoms may be the $Q_2^1\Pi_u$ state of H_2^+ .

References

- 1) S. Arai, T. Yoshimi, M. Morita, K. Hironaka, T. Yoshida, H. Koizumi, K. Shinsaka, Y. Hatano, A. Yagishita and K. Ito
Z. Phys., D4, 65 (1986)

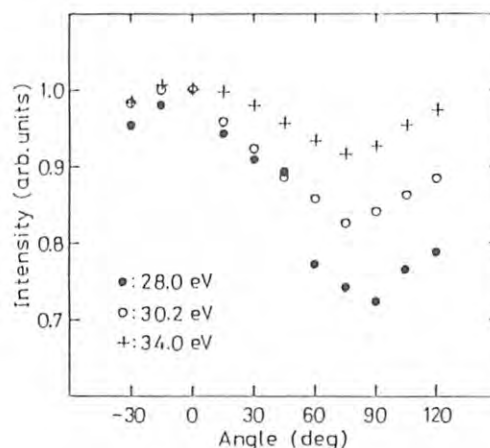


Fig.1

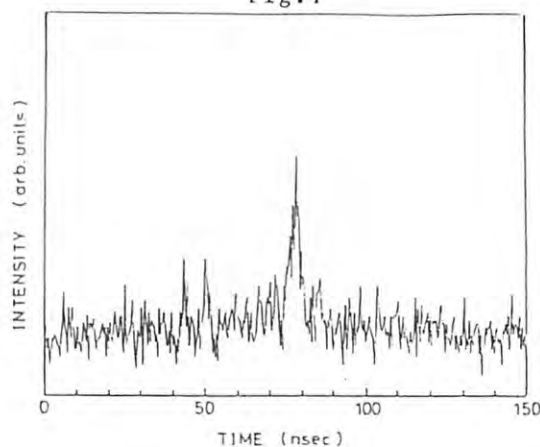


Fig.2

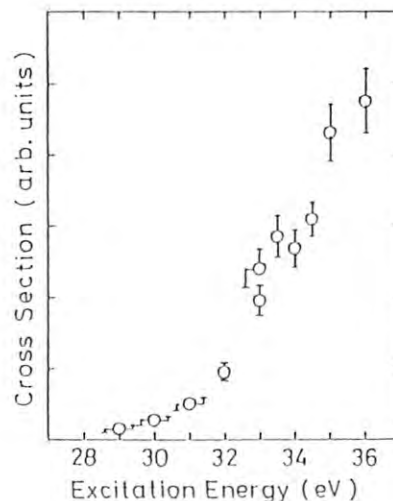


Fig.3

KINETIC ENERGY ANALYSIS OF PHOTOFRAGMENTS
PRODUCED IN DISSOCIATIVE PHOTOIONIZATION OF O₂ IN THE VUV REGION

M.Ukai, K.Ito, P.Lablanquie*, and A.Yagishita

Photon Factory, National Laboratory for High Energy Physics, Oho-machi, Ibaraki 305
*LURE, Bât 209D, Centre Université de Paris-Sud, 91405 Orsay-Cedex, France

Molecular photoionization process in the VUV region is closely coupled with dissociation process, and it is of great importance to obtain kinetic energy spectra and angular dependence of ionic fragments to elucidate dynamic behavior of the ionic and the highly excited states of molecules^{1,2}.

According to the kinetic energy analysis of O₂⁺ photoions^{4,5}, molecular ions in the B²Σ_g⁻ state predissociate almost exclusively to the 1st dissociation limit, O⁺(⁴S)+O(³P), to emit an ionic fragment with the kinetic energy of about 1eV. Predissociation of other electronic states of O₂⁺ does not lead to O⁺ ions with kinetic energy of 1eV below the photon energy of 23.8eV.

Conventionally, photoionization process has been studied by using the state-selected photoelectron spectroscopy³. However, it has been very difficult to apply the conventional photoelectron spectroscopy for investigations of the photoionization process near the ionization threshold because of experimental difficulties.

In the present experiment, dissociative photoionization of O₂ molecules has been studied by means of kinetic energy analysis of photoions. Photoions produced in collision with VUV photons dispersed by a 1m Seya-Namioka monochromator are extracted, energy analyzed, and detected at right angle with a parallel plate electrostatic analyzer combined with a position sensitive detector⁶. The analyzer system is rotatable in the plane perpendicular to the photon beam from -90 to 90 degree with respect to the polarization axis of SR.

Figure 1 shows obtained kinetic energy spectra. At 61.2nm (below the threshold of the B state), a single peak is observed at around zero kinetic energy, which corresponds to O₂⁺ ions with thermal

energy. On the other hand at 60.0nm (above threshold), another peak appears at 1eV kinetic energy as mentioned above. An excitation spectrum for this energetic ion is shown in figure 2.

The onset of this peak at 20.3eV coincides with that of the O₂⁺(B²Σ_g⁻) state. "Step up" structures just above the onset are due to the respective vibrational levels of the B state. The pronounced structure with double windows at around 21.0eV corresponds to the autoionization of the vibronic Rydberg states of the c⁴Σ_g⁻-3sσ_g v'=0,1 down to the B state. Others due to the Rydberg series of the c⁴Σ_g⁻-nsσ_g and ndσ_g states can also be observed above 23eV. The cross section has a broad maximum at about 21.7eV, which corresponds to the σ_u shape resonance.

Weak anisotropy of angular intensity distribution of O⁺ ions is observed. The anisotropy parameter is determined to be about 0.3 and does not show strong variation with photon energy.

At the photon energy above 29eV an unidentified peak is observed at 5eV kinetic energy⁴. This peak shows strong dependence on the photon energy and detection angle.

- 1) M.Ukai, A.Kimura, S.Arai, P.Lablanquie, K.Ito, & A.Yagishita, Chem.Phys.Lett., **135**, 51(1987).
- 2) A.Tabche-Fouhaile, I.Nenner, P.M.Guyon, & J.Delwiche, J.Chem.Phys., **75**, 1129(1987).
- 3) P.Morin, I.Nenner, M.Y.Adam, M.J.Hubin-Franskin, J.Delwiche, H.Lefevre-Brion, & A.Giusti-Suzor, Chem.Phys.Lett., **92**, 609(1982).
- 4) P.H.Doolittle, R.I.Shoen, & K.E.Schubert, J.Chem.Phys., **49**, 5108(1968).
- 5) T.Akahori, Y.Morioka, M.Watanabe, T.Hayaishi, K.Ito, & M.Nakamura, J.Phys., **B18**, 2219(1985).
- 6) A.Yagishita, Jpn.J.Appl.Phys., **25**, 657(1986)

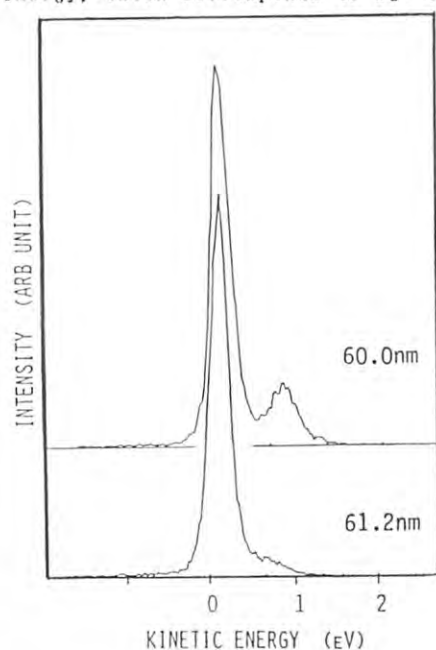


Fig.1

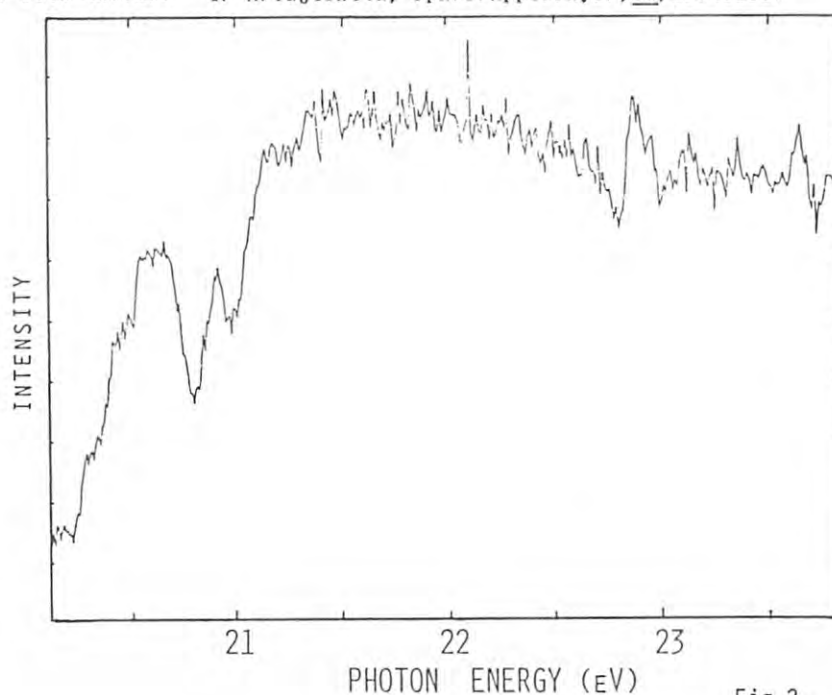


Fig.2

VACUUM-ULTRAVIOLET ABSORPTION OF Cl_2 AND HCl BETWEEN 33 AND 105 nmShin YOKOYAMA, Ken-ichirou TANAKA⁺, Masatoshi UKAI⁺⁺, Dai YUI, Yasumitsu IKEDA and Mitsuo KAWABEInstitute of Materials Science, University of Tsukuba
Sakura-mura, Ibaraki 305⁺Photon Factory, National Laboratory for High Energy Physics
Oho-machi, Tsukuba-gun, Ibaraki 305⁺⁺Department of Chemistry, Faculty of Science, Tokyo Institute of Technology
Oukayama, Meguro-ku, Tokyo 152Introduction

Recently, photochemical reaction using synchrotron radiation has been applied to semiconductor processes such as etching of Si ,^{1,2)} and SiO_2 ¹⁾ and deposition of silicon nitride³⁾. However, the optical properties of the reaction gases used in the photochemical processing are known very little especially in the vacuum-ultraviolet region (<100 nm). Cl_2 and HCl gases are often used in the plasma-etching⁴⁾ and photochemical etching of GaAs ⁵⁾. For these gases several researchers measured the absorption coefficients⁶⁻¹²⁾. However, there are no data at the wavelength shorter than 70 nm excepting extreme ultraviolet region (>200 eV). The absorption data and the dissociation procedure will become important in the near future with advancement of the photochemical processing. In this report the absorption data of Cl_2 and HCl are exhibited between 33 and 105 nm.

Experimental and Results

Detailed experimental technique and equipment were reported elsewhere¹³⁾. The absorption cross sections were measured with an ionization chamber as shown in Fig. 1, with four ion collection plates. An absorption coefficient, α , can be obtained from the ion current, I_1 and I_2 using the following equation:

$$\alpha = \sigma_t N = \ln(I_1/I_2)/L, \quad (1)$$

where L is the distance between electrodes as shown in Fig. 1, σ_t is the absorption cross section and N is the molecular density of the sample gas. The value of N was calculated from the pressure monitored by the baratron (MKS type 222B). Figure 2 shows the absorption spectra for Cl_2 and HCl gas. The oscillation structure of HCl observed for the wavelength larger than 70 nm is quite similar to the data after Terwilliger and Smith⁹⁾. The assignment of the structure of Cl_2 between 80 and 100 nm is now in progress.

References

- 1) T. Urisu and H. Kyuragi, 2nd Topical Meeting on Microphysics of surfaces, Beams and Adsorbates, Feb. 1987)
- 2) N. Hayasaka et al., Nikkei Microdevices No.4, 1987, p.42. (in Japanese)
- 3) H. Kyuragi and T. Urisu, J. Appl. Phys. **61**, 2035 (1987).
- 4) K. Asakawa and S. Sugata, Oyobuturi **54**, No. 11, 1136 (1985). (in Japanese)

- 5) S. Yokoyama, Y. Yamakage, and M. Hirose, Proc. 12th Int. Symp. on Gallium Arsenide and Related Compounds (The Inst. Physics by Adam Hilger Ltd, Karuizawa, Japan) p. 325.
- 6) S. T. Stephenson, R. Krogstad, and W. Nelson, Phys. Rev. **84**, 806(1951).
- 7) W. Hayes and F. C. Brown, Phys. Rev. **A6**, 21(1972).
- 8) D. Thomas and A. L. Smith, J. Chem. Phys. **63**, 1008(1975).
- 9) D. T. Terwilliger and A. L. Smith, *ibid*, **45**, 366(1973).
- 10) T. A. Jacobs and R. R. Giedt, J. Quant. Spectrosc. Radiat. Transfer. **5**, 457(1965).
- 11) A. A. Zakharyan and V. M. Novikov, Soviet J. Opt. Tech. **39**, 119(1972).
- 12) D. J. Seerry and D. Britton, J. Phys. Chem. **68**, 2263(1964).
- 13) Y. Hatano et al., Photon Factory Activity Report 1982/83 (1984) p. VI87.

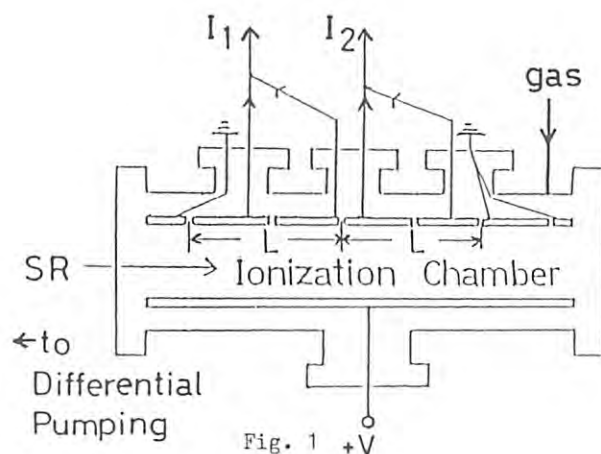


Fig. 1

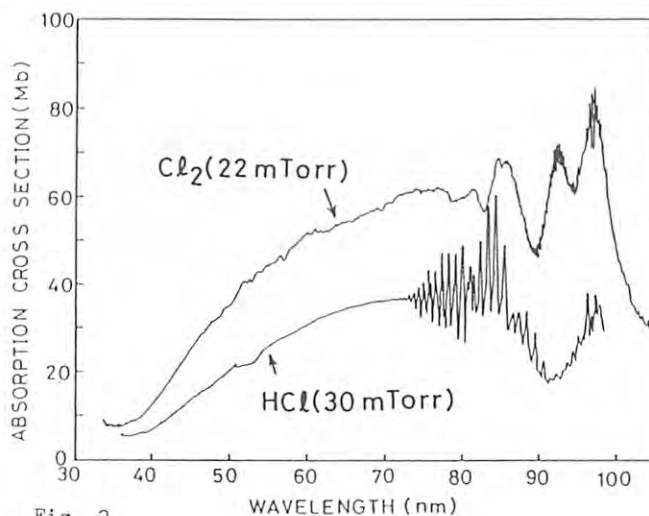


Fig. 2

Shingo TERAKADO, Masao NAKAO, Atsuo MIZUKAMI, Ken-ichiro TANAKA[†] and Jun-ichi CHIKAWA[†]

SANYO Tsukuba Research Center,

2-1 Koyadai, Yatabe-machi, Tsukuba-gun, Ibaraki 305

[†]Photon Factory, National Laboratory for High Energy Physics,
Oho-machi, Tsukuba-gun, Ibaraki 305

Introduction

Recently, photochemical etching techniques which will be capable of realizing maskless, resistless and damageless process of semiconductor, have been investigated extensively.¹⁻²⁾ In particular, the technique using synchrotron radiation (SR) as a light source, can be expected to be new one, because gases used in such etching processes have large absorption cross sections in the vacuum UV (VUV) region. Reactive gases excited by the VUV are immediately decomposed or ionized, and react with the substrate.

Experimental

Experiments were carried out in the beam line BL-12A at the photon factory. The wavelength region used in the reaction chamber was longer than 105 nm, because LiF windows were set into the entrance of the chamber filled with reactive gases connected to the beam line, to keep the high vacuum. Experimental setup is shown in Fig. 1. Two kinds of gases were used in the experiment. One was 10 % Cl₂ reactive gas diluted with Ar, the other was pure Ar gas used for the protection of the LiF window. Each gas was fed into the reaction chamber at the same pressure of 1.33×10^{-3} Pa through a variable leak valve and a feeding line as shown in Fig. 1. An n-GaAs (100) substrate fixed on a Mo holder was heated from room temperature to 225 °C by W ribbon heater. The substrate was set perpendicularly to the radiation beam. The etched thickness was measured by using DEKTAK. The etching profile of GaAs surface was directly observed by scanning electron microscope (SEM).

Results and Discussion

Etching rates of n-GaAs (100) by Cl₂ as a function of the substrate temperature are shown in Fig. 2. The irradiation time for the calculation of the etching rates was normalized by the standard ring current 100 mA; that is, the dose is defined as the product of the real irradiation time and the average ring current during the etching. Then the normalized irradiation time is the amount of dose divided by 100 mA. In this figure, a solid line shows the etching rate with SR and a dotted line shows that without SR. The etching rate increases with the substrate temperature. Below 200 °C, it was found that the etching rate of GaAs with SR was higher than that without SR, and etching product was remained on the substrate surface. When the substrate temperature was above 200 °C, both of the etching rate with and without SR indicated almost the same, and the substrate surface had no product. These results indicate that the etching of GaAs

using Cl₂ as a reactive gas was activated very much by the addition of the VUV from SR, and the etching product remained on the surface was supposed to be GaCl₃, because GaCl₃ evaporates at about 201 °C, could not exist on the substrate surface above 201 °C.³⁾ The GaAs substrate used for the experiment shown in Fig. 2 was covered with stripe-pattern-shaped Au mask of about 50 nm thickness. The etching reaction in this experiment was observed especially on the boundary between the GaAs surface and the Au mask. Based on this result, it is thought that the Au mask functions as catalyst, because etching did not occur from the boundary at any temperature when a polyimide mask was used. It was found from SEM observation that the etching occurred on both the irradiated and the non irradiated region. Therefore it was concluded that Cl₂ gas is excited in gas-phase and reacts with the substrate.

References

- 1) D. J. Ehrlich and J. Y. Tsao, J. Vac. Sci. Technol. B1, 969(1983)
- 2) T. J. Chuang, in the 18th Conference on Solid State Devices and Materials, 193(1986)
- 3) M. Hirose, S. Yokoyama and Y. Yamakage, J. Vac. Sci. Technol. B3, 1445(1985)

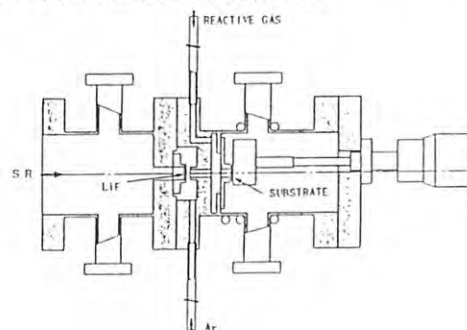


Fig. 1 Experimental apparatus used for SR-assisted photochemical etching.

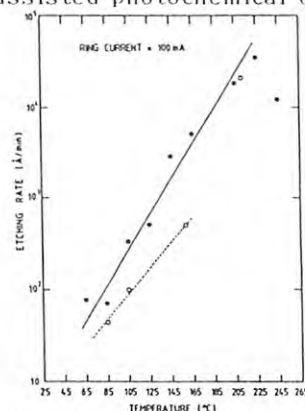


Fig. 2 Dependence of etching rate on substrate temperature.

PHOTOELECTRIC ABSORPTION MEASUREMENTS IN THE FOCAL PLANE SCANNING MODE
OF THE 6VOPE FACILITY AND ITS APPLICATION TO KRYPTON IN THE VUV REGION

Kenji ITO¹, Kengo MAEDA², Kiyoshi UEDA³, Yumio MORIOKA⁴ and Takeshi NAMIOKA³

1) Photon Factory, National Laboratory for High Energy Physics, Tsukuba-gun, Ibaraki 305, Japan.

2) Faculty of Education, Kumamoto University, Kurokami, Kumamoto 860, Japan.

3) Research Institute for Scientific Measurements, Tohoku University, Katahira, Sendai 980, Japan.

4) Institute of Physics, University of Tsukuba, Niihari-gun, Ibaraki 305, Japan.

INTRODUCTION

The 6VOPE facility, which consists of a 6.65-m Vertical dispersion Off-Plane Eagle spectrograph/monochromator and a specially designed predisperser system of zero-dispersion type, is installed at BL12B for high-resolution spectroscopic studies in the VUV region by using photographic and photoelectric modes.

With respect to the photographic mode, we have already shown the highest resolving power ($\lambda/\Delta\lambda = 2.5 \times 10^5$) ever demonstrated in the VUV region, by taking the absorption spectra of rare gases in the 6th - 10th order of the main grating in the wavelength region of 50 - 90 nm.

The photographic mode has a great advantage in determining absolute wavelengths of spectral lines, while the photoelectric mode is required in order to obtain accurate cross sections of photoabsorption and photoemission. In this report, we describe the details of the photoelectric mode, i.e., the focal plane scanning mode, and its application to the measurement of photoabsorption cross section of krypton atom in the VUV region.

EXPERIMENTAL

1) Focal Plane Scanning Mode

In the focal plane scanning mode, the exit slit and photon detector unit scans along the focal plane of the main grating. The scanning consists of a linear translation of the exit slit and detector unit, and a rotation of the whole system including the guiding mechanism for the translation. These two motions are realized by two stepping motors, and are linked 80 through a minicomputer. The slit and detector unit moves over 250 mm at a rate of 2 $\mu\text{m}/\text{step}$, i.e., 2.5×10^{-4} nm in the first order. In order to initialize a scan, one enters start-, stop- and step wavelengths, and a dwell time into the computer. For every step, it calculates the numbers of output pulses for the stepping motors, and controls the two motions by checking the readings of the encoders connected to the stepping motors. A nude type electron multiplier with a CsI coated cathode is used as a photon detector. The counting rate is ~ 6 kcps at 86 nm in the 6th order with 10- μm widths from the entrance and exit slits at a 200-mA storage current in the PF ring.

2) Absorption Measurements

Since the realignment of

the bending magnets during the summer shut-down in 1986, the SR beam is enough stable to carry out the photoelectric measurements with the 6VOPE facility. The main spectrometer tank containing sample gases is used as an absorption cell. The problem is how to keep the sample-gas pressure in the tank constant, and how to decide the pressure accurately during a scan. We estimate the uncertainty in the column density is less than several percent.

With an assumption that the intensity of the scattered light has a uniform distribution on the focal plane, the intensity of the dispersed light at a position corresponding to a wavelength λ_0 on the focal plane with an absorption by sample gas of which column density is $n\ell$ is represented by,

$$I(\lambda_0) = i_0(\lambda_0)\exp(-\sigma(\lambda_0)n\ell) + i_s\exp(-\sigma_s n\ell)$$

where $i_0(\lambda_0)$ and i_s are the intensities of the incident and scattered lights without absorption, and $\sigma(\lambda_0)$ and σ_s the absorption cross sections by sample gas for the light of wavelength λ_0 and for the scattered light. We measured $I(\lambda_0)$ at various pressures of sample gas and estimated that i_s is 10 ± 1 percent of $i_0(\lambda_0)$.

We have measured the photoabsorption spectrum of krypton atom in the wavelength region of 84.5 - 88.5 nm. A portion of the spectrum is shown in Figure 1. The resolution is estimated to be $\sim 6 \times 10^{-4}$ nm, which is the highest one ever shown in the photoelectric method for this wavelength region.

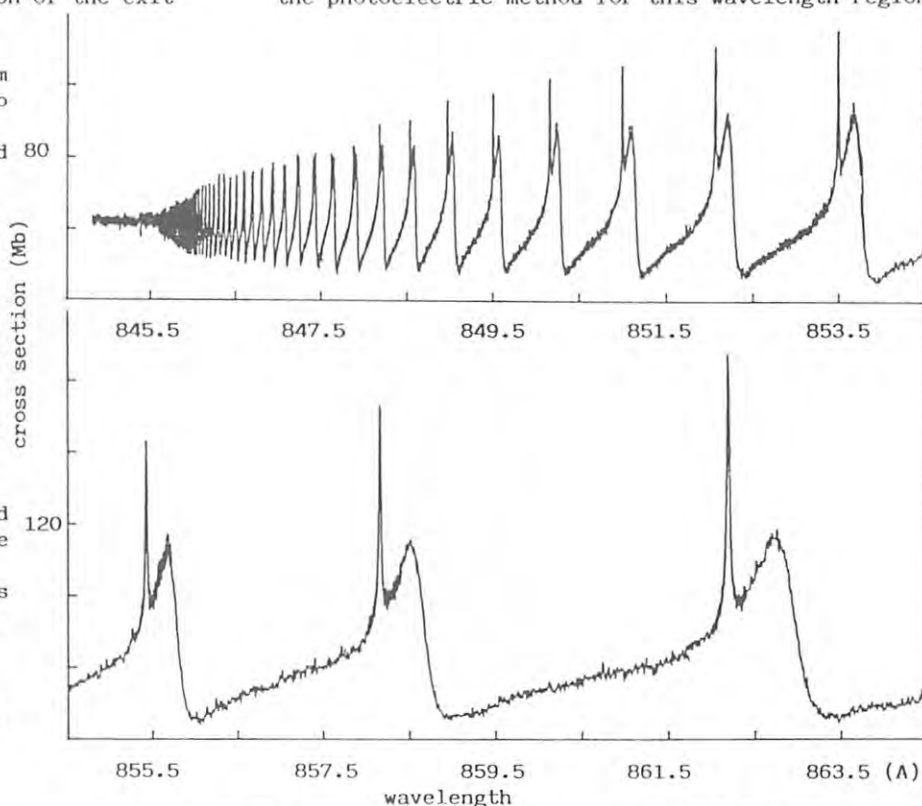


Figure 1. A portion of absorption spectrum of krypton atom.

ABSORPTION SPECTRUM OF THE NEON ATOM IN THE VACUUM-ULTRAVIOLET REGION

Kenji ITO*, Kiyoshi UEDA#, Kouichi YOSHINO§, Yumio MORIOKA\$ and Takeshi NAMIOKA#

*Photon Factory, National Laboratory for High Energy Physics, Tsukuba-gun, Ibaraki 305, Japan.

#Research Institute for Scientific Measurements, Tohoku University, Katahira, Sendai 980, Japan.

§Harvard-Smithsonian Center for Astrophysics, 60 Garden St., Cambridge, MA 02138, U.S.A.

\$Institute of Physics, University of Tsukuba, Niihari-gun, Ibaraki 305, Japan.

INTRODUCTION

We report the absorption spectrum of Ne I in the region of 565 - 595 Å obtained by using the 6VOPE facility/1/, the high-resolution VUV spectrograph/monochromator installed at the BL-12B of the Photon Factory. We have extended the five Rydberg series to higher members, e.g., $n=63$ for $nd(3/2)_1^o$ series, and derived the two ionization potentials, $I_{3/2}$ and $I_{1/2}$, with the single channel quantum-defect analysis. We also applied the five channel quantum-defect analysis to the observed term values, and obtained a set of the parameters from the multichannel quantum-defect theory (MQDT) that well reproduces the term values observed in the present measurement.

EXPERIMENTAL

The absorption spectrum of neon gas was registered on $2 \times 10''$ Kodak SWR plates for the wavelength region of 565 - 595 Å in the 10th spectral order of a 6.65-m, 1200-grooves/mm, 5500-Å blaze, Os-coated grating. Tank neon of research grade was used without further purification and flowed through the main spectrograph tank at a pressure of 10^{-3} - 10^{-5} Torr. Exposure time was 30 - 100 min. under a normal operational condition of the storage ring. The detailed procedure to determine absolute wavelengths of absorption lines on the photographic plates was described elsewhere/2/.

RESULTS AND DISCUSSION

In Figure is shown a portion of the absorption spectrum of neon gas for 572.4 - 575.6 Å range taken in the 10th spectral order. Neon pressure in the tank was 1×10^{-3} Torr and exposure time was 45 min.

We extended five Rydberg series up to $n=44$, 15, 63, 45, and 53 for the $ns(3/2)_1^o$, $nd(1/2)_1^o$, $nd(3/2)_1^o$, $ns'(1/2)_1^o$ and $nd'(3/2)_1^o$ series, respectively.

If the Rydberg series is not perturbed, term values are given by the Rydberg formula

$$I - E_n = \text{Ryd} / (n - \mu)^2$$

where I is the series limit, E_n the term value with the principal quantum number n , Ryd the Rydberg constant, and μ the quantum defect. We obtained

$$I_{3/2} = 173930.0 \pm 0.2 \text{ cm}^{-1} \text{ from the } ns(3/2)_1^o \text{ and } nd(3/2)_1^o \text{ series,}$$

$$I_{1/2} = 174710.4 \pm 0.2 \text{ cm}^{-1}$$

from the $ns'(1/2)_1^o$ and $nd'(3/2)_1^o$ series.

Furthermore, we applied the MQDT to the analysis of the five Rydberg series obtained in the present measurement. The fitting procedure to calculate the energy-dependent quantum-defects are described in detail elsewhere/3/. It is found that the observed term values below the $I_{3/2}$ limit are well reproduced by using the MQDT parameters from the present analysis. In order to check further the quality of the parameters obtained here, we derived real and imaginary parts of the complex quantum defect for the $ns'(1/2)_1^o$ and $nd'(3/2)_1^o$ series. The complex quantum defect thus derived semiempirically shows a better agreement with the experimental values than those with the ab initio calculation. We emphasize the reliability and accuracy of the MQDT parameters obtained from this analysis.

REFERENCES

- /1/. K. Ito, T. Namioka, Y. Morioka, T. Sasaki, H. Noda, K. Goto, T. Katayama and M. Koike, Appl. Opt., **25**, 837 (1986).
- /2/. K. Ito, K. Yoshino, Y. Morioka and T. Namioka, Phys. Scr., **36**, 88 (1987).
- /3/. K. Ueda, J. Opt. Soc. Am., **B4**, 424 and 648 (1987).

This work is supported in part by Japan Society for Promotion of Science and National Science Foundation under a Japan-USA Cooperative Research Program.

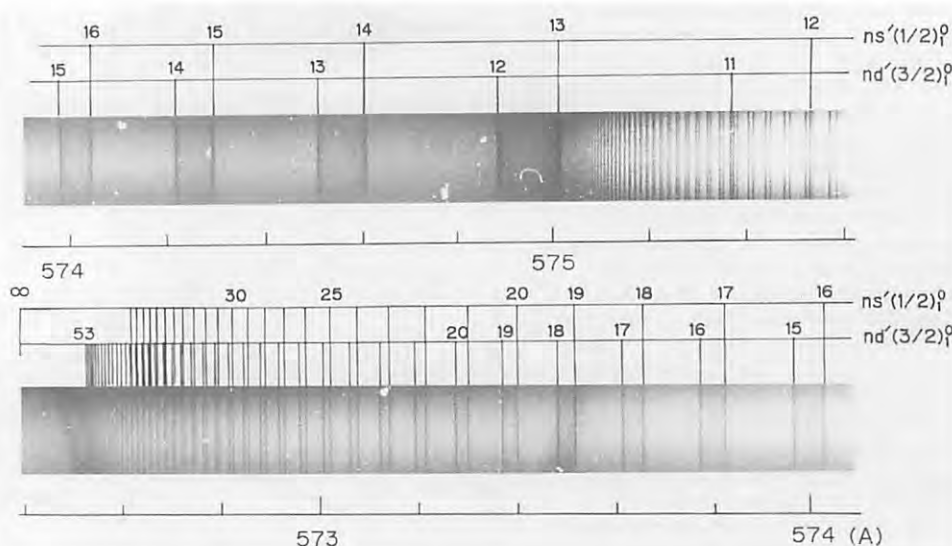


Figure : A portion of absorption spectrum of neon gas

HIGH-RESOLUTION MEASUREMENTS OF PHOTOABSORPTION COEFFICIENTS FOR CARBON MONOXIDE ABSORPTION BANDS BETWEEN 94.0 nm AND 100.4 nm

K. Yoshino, G. Stark, P. L. Smith, W. H. Parkinson, K. Ito¹ and T. Namioka²

¹Harvard-Smithsonian Center for Astrophysics, 60 Garden St., Cambridge, MA 02138, U.S.A.

²Photon Factory, National Laboratory for High energy Physics, Tsukuba-gun, Ibaraki 305, Japan.

²Research Institute for Scientific Measurements, Tohoku University, Katahira, Sendai 980, Japan.

INTRODUCTION

Observations and studies of interstellar CO provide important insights into the formation and properties of interstellar clouds. CO is believed to be the most abundant molecule after H₂, is used as a tracer of the large-scale distribution of molecular gas in galaxies. This application of CO observations requires that the abundance and excitation, and, therefore, the physical and chemical properties, of CO be known.

An important process for which more data are needed is photodissociation. Destruction of CO by this means occurs through line absorptions, at wavelengths between 91.2 nm and 111.8 nm, into predissociating states. In diffuse clouds, the rate of photodissociation of CO is reduced because of shielding by atomic and molecular hydrogen lines that are accidentally coincident with CO absorption features. On the other hand, in dense clouds, dissociation of CO is enhanced by emission from H₂ that has been excited by cosmic-ray-generated secondary electrons. Quantitative understanding of these effects requires high-resolution spectral data so that the molecular states that contribute can be identified and their line positions, line widths, and absorption coefficients, or band oscillator strengths, can be determined.

EXPERIMENTAL

The present measurements were made with the 6VOPE facility at the Photon Factory. The 5th order of 1200 line mm⁻¹ grating and 10-μm entrance exit slit were used. The spectrometer tank contained the CO and was used as the absorption cell. The nominal absorption path length was 12.5 m, and typical tank pressure were 5 × 10⁻⁵ to 5 × 10⁻⁴ Torr. We estimate that the column density during the measurements could be determined with an uncertainty of ±10 percent. Most spectral region were scanned 0.15 nm portions. the scans were begun with no gas in the main tank. After measuring the background continuum level, I₀, over 0.01 nm, the gas was injected. After 0.13 nm of the spectrum, I, had been scanned, the tank was evacuated and a final short portion of the continuum was studied. A linear interpolation was used to approximate I₀ during the scanning of 0.13 nm. I₀ and I were comprised, in part, of scattered light, so that their relationships to the actual values of background, i₀, and signal, i, were:

$i_0 + s i_0 = I_0$ and $i + s i_0 = I$,
where $s i_0$ is the scattered signal. Thus α is given by:

$$\alpha/n = (1/\ell) \ln \left(\frac{I_0/(1+s)}{I - s I_0/(1+s)} \right)$$

where ℓ is the length of the absorbing column. s was determined by considering absorption data obtained at two values of absorber column density for the J(0), W(0), L(0), and L'(0) bands.

The four measurements of s gave values that clustered around $s=0.22 \pm 0.07$.

A small portion of the data obtained are presented in Figure 1. Because α/n is a temperature-dependent quantity, we have chosen not to call it a "cross section". The apparent band head at 96.87 nm is actually a superposition of the P-branch of the L(0) band and the R-branch of the L'(0) band. The uncertainty for the α/n in Figure 1 was estimated to be ± 20 percent.

RESULTS

Our absorption coefficient data are presented in Table 1. In order to facilitate comparison, we have integrated our data over the same wavelength ranges as used by Letzelter et al. Our integrated values are greater than those by Letzelter et al. for all bands except the blend of L(0), L'(0), and K(0). The discrepancy may be attributable to the difference between the resolving powers of the spectrometers used.

This research was supported in part by NASA Grant NSG-7304 to Harvard University and by a joint JSPS-NSF Cooperative Research Program.

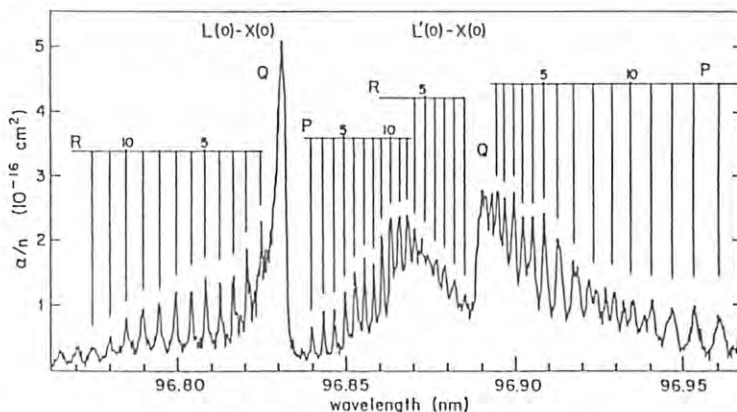


Figure 1. Absorption Coefficient for the L(0), and L'(0) Bands of CO.

Table 1. Integrated Values of α/n (in 10^{-16} cm^2)

wavelength range(nm)	assignment	this work	*Letzelter et al.
100.148-100.438	F(0)	0.99 ± 0.30	0.706
98.868- 99.000	G(0)	0.10 ± 0.03	0.04
98.370- 98.724	J(0)	2.3 ± 0.46	1.32
97.243- 97.502	W(0)	1.2 ± 0.24	1.01
96.735- 96.859	L(0)	0.72 ± 0.14	nr
96.859- 96.977	L'(0)	1.5 ± 0.30	nr
96.977- 97.180	K(0)	1.3 ± 0.26	nr
94.090- 94.222	S(0)	2.9 ± 0.60	2.02
96.735- 97.180	L + L' + K	3.5 ± 0.70	3.4

*)Letzelter et al., Chem. Phys., 114, 273 (1987). nr)not resolved.

HIGH RESOLUTION ABSORPTION SPECTRA OF H_2O AND D_2O IN THE V.U.V. REGIONYumio MORIOKA, Kenji ITO,⁺ Kengo MAEDA,⁺⁺ and Takeshi NAMIOKA⁺⁺⁺Institute of Physics, University of Tsukuba, Sakura-mura,
Ibaraki 305⁺ National Laboratory for High Energy Physics, Oho-machi,
Ibaraki 305⁺⁺ Faculty of Education, Kumamoto University, Kurokami,
Kumamoto 860⁺⁺⁺ Research Institute for Scientific Measurements,
Tohoku University, Katahira, Sendai 980Introduction

H_2O and D_2O molecules have been studied in the various wavelength regions by many investigators. High resolution absorption spectra in the V.U.V. region was investigated by Johns¹⁾. However, the linear H_2O and D_2O were not found yet. We confirmed by the rotational analysis the existence of the linear states of H_2O and D_2O in the 1140 Å region.

Experimental and Results

The light source was synchrotron radiation at the Photon Factory. The spectrum was obtained with a high-resolution spectroscopic facility consisting of 6.65 m Vertical dispersion Off-Plane Eagle spectrograph and a unique predisperser system of zero dispersion type²⁾ in the 12B line.

In the figure is shown a densitometer trace of the spectrogram of H_2O , which was taken at a pressure of 3×10^{-3} Torr and with an exposure time of one hour. Triatomic molecules generally show very complicated spectral features. The structure of the spectrum is, however, very simple as is seen in the figure.

Furthermore, the Q branch is missing, and this suggests that the transition is like $\Sigma-\Sigma$ type. Since the energies of the rotational levels of the ground state are known from the infrared data³⁾, the molecular constants of the excited state can be derived. The band origin is 87377.6 cm^{-1} and the rotational constant of the excited state B' 8.1 cm^{-1} .

The linearity of H_2O in this excited state is evident from the following points. (1) the level in the excited state are degenerate (2) their energies can be represented by a simple formula $B'J(J+1)$ and (3) only the spectrum of $K_a=0$, that is $\Sigma-\Sigma$ transition, presents.

We made also an experiment on D_2O and observed the same spectral feature, except for the rotational constants B' being about one half that of H_2O , as expected from the moment of inertia.²⁾ The band origin was found to be 87330.0 cm^{-1} and B' was 4.1 cm^{-1} .

References

- 1) J. W. C. Johns: Can. J. Phys. 41 (1963) 209
- 2) K. Ito, T. Namioka, Y. Morioka, T. Sasaki, H. Noda, K. Goto, T. Katayama and M. Koike Appl. Opt. 25 (1986) 837
- 3) W. S. Benedict and E. K. Plyler: J. Res. Natl. Bur. Std. 46 (1934) 246

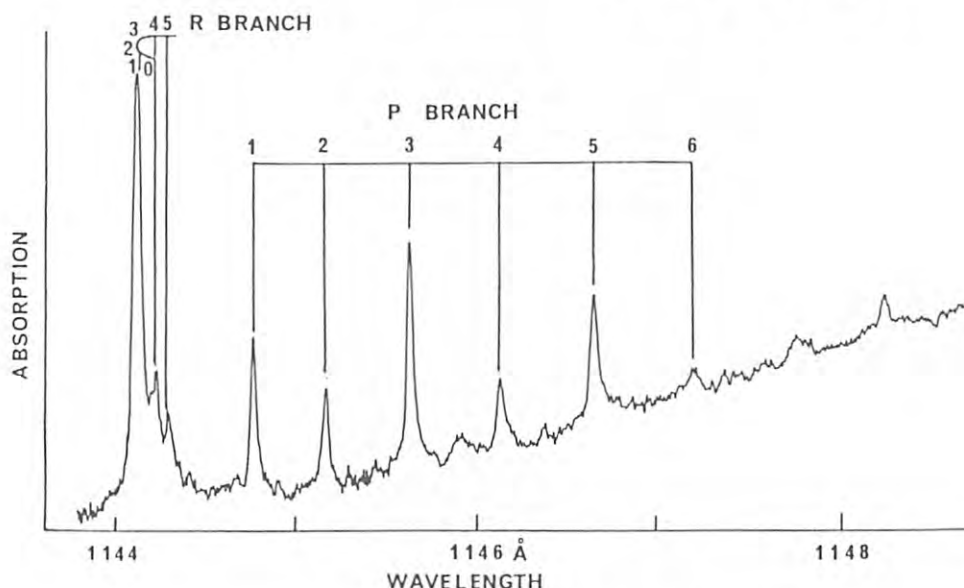


Fig.1. The rotational spectrum of H_2O in the 1144 Å region

BASIC CHARACTERISTICS OF MICROCHANNEL PLATES FOR PLASMA X-RAY DIAGNOSTICS

Naohiro YAMAGUCHI, Takashi KONDOH, Teruji CHO, Sadao AOKI*

Hideki MAEZAWA** and Masaharu NOMURA**

Plasma Research Center, University of Tsukuba, Sakura, Ibaraki 305

* Institute of Applied Physics, University of Tsukuba, Sakura, Ibaraki 305

** Photon Factory, National Laboratory for High Energy Physics, Oho, Ibaraki 305

Introduction

X-ray measurement is an important method to diagnose high temperature plasmas. In general spatial and spectral resolutions are required together with temporal resolution. Microchannel plates (MCPs) have often been used as the two-dimensional or position sensitive detector in X-ray imaging system or XUV spectrometer. The MCP calibrated in this experiment is prepared for X-ray tomography measurement on the GAMMA10, axisymmetrized tandem-mirror plasma-confinement device¹⁾. In this measurement system MCPs detect X-ray radiations from different chord of a plasma with a slot hole imaging geometry. It is necessary to investigate the X-ray detection characteristics of MCPs for wide energy range and various angle of incidence.

Experimental and Results

The specification of the MCP used (Hamamatsu F1943-22MX) is as follows: channel diameter 15 μm , length to diameter ratio 40, channel pitch 19 μm , open area ratio 57 % and electrode material Fe-Cr. Two channel plates are assembled in tandem configuration. The experiment has been carried out at the BL-7C, a double crystal (Si(111)) monochromator beam line (5-20 keV). In order to suppress the higher order reflected X-ray, the setting of crystals has been kept slightly deviated from the parallel location. The incident photon flux has been monitored by an ionization chamber with capton windows. MCPs were mounted on a rotatable stage in a vacuum chamber in order to change the incident angle of X-ray beam. MCPs were operated at unsaturated current-detection mode.

The current response as a function of incident angle is shown in Fig. 1 for different

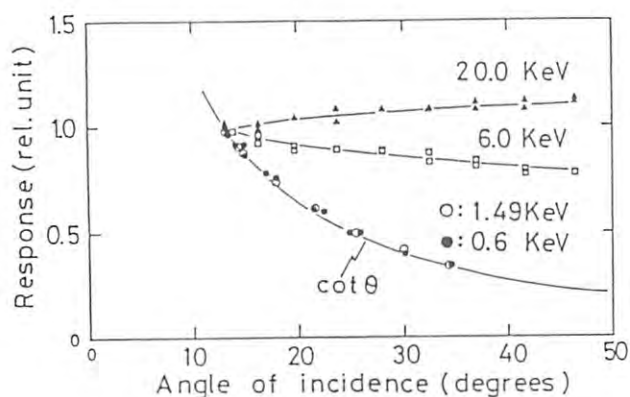


Fig.1 Relative X-ray detection efficiency vs incident angle to the channel axis. Parameters are X-ray energy.

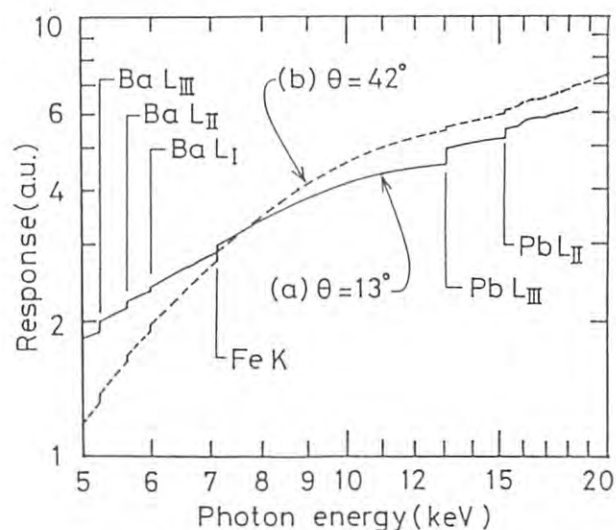


Fig.2 Current response for the X-ray energy range from 5 to 20 keV. The parameter is incident angle of X-rays.

X-ray energies together with the results of the lower energy case which has been obtained previous experiment²⁾. The response curve for the higher energy X-ray is rather flat and does not indicate the $\cot\theta$ dependence, where θ is the angle of incidence of X-rays, which comes from the change of the irradiated area in a channel wall. High energy X-rays can penetrate through the channel wall, then multiple channels contribute to produce photoelectrons. The number of channels which X-rays pass through will increase as the angle of incidence increases. Thus, the dependence of $\cot\theta$ for the ideal single cylindrical photocathode model is lost.

The current response for the X-ray energy range from 5 to 20 keV is shown in Fig. 2 for the two different incident angles. Some discontinuous jumps are found at the absorption edges of MCP glass and input-surface-electrode materials.³⁾

References

- 1) M. Inutake et al., Phys. Rev. Lett. 55, 939 (1985).
- 2) N. Yamaguchi et al., Photon Factory Activity Report 1986, Proposal No.85-145.
- 3) T. Kondoh et al., to be published in Rev. Sci. Instrum.

DEEP SUBMICRON PATTERN REPLICATION AND MEASUREMENT OF TEMPERATURE RISE DISTRIBUTION FOR X-RAY MASK MEMBRANE IN SR LITHOGRAPHY

Ichiro MORI, Haruki KOMANO, Masaru HORI, Yukiko KIKUCHI, Yasuhiro HORIIKE and Ken-ichiro TANAKA⁺

VLSI Research Center, Toshiba Corporation
Komukai-Toshiba-cho, Saiwai-ku, Kawasaki 210

⁺Photon Factory, National Laboratory for High Energy Physics
Oho-machi, Tsukuba-gun, Ibaraki 305

Introduction

X-ray lithography using synchrotron radiation (SR) is a promising technology for finer microfabrication of VLSI with less than 0.25 μm feature sizes.¹⁾ This report presents recent results of deep submicron pattern replications and measurements of temperature rise distribution for X-ray mask membrane by means of a thermographic system.

Experimental and Result

The beam is deflected by 2° using a silicon carbide (SiC) plane mirror. This mirror can be scanned for a large and uniform vertical-illumination area. A vacuum chamber is located at a distance of 34 m from the source and equipped with a 5 μm thick aluminum (Al) filter and a shutter for exposure time control. An X-ray mask and a silicon wafer are exposed in the vacuum chamber ($< 2 \times 10^{-7}$ Torr). The spectrum has its maximum at 8 Å which is optimally suited for the SR lithography purpose.

X-ray mask membranes used for this study are 1~1.5 μm thick silicon nitride (SiN_x) films deposited by low pressure chemical vapor deposition. An absorber pattern on the membrane is fabricated by an electron beam writing and subsequent gold (Au) electroplating technique in the resist space patterns.

Figure 1 shows 0.25 μm square patterns replicated in 1 μm thick PMMA. 0.2 μm lines and spaces patterns with a steep profile were also obtained. Mask-wafer gap was 20 μm . Exposure time was 60 seconds at a 200 mA ring current. Resist development was carried out by isoamyl-acetate (IAA). This developer was useful for precise replications of deep submicron pattern

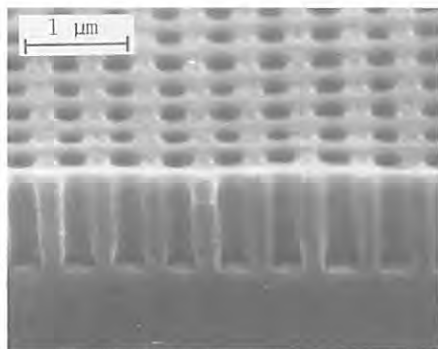


Fig.1. 0.25 μm square patterns replicated in 1 μm thick PMMA.

because of its high γ value in the case of high dose regions.

A thermographic system (JEOL: THERMOVIERER JIG-3200) is located at an angle of 145° with respect to the SR beam direction. Infrared rays from a mask membrane are detected by a HgCdTe sensor through a zinc selenide (ZnSe) window of the vacuum chamber. The read out data were corrected with emissivity, reflectivity and transparency of the window and the membrane.

Figure 2 shows a schematic of X-ray mask membrane and a temperature distribution of the membrane. At a 203 mA ring current, temperature rise at the center of the irradiated region was 50 °C. In this case the absorbed power was estimated to be 30 mW/cm². The temperature rise was measured to be proportional to the ring current. The experimental values of the temperature rise and the thermal diffusion length coincide with theoretical values, which are derived from a one dimensional model.²⁾

References

- 1) A.Heuberger, Microelectronic Engineering, 3, 535 (1985).
- 2) K.Heinrich, H.Betz and A.Heuberger, J. Vac. Sci. Technol., B1, 1352 (1983).

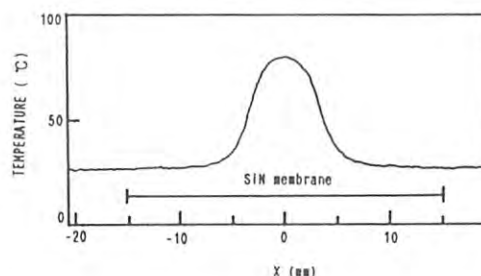
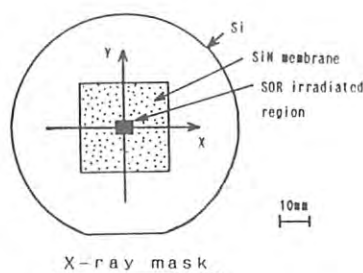


Fig.2. Schematic of X-ray mask membrane and temperature distribution.

A METHOD OF PATTERN REDUCTION IN SR X-RAY LITHOGRAPHY

Shigeo SUZUKI, Mitsuaki HARADA, Mitsuaki MORIGAMI, Jun-ichi NISHINO, Shuji FUJIWARA, Takashi GOTO, Kazuhiro KANEDA, Shun-ichi KOBAYASHI, and Masami ANDO¹

Tsukuba Research Center, Sanyo Electric, Co. Ltd.
Koyadai, Yatabe-machi, Tsukuba-gun, Ibaraki 305
¹Photon Factory, National Laboratory for High Energy Physics
Oho-machi, Tsukuba-gun, Ibaraki 305

Introduction

The reduction of the pattern in sub-micron scale has not been successfully done in X-ray lithography because of the lack of the lens. NTT has obtained images of 4 microns by using a multilayer synthetic mirror of Schwarzschild type. We have tried to reduce the size of the image by using X-ray diffraction phenomenon in crystal.

When the crystal is highly absorbing, the reflecting region is restricted near the surface. Intensity distribution in the incident X-rays is projected into the diffracted beam either in reduced or enlarged scale, if the asymmetric Bragg reflection is used. Experiment has been carried out at the beamline BL-12C of the Photon Factory.

Experimental

When the crystal surface is not parallel to the reflecting plane, the width of the reflected beam is different from that of the incident beam. The ratio n of the beam width is given by

$$n = \sin(\theta - \alpha) / \sin(\theta + \alpha)$$

where θ is the Bragg angle, and α is the offset angle of the surface from Bragg plane. In case of Fig.1, α is $0 < \alpha < \theta$, and the pattern size is reduced by the factor n . We have chosen wavelength $\lambda = 4.26 \text{ \AA}$, the offset angle $\alpha = 22^\circ$ and 111 reflection ($\theta = 34.7^\circ$). Then $n = 0.263$.

A SiC mirror coated with Pt was inserted between the light source and the monochromator, and high energy component ($\lambda < 3 \text{ \AA}$) was cut to avoid the undesirable Bragg reflection due to higher harmonics. Furthermore a Be filter of 200 \mu m thick was used to protect the resist film from the scattered light with the long wavelength. A mask which has an L shape pattern as shown in Fig.2(a) was set in the incident beam. A resist film which was coated on a Si wafer was put in the reflected beam.

A mask pattern has been prepared with a focussed ion beam technique. Absorber of X-rays is gold film which was supported by SiN membrane. InSb crystal was chosen, because it is heavy and the reflectivity is relatively high.

As the setting of a monochromator and a reduction mirror crystal, both (+,+) and (+,-) settings have been tried for pattern replication.

Resist films which we used in this experiment were positive type EBR-9 (TORAY) and negative type MES-X (JSR) which includes Cl and is sensitive to X-ray of 4.4 \AA . Orientation of the monochromator crystal was adjusted by a Huber goniometer and its angle was read with an encoder. A reduction mirror was set on a holder which sits on a rotating axis. Its orientation was adjusted manually. The distance from the resist film to mask along the

path of the X-ray beam was about 10 mm. The excitation of Bragg reflection was detected by watching brightness of an image on a fluorescent screen which was set behind the resist film.

Results and Discussion

A replicated image obtained in a (+,+) setting is shown in Fig.2(b). The size of the image was reduced to $n = 0.263$ times of original pattern only in vertical direction. Width of a gap A in Fig.2(a) was reduced from 10 to about 2.5 \mu m as shown in Fig.2(b). Exposure was about 3000 Amp·sec. The fringe-like pattern B in Fig.2(b) are possibly due to the fact that the total reflection mirror is not flat. We were not successful to reduce the pattern of 1 or 2 microns to a half or a quarter micron in this experiment. The reason is that the monochromatized X-ray was not ideally plane-parallel and that the angular width of the 111 reflection of InSb was too large.

Our method is not useful at this moment from the practical point of view, because only the small part of the incident X-ray is used and the exposure time is too long. But it may be used in the future, if either the intensity of the source or the sensitivity of the resist were improved by two or three orders of magnitude.

This work was performed as a joint work between KEK-PF and SANYO Electric Co.Ltd.

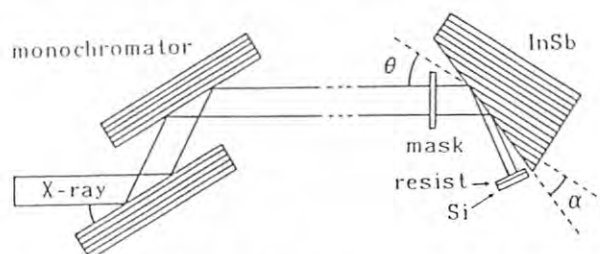


Fig.1 Experimental arrangement used in SR X-ray lithography.

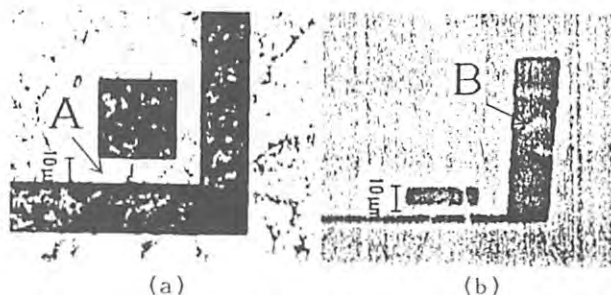


Fig.2 A mask pattern (a) and a replicated image (b) which was reduced in the vertical direction.

CRYSTAL STRUCTURE ANALYSIS OF *PSEUDOMONAS* ISOAMYLASE

Kunio MIKI, Kazuhiro MASUDA, Masaki YAMANAKA, Kenji MASAKI, Nobutami KASAI, and Yoshinori SATOW*

Department of Applied Chemistry, Faculty of Engineering, Osaka University, Yamadaoka, Suita, Osaka 565

*Photon Factory, National Laboratory for High Energy Physics, Oho-machi, Tsukuba-gun, Ibaraki 305

Introduction

We have been carrying out the crystal structure analysis of *Pseudomonas* isoamylase isolated from *Pseudomonas amyloclavata* to understand the catalytic mechanism of this enzyme at an atomic resolution. The enzyme has a molecular weight of about 90,000 and catalyzes the cleavage of α -(1,6)-D-glucosidic linkage in amylopectin and glycogen. We describe here the further progress of our structure analysis obtained after the previous activity report.¹⁾

Experimental

The intensity data were collected by the rotation method due to the large unit-cell dimensions of the crystal.²⁾ A Huber rotation/precession camera equipped on a Rigaku RU300 rotating anode generator (Cu-K α radiation) was used for the data collection of the native crystals. On the other hand, rotation photographs of heavy-atom derivatives were taken on a four-circle diffractometer associated with the BL14A beam line at the KEK Photon Factory. Two heavy atom compounds, $\text{Sm}(\text{NO}_3)_3$ and HgCl_2 were found to be well soaked into the crystals. A rotation photograph of the Hg derivative is shown in Fig. 1. The film evaluation and crystallographic calculation were done by using FILME and PROTEIN programs, respectively, both of which were developed at Max-Planck-Institut für Biochemie, Munich. All the computations were carried out at the Crystallographic Research Center, Institute for Protein Research, Osaka University.

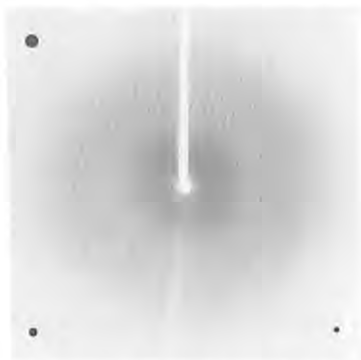


Fig. 1. A rotation photograph of the HgCl_2 derivative taken at the Photon Factory.

Results and Discussion

Intensity data for the native and derivative crystals hitherto collected were summarized in Table 1. The difference Patterson functions were calculated at 6 Å resolution for both derivatives. Fig. 2 represents one of the Harker sections where a peak corresponding to a plausible self-vector between heavy-atoms is indicated. Only one possible heavy-atom site was

located at the present stage for each derivative. These heavy-atom positions were referred to a common origin and refined by the least-squares procedure. At this stage, the electron density map, which was based on the phases obtained from these heavy-atom positions, was preliminarily calculated at 6 Å resolution. The map showed high and low regions of electron densities which might correspond to molecule and solvent regions, respectively. However, the molecular boundary was not so clear enough to determine the molecular size, which implies the necessity of the further improvement of the phase angles.

Table 1. Summary of intensity data collection

	native	$\text{Sm}(\text{NO}_3)_3$	HgCl_2
X-ray source	RU300	SR	SR
Wavelength(Å)	1.5418	1.58	1.54
No. crystals used	11	2	2
Rotation range(°)	0-90	0-67	0-42
No. total reflns.	90,348	47,333	27,866
No. unique reflns.	29,796	24,528	16,113
Completeness	0.833	0.686	0.451
Rmerge	0.117	0.085	0.094

1) RU300: Rigaku rotating anode generator

SR: synchrotron radiation at BL14A

2) Completeness: for 2.6 Å resolution

3) $R_{\text{merge}} = \Sigma(I - \langle I \rangle) / \Sigma I$.

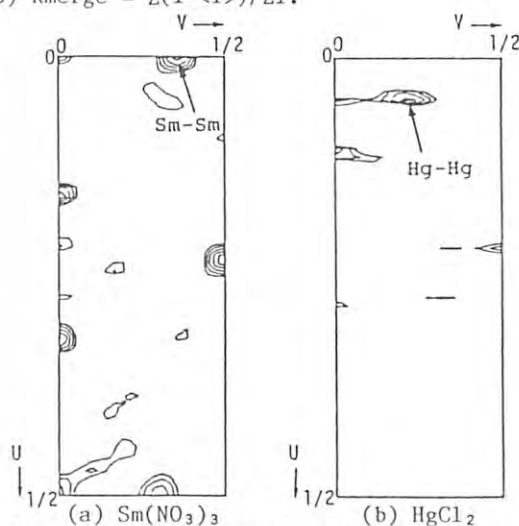


Fig. 2. Harker sections ($w=1/2$) of the difference Patterson functions at 6 Å resolution.

References

- 1) K. Miki, K. Masuda, K. Masaki, N. Kasai, and Y. Satow, Photon Factory Activity Report 4, 1986, p.269.
- 2) S. Sato, Y. Hato, Y. Ii, K. Miki, N. Kasai, N. Tanaka, and T. Harada, J. Mol. Biol., 160, 669(1982).

USE OF APOENZYME CRYSTAL IN STRUCTURE ANALYSIS OF SERRATIA PROTEASE

Yoshio KATSUYA, Yasuo HATA, Mamoru SATO, Nobuo TANAKA, Yukiteru KATSUBE and Yoshinori SATOW
 Institute for Protein Research, Osaka University, Suita, Osaka 565
 * Photon Factory, National Laboratory for High Energy Physics,
 Tsukuba, Ibaraki 305

Introduction

The X-ray crystal structure determination of serratia protease with a zinc metal in the active center has been carried out in our laboratory. The 2.5 Å resolution data of the native, U- and Hg-derivative crystals were collected with oscillation photography. Some reasonable heavy-atom binding sites were obtained for each derivative crystal from a difference Patterson and a difference Fourier maps. However, the contribution of Hg-sites to phase determination was very small. A preparation of another derivative crystal was required for phase determination. Many preparations of heavy-atom derivatives were tried, but none of them succeeded. Then the use of the apoenzyme crystal was tried for phase determination. The method that the zinc metal was removed from the native crystal was applied to prepare the apoenzyme crystal for keeping the isomorphism of the apoenzyme crystal to the native crystal. Diffraction intensity measurements for apoenzyme crystals were carried out at the synchrotron radiation facilities of Photon Factory (PF), because rapid measurements were required considering the apoenzyme crystal was unstable for X-ray irradiation. This report deals with the use of the apoenzyme crystal for the analysis.

Experimental

Native crystals were obtained by the dialysis method as reported previously (1). Crystals of the apoenzyme were prepared by soaking those of the native enzyme in 35% saturated ammonium sulfate solution containing 10% (w/v) EDTA. The soaking period was 5 days. The preparation process of the apoenzyme was checked by casain-plate method for the protease activity assay.

The sample for the assay was prepared by dissolving a few EDTA-treated crystals in 0.1M phosphate buffer (pH7) and put in a casain-plate with a solution of the native enzyme in the neighbouring site for the comparison of the enzyme activity between them. The casain-plate after 24 hour incubation was washed by 5% TCA. Then the casain-plate displayed two sizes of circular marks corresponding to the amount of the digested casain: 6mm diameter for the prepared apoenzyme and 15mm diameter for the native enzyme. From this result, the enzyme in the EDTA-treated crystal was estimated to have 20% of the original enzyme activity.

The four-circle diffractometer at the beam line BL-14A in PF was used for data collection. Intensity measurements were carried out with X-ray beam with the wavelength of 1.2 Å. Each reflection peak was scanned twice in the omega-scan method to measure its integrated intensity. The scan width was 0.2 degree and the scan speed was 8 degree/min. Before and after the scan of the

peak, the background intensity was measured for 0.3 sec. The diffraction data of apoenzyme crystals were collected up to 3.3 Å resolution using seven crystals.

Results and Discussion

The observed data were corrected for the Lorentz-polarization factor, X-ray absorption and irradiation damage, and intensity change of the incident X-ray. The scaling of the intensity data between the different crystals was done to obtain one data set of 11,560 independent reflection at 3.3Å resolution. The R-value in the scaling was 3.29% (Table I) which is comparable with the values of 2.42% and 4.24% for the native and PCMBs derivative, respectively, obtained in PF (2).

The difference Patterson map between the native data set obtained with oscillation photography and the apoenzyme data set obtained by a diffractometer in PF was calculated and compared with that between the native data and the apoenzyme data set which were both obtained by a diffractometer in PF. The ratio of rms intensity differences between two data sets in both calculation were 0.14 and 0.23, respectively. There were some common peaks between both the difference Patterson maps. The interpretation of the difference-patterson map was carried out using three Harker sections to obtain one position regarded as the zinc site of the enzyme. The refinement of the possible zinc site have been carried out, and the possibility of the site has been investigated.

References

- 1) Y. Katsuya, K. Hamada, Y. Hata, N. Tanaka, M. Sato, K. Kakiuchi, Y. Katsube and K. Miyata, J. Biochem., **98**, 1139 (1985)
- 2) Y. Katsuya, Y. Hata, M. Sato, N. Tanaka, Y. Katsube and Y. Satow, Photon Factory Activity Report **No.4**, 273 (1986)

Table I

Crystal	No of Ref	Overlap	R-value
AP01	2114	354	
2	1871	654	
3	1828	624	
4	1542	548	3.29%
5	1455	421	
6	1982	334	
7	2336	137	

Intensity Measurements with Short Wave-Length X-rays; Structure Refinement of Ilmenite

Masataka OHGAKI¹, Kiyooki TANAKA¹, Fumiyuki MARUMO¹, Fumihiko TAKEI²,
Yoshinori SATOU³

1. The Research Laboratory of Engineering Materials, Tokyo Institute of Technology,
Nagatsuta 4259, Midori-ku, Yokohama 227
2. The Institute for Solid State Physics, The University of Tokyo
Roppongi, Minato-ku, Tokyo, Japan
3. Photon Factory, National Laboratory for High Energy Physics,
Oho-machi, Tsukuba, Ibaraki, 305

Introduction

Studies of electron-density distributions have been intensively carried out on inorganic crystals with the X-ray diffraction method for the last decade. As a result, qualitative knowledges are much accumulated, for example, on distributions of d electrons in various crystal fields, hydrogen bondings, net charges of ions in ionic crystals, etc. However, it is required to increase accuracy of observed structure factors to obtain electron-density distributions worthwhile for quantitative examinations.

One of the most important problems lies in correction for extinction. The present study was undertaken with the intention to obtain diffraction data of ilmenite FeTiO_3 with reduced extinction effects. Electron-density distribution in ilmenite was already studied by making use of the conventional X-ray source by the present authors. We can compare the two results.

Experimental

The crystal used was synthesized with an infrared-heating floating-zone furnace (Takei, et al., 1982). The crystal is rhombohedral with the space group $R\bar{3}$ and the hexagonal cell dimensions of $a=5.08854(7)$ and $c=14.0924(3)$ Å.

The data collection was carried out on a four-circle diffractometer at BL-14A. The following experimental conditions are adopted; collimator: 1mm, scan mode: ω -scan, scan width: 0.5° , scan speed: $2^\circ/\text{min}$, max of 2θ : 43.0° , diameter of specimen: 0.145 mm. For weak reflections measurement was repeated up to 10 times, when $(F)/F$ was less than 0.010. The correction for incident beam fluctuation was performed by monitoring the intensity of incident beam with an ion-chamber. The wavelength was set to $0.349650(5)$ Å using Si(333) double monochromator. The reflections of different orders were cut by CeO_2 filter. Total of 1058 reflections were measured, 631 (489 independent) with $|F_o| > 3\sigma(|F_o|)$ and omitted the reflection of measured in instability condition of incident beam were used.

The refinement was carried out with a modified version of the full-matrix least-squares program LINKT, which includes the extinction corrections after Becker and Coppens (1974, 1975) and the connections for anharmonic thermal vibrations of Tanaka and Marumo (1983). Least-squares calculations assuming the type II extinction effects with a Gaussian mosaic-spread distribution gave smaller R and Rw values than those with the type I extinction corrections. The final refinement was performed on the assumption of partial disorder of the cations. The chemical formula was assumed as $(\text{Fe}_q \text{Ti}_r)(\text{Ti}_u \text{Fe}_v)\text{O}_{q+v+2(r+u)}$, and the population parameters were refined with normalization of the value of the larger one between

$q+r$ and $u+v$ to unity. Finally the R and Rw values reduced to 0.0206 and 0.0204, giving the values 0.97(2) 0.027(3), 0.916(3) and 0.073(2) for q, r, u and v, respectively. The final atomic parameters are compared in Table 1 with those obtained from the diffraction data collected with a conventional X-ray source.

Table 1 Positional and thermal parameters (Å²)

	SR	Mok
Fe X	0	0
Y	0	0
Z	0.35548(2)	0.35542(1)
U_{11}	0.00677(9)	0.00627(3)
U_{22}	0.00614(12)	0.00607(4)
Ti X	0	0
Y	0	0
Z	0.14848(3)	0.14840(1)
U_{11}	0.00488(10)	0.00490(3)
U_{22}	0.00512(13)	0.00512(13)
O X	0.31720(24)	0.31725(9)
Y	0.02326(24)	0.02352(9)
Z	0.24483(7)	0.24495(3)
U_{11}	0.0049(3)	0.0052(1)
U_{22}	0.0052(4)	0.0060(1)
U_{33}	0.0063(3)	0.0069(1)
U_{12}	0.00192(3)	0.00224(9)
U_{13}	0.00070(3)	0.00027(8)
U_{23}	0.00170(3)	0.00157(8)

The form of the anisotropic temperature factor is defined as $\exp[-2\pi^2(h^2a^{*2}U_{11}+k^2b^{*2}U_{22}+l^2c^{*2}U_{33}+(1/2)hka^*b^*U_{12}+...$



Fig. 1 Section of the difference Fourier map. Contours are at intervals of $0.20e \cdot \text{\AA}^{-3}$. Negative and zero contours are in broken and dashed-dotted lines, respectively.

Result

The obtained populations give the chemical formula of $(\text{Fe}_{0.97}\text{Ti}_{0.03})(\text{Ti}_{0.92}\text{Fe}_{0.07} \text{O}_{0.01})\text{O}_3$ for the present crystal. The atomic parameters in the present study were not so different from those obtained from the data collected with a molybdenum X-ray tube.

Since X-rays with short wavelength are used, the isotropic extinction correction factor is 0.959 for the reflection with the largest extinction effect. Because of the small extinction effects, anisotropic parameters for the extinction corrections were unable to be determined. Fig. 1 shows the section of the difference Fourier map parallel to (010) including Fe and Ti atom, and passing near the O atom site. Fairly high peaks are observed around the transition metal atoms. Examinations are in progress, if those peaks are due to the aspherical distributions of d electrons. The final R and Rw factors are larger for the SR data than the previous data, in spite of the smaller extinction effect in the experiment with SR. This is probably due to the following fact: 1) SR is less stable than X-rays from conventional generators, 2) accumulated counts were much smaller in the present measurements than those with Mok α radiation from the sealed tube (in the strongest reflection about 1/8), because of the shorter wave-length in the SR experiment, 3) though monitoring was carried out for the whole incident beam, only a part of the beam fell upon the specimen. This is a possibility that the average intensity fluctuation is different from that in the portion of the beam which fall on the specimen.

A SINGLE CRYSTAL DIFFRACTION STUDY OF THE NATURAL ZEOLITE COWLESITE

Gilberto ARTIOLI¹, Glaucio GOTTARDI¹, Romano RINALDI², Yoshinori SATOW³, Hiroyuki HORIUCHI⁴, Jinhua YE⁴, Haruo SAWADA⁴, Masahiko TANAKA⁴ and Masayasu TOKONAMI⁴.

1. Istituto di Mineralogia e Petrologia, Università di Modena.
2. Dipartimento di Scienze della Terra, Università di Cagliari.
3. Photon Factory, National Laboratory for High Energy Physics.
4. Mineralogical Institute, Faculty of Science, University of Tokyo.

Introduction

X-ray diffraction intensities of quality good enough for structural analysis have been collected on the natural zeolite cowlesite¹. The crystals for this study were from a specimen from North Ireland, where cowlesite is found in small radial aggregates. The small size of the crystals and their structural imperfections prevented data collection with conventional x-ray sources. All crystals show streaky diffractions along two reciprocal lattice directions (a^* and b^*), indicating structural complexities.

Experimental

The crystal used in the experiment was prismatic, with dimensions 0.4 x 0.06 x 0.03 mm. and was mounted with the direction of elongation (crystallographic c^* axis) slightly off the ϕ axis of the diffractometer. The intensity measurement was carried out with the Rigaku diffractometer at the beam line BL-14A of Photon Factory. X-rays out of the wiggler were monochromatized to $\lambda=1.2\text{\AA}$ with a double flat crystal monochromator (Si(111)). A single omega-scan was used for each reflection, with a scan speed of four degrees per minute and a scan width of 1.6° for reflections with $2\theta < 56^\circ$ and 1.8° for reflections with $56^\circ < 2\theta < 65^\circ$. The background intensity was measured for 4.0 sec. before and after peak scan. Correction of anomalously high values of background sampled on streaky reflections was obtained by polynomial fitting of order 6 of the background counts of the unobserved reflections (Fig. 1). 5105 intensities were collected up to $2\theta = 65^\circ$. Observed data were corrected for Lorentz-polarization, absorption and were normalized by primary beam monitor counts to account for the intensity decay of the

x-ray source.

Discussion

The cell parameters obtained by least-squares fit of 41 observed 2θ values are: $a=23.249(5)$, $b=30.629(3)$, $c=24.964(4)$ Å. The cell parameters are consistent with those reported by Nawaz² and are doubled with respect to the originally reported values³. Preliminary data confirm orthorhombic space group symmetry. The lattice type is primitive, although very few reflections with $h+l=2n$ are significantly ($>3\sigma$) observed, indicating that at least part of the structural atoms are consistent with a B lattice. Structural analysis is at present on progress.

1. G. Gottardi and E. Galli, 'Natural Zeolites', Springer, Berlin (1985)306.
2. R. Nawaz, Mineral. Mag., **48** (1984)565.
3. W.S. Wise and R.W. Tschernich, Am. Mineral., **60** (1975)951.

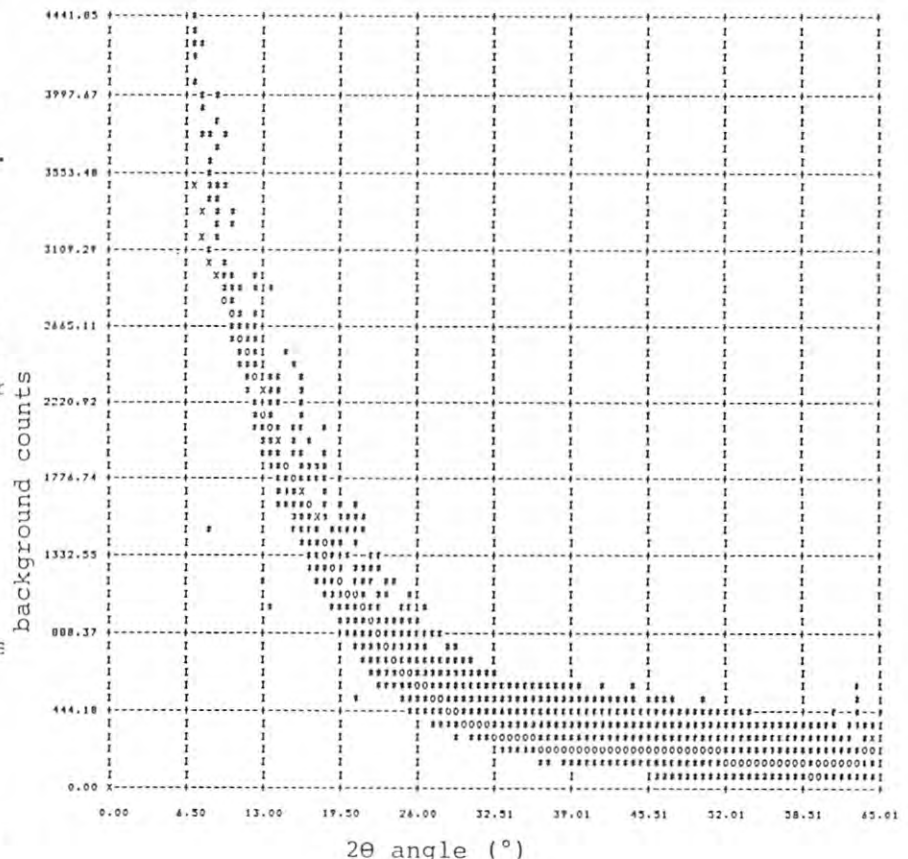


Fig. 1

THE STRUCTURAL STUDY ON THE SMSI CATALYSTS BY MEANS OF THE
POLARIZED TOTAL REFLECTANCE FLUORESCENT EXAFS METHOD(2).

Kiyotaka ASAKURA¹, Yasuhiro IWASAWA¹, Haruo KURODA¹, and Yoshinori SATOW²

¹ Department of Chemistry, Faculty of Science, the University of Tokyo, Hongo, Tokyo 113.

² Photon Factory, National Laboratory for High Energy Physics, Oho-machi, Ibaraki 305.

Metal-deposited inorganic oxide single crystals (TiO_2 , SiO_2 etc.) are considered as a model system for the supported metal catalysts¹⁾. The electronic properties and chemisorption properties of the deposited metal have been studied by many workers but the structure of the deposited metal has not yet been investigated sufficiently. Although EXAFS spectroscopy is one of the most appropriate candidates for the structure analysis, conventional EXAFS spectroscopy is not so surface sensitive. Surface EXAFS with detecting Auger yield can enable one to obtain the surface structure. The other possibility is using the total reflectance with X-ray fluorescence detection. We have shown the possibility of the total reflectance EXAFS with fluorescence detection of the $\text{Os}_3(\text{CO})_{12}$ deposited on TiO_2 single crystal²⁾. In this paper we will report the configuration of $\text{Os}_3(\text{CO})_{12}$ on TiO_2 single crystal by using the polarization dependency of Os L_3 -edge EXAFS.

Experimental

The experimental set up and preparation of the sample were described previously²⁾. The EXAFS spectra were taken at BL-14A using the wiggler radiation.

Results and Discussion

Fig.1 and Fig.2 shows the EXAFS spectra taken with the parallel and perpendicular polarization in respect to the surface normal. The detector was always placed to the direction parallel to the polarization vector. Although the polarization dependency of L_3 -edge is not so sharp compared to that of K-edge, yet no remarkable change was observed in the spectra with two different directions. Possibly this may be due to the thermal motion of the Os_3 cluster on the TiO_2 which averages the orientation of the Os_3 against surface plane. Thus the Os_3 cluster might be fluttering on the TiO_2 surface.

1) H.Onishi, T.Aruga, C.Egawa, and Y.Iwasawa, *surf.sci.*, to be published.

2) K.Asakura, Y.Iwasawa, H.Kuroda, and Y.Satow, *PF activity Report.*, 4, 265(1986).

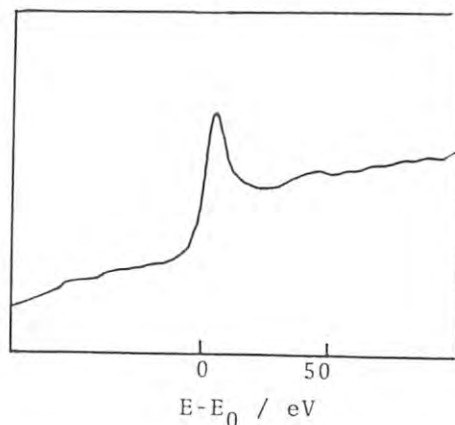


Fig.1 The Os L_3 -edge spectrum with the polarization parallel to the surface normal.

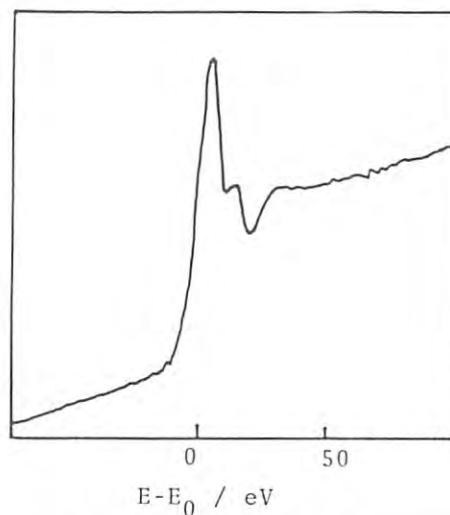


Fig.1 The Os L_3 -edge spectrum with the polarization perpendicular to the surface normal.

MEASUREMENT OF A CERIUM K-EDGE EXAFS SPECTRUM OF CERIUM OXIDE

Yoshinori SATOW, Kiyotaka ASAKURA* and Haruo KURODA*

Photon Factory, National Laboratory for High Energy Physics,
Oho-machi, Tsukuba-gun, Ibaraki 305,
and *Department of Chemistry, Faculty of Science, the University of Tokyo,
Hongo, Bunkyo-ku, Tokyo 113.

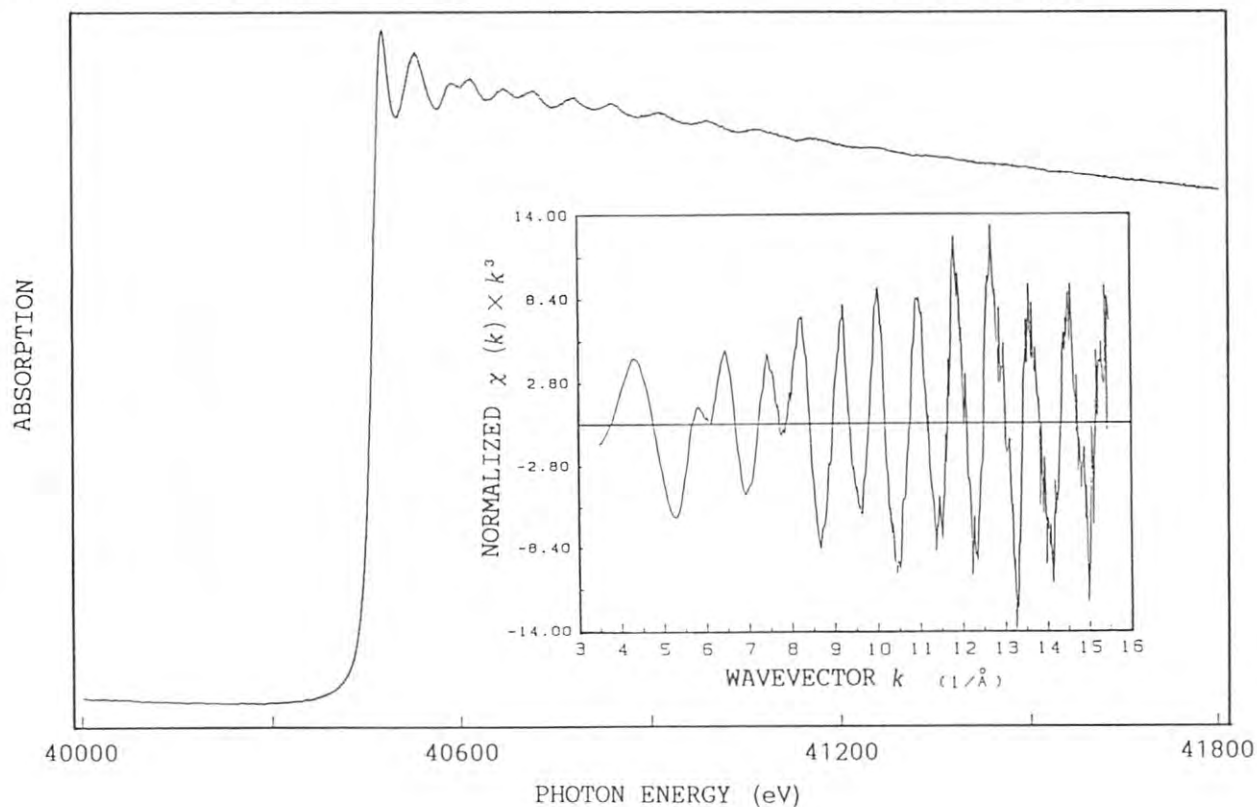
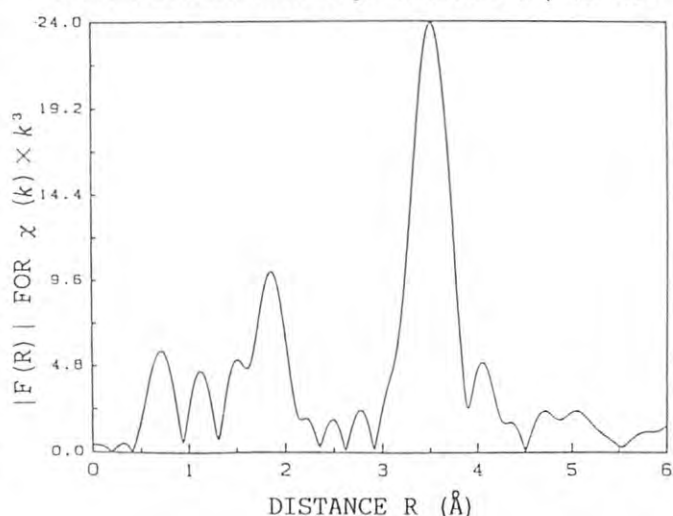
Here we report a measurement of a Ce K-edge (threshold energy at 40.45 keV) EXAFS spectrum of CeO_2 . The measurement was carried out at the beamline 14A. A double-crystal monochromator was used to obtain a good energy resolution. A pair of flat Si (553) crystals in the monochromator produce X-rays whose energy range from 22.7 keV to 84.5 keV. Intensity measurements of X-rays were made by use of paired ion-chambers, 14 cm and 28 cm long (krypton gas was used). The details of the experimental arrangement are to be described elsewhere¹⁾.

A preliminary measurement of a K-edge EXAFS spectrum was previously reported on the powder sample of CeO_2 ²⁾. The measurement, in which attained energy resolution was worse than that of the present experimental arrangement (~ 6 eV), was performed up to only 500 eV above the edge. A spectrum of the CeO_2 sample has been measured with the present arrangement. The spectrum (Fig. 1) shows discernible EXAFS oscillations extending beyond 15 \AA^{-1} in k , or 860 eV above the edge. Particularly, oscillations mainly attributable to contributions from the large back-scattering amplitude of Ce are clearly noticeable at the high- k ($\sim 12 \text{ \AA}^{-1}$) region.

Two peaks at 1.8 \AA and 3.6 \AA in the Fourier transform of the spectrum (Fig. 2) are attributed to Ce-O and Ce-Ce radial distributions, respectively. The analysed distances are well consistent with those from the crystal structure.

¹ Y.Satow, K.Asakura & H.Kuroda; to be published in J. Phys. C: Solid State Phys.

² K.Asakura, Y.Satow & H.Kuroda (1986); Proc. Int. Conf. EXAFS and Near Edge Structure IV, C8-185.



DEVELOPMENT OF A PPAC AND CONSTRUCTION OF AN ALCD

Hiroyuki Takahashi, Shuji Namatame, Koh-ichi Mochiki, Ken-ichi Hasegawa and Yoshinori Satow.*

Department of Nuclear Engineering, University of Tokyo, Bunkyo-ku, Tokyo, 113, Japan

*Photon Factory, KEK, Oho-machi, Tsukuba-gun, Ibaraki, 305, Japan

Introduction

Since 1981, We have been developing fast two-dimensional X-ray detectors. Especially a fast MWPC (Multi Wire Proportional Chamber) has a capability of handling a counting rate of 1 Mcps and good uniformity over the whole sensitive area [1]. However, there still exists a problem on this detector : that is a poor spatial resolution(2 mm FWHM).

We present here two devices to improve this characteristic. They are a parallel plate avalanche chamber (PPAC) and an area-to-line conversion detector (ALCD).

Development of a PPAC

Fig.1 describes a structure of a PPAC which is composed of an anode, a cathode and a grid electrode where a PR gas is filled over the detector. A weak electric field is applied in the space between the cathode and the grid. That forms an electron drift region : the most part of the sensitive volume of this detector. Electrons produced by incident photons drift toward the grid and enter the multiplication region between the grid and the anode where a very high electric field is applied. In this region they are multiplied by 10^3 - 10^4 to give sufficient charges in the position measurement.

The method to determine a position of the electron swarm arriving at the anode surface has many variations. However, we adopted in this study a charge-division method which utilizes a simple construction of a PPAC. This method uses two plane resistive electrodes. One is used as the anode plate. And the other is used as the position readout electrode set closely behind the anode plate. From this readout electrode we can derive a differentiated pulse of the anode signal. Then each electrode functions a one-dimensional position sensor. With this method a rather simple two-dimensional position sensing system can be realised to give a high reliability.

Table 1 shows a summary of our PPAC. The resolution of 1.3 mm FWHM is attained by now. Another approach to a PPAC having a faster readout is planned and examined.

Fig.1 Principle of PPAC

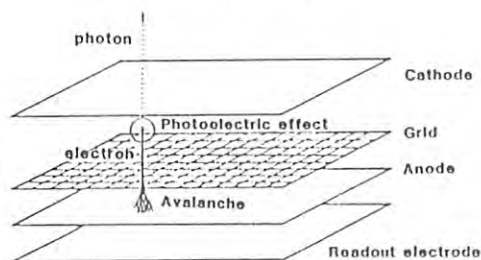


Table 1. Summary of a PPAC

Effective area	: 90 mm x 90 mm
Gas(flow type)	: Ar/CH ₄ 10%, 1 atm.
Drift Region depth	: 15.0 mm
Anode-Grid gap length	: 1.5 mm

Preliminary test of an ALCD

A new two-dimensional position-sensitive detector with a bundle of narrow optical fibers based on the area-to-line conversion technique has been made for a trial and a preliminary test has been carried out[2]. This detector consists of optical fibers with a Gd₂O₂S phosphor sheet, a light sensor and a readout circuit[3]. The light sensor is an amorphous silicon linear image sensor which is usually used as a part of facsimile.

(a) Principle

Incident X-rays are converted into visible light by the phosphor sheet. The light is transmitted through optical fibers to the sensor. Then two-dimensional image is converted into sliced successive one-dimensional patterns (as shown in fig.2). Converted one-dimensional signals are accepted by the linear image sensor and are processed by the readout circuit and a small computer. The advantage of ALCD is that its spatial resolution remains unchanged even with extending sensitive area.

(b) Characteristics

This ALCD has a sensitive area of 5.0 x 2.5 mm² which consists of 200 optical fibers (0.25 mmφ). A spatial resolution of 0.50 x 0.50 mm² was measured. The sensor output I is presented by the following formula:

$$I = I_0 \cdot R \cdot M \cdot A$$

where

I_0 : the sensor output without optical coupling
 $R=0.3$ (measured):light collection efficiency
 $M=0.6$ (measured):fiber-sensor coupling efficiency
 $A=0.98$:attenuation factor in the optical fiber.
 Then I / I_0 ratio of 0.17 was measured. The greater part of the sensor output is determined by the factor R and M . The ideal R and M are larger than the present values. We are now testing a few fabrication methods to improve characteristics required for applications.

(c) Applications

We used this ALCD for X-ray radiography. Fig.3 shows examples of two-dimensional patterns.

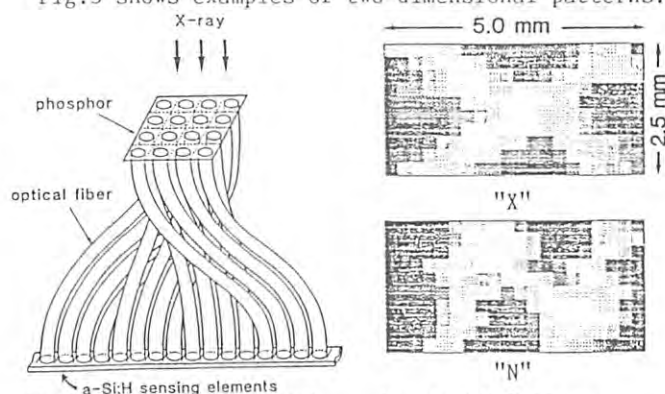


Fig.2 Principle of ALCD

Fig.3 2-D Patterns

References

- [1]K.Hasegawa,K.Mochiki,M.Koike,H.Takahashi and Y.Satow; Photon Factory Activity Report No.4, (1986) 268.
- [2]K.Mochiki,K.Hasegawa,S.Namatame; Submitted to Nucl. Instrum. Meth. Phys. Res.
- [3]K.Hasegawa,K.Mochiki,M.Koike,Y.Satow, H.Hashizume and Y.Iitaka; 319 Nucl. Instr. and Meth. A252 (1986) 158.

DYNAMICAL PHENOMENA IN GRAZING-INCIDENCE X-RAY DIFFRACTION BY PERFECT CRYSTALS

Osami SAKATA, Yoshiharu SAITO, Hiroyuki KUSUHARA, Takumi NAKAHATA, Ichiro MINATO and Hiroo HASHIZUME
Research Laboratory of Engineering Materials, Tokyo Institute of Technology
Nagatsuta, Midori, Yokohama 227

Introduction

We have formulated a dynamical X-ray diffraction theory for perfect crystals under grazing incidence conditions [1]. The concept of 3D dispersion surface and wave fields provides a wave-optical explanation to such physically interesting phenomena as the two separate critical angles of total reflection and the extinction of out-going diffracted waves at special values of the incidence angles. The theory also permits calculation of intensity curves for the specularly reflected and diffracted waves as functions of incidence angles.

Geometry and wave intensities

Figure 1 shows the geometry where an X-ray plane wave is incident on a flat surface of a perfect crystal at glancing angle ϕ_0 and deviation angle $\Delta\theta$ from the exact Laue incidence for a net plane perpendicular to the crystal surface. For small ϕ_0 and $\Delta\theta$, we have specular wave K_s and diffracted wave K_h propagating out of the crystal and two wave fields (k_{0j} , k_{hj} ; $j = 1, 2$) generated in the crystal. An inspection of the 3D dispersion surface taking account of the principle of wave-vector continuity on the boundary surface reveals that the 2D reciprocal space formed by sectioning the 3D space by a plane parallel to the crystal surface is divided into four regions, I to IV, where zero, one, one and two wave fields exist in the crystal respectively [1]. When the projected wave point for the incident wave is located in region I, simple specular reflection occurs with no wave field formed even when $\Delta\theta = 0$. In region II, where $\phi_0^2 < -2\Delta\theta \sin 2\theta_B$, the tangential component of the internal wave vector k_{h2} has a modulus greater than $K (= 1/\lambda)$ so that no vacuum wave can couple with it. Hence the external diffracted wave K_h is evanescent and the standing wave is localized in a shallow layer, several 10 Å thick, above the interface [2].

The intensity formulae are derived from a set of standard boundary conditions. At $\Delta\theta$'s close to zero, the specular intensity curves $I_s(\phi_0; \Delta\theta)$ show double steps at ϕ_{c1} and ϕ_{c2} , critical angles of total reflection for the two wave fields. Also, the diffracted intensity curves $I_h(\phi_0; \Delta\theta)$ have peculiar shapes with a quite high peak flanking a plateau in the low ϕ_0 side [3].

Experimentals

We have designed an experiment to observe the characteristic features of the intensity curves. The (111) surface of a germanium single crystal was mirror polished to such a flatness that the macroscopic corrugation was less than 1 μm over a 1 cm^2 area. This specimen was set horizontal-

ly with the polished surface upward in a double-crystal diffractometer of non-dispersive arrangement for the 220 reflection at the BL14B work station. The first crystal used a 21.88° cut angle and delivered a beam of 10 μrad in horizontal divergence at $\lambda = 1.543 \text{ \AA}$. The beam was further limited by a horizontal slit to illuminate the selected area on the specimen surface. The vertical beam divergence was ca. 70 μrad .

Figure 2 shows the specular and diffracted intensity curves, $I_s(\phi_0; \Delta\theta)$ and $I_h(\phi_0; \Delta\theta)$, measured at a fixed value of $\Delta\theta$. The predicted double steps are clearly seen on $I_s(\phi_0; \Delta\theta)$. However, a comparison of the experimental and theoretical curves show systematic discrepancies: the observed $I_s(\phi_0; \Delta\theta)$ is lower in zero-angle reflectivity and higher in plateau reflectivity than the theoretical curve. Also the observed $I_h(\phi_0; \Delta\theta)$ has a lower peak reflectivity. Similar but different disagreements are also found in $I_s(\Delta\theta; \phi_0)$ and $I_h(\Delta\theta; \phi_0)$ curves. Specimen misorientation, surface micro roughness and damaged surface layer are being examined as possible sources of the disagreements.

References

- [1] O. Sakata & H. Hashizume: Report RLEMTIT 12, 45 (1987).
- [2] P.L. Cowan: Phys. Rev. B 23, 5437 (1985).
- [3] A. Afanas'ev & M.K. Melkonyan: Acta Cryst. A39, 207 (1983).

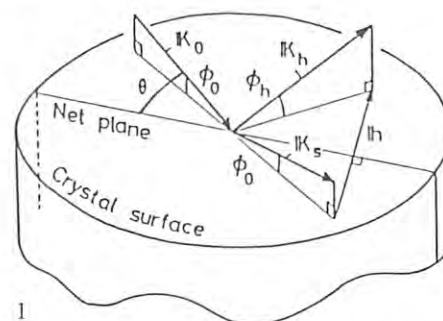


Fig. 1

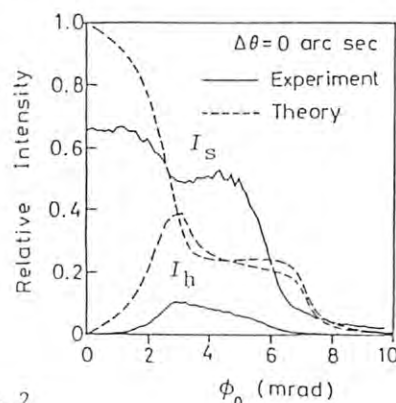


Fig. 2

ANGLE-DISPERSIVE X-RAY DIFFRACTION BY WATER MOLECULES

Hiroshi TAKEUCHI, Atsuhiko SUWA, Teruhisa SAKURAI,
Toshiyuki MITSUHASHI⁺, Tetsuya ISHIKAWA⁺ and Shigehiro KONAKA

Department of Chemistry, Faculty of Science, Hokkaido University,
Kita-ku, Sapporo 060

⁺Photon Factory, National Laboratory for High Energy Physics,
Oho-machi, Tsukuba-gun, Ibaraki 305

Introduction

It is possible to study the charge densities in molecules by X-ray diffraction by gases. In the present study, the energy spectra of H₂O have been measured using an angle-dispersive type diffractometer placed on the BL-14B experimental station. Elastic, inelastic and total intensities of scattered X-rays were obtained from the observed spectra and compared with the theoretical ones.

Experimental

A silicon (111) monochromator was used to obtain the incident X-rays with the wavelengths of 1.543 Å/n (n=1,3,4,5). The ω -2 θ horizontal type diffractometer and the sample cell constructed by Mitsuhashi et al.¹⁾ were used. Scattered intensities were measured by using a pure-Ge SSD with an energy-resolution of 170 eV. Energy spectra were observed at scattering angles between 7.5° and 75.8°. The temperature of the sample cell was kept to be about 146°C. In the latter half of the experiment, a scintillation counter was used to monitor the fluctuations of the scattered intensity at a fixed angle. The signals from the SSD were stored in a multichannel analyzer. For the determination of the polarization factor, the scattered intensities by air were measured by mounting the scintillation counter on a χ - ϕ circle.

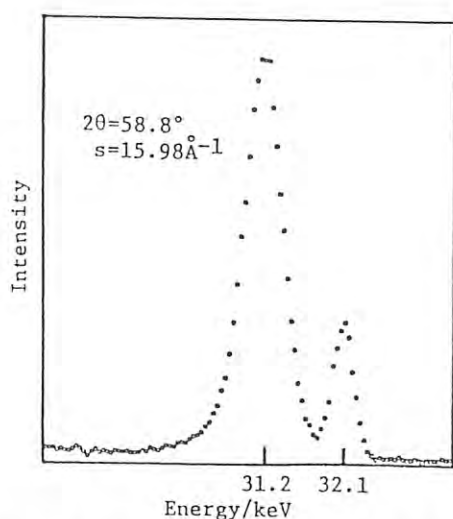


Fig. 1. Energy spectra of the X-rays scattered by H₂O

Results

Figure 1 shows one of the observed energy spectra. Separation of inelastic scattering peaks from elastic ones was clearly seen at s -values ($s=(4\pi/\lambda)\sin\theta$) larger than 10 Å⁻¹. The increase of the separation with increasing s -value was consistent with the classical theory of the Compton shift (see Fig. 2).

Experimental total intensities were determined according to the following procedure: (1) normalization by using the monitor counts; (2) background correction; (3) normalization regarding the effective scattering volume; (4) polarization correction; (5) absorption correction. Resulting data are compared with the theoretical total intensities based on an SCF-MO wavefunction²⁾ in Fig. 3. Systematic differences are found between the experiment and the theory at small s -values.

References

- 1) T. Mitsuhashi et al., Photon Factory Activity Report 1983/1984, p. VI-172.
- 2) M. Kumar, A. N. Tripathi and V. H. Smith, Jr., Int. J. Quantum Chem. **29**, 1339 (1986).

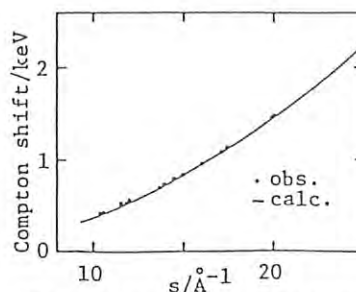


Fig. 2. Observed and calculated Compton shifts of H₂O

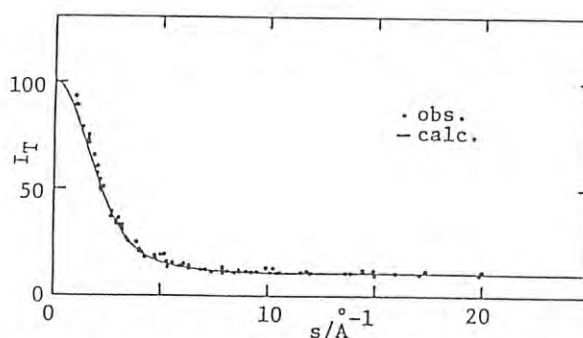


Fig. 3. Total scattered intensities for H₂O

NUCLEAR EXCITATION BY SYNCHROTRON RADIATION

Takeshi MUKOYAMA, Harumi KAJI,[†] Kenji YOSHIHARA,[†] Tetsuo NAKAJIMA* and Hisashi KOBAYAKAWA*

Institute for Chemical Research, Kyoto University, Kitashirakawa-Oiwake-cho, Sakyo-ku, Kyoto 606

[†]Department of Chemistry, Faculty of Science, Tohoku University, Aoba, Aramaki, Sendai 980

*KEK, National Laboratory for High Energy Physics, Oho-machi, Tsukuba-gun, Ibaraki 305

Introduction

Nuclear excitation by photons has been studied for long time using the bremsstrahlung radiations from accelerators or Compton-scattered γ rays from radioisotopes. The production of excited states has been confirmed by observing the induced activity. Owing to narrow widths of activation levels, intense photon beam are necessary and the produced activity is in general weak.

Recently we have attempted to excite the Os nucleus by synchrotron radiation.¹ We have succeeded to detect the L-shell x rays emitted following internal conversion from the isomeric state of ^{185}Os . This is the second report of our project and here we present our preliminary result for rhodium.

Experimental

The metallic foil of natural rhodium with 13-mm diam and 1.18-g/cm² thick was irradiated by the photon beam at the BL-14C line (wiggler line). Considering the narrow nuclear level widths, we did not use a monochromator and the target was irradiated by a white beam. The beam current was about 150 mA at the storage ring.

The natural rhodium consists of 100% ^{103}Rh nuclide. This nuclide has an isomeric state with the energy of 39.75 keV and the life time of 56.1 m. We used this level to detect the nuclear excitation. When the ^{103}Rh nucleus is excited to this level or higher energy states which cascades down to it, we can observe the induced activity due to long life of this isomeric state. Since the deexcitation from ^{103m}Rh takes place mainly through K-shell internal conversion, we measured the K x rays following this process.

The irradiation period of the target was chosen to be 4 h. After irradiation, the target was removed from the beam line and its induced activity was measured with a Ge low-energy photon spectrometer (LEPS) for 4 h. This experimental procedure was repeated 10 times.

Results and discussion

The typical example of the observed K-x-ray spectrum is shown in Fig. 1. The experimental data scatter due to low counting statistics. However, it can be seen in the figure that there are two peaks corresponding to the $K\alpha$ - and $K\beta$ -x-ray energies of Rh.

The study of nuclear excitation of ^{103}Rh by photons was reported by Ikeda and Yoshihara.^{2,3} They irradiated the Rh samples by γ rays from the ^{60}Co irradiation facility and observed conversion electrons from the isomeric state with a gas-flow-type proportional counter. From the decay curve of the induced activity, they confirmed the formation of the isomeric state. However, it was not clear which levels were excited.

In the low-energy region of the level scheme of ^{103}Rh , there are four excited states; 39.75,

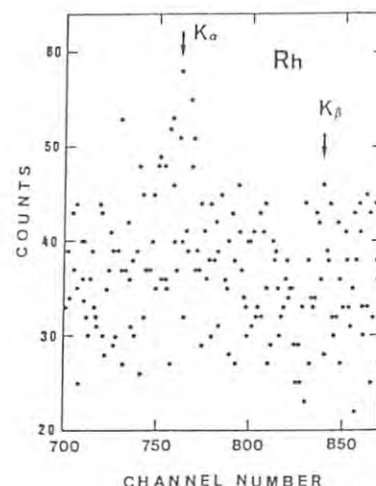


Fig. 1. K x rays from Rh.

93, 295 and 357 keV. Since we used the white beam, all these levels can be considered as a candidate for an activation level. Considering the energy spectrum of the synchrotron radiation, the photon flux with the energy higher than 100 keV would be small. There has been reported no direct transition between the 93-keV level and the ground state. This E4 transition, if it exists, may be weak. On the other hand, the level width of the 39.75 keV is very narrow because of long life time and the fraction of the photon spectrum available to excite this level directly is probably small. These facts indicate that the probability for nuclear excitation by synchrotron radiation is very small, as has been observed above.

In addition to the nuclear transition, there is a possible source for K-x-ray emission from Rh target; photoelectric effect due to the background radiations from the surroundings. This contribution is small, but we must be careful when we subtract the background.

In conclusion, we have observed the nuclear excitation of ^{103}Rh by synchrotron radiation. However, the counting statistics is very poor and the careful data processing of the measured spectra, including the background subtraction, is necessary. The further analysis of the experimental data is in progress.

References

- 1) T. Mukoyama, H. Kaji, K. Yoshihara, T. Nakajima and H. Kobayakawa, Photon Factory Activity Report 1986, 283 (1986).
- 2) N. Ikeda and K. Yoshihara, Radioisotopes, 5, 11 (1956).
- 3) N. Ikeda and K. Yoshihara, Radioisotopes, 8, 24 (1959).

IN SITU OBSERVATION OF THE STRUCTURE CHANGE IN VACANCY-RICH TiO ($x=0.84, 1.0, 1.25$) AT HIGH PRESSURES AND TEMPERATURES

Toru FUJIMURA, Hiroshi IWASAKI[†], Yoshihiko TSUCHIDA^{††}
Osamu TERASAKI^{†††}, Takumi KIKEGAWA[†] and Osamu SHIMOMURA^{††††}

The Research Institute for Iron, Steel and Other Metals
Tohoku University, Sendai 980

[†] Photon Factory, National Laboratory for High Energy Physics
Oho, Ibaraki 305

^{††} Institute for Solid State Physics, University of Tokyo
Minato-ku, Tokyo 106

^{†††} Department of Physics, Faculty of Science
Tohoku University, Sendai 980

^{††††} National Institute for Research in Inorganic Materials
Sakura, Ibaraki 305

Introduction

Titanium monoxide has the rocksalt(B1)-type structure, but contains an abnormally large number of vacancies which are distributed randomly both in titanium and oxygen sublattices at temperatures higher than 800°C. At lower temperatures these vacancies are arranged in an ordered fashion and a monoclinic superstructure is formed¹⁾. We have made an investigation to see how pressure affects the ordering of vacancies employing the multi-anvil-type high-pressure apparatus MAX-80²⁾. Since the order-disorder reaction in the oxide occurs rapidly, it is necessary to do in-situ observation at elevated pressures and temperatures. Use of synchrotron radiation of high brilliance is indispensable to the detection of weak reflections from the sample enclosed in the high pressure cell.

Experimental Procedures

Three kinds of samples with different compositions (TiO with $x=0.84, 1.0, 1.25$) were prepared. They were in the form of powder and quenched from above the order-disorder transition temperature. The sample was placed in the center of a cube made of a mixture of boron and epoxy resin and compressed by six tungsten carbide anvils having a squared face. Synchrotron radiation from the vertical wiggler (BL-14C) was introduced through one edge into the cube and diffracted beams from the sample as well as from the pressure marker (NaCl) were taken out through the opposite edge. Recording of the diffraction pattern was made in an energy dispersive mode using a pure Ge solid state detector.

Experimental Results

First, pressure was increased at ambient temperature up to 7.7 GPa using the sample with $x=1.0$, but no change, except the shift of the reflection positions due to volume contraction, was observed. When temperature was raised while pressure was kept constant, new diffraction lines (indicated by the arrows) appeared in addition to the lines from the B1-type structure, as shown in Fig. 1. These new lines can not, however, be explained by any possible superstructure models based on the B1-type structure. Instead they are indexed in terms of

a hexagonal lattice identical to that proposed for the structure of the delta-phase of the composition Ti_2O_3 ³⁾. Prolonged holding of the sample did not increase the volume ratio of the delta phase to that of the B1-phase. Effect of high pressure is thus to suppress the ordering of vacancies and to make precipitate the phase rich in Ti content, an effect not hitherto found for metal oxides. Similar results were obtained for the sample with $x=0.84$, but not for the sample with $x=1.25$.

Besides the formation of the delta-phase, unusual change in the lattice parameter of the remaining B1-phase was observed at high pressures. In an isothermal compression and decompression run at 700°C, a clear hysteresis exists with the lattice parameter after compression increased appreciably as compared with that before compression. This is due to the annihilation of vacancies during compression at elevated temperatures.

References

- 1) D.Watanabe et al.: Act Cryst. **23** (1967) 307.
- 2) O. Shimomura et al.: Solid State Physics under Pressure, ed. S. Minomura (KTK Sci. Pub., 1985) p.351.
- 3) S. Andersson: Ark. Kemi **15** (1959) 247.

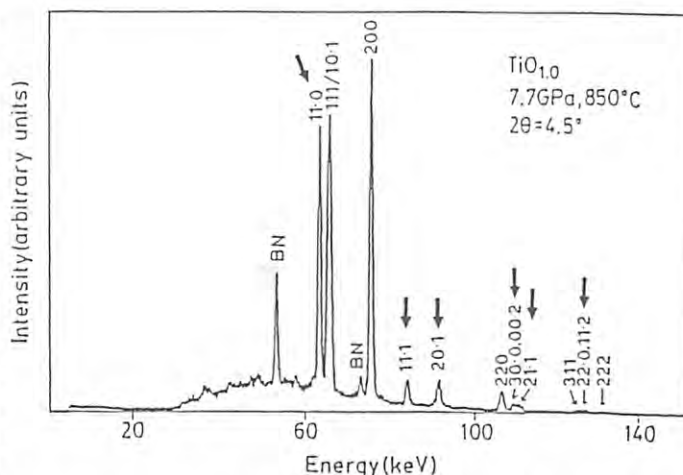


Fig. 1 Diffraction pattern of $TiO_{1.0}$ held at 7.7 GPa and 850°C.

HIGH RESOLUTION MOMENTUM DENSITY MEASUREMENT FOR SILICON USING 29.5 keV SYNCHROTRON RADIATION

Fumitake ITOH, Masaki SAKURAI, Nobuaki SUZUKI, Kenji SUZUKI
Nobuhiro SHIOTANI*, Nobuhiko SAKAI*, Hirokazu FUJIMAKI*
Hiroshi KAWATA**, Yoshiyuki AMEMIYA** and Masami ANDO**

Institute for Materials Research, Tohoku University, Sendai 980

*Institute of Physical and Chemical Research, Wako, Saitama 351-01

**KEK, National Laboratory for High Energy Physics, Oho-machi, Tsukuba-gun, Ibaraki 305

Introduction

In our previous works¹⁻²⁾, it has been shown that the momentum resolution of 0.13 atomic unit(a.u.) could be achieved in our Compton spectrometer for the incident X-ray energy of 29.5 keV from the synchrotron radiation.

In this paper, we report further developments in the spectrometer and some experimental results on electron momentum distribution in Si single crystals.

Experimental

Our previous monochromator of Si(111) was now replaced by Ge(220) to improve the energy resolution and to increase the intensity. The spatial resolution and detecting efficiency of the position sensitive proportional counter was improved by employing the operating condition of a pressure of 10kg/cm² of a mixture gas of Xe+10%CH₄ and an applied voltage of 4.8 kV. The overall momentum resolution of 0.1 a.u. has been achieved for incident energy of 29.5 keV.

Results and Discussion

Compton profiles for Si single crystals along [100],[110] and [111] directions were measured. The specimens were cut from a single crystal rod and shaped into a slice of 20 mm x 20

mm x 1.5 mm and finally finished by a chemical etching process to remove the surface distortion. About 2×10^4 counts were accumulated at the Compton peak of each profile during 2.5 days. The Compton profiles for Si are shown in Fig.1. Various corrections are made; background subtraction, analyzer and detector efficiency corrections and non-relativistic Compton scattering cross section correction. It is found that each profile reflects the fine structure of the Jones zone. Figure 2 shows one of the Compton profile anisotropies $J_{100}(p_z) - J_{110}(p_z)$. The present result is in qualitative agreement with a theoretical prediction based on the pseudopotential method³⁾. However, some quantitative disagreement between the experiment and the theory is found to exist.

References

- 1) F. Itoh, M. Sakurai, Y. J. Chen, K. Suzuki, N. Shiotani, N. Sakai, Y. Amemiya, H. Kawata and M. Ando, Photon Factory Activity Report No.3, 1985/86, p.259.
- 2) F. Itoh, M. Sakurai, N. Suzuki, K. Suzuki, N. Shiotani, N. Sakai, H. Fujimaki, H. Kawata, Y. Amemiya and M. Ando, Photon Factory Activity Report No.4, 1986, p.277.
- 3) H. Nara, T. Kobayashi and K. Shindo; J. Phys. C 17 (1984) 3967.

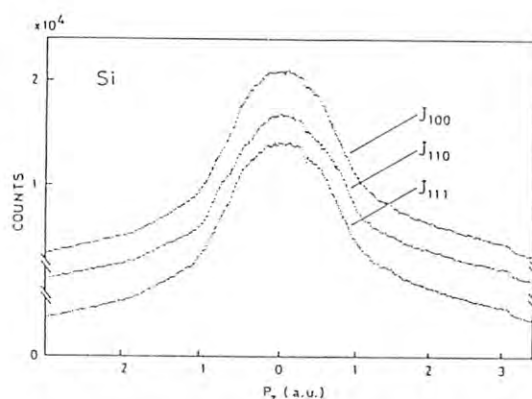


Fig.1. Compton profiles $J(p_z)$ for Si along [100],[110] and [111] directions.

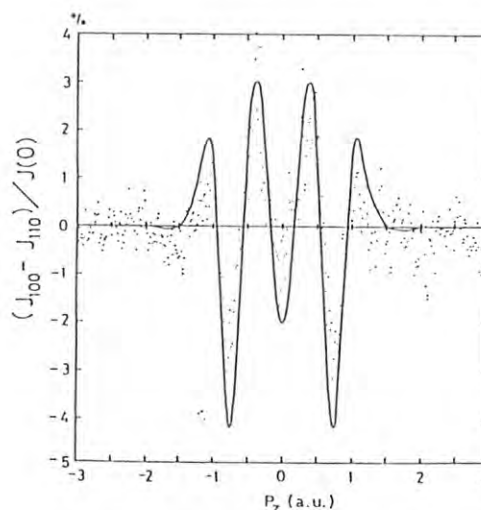


Fig.2. Compton profile anisotropy $J_{100} - J_{110}$ for Si. The solid line indicates the theoretical anisotropy based on the pseudopotential method³⁾.

TIME-RESOLVED X-RAY STUDIES OF THE AGGREGATION OF BLEACHED RHODOPSIN

Toshiaki HAMANAKA*, Yuji KITO**, Kenji HIRAKI**, Katsuzo WAKABAYASHI*

Yoshiyuki AMEMIYA*** and Toshio MITSUI*

* Department of Biophysical Engineering, Faculty of Engineering Science, Osaka University, Toyonaka, Osaka 560

** Department of Biology, Faculty of Science, Osaka University, Toyonaka, Osaka 560

*** National Laboratory for High Energy Physics, Oho-machi, Tsukuba-gun, Ibaraki 305

Introduction

The initial step of the visual process is the absorption of light by the visual pigment. The vertebrate rod visual pigment, a rhodopsin, exhibits the complex sequence of spectral intermediates on illumination. The metarhodopsin I \rightarrow metarhodopsin II step is considered to be responsible for the initiation of the transduction mechanism. In previous reports, we have described the time course of aggregation of detergent-solubilized bovine rhodopsin after light illumination, which was investigated by small-angle x-ray scattering at various temperatures and bleaching ratios^{1), 2)}. There, the zero-angle x-ray scattering intensity at time t , $I_A(0,t)$, was obtained by fitting intensity data to a single Gaussian function. In the present study, we have analysed intensity data by using the sum of two Gaussian functions, one of which corresponds to the scattering from monomeric rhodopsin molecule and the other to oligomer.

Analysis

The x-ray scattering intensity was approximated at small angle by a following equation,

$$I(h,t) = I_A(0,t) \exp(-R_A^2 h^2/3) + I_B(0,t) \exp(-R_B^2 h^2/3)$$

Here, $I_A(0,t)$ and $I_B(0,t)$ stand for the zero-angle scattering intensity at time t from monomer and oligomer, respectively and h is $4\pi \sin\theta/\lambda$, the length of scattering vector, where 2θ is scattering angle and λ the wavelength. The 35 Å was assigned to R_A , the radius of gyration of monomer and 57-58 Å to R_B , the radius of gyration of oligomer. The fitting of intensity data to $I(h,t)$ was done by a Simplex method over the range of $0.014 < h < 0.033 \text{ Å}^{-1}$.

Results

Figure 1 shows time courses of $I_A(0,t)$, the zero-angle x-ray scattering intensity from monomeric rhodopsin molecule solubilized with lauryl ester of sucrose (LM), after light illumination. The decrease in scattering intensity of monomer observed in the dark is due to the radiation damage of rhodopsin by x-ray. The ratio of the zero-angle intensity at the final stage of aggregation to the initial one is presented as a function of bleaching ratio in Fig.2. The amount of monomer remained agrees with unbleached rhodopsin if the correction to radiation damage is considered. This suggests that the aggregation occurs only between bleached rhodopsins but not between bleached and unbleached rhodopsins.

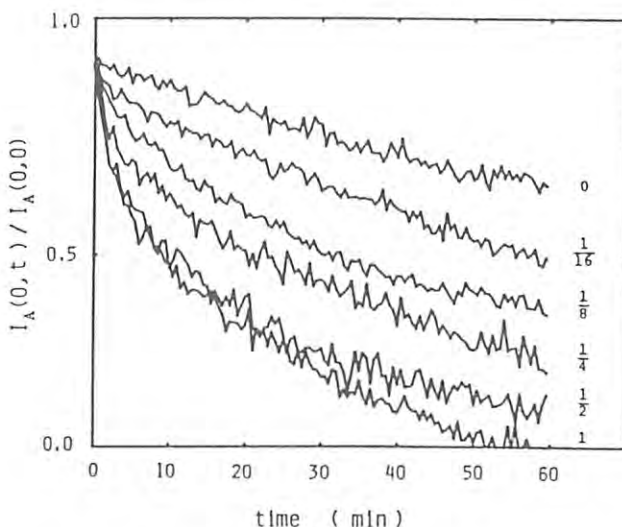


Figure 1. Time course of the change in zero-angle x-ray scattering intensities from monomer of the LM-solubilized bovine rhodopsin after light illumination at 35 °C. The relative powers of a flash light are given in the figure. X-ray intensities were accumulated over time frames of 30 s. $I_A(0,t)$ stands for the zero-angle x-ray scattering intensity at time t , which was obtained as described in Analysis.

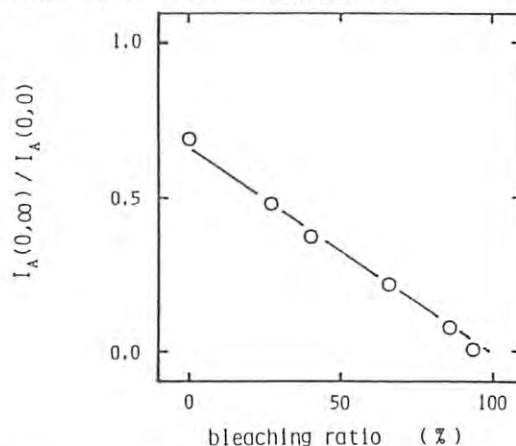


Figure 2. The dependence of $I_A(0,\infty)/I_A(0,0)$, which corresponds to the relative amount of monomeric rhodopsin at final stage of aggregation, on the bleaching ratio. The bleaching ratio was estimated by absorbance at 500 nm of samples after light illumination.

References

- 1) T. Hamanaka et al., Photon Factory Activity Report (1984/85) VI-167.
- 2) T. Hamanaka et al., Photon Factory Activity Report (1986) 293.

X-RAY DIFFRACTION STUDIES OF GLUTARALDEHYDE AND TRITON X-100 TREATED PURPLE MEMBRANE DURING ITS PHOTOCYCLE

Tomoya URUGA, Toshiaki HAMANAKA, Katsuzo WAKABAYASHI,
Yoshiyuki AMEMIYA* and Toshio MITSUI

Department of Biophysical Engineering, Faculty of Engineering
Science, Osaka University, Toyonaka, Osaka 560

* Photon Factory, National Laboratory for High Energy Physics,
Oho-machi, Tsukuba-gun, Ibaraki 305

Introduction

The purple membrane (PM) from *Halobacterium halobium* consists of a two-dimensional crystal of a sole protein, bacteriorhodopsin (bR), and lipid. Upon absorbing light, bR undergoes a photochemical reaction cycle through several intermediates (K,L,M,O). During the photocycle, bR transports protons across the membrane.

Under continuous light irradiation, bR exists as a mixture of the light-adapted form and the photo-intermediates. In native PM under the room temperature, the ratio of the intermediates to light-adapted form is quite low, since the lifetime of the intermediates is very short. Then, we have tried to lengthen the lifetime of the M intermediate by modifying PM as described below and examined the effects of light upon the structure of the modified PM by X-ray diffraction procedure.

Materials and Methods

PM was isolated from *Halobacterium halobium*. Glutaraldehyde and Triton X-100 treated PM (G-T-PM) suspension was prepared following Lam *et al.* (1) and concentrated to OD=27 at 559nm. Sample irradiation was performed by a 500W tungsten lamp and filtered through a 500nm high-path yellow glass filter (Toshiba Y-50) and a blue glass filter (Toshiba IRA-05) with a 1cm path of 10% CuSO₄ solution to absorb infrared light. In all experiments, sample was kept at 5°C by water cooling device. X-ray diffraction studies were performed at small-angle X-ray diffractometer, BL15A. The wavelength of incident beam was 1.48Å. The diffraction patterns were recorded by using PSPC. Sample to detector distance was 38cm.

Results

Diffraction patterns from G-T-PM suspension were collected for 5min. under intense light irradiation and unirradiation. To avoid damage due to X-ray irradiation, the sample was changed after the collection of a data set. 8 data sets were obtained and added up, respectively. The background scattering from the buffer solution was subtracted. Each diffraction pattern was folded back at reciprocal space origin and smoothed. The result is shown in Fig.1. Under light irradiation, the lattice constant enlarged from 59.0Å to 59.7Å and the crystalline order of bR became worse and rather large intensity changes were observed for each Bragg reflection.

Spectroscopic experiments show that, under the present experimental conditions, most of bR are converted to M state. Since such changes

in diffraction were not observed in native PM, these differences between the diffraction patterns reflect the conformational changes of bR in M state from light-adapted form but not any heat effects.

As deoxycholate treated PM²⁾, it seems that some of lipid molecules are extracted and the neighboring bR trimers are directly contacted in G-T-PM. This may cause the conformational changes during the photocycle to influence the unit cell dimension and lattice order.

Further analyses are performed to obtain the structural information of M intermediate in more detail from the diffraction data set of G-T-PM.

References

- 1) E. Lam and L. Packer, Archives of Biochem. Biophys., **221**, 557 (1983)
- 2) R. M. Glaeser, J. S. Jubb and R. Henderson, Biophys. J., **48**, 775 (1985)

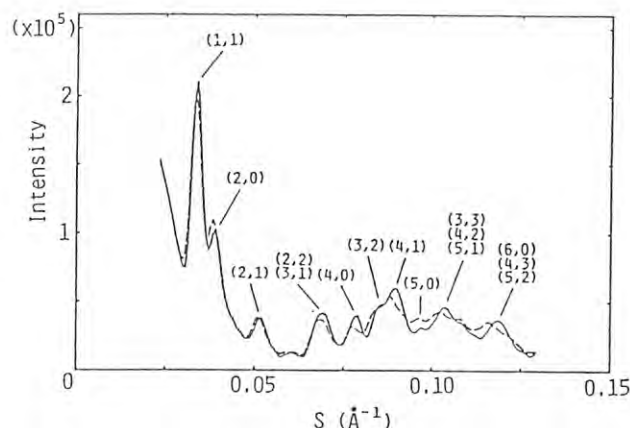


Fig.1 X-ray diffraction patterns from G-T-PM. The solid curve is for unirradiated sample and the dashed curve is for irradiated sample. Temperature, 5°C; pH, 7. The total counting time was 40min. for each curve.

DEVELOPMENT OF SPECIMEN CHAMBER FOR LIGHT IRRADIATION AT LOW TEMPERATURE
AND ITS APPLICATION TO BACTERIORHODOPSIN PHOTOCYCLE IIIFumio TOKUNAGA¹, Mikio KATAOKA¹, Masayoshi NAKASAKO¹ and Yoshiyuki AMEMIYA²

1. Department of Physics, Faculty of Science, Tohoku University, Sendai, Miyagi 980

2. Photon Factory, National Laboratory for High Energy Physics, Oho-machi, Tsukuba-gun, Ibaraki 305

INTRODUCTION

The investigation on dynamical structure of protein reactions is very important to understand the relation between structure and function. However, the protein reactions in solution is too rapid and non-synchronous to detect the dynamical structure. In order to overcome these difficulties, we developed the low temperature X-ray scattering chamber and applied to the structural study of M-intermediate appearing in bacteriorhodopsin (bR) photocycle.¹ bR is a sole protein in purple membrane of *Halobacteria*. It transports hydrogen ion during the photocycle and M-intermediate is considered to be the most important for the function.

By improving the chamber and sample conditions, we could obtain more informative diffraction patterns from M-intermediate.

EXPERIMENTAL

X-ray diffraction experiments were performed at BL-15A with use of the low temperature specimen chamber. Dry ice-acetone system (-77°C) was used as a coolant. Exposure time was 900sec for each record of diffraction patterns.

Purple membranes were suspended in high salt high pH solution (2M Arg-HCl or NaCl, pH 11). In this condition, M-intermediate was generated within 15min with intense yellow light (>530nm) at -77°C. Trans-bR was regenerated with purple light (420nm).

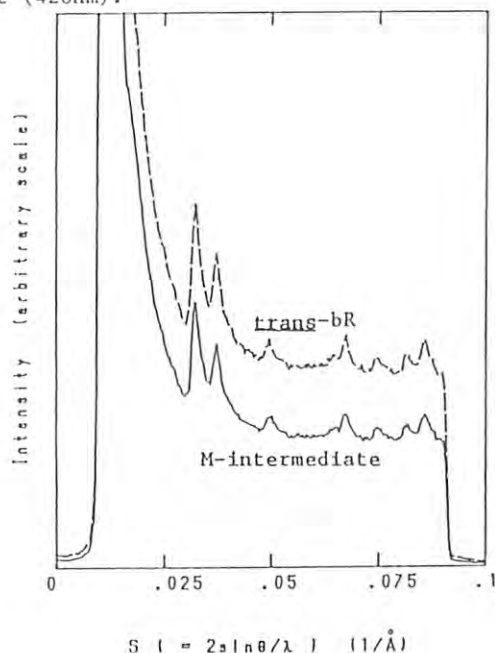


Fig. 1 Diffraction patterns from M-intermediate and trans-bR at -77°C

RESULTS

Lowering the temperature, the diffraction pattern from purple membrane is slightly changed. The lattice constant of purple membrane decreases about 1Å and the integrated intensities of Bragg peaks also decrease to ca.70%. These results are sufficiently reproducible.¹ Zaccai reported the low temperature neutron diffraction on purple membrane,² however it is inconsistent with our results. Now these results are under analysis.

Fig.1 shows the diffraction patterns from M-intermediate and trans-bR at -77°C. No difference is seen between two diffraction patterns; the intensities of Bragg peaks are not changed up to (41) reflection. The region from (31) to (41) reflection was newly recorded by improvement of the chamber. This region contains information about α -helices packing in bR trimer. These results indicate that there are no significant structure changes during the photocycle from trans-bR to M-intermediate at -77°C.

However, because the spectroscopic observation on M-intermediate gives information only about the small region around the chromophore retinal, there remains the possibility that global structure change does not occur at -77°C by reason of quenching of thermal vibrations in bR. To examine this possibility, we are now developing new specimen chamber (Fig.2). In this chamber, sample temperature is freely controlled with low temperature nitrogen gas. So we will be able to study the structure of M-intermediate in various temperature at the range of -40°C - -77°C where M-intermediate is sufficiently stable.

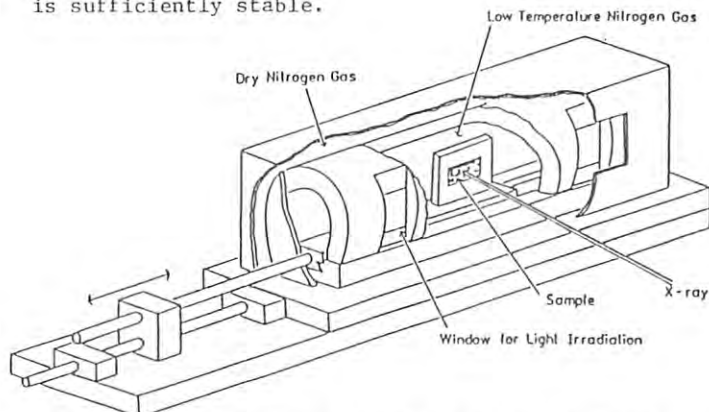


Fig. 2 Outline of under developing new specimen chamber for low temperature X-ray diffraction experiment.

REFERENCES

1. F. Tokunaga et.al. PF Activity Report #4, 295 (1986)
2. G.Zaccai J. Mol. Biol. 194, 569 (1987)

X-RAY DIFFRACTION OF BACTERIORHODOPSIN WITH NITRATED TYROSINE RESIDUES III.

Fumio TOKUNAGA¹, Mikio KATAOKA¹, Masayoshi NAKASAKO¹, Hiroyuki HIGASHIYAMA¹,
Yoshiyuki AMEMIYA² and Toshiaki HAMANAKA³

1. Faculty of Science, Tohoku University, Sendai, Miyagi 980
2. Photon Factory, National Laboratory for High Energy Physics, Oho-machi, Ibaraki 305
3. Faculty of Engineering Science, Osaka University, Toyonaka, Osaka 560

INTRODUCTION

Bacteriorhodopsin (bR) in purple membrane (PM) of *Halobacteria* translocates protons across the membrane by the use of light energy. Tetra-nitromethane (TNM) treatment was effectively applied to investigation of the proton pumping mechanism of bR^{1,2}, because the reaction of TNM with PM requires light illumination and TNM reacts with tyrosinate to bring nitration. TNM treatment of bR brings blue-shift of absorption maximum, as is similar to iodination. Our previous reports³⁻⁵ on iodination indicate that the blue-shift is closely related to the disorder induced in the PM structure. We also demonstrated that the disorder induced by nitration is not so large as iodination³. There are two conflicting reports on the structure of TNM treated PM. Scherrer et al.² stated that the crystalline structure is maintained after TNM treatment, while Lemke et al.¹ reported that the crystalline structure is completely lost. Therefore we investigated more precisely on the absorption spectral change and diffraction pattern of TNM treated PM.

EXPERIMENTAL

Preparation of PM and TNM treatment was performed according to the method reported previously⁶. X-ray diffraction was performed at BL-15A.

RESULTS AND DISCUSSION

We found that the reaction of TNM with PM can be separated into two steps⁶ (Fig. 1). The first step which is proceeded under red light (>600nm) illumination is characterized by the blue-shift of the spectrum and the decrease of maximum absorbance. The second step which is required further illumination by yellow light (>500nm) is characterized by the decrease of the absorbance. The second step did not show any spectral shift.

The product of red light

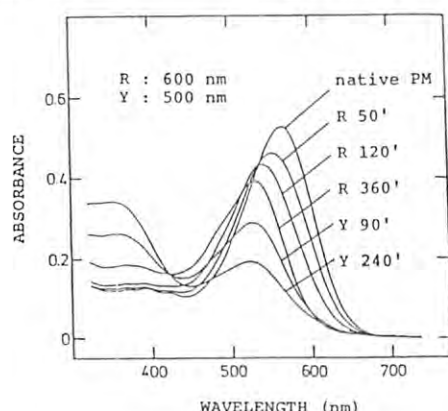


Fig. 1. Absorption spectral change by TNM under illumination. R indicates red light illumination. Y indicates yellow light illumination after red light illumination for 360 min. The number expresses the illumination time in minutes.

illumination shows the same X-ray diffraction profiles as that of the native PM (R50'-R360', Fig. 2). Further yellow light illumination induced the distortion in the crystalline structure (Y90'). Finally the crystalline structure was disappeared (Y240'). We can consider that the observation by Scherrer et al.² is corresponding to the first step, and that by Lemke et al.³ is corresponding to the final stage of the second step.

The present result indicates that the blue-shift by TNM treatment is not concomitant with the loss or the distortion of crystalline structure. The cause of the blue-shift by TNM is far different from that by iodination. From analogy with the study on PM with analogue retinal, the blue-shift without lattice distortion is attributed to the modification of retinal. In fact, the analysis of chromophoric retinal extracted from the TNM treated PM revealed that retinal is modified by TNM under red light illumination⁶.

Present results demonstrate that the conclusion concerning to the nitration of PM should be re-examined carefully.

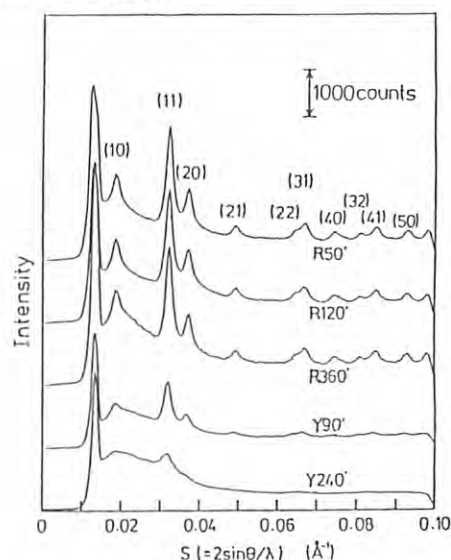


Fig. 2. X-ray diffraction pattern of the TNM treated PM. The samples were the same as in Fig. 1.

REFERENCE

1. H. D. Lemke and D. Oesterhelt (1981) *Eur. J. Biochem.*, 115, 595
2. P. Scherrer, and W. Stoeckenius (1984) *Biochemistry*, 23, 6195
3. F. Tokunaga et al. (1985) *PF Activity Report*, 3, 161
4. F. Tokunaga et al. (1986) *PF Activity Report*, 4, 296
5. M. Kataoka et al. (1986) *Photobiochem. Photobiophys.*, 13, 187
6. H. Higashiyama and F. Tokunaga (1987) *FEBS Lett.*, 218, 287

CHANGES IN THE EQUATORIAL INTENSITIES ON ACTIVATION OF OVERSTRETCHED FROG SKELETAL MUSCLE

Naoto Yagi, Ichiro Matsubara and Yoshiyuki Amemiya*

Department of Pharmacology, Tohoku University School of Medicine,
2-1 Seiryomachi, Sendai 980

*Photon Factory, National Laboratory for High Energy Physics,
Oho-machi, Tsukuba-gun, Ibaraki 305

INTRODUCTION

Muscle contraction is regulated by the sarcoplasmic Ca concentration. The structural changes associated with this regulation mechanism have been studied by X-ray diffraction technique. Recently, intensity changes of some layer-lines in the X-ray diffraction pattern from skeletal muscles were identified as being due to conformational changes of the thin filaments¹⁻²⁾. In the present study, intensity changes on the equator were studied.

EXPERIMENTAL

Semitendinosus muscles from bullfrogs (*Rana Catesbeiana*) were stretched so that there was no overlap between thick and thin filaments (sarcomere length $> 4.0\mu$), and stimulated either by a 1-sec train of electrical pulses (20Hz) or by a single stimulus at 6°C. The intensity distribution along the equator was measured by a position sensitive detector at BL15A with a time resolution of up to 4msec.

RESULTS

The equatorial intensity changed only slightly during stimulation. However, the difference between equatorial intensity distributions from resting and contracting muscles showed decrease in the region $0.05-0.08\text{nm}^{-1}$ (Figure 1). The time course of the intensity change in this region was measured after a single stimulus (Figure 2). It reached a minimum at 30msec after a stimulus and recovered at 150msec. This time course is faster than that found with myosin-related reflections³⁻⁴⁾ but is very similar to that of the second layer-line from the thin filament¹⁻²⁾.

DISCUSSION

Since other components of muscle, including thick filaments, also contribute to the equatorial intensity, it is difficult to measure contribution from thin filaments alone. However, in highly stretched muscles structural changes of the thick filament do not occur during activation⁵⁾. Also, the time course of the intensity change suggests that it is due to structural change in the thin filament.

The radius of gyration of the thin filament is equivalent to that of a solid cylinder with a diameter of about 7nm ⁶⁾. Since the fourier transform of this cylinder ($J_1(x)/x$) has a first zero at 0.17nm^{-1} , decrease in intensity at $0.05-0.08\text{nm}^{-1}$ indicates that the diameter of the thin filament apparently increased. Detailed analysis of the result, using more realistic models of the thin filament, is in progress.

REFERENCES

- 1) M.Kress, H.E.Huxley, A.R.Faruqi & J.Hendrix, *J.Mol.Biol.* **188** 325-342 (1986).
- 2) N.Yagi, I.Matsubara & Y.Amemiya, Photon Factory Activity Report 1986 pp297.
- 3) N.Yagi, E.J.O'Brien & I.Matsubara, *Biophys.J.* **33** 121-138 (1981).
- 4) K.Wakabayashi, H.Tanaka, Y.Amemiya, A.Fujishima, T.Kobayashi, T.Hamanaka, H.Sugi & T.Mitsui, *Biophys.J.* **47** 847-850 (1985).
- 5) N.Yagi & I.Matsubara, *Science* **207** 307-308 (1980).
- 6) P.Matsudaira, J.Bordas & M.H.J.Koch, *Proc. Natl. Acad. Sci. USA* **84** 3151-3155 (1987).

Figure 1

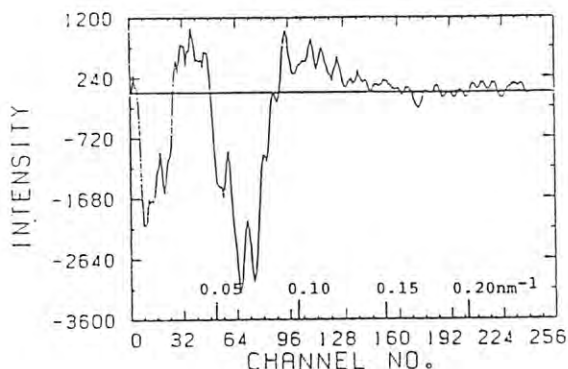
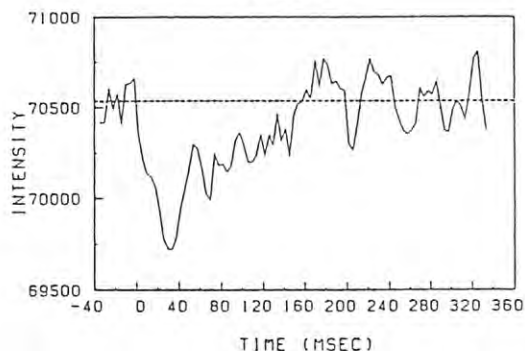


Figure 2



An X-ray diffraction study of chemically skinned cardiac muscle

Y. Saeki*, I. Matsubara, N. Yagi and Y. Amemiya†

Department of Pharmacology, Tohoku University School of Medicine,
Seiryō-machi, Sendai 980.*Department of Physiology, Tsurumi University School of Dental Medicine,
2-1-3 Tsurumi, Tsurumi-ku, Yokohama 230.†KEK, National Laboratory for High Energy Physics,
Oho-machi, Tsukuba-gun, Ibaraki 305.

The contractile mechanism of cardiac muscle is believed to be essentially the same as that of skeletal muscle. Namely, myosin heads attach to actin forming the cross-bridges which, in turn, produce the sliding force between the thick and the thin filaments. However, the details of such a cross-bridge mechanism differ between the two types of muscle. For instance, in cardiac muscle during relaxation, many myosin heads appear to be attached to actin without producing tension. On the other hand, in relaxed skeletal muscle most myosin heads are detached from actin. To clarify the origin of such a difference we have been studying the effect of intracellular calcium concentration on the behaviour of myosin heads. In this report, we first describe the previous X-ray diffraction experiment which we carried out with a rotating-anode X-ray generator, and secondly the progress of a similar experiment performed with synchrotron radiation.

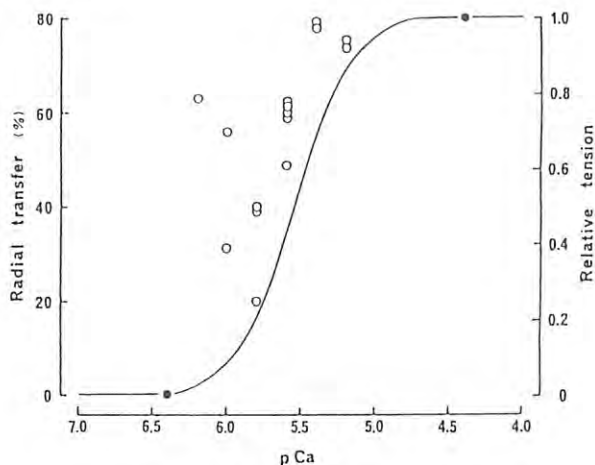


(Fig. 1)

A papillary muscle, isolated from the right ventricle of the rat, was treated for 1 hr with saponin (250 μ g/ml) to make the sarcolemma permeable to the solutes of the bathing solution. The muscle, thus skinned, was soaked in solutions of various calcium concentrations to obtain various grades of contraction

at room temperature (18–21 °C) at a sarcomere length of 2.1–2.2 μ m. The threshold concentration for tension production was pCa 6.2, and the maximum tension was reached at pCa 5.0 (see the curve in Fig. 1). Each isometric contraction was continued for 5–10 min during which the X-ray diffraction pattern was recorded using a low-angle camera combined with a rotating-anode X-ray generator. From the intensities of the 1,0 and the 1,1 equatorial reflections, the fraction of myosin heads transferred to the vicinity of the thin filaments was calculated. During the maximum contraction at pCa 5.0 to 4.4, about 80 % of myosin heads were found in the vicinity of the thin filaments (see the circles in Fig. 1). An unexpectedly large fraction of myosin heads was transferred to the thin filaments at lower calcium concentrations; at pCa 6.2 to 5.8, where the average tension was less than 20 % of the maximum, the average fraction of myosin heads transferred was 40 %, almost half of that during the maximum contraction. On the other hand, in skeletal muscle no large transfer was observed at low calcium concentrations when tension was small. These results suggest the possibility that, in cardiac muscle at low intracellular calcium concentrations, many myosin heads may be attached to actin without producing tension.

In the experiments with synchrotron radiation, the equatorial reflections can be recorded within 30 sec. This makes it possible to keep the muscle in a good physiological condition during each X-ray exposure. Fig. 2 shows a typical set of relaxed (left) and active (right) patterns from a muscle. The data obtained so far do not contradict the previous results.

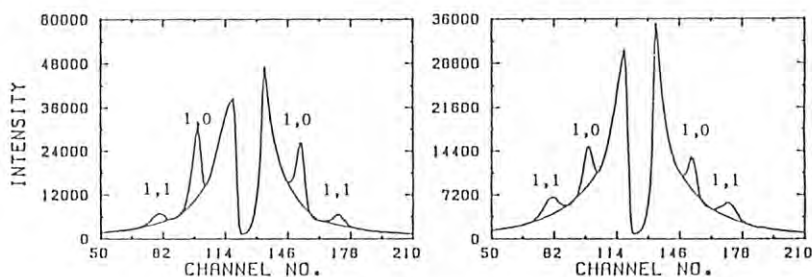


(Fig. 2)

X-RAY DIFFRACTION OF SKELETAL MUSCLE UNDER THE INHIBITORY ACTION OF 2,3-BUTANEDIONE-2-MONOXIME

Keisuke HORIUTI, Naoto YAGI[†], Yoshiyuki AMEMIYA^{*},
Shigeru TAKEMORI, Masaru WATANABE, Yoshiki UMazUME
and Ichiro MATSUBARA[†]

Department of Physiology, Jikei University School of Medicine,
Nishi-shimbashi, Minato-ku, Tokyo 105

[†]Department of Pharmacology, Tohoku University School of
Medicine, Seiryō-machi, Sendai 980

^{*}Photon Factory, National Laboratory for High Energy Physics,
Oho-machi, Tsukuba-gun 305

Introduction

X-ray diffraction analysis of muscle structure is unique in molecular biology of muscle contraction for it enables us to observe the structure of muscle filaments in living cells, and intensive x-ray studies have been carried out to elucidate the mechanism of contraction.

On the equator of x-ray diffraction from skeletal muscle we observe two major reflections, (1,0) and (1,1). On contraction the intensity ratio ($I(1,0)/I(1,1)$) of the two shows a decrease. This has been interpreted as a result of projections of myosin filaments approaching actin filaments so as to generate the sliding force between the filaments¹⁾.

Recently^{2,3)} it has been found that a chemical agent, 2,3-butanedione-2-monoxime (b.d.m.) has a strong inhibitory effect on contraction of living muscles and that this effect is mainly a result from a direct action of the agent on the contractile proteins *per se*. In a preliminary experiments with a x-ray generator in our laboratory, it was suggested that, even when muscle contraction was strongly suppressed by b.d.m., the decrease of $I(1,0)/I(1,1)$ of the muscle was well preserved.

The aim of the present study is to confirm the above result and to extend the experiments using the x-ray beam with high intensity at Photon Factory in order to clarify the molecular mechanism of the action of b.d.m.

Experimental and Discussion

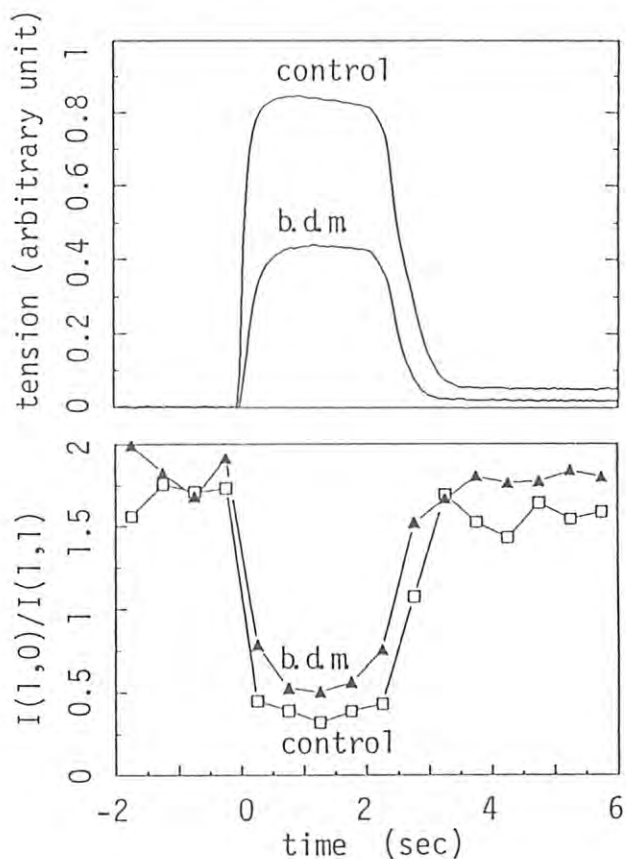
Sartorius muscle of *Rana nigromaculata* was isolated and the mounted on the tension measurement apparatus and cooled down to 5°C by lowering the temperature of circulating Ringer solution. Muscle contraction was elicited by electrical stimulation through a pair of platinum electrodes. X-ray diffraction was recorded by using a position sensitive photon counter. Application of b.d.m. was done by leaving muscles in the Ringer solution containing 3 mM of the agent for several hours.

The upper traces of the figure shows the tension records of a muscle before and after the application of b.d.m. The maximum tension level was suppressed to half by the agent. The lower graph shows the time course of the change

in $I(1,0)/I(1,1)$. The effect of b.d.m. on the ratio was disproportionately small compared with that on the maximum tension. B.d.m. seems to inhibit the interaction between myosin and actin after the process of binding of these proteins.

References

- 1) J. C. Haselgrove and H. E. Huxley, *J. Mol. Biol.* **77**, 549-568 (1973)
- 2) L. A. Mulieri and N. A. Alpert, *Biophys. J.* **45**, 47a (1984)
- 3) K. Horiuti, H. Higuchi, Y. Umazume, M. Konishi, O. Okazaki and S. Kurihara, *J. Mus. Res. Cell Motil.* *in press*



EFFECT OF SLOW LENGTH CHANGES ON THE EQUATORIAL X-RAY DIFFRACTION INTENSITIES OF FROG SKELETAL MUSCLE AT SHORT AND LONG SARCOMERE LENGTHS

Hiroyuki IWAMOTO, Hidehiro TANAKA, Katsuzo WAKABAYASHI*, En-Zhong WANG*, Yoshiyuki AMEMIYA** and Haruo SUGI

Department of Physiology, School of Medicine, Teikyo University, Itabashi-ku, Tokyo 173
 *Department of Biophysical Engineering, Faculty of Engineering Science, Osaka University, Toyonaka, Osaka 560

**Photon Factory, National Laboratory of High Energy Physics, Oho-machi, Tsukuba-gun, Ibaraki 305

When a skeletal muscle is slowly stretched during contraction, the force is increased. After the end of stretch, the force falls back but remains above the isometric level¹⁾, although the number of interacting crossbridges is supposed to have decreased. Attempts to explain this phenomenon have been made by observing the changes in equatorial reflection intensities during and after slow stretches²⁾. As the effect is dependent on muscle length³⁾, we measured the dependence on the muscle length of the equatorial X-ray intensity changes during slow stretches and releases.

The sartorius muscles of *Rana catesbeiana* were used. The experimental conditions were similar to those described previously⁴⁾. The starting length of the muscle was either 110% (long length) or 80% (short length) of the slack length. The duration of the stretch or release was 250ms, and its amplitude was 4% slack length.

The responses of the force, intensities of 1,1 and 1,0 reflections to slow stretch at long length are shown in Fig. 1a. The intensity of 1,1 showed a concomitant decrease followed by a partial recovery. This response of 1,1 reflection was similar to that at the slack length⁴⁾, though the modest increase of 1,0 reflection observed at the slack length was less conspicuous. The slow release had opposite effects on these reflections as have been observed at the slack length (Fig. 1b).

The response of 1,1 reflection to the slow stretch at the short length was similar to that

at longer lengths but its recovery after the stretch was more complete (Fig. 2a). The change of 1,0 reflection during stretch was more conspicuous. The response of 1,1 reflection to the slow release at the short length showed a marked contrast to that at longer lengths; it did not increase during the release but showed a decrease during and after the release. The 1,0 reflection increased in intensity during and after the release (Fig. 2b).

Thus, the responses to slow length changes of the equatorial reflections at the long length was similar to those at the slack length but those at the short length showed definite differences. The difference in the amount of filament overlap and an inactivation effect at short lengths⁵⁾ may constitute a part of possible explanations of these differences.

References

- 1) Abbott, B.C. and Aubert, X.M. (1952) *J. Physiol.*, 117, 77-86.
- 2) Tanaka, H., Hashizume, H. and Sugi, H. (1984) in *Contractile Mechanisms in Muscle* (eds. Pollack, G.H. and Sugi, H.) 193-201 (Plenum Press, New York).
- 3) Edman, K.A.P., Elzinga, G. and Noble, M.I.M. (1978) *J. Physiol.*, 281, 139-155.
- 4) Tanaka, H., Kobayashi, T., Amemiya, Y. and Sugi, H. (1984) *Photon Factory Activity Report*, 1983/84, VI-139.
- 5) Taylor, S.R. and Rüdel, R. (1970) *Science* 167, 882-884.

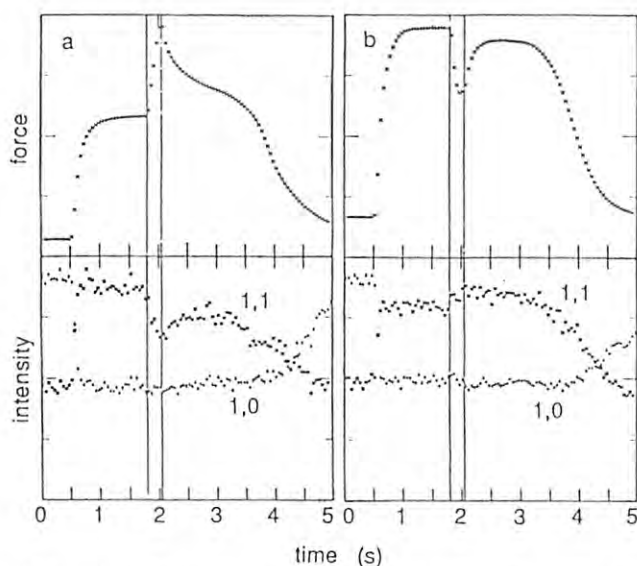


Fig. 1. Effect of slow length changes to contractile force and equatorial reflection intensities at the long length. a: effect of stretch; b: effect of release. Upper panel: force, lower panel: reflection intensities. All in arbitrary units. Vertical lines mark the duration of length change.

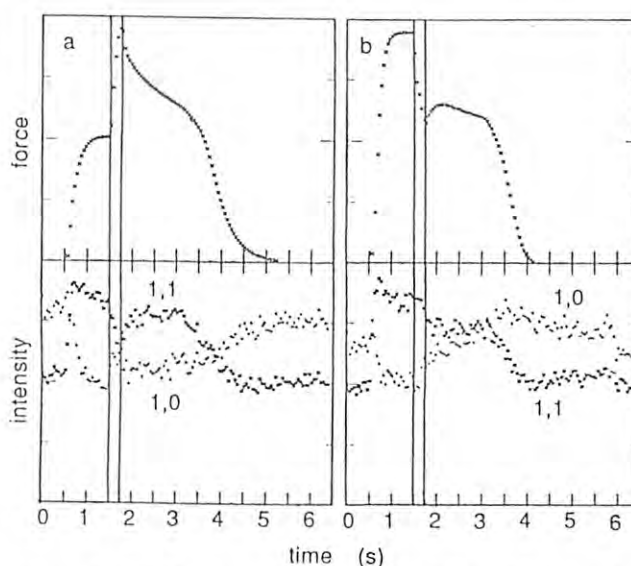


Fig. 2. Effect of slow length changes to contractile force and equatorial reflection intensities at the short length. a: effect of stretch; b: effect of release. Upper panel: force, lower panel: reflection intensities. All in arbitrary units. Vertical lines mark the duration of length change.

USE OF SKELETAL MUSCLE FIBER BUNDLE AS A MATERIAL FOR DYNAMIC X-RAY DIFFRACTION STUDIES

Hiroyuki IWAMOTO, Takakazu KOBAYASHI, Katsuzo WAKABAYASHI*, En-Zhong WANG*, Yoshiyuki AMEMIYA** and Haruo SUGI

Department of Physiology, School of Medicine, Teikyo University, Itabashi-ku, Tokyo 173

*Department of Biophysical Engineering, Faculty of Engineering Science, Osaka University, Toyonaka, Osaka 560

**Photon Factory, National Laboratory of High Energy Physics, Oho-machi, Tsukuba-gun, Ibaraki 305

The strong synchrotron radiation of X-ray has enabled us to make measurements of the intensity using skeletal muscle with a time resolution of millisecond order. H.E. Huxley and his colleagues were the first to make time-resolved measurements of the intensity changes during the mechanical transients after a quick stretch or release, using synchrotron radiation¹⁾. Most of the dynamic X-ray diffraction studies of muscles, including their works, have been done using whole sartorius muscles of the frog, because their thickness and width are suitable to give strong reflections at the wavelength used (1.5Å). At the same time, however, that material has disadvantages for dynamic measurements, e.g., inhomogeneity in the behavior of fibers and a large end-compliance. For this reason, it is difficult to make a close comparison between the X-ray diffraction data and the results of the mechanical measurements, which have been done using single muscle fibers. On the other hand, the diffraction from a single fiber is too weak to make dynamic measurements of reflections, especially weak meridional reflections. Moreover, it should be prepared and handled with particular carefulness. Those difficulties have requested us to seek a new material which is suitable for both X-ray and mechanical measurements. A small fiber bundle was tested as a candidate which meets that requirement.

A small bundle consisting of 10~30 muscle fibers excised from the semitendinosus muscle of the frog, *Rana japonica*, with pieces of

tendon at its ends. Its length was about 10 mm. The bundle was then transferred to the experimental chamber made of acrylate resin. One end of the bundle was connected to the force transducer and the other to the extension of the servo-controlled moving-coil length driver, which was capable of a 0.5% length step complete within 1 ms.

The bundle was able to maintain active force for 100 repeats of 0.5 s tetani when it was stimulated every 1 min. The relaxation was not slowed by repeated contractions. Fig. 1 shows an example of the record of 0.5 s tetanic contraction, during which a 1% quick release was applied. The four phases of force transients²⁾ are clearly observed in the figure. This shows that the fiber bundle can be used in place of a single fiber for mechanical measurements. Time-resolved measurements of the meridional reflection intensities were made with 5 ms time resolution. Fig. 2 shows the time course of intensities of 14.3 and 21.5 nm meridional reflections from myosin, during a 0.5 s tetanus with a 1% quick stretch. Intensities from 80 contractions were summed. In spite of the small size of the material, the drop in 14.3 nm reflection was clearly resolved after the stretch. This result also proves usefulness of the material in dynamic X-ray diffraction studies.

The present study showed that a fiber bundle meets the requirement mentioned above. It will provide further information about the mechanism of muscle contraction.

References

- 1) Huxley, H.E., Simmons, R.M., Faruqi, A.R., Kress, M., Bordas, J. and Koch, M.H.J. (1981) *Proc. Natl. Acad. Sci. USA* 78, 2297-2301.
- 2) Huxley, A.F. and Simmons, R.M. (1971) *Nature* 233, 533-538.

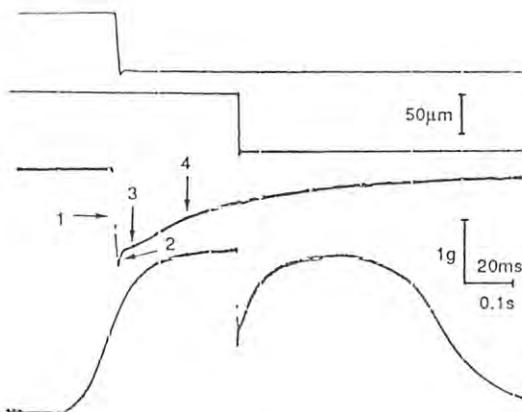


Fig. 1. Record of a 0.5 s tetanic contraction of the fiber bundle from the semitendinosus muscle. A 1% quick release was applied during contraction. Four traces show length in fast time base, length in slow time base, force in fast time base and force in slow time base, from top to bottom respectively. Note that the four phases of force transients are clearly seen.

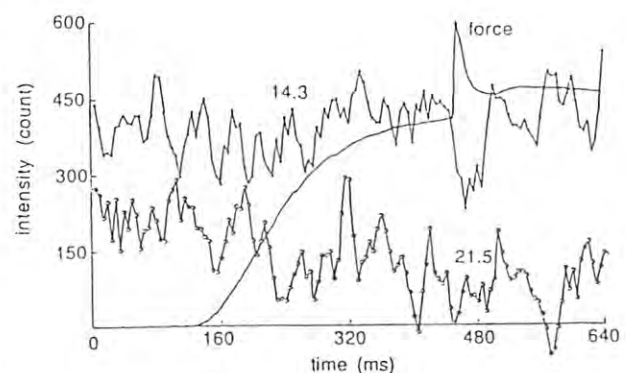


Fig. 2. Intensity changes of meridional reflection during a 0.5 s tetanic contraction. A 1% quick stretch was applied. Sum of intensities from 80 contractions.

ANALYSIS OF THE INTENSITY CHANGE OF THE ACTIN-BASED LAYER LINES IN THE TWO-DIMENSIONAL X-RAY DIFFRACTION PATTERN FROM A FROG SKELETAL MUSCLE DURING ISOMETRIC CONTRACTION

Katsuzo WAKABAYASHI*, Yutaka UENO*, Yoshiyuki AMEMIYA** and Hidehiro TANAKA***

* Department of Biophysical Engineering, Faculty of Engineering Science, Osaka University, Toyonaka, Osaka 560

** Photon Factory, National Laboratory for High Energy Physics, Oho-machi, Tsukuba-gun, Ibaraki 305

*** Department of Physiology, School of Medicine, Teikyo University, Itabashi-ku, Tokyo 173

Introduction

We reported that intensity distributions of the actin-based layer lines in the two-dimensional diffraction patterns from isometrically contracting muscles (recorded with the imaging plate [1]) were measured and the calculated Patterson function showed no distinct contribution from the myosin heads which might be binding to the actin [2]. Thus, the intensity changes of them were assumed to be due to the structural changes within the thin filament which would be taken place by interaction with the myosin heads combined with Ca^{2+} -activation. On this basis, the modelling studies have been done to interpret the observed intensity changes of the actin-based layer lines. We show that the intensity changes can be explained mainly by changes in the structure of actin subunit and in position of the tropomyosin.

Results

In model calculations, we assumed that intensities of the outer layer lines above 7 nm axial spacing are mainly determined by the form factor of the F-actin. We constructed the model of an actin subunit based on the crystallographic analysis of the actin molecule [3]. According to it, the actin monomer consists of two domains with unequal size. These domains were approximated by gaussian spheres. This actin molecule was arranged to generate the F-actin. We calculated the layer-line intensities by changing parameters such as the positions of two domains, their size and relative weights to fit the observed intensities by the least-square fitting. We found two possible solutions for the actin structure in the resting state. A common feature of the solutions was that the large domain of the subunit is at high radius and a small domain at small radius and with the long axis tilted along the 5.9 nm-pitch helical track. The axial separation between two domains was about 1.1 nm. The difference between two solutions was in the distance between the domains: one has a close contact between them and the other has them separated. The longest dimensions were 6.3 nm and 7.0 nm, respectively and the shortest was about 3 nm. Starting from each solution obtained in the resting state, we examined whether the intensity increase in the outer layer lines during contraction could be generated by changing the actin structure. This could be done, and there were two possible solutions. They were obtained mainly by decreasing the volume (ca. 20%) of each domain and by changing the distance and angle between two domains. Again we had two models in the active state: one has the contact-domain structure and the other the separate-domain structure. They are schematically presented in Fig. 1 in which the change in various parameters is shown. Next, we incorporated the tropomyosin molecules (TM) into the F-actin. The positioning of TM was determined so as to further fit the observed low-angle layer lines at high radius. We found that there were respectively two different positions of TM in each model in the

resting and in the active states. In one model of the resting state, TM molecules were in contact with the boundary between two domains of an actin subunit and in the other model, they were in contact with the large domain. In both cases, TM molecules were located at a radius of about 3.5 nm and at the angular positions of $\pm 45^\circ$ from the line joining the center of the large domain of the actin subunit and the filament axis. In the active state, TM molecules shift centrally: they move away by about 1 nm or 2 nm radially and by about 25° azimuthally. Figure 2 shows the positions of TM in the resting and active states.

At present stage, the crystallographic R-factor was about 0.25 in our models.

References

- 1) Y. Amemiya et al.: Science 237 (1987) 164.
- 2) K. Wakabayashi et al.: PF Activity Report 4 (1986) 303 and Y. Ueno et al.: ibid 304.
- 3) W. Kabsch et al: EMBO J. 4 (1985) 2113.

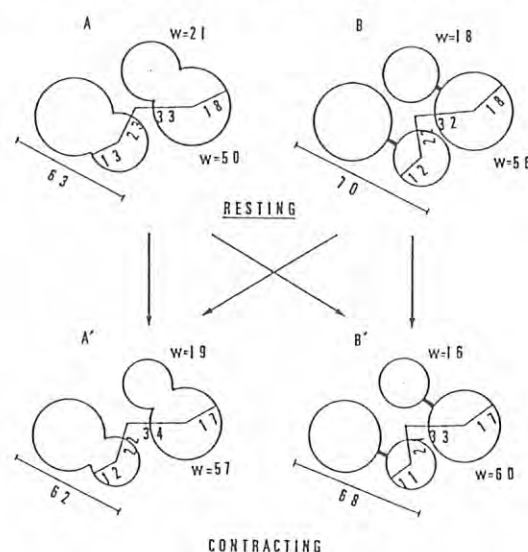


Fig. 1 Schematic representation of cross-section views of the F-actin models. Numbers (in Å unit). w, weight of the domain. Arrows indicate possible transitions.

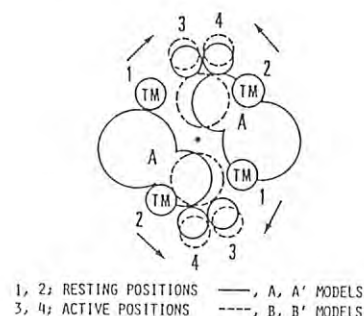


Fig. 2 Position of the tropomyosin molecules and possible movements.

INTENSITY CHANGES OF THE SECOND ACTIN LAYER-LINE REFLECTION AND THE EQUATORIAL REFLECTION AT THE HIGH RADIAL POSITION OF 0.21 nm^{-1} FROM TETANIZED FROG SKELETAL MUSCLES WITH NON-OVERLAP SARCOMERE LENGTH

Katsuzo WAKABAYASHI*, Hiroyuki IWAMOTO**, Hidehiro TANAKA**, En-Zhong WANG*, Toshiaki HAMANAKA*, Takakazu KOBAYASHI**, Haruo SUGI**, Toshio MITSUI* and Yoshiyuki AMEMIYA***

* Department of Biophysical Engineering, Faculty of Engineering Science, Osaka University, Toyonaka, Osaka 560

** Department of Physiology, School of Medicine, Teikyo University, Itabashi-ku, Tokyo 173

*** Photon Factory, National Laboratory for High Energy Physics, Oho-machi, Tsukuba-gun, Ibaraki 305

Introduction

The reflections on the equator and on the second actin-based layer line at the high radial position of about 0.21 nm^{-1} increase in intensity during isometric contraction of frog skeletal muscles [1,2]. The change of these reflections was investigated with the muscle of the non-overlap length of the thin and thick filaments during contraction. Results are reported in comparison with the muscle of the full-overlap.

Results

Semitendinosus muscles of the bullfrog were mounted with the fibre axis parallel to and in between the parallel electrodes. They were isometrically stimulated with a train of 3 ms pulses at 40 Hz to produce a maximum tension of 2.1 s duration at 4°C . This was repeated 10 times at intervals of 1 min for each muscle. The muscle was stretched to the sarcomere length of $\geq 4 \mu\text{m}$. Experiments were also done with the muscle of the full-overlap length ($\sim 2.4 \mu\text{m}$) before and after stretching as controls. Intensity was measured by setting the PSPC with its long axis parallel to the meridian at the radial position of 0.21 nm^{-1} . The PSPC covered the radial range of $0.20 - 0.22 \text{ nm}^{-1}$, where the peaks of the equatorial and the second layer-line reflections sit. Tension and intensity were measured with a time-resolution of 50 ms and the data from four muscles were added. We confirmed that the muscle before and after stretching showed nearly the same changes of tension and intensity by stimulation. Figure 1 shows the results. Intensities of the equatorial and the second layer-line reflections from the full-overlap muscle increased by about 40% relative to the resting values. At the non-overlap length, the equatorial intensity remained unchanged, and the second layer-line reflection increased but the maximum value (about 15% increase) was less than that in the full-overlap muscle. Provided that the present result is correct (cf. [1]), it is suggested that the other structure components as well as the regulatory proteins are responsible for the intensity increase of the second layer-line reflection from the full-overlap muscle during contraction. Wakabayashi et al. [3] noted that the structural change of the actin subunit induced by interaction with the myosin heads might contribute to the intensity change of this reflection. The intensity increase of the equatorial reflection during contraction may be due in large part to the binding of the myosin heads to actin [1]. It is worthwhile to mention that the intensity on the first layer line in this region increased in the overlap muscle but decreased slightly in the non-overlap muscle during contraction (see Fig. 1).

References

1) M. Kress et al.: J. Mol. Biol. 194 (1986) 325.

2) Y. Amemiya et al.: Science 237 (1987) 164.

3) K. Wakabayashi et al.: In Molecular Mechanism of Muscle Contraction, ed. by H. Sugi and G. H. Pollack (Plenum Press, 1987) in press.

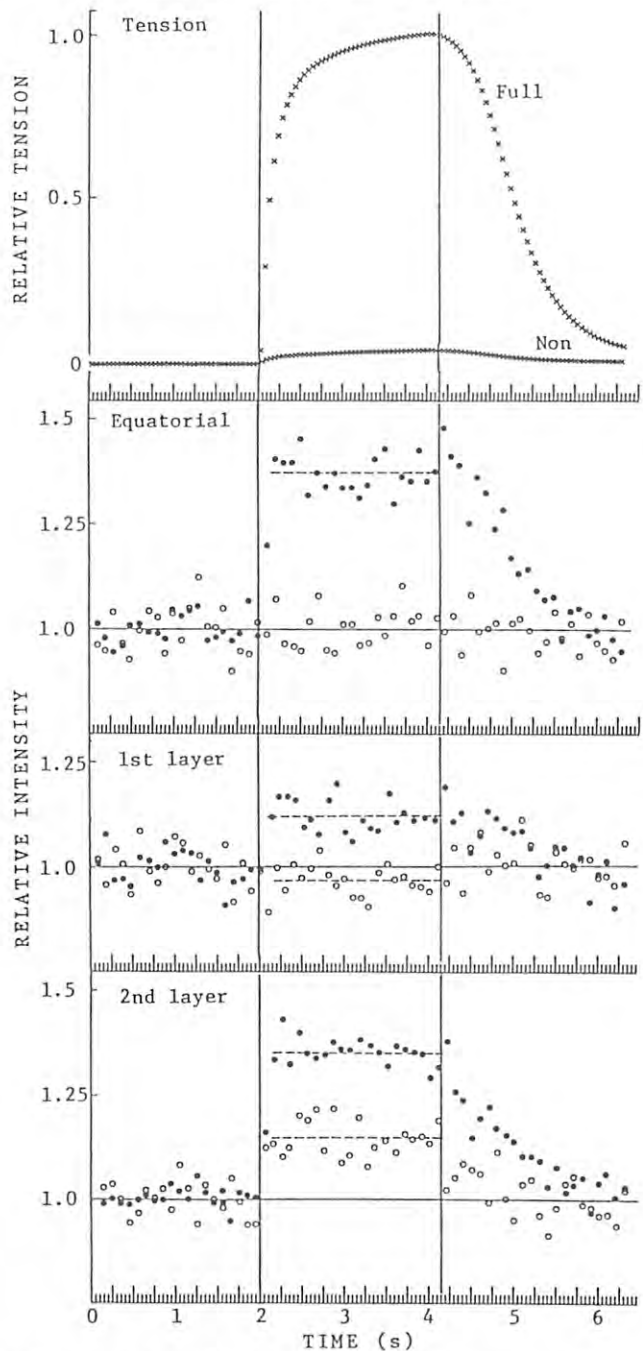


Fig. 1 Intensity changes on the equator, the first and second actin layer lines at the radial position of 0.21 nm^{-1} . Top, tensions. In intensity data, (o) non-overlap and (●) overlap muscles.

INTENSITY CHANGE OF THE 7.2 NM MYOSIN MERIDIONAL REFLECTION FROM TETANIZED FROG SKELETAL MUSCLE DURING SINUSOIDAL LENGTH CHANGES

Katsuzo WAKABAYASHI*, Hidehiro TANAKA**, Hiroyuki IWAMOTO**, En-Zhong WANG*, Takakazu KOBAYASHI**, Toshiaki HAMANAKA*, Yoshiyuki AMEMIYA***, Haruo SUGI** and Toshio MITSUI*

* Department of Biophysical Engineering, Faculty of Engineering Science, Osaka University, Toyonaka, Osaka 560

** Department of Physiology, School of Medicine, Teikyo University, Itabashi-ku, Tokyo 173

*** Photon Factory, National Laboratory for High Energy Physics, Oho-machi, Tsukuba-gun, Ibaraki

Introduction

Intensity change of the 7.2 nm myosin meridional reflection (the 6th order of the basic repeat, 42.9 nm of the thick filament) from isometrically tetanized frog skeletal muscle was studied during sinusoidal length changes by time-resolved X-ray diffraction technique. It has been reported that the intensity of this reflection does not change upon quick length change [1]. We show here that it behaves as do the 14.3 nm reflection during sinusoidal length changes as well as in the course of tension development.

Results

Sartorius muscles of the bullfrog with the sarcomere length of $\sim 2.4 \mu\text{m}$ were isometrically stimulated with a train of 3 ms pulses at 30 Hz to produce a maximum tetanic tension of 1.0 s duration at 4°C . When the tension reached a steady level, sinusoidal length changes of amplitude $\sim 1\%$ at frequency 5 Hz were applied to the muscle. This was repeated 10 times at intervals of 20 s for each muscle. Intensity measurements were done on the meridian by setting the PSPC with its long axis parallel to the meridian. In order to simultaneously measure the weak 7.2 nm reflection and the strong 14.3 nm reflection, a filter ($\sim 100 \mu\text{m}$ thick Al) was put in the strong region as shown in Fig. 1 to avoid excessive counting rate of the PSPC and to raise S/N ratio of the weak reflection. Tension and intensity were measured with a time-resolution of 10 ms and the data from several muscles were added.

Figure 2 shows a typical example of the results. The intensity of the 7.2 nm reflection ($I_{7.2\text{nm}}$) increased with development of tension, being about a 1.4-fold increase at the plateau phase of the tension relative to the resting value. The intensity of the 14.3 nm reflection ($I_{14.3\text{nm}}$) increased by about a 1.7-fold of the resting value at the plateau phase. During sinusoidal length changes, $I_{7.2\text{nm}}$ oscillates with large decrease in the stretching phase. Its intensity minima were observed around the tension peaks where deeper troughs of $I_{14.3\text{nm}}$ appeared. As was reported previously [2], $I_{14.3\text{nm}}$ exhibited two peaks and troughs within each cycle of the applied length changes. Although the existence of the doublet peaks within one cycle of the length changes was not clear, $I_{7.2\text{nm}}$ behaved as a whole similarly to $I_{14.3\text{nm}}$ during sinusoidal length changes as well as in the course of tension development. This suggests that the myosin heads which are interacting with the actin contribute to the intensity of the 7.2 nm reflection, though the main component of this reflection has been considered to be due to the thick filament backbone [2].

References

- 1) H. E. Huxley et al.: J. Mol. Biol. 169 (1983) 469.
- 2) K. Wakabayashi et al.: Biophys. J. 47 (1986)

471. Also see H. Tanaka et al.: Photon Factory Activity Report 3 (1985) VI-176.

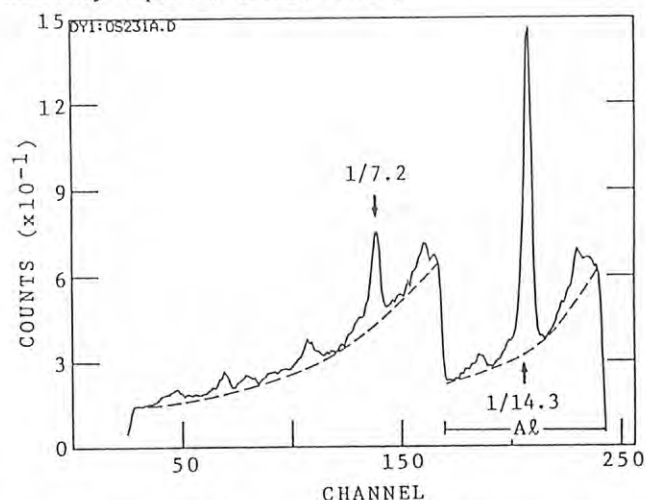


Fig. 1 The region covered with an $\Delta\lambda$ attenuator.

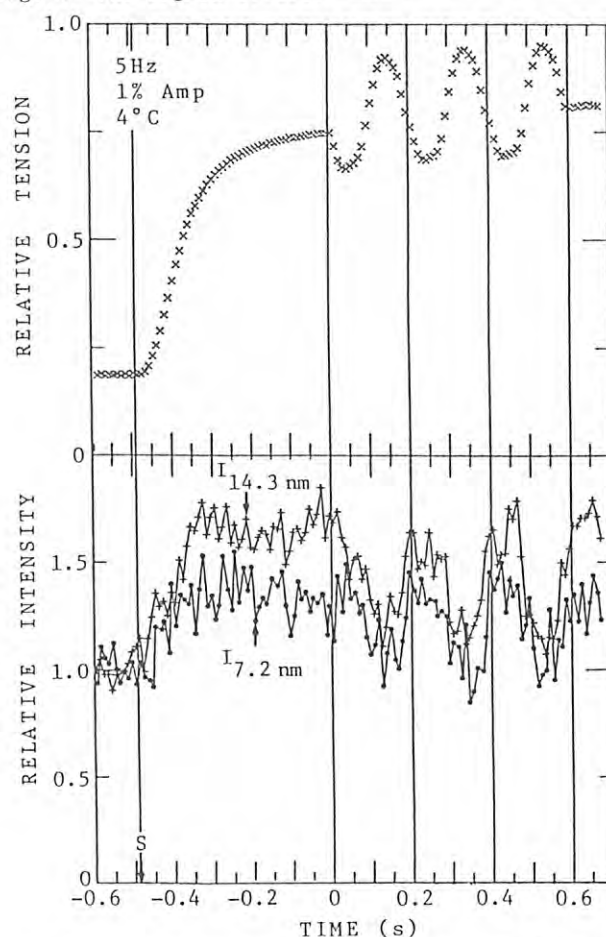


Fig. 2 Intensity change of the 7.2 nm reflection in comparison with the 14.3 nm reflection. Upper, tension and lower, intensity. S, stimulation.

DIFFRACTION STUDIES OF MUSCLE CONTRACTION BY SINUSOIDAL LENGTH CHANGE
— THEORETICAL MODEL AND EXPLANATION OF EXPERIMENTAL RESULTS —

Toshio MITSUI and Hiroyuki OHSHIMA[†]

Department of Biophysical Engineering, Faculty of Engineering Science,
Osaka University, Toyonaka, Osaka 560

[†]Faculty of Pharmaceutical Science, Science University of Tokyo,
Shinjuku-ku, Tokyo 162

The aim of our synchrotron radiation studies of muscle is to understand molecular mechanism of the filament sliding in contracting muscle. The problem is, however, very complicated having many parameters to be determined. Thus any theoretical model for muscle contraction should be constructed based upon various informations supplied by biological, biochemical and physiological studies in addition to X-ray structural study, and should explain experimental results in these fields.

Recently evidence seems to be accumulating that muscle contraction may not be associated with the power stroke of the crossbridges, and a new model called a self-induced translation model was proposed for myosin motion in contracting muscle. Outline of the model is given in the abstract of recent international congress [1], and here we give three examples of our calculations with the model, which are in good agreement with experimental observations. Figure 1 shows calculated time course of the intensity of the 14.3 nm meridional reflection in comparison with the experimental results obtained by Wakabayashi et al. at the Photon Factory [2]. Figure 2 shows calculated V/V_{\max} as a function of P/P_0 , where V is the shortening velocity and P is the tension produced by muscle, P_0 being the isometric tension. Figure 3 gives rate of energy liberated in shortening muscle as a function of P/P_0 .

References

- 1) T. Mitsui and H. Ohshima: in Abstracts of the 9th International Biophysics Congress at Jerusalem (1987) p.158.
- 2) K. Wakabayashi et al.: Biophys. J. **49** (1986) 581. Also see H. Tanaka et al.: PF Activity Report **3** (1985) VI-176.

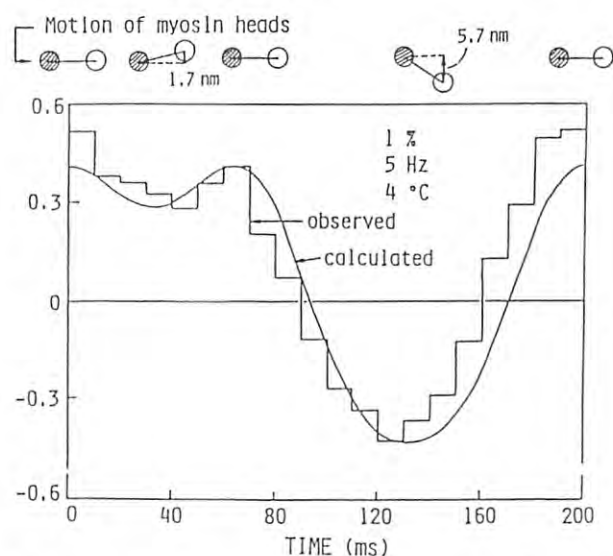


Fig. 1 Calculated time course of $I_{14.3}$ for the sinusoidal length change in comparison with the results by Wakabayashi et al. [2].

- 3) T. Tsuchiya et al.: in Cross-Bridge Mechanism in Muscle Contraction, ed by H. Sugi and G. H. Pollack (Univ. of Tokyo, 1979) p.225.
- 4) T. Yamada and E. Homsher: in Contractile Mechanism in Muscle, ed. by G. H. Pollack and H. Sugi (Plenum Press, 1984) p.883.

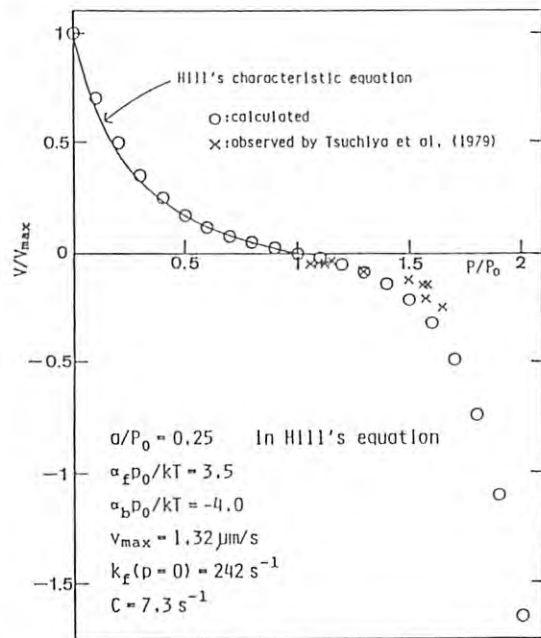


Fig. 2 Calculated force-velocity relation (o) in comparison with Hill's characteristic equation (solid line) for $P < P_0$ and with observation (x) by Tsuchiya et al. [3] for $P > P_0$.

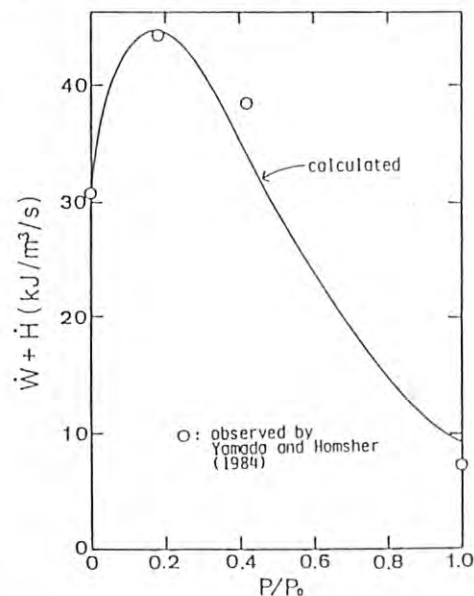


Fig. 3 Calculated rate of energy liberation in comparison with the observation (o) by Yamada and Homsher [4].

SMALL ANGLE X-RAY DIFFRACTION OF A MOLLUSCAN SMOOTH MUSCLE CONTRACTING
TONICALLY IN RESPONSE TO ACETYLCHOLINE

Yoshiko TAJIMA, Kazuyuki OKADA, Osamu YOSHIDA, and Yoshiyuki AMEMIYA*

Department of Physics, Tokyo Metropolitan University, Setagaya-ku, Tokyo 158

* Photon Factory, National Laboratory of High Energy Physics, Oho-machi,
Tsukuba-gun, Ibaraki 305Introduction

Small angle x-ray diffraction of the anterior byssus retractor muscle of *Mytilus edulis* (ABRM) in the tonically contracted state was carried out to take good diffraction patterns for structure analysis of the thin filaments. It was attempted to take x-ray patterns in a very short time while tonic tension was maintained high.

Experimental and Results

Tonic contraction was produced by stimulation with acetylcholine at 20°C¹⁾. The muscles were soaked in solutions containing 10^{-4} M acetylcholine in the artificial sea water for 2 min at intervals of 10 min (Fig. 1). The tonic tension reached maximum after three stimuli. Because the redevelopment of tension after quick release was only 20 %, the muscles were almost inert, and the high tension level was mostly due to catch tension²⁾. The redevelopment of tension was about 30 % in a previous experiment in which tonic tension was maintained for long time by iterative spontaneous contraction³⁾. Therefore, the muscles were less active and reached a higher level of the catch state in this work than in the previous work.

After the third stimulation with acetylcholine, the muscles were exposed to x-rays for 30 sec, and the diffraction patterns were recorded on imaging plates. It was successful to take diffraction patterns from the highly-oriented thin filaments. Figure 2 shows a diffraction pattern from a ABRM developing tonic tension of 8.3 Kg/cm². The 194 Å ($l=4$) layer line which was not detectable in the relaxed state became apparent. It became stronger than the 51 Å ($l=15$) and 71 Å ($l=11$) layer lines (Fig. 2b) in resemblance to the diffraction pattern from the contracting frog skeletal muscle⁴⁾. Because of

overlap between the 388 Å ($l=2$) layer line from the thin filaments and the 362 Å layer line from paramyosin, the 388 Å layer line looks as if it is much stronger than the 194 Å layer line³⁾ (Fig. 2c), but actually, the former is only a little stronger than the latter. The same relative intensity changes among those layer lines were also observed in the ABRM developing tonic tension of 4 Kg/cm².

References

- 1) B. M. Twarog, J. Physiol., 192, 847 (1967).
- 2) B. R. Jewell, J. Physiol., 149, 154 (1959).
- 3) Y. Tajima, M. Sasaki, T. Asano, Y. Amemiya, and J. Miyahara, Photon Factory Activity Report, 289 (1986).
- 4) K. Wakabayashi, Y. Ueno, Y. Amemiya, H. Tanaka, and J. Kurihara, Photon Factory Activity Report, 303 (1986).

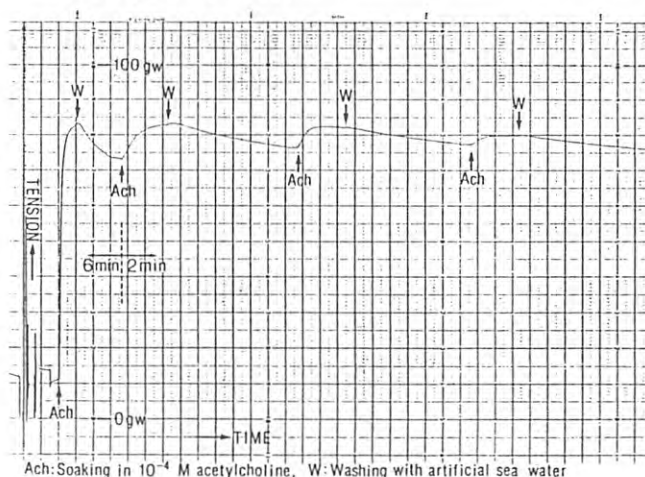
Ach: Soaking in 10^{-4} M acetylcholine, W: Washing with artificial sea water

Fig. 1

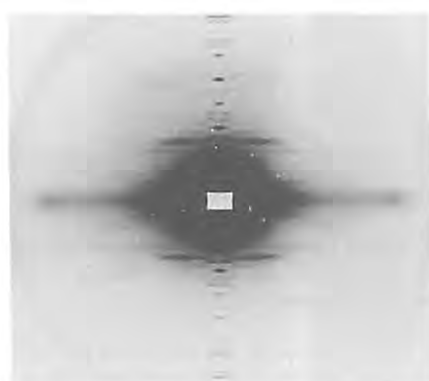
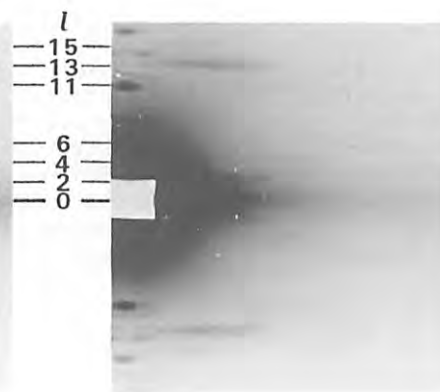


Fig. 2 (a)



(b)



(c)

TIME-RESOLVED SMALL-ANGLE X-RAY SCATTERING STUDY OF TOBACCO MOSAIC VIRUS PROTEIN
ASSOCIATION INDUCED BY SALT CONCENTRATION JUMP

Hideo INOUE¹, Yoh SANO¹, Hiroshi KIHARA², Katsuzo WAKABAYASHI³ and Yoshiyuki AMEMIYA⁴

1. National Institute of Agrobiological Resources, Yatabe, Tsukuba-gun, Ibaraki 305

2. Department of Physics, Jichi Medical School, Minamikawachi, Tochigi 329-04

3. Department of Biophysical Engineering, Faculty of Engineering Science, Osaka University, Toyonaka, Osaka 560

4. National Laboratory for High Energy Physics, Oho-machi, Tsukuba-gun, Ibaraki 305

Introduction

It has been known that the coat protein of tobacco mosaic virus (TMVP) self-associates to form several kinds of aggregates depending upon pH, temperature, ionic strength and the protein concentration. We have continued the time-resolved SAXS measurements of TMVP self-association from A-protein (around trimer of subunits) to a double-layer disk (34 subunits) to multi-layer disks induced by a jump of ionic strength. The shape analysis of TMVP aggregates was performed by comparing the scattering curves with model calculations.

Experimental

X-ray experiments have been carried out with the Muscle Diffractometer BL-15A. A jump of ionic strength from 5mM to 50mM or 100mM were performed with a stopped-flow apparatus designed for the X-ray experiments. The details of the experiments have already described¹⁾.

Results

Experimental data obtained were analyzed by means of two kinds of plot: plotting logarithm of scattered intensities $I(h)$, being a function of the momentum transfer $h (=4\pi \sin \theta / \lambda)$, of each frame against squares of h ("Guinier plot"), and plotting $\log(I(h) \cdot h^2)$ against h^2 . Under less favorable conditions for the protein aggregation a $\log I(h)$ vs h^2 plot can be better fitted by the two exponential term approximation method:

$$I(h) = a(1)\exp[-R_g(1)^2 h^2 / 3] + a(2)\exp[-R_g(2)^2 h^2 / 3].$$

An example is the ionic strength jump from 5mM to 50mM at 15°C. Re-examination of our SAXS data is under way to determine which analysis to be applied for each condition.

Shape Analysis

The analysis of SAXS measurements shows the ionic strength jump induces TMVP to aggregate to the double-layer disk and further stacking of the disk. A single layer of disk is composed of 17 monomers. Assuming these disks to be a hollow cylinder, we calculated the scattering intensity of hollow cylinders according to Furuno, et al.²⁾ as a function of a height, i.e., a number of layer. The parameters used are as follows; the outer radius: 9.0nm, the inner radius: 2.0nm, the half height of one layer: 1.15nm. Logarithms of scattering intensity of model calculations are plotted against h in Fig. 2 with variation of a number of layer from 2 to 12. As a comparison the scattered intensity curve of TMVP in 100mM PB at 25°C was

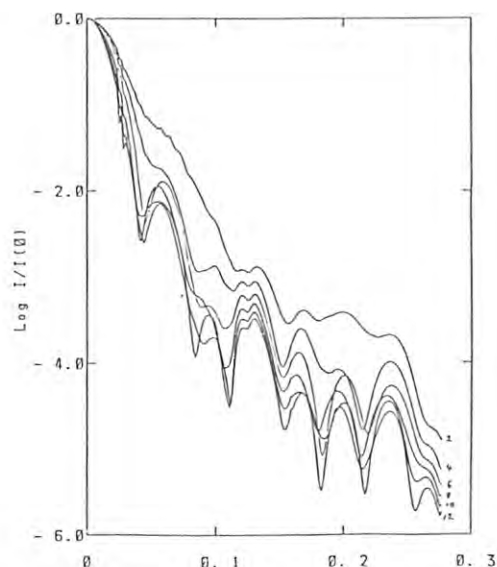


Fig. 1. Model calculation of scattered intensity curve for hollow cylinders plotted against the momentum transfer.

shown in Fig. 2, where a triple- or quadruple-layered double disk was suggested from the Guinier plot. It is desirable to extend the scattering measurements to a considerably wide angular range in order to determine definitely the shape of the aggregates.

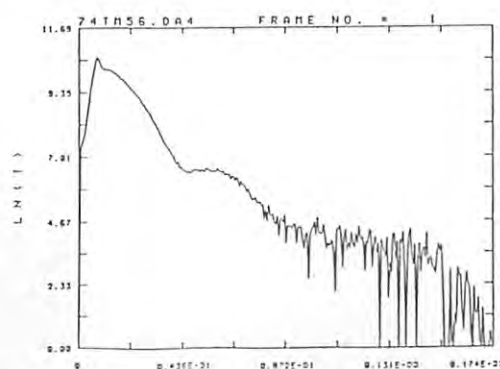


Fig. 2. Plot of logarithm of the scattered intensity of TMV protein in 100mM PB at 25°C against the momentum transfer.

1) H.Inoue, Y.Sano, H.Kihara, K.Wakabayashi and Y.Amemiya : Photon Factory Activity Report 4(1986)307.

2) T.Furuno, A.Ikegami, H.Kihara, M.Yoshida and Y.Kagawa : J. Mol. Biol. 170(1983)137-153.

CONFORMATIONAL CHANGE OF OVOMACROGLOBULIN CAUSED BY INTERACTION WITH CHYMOTRYPSIN

Hideo ARAKAWA, Atsushi IKAI, Yoshiaki TAKEIRI*, Yoshiyuki AMEMIYA**, Katsuzo WAKABAYASHI*** and Hiroshi KIHARA****

Dept. of Biophysics & Biochemistry, Univ. of Tokyo, Hongo, Tokyo, *Hamamatsu Photonix, Hamamatsu, **Photon Factory, National Laboratory for High Energy Physics, Oho-machi, Tokuba, ***Dept. of Bioengineering, Osaka Univ., Osaka, ****Jichi Medical College, Minami-Kawachi, Tochigi

Introduction

The time resolved change of the X-ray small angle scattering from the mixture of ovomacroglobulin and chymotrypsin was successfully recorded for the first time. Ovomacroglobulin is a homologous protein of serum α_2 -macroglobulin. Both proteins "trap" various kinds of proteinases. The trapping of proteinases by macroglobulins is accompanied by decreases in their hydrodynamic volumes and electron microscopic images. We tried to analyze the change with time-resolved X-ray scattering.

Results

Equal volume solutions of ovomacroglobulin and chymotrypsin were mixed in a stopped flow apparatus and, within a few milliseconds, the mixture was led to a thin quartz cell for the measurement of X-ray scattering. The scattering curve was recorded every 200ms and the radius of gyration was calculated for each curve. The result

is given in Fig.2. The radius of gyration decreased from 76Å to 69Å with an approximate half time of 4s under the given condition (10°C, conc. of ovomacroglobulin and chymotrypsin, 10mg/ml and 1mg/ml). The static data before and after the reaction was completed are given in Fig.1. There is a clear decrease in the scattering intensity in the mid-angle region after the reaction. This change is considered to be due to the filling of the inner cavity of ovomacroglobulin by chymotrypsin. We are trying to correlate the kinetics of conformational change observed here with similar data from fluorescence kinetics experiments.

References

1. Nishigai, M., Osada, T. and Ikai, A., Biophys. Biochem. Acta., (1985) 831, 236-241
2. Branegard, B., Osterberg, R. and Sjöberg, R., (1980) Int. J. Biol. Macromol. 2, 321-323

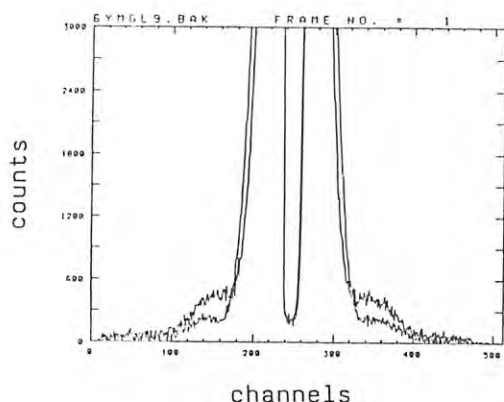


Figure 1

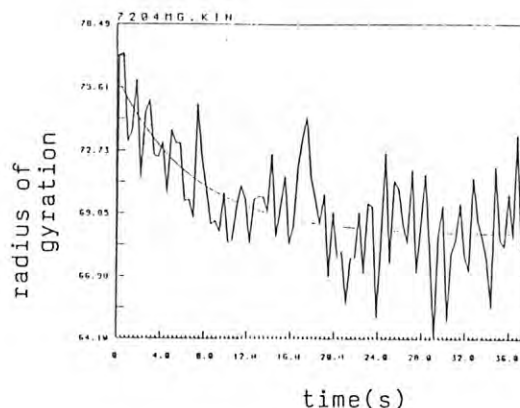


Figure 2

STOPPED-FLOW X-RAY SCATTERING STUDY VII. DISSOCIATION OF HEMOCYANIN FROM *Limulus polyhemus* AND *Panulirus japonicus*.

Yoshihiko IGARASHI¹⁾, Kazumoto KIMURA²⁾, Akihiko KAJITA¹⁾, Nobuo MAKINO³⁾, Yoshiaki TACHI-IRI⁴⁾, Osamu HASEGAWA⁵⁾, Takaki YAMAMURA⁶⁾, Yoshiyuki AMEMIYA⁷⁾, Katsuzo WAKABAYASHI⁸⁾, and Hiroshi KIHARA⁹⁾

- 1)Department of Biochemistry and 2)Medical Electronics Center, Dokkyo University Medical School, Mibu, Tochigi
- 3)Division of Biochemistry, School of Basic Medicine, Tsukuba University, Tsukuba, Ibaraki
- 4) Hamamatsu Photonics, Hamamatsu, Shizuoka
- 5) Department of Chemistry, Faculty of Science, Science University of Tokyo, Kagurazaka, Shinjuku, Tokyo
- 6) International Life Science Institute, Takarazuka, Hyogo
- 7) Photon Factory Division, National Laboratory for High Energy Physics, Oho-machi, Tsukuba, Ibaraki 305
- 8) Department of Biological Engineering, Faculty of Engineering Science, Osaka University, Osaka 560
- 9) Jichi Medical School, School of Nursing, Minamikawachi, Tochigi 329-04

1. Introduction

Hemocyanin is an oxygen binding protein of high molecular weight. It dissociates into subunits of lower molecular weight. In the present study, kinetics of this dissociative process was monitored by stopped-flow X-ray scattering method. In the experiments, two types of hemocyanin were used, from *Limulus polyhemus* and from *Panulirus japonicus*. Their molecular weights are 3.6×10^6 and 4×10^5 respectively.

2. Results and Discussion

Hemocyanin from *Limulus polyhemus* was degraded on mixing with EDTA. It dissociated into monomers via at least two dissociative processes. In the experiments, two types of experiments were planned; dissociation from the native protein (=48-mer) to monomers and the native protein to 24-mer. The former experiment shows two decay processes were observed. From the latter experiments, we can confirm that a subpeak, observed in native protein, disappeared at 24-mer state within 10 s. Another hemocyanin from *Panulirus japonicus* (=6-mer) was also dissociated on mixing with EDTA at pH 9.5. Also in this case, the dissociation process was biphasic.

3. References

1. Y. Amemiya, K. Wakabayashi, T. Hamaoka, T. Wakabayashi, T. Matsushita, and H. Hashizume (1983) Nuclear Inst. Methods, 208, 471-477.
2. T. Nagamura, K. Kurita, E. Tokikura, and H. Kihara (1985) J. Biochem. Biophys. Methods, 11, 277-286.

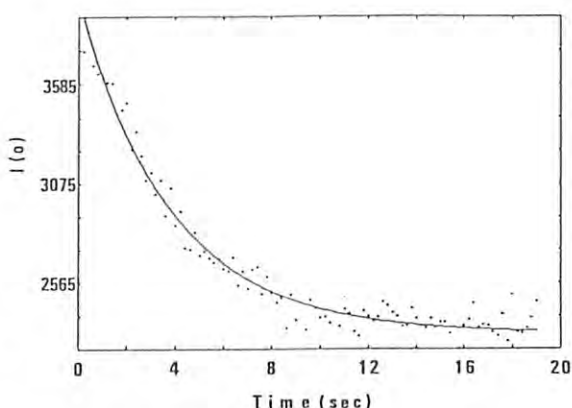


Fig. 1 Time course of the dissociation of *Limulus polyhemus* 48-mer to 24-mer in Tris-HCl, I=0.01, 10 mM EDTA, pH 7.0.

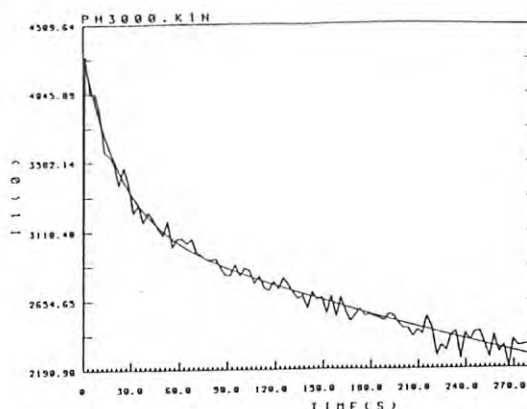


Fig. 2 Time course of the dissociation of *Panulirus japonicus* 6-mer to monomer in 50 mM ehtanolamine, 25 mM EDTA, pH 9.5.

SLOW CHANGE OF P_{β}' STRUCTURE AFTER TEMPERATURE JUMP
ACROSS MAIN TRANSITION IN DIMYRISTOYLPHOSPHATIDYLCHOLINE

Morio AKIYAMA, Shinji MATSUOKA⁺, Satoru KATO⁺, Ichiro HATTA⁺,
Yoshiyuki AMEMIYA⁺⁺ and Yoshio TERAYAMA

Department of Physics, Sapporo Medical College
Chuo-ku, Sapporo 060

⁺Department of Applied Physics, Faculty of Engineering,
Nagoya University, Chigusa-ku, Nagoya 464

⁺⁺Photon Factory, National Laboratory for High Energy Physics
Tsukuba-gun, Ibaragi 305

Introduction

In multilamellar phospholipids, it requires 4-30 minutes to reach the equilibrium after the temperature change across the pretransition which causes the formation or disappearance of undulation (ripple) in the lamella and a change in the repeat period of the lamellae stack¹⁾. On the other hand, the main transition has been thought to be completed in less than 1 sec²⁾. The existence of slow process in the main transition has not been noticed.

In this paper, the slow change of the lattice parameters of P_{β}' phase is described. The lattice parameters were calculated from the reflection of small angle X-ray diffraction after temperature jump across the main transition ($L_{\alpha} \rightarrow P_{\beta}'$).

Experimental

Dimyristoylphosphatidylcholine 60% water content was prepared by the usual method. Samples were sealed in aluminium cell with two windows of polyester film. The thickness of the cell was 1 mm. Temperature-controlled fluid was made to flow around the cell. The temperature jump was achieved by switching the flow from two individually temperature-controlled fluid baths. A small angle X-ray diffraction was performed at BL-15A. The wavelength of the X-ray was 1.55 Å.

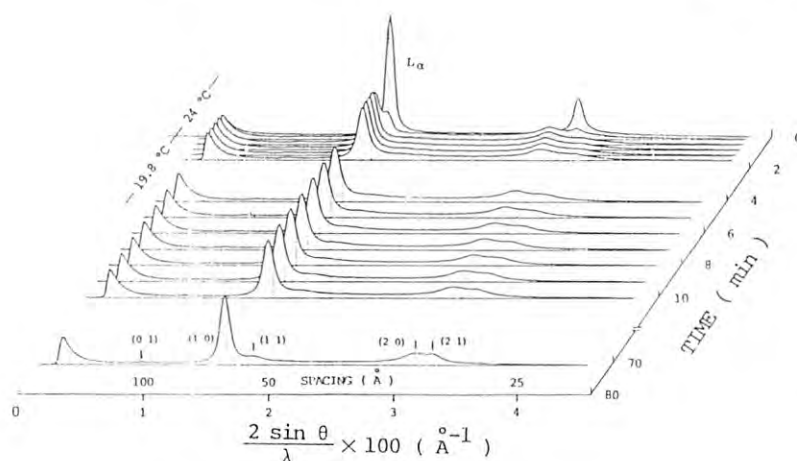


Fig.1 Small angle X-ray diffraction profiles after the temperature jump from 24°C to 19.8°C.

Results and Discussion

X-ray diffraction profiles at various times after the temperature jump from 24°C (L_{α}) to 19.8°C (P_{β}') are shown in Fig. 1. Five reflections (0 1), (1 0), (1 1), (2 0), (2 1) can be seen. The peak position of each reflections shift as time passes. The reflections (1 0), (2 0) and (2 1) shift from the small angle side to the large angle side, and the reflections (0 1) and (1 1) shift to the opposite direction.

Two dimensional lattice parameters a , b and γ at various time were calculated from the spacing of the five reflections. These are shown in Fig.2 as a function of time. Remarkable change occurs in a and γ . The parameter b , which corresponds to the repeat period of the ripples, does not change so much.

The repeat period of lamellae stack increases immediately after the temperature jump from 66.2 Å (L_{α}) to 71.1 Å and decreases slowly to 67.0 Å (P_{β}'). This slow decrease corresponds to the decrease of the parameter a . The decrease of γ may be due to the avoidance of interlamella repulsive interaction.

References

- 1) B. R. Lentz, Y. Barenholz and T. E. Thompson: Biochemistry 15 (1976) 4521
- 2) T. Y. Tsong and M. I. Kanehisa: Biochemistry 16 (1977) 2674

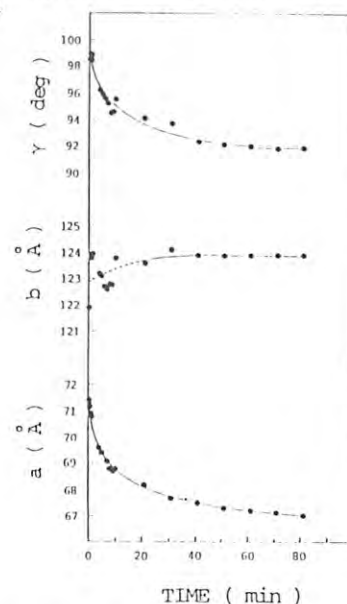


Fig.2 Lattice parameters of P_{β}' phase after the temperature jump.

DYNAMICAL STRUCTURE CHANGE DURING REVERSION IN AL-ZN ALLOYS

Kozo OSAMURA¹, Hiroshi OKUDA¹, Yoshiyuki AMEMIYA² and Hiroo HASHIZUME³¹ Department of Metallurgy, Kyoto University, Sakyo-ku, Kyoto 606² Photon Factory, National Laboratory for High-Energy Physics,
Tsukuba-gun, Oho-machi, Ibaraki 305³ Research Laboratory for Engineering Materials, Tokyo Institute of Technology,
Nagatsuda, Midori-ku, Yokohama 227Introduction

It is well known that metastable G.P. zones dissolve partially or completely into matrix when the sample is held at higher temperatures than the pre-aged temperature. In the present paper, the structure change during reversion process for Al-Zn alloys has been investigated by means of in-situ SR-SAS measurements. An analytical model describing the collapse of zone during reversion has been proposed.

Experimental Procedure

The alloys used here were Al-6.8at%Zn and 15at%Zn. After the solution treatment at 573 K for 3.6 ks, the specimen was quenched into brine and then pre-aged at 313 K for 60 ks to form metastable G.P. zones. The reversion treatment was done at temperatures, where the temperature range is conventionally divided into two parts by the zone solvus. The measurements were performed using time-resolved SAS apparatus installed at BL-15A in Photon Factory, National Laboratory for High Energy Physics, KEK.

Results and Discussion

The time dependence of the radius of gyration R_g for Al-6.8at%Zn alloy is shown in Fig. 1. While the integrated intensity decreases monotonously during the process, it was found that the radius remains constant at first, and beyond a certain critical time, it increases rapidly as indicated by the arrow in the figure. The reversion process was divided into two stages. The change of structure parameters for Al-6.8at%Zn alloy reverted at 443 K is shown in Fig. 2. Within the time of 5 sec, it is found that the volume fraction did not change, while the quantity $\Delta\rho/\Delta\rho_0$ decreased suggesting the decrease of solute concentration inside the zone. This behaviour can be explained in terms of local equilibrium at the interface as shown in Fig. 3. Fig. 3(a) shows schematically the composition dependence of free energy in this alloy system. At the pre-aging temperature T_1 , the alloy decomposed into two phases. When the sample is heated up abruptly to a temperature T_2 , which is lower than the critical temperature T_c , the alloy composition c_0 comes to lie within the one-phase region. Therefore the zone becomes unstable and tends to dissolve to the matrix. During this process, it is reasonable to assume the local equilibrium, by which both compositions of the zone and the matrix at the interface, $c_m^I(T_2)$ and $c_p^I(T_2)$ are fixed from the free energy-composition curve at T_2 . In the successive period, that is, the later stage, both quantities R_g and L increased rapidly. The former change can be explained in terms of the diffuse tail of

concentration profile outside the zone/matrix interface. When the location of the interface reduces, R_g increases apparently and then the zone with smaller size dissolves faster resulting in increase of average interparticle distance. When the pre-aged specimen is held at the temperature below the zone solvus, the structure change is found to be terminated into three stages. In the first two stages, the zones formed at the pre-aged temperature are partially dissolved. The behaviour is similar to that for the reversion above the zone solvus. At the later stage, that is, at the third stage, the coarsening of the zones occurs.

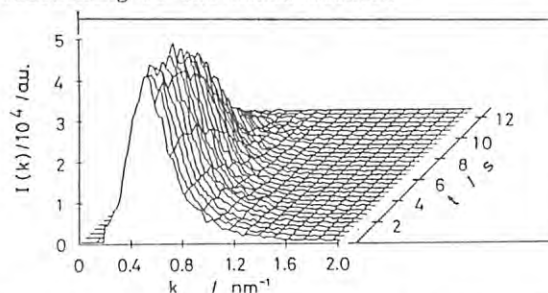


Fig. 1 In-situ SAS diagram for Al-15Zn alloy during reversion at 523 K.

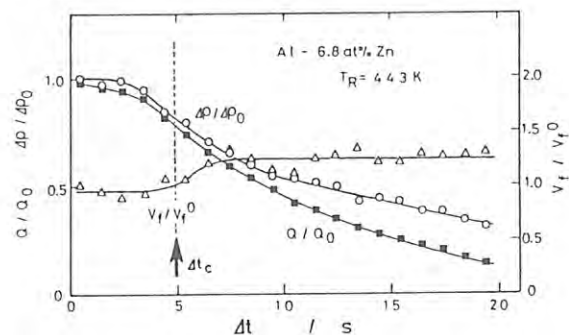


Fig. 2 Change of structure parameters as a function of reversion time.

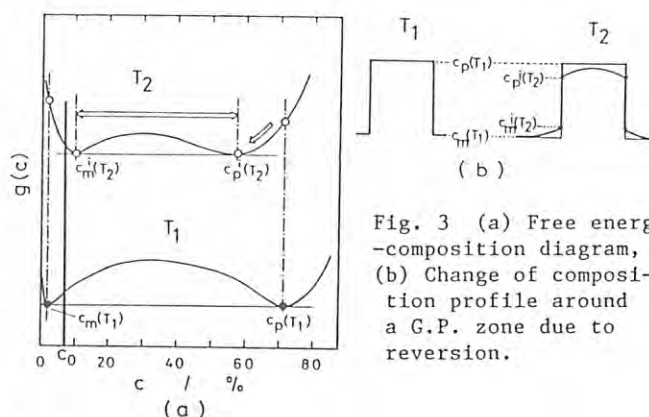


Fig. 3 (a) Free energy-composition diagram, (b) Change of composition profile around a G.P. zone due to reversion.

DYNAMICAL STRUCTURES DURING DECOMPOSITION IN Al-Li ALLOYS

Tatsuo SATO, Hiroyasu TEZUKA, Yoshiyuki AMEMIYA*, Hiroo HASHIZUME**, Tsuneo TAKAHASHI***

Department of Metallurgical Engineering, Faculty of Engineering, Tokyo Institute of Technology, O-okayama, Meguro-ku, Tokyo 152

* National Laboratory for High Energy Physics, Oho-machi, Tsukuba-gun, Ibaraki 305

** The Research Laboratory of Engineering Materials, Tokyo Institute of Technology, Nagatsuda, Midori-ku, Yokohama 227

*** Department of Metallurgical Engineering, Faculty of Engineering, Chiba Institute of Technology, Tsudanuma, Narashino 275

Introduction

Dynamical structures of GP zones in Al-Cu alloys were previously investigated by the small-angle scattering technique of synchrotron radiation. In Al-Cu alloys, platelet GP zones were found to be formed in the initial stage of decomposition, while in Al-Li alloys spherical precipitates are formed with a $L1_2$ -type ordered structure. In this work, structures and decomposition phenomena in Al-Li alloys were dynamically examined to clarify the differences in the formation kinetics between Al-Cu and Al-Li alloys.

Experimental

Polycrystalline specimens of Al-2.15 and -2.70wt%Li alloys were prepared. Diffuse scattering intensities at small angles were measured dynamically by the time-resolved technique using the small-angle scattering instrument at the BL-15A station. Specimens were solution treated at 793K and quenched into ice water, and subsequently annealed at various temperatures.

Results and Discussion

Small-angle scattering intensities for the specimens isothermally aged at 323K were continuously measured. Scattering intensities increased rapidly with the increase in aging time immediately after quenching. The diffuse scattering at small angles is due to the formation of Li aggregates which have the ordered domains morphology. Guinier radius of domains was determined from the scattering intensities and are shown in Fig.1. Guinier radii for both alloys show very rapid initial rises within 1ks and subsequently show extremely small changes. These demonstrate the fast and slow reaction processes in Al-Li alloys, which were already found out in Al-Cu alloys. The behavior of Guinier radius increase is almost similar for both Al-Li alloys. The time dependence of the calculated integrated intensities for both alloys were also similar to that of Guinier radii, although the

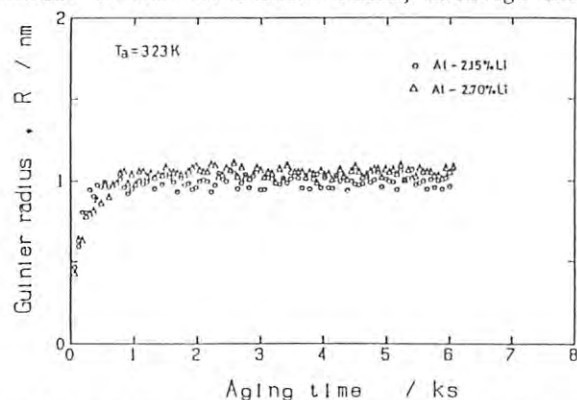


Fig.1 Changes in Guinier radius during aging at 323K.

values of the integrated intensities were higher for an Al-2.70%Li alloy than for an Al-2.15%Li alloy. Scattering intensities during heating at a constant rate of 0.03K/s are shown in Fig.2 for an Al-2.70%Li alloy. Changes in the intensities are very small up to about 400K, while intensities at smaller angles increase remarkably above 400K. Guinier radius of precipitates is shown in Fig.3. Characteristic change in Guinier radius is seen against temperatures. Guinier radius increases gradually with the increase in temperatures up to ~350K and then shows almost no changes, subsequently increases again above 410K. The increase in Guinier radius at lower temperatures is due to the formation of ordered domains which were demonstrated in Fig.1, while the increase at higher temperatures is due to the formation and growth of δ' particles. Furthermore, various structure parameters were determined and the decomposition kinetics accompanying ordering process were discussed.

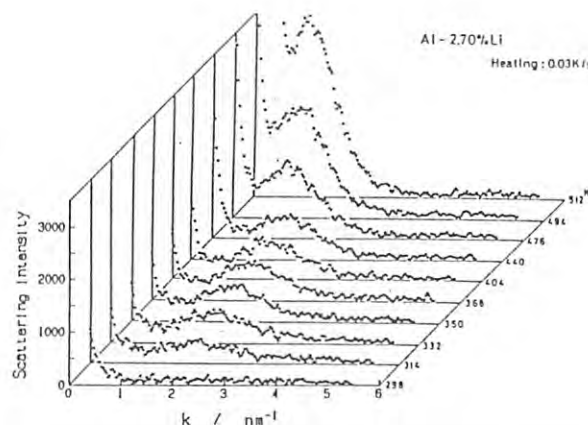


Fig.2 Small-angle scattering intensities for an Al-2.70%Li alloy during heating.

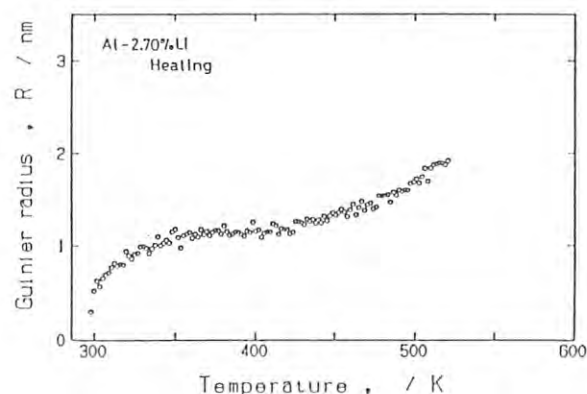


Fig.3 Changes in Guinier radius during heating.

Time-Resolved Small Angle X-ray Scattering of Polyethylene under Stretching Process

Toshiro Kojima, Hideo Nomura, Kazuhiro Chikaishi and Yoshiyuki Amemiya⁺

Sumitomo Chemical, Takatsuki Research Laboratory,
Tsukahara, Takatsuki, Osaka 569

⁺Photon Factory, National Laboratory for High Energy Physics,
Oho-machi, Tsukuba-gun, Ibaraki 305

Introduction

Structural changes under stretching of some polymers are very interesting phenomena. We have executed the 'in-situ' SAXS observation of polyethylene films using a stretching machine. The SAXS patterns of stretched polyethylene were observed statistically by Kasai et. al.¹⁾ before. In our experiments, the observation of SAXS and stretching of specimens were executed simultaneously. The observed SAXS patterns were changed according to the stretching, and we observed them by PSPC (Position Sensitive Proportional Counter).

Experiments

When we start to stretch some polyethylene films, a symmetric SAXS pattern in the early stage begins to be asymmetric. Then it will be a pattern with four points of diffractions.²⁾ We did measurements by PSPC which were parallel and perpendicular to the stretching direction. The specimens which we used were linear low density polyethylene films (Sumikasene-L FA101). The stretching speed of this experiments was about 200mm/min. The specimen was made 10% longer in a second at this speed.

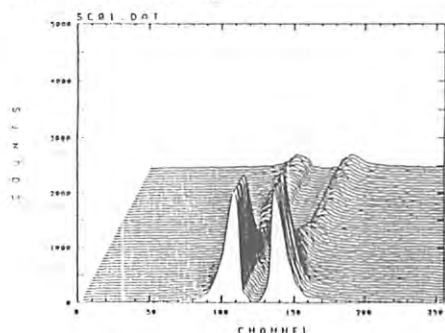


Fig.1

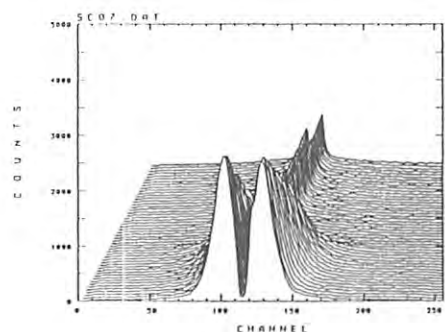


Fig.2

This was the fastest speed of this stretching machine.³⁾ The specimen size was 26(L)x15(W)x0.5(T)mm³. The observed SAXS pattern parallel to the stretching direction is shown in Fig.1. In this figure, the time resolution of PSPC accumulation was 1 sec. We can find the decrease of intensity of the first symmetric pattern. The peak position moves to higher angle by stretching. A pattern perpendicular to the stretching direction is shown in Fig.2. In this figure, new reflection was not appeared, but only diffuse scattering was observed. The tension curve versus the stretching time is shown in Fig.3.

Discussion

The first decreasing of the scattered intensity was due to the thinning of the specimen. The long period which was perpendicular to the stretching direction got bigger once, then got smaller (Fig.4). The crystalline reorientation was induced by the stretching. Crystalline models for this structural change will be described in elsewhere.

References

- 1) N. Kasai and M. Kakudo: J. Polymer Science A2 (1964) 1955.
- 2) Y. Amemiya et. al.: Photon Factory Activity Report 1986 p.306.
- 3) T. Kojima, H. Nomura, K. Chikaishi and Y. Amemiya: Photon Factory Activity Report 1987.

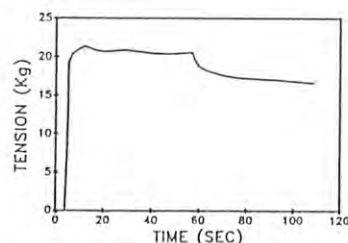


Fig.3

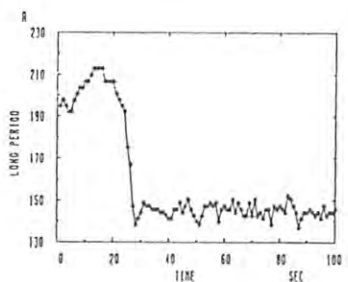


Fig.4

Development of a Stretching Device of Synthetic Polymers for Time-Resolved X-ray Scattering

Toshiro Kojima, Hideo Nomura, Kazuhiro Chikaishi and Yoshiyuki Amemiya[†]

Sumitomo Chemical, Takatsuki Research Laboratory,
Tsukahara, Takatsuki, Osaka 569

[†]Photon Factory, National Laboratory for High Energy Physics,
Oho-machi, Tsukuba-gun, Ibaraki 305

Introduction

The critical phenomena under stretching or crazing of some polymers are very interesting. For these analysis Small Angle X-ray Scattering Method is very powerful technique. But since the scattered x-ray intensity is very weak, we could not observe it in the real-time process before. By using the synchrotron radiation, we can execute the real time 'in-situ' observation under stretching. For this purpose we developed a stretching machine for some polymers, such as polyethylene or polypropylene.

Machine Feature

We show a block diagram and a photograph of this machine in Fig.1 and Fig.2.

(1)Method for Stretching

The specimen is stretched by a stepping motor. Both sides of specimen are drawn by one stepping motor simultaneously with the same velocity in the opposite direction. By this method the position which x-ray beam irradiates is not moved during the stretching.

(2)Velocity for Stretching

We can change the stretching velocity by choosing the oscillation frequency of stepping motor driver. The maximum speed is about 200mm/min. Eight steps of velocity are available. The stretching velocity is decided by following equation,

$$V = F \times 2^{-n}$$

where V is the stretching velocity, F is the frequency of oscillator and n is the velocity step.

(3)Temperature of Specimen

The highest temperature of specimen is about 200 C.

(4)Maximum Tension

The maximum tension of a specimen is 200kg. This tension is monitored by a load cell.

(5)Holder of Specimen

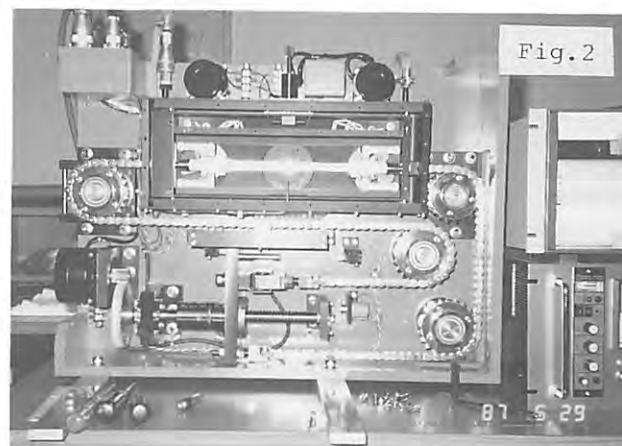
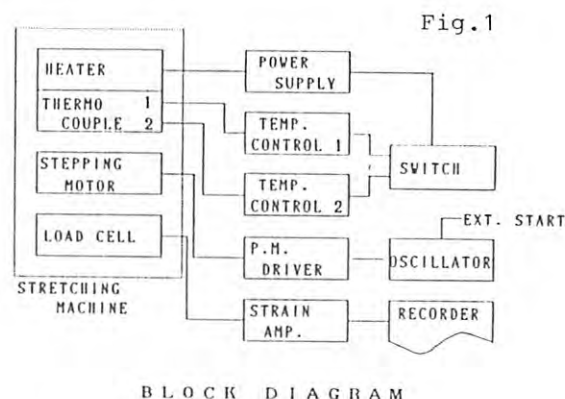
The specimen holder is supported by two rails in order to hold the vertical position of a specimen precisely, when it is weakened above the glass transition temperature.

(6)Controller

All functions of this machine are controlled from the another unit, and the external control of this unit is available. So we can make a coincidence of the data accumulation and the stretching. The temperature, stretching tension and stretched distance are recorded on a x-t recorder.

Application

We executed stretching experiments of some polyethylene and polypropylene. Experimental details will be described in elsewhere.



Imaging Analysis by Photoacoustic X-ray Absorption Spectroscopy

Tsutomu Masujima¹, Hideo Imai², Hideaki Shiwaku¹, Hiroshi Kawata⁸, Yoshiyuki Amemiya⁸, Atsuo Iida⁸, Masaharu Hoshi³, Chieko Nagoshi⁴, Shuzo Uehara⁵, Mikio Kataoka⁶, Minoru Danno⁷, Tetsuya Ikeda⁷, Hiroshi Makihara⁷, Hisanobu Yoshida¹ and Masami Ando⁸

- 1.Inst. Pharmaceutical Sci., Hiroshima Univ. School of Med., Kasumi 1-2-3, Hiroshima 734
- 2.Faculty of Pharmaceutical Sci., Fukuyama Univ., Higashimura-cho, Fukuyama 729-02
- 3.Research Inst. for Nuclear Medicine and Biology, Hiroshima Univ. Kasumi, Hiroshima 734
- 4.Inst. for Nuclear Study, Univ. of Tokyo, Tanashi, Tokyo 188
- 5.Lab. of Physics, School of Health Sci., Kyushu Univ., Maidashi, Higashiku, Fukuoka 812
- 6.Dep. of Physics, Faculty of Sci., Tohoku Univ., Sendai, Miyagi 980
- 7.Mitsubishi Heavy Ind. Ltd., Technical Head Quarters, Hiroshima Technical Inst. Kan-on-shinmachi, Hiroshima 733
- 8.KEK, National Laboratory for High Energy Physics, Oho-machi, Ibaraki 305

Introduction

Photoacoustic imaging method is useful for the analysis of localization of various components in two-dimension.¹⁾ Photoacoustic method has one advantage which can be applied to the non-destructive depth-profiling. Thus, in future, 3-dimensional analysis should be possible by this method. For the development of this possibility, the model experiments were performed.

Experimental

Focused X-ray beam at Beam Line 15A was used for this study. In order to improve the resolution, the focused beam (about 1x1.5 mm) was cut into 0.9-0.5 mm ϕ by apertures which were set just in front of the cell. Modulation frequency was 10 Hz. Scanning X-Y stage which was originally developed for the laser microscopy¹⁾ was set perpendicular to the surface of the iron-base table. The scanning and data acquisition were controlled by PC-9801VM2 microcomputer (NEC) with the original program which was developed for the imaging immunoassay.¹⁾ Various size and shape of metal foils were glued on the paper to have a model patterned sample.

Results and Discussion

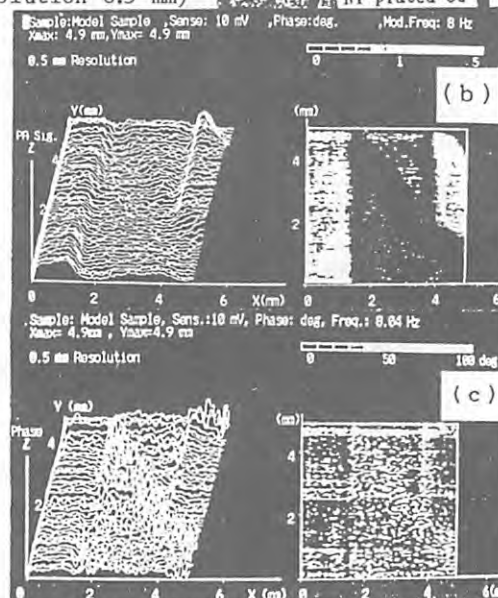
Figure 1(a) shows the microscopic picture of the model sample. The photoacoustic imagings of this sample were Fig.1(b)(photoacoustic signal amplitude) and (c)(photoacoustic phase). Since the wavelength of X-ray was 1.48Å at which the K-edge region of Ni locates, the image of signal amplitude (a) shows high region where Sn and Ni foils locate, both of which have high absorption coefficient at this wavelength. Ni-plated Cu and Cu foils gave small signal regions due to the small absorption coefficient or small amount of Ni. Even the same sample region, the difference in the amplitude can be seen. This is mainly due to the difference in the thermal state of the foil. At the high amplitude region, the metal foil

was not glued and thus was free from the backing material. In other words, this method also reveals not only the absorption profile but also the thermal circumstances. Phase image (c) was also displayed by the data processing program. The backing material(paper) gave small signal, thus phase image was noisy. In other regions, the phase values were a little different depending on the sample which seems to show the difference in the depth of the point where the heat is mainly generated. Precise data analysis is under progress.

Reference

- 1)T.Masujima, Y.Munekane et al.,Proc. of 5th International Topical Meeting on Photoacoustics and Photothermal Phenomena, Springer-Verlag Heiderberg, in press.

Figure 1. (a)The picture of a model sample, (b)image of photoacoustic signal amplitude for a model sample, and (c)image of phase for a model sample.(chopping freq. 10 Hz, resolution 0.5 mm)



X-ray Photoacoustic Effect of Gas Phase

Tsutomu Masujima¹, Yoshiyuki Amemiya², Hiroshi Kawata², Sachiko Sakura³, Masaharu Hoshi⁴, Shuzo Uehara⁵, Chieko Nagoshi⁶, Takayuki Sano⁷, Hisanobu Yoshida¹, Hideo Imai³, and Masami Ando²

1.Inst. Pharmaceutical Sci., Hiroshima Univ. School of Medicine, Kasumi, Hiroshima 734

2.KEK, National Laboratory for High Energy Physics, Oho-machi, Ibaraki 305

3.Faculty of Pharmaceutical Sci., Fukuyama Univ., Higashimura-cho, Fukuyama 729-02

4.Research Inst. for Nuclear Medicine and Biology, Hiroshima Univ., Kasumi, Hiroshima 734

5.Lab. of Physics, School of Health Sci., Kyushu Univ., Maidashi, Higashiku, Fukuoka 812

6.Inst. for Nuclear Study, Univ. of Tokyo, Tanashi, Tokyo 188

7.Faculty of Sci., Hiroshima Univ., Higashi-senda, Hiroshima 730

Introduction

X-ray photoacoustic effect of solid materials¹⁾ was observed by microphonic detection¹⁾ and revealed several aspects of the informations²⁾ which are included in the heat generation effect by X-ray absorption. It is interesting to study whether this effect can be found in other phases of the materials. The gas phase is the one which can be detectable by microphonic photoacoustic method. In order to check this possibility, the cell was modified for the measurement of this phase. Using focused beam, it was found that photoacoustic effect was observed even for this case. This finding expands the types of materials wider than before for photoacoustic X-ray absorption spectroscopy.

Experimental

The focused beam at Beam Line 15A at wavelength of 1.56Å was used for this experiment. Photoacoustic cell for gas phase measurement is shown in Fig. 1. The optical path was 10 cm (x6 mmφ) with beryllium windows (18 mmφ, 0.5mm thick) at both ends. The microphone was set at the end of the stainless micro-tube which was connected to the center of cell body. Argon and Xenon gas and air were measured. Other Photoacoustic apparatuses¹⁾ were the same as detailed elsewhere.¹⁾

Results and Discussion

Figure 2 shows some typical signal shapes of X-ray photoacoustic effect seen for the gases. The rising-up time of the signal after the starting of irradiation of X-ray is usually faster than that for solid phase. It shows that the gas has lower heat diffusivity and less heat capacity than those for the solids. The signal intensities for various samples did not show linear dependence on the absorption coefficients. When the transit X-ray beam was monitored by a fluorescence plate, only Xe gas was found to be opaque for 10 cm optical path. Thus one reason of the non-linear dependence should be the difference in gross absorption of X-ray beam. Other reason might be the difference in the

ionization rate of gases. The mechanism of the X-ray photoacoustic phenomena for gas phase is still under speculation and should be 1) some energy dissipation process into the heat energy and 2) ionization. In contrast to the solid phase, ionization process should be rather direct contribution for the photoacoustic effect.

Various gases and various states of samples are under the investigation by this method.

References

- 1) T.Masujima, H.Kawata, Y.Amemiya, N.Kamiya, T.Katsura, T.Iwamoto, H.Yoshida, H.Imai, M.Ando, Photon Factory Activity Report, 4, 114 (1986), and Chemistry Letters, 1987, 973.
- 2) T.Masujima, M.Hoshi, Y.Sugitani, T.Sano, C.Nagoshi, H.Yoshida, H.Imai, H.Kawata, Y.Amemiya, M.Ando., Photon Factory Activity Report, 4, 115 (1986), and Other papers in Photon Factory Activity Report, 5 (1987) in press.

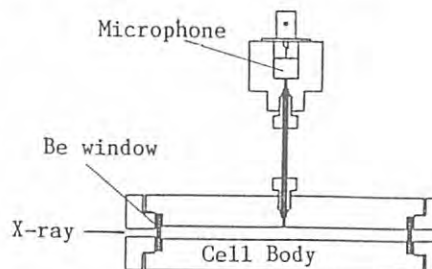


Figure 1. X-ray photoacoustic cell for the measurement of gas phase.

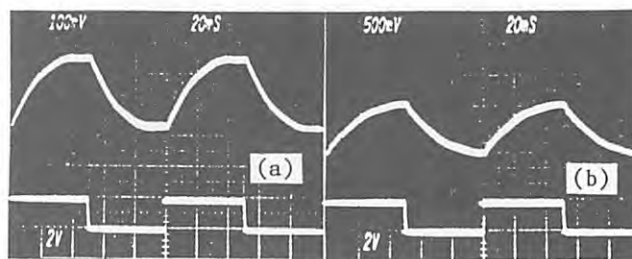


Figure 2. Photoacoustic X-ray absorption signal for gas samples. (a) Ar gas; (b) Xe gas (Chopping freq. 10 Hz)

PHOTOACOUSTIC DOSIMETRY (PAD)
- TEST OF METAL POWDER AS TARGETS -

Masaharu HOSHI¹, Tsutomu MASUJIMA², Shuzo UEHARA³, Chieko NAGOSHI⁴,
Yoshinori SUGITANI⁵, Hiroshi KAWATA⁶, Yoshiyuki AMEMIYA⁶, Katsumi KOBAYASHI⁶,
Di CHEN⁷, Shozo SAWADA¹ and Masami ANDO⁶

1. Research Institute for Nuclear Medicine and Biology, Hiroshima University, Kasumi, Hiroshima 734
2. Institute of Pharmaceutical Science, School of Medicine, Hiroshima University, Kasumi, Hiroshima 734
3. Laboratory of Physics, School of Health Sciences, Kyushu University, Higashi-ku, Fukuoka 812
4. Institute for Nuclear Study, University of Tokyo, Tanashi, Tokyo 188
5. Department of Chemistry, Tsukuba University, Sakura-mura, Ibaraki 305
6. KEK, National Laboratory for High Energy Physics, Oho-machi, Ibaraki 305
7. Beijing Institute of Radiation Medicine, 27 Tai-Ping Road, Beijing, China

Introduction

Photoacoustic spectroscopy (PAS) was applied to the dosimetry for synchrotron orbital radiation. 1,2,3) Metal foils such as Cu, Ni and Sn were found to be a sensitive target materials. We also obtained signals from plastic sheets such as Mylar and polypropylene. In this study, we tested powder samples as target. Powder will be a useful target, since heat conduction is mostly limited within small powder particle, of which characteristics are much different from metal foils.

Experiment and Results

Metal powder samples of Cu (10 μ , 100 mesh, 325 mesh), Sn (325 mesh), Al (10 μ , 200 mesh) and Fe (200 mesh) were used as target and, in addition to these, 200 - 300 mesh of Al_2O_3 powder was also used. Targets were prepared as follows; (1) both sticky tape was pasted on the top of sticky (only bottom) paper tape, (2) 8 mm or 9 mm in diameter piece was cut by scissors as a target base, (3) small amount of powder was pressed on the prepared target base. This target was pasted on the inside of a beryllium window of the photoacoustic cell. The system of the photoacoustic X-ray absorption spectroscopy (PAXAS) were detailed in refs. 1,2,3) and the measurement was performed at the beam-line 15A. The X-ray energy was 8.0 keV and maximum intensity

was about 8 kR/min. Photoacoustic signal intensities obtained from 10 μ of Cu powder, as a function of weight of the powder, are shown in Fig. 1. Target size was 9 mm in diameter. In Fig. 2, the signals from 10 μ of aluminum, 200 mesh aluminum, 200 mesh iron and 200-300 mesh aluminum oxide are also shown as a function of weight. Target size was 8 mm in diameter. Fig. 1 shows scintillation over 30 mg. This indicates limited X-ray transmission in the target material and limited heat transfer to the surface. In Fig. 2 signals from different materials with different sizes are shown. This results are useful for the analysis of the heat transfer and emission of acoustic signals.

References

- 1) T. Masujima, M. Hoshi, Y. Sugitani, T. Sano, C. Nagoshi, H. Yoshida, H. Imai, H. Kawata, Y. Amemiya and M. Ando: Photon Factory Activity Report (1985/86) p.315 (1986).
- 2) M. Hoshi, T. Masujima, C. Nagoshi, Y. Sugitani, T. Sano, S. Sawada, H. Kawata, Y. Amemiya and M. Ando: Photon Factory Activity Report (1985/86) p.313 (1986).
- 3) T. Masujima, H. Kawata, Y. Amemiya, N. Kamiya, T. Katsura, T. Iwamoto, H. Yoshida, H. Imai and M. Ando: Chem. Letters 973 (1987).

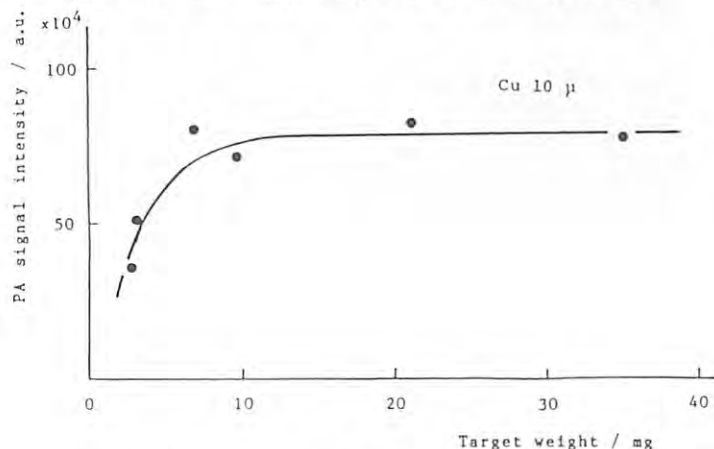


Fig. 1. Photoacoustic signals from Cu metal powder targets.

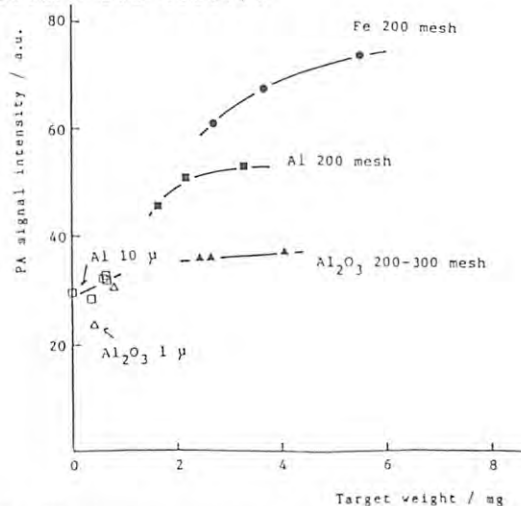


Fig. 2. Photoacoustic signals from Fe, Al and Al_2O_3 powder targets.

CORRELATION PHOTOACOUSTIC MEASUREMENT WITH SYNCHROTRON RADIATION
AS EXCITING SOURCEYoshinori SUGITANI⁺ and Kenji KATO⁺⁺⁺ Department of Chemistry, The University of Tsukuba,
Sakura-mura Ibaraki 305⁺⁺ National Chemical Laboratory for Industry,
Yatabe-machi, Ibaraki 305Introduction

Correlation photoacoustic measurement has been successfully carried out with the use of synchrotron radiation as an exciting source. The technique has two futures: one is the measurement of impulse response curve, and the other is that of the time resolved spectra of a sample. These are referred to as the first and the second kind of correlation photoacoustics, respectively^{1,2)}. The former, which has been done in the present study, can give different information on thermal and structural properties than the conventional photoacoustic method^{3,4)}.

Experimental and Results

The experiment was made at the beam lines BL4A and BL15A. A mechanical random chopper (containing 2 series of M-sequence, $n=31$) was used to modulate the X-ray beam. Chopper speed was varied from 1 to 8RPS. The photoacoustic cell was made of brass with Be windows (10mm diameter and 0.25mm thick). The signal was detected by condenser microphone. The preamplified signal was introduced into signal analyzer (IWATSU, SM2100C), and the cross correlation between photoacoustic and reference signal was obtained by integration upto 100 or 400 times. The reference signal was obtained at an optical coupler installed at the chopper. Sheets of copper foil (thickness 1 to 300 μm and diameter 10 to 15mm) and laminated sheet of copper foil and adhesive tapes were used as samples.

Figure 1 shows a correlation photoacoustic spectra obtained for the copper foil with thickness of 10 μm by integration of 100 times. T_0 and T_f is defined as the time difference

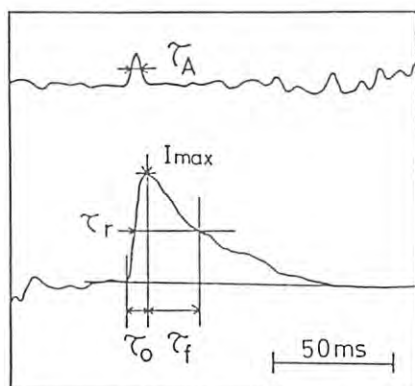


Fig. 1. Auto-correlation and impulse response curve.

between the excitation and the top of the peak and that between the top and the half height point, respectively. T_A is FWHM of an auto correlation spectra of reference signal and gives a limit of time resolution of the measuring system.

Figure 2 shows plots of T_f , T_0 and I_{max} versus sample thickness at constant chopper speed (4RPS). The maximum value of T_0 and T_f were obtained for the samples with the thickness of 50 and 10 μm , respectively. Optical penetration depth of copper for 1.37A irradiation is calculated to be about 30 μm . In the sample with thickness larger than the optical penetration depth, heat diffusion occurs and temperature of the sample surface is considered to be decreased rapidly. Supposing that heat diffusion in the sample is neglected, T_f will show a monotonic change with the increase of the sample thickness. Therefore the decrease of T_f for thick sample is considered to be due to the dissipation of heat in the sample. As for T_0 , contribution of the heat from deep level of the sample will cause an increase to the T_0 , but the dissipation of heat cancels out the contribution from deep region. On the other hand, heat radiation from sample surface of thin foils will cause the shorter T_f and larger I_{max} .

References

- 1) K. Kato, S. Ishino, and Y. Sugitani: Chem. Lett. (1980) 783.
- 2) Y. sugitani A. Uejima and K. Kato: J. Photoacoust. 1 (1982) 217.
- 3) T. Masujima et. al.: Chem. Lett. (1987) 973.
- 4) K. Kato, Y. Kobayashi, S. Aoki and Y. Sugitani: Anal. Sci., 3(1987) 275.

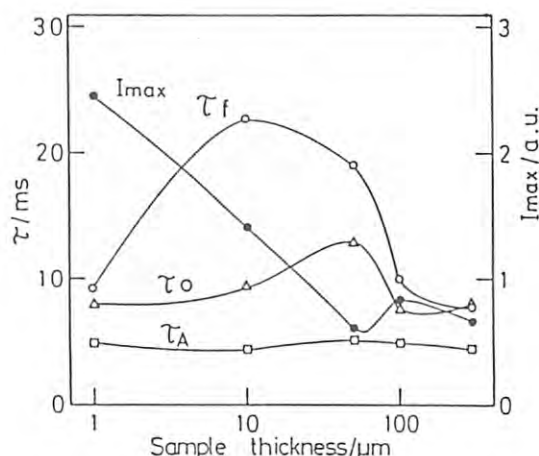


Fig. 2. Dependence of the parameters on sample thickness.

NON-DESTRUCTIVE INVESTIGATION OF THE SURFACE-DAMAGED-LAYER OF (MN,ZN) FERRITE BY X-RAY DIFFRACTION NEAR ABSORPTION-EDGE.

Yoshiro AKAGI, Mariko ISINO, Yoshiharu NAKAJIMA, and Hiroshi KAWATA*

Material Research and Analysis Center, SHARP Cooperation,
2613-1 Ichinomoto, Tenri, Nara, 632 Japan

*Photon Factory, National Laboratory for High Energy Physics,
Oho-machi, Tsukuba-gun, Ibaraki, 305 Japan

Introduction

A single crystal of ferrite, $\text{MO} \cdot \text{Fe}_2\text{O}_3$ ($\text{M}=\text{Mn}, \text{Zn}$, etc.), has been currently used as a magnetic recording device because of its excellent frequency-response. So far, details of surface-damaged-layer which originates from working processes have been studied¹⁻²⁾ by a destructive analysis, such as measurements of chemical etching rate and/or etching-pit density.

In this note, the experimental result obtained from non-destructive analysis is reported based on the fact that a penetration-depth of an X-ray incident on a specimen strongly depends on the wavelength near its absorption-edge of an element.

Experimental

Double-crystal X-ray diffraction technique was employed by using the Beam Line 15-A facilities and vertical three-axis goniometer system. Single crystal of silicon with the asymmetric (511) Bragg-case diffraction was used as the first monochromating crystal under parallel setting. For the second crystal, a specimen of (Mn,Zn) ferrite ($1 \times 3 \times 10 \text{ mm}^3$) was mounted with its normal perpendicular to the crystallographic (111) plane. K-absorption-edge of Sn, $\lambda = 0.42467 \text{ \AA}$, was used as a reference for calibration. The wavelength of X-rays incident on the specimen was varied from 0.5 to 1.8 \AA to change the penetration-depth of an X-ray.

The specimen of (Mn,Zn) ferrite was ground with the aid of carborundum (#2000) after cutting from a single crystal grown by Bridgeman method. Destructive analysis was also carried out for a comparison with the present experiment with the aid of HCl as an etchant.

Results and Discussion

Fig.1 shows the wavelength dependence of a half-width obtained from a rocking-curve measurement. Abrupt change in a half-width is observed around the wavelength of 1.7 \AA , corresponding to the K-absorption-edge of iron (1.74346 \AA) which is the main element of the present specimen. This experimental fact can only be explained by a difference in a

penetration-depth of an X-ray above and below the absorption-edge, and thus indicates that the topmost surface of the specimen is composed of structurally damaged layer. From an analysis of chemical-etching rate which is sensitive to defects, the surface-damaged-layer of the present specimen is found to reach a depth of 8 to 10 \mu m .

Taking into account the values of mass absorption coefficients and a geometrical factor, calculated value of a penetration-depth of an X-ray incident on the present specimen becomes 5 \mu m at $\lambda = 1.6 \text{ \AA}$ and 15 \mu m at $\lambda = 1.7 \text{ \AA}$, respectively. These values obtained by the present, non-destructive method are found to well explain the thickness and the structure of a surface-damaged-layer.

References

- 1) Y. Kawai, M. Tanaka and T. Ogawa, Phys. Stat. Solids A55, K119 (1979)
- 2) J. E. Knowles, J. Phys. D:Appl. Phys. 3, 1346, (1970)

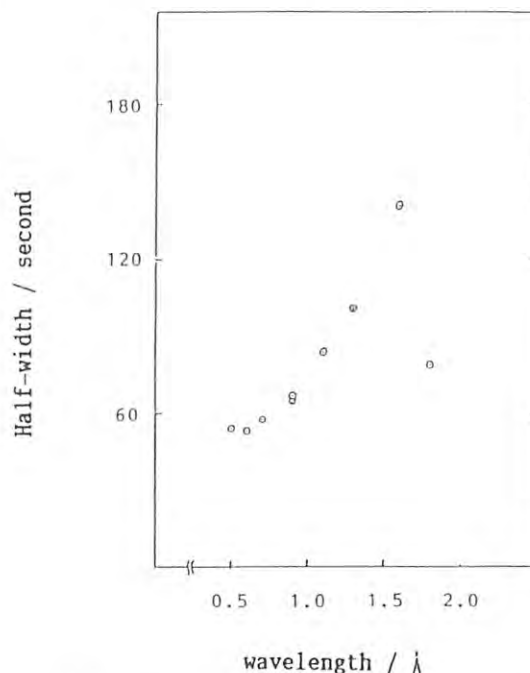


Fig.1. SR determination of a half-width of an X-ray diffraction (O) versus X-ray wavelength from 0.5 to 1.8 \AA at the KEK PF BL-15A station.

X-RAY TOPOGRAPHIC AND GONIOMETRIC STUDY OF LATTICE MISMATCHES IN InAlAs FILMS ON InP SUBSTRATES

Osamu NITTONO, Masao IRIKURA, Hiroyuki HOSHIYA, Hiroshi SUGIYAMA and Saburo SHIMIZU⁺Department of Metallurgy, Tokyo Institute of Technology,
O-okayama, Meguro-ku, Tokyo 152⁺ ULVAC Corporation, Hagisono, Chigasaki, Kanagawa 253Introduction

InAlAs films on InP substrates are promising ones as optical and electronic devices. However, it seems unlikely that device techniques have been well established for processing such films, and in order to meet the requirements of recent developments in devices, various kinds of parameters must be controlled completely by varying composition on the basis of stoichiometry. In the present study, the lattice mismatches and crystal defects in the InAlAs/InP system wafers prepared under various MBE growth conditions were examined by X-ray topography and X-ray goniometry.

Experimental

InAlAs films (0.4 μm thick) were grown onto (100) InP substrates (0.35 mm thick) by a conventional MBE growth method under the following conditions: substrate temperature of 580°C, a molecular flux of $2 \times 10^{14}/\text{cm}^2 \cdot \text{s}$ for both Al and In elements and under various As pressures. The film composition was evaluated by a photoluminescence method at 77 K. From RHEED observations, these films were found to be grown epitaxially on the (100) InP substrates. The lattice spacing of each film was investigated by a conventional X-ray diffractometer and more precisely by a double-crystal diffractometer. The crystal defects in the InAlAs/InP wafers were also examined by synchrotron X-ray Laue topography.

Experimental Results and Discussion

From the lattice spacing obtained from a peak separation in rocking curve, each film composition was also evaluated on the basis of the Vegard's law for the $(1-x)\text{InAs}-x\text{AlAs}$ alloy system. As a result, it was found that the mole fraction x of AlAs in deposited films approaches to a saturated value with increasing As pressure, as previously reported¹⁾. This suggests that the composition of

deposited InAlAs film is remarkably dependent upon the As pressure, as expected from the concept of Heckingbottom²⁾. Furthermore, the characteristic features of the lattice mismatches in the epitaxial films were investigated by measuring in detail the reflection profiles of the rocking curves from both the epitaxial film and the substrate by means of the (InP400, InAlAs400) setting goniometry, and summarized in Table. It is shown that, the sample A, which was prepared under a high As pressure, shows a small deviation from the lattice spacing of the InP crystal, and the sample D prepared at a low As pressure shows a large deviation. The lattice spacing of the (400) planes parallel to the substrate surface and the lattice mismatch for each wafer suggest that the deposited film is in a tensile stress state and thus the epitaxial film is deformed elastically in the direction normal to the substrate surface and consequently has a smaller interplanar spacing than the InP crystal. However, the sample A shows the largest half-value width, although its lattice spacing is the nearest to that of the InP crystal. This can be expected from the bending of wafer. In fact, this was confirmed by taking X-ray topographs using parallel incident X-ray beam. Therefore, the other wafers are also considered to be slightly bent, although each wafer was not examined. The observed large mismatches suggest the generation of misfit dislocations on the process of MBE growth. However, they were not observed on the present SR Laue topographs. This is probably because epitaxial film is too thin and the substrate is thick. In order to observe such misfit dislocations directly by X-ray topography, the thicknesses of both epitaxial film and substrate crystal must be taken into consideration³⁾.

References

- 1) T. Nakagawa, S. Shimizu et al.: Collected Abstracts of 1986 Autumn Meeting of OYO BUTURI, 27a-L-5.
- 2) R. Heckingbottom: J. Vac. Sci. Tech., **B3** (1985) 572
- 3) S. Kishino and M. Ogirima: Phil Mag. **31** (1975) 1239.

Table Characteristic features of $\text{In}_{1-x}\text{Al}_x\text{As}$ / InP system wafers

Sample	P_{As_4} (10^{-6}Torr)	x (PL)	x (Vegard's law)	spacing d_{400}	half-value with for substrate	lattice mismatch ($a_s - a_f$)/ a_s *
A	26.0	0.53	0.5532	1.4595	18.5"	2.62×10^{-3}
B	13.5	0.58	0.6037	1.4544	13.7"	4.30×10^{-3}
C	7.5	0.69	0.6579	1.4490	15.5"	6.0×10^{-3}
D	3.2	0.68	0.6926	1.4456	12.5"	8.0×10^{-3}
InP	----	----	----	1.46718	11.5"	-----

* $(a_s - a_f)/a_s = [(1-v)/(1+v)] [(a_s - a_f^*)/a_s]$, where $v = 1/3$.

DIRECT OBSERVATION OF LATTICE DEFECTS IN SOLID HELIUM BY SR X-RAY TOPOGRAPHY

Hideji SUZUKI, Izumi IWASA⁺, Tetsuo NAKAJIMA⁺⁺, Ichiro YONENAGA⁺⁺⁺

Tokyo Engineering University, 1404 Katakura, Hachioji, Tokyo 192

⁺Fundamental Technology Research Lab. Fuji-Xerox Co. Ltd., Ebina, Kanagawa 243-04

⁺⁺KEK, National Laboratory for High Energy Physics, Oho-machi, Tsukuba-gun, Ibaraki 305

⁺⁺⁺Institute for Materials Research, Tohoku University, Sendai 980

Introduction

We succeeded to observe the process of martensitic transformation between the hcp and bcc structures¹⁾, and also dislocations in solid helium-4 by X-ray topography^{2,3)}. The equipment used in this experiment is the same as that reported in the previous activity report⁴⁾.

Results and Discussions

Figure 1 shows successive changes of the topograph, 2134 reflection of the initial hcp structure, (a) is an annealed hcp crystal with the hcp structure, (b) transformed into the bcc structure, (c) reverse transformation: partially transformed to the hcp structure. The sharp white and black bands in (a) are small angle boundaries with misfit angles smaller than 0.1 degrees. The successive changes of the topograph in the course of martensitic transformation is well described by the mechanism proposed by Burgers⁵⁾.

The extinction distance calculated for the case of Fig. 1 is 2.5 mm and the distance between neighboring dislocations is shorter than 0.01 mm, so that the multiple reflection of X-rays is negligible. Therefore, the image of dislocations in solid helium is caused only by the orientation contrast. An estimation indicates that the image contrast of a dislocation is similar to that of a hollow cylinder with a diameter of about 1 μm . In a region, where many images of dislocations are superposed, the reflected X-ray intensity decreases considerably, so that it is most natural to suppose that the whitish regions in Fig. 1 (a) are the region of high density of dislocations.

Figure 2 shows a highly magnified topograph of the region A in Fig. 1(a). There are complicated images caused by overlap of those of many dislocations. However, sometimes we can observe individual dislocations with helical configuration with diameters of about 2 μm . Such helical dislocations are created from screw dislocations in non-equilibrium concentration of vacancies absorbing or creating vacancies to be in local equilibrium with vacancies.

References

- 1) H. Suzuki, T. Nakajima and I. Iwasa: 14th Int. Conf. Crystals Collected Abstracts (1987) C-264.
- 2) H. Suzuki, I. Iwasa and T. Nakajima: Proc. LT18 Suppl. 26-3 (1987) 405.
- 3) H. Suzuki: Kotaibutsuri 22 (1987) 983.
- 4) I. Iwasa et al.: Photon Factory, Activity Report # 4 (1986) 320.
- 5) A.J. Williams, R. W. Cahn and C. S. Barrett: Acta Met. 2 (1954) 117.

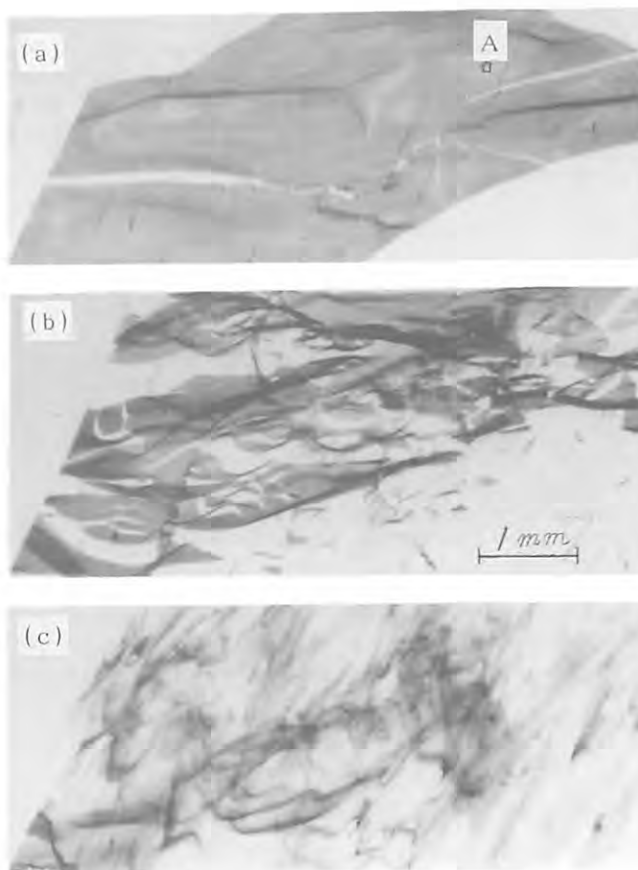


Fig. 1 Successive change of section topograph, reflection 2134 of the initial hcp crystal.

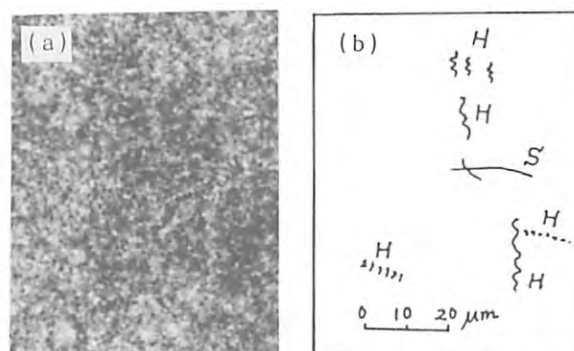


Fig. 2 (a) is highly magnified topograph of the region A in Fig. 1 (a). In (b) curves show isolated dislocations observed in (a). A letter H indicates a helical dislocation.

SECTION TOPOGRAPHY USING A HIGH-ORDER REFLECTION AND ITS APPLICATION

Yoshimitsu SUGITA, Satoshi IIDA, Hiroshi SUGIYAMA, Hiroshi TAKENO,
Yasuyoshi YAGOU, Hiroshi KAWATA*, and Jun-ichi CHIKAWA*

Department of Physics, Toyama University, 3190 Gofuku, Toyama 930

*Photon Factory, National Laboratory for High Energy Physics
Oho-machi, Tsukuba-gun, Ibaraki 305

We have measured the static Debye-Waller factor(DWF) of a heat-treated Czochralski(CZ) silicon crystal by analyzing the Pendellösung oscillation in a section topograph. With a laboratory x-ray source (MoK α), the static DWF's were measured as a function of scattering vector, (220) to (880). A linear relationship was observed between the static DWF and the square of the magnitude of the scattering vectors.¹⁾²⁾ From these results, combined with the results of the infrared absorption measurement of 1107 cm⁻¹ peak, we inferred the size of precipitates responsible for the static DWF.

Synchrotron radiation is necessary for more larger scattering vector which becomes more sensitive to lattice strain. We tried in this investigation the section topography with an extremely large scattering vector of silicon crystals having a wide variety of crystalline perfection. As a consequence, it may be possible to detect a very small strain fields caused by a cluster of impurities and or point defects. Also, we may infer the shape of a precipitate from inspecting the linear relationship of the static DWF and the square of scattering vector, in particular in a large scattering vector.

The experiments are now in progress and some results obtained so far will be described.

The experimental arrangement used is given in Fig.1. In order to avoid the polarization effect the scattering plane was made to be perpendicular to the direction of the polarization of radiation. Experiments were carried out using 0.4 Å x-ray beams monochromated with a silicon channel cut monochromator and (100)

silicon crystals with 3.1 mm in thickness.

Section topographs were taken in the (440) to (14 14 0) reflections. A static DWF was determined by analyzing the intensity distribution of the Pendellösung oscillations in a topograph, which was obtained with a microdensitometer. For the details of the analysis the reader is referred to the previous papers.¹⁾²⁾ The exposure times were varied from 0.1 to 16 h, depending on the reflection used and the degree of crystalline perfection of the crystals. Two samples were examined; one is an as-grown CZ reference crystal and another is a heat-treated CZ crystal at 800 C for 100 h.

Figure 2 is a (660) topograph of an as-grown CZ silicon, from which the static DWF of 0.045 was derived. This value is somewhat larger than as expected for a usual as-grown CZ crystal.²⁾ In more larger scattering vectors, (10 10 0) to (14 14 0), we could not observe Pendellösung oscillations, for the Pendellösung fringes were severely deformed by unexpected surface damages. We failed to determine the static DWF of the heat-treated sample, for the Pendellösung oscillations were disturbed by the generation of swirl defects running almost parallel to the the Pendellosung fringes (Fig. 3).

References

- 1) Y.Sugita et al.: Photon Factory Activity Report (1984/85) VI184 p.256.
- 2) Y.Sugita et al.: to be published in Jpn.J. Appl.Phys. 26(1987) No.11.

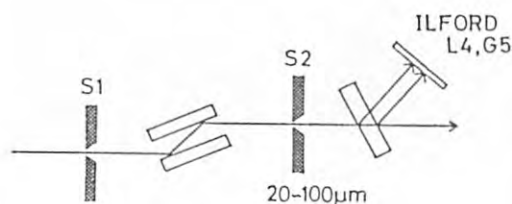


Fig.1. Experimental arrangement.

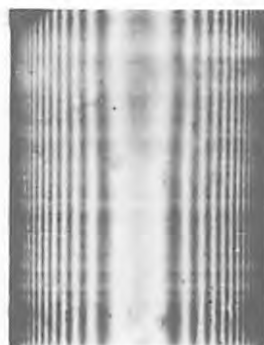


Fig. 2. (660) topograph of the as-grown CZ crystal.

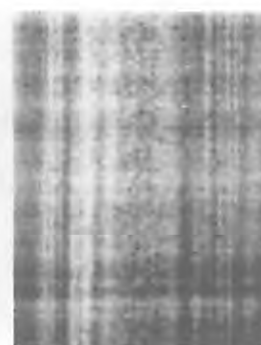


Fig. 3. (660) topograph of the heat-treated CZ crystal.

GENERATION OF LATTICE DEFECTS IN ICE AT A TEMPERATURE CLOSE TO THE MELTING POINT

Takeo HONDOH, Akira GOTO, Hidenori ANZAI and Shinji MAE

Department of Applied Physics, Hokkaido University, Sapporo 060, Japan

Introduction

X-ray topographic observations were carried out on wedge-shaped single crystals of ice for clarifying thermal behavior of dislocations near the melting temperature. According to the X-ray diffraction theory¹⁾, generation of very small defects invisible by X-ray topography can be detected by changes in spacing and visibility of Pendellösung fringes (abbreviated to P--fringes). Two cases were investigated: (1) generation by temperature change and (2) generation as premelting phenomenon in equilibrium near the melting temperature.

Experimental and Results

Specimens were carefully formed to a wedge shape with a wedge angle of about 15° by planing without chemical polishing. The specimen formed was fixed by freezing a water droplet to a specimen chamber shown in Fig.1. The chamber was cooled by circulating cooling liquid of which temperature was precisely controlled within $\pm 0.02^\circ\text{C}$. A high-speed X-ray topography camera²⁾ installed at Photon Factory was used. The observations were made mainly by 0002 and 10 $\bar{1}0$ reflections.

Fig.2 shows a series of X-ray topographs recorded on a video tape during cooling from -0.5°C to -5.2°C . Strong distortion of P-fringes are seen in the right-hand side of the specimen even before cooling ($t=0\text{s}$). This distortion must be caused by strain fields due to the defects along the right side surface, which were generated during heat treatment. At $t=75\text{s}$, spacing of P-fringes decreases and dark areal images appear in the central part of the figure. The P-fringes are blurred by the strong dark areal images at $t=150\text{s}$. As the dark areal images disappear at $t=390\text{s}$, the small dot images appear instead and the P-fringes are recovered. These dot images grow up to circular ones during aging at -5.2°C .

Although this growth process is similar to the previous observations on dislocation loops in a lower temperature range³⁾, the image of the defects observed here are different from those of dislocation loops. Detail of the structure is not known yet. Changes in spacing and visibility of P-fringes from $t=0$ to 150s must be caused by generation of very small defects which are observed as the dark areal images in the X-ray topograph.

As described above, defects are easily generated by a small temperature change in temperatures near the melting point. On the other hand, spontaneous generation of dislocations close to the melting temperature was suggested recently as a premelting phenomenon by Tamura et.al. from their experimental results on ultrasonic attenuation in ice⁴⁾. According to their results, the density of the dislocations generated at -0.1°C is of the order of 10^7 cm^{-2} , by which remarkable change in visibility of the P-fringes can be expected. However, no remarkable change in spacing and visibility of P-fringes and no defect generation were found provided that the temperature was kept constant.

References

- 1) N.Kato: Acta Cryst. A36(1980)763.
- 2) S.Suzuki, M.Ando, K.Hayakawa, O.Nittono, H.Hashizume, S.Kishino and K.Kohra: Nucl. Instr. Meth. Phys. Res. 227(1984)584.
- 3) T.Hondoh, T.Itoh and A.Higashi: J.J. Appl. Phys. 20 (1981)L737.
- 4) J.Tamura, Y.Kogure and Y.Hiki: J. Phys. Soc. Japan 55(1986)3445.

Fig.2 A series of X-ray topographs taken during cooling.

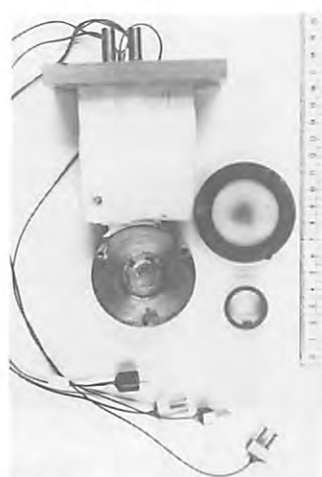
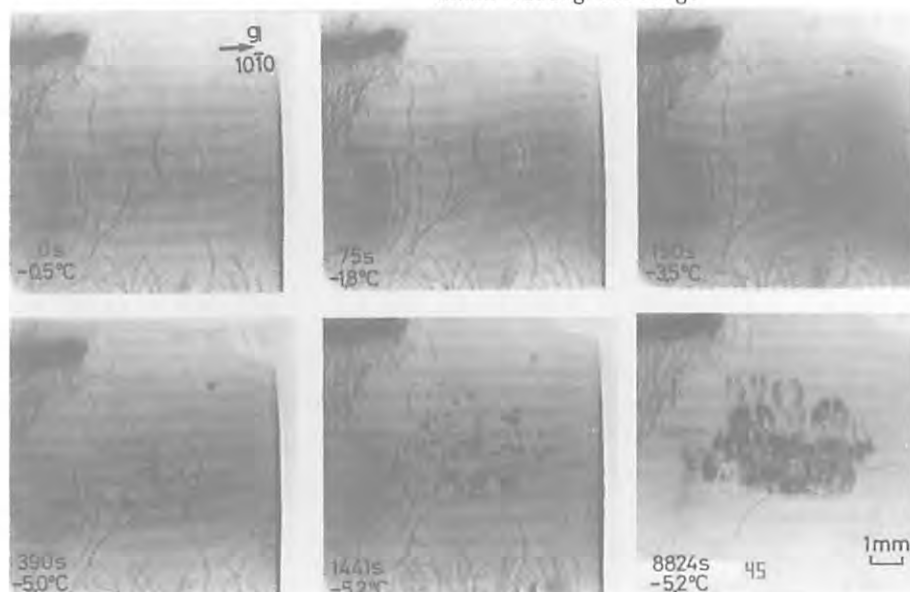


Fig.1 A specimen chamber



STRUCTURAL STUDY OF GaAs/AlAs SUPERLATTICES

Susumu Nanao, Shun Koshiba, Masataka Masuda, Yasuhiro Watanabe, Osamu Tsuda,
Hiroshi Kawata* and Masami Ando*

Institute of Industrial Science, University of Tokyo
7-22-1 Roppongi, Minato-ku, Tokyo 106, Japan.

* Photon Factory, National Laboratory for High Energy Physics
Ohomachi, Tsukuba-gun, Ibaraki 305, Japan

1. Introduction

Molecular beam epitaxy (MBE) provides high quality (Al,Ga)As/GaAs heterostructures, which enables the fabrication of novel devices such as quantum-well lasers and heterostructure transistors. The microscopic structures of the interfaces have significant effects on the characteristics of such heterostructure devices.

In the present study, the precise X-ray diffraction measurements were carried out for the X-rays just below the Ga K-edge, which provides novel information for the superlattice (SL) structure and the growth-interruption effects on the heterointerfaces through the differential information of the Ga atom arrangements.

2. Experimental

Two SL sample with the same (GaAs₆/AlAs₂)₁₂₀ structure were epitaxially grown while monitoring the in-situ RHEED oscillation in a RIBER 2300 system. One of the samples was forced to undergo growth-interruptions at every AlAs/GaAs and GaAs/AlAs heterointerface with time periods of 60 s and 30 s.

The rocking curves of the (200) substrate peak, and the 0th peak, the +1 and -1 SL satellite peaks were measured for two X-Ray energies (10.36keV and 10.16keV) beneath the K-absorption edge of Ga.

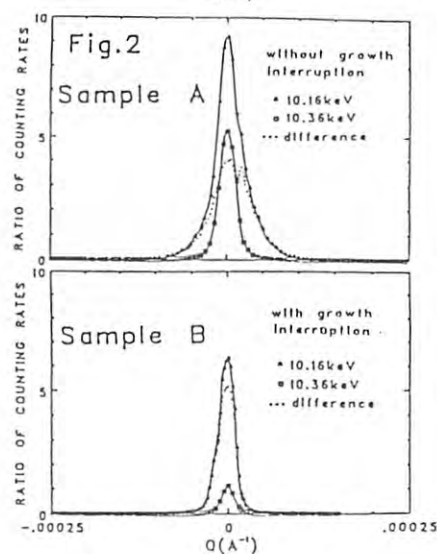
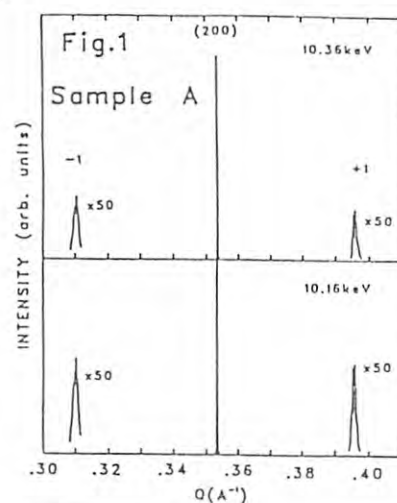
3. Results and Discussions

Figure 1 shows the overview of the diffraction profiles of the two X-ray energies, where the direction of scanning is <001>. When the energy of the X-ray was changed from 10.16keV to 10.36keV, the integral intensities decreased by about 20% for the main peak and by about 50% for the satellite peaks. These decreases were caused by the rapid decrease of the form factor of Ga with the increase of X-ray energy towards the absorption edge. The differential profile for the two X-ray energies reflects the atomic arrangement of Ga atoms and has a structure

unique to sample A.

Figure 2 illustrates the profiles of the 0th peak for the scanning of the <110> direction (this direction lies within the plane parallel to the interface) and the differential profiles for the two X-ray energies. The FWHM of the energy differential peaks of sample B are far narrower than that of sample A, which indicates that the growth interruption improved the degree of order in the arrangement of Ga atoms.

Thus all the data reflect the effect of the growth interruption which makes the interfaces smooth and clean. The detailed quantitative analysis are ongoing.



X-RAY PARAMETRIC FREQUENCY CONVERSION

Kazumichi NAMIKAWA, Masami ANDO*, Misao OHI, Shinichi ITOH**, Hiroshi KAWATA*

Department of Physics, Tokyo Gakugei University, Nukuikita-Machi, Koganei-Shi, Tokyo 184

* Photon Factory, National Laboratory for High Energy Physics, Oho, Tsukuba-Shi, Ibaraki 305

** Faculty of Engineering, Tokyo Institute of Polytechnics, Atsugi-Shi, Kanagawa 243

Introduction

When a dielectric crystal is irradiated by an intense laser beam, an oscillatory charge distribution is induced in coincidence with the lattice periodicity. An X-ray scattered from such charge distribution is different from the incident X-ray in frequency by that of the laser beam. Such phenomenon has been named as X-ray parametric frequency conversion.

This phenomenon is applicable to investigation of an excited valence charge distribution, which is an indispensable knowledge as well as a spectroscopic information to through understanding of the physics of excited state. A high resolution X-ray spectroscopy is also possible if this phenomenon is utilized with an intense monochromatic X-ray beam and variable wavelength laser. This is a preliminary report to observe the X-ray parametric frequency conversion.

Phase-matching Condition

X-ray parametric frequency conversion takes place only when so called phase-matching condition is fulfilled. This is nothing more than the energy and momentum conservation condition. This condition is realized by means of refraction and Bragg reflection, as follows. Fig. 1 illustrates the phase-matching condition.

$$\begin{aligned}\omega_i + \omega_l &= \omega_o, \\ k_i + k_l + G &= k_o, \\ k_l &= \frac{\omega_l}{c} n,\end{aligned}$$

where, ω_i , ω_l and ω_o is the frequency of the laser light, incident X-ray and scattered X-ray, respectively, k_i , k_l and k_o is the wave vector of the laser light, incident X-ray and scattered X-ray, respectively, while G is a reciprocal vector.

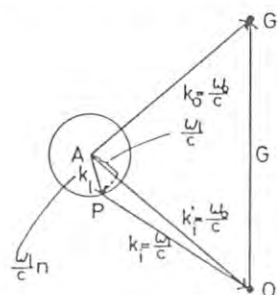


Fig. 1

Experimental

Experimental setup is illustrated in Fig. 2, where the X-ray and the laser beam is in the same plane; polarization of both beam is perpendicular to the plane. X-ray from the bending magnet BM15 was monochromated to 8.8615 keV by a Si(220) channel-cut type monochromator. A 532 nm laser beam, the 2nd higher harmonics of Nd-YAG laser, was focused on a KDP single crystal mounted with a-axis perpendicularly to the plane as illustrated in Fig.2.

We are indebted to Marubun Corp. and Mr. Y. Ohtake for the loan of Nd-YAG laser.

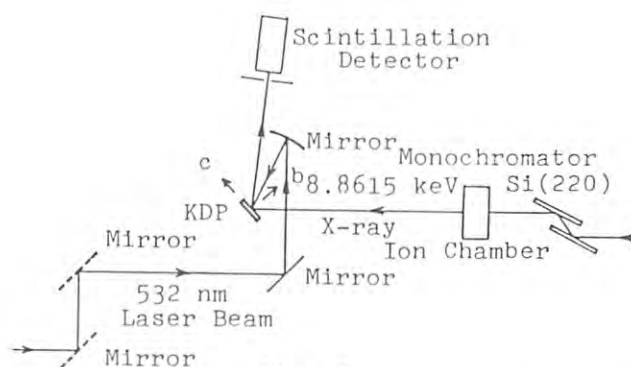


Fig. 2

The phase-matching condition is fulfilled at the low angle side tail of the rocking curve of the 080 Bragg reflection for the incident X-ray. However, the scattering probability of the present phenomenon is so small that it is hopeless to observe a satellite peak directly in rocking curve. We instead tried to observe the difference in intensity between the two time interval, one with the laser beam on, another with the laser beam off. The time chart is shown below in Fig.3.

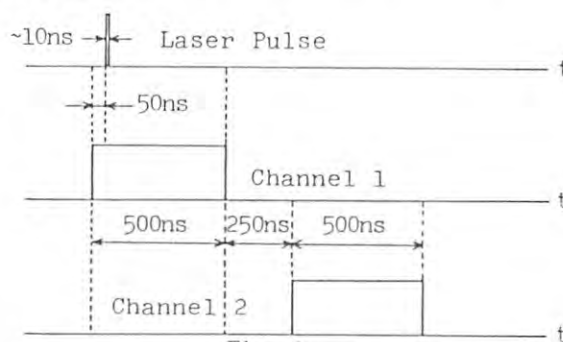


Fig. 3

Results and Discussion

The difference in intensity between the two time interval amounted to about 1%. If this difference is attributed to the X-ray parametric frequency conversion, then the scattering amplitude becomes 10^2 times or so larger than the theoretical prediction. This is by no means unacceptable, because the susceptibility of the bonding electron in a dissociating crystal is supposed to be much larger than that in a steady state. The focused area of the present sample was dissociated by an intense laser irradiation. However, other effects, such as nonlinear dc field or a thermal expansion produced by an intense laser pulse are also probable to cause the difference in intensity. More confident experiment is under preparation to eliminate these probability.

X-Ray Topography of LEC GaAs Crystal (I)

Tomohisa KITANO, Tetsuya ISHIKAWA*, Haruhiko ONO and Junji MATSUI

Fundamental Research Laboratories, NEC Corporation, 4-1-1
Miyazaki, Miyamae-ku, Kawasaki 213

* Photon Factory, National Laboratory for High Energy Physics,
Oho-machi, Tsukuba-gun, Ibaraki 305

Introduction

Dislocation distribution in (001) undoped GaAs wafers grown by an LEC method has been reported to exhibit the so-called W-shaped pattern along the diameter and four-fold symmetry on the entire wafer. Dislocation bundles were formed at the lineages and cell walls, resulting in the lattice being strongly tilted¹⁾. Reduction of dislocation density did not affect the variation of lattice spacing, but strongly affect the lattice tilt²⁾. In the present work we investigated strain field in (001) undoped LEC GaAs wafers using PWXRT. Explanation of the observed strain field was made from the viewpoint of ease of slip dislocation generation on the basis of the calculation of Schmid factor magnitude.

Experimental

Plane wave X-ray was obtained by the double crystal monochromator of (+,+) setting³⁾. The first and second crystals were (111) FZ Si. The first crystal was aligned as a monochromator to give 111 symmetric reflection and the second one as a collimator to give 553 asymmetric reflection. (001) LEC undoped GaAs crystal was aligned as a specimen at the third crystal and (008) symmetric reflection was used. A series of topographs was taken around the Bragg peak at intervals of 10 arc seconds for high and low dislocation density GaAs wafers.

Results and Discussion

Figure 1 (a) and (b) show the superimposed pattern taken for the undoped GaAs wafers with high and low dislocation density at eleven angular positions. Pronounced local strain fields were observed at eight positions between $\langle 110 \rangle$ and $\langle 100 \rangle$ radii near the periphery for a low dislocation density wafer (Fig. 1 (a)). By anomalous X-ray transmission topography, it was also observed that slip dislocations were generated along $\langle 110 \rangle$ from the periphery between $\langle 10 \rangle$ and $\langle 100 \rangle$ radii. The eight-fold circular strain field observed by PWXRT might be attributed to these slip dislocations. Explanation for slip dislocations to be preferentially generated from the periphery between $\langle 110 \rangle$ and $\langle 100 \rangle$ radii should be made. Assuming that major thermal stress was applied to tangential direction at the round ingot surface, the stress contribution to each crystallographic direction for twelve slip systems in a zincblende structure was calculated. Figure 2 shows the distribution of Schmid factor magnitude in a (001) stereographic projection. For eight out of the twelve slip systems considered the respective Schmid factor has its maximum value between $\langle 110 \rangle$ and $\langle 100 \rangle$ radii, from which directions slip dislocation can be preferentially generated. The Burgers vectors of the slip dislocation intersect the (001) plane with an angle of 60° . While, pronounced four-fold strain fields were observed at four positions near 100 radii for a high

dislocation density wafer as shown in Fig. 1 (b). This four-fold strain fields were attributed to the intersection of slip dislocations of different slip systems, generated along $\langle 110 \rangle$ from the periphery between $\langle 110 \rangle$ and $\langle 100 \rangle$ radii.

References

- 1) T. Kitano, J. Matsui and T. Ishikawa: Jpn. J. Appl. Phys. 24 (1985) L948.
- 2) T. Kitano, T. Ishikawa and J. Matsui: Jpn. J. Appl. Phys. 25 (1986) L282.
- 3) T. Ishikawa, T. Kitano and J. Matsui: Jpn. J. Appl. Phys. 24 (1985) L968.

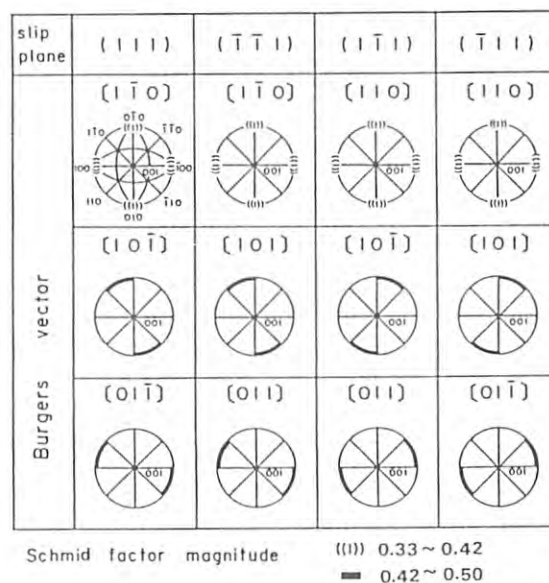
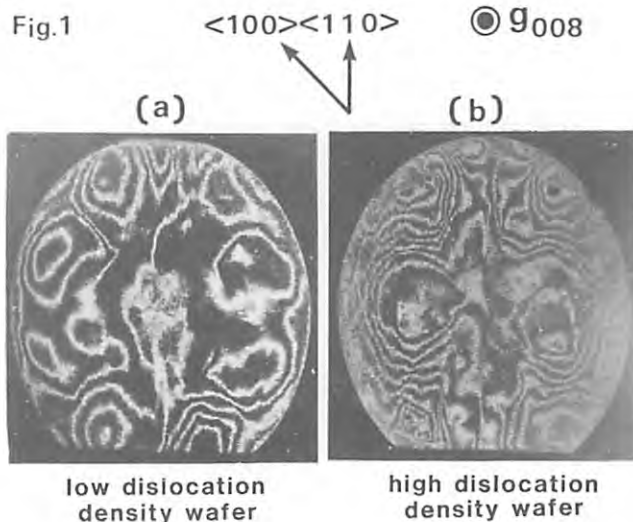


Fig. 2

Fundamental Research Laboratories, NEC Corporation, 4-1-1
Miyazaki, Miyamae-ku, Kawasaki 213

* Photon Factory, National Laboratory for High Energy Physics,
Oho-machi, Tsukuba-gun, Ibaraki 305

Introduction

Great inner stress and/or lattice distortions mainly due to thermal stress are frozen in undoped GaAs crystal grown by LEC method. It was reported that the threshold-voltages of FET was affected by two kinds of lattice distortions: One was the lattice distortion concerned with dislocation¹, and the other with variation of lattice spacing². In the present work we investigated lattice distortions in undoped LEC GaAs crystal using plane wave X-ray topography and separated variation of lattice spacing from lattice inclination quantitatively as indicated by Kikuta et al.³⁾

Experimental

A plane wave topographic camera at Photon Factory was used in the present work. Details of experimental arrangement was already reported⁴⁾. (001) undoped LEC GaAs wafer was cut to a thickness of about 3mm to avoid wafer bending due to relaxation of the frozen-in strain field. Two series of X-ray topographs were taken around the Bragg peak at 0° and 180° rotation around [001] axis.

Results and Discussion

Figure 1 shows the superimposed pattern of the topographs taken at nine positions with an interval of 10 arc sec. Dislocation distribution exhibited typical four-fold symmetry and EPD was about $4 \times 10^4 \text{ cm}^{-2}$. Figure 2 shows calculated results of distributions of (a) lattice inclination around [110] axis and (b) lattice spacing. Lattice was strongly inclined to the negative direction on the left hand periphery, and the positive direction on the right hand periphery. It was also strongly inclined to the positive direction at the left hand side of the wafer core, and to the negative direction at the right hand side of the wafer core. Lattice inclination gradually varied along [110]. Consequently, two 'eyes' due to variation of lattice inclination was observed. Variation of lattice inclination around [110] axis exhibited two-fold symmetry, or W shaped pattern along [110] diameter and was strongly related to the dislocation distribution. Degree of lattice inclination around the four [100] radii region changed from a value less than -40 arc sec to a value larger than +40 arc sec. It was observed that lattice spacing was small near the center of the wafer, and became larger toward the periphery. Degree of variation of lattice spacing changed from -1×10^{-5} to $+1 \times 10^{-5}$ on the wafer. Reducing dislocation density by the proper thermal gradient environment, degree of lattice inclination was much reduced to such values from -5 arc sec to +5 arc sec on the wafer, while the degree of variation of lattice spacing was nearly

the same as that shown in Fig.2 (b). Reduction of dislocation density did not affect the variation of lattice spacing, but strongly affect lattice inclination. It was assumed that the variation of lattice spacing was related to the distribution of native defects such as vacancies, interstitial atoms and anti-site atoms. We must further investigate the interaction between dislocation and native defects.

References

- 1) Y. Nanishi et al.: Jpn. J. Appl. Phys. 21(1980)L335.
- 2) Y. Takano et al.: Jpn. J. Appl. Phys. 24(1985)L239.
- 3) S. Kikuta et al.: Jpn. J. Appl. Phys. 5(1966)1047.
- 4) T. Ishikawa et al.: Jpn. J. Appl. Phys. 24(1985)L968.

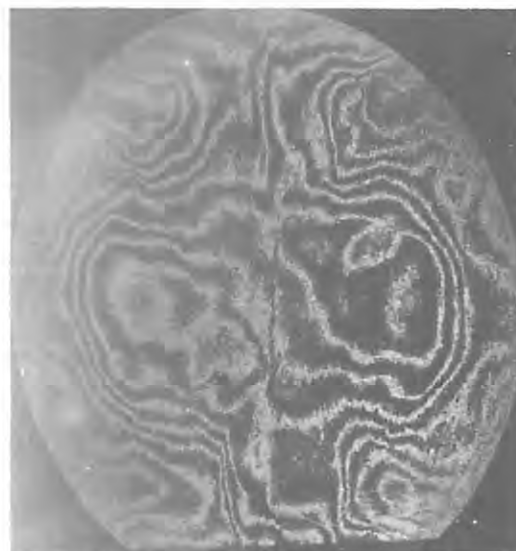


Fig.1 Superimposed pattern of topographs for undoped LEC GaAs crystal.

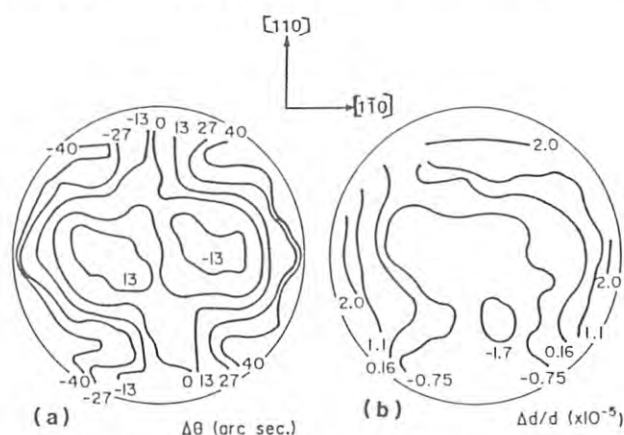


Fig.2 Distributions of lattice inclination around [110] axis and lattice spacing.

TIME-RESOLVED X-RAY MEASUREMENT SYSTEM FOR STUDYING THE STRUCTURAL CHANGE UNDER LASER IRRADIATION

Seiji KAWADO¹⁾, Shigeryu KOJIMA¹⁾, Tetsuya ISHIKAWA²⁾,
Toshio TAKAHASHI³⁾, and Seishi KIKUTA⁴⁾

1) Sony Corporation Research Center, Hodogaya-ku, Yokohama 240

2) Photon Factory, National Laboratory for High Energy Physics,
Oho-machi, Tsukuba-gun, Ibaraki 305

3) The Institute for Solid State Physics, The University of Tokyo,
Roppongi, Minato-ku, Tokyo 106

4) Department of Applied Physics, Faculty of Engineering, The
University of Tokyo, Hongo, Bunkyo-ku, Tokyo 106

Introduction

A time-resolved x-ray measurement system has been developed to investigate the annealing behavior and photo-acoustic effect²⁾ of semiconductor crystals caused by pulsed laser irradiation.

Optical arrangement and laser equipment

An example of the optical arrangement is shown in Fig.1. The monochromatic x-ray beam ($\lambda=1.54\text{\AA}$) was obtained by the 111 symmetric reflection of the first Si(111) crystal, and in the case of the elimination of the third harmonics the (110) Si crystal was used as the second monochromator. The sample was (111) Si and the dielectric mirror system led a pulsed laser beam to the sample surface. The YAG laser equipment provided a pulsed beam about 15ns wide with a diameter of 8mm and its maximum power was about 700 mJ/pulse at 1.06 μm .

Detection system

Figure 2 shows an example of the detection system using a plastic scintillation counter coupled with a gating MCP-PMT³⁾. The Q-switched trigger pulse of the YAG laser and two additional delayed pulses were used at 10Hz for the start signal of the TAC. These pulses were also used for the gate signal of the MCP-PMT in the form of 15V height and 50ns width. When the x-ray photon entered the MCP-PMT, it generated the stop signal of the TAC. The SCA output

signal was then counted by three scalars connected with the multiplexer.

Rocking curve measurement

Rocking curves were measured at the time intervals of μs and ms after the laser flashing. The rocking curves obtained from the (111) Si crystal irradiated by the laser beam with the power of 450 mJ/pulse are shown in Fig.3. A remarkable change of the profile was found at several μs after the laser flashing. The detailed study is in progress.

References

- 1) B.C. Larson et al., Phys.Rev.Lett., 48, 337 (1982).
- 2) K. Hoh, Electron.Lett., 16, 931 (1980).
- 3) T. Takahashi et al., Photon Factory Activity Report 1984/85, VI-151.

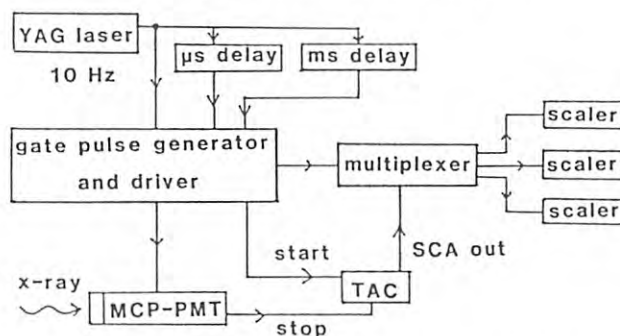


Fig.2. Block diagram of the detection system.

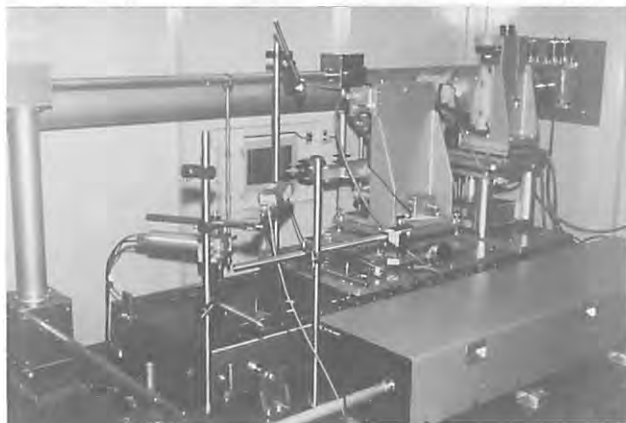


Fig.1. Experimental arrangement.

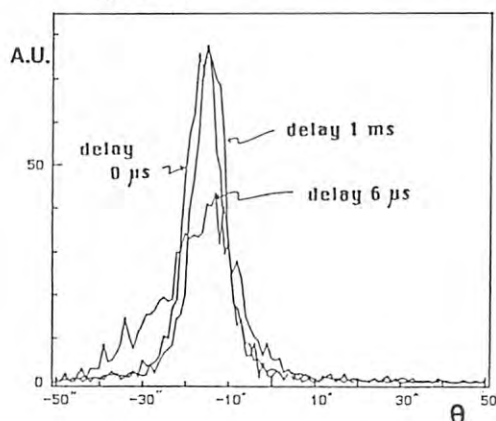


Fig.3. Time-resolved profiles of (111)Si under the pulsed laser irradiation.

OBSERVATION OF MICRODEFECTS IN A THIN SILICON CRYSTAL

BY MEANS OF ULTRA-PLANE WAVE TOPOGRAPHY

Yoshinori CHIKAURA, Hideki KI-I, Masato IMAI* and Tetsuya ISHIKAWA**

Department of Physics, Faculty of Engineering, Kyushu Institute
of Technology, Sensui-cho, Tobata-ku, Kitakyushu 804

* R & D Division, Komatsu Electronic Metals Co., Ltd., Hiratsuka 254

** Photon Factory, National Laboratory for High Energy Physics,
Oho-machi, Tsukuba-gun, Ibaraki 305Introduction

In order to observe smaller micro-defects in silicon crystals, plane-wave topography using synchrotron X-radiation has been successfully applied to thin crystals. In the last activity report(1) we described our nearly-plane wave topography using (+,-) double crystal arrangement. The angular spread of the incident beam to a thin specimen was almost one-third of the angular range of the selected diffraction in the symmetrical case. Thickness of the specimen was approximately the extinction distance ($\sim 40\mu\text{m}$) for 220 reflection used ($\sim 0.71\text{ \AA}$). The experiment revealed microdefect images which could not be observed in a normally thick ($\sim \mu\text{m}$) crystal. Because of the fairly large angular spread of the incident beam used, however, the sensitivity to minute strain around microdefects seemed not so outstanding as expected.

In the present experiment, thus, by heightening the level of plane wave we tried to improve the detectability, and obtained successful results.

Experimental and Results

The principle of the experimental set-up is shown in Fig.1. The X-ray beam is collimated in two asymmetricaly cut silicon crystal, C1 and C2. A forecrystal F reduces background noise

before the collimators. The wave length of the X-ray beam was estimated to be approximately 0.70 \AA . 220 reflection was investigated. The collimators C1 and C2 have an asymmetry factor $b_1 = b_2 = 40$, respectively. The divergence of the beam is 0.008 seconds in arc, less than 0.40% of the angular range of the selected diffraction in the symmetrical case, 2.0 seconds in arc.

Original material of the specimen is a phosphor-doped, n-type bulk crystal, CZ-grown, oxygen content 1.6×10^{18} atoms/cm, as measured by infrared spectroscopy. 0.6 mm thick wafers were cut from the bulk crystal so as to make the surface normal $[001]$. The wafers were then annealed in dry oxygen at 800°C during 8 hrs. Finally they were thinned to $80 - 100\text{ }\mu\text{m}$, only twice as thick as the extinction distance for 220 reflection by mechanochemical etching.

Fig. represents an example of observed defect images, which depend strongly on the diffraction condition. We have obtained quite clear contrast of microdefects which have not been observed by the other X-ray topography.

References

- 1)Y. Chikaura, M. Imai and T. Ishikawa: Jpn. J. Appl. Phys., 26(1987)L 889
- 2)Y. Chikaura, M. Imai and T. Ishikawa: Photon Factory Activity Report, #4(1986)327, ed by National Laboratory for High-Energy Physics

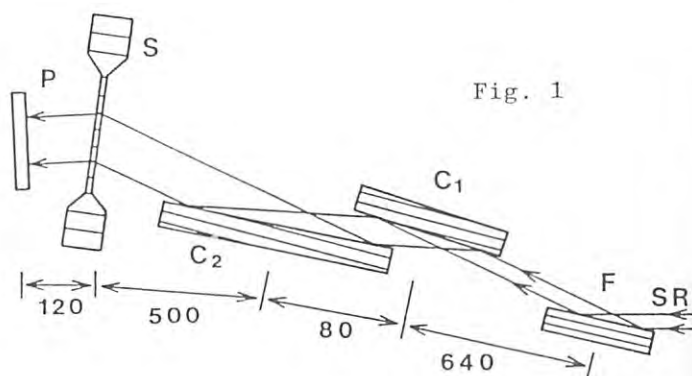


Fig. 1

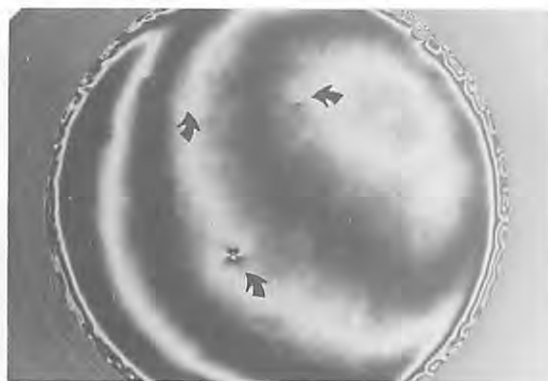


Fig. 2

A NEW GRAZING INCIDENCE MONOCHROMATOR FOR UNDULATOR RADIATION, MMM(Muramatsu-Maezawa Monochromator)-22. (1) DESIGN CONCEPT

*

Hideki MAEZAWA and Yasuji MURAMATSU

Photon Factory, National Laboratory for High Energy Physics, Ohomachi, Tsukuba-gun, Ibaraki 305

* NTT Applied Electronics Laboratories, Musashino-shi, Tokyo 180

INTRODUCTION

BL16 is a beam line designed to exploit high-brightness synchrotron radiation from a MPW(Multi Pole Wiggler) which can provide wiggler and undulator radiation. The beam line BL16 is composed of two lines. One is a main line(BL16A) for wiggler radiation and the other is a branch line(BL16C) for undulator radiation.

In order to monochromatize the undulator radiation effectively, a new monochromator should be developed. The monochromator must be matched with the radiation characteristics, and satisfied with "high resolution", "high brightness", "high accuracy" and "easy operability". In this point of view, the new monochromator for undulator radiation was designed.

DESIGN CONCEPT will be described in this paper, and OPTICAL DESIGNING and MECHANICAL DESIGNING will be described elsewhere.

DESIGN CONCEPT

(1) MATCHING FOR BL16-UNDULATOR: The MPW is composed of 53-pole permanent magnets, and their period length is 12 cm. Magnetic field is variable up to 1.5 tesla; thus a wiggler mode(1.5 tesla) and an undulator mode(0.05-0.5 tesla) can be chosen. Figure 1¹⁾ shows the radiation spectra in the Photon Factory. Photon energy range of the BL16 undulator radiation(1st harmonics) is 40eV - 400eV. Beam size and divergence are $\sigma_x = 0.655\text{mm}$, $\sigma_y = 0.225\text{mm}$, $\sigma_x' = 0.203\text{mrad}$, $\sigma_y' = 0.0117\text{mrad}$ in a low-emittance mode (2% coupling).

It is necessary for the monochromator to have a full coverage of the photon energy range and to accept the divergence.

(2) OPTICAL ARRANGEMENT: In order to design the monochromator with "high resolution" and "high brightness", a radiation source point should be regarded as an entrance slit itself, and diffracted rays can be focused enough to go through an exit slit. Moreover, the monochromator should be placed at an arbitrary position in a beam line because of the parasitic character of the branch beamline.

A combination of two cylindrical mirrors, which can be placed in tandem asymmetrically on positions between the source point and an exit slit, can focus the reflected rays vertically satisfying the 2nd-order focusing condition. If the rear mirror is replaced by a concave grating, then the diffracted rays can be focused enough to go through the exit slit with a fair resolution even without an entrance slit. An asymmetric mounting can be achieved by this arrangement. Therefore, the combination of a cylindrical mirror and a concave grating will be tried for the basic

optical arrangement. Incident angles of the mirror and the grating were set at 87° - 89° . Groove density of the grating is 1200 or 2400 lines/mm to cover the photon energy range of the undulator radiation. The radius of curvature of the grating is 2m.

Three pre-focusing mirrors(a branch mirror, a deflection mirror and the cylindrical mirror) and one re-focusing mirror will be needed to fix the focal point on a sample position. The number of these mirrors is the same as BL11A which equips a Grasshopper monochromator. However, resolution and brightness of this arrangement can be higher than that of the Grasshopper.

(3) MECHANICAL SYSTEM: In order to scan with high accuracy, the deflection mirror(M1), the cylindrical mirror(M2), and the grating(G) should be linked mechanically. All translations and rotations of M1, M2 and G should be achieved by linking only to a linear translation of the grating.

A new alignment system in a grazing incidence monochromator should be developed to achieve the "easy operability". Therefore, the new system which is composed of a knife edge and a photocathode plate was designed and constructed.

REFERENCES

- 1) Photon Factory Activity Report 1986, p.80.

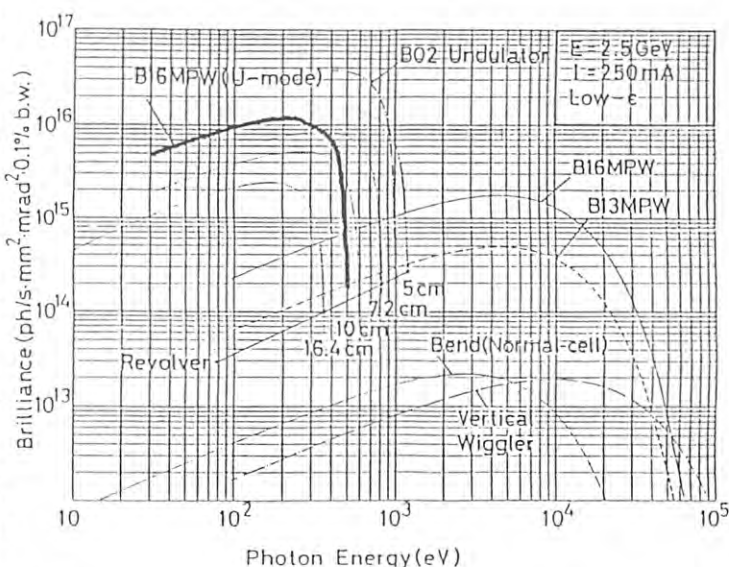


Fig.1 Synchrotron radiation spectra in the Photon Factory.

A NEW GRAZING INCIDENCE MONOCHROMATOR FOR UNDULATOR RADIATION, MMM(Muramatsu-Maezawa Monochromator)-22. (2)OPTICAL DESIGNING

Yasuji MURAMATSU and Hideki MAEZAWA

NTT Applied Electronics Laboratories, Musashino-shi, Tokyo 180

* Photon Factory, National Laboratory for High Energy Physics,
Oho-machi, Tsukuba-gun, Ibaraki 305

INTRODUCTION

A monochromator which will be equipped at a beamline BL16C must be a undulator matched monochromator. In order to match the monochromator to undulator radiation characteristics, a new optical arrangement system should be tried. The system is basically composed of a cylindrical mirror and a concave grating. Optical designing of the system and the best optical parameters will be described.

CALCULATION PROCESS

In order to determine the best optical parameters, optical calculations were carried out. The calculation processes are as follows:
(1): Fig. 1 shows a optical system of the cylindrical mirror and the concave grating. The lengths from a point source to the mirror, from the mirror to a matching point, from the matching point to the grating, and from the grating to a focussing point are rm_1 , rm_2 , rg_1 and rg_2 , respectively. An incident angle of the mirror and that of the grating are α , and a diffract angle is β . Radii of the mirror and the grating are R_m and R_g , respectively. The position and the vector at a matching point of a forward ray which is radiated from the point source to the mirror can be calculated. These calculation formulas can be expressed as 2nd order polynomials for δ which is a radiation angle of the forward ray.
(2): The position and the vector at the matching point of a backward ray which is radiated from the focussing point to the grating can be calculated as the same way of the forward ray.
(3): The positions and the vectors of the forward ray and the backward ray can be matched at the matching point. This process gives the 2nd order focussing condition.

OPTICAL PARAMETERS AND RAYTRACING

Optical calculations can be carried out taking into account that ray tracing profiles at the focussing point are within 20 micron throughout the undulator radiation spectra(1st harmonics: 50eV - 600eV). The best optical

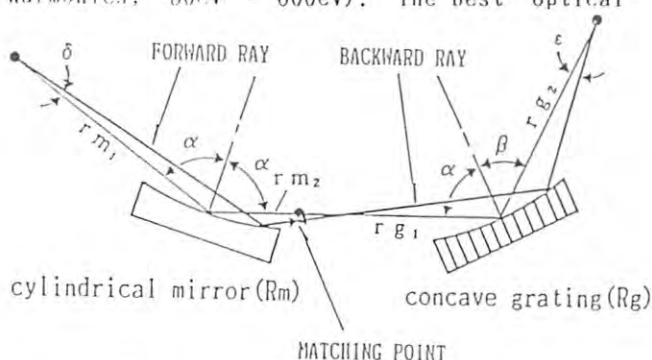


Fig.1. Optical system of a cylindrical mirror and a concave grating.

parameters were determined to be $\alpha = 87.0^\circ$, $R_g = 1.9995m$, $R_m = 1.795760m$, $rm_1 = 22.0m$, $rm_2 = 0.047092m$, $rg_1 = 0.078762m$ and $rg_2 = \cos^2\beta / ((\cos\alpha + \cos\beta)/R_g - \cos^2\alpha/rg_1)$.

Fig. 2 shows the ray tracing profiles along a exit slit width (Z) at photon energy of 100eV, 200eV, 300eV, 400eV, 500eV and 600eV, where 2400 lines/mm grating is used. Diffracted rays with photon energy from 100eV to 600eV can be focussed within 20 micron. This result means that the best optical parameters will achieve a unique monochromator with 'high resolution' and 'high brightness'.

ACKNOWLEDGMENT

The authors wish to express their thanks to Prof. T. Namioka of Tohoku University for his encouragement and cooperation in this work.

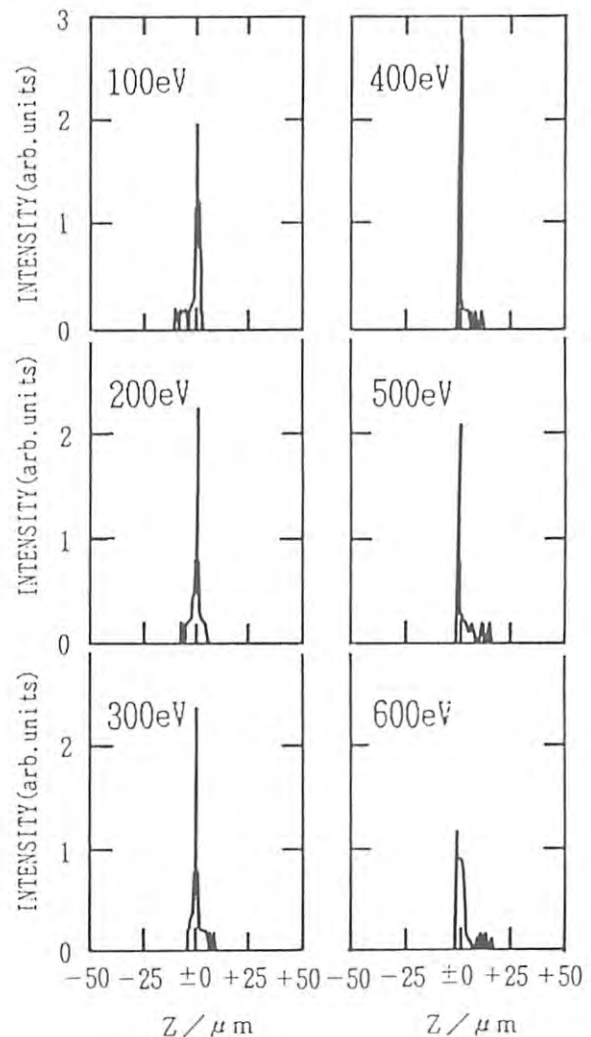


Fig.2. Ray tracing profiles at a focussing point along an exit slit width(Z).

A NEW GRAZING INCIDENCE MONOCHROMATOR FOR UNDULATOR RADIATION, MMM(Muramatsu-Maezawa Monochromator)-22. (3)MECHANICAL DESIGNING

Yasuji MURAMATSU and Hideki MAEZAWA

NTT Applied Electronics Laboratories, Musashino-shi, Tokyo 180

* Photon Factory, National Laboratory for High Energy Physics, Oho-machi, Tsukuba-gun, Ibaraki 305

INTRODUCTION

The monochromator MMM-22 which will be equipped at a beamline BL16C is designed with a new optical system that is composed of a cylindrical mirror and a concave grating. The best optical parameters were determined and reported on the previous paper, (2)OPTICAL DESIGNING. Mechanical designing concepts of MMM-22 are a mechanically linked simple mechanism and easy operability.

MECHANICAL DESIGN

Figure 1 shows a BL16C beamline optics. Undulator radiation is reflected by a branch cylindrical mirror M0 which is a Pt-coated all-SiC mirror. The radiation is focussed on an exit slit S horizontally. The reflected rays are deflected by a front plane mirror M1 into a front cylindrical mirror M2 and a concave grating G. Diffracted rays are focussed on S vertically. Exit rays are refocussed on a sample position both horizontally and vertically by a bent cylindrical rear mirror M3. MMM-22 is composed of the optical elements, M1, M2, G, S and M3. Optical brightness and cutting efficiency of high order radiation are dependent on an angle ϵ . In order to obtain high optical brightness and high cutting efficiency, ϵ is set at about 7.5° . M1, M2 and G are mounted on a same stage, and the relative position of them are fixed. Incident angles of M2 and G are fixed at 87.0° . G can be moved along a straight G-rail by a ball-screw. According to the G moving, G and M2 can be rotated and M1 can be moved straight along a straight M1 rail. The rotation angle and a length between G and S are satisfied with focussing conditions.

Figure 2 shows the side view of MMM-22. It is composed of a main chamber which includes M1, M2, G and S and a M3-chamber. Fine optical alignment of M1, M2, G and S can be achieved from outside of the chambers, because of use of flexible shaft micrometers and a new alignment system. This is another attractive point of MMM-22.

The simple mechanism and the alignment system will make MMM-22 a unique monochromator with high accuracy and easy operability.

ACKNOWLEDGEMENT

The authors wish to express their thanks to K. Akiyama of Toyama Corporation for his expert workmanship in this work.

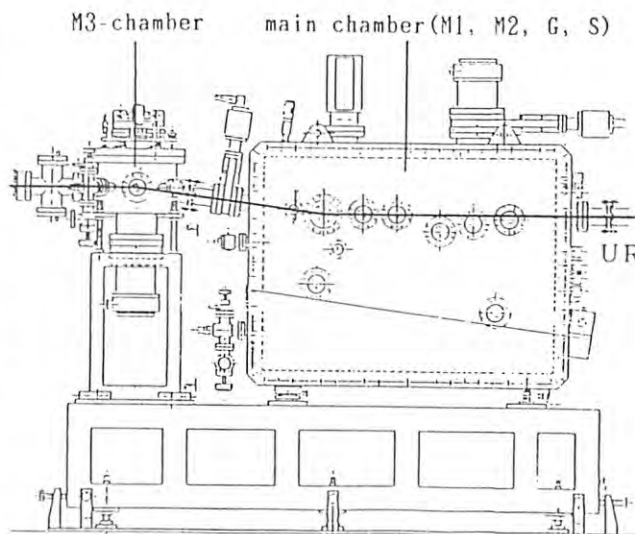


Fig.2. The side view of MMM-22.

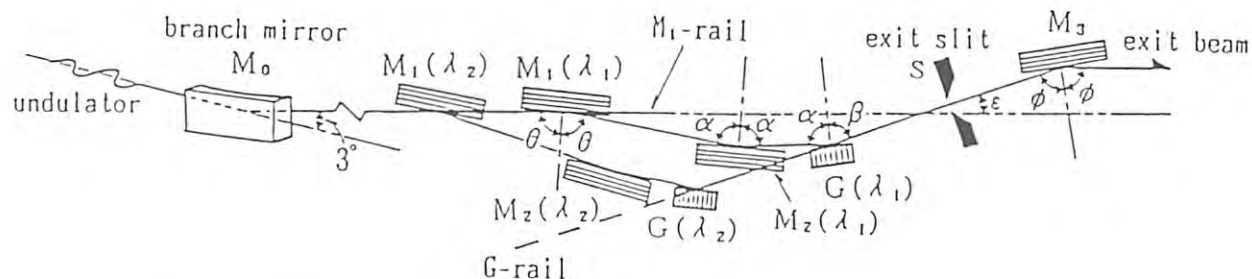


Fig.1. BL16C beamline optics showing the branch mirror M0, front plane mirror M1, front cylindrical mirror M2, concave grating G, exit slit S and rear bent cylindrical mirror M3 at two positions corresponding to wavelength λ_1 and λ_2 ($\lambda_1 < \lambda_2$).

MEASUREMENTS OF PRESSURE DEPENDENCE OF DEBYE TEMPERATURE OF ALUMINUM

Akihito MATSUMURO¹⁾, Masafumi SENOO²⁾, Ikuya FUJISHIRO²⁾, Yuichi NAKAMURA²⁾
 Masaru KOBAYASHI¹⁾, Toshihiro NAGASAKA¹⁾, Koichi MURATA¹⁾, Kazuyuki KASUMI¹⁾
 Osamu SHIMOMURA³⁾, Takumi KIKEGAWA⁴⁾

- 1) Department of Mechanical Engineering, Faculty of Engineering, Nagoya University,
 Chikusa-ku, Nagoya 464
 2) Department of Mechanical Engineering, Faculty of Engineering, Mie University, Tsu-shi, Mie 514
 3) National Institute for Research in Inorganic Materials, Sakura, Ibaraki 305
 4) Photon Factory, National Laboratory for High Energy Physics, Oho-machi, Ibaraki 305

Introduction

It is known from BCS theory that superconductivity temperature T_c depends strongly on Debye-temperature Θ which is an important parameter in solid-state lattice vibration. So determination of Θ under high pressure will enable us to estimate pressure dependence of T_c . The purpose of this study is to determine Θ of aluminum under high pressure by X-ray diffraction using energy dispersive method.

In order to avoid errors caused by the optical system, the method used in the determination of Θ is characterized by using data at a constant volume instead of a constant load.

Experimental

Particle diameter of aluminum powder was 5-10 μm . Water glass was added to the powder to suppress growths of particles. Sample was preformed by a hand press and annealed at 200 °C to remove residual strain. Fig.1 shows the sample assembly. Each diffraction pattern was measured for 300 s with a 50 °C increment from room temperature to 400 °C under a constant load using MAX80 with 6 mm truncation anvil. About ten diffraction lines from (111) were adopted and fitted to Gaussian distribution. The integral intensity were compared for two points with constant volume. From eq.(1) $\Delta 2B$ was obtained from intensity ratio and $(\sin \theta / \lambda)^2 = (1/2d)^2$ using the method of least square. And Θ was obtained by using eq.(2) and measured ΔT .

$$-\ln(I_2/I_1) = \Delta 2B (\sin \theta / \lambda)^2 \quad (1)$$

$$\Delta 2B = \frac{12 h^2 \Delta T}{m k \Theta^2} \quad (2)$$

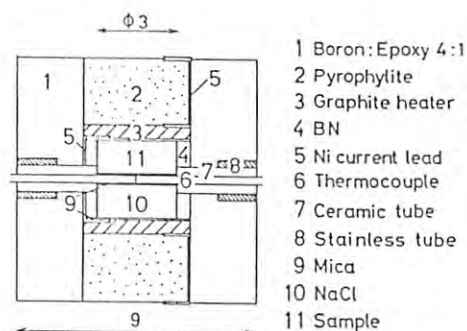


Fig.1 Sample assembly

where h is Planck's constant, k Boltzmann's constant and m the atomic mass.

Results

Fig.2 shows the results of volume dependence of Θ . Each value has about $\pm 30\text{K}$ error. In order to estimate volume dependence of Θ , data were fitted to eq.(5), which is derived from eq.(3) and (4) 1), by the least square method.

$$\gamma = - \frac{\partial \ln \Theta}{\partial \ln V} \quad (3)$$

$$\gamma = \gamma_0 (V/V_0)^\Lambda \quad (4)$$

$$\Theta = \Theta_0 \exp [\gamma_0 / \Lambda \{ 1 - (V/V_0)^\Lambda \}] \quad (5)$$

Calculated result is shown by the solid line in Fig.2, giving $\Theta_0=372\text{K}$, $\gamma_0=3.2$ and $\Lambda=0.3$. Θ_0 and γ_0 are Debye-temperature and Grüneisen constant, respectively, at room temperature and pressure. $\Theta=428\text{K}$ (OK) were calculated from elastic constants ²⁾ and $\gamma_0=2.34$ were reported ³⁾ and Λ is known to be nearly unity. The obtained Θ was lower than that calculated, but this result can be explained since Θ from X-ray is lower than that from elastic constants and heat capacity. γ_0 is a little large, but the result showing Θ increase when volume decrease is reasonable.

Reference

- 1) Decker, D.L., J. Apply. Phys., 42-8 (1971). 3239
- 2) Girifalco, L.A., "Statistical Physics of Materials", (1973). 83. John Wiley & Sons.
- 3) Read, T.D., Trans. ASME, Ser. H. 99-2 (1977). 181

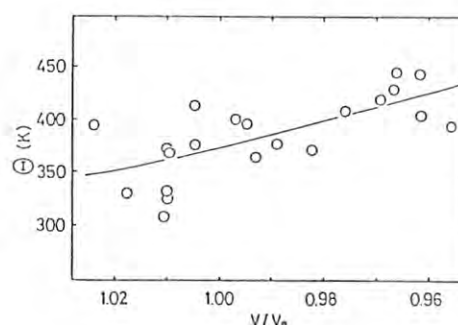


Fig.2 Volume Dependence of Debye-Temperature

STRUCTURE OF LIQUID GALLIUM UNDER PRESSURE

Kazuhiko TSUJI, Osamu SHIMOMURA*, Kenichi YAOITA,
Motoharu IMAI, Osamu ENDO and Hirohisa ENDO**

Department of Physics, Faculty of Science and Technology,
Keio University, Hiyoshi, Kohoku-ku, Yokohama 223

* National Institute for Research in Inorganic Materials,
Sakura-mura, Ibaraki 305

** Department of Physics, Faculty of Science,
Kyoto University, Sakyo-ku, Kyoto 606

Introduction

In Fig. 1, phase diagram for gallium¹⁾ is shown. The melting temperature of gallium decreases with increasing pressure. According to Clausius-Clapeyron equation, the density of liquid gallium is higher than that of α -Ga. To interpret the negative slope of melting curve, two species model was proposed where substance in liquid state consists of two species, the normal form and another form similar to the high pressure phases. In liquid selenium, the continuous phase transition to high pressure phase observed at lower pressure than the transition pressure of crystalline selenium.²⁾

There are two high pressure polymorphs of gallium, β -Ga at low temperature and γ -Ga at high temperature. The structure of β -Ga is body centered tetragonal, two atoms per unit cell. The structure of γ -Ga is orthorhombic, 40 atoms per unit cell.

Experimental

Measurements of high pressure and high temperature x-ray diffraction were performed using cubic-anvil apparatus (MAX80). The specimen of gallium was put in a capsule of teflon. X-rays from AR were diffracted by the specimen and detected by a Ge SSD in the energy range of 40-120 keV. Structure factor $S(Q)$ for liquid Ga was obtained from the diffraction intensity by taking into account the energy distribution of incident white x-ray, the absorption by specimen and pressure-transmitting medium, the form factor, etc..

Results and discussion

Examples of $S(Q)$ for liquid gallium under pressure are shown in Fig. 2. With increasing pressure, the peak positions shift towards higher Q . In Fig. 3, $S(Q)$ for gallium in various phases³⁻⁵⁾ are compared for reference. If the structure of liquid Ga is similar to that of

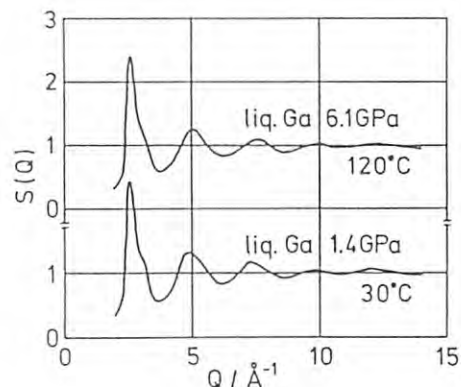


Fig. 2

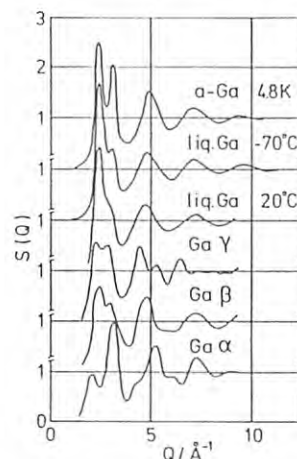


Fig. 3

γ -Ga, then the intensity of subpeak which appears at high Q side of the first peak increases with pressure and the position of second peak shifts towards low Q . However, at 6.1 GPa where the crystalline structure is γ -Ga at high temperature, $S(Q)$ for liquid gallium is similar to that for β -Ga, low temperature phase at high pressure. Detailed analysis is in progress.

References

- 1) A. Jayaraman, W. Klement Jr., R. C. Newton and G. C. Kennedy: J. Phys. Chem. Solids 24 (1963) 7.
- 2) K. Tsuji, O. Shimomura, K. Tamura and H. Endo: Proc. 6th Intern. Conf. Liquid and Amorphous Metals (August, 1986, Garmisch-Partenkirchen).
- 3) A. Bizid, A. Defrain, R. Bellissent and G. Tourand: J de Physique 39 (1978) 554.
- 4) A. Bizid, L. Bosio, H. Curien, A. Defrain and M. Dupot: Phys. Stat. Sol. (a) 23 (1974) 135.
- 5) A. Bererhi, L. Bosio and R. Cortes: J. Non-Cryst. Solids 30 (1979) 253.

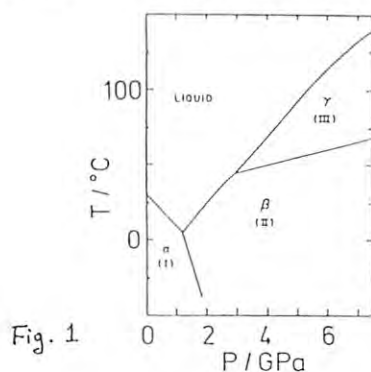


Fig. 1

MEASUREMENT OF Ni_2SiO_4 OLIVINE-SPINEL TRANSFORMATION KINETICS AT HIGH PRESSURE AND TEMPERATURE

David C. RUBIE^{*}, Yoshihiko TSUCHIDA^{*}, Wataru UTSUMI^{*},
Takumi KIKEGAWA^{**}, Osamu SHIMOMURA^{***} and Takehiko YAGI^{*}

Department of Geology, The University, Manchester M13 9PL, U.K.

^{*}Institute for Solid State Physics, The University of Tokyo,
Roppongi, Minato-ku, Tokyo 106

^{**}Photon Factory, National Laboratory for High Energy Physics
Oho-machi, Tsukuba-gun, Ibaraki 305

^{***} National Institute for Research in Inorganic Materials,
Sakura-mura, Ibaraki 305

Introduction

The kinetics of high-pressure mineral transformations may be of considerable importance in affecting the dynamics of convection in the Earth's mantle. In this study, the kinetics of the olivine to spinel transformation in Ni_2SiO_4 have been investigated in order to evaluate the effects of temperature (T) and pressure (P) on reaction rates. The very high intensity and wide energy range of the accumulator ring enables fast reaction rates to be measured in low-symmetry crystals.

Experimental

Experiments were carried out using the MAX-80 high-pressure, high-temperature, X-ray diffraction apparatus. Ni_2SiO_4 olivine powder was first hot-pressed to reduce the dislocation density and porosity, and to eliminate ultrafine-grained particles by grain growth. Pressure-temperature conditions were then changed to initiate transformation to spinel. On attaining the required P-T conditions, diffraction patterns were generally collected for 100 sec every 2 minutes until the olivine was completely transformed. (Fig.1). In one experiment (980°C, 3.6 GPa), diffraction profiles were collected at 30 sec intervals. Kinetics were measured at six different P-T conditions.

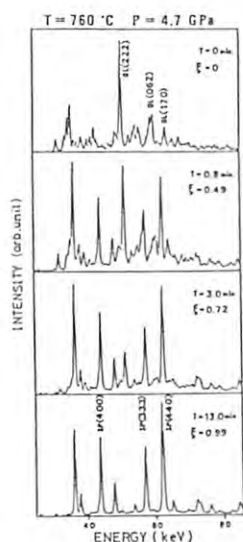


Fig.1.

Results

The position of the Ni_2SiO_4 olivine-spinel phase boundary was found to correspond closely to that determined by Akimoto et al. (1), i.e. about 0.4 GPa lower than the estimate of Ma (2).

The relative intensities of three olivine peaks and three spinel peaks, in the energy range 40-65 KeV, have been used to estimate the volume fraction of spinel as a function of time (Fig.1). The different forms of the transformation-time curves (Fig.2) result from the variation of rates of nucleation and growth with temperature and pressure. Modelling studies, combined with microstructural observations (using transmission electron microscopy), will be made to evaluate the variation of nucleation and growth rates with pressure and temperature.

References

- 1) S. Akimoto, H. Fujisawa and T. Katsura: J. Geophys. Res., 70 (1965) 1969.
- 2) C.B. Ma: J. Geophys. Res., 79 (1974) 3321.

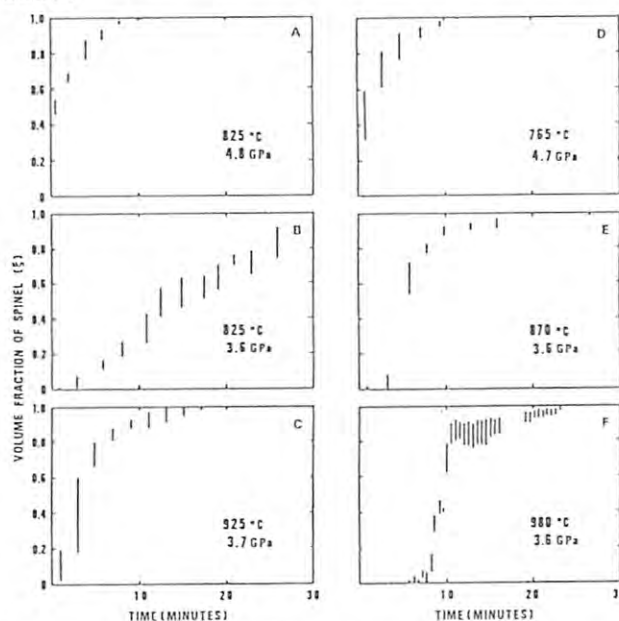


Fig.2. Transformation-time diagrams. The bars show the uncertainties in the estimates of the volume fraction of spinel.

Hydrostatic Compression of MgO-FeO to 6.2 GPa: X-ray Measurement Using Synchrotron Radiation

M.H.Manghuni¹, L.C.Ming¹, O.Shimomura², J.Sasaki³,
T.Yagi³, S.Akimoto⁴, E.Ito⁴, N.Nakagiri⁵

¹Hawaii Institute of Geophysics, University of Hawaii,
Honolulu, Hawaii 96822, U.S.A.

²National Institute for Research in Inorganic Materials,
Sakura-mura, Ibaraki 305, Japan

³Institute for Solid State Physics, University of Tokyo,
Roppongi, Minato-ku, Tokyo 106, Japan

⁴Institute for Study of the Earth's Interior, Okayama University,
Misasa, Tottori 682-02, Japan

⁵Research Development Corporation of Japan,
Toyosato, Ibaraki 300-26, Japan

Introduction

Fe/Mg ratio in magnesiowüstite ($(\text{Mg},\text{Fe})\text{O}$), which exists in the lower mantle of the earth, has been thought to be about 0.1. Recent various experimental facts suggest that this value may be larger than 0.1. From the geophysical point of view, it is essentially important to investigate the influence of the chemical composition to the characteristics of these materials under pressure. As the first stage of this study, we precisely investigated the compositional dependence of the compressibility of this system under hydrostatic condition at room temperature.

Experimentals

MgO sample was prepared by neatly crushing a single crystal, and $(\text{Mg}_{0.5}\text{Fe}_{0.5})\text{O}$ was prepared by coprecipitation method. These sample was immersed in a teflon capsule together with NaCl pressure marker. Alcohol mixture was used as pressure transmitting medium. The samples were pressurized by the MAX80 and diffraction profiles were collected with an energy dispersive method. Typical measuring time is about 500sec.

Experiments were performed at the test beam line at AR with the beam condition of 6.5GeV and 5 to 20 mA.

Results

A typical diffraction profile of $(\text{Mg}_{0.5}\text{Fe}_{0.5})\text{O}$ is shown in Figure 1. At least four or five diffraction lines for each of the two samples and NaCl at each run.

Hydrostatic compression data were obtained to 6.2 GPa for MgO (38 data points) and $(\text{Mg}_{0.5}\text{Fe}_{0.5})\text{O}$ (33 data points). Best fits to the pressure-volume data, using the Birch-Murnaghan equation and assuming K'_0 (where K_0 is the isothermal bulk modulus) values of 4.15 for MgO and 4.5 for $(\text{Mg}_{0.5}\text{Fe}_{0.5})\text{O}$, give the following values:

$$K_0 = 158.06 \pm 1.0 \text{ GPa for MgO}$$

$$K_0 = 157.24 \pm 0.7 \text{ GPa for } (\text{Mg}_{0.5}\text{Fe}_{0.5})\text{O}.$$

One striking feature is that the difference in the compression behavior of these two materials is indistinguishable in the pressure range of this study.

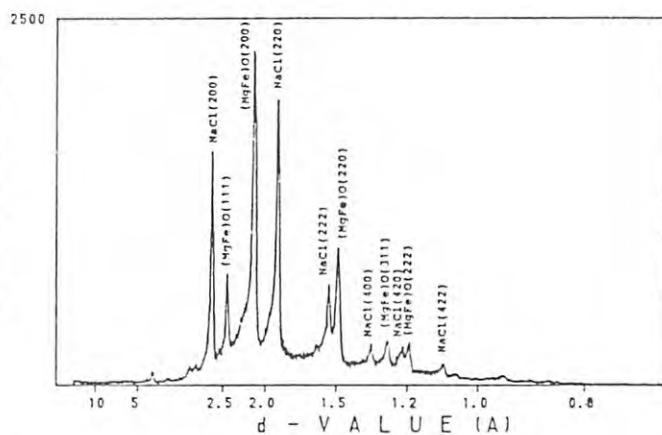


Figure 1. A diffraction pattern of $(\text{Mg}_{0.5}\text{Fe}_{0.5})\text{O}$ at 5.9 GPa.

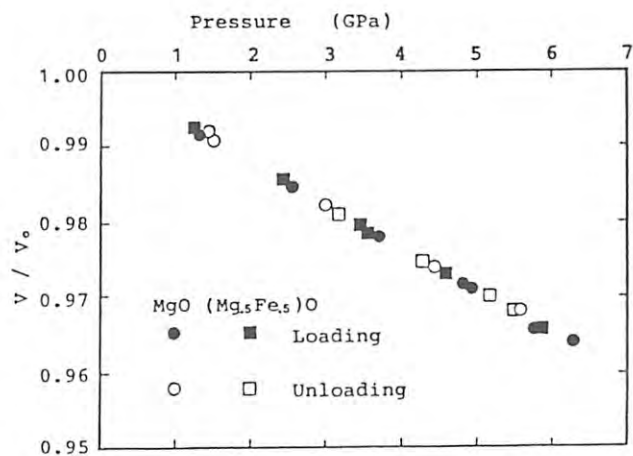


Figure 2. Volume-Pressure relation of MgO and $(\text{Mg}_{0.5}\text{Fe}_{0.5})\text{O}$ at room temperature.

HIGH PRESSURE GENERATION WITH A MULTIPLE ANVIL SYSTEM USING SINTERED DIAMOND ANVILS

E.Ohtani¹, O.Shimomura², M.Togaya³, A.Yoneda⁴, H.Sawamoto⁴, E.Itoh⁵, A.Onodera³, K.Suito³,
A.Matsumuro⁴, H.Hasizume⁴, I.Sakamoto³, W.Utsumi⁶, N.Kagawa¹, S.Tanaka⁴ and T.Kikegawa⁷

¹Ehime Univ., Matsuyama 790, Japan

²NIRIM, Sakura-mura, Ibaraki 305 Japan

³Osaka Univ., Toyonaka, Osaka 560, Japan

⁴Nagoya Univ., Chikusa-ku, Nagoya 464, Japan

⁵Okayama Univ., Misasa, Tottori 682-02, Japan

⁶ISSP, Roppongi, Tokyo 106, Japan

⁷KEK-PF, Oho-machi, Ibaraki 305, Japan

Introduction

Pressure generation of MAX80 is so far limited to about 13GPa mainly because anvils are made of tungsten carbide. One promising method to expand the pressure range is to adopt a double stage configuration. In a large pressure system, a pressure of 30GPa is generated by using a double stage configuration in which 8 truncated cubes are compressed by six first stage anvils. As this pressure is far above the yield pressure of tungsten carbide, the anvils are frequently broken after the experiments. This difficulty may be solved by using sintered diamond as anvils at the second stage. We test this possibility using the MAX80 system as a proto-type of the large volume high temperature and ultra-high pressure system.

Experimentals

Sintered diamond cubes (4.85mm cube, De Beers SYNDAX L555) were used as the second stage. A corner of each anvils was truncated by 0.5mm or 1.0 mm. A magnesia pressure transmitting medium was placed in a room composed by these truncations (Fig.1;top). The assemblage of the cubes was compressed by cubic anvils with edge size of 12mm (Fig.1;middle).

Experiments were performed at the test beam line at AR. Pressure was calibrated by measuring the lattice constant of Au which was set the center of the pressure transmitting medium. Diffraction profiles were measured by an energy dispersive method. In this double stage configuration, diffracted X-rays should pass through the second stage of anvil (Fig.1;bottom). The present sintered diamond is a mixture of diamond and SiC. So, X-ray could pass through above 30 keV.

Results

Figure 2 shows the diffraction patterns of Au at various pressure for truncated edge length (TEL) = 0.5mm. Mainly two diffraction peaks of Au were used to determine the lattice constant. The diffraction energies are obtained by referring to the characteristic X-rays of Au, which made it possible to determine the accurate pressure. The maximum pressure of 41 GPa was attained with applied load of 100 ton. The pressure difference at the position 1mm apart from the center was 1GPa at 20GPa. After the compression to the maximum pressure, the deformation of the surface of the anvils were not recognized.

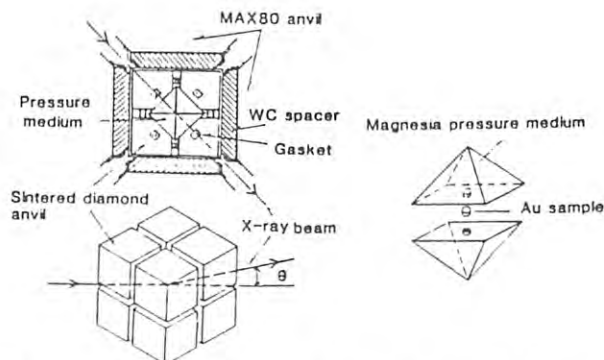


Figure 1. Configuration of the double stage system.

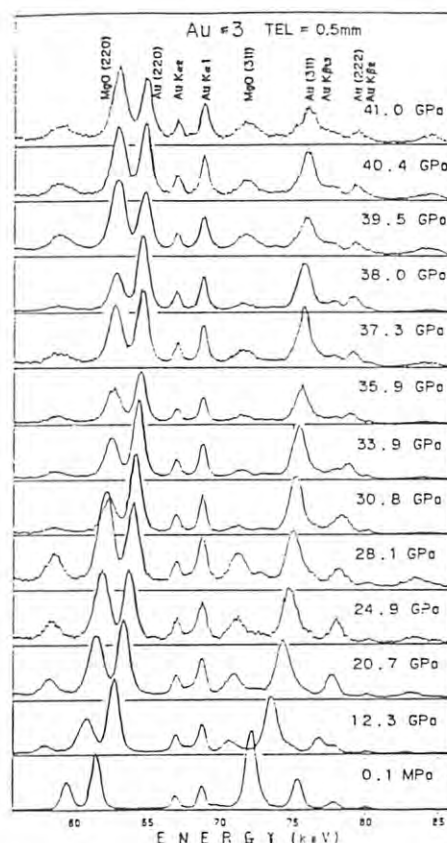


Figure 2. X-ray diffraction patterns of Au at various pressure with TEL=0.5mm anvil.

ANIMAL EXPERIMENTS BY K-EDGE SUBTRACTION ANGIOGRAPHY USING SR

Izumi ANNO⁽¹⁾, Tohru TAKEDA⁽¹⁾, Yasuro SUGISHITA⁽¹⁾, Masaki KAKIHANA⁽¹⁾, Sadanori ONTSUKA⁽¹⁾,
 Katuyuki NISHIMURA⁽²⁾, Kazuyuki HYODO⁽³⁾, Keisuke KONISHI⁽³⁾, Fukashi TOYOFUKU⁽⁴⁾, Masami ANDOH⁽³⁾,
 Akio SUWA⁽³⁾, Shin HASEGAWA⁽⁵⁾, Eiichi TAKENAKA⁽⁴⁾, Ryosuke HOSAKA⁽⁶⁾, Masayoshi AKISADA⁽¹⁾

- 1) Faculty of Medicine, The University of Tsukuba, Sakura, Ibaraki, Japan
- 2) Department of Radiology, Saitama Medical School, Moroyama, Iruma, Saitama, Japan
- 3) The National Laboratory for High Energy Physics, Ohho, Ibaraki, Japan
- 4) Department of Dentistry, Kyushu University, Fukuoka, Japan
- 5) Department of Electronics, The University of Electronics Communication, Chofu, Tokyo, Japan
- 6) Department of Radiology, National Self Defence Medical College, Saitama, Japan

Introduction

Digital subtraction angiography (DSA) is a technically advanced, noninvasive mean of sequential imaging of the vascular system. However, because of misintegration artifact due to motion such as respiration, peristalsis, and swallowing, coronary intravenous DSA has not yet been succeeded in clinical use.

The K-edge subtraction method, using the K-edge discontinuity in the attenuation coefficient of iodine, may provide a solution to this problem. Some experimental studies using this method have been performed, however clinical application has not yet been developed due mainly to the insufficient intensity.

Purpose

We are going to make the synchrotron radiation digital subtraction angiography in the above policy and in the future going to apply to the coronary ischemic disease.

Materials and Methods

Three dogs were examined to evaluate the ability of a prototype synchrotron radiation DSA unit, that we are now constructing. The dogs we used weighted approximately 15 kg in each. Six french size pigtail polyethylene catheter with multiple side holes were introduced via right femoral vein into the right atrium by the cutdown methods under conventional X-ray fluoroscopic control. The dogs were handled under general anesthesia by intravenous administration of Ketalar. The respiration of the dogs were controlled by mechanical ventilator. The respirations were hold when taking the images.

Approximately 10 to 15 ml of 76% water soluble iodinated contrast medium (Urografin 76, Schering) was injected by the automatic electronic injector at the rate of approximately 10 ml per second, respectively. Three or 4 times injection were done in each dog so as not to exceed the normal threshold excretion via renal system. Some times we used 100 microgram of nitroglycerine intravenously to dilated the coronary arteries, and also some times we used 0.1

mg/kg beta blockage agent (INDERAL) to decrease the heart rate. Subsequently, the heart rate of the dogs were decreased from 200/sec to 100. These technique is usually taken in human examinations.

The sequential images were now detected by image intensifier (RTP9204F, TOSHIBA) and recorded high signal to noise ratio videorecording system (C1900, HAMAMATSU PHOTONICS), because digital recording system had not been available until then.

The blockdiagrams of our synchrotron radiation DSA are shown in Fig. (1).

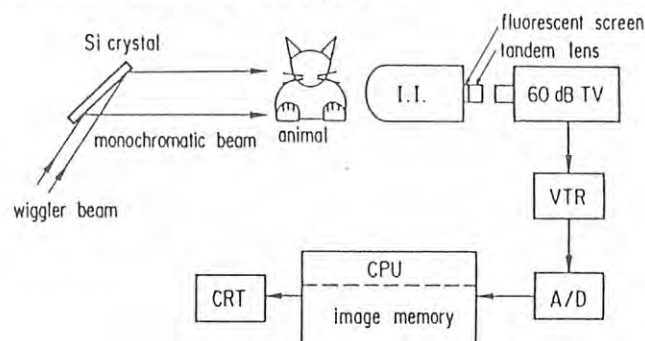


Fig. 1 Schematic diagram of the experimental system

Results

The coronary arteries are well visualized in each dog, especially in one that is given nitroglycerine. However, when there is a superimposition to the left ventricle, the coronary arteries are not fully visualized.

References

- 1) M. Akisada, K. Hyodo, M. Ando, et al. Synchrotron radiation at the photon factory for non-invasive coronary angiography: Experimental studies, Journal of Cardiology Vol. 16 No.3, p.527-534, 1986.
- 2) A. Akisada, M. Ando, K. Hyodo, S. Hasegawa, K. Konishi, K. Nishimura, A. Maruhashi, F. Toyofuku, A. Suwa and K. Kohra. An attempt at coronary angiography with a large size monochromatic SR beam. Nucl. Inst. Meth. Phys. Res. A246 (1986) 713-718.

X-RAY K-EDGE SUBTRACTION TELEVISION SYSTEM

Kiwamu SUZUKI, Shin HASEGAWA, Hiroshi FUKAGAWA, Chousaku NODA, Masami ANDO,[†]
 Kazuyuki HYODO,[†] Masayoshi AKISADA,^{††} Katsuyuki NISHIMURA,^{†††}
 Fukae TOYOFUKU,^{††††} Eiichi TAKENAKA^{†††††} and Ryosuke HOSAKA^{†††††}

The University of Electro-Communications, Chofu, Tokyo 182

[†]National Laboratory for High Energy Physics (KEK), Oho, Ibaraki 305

^{††}University of Tsukuba, Sakura, Ibaraki 305

^{†††}Saitama Medical School, Moroyama, Saitama 350-04

^{††††}Kyushu University, Fukuoka, Fukuoka 812

^{†††††}National Self Defence Medical College, Tokorozawa, Saitama 356

Introduction

An X-ray K-edge subtraction television system was investigated. The phantom is irradiated by two monochromatized X-ray beams slightly higher (HX) and lower (LX) than the K-absorption edge of iodine (33.17keV), alternately, by means of vibrating single crystal monochromator combined with synchrotron X-ray beam. The subtraction of the successive two images produced by these beams results in images that enhances signals arising from attenuation by iodine and suppresses signals by other materials.

System

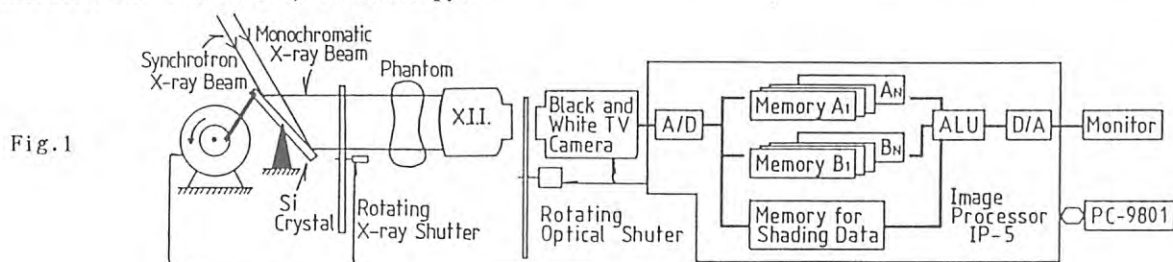
The experimental system has three groups of frame memories (512 × 512 pixels, 8bits each, two for image data, one for shading data). The memorized image data of successive two frames, one of which is obtained by HX and stored in memory A, the other by LX in memory B are processed by a personal computer (PC-9801) and an image processor (IP-5), as shown in Fig.1.

The contents of the data processing are as follows;

- (1) Correction of the shading originating from the non-uniformity of X-ray irradiation. The shading data was taken before the setting of phantoms and memorized in the memory.
- (2) Correction of dynamic range and brightness level between two images.
- (3) Logarithmic transformation.
- (4) Subtraction.
- (5) Addition of constant number to every image data to prevent pixels having negative number (complementary number) be displayed as white dots.
- (6) Gamma correction (enhancement of contrast).

Experimental Results

The iodine phantom with an aluminum step wedge and a lucite plate of 4cm thickness, as an absorber, was examined by fluoroscopy.

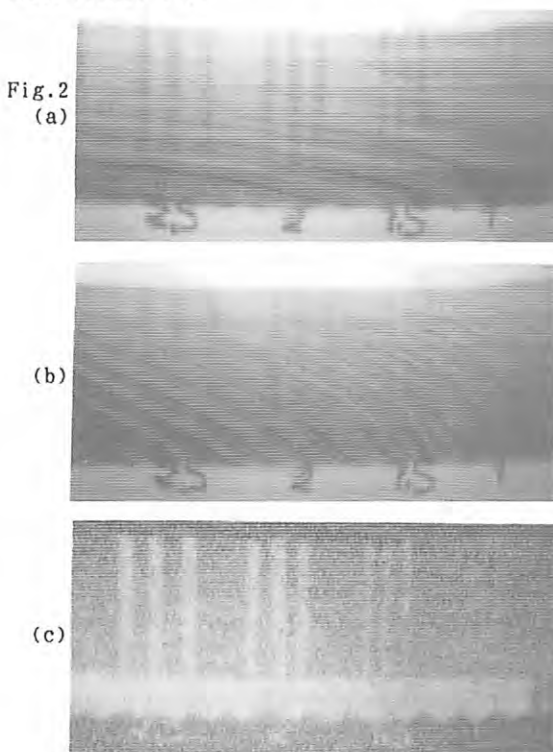


The fluoroscopic images taken by X-rays having different photon energy, HX and LX, are shown in Fig.2(a) and (b), respectively. The resulting image of the processing is shown in Fig.2(c).

Contrast material in the phantom can be identified in Fig.2(a), but cannot be identified in Fig.2(b). The iodine chart image is enhanced by signal processing, as shown in Fig.2(c).

Reference

- 1) M.Akisada, M.Ando, K.Hyodo, S.Hasegawa, K.Konishi, K.Nishimura, A.Marubishi, F.Toyofuku, A.Suwa and K.Kohra : Nucl. Instrum. Methods A246 (1986) 713.



Author Index

A		Endo, H.	203, 366	Hatano, Y.	302
Aibara, S.	155	Endo, O.	160, 163, 366	Hatsukade, I.	276
Aiura, Y.	288, 289, 298, 299	Endo, S.	290	Hatta, I.	342
Aizaki, N.	190, 191	Endo, T.	188	Hayaishi, T.	268, 269, 270, 271
Akagi, Y.	351	Esaki, N.	248	Hayakawa, K.	188
Akai, T.	218			Hayakawa, S.	130, 135, 136
Akimoto, J.	222	F		Hayase, S.	145
Akimoto, K.	190, 191, 192, 193	Fujii, K.	189	Hayashi, S.	128
Akimoto, S.	368	Fujii, Y.	147, 159	Hieda, K.	127, 128, 129, 285, 286, 287
Akisada, M.	371, 370	Fujimaki, H.	324	Higashi, T.	155
Akiya, H.	120	Fujimori, A.	295, 297, 298, 301	Higashi, Y.	166
Akiyama, M.	342	Fujimoto, K.	157	Higashiyama, H.	328
Amemiya, Y.	140, 158, 251, 252, 254, 255, 257, 324, 325, 326, 327, 328, 329, 330, 331, 332, 333, 334, 335, 336, 338, 339, 340, 342, 343, 344, 345, 346	Fujimura, T.	161	Higuchi, Y.	157
Ando, M.	125, 126, 139, 140, 166, 312, 324, 347, 348, 349, 356, 357, 370, 371	Fujimura, T.	323	Hirabayashi, M.	149, 150
Anno, I.	370	Fujisawa, H.	275	Hiragi, Y.	229, 248, 251, 253, 254, 255, 256, 257, 258, 259, 260, 262, 264
Anzai, H.	355	Fujisawa, T.	263	Hiraki, K.	325
Aoki, H.	251	Fujishiro, I.	365	Hirano, T.	223
Aoki, K.	159	Fujita, K.	173	Hirano, T.	187, 188
Aoki, S.	125, 126, 130, 310	Fujiwara, S.	254	Hirayama, H.	190, 191
Arai, A.	277	Fujiwara, S.	312	Hirosawa, I.	190, 191, 192
Arai, H.	301	Fukagawa, H.	371	Hirose, K.	192
Arai, S.	302	Fukagawa, T.	205	Honda, K.	250
Arakawa, H.	340	Fukamachi, T.	162, 165	Hondoh, T.	355
Arber, J.M.	184	Fukase, T.	211	Hori, M.	311
Artioli, G.	316	Fukamoto, N.	250	Horiike, Y.	311
Asakura, K.	180, 182, 232, 235, 238, 239, 243, 244, 245, 246, 317, 318	Fukunaga, T.	201	Horiuchi, H.	198, 316
Azami, A.	286	Fukuoka, A.	236, 241	Horiuti, K.	331
Ashida, T.	156	Fukushima, T.	233, 242	Hosaka, R.	370, 371
		Fukutani, H.	155, 288, 289, 290, 291, 295, 298	Hoshi, M.	139, 140, 347, 348, 349
		Funabashi, M.	281, 282, 283, 284	Hoshino, H.	203
		Funabiki, T.	178, 224, 240	Hoshiya, H.	352
		Furusawa, Y.	129, 285, 286, 287	Hosoya, S.	301
		Furuya, M.	261	Howe, r.f.	245
		Futemma, T.	289	Hyodo, K.	125, 126, 370, 371
		G		I	
		Garner, C.D.	184	Ichikawa, M.	236, 241
		Gohshi, Y.	130, 131, 132, 134, 135, 136, 137	Ichimura, T.	251
		Gonda, S.	206	Idei, Y.	167
		Goto, A.	355	Igarashi, Y.	341
		Goto, T.	312	Iguchi, Y.	122
		Gottardi, G.	316	Ihara, H.	149, 150
		Gouhara, K.	200	Iida, A.	121, 130, 131, 132, 133, 135, 136, 137, 138, 347
		Guo, P.	270	Iida, S.	354
		H		Iizuka, T.	148
		Haga, N.	198	Ikai, A.	340
		Hamada, I.	214	Ikawa, H.	170
		Hamanaka, T.	325, 326, 328, 335, 336	Ikeda, S.	176, 225
		Hamaya, N.	148	Ikeda, T.	140, 347
		Hanyu, T.	279, 296	Ikeda, Y.	304
		Harada, J.	146	Ikegami, K.	151
		Harada, K.	183	Ikemoto, I.	272, 273
		Harada, M.	312	Imafuku, M.	222
		Haruta, M.	237	Imai, H.	139, 140, 347, 348
		Hase, K.	159, 161	Imai, K.	142, 174
		Hasegawa, K.	319	Imai, M.	361
		Hasegawa, O.	341	Imai, M.	163, 366
		Hasegawa, S.	370, 371	Imura, T.	209, 210
		Hasegawa, Y.	144	Inada, M.	254
		Hashimoto, H.	138	Inoko, Y.	254, 263
		Hashizume, H.	320, 343, 344	Inoue, H.	262, 339
		Hasnain, S.S.	184	Inoue, Y.	216
		Hata, Y.	314,	Inui, M.	203
				Inukai, J.	182, 244, 245
B					
Bamba, N.	205, 217				
Bando, K.	243				
Burchard, W.	264				
C					
Cao, J.	277				
Chen, D.	349				
Chikaishi, K.	345, 346				
Chikaura, Y.	361				
Chikawa, J.	305, 354				
Cho, T.	310				
D					
Daimon, H.	167				
Danno, M.	347				
Dannon, J.	196				
Dobson, B.R.	184				
Domen, K.	238				
Donkai, N.	253, 258, 264				
E					
Eady, R.R.	184				
Edamoto, K.	299, 300				
Ehara, K.	165				
Ejima, Y.	129				
Emura, S.	171, 202, 206, 212, 215				

Irie, T.	290	Kato, Y.	257	Kosugi, N.	179, 231, 214, 219,
Irikura, M.	352	Katsube, Y.	257, 314		233, 234, 236, 241, 247, 272, 273,
Ishigame, M.	297	Katsuya, Y.	314		281, 282, 283, 284
Ishiguro, T.	151, 152, 153, 154	Kawabe, M.	304	Koto, K.	202, 206, 212, 215,
Ishii, H.	296	Kawado, S.	360		216
Ishii, Y.	115, 116	Kawaguchi, A.	258	Koumyouji, D.	215
Ishikawa, M.	133	Kawai, J.	280	Koyano, I.	271
Ishikawa, T.	121, 193, 267, 321,	Kawamura, H.	160	Kudo, A.	238
	358, 359, 360, 361	Kawamura, K.	213	Kurahashi, M.	250
Ishino, M.	351	Kawamura, T.	165	Kuranaka, S.	198
Itikawa, Y.	268, 269	Kawamura, T.	112, 113, 114, 115,	Kurita, K.	251
Ito, H.	171, 202, 206		116, 117	Kuroda, H.	167, 168, 169, 179,
Ito, K.	303, 306, 307, 308,	Kawase, Y.	189, 193		180, 182, 214, 219, 231, 232, 233,
	309	Kawashima, T.	135, 136, 142, 223		234, 235, 236, 238, 239, 241, 242,
Ito, T.	128, 129, 285, 287	Kawata, H.	139, 140, 166, 324,		243, 244, 245, 247, 281, 282, 283,
Ito, Y.	302		347, 348, 349, 351, 356, 354, 357		284, 317, 318
Itoh, E.	368, 369	Kawata, Y.	156	Kuroda, H.	189
Itoh, F.	201, 324	Kihara, F.	206, 212	Kuroda, S.	151
Itoh, K.	175	Kihara, H.	339, 340, 341	Kuroda, Y.	217
Itoh, S.	357	Kihara, N.	275	Kuroiwa, Y.	147
Itoh, T.	252	Ki-i, H.	361	Kusaba, K.	174
Itoh, Y.	268, 269	Kikegawa, T.	159, 160, 161, 323,	Kusuhara, H.	320
Iwabuchi, Y.	252		365, 367	Kuwabara, R.	182, 244, 245
Iwamoto, H.	332, 333, 335, 336	Kikuchi, K.	272, 273	Kyuragi, H.	120, 123
Iwasa, I.	353	Kikuchi, M.	174		
Iwasaki, H.	149, 150, 323	Kikuchi, S.	124		L
Iwasawa, Y.	180, 182, 232, 235,	Kikuchi, Y.	311		
	239, 243, 244, 245, 246, 317	Kikuta, S.	267, 360	Lablanquie, P.	303
Iwase, K.	288	Kim, E.	259	Li, G.	268
Iwazumi, T.	207, 208	Kimata, M.	197		M
Izawa, A.	159, 164	Kimura, K.	341		
Izumi, M.	207, 208	Kimura, K.	172	Mae, S.	355
Izumi, Y.	182, 244, 245	Kimura, M.	260	Maeda, F.	301
Izumi, Y.	251	Kimura, T.	236, 241	Maeda, H.	171, 205, 211, 217,
		Kimura, Y.	149, 150		221, 237, 248
	K	Kinjo, Y.	124	Maeda, I.	128
Kageyama, H.	237	Kitajima, Y.	281, 282, 283, 284	Maeda, K.	306, 307, 309
Kagoshima, Y.	125, 124, 126	Kitamoto, S.	276	Maehama, S.	300
Kaji, H.	322	Kitamura, M.	120, 123	Maekawa, H.	213
Kajita, A.	341	Kitano, T.	193, 194, 195, 358,	Maekawa, T.	213
Kajiwara, K.	243, 253, 256, 258,		359	Maeyama, S.	112, 113, 114, 115,
	259, 260, 262, 264	Kito, Y.	325		116, 117
Kakihana, M.	370	Klabunde, K. J.	181	Maezawa, H.	121, 122, 123, 124,
Kakuchi, M.	125, 126	Kobayakawa, H.	322		125, 126, 310, 362, 363, 364
Kambara, K.	290	Kobayashi, K.	124, 127, 128, 129,	Maezawa, H.	127, 128, 129, 285,
Kamigaki, K.	145		139, 140, 263, 285, 286, 287, 349		286, 287
Kamijo, N.	237	Kobayashi, M.	288	Makihara, H.	140, 347
Kamon, K.	211, 221	Kobayashi, M.	119	Makino, N.	341
Kamosaki, T.	302	Kobayashi, M.	365	Manghnani, M. H.	368
Kanai, H.	181	Kobayashi, S.	312	Marumo, F.	170, 172, 177, 213,
Kanamaru, F.	212, 215, 216	Kobayashi, T.	333, 335, 336		315
Kaneda, K.	312	Kobayashi, T.	237	Maruyama, H.	205
Kaneko, K.	179	Kobayashi, Y.	114	Maruyama, T.	288
Kaneko, T.	119	Kobayashi, Y.	250	Masaki, K.	313
Kanisawa, K.	288	Kobuke, M.	156	Masaki, N.	260
Kasai, N.	313	Kogiso, M.	199	Masuda, K.	313
Kashihara, Y.	146	Koide, T.	274, 275, 278, 288,	Masuda, M.	168, 169
Kashiwagura, N.	146		295, 297, 298, 301	Masuda, M.	356
Kashiwase, Y.	199	Koike, Y.	218	Masuda, S.	292, 293, 294
Kasumi, K.	365	Koizumi, H.	302	Masujima, T.	139, 140, 347, 348,
Kataoka, M.	139, 140, 251, 252,	Koizumi, T.	265, 268, 269		349
	254, 255, 257, 259, 261, 262, 263,	Kojima, I.	250	Matsubara, E.	183
	327, 328, 347	Kojima, S.	360	Matsubara, I.	329, 330, 331
Katayama, Y.	203	Kojima, T.	345, 346	Matsubara, T.	149, 150
Kato, H.	288, 289, 290, 291,	Komano, H.	311	Matsubayashi, N.	225, 231, 247
	292, 293, 294, 295, 296, 298, 299,	Konaka, S.	321	Matsui, J.	190, 191, 192, 193,
	300	Kondo, Y.	279		194, 195, 358, 359
Kato, K.	350	Kondoh, N.	173	Matsumoto, A.	179
Kato, N.	200	Kondoh, T.	310	Matsumuro, A.	365
Kato, S.	342	Konishi, K.	370	Matsuo, T.	265, 268, 269
		Koshiha, S.	356	Matsuoka, S.	342
				Matsusaka, H.	204

Matsushita, T.	147, 148, 149, 150,	Nakao, M.	305	Parkinson, W. H.	308
151, 152, 153, 154, 158, 184		Nakasako, M.	255, 261, 327, 328	Phizackerley, R.	158
Matsuura, E.	207, 208	Nakatani, S.	267	R	
Miki, K.	313	Nakayama, S.	277		
Minato, I.	320	Nakayama, T.	176	Rao, L.	236, 241
Ming, L. C.	368,	Namatame, S.	319	Richtering, W.	264
Minoura, M.	199	Namba, H.	167, 168, 169	Rinaldi, R.	316
Misu, A.	288	Namikawa, K.	357	Rubie, D. C.	367
Mitsubashi, T.	321	Namioka, T.	277, 306, 308, 309		
Mitsui, T.	325, 326, 335, 336,	Nanao, S.	356	S	
337		Nasu, H.	209, 210		
Miyahara, T.	112, 113, 114, 115,	Nasu, T.	201	Saeki, Y.	330
116, 117, 167, 289, 295, 296, 297,		Nihei, Y.	280	Sagawa, Y.	246
298, 300, 301		Niki, R.	253	Saigo, S.	148
Miyake, A.	276	Nishi, F.	165	Saito, K.	272, 273
Miyana, T.	176, 225	Nishijima, A.	231, 247	Saito, K.	118
Miyazaki, E.	300	Nishimura, K.	370, 371	Saito, Y.	320
Mizukami, A.	305	Nishimura, Y.	178	Saitoh, N.	134
Mizuki, J.	190, 191, 192, 193	Nishino, J.	312	Sakabe, K.	155
Mizuta, M.	194	Nitto, O.	352	Sakabe, N.	155
Mizutani, H.	178, 224, 240	Noda, C.	371	Sakai, J.	261
Mizutani, T.	192	Noda, Y.	221	Sakai, N.	324
Mochiki, K.	319	Nomachi, I.	174, 223	Sakamoto, K.	187
Mochizuki, A.	135, 136	Nomura, H.	345, 346	Sakamoto, K.	152
Mori, I.	311	Nomura, M.	139, 170, 173, 175,	Sakamoto, T.	152
Mori, K.	122	184, 203, 226, 227, 228, 230, 310		Sakane, H.	176
Mori, M.	162, 199	Nukui, A.	141, 144	Sakashita, H.	145, 211
Mori, T.	285			Sakata, M.	146, 200
Morigami, M.	312		0	Sakata, O.	320
Morikawa, H.	144, 170, 172, 175,			Sakisaka, Y.	292, 293, 294, 299
177		Oda, K.	173	Sakiyama, F.	156
Morimoto, T.	217	Oda, T.	259	Sakura, S.	139, 348
Morimoto, Y.	157	Ogasawara, S.	233, 242	Sakurai, H.	248
Morioka, Y.	270, 306, 307, 309	Ogata, K.	143	Sakurai, K.	130, 131, 132
Morita, Y.	155	Ogura, S.	218	Sakurai, M.	201, 324
Moriwaki, H.	217	Ohgaki, M.	315	Sakurai, T.	249
Moriya, A.	217	Oh, M.	357	Sakurai, T.	321
Mukai, S.	206	Ohshima, H.	337	Sano, M.	249
Mukoyama, T.	265, 322	Ohshima, K.	162	Sano, T.	139, 140, 348
Murakami, E.	270	Ohsumi, K.	141, 142, 144, 175	Sano, T.	272, 273
Muramatsu, Y.	362, 363, 364	Ohta, T.	169, 272, 273, 281,	Sano, Y.	259, 262, 339
Murashita, T.	119	282, 283, 284		Sasaki, A.	153, 154
Murata, K.	149, 150	Ohtani, E.	369	Sasaki, K.	155
Murata, K.	365	Ohtsuka, S.	370	Sasaki, M.	129
Murata, T.	171, 248	Ohwada, H.	290, 291	Sasaki, S.	147, 196, 197, 198,
Murata, Y.	167	Oishi, Y.	161	199, 200	
Muroga, Y.	251	Okabe, Y.	301	Sasaki, T.	270
Myoren, H.	209, 210	Okada, K.	338	Sato, K.	205
		Okada, K.	189	Sato, M.	257, 314
		Okai, B.	164	Sato, M.	301
		Okuda, H.	343	Sato, S.	274, 278, 295, 297
		Okuno, M.	213	Sato, T.	344
		Okuyama, K.	159, 160, 161	Sato, T.	271
		Omote, K.	200	Sato, T.	231, 247
		Onchi, M.	292, 293, 294, 299	Sato, Y.	268, 269, 271
		Onishi, T.	238	Satow, Y.	158, 313, 314, 315,
		Ono, H.	358	316, 317, 318, 319	
		Onoda, M.	301	Sawada, H.	198, 316
		Onodera, A.	369	Sawada, S.	349
		Osaka, Y.	209, 210	Sawamoto, H.	369
		Osamura, K.	343	Senoo, M.	365
		Oshima, M.	112, 113, 114, 115,	Senzaki, K.	149
		116, 117		Sham, T. K.	283
		Owari, M.	280	Shamoto, S.	301
		Oyanagi, H.	148, 149, 150, 151,	Shiba, S.	160, 161
		152, 153, 154, 203, 207, 208, 213		Shibata, H.	265
		Ozawa, H.	141, 144	Shibata, K.	173
		Ozawa, T.	198	Shibayama, N.	148

Shimada,H.	231,247	Takeda,Y.	153,154	Umazume,Y.	331
Shimizu,F.	204	Takei,F.	315	Umetani,K.	186
Shimizu,S.	352	Takeiri,Y.	340	Uno,R.	141,142,143,144
Shimizugawa,Y.	144,170,172	Takemori,S.	331	Urabe,K.	170
Shimoda,N.	174	Takemura,K.	159,161	Urakawa,H.	253,258,260,262,
Shimomura,O.	159,160,161,323, 365,366,367,368,369,371	Takemura,K.	220	264	
Shin,S.	297	Takenaka,E.	370,371	Urisu,T.	120,123
Shinoda,Y.	114	Takeno,H.	354	Uruga,T.	326
Shinohara,K.	124	Takeuchi,H.	321	Usami,K.	187
Shinsaka,K.	302	Takizawa,T.	290,291	Usami,N.	287
Shiotani,N.	324	Tamura,K.	203	Ushikubo,T.	218
Shirotnani,I.	160	Tan,B.J.	181	Usuda,K.	166
Shiwaku,H.	140,347	Tanaka,H.	248	Utsugi,Y.	118
Smith,B.E.	184	Tanaka,H.	332,334,335,336	Utsumi,W.	367
Smith,P.L.	308	Tanaka,K.	284	Utsumi,Y.	123
Soda,K.	248	Tanaka,K.	271,273,302,304, 305,311		W
Stark,G.	308	Tanaka,K.	177,315		
Stevenson,A.W.	146	Tanaka,M.	198,316	Wada,K.	218
Sueno,S.	175	Tanaka,N.	257,314	Wakabayashi,K.	325,326,332,333, 334,335,336,339,340,341
Suga,S.	167	Tanaka,T.	178,181,224,240	Wakita,H.	227,228,229,230
Sugawara,H.	165	Tanase,T.	204	Wang,E.	332,333,335,336
Sugi,H.	332,333,335,336	Taniguchi,M.	167	Waseda,Y.	183
Sugi,M.	151	Tasumi,M.	261	Watanabe,H.	195
Sugishita,Y.	370	Tatsumi,T.	190,191	Watanabe,H.	250
Sugita,Y.	354	Tawara,H.	265	Watanabe,I.	176,225
Sugitani,Y.	222,349,350	Terada,N.	149,150	Watanabe,M.	124
Sugiyama,H.	352,354	Terakado,S.	305	Watanabe,M.	331
Sugiyama,K.	183	Terasaki,O.	323	Watanabe,N.	298
Sumiyama,K.	220	Terauchi,H.	145,211,221	Watanabe,Y.	356
Susaki,J.	368	Terayama,Y.	342	Wilkins,S.W.	146
Suwa,A.	321	Tezuka,H.	344		X
Suwa,A.	370	Togaya,M.	369		
Suzuki,H.	353	Tohji,K.	266	Xu,Q.	213
Suzuki,K.	201,324	Toida,T.	156		Y
Suzuki,K.	285	Tokiwa,A.	174		
Suzuki,K.	371	Tokonami,M.	196,198,316		
Suzuki,N.	324	Tokumoto,M.	149,150		
Suzuki,M.	286	Tokunaga,F.	255,261,327,328		
Suzuki,R.	186	Tokushige,M.	259	Yagi,K.	292,293,294,298
Suzuki,S.	312	Tokutomi,S.	261	Yagi,N.	329,330,331
Suzuki,S.	249	Tomiki,T.	289	Yagi,T.	367,368
Suzuki,S.	299	Tonuma,T.	265	Yagishita,A.	265,268,269,270, 302,303
Suzuki,T.	122	Toriumi,K.	204	Yagou,Y.	354
Suzuki,T.	134	Toshima,N.	246	Yakushi,K.	214
Suzuki,T.	179	Toyama,S.	155	Yamada,O.	205
Suzuki,T.	301	Toyofuku,F.	370,371	Yamada,T.	129
Suzuki,Y.	187,188	Toyoshima,I.	284	Yamada,Y.	112
		Toyota,N.	211	Yamaguchi,N.	310
		Tsuburaya,K.	160	Yamaguchi,S.	279
		Tsuchida,Y.	323,367	Yamaguchi,T.	226,227,228,229, 230
		Tsuchitani,R.	178	Yamamoto,M.	277
		Tsuji,K.	160,163,164,366	Yamamura,T.	341
		Tsukada,M.	256	Yamanaka,M.	313
		Tsunemi,H.	276	Yamanaka,T.	141,142,143
		Tsunetomo,K.	209,210	Yamane,M.	172
		Tsunoda,Y.	162	Yamane,T.	156
		Tsutsui,H.	156	Yamashita,H.	224
			U	Yamashita,H.	240
		Udagawa,Y.	266	Yamashita,K.	276
		Ueda,K.	186	Yamashita,S.	229
		Ueda,K.	268,271,306,307	Yamazaki,H.	205
		Uehara,S.	139,347,348,349	Yanagihara,M.	274,275,277,278, 279,296
		Ueki,T.	251,252,254,255, 257,259,262,263	Yanase,Y.	229
		Uemura,K.	260	Yano,S.	204
		Ueno,Y.	276	Yao,M.	203
		Ueno,Y.	334	Yao,T.	149,150,151,152, 153,154
		Ueyama,K.	167		
		Ukai,M.	302,303,304		
Tabira,Y.	172,175,177				
Tachi-iri,Y.	341				
Tagai,T.	175,196				
Tagawa,H.	251,256				
Tajima,H.	219				
Tajima,Y.	338				</

Yaoita, K.	163, 366	283, 284	Yoshihara, K.	322	
Yasuami, S.	166	Yonaha, K.	155	Yoshimoto, J.	164
Yasuda, H.	220	Yoneda, T.	292, 293, 294, 299	Yoshimura, J.	238
Yasuoka, N.	157	Yonenaga, I.	353	Yoshimura, Y.	231, 247
Yata, O.	230	Yoneyama, M.	151	Yoshino, K.	307, 308
Ye, J.	198, 316	Yonezawa, T.	246	Yoshino, M.	268, 269
Yokoi, K.	225	Yoshiasa, A.	202, 206, 212, 215, 216	Yoshitake, H.	180, 182, 235, 239, 244, 245
Yokokawa, T.	213	Yoshida, H.	301	Yoshizaki, R.	207, 208
Yokouchi, H.	186	Yoshida, H.	139, 140, 347, 348	Yoshizawa, M.	162, 165
Yokoya, A.	287	Yoshida, O.	338	Yui, D.	304
Yokoyama, S.	304	Yoshida, S.	178, 181, 224, 240	Yukino, K.	144
Yokoyama, T.	233,	Yoshihara, H.	119	Yuri, M.	288
Yokoyama, T.	234, 242, 281, 282,				

Subject Index

1s absorption edge 279
1s-3d transition 219
2p-shell 268

A

Absorption 267, 304
- edge 127, 131, 132, 275
- spectra 272, 273
- spectroscopy 151
Actin structure 334
AES 283
Ag(111) 300
AgBr 212
AgBr-Ag₂O-GeO₂ Glass 172
Aggregation 253, 325
AgI 212
Al-Li alloy 344
Al₂O₃ 289
Al-Zn alloy 343
Aldolase 257
AlGaAs 194
Alkali halides 171
Aluminum 365
Aminotransferase 155
Amorphous 209, 210, 222
- alloys 201, 220, 224
- semiconductors 163
Amphiphile 264
Amulase 313
Angiography 186
-, coronary 370
Anomalous dispersion 157, 198
Anomalous scattering 144, 183
-- factor 165
Anomalous transmission 199
Apoenzyme 314
Archaeology 136, 135
Art 135
Ascorbate oxidase 249
Association 262
Asymmetric disorder 234
Auger 268
- effect 128, 286
- process 270

B

Ba₂YCu₃O_y 149, 150
Bacteriorhodopsin 326, 328
-, solubilized 255
Band structure 290, 291, 292, 293, 294, 299
Barium 268

Bi₂O₃ 202
Bimetal 246, 283
Bimetallic 236, 241
Bleaching 325
Br-dCMP 127
Brome 172
Bromine 128
Butanedionemonoxime 331

C

C₄H₈ oxidation mechanism 180
C-2 epimerization 204
CaF₂ 112
Calcium 269
Carbohydrates 204
Carbon fiber 179
Carbon monoxide 308
Casein 253
Catalyst 178, 231, 233, 236, 241, 244, 246, 247
-, attached Co oxide 235
-, attached Se-Nb 182
-, bimetallic 181
-, one-atomic layer ZrO₂ 239
-, Rh dimer carbene 243
-, supported gold 237
-, supported metal 233, 242
Cd₃InGaS₄ 290
CdIn₂S₄ 290
Cell killing 285
CeO₂ 297
Ceramics 187
Cerium 295
- EXAFS 170
- oxide 318
Cesium 268
Chalcogenide film 118
Charge density 321
Chemical shift 131, 132,
Chemical state imaging 132
Chemisorption 300
Chromatin 254
Chromium 162
Cl₂ 304
Cluster 236, 241, 246
CO hydrogenation 243
Co-Mn/SiO₂ 181
Cobalt (III) 176
Colorant 136
Complex 229
Composite oxide 240
Compressibility 368
Compton scattering 321

Computed tomography 187
 Copper 213,227,228,249
 -, solution 226
 Core 271
 - exciton 288
 Correlation 350
 - function 256
 Cowlesite 316
 Cr(110) surface 299
 Critical phenomena 207
 Cross-bridge 330
 Crystal 117
 - spectrometer 121
 - structure 197,314,316
 - truncation rod 146
 Crystallization 215,224
 Cu-mordenite 217
 Cu-Zr 224

D

d-f hybridization 296
 Debye temperature 234,365
 Decomposition 344
 Deformation softening 173
 Depth-profiling 140
 Detector 187,319
 Diamond 168
 - anvil cell 175
 Diffraction 183
 Discharge cleaning 278
 Dislocation 195,353,358,359
 Disordered materials 183
 Dissociation 341
 Dissociative photoionization 303
 DNA 128,286
 Doping 195
 Doubly excited state 302
 DSA 370
 DX center 194
 Dynamical structure 344
 Dynamical X-ray diffraction 320

E

EDTA 176
 Electronic structure 168,301
 Embryo 221
 Energy dispersive 143
 Energy subtraction 186
 Enzyme 313
 Equatorial reflection 332
 Etching 120,305
 EXAFS 113,139,152,170,172,175,176,177,178,180,
 181,182,194,195,201,202,203,205,206,207,208,
 209,210,212,213,215,216,217,218,220,221,224,
 223,225,226,227,228,229,231,232,234,235,237,
 238,239,240,243,244,245,250,266,282,284,317,
 318
 -, surface-sensitive 152
 Excitation spectra 279

F

Fe(100) 284
 Fe-Ag 220
 Fe-Sn 240
 Fe-Ti 220
 FeO 368
 Fiber bundle 333
 Fluorescence EXAFS 153,154,171
 -, total reflectance 317

Fluorite-type 202
 Fragmentation 271

G

GaAlAs 137
 GaAs 112,114,305,309,358,359
 - composition 166
 Garnet 177
 Gas 348
 Gd₂O₃ 202,215,
 Ge-Se glasses 144
 Germanium perfect crystal 320
 GeSnO 209
 GeTe 210
 Glass 136,230
 Glaze 136
 Graphite 266
 -, neutron-irradiated 298
 Grating 116,278
 Grazing incidence 137,138,190,191,192,193,320
 Guinier plot 262

H

H₂ 302
 H₂O 309,321
 Hair 134
 HCl 304
 Heme 148
 Hemocyanin 341
 Hemoglobin 148
 Heterostructure 356
 High pressure 147,159,160,161,163,164,174,175,323,
 366,367,369
 --, in-situ 235
 High resolution 306,307,308,309
 High T_c superconductor 149,150,219,301
 Holography 118
 HPLC 127
 Human chromosome 124
 Hydrogen adsorption 293
 Hydrogenase 157

I

Ice 355
 Ilmenite 315
 Image detection 280
 Image sensor 188,319
 Imaging 135,347
 - plate 155,156,157,158,161,334,338
 Imogolite 258
 Impurity 171,194
 InAlAs 352
 Incommensurate 162
 Inner shell excitation 268
 InP 352
 InSb(222) 164
 Insulator 114
 Interface 112
 - roughness 276
 Interference fringe 165
 Interstitial atom 173
 Ionic conductor 202,212
 Iron 177
 - base alloy 205
 - oxide 179

K

K-edge 287,318,370

- subtraction 371
- K-shell absorption 285
- KAMON 211
- KBr 279
- KBSi₃O₈ 197
- KCl 279
- Kinetic energy analysis 303
- Kinetics 325,367
- Krypton 306

L

- Langmuir-Blodgett monolayers 151
- Lanthanide 318
- Laser irradiation 360
- Lattice defects 355
- Lattice mismatches 352
- Lattice parameter 166
- Lattice relaxation 194
- Laue diffraction 158
- Layer compound 238
- Layered structure 138
- LEC 358,359
- Liquid 203
 - Ammonia 227
 - crystal 264
 - metal 366
- Lithography 189,311,312
- Local equilibrium 343
- Local structure 149,221,240
- Low temperature 163,164
- Lyotropic mesophase 258

M

- Magnetic moment 159
- Manganese 159,250
- Martensite 198
- Martensitic transformation 205,353
- Mask membrane 311
- Melting 355
- Meridional reflection 333
- Metal 250
- Metal-nonmetal transition 203
- Metamict 222
- MgO 368
- Microanalysis 347
- Microchannel plate 310
- Microcrystal 197,252
- Microdefect 361
- Microradiography 188
- Microscope 125,126,
- Mineralogy 222
- Mirror 278
- Mixed chemical states 131
- Mixed-valence 225
- Mo(Co)₆/NaY 245
- Moessbauer analysis 222
- Molybdenum 225,231,247
- Momentum density 324
- Monochromatic X-rays 128,133,286
- Monochromator 115,116,117,166,167,169
- Monolayer heterostructure 152
- Mosaic virus 262
- Multicopper oxidase 249
- Multilayer 115,276
 - mirror 123
- Multiple charged ions 265
- Muscle 329,334,337,
 - contraction 330,334,335,336
 - heart 330
 - skeletal 331,332,333

- frog 334,335
- Myosin 330
 - motion 337
 - reflection 336
- Mytilus 338

N

- Na-DBDTC 133
- NaCl 288
- Nb₂O₅ 218
- Neon 307
- Ni(110) surface 292,293,294
- Ni(111) 281,282
- Ni(mnt)₂ 272
- Nickel 148,204,229,238
- Niobic acid 218
- NMR 127
- NO 300
- Nonequilibrium alloys 220
- Nuclear excitation 322
- Nucleosome 254

O

- O₂ 303
- One-dimensional compound 208
- Optical constant 274,275,277,290,291
- Ordered structure 344
- Ordering 196
- Organic conductor 272,273
- Organometallic molecules 271
- Os₃(CO)₁₂/TiO₂ 317
- Oscillating mirror 189
- Outgassing 119
- Ovomacroglobulin 340
- Oxidation 114
- Oxygen 113
 - adsorption 292,294
 - vacancies 149,150

P

- p.A. scattering 122
- Paladium 246
- Parallel plate 319
 - analyzer 303
- Parametric conversion 357
- Partial pair distribution 144
- Pattern replication 311
- Pd-Si 201
- Phase diagram 264
- Phase problem 267
- Phase transformation 174,323,367
- Phase transition 160,163,164,207,299,342,
 - pressure-induced 147
- Phospholipid 342
- Phosphorus 160,285,286,287
- Photoacoustic dosimetry 349
- Photoacoustic spectroscopy 139
- Photoacoustics 139,140,347,348,349,350
- Photocatalysis 178
- Photocatalyst 238
- Photodissociation 302
- Photoelectron diffraction 280
- Photoelectron spectroscopy 280
- Photoemission 112,114,296,298
 - angle-resolved 292,293,294,299,300
- Photoionization 265,268,269,270,271
- Photon counting 200
- Photon stimulated desorption 119
- Photoreaction 327

Phthalocyaninato nickel complex 214
 Phytochrome 261
 Pickup tube 188
 Piezorefectivity 288
 PIPICO (Photoion-photoion coincidence) 271
 Plant leaf 250
 Plasma diagnostics 310
 Platinum 246
 Polarized 273
 Polyethylene 345
 Polymethylmethacrylate 124
 Potassium 269
 Powder diffraction 142
 Powder diffractometer 141
 Precipitate 344
 Premartensite 221
 Pressure dependence 365
 Profile analysis 143
 Protease inhibitor 340
 Protein crystallography 158,313
 -,myelin 260
 -,P2 260
 PSD 319
 Purple membrane 326,327,328

Q

Quantum-size-effect 252

R

Radiobiology 129
 Rare earth 295
 -- compounds 296
 RDF 144
 Reconstruction 281,282
 Reduction 312
 Reflectance 274,275,277,289
 -,near-normal 297
 Relaxation 224
 Reliability 189
 Repair 285
 Replica method 124
 Resonance absorption 287
 Resonant photoemission 295,301
 Resonant scattering 165
 Reversion 343
 Rh-Fe 236,241
 Rhodium 277,322
 Rhodopsin 325
 Rotation photograph 313
 Ruthenium 277

S

Sarcomere length 332
 SDW 162
 Se K-edge 248
 Sea water 133
 Section topography 354
 Selective excitation 131,132,
 Selenium 203,223
 Selenocysteine 248
 Self-trapped exciton luminescence 279
 Semi-dilute 251
 Semiconductor 206,252
 Sensor 240
 Serratia protease 314
 Short wavelength 315
 Si(111) 267
 SiC 274
 Silica 241

Silicon 119,146,324,354,360,361
 -,Cz 193
 - diode 319
 - oxide film 113
 Silk 256
 Sintered diamond 369
 Sinusoidal length change 336,337
 Site occupancy 198,205,207,213,219,250
 Small-angle X-ray diffraction 326
 Small-angle X-ray scattering (SAXS) 251,253,254,
 255,256,257,258,259,260,261,262,263,264,340,
 345,346
 -,in-situ 343
 SMSI 232,317
 Sodium borate 213
 Soft X-ray 117,123,125,126,167,274,275,362,363,364
 - inelastic scattering 122
 Solid 229
 - helium 353
 Solid solution 212
 -,perovskite-type 216
 -,AgI type 212
 Solution 127,229
 Solution strengthening 173
 Solvation 227,228
 Spin state of Co^{4+} ion 216
 SrCoO_3 216
 SrMnO_3 216
 Static Debye-Waller factor 354
 Stopped-flow X-ray scattering 341
 Structure analysis 156,255,327,334
 Structure change 201
 Sulfur 281,282,284
 Superconductor 142,208
 Superlattice 356
 -,strained layer 153
 Superstructure 190,191,192,196
 Surface 168,169,281,282,283,284,300
 - analysis 137
 - roughness 274
 - structure 233,267
 Synthetic polymer 346

T

(TMTTF)₂ClO₄ 273
 Ta_2O_5 218
 Tantalalic acid 218
 Tellurium 203
 Tensile deformation 201
 TeO_2 291
 Tetranitromethane 328
 Thermal diffuse scattering 199
 Thermal expansion 234
 Thermography 311
 Threshold electron 270
 Time-resolved measurement 158,257,339,345,346,360
 TiO_2 one-atomic layer 244
 Titanium monoxide 323
 TMV protein 339
 TOF 265
 Tonic contraction 338
 Total reflection-diffraction 320
 Trace element 133
 Troponin-C 263
 Trypsin 156
 Tryptophanase 259

Tyrosine residues 328
 U
 Ultra fine particles 242
 Undulator radiation 121,124,362,363,364
 UPS 168
 Urbach tail 289
 V
 V_2O_5 174
 $V_2O_5-P_2O_5$ 180
 Valence fluctuation 297
 Valency 219
 Vanadium 178
 Vanadium oxides 174
 Vitamin B6 155
 VUV 116,169,303,304,305,306,307,308,309,362,363,364
 W
 Wolter mirror system 130
 X
 X-ray absorption 139,140,249,347,348
 X-ray contact microscopy 124
 X-ray diffraction 142,190,191,192,199,267,328,329,
 332,333,334,335,336,337,338,342
 -,gas 321
 -,low temperature 327
 X-ray fluorescence 121,130,131,132,134,135,136,137,
 138
 X-ray goniometry 352
 X-ray lithography 123
 X-ray microbeam 130
 X-ray optics 123
 X-ray plate 118
 X-ray raman 266
 X-ray television 371
 X-ray topography 193,352,353,355
 -,plane wave 361
 XANES 173,174,176,178,223,281,283,284
 -,polarized 214
 Xenon 265
 Y
 Yeast 287
 Z
 Zeolite 217,236,316
 Zinc(II) bromide 230
 Zirconia 215
 Zn/Zinc 175
 Zone plate 125,126

LIST OF PUBLICATIONS

(Continued from the publication list in Photon Factory Activity Report 1986)

1986

- K.Asakura, Y.Iwasawa and H.Kuroda
Structure Determination of $\text{Ru}_3(\text{CO})_{12}$ Catalysts Supported on Inorganic Oxides by Means of EXAFS
J. Chem. Soc. Jpn., (1986) 1539. (in Japanese).
- K.Asakura, Y.Iwasawa and H.Kuroda
EXAFS and XANES Studies on the Local Structures of Metal Ions in Metal Doped MgO Systems
J. Phys. (Paris), Colloq., 47 (1986) C8-317.
- K.Asakura, Y.Iwasawa and H.Kuroda
The Studies about the Local Structures of the Metal Ions Added to MgO and Their Effects on the Catalytic Nature of MgO
Shokubai, 28 (1986) 120.
- K.Asakura, Y.Satow and H.Kuroda
Ce K-edge EXAFS Spectrum of CeO_2
J. Phys. (Paris), Colloq., 47 (1986) C8-185.
- S.Harada, M.Yasui, K.Murakawa, N.Kasai and Y.Satow
Crystal Structure Analysis of Cytochrome c' by the Multiwavelength Anomalous Diffraction Method Using Synchrotron Radiation
J. Appl. Cryst., 19 (1986) 448.
- K.Hasegawa, K.Mochiki, M.Koike, Y.Satow, H.Hashizume and Y.Iitaka
High-Count Rate Position-Sensitive Detectors for Synchrotron Radiation Experiments
Nucl. Instrum. & Methods, A252 (1986) 158.
- Y.Hatano
The Study of Reaction Dynamics Using the Pulse Profile of Synchrotron Radiation
Gakujutsu Geppou, 39 (1986) 16. (in Japanese).
- T.Hayaishi, Y.Morioka, T.Akahori, M.Watanabe, A.Yagishita and M.Nakamura
Multiple Photoionization from 3p Excitation of Kr and 4p Excitation of Xe
Z. Phys. D, 4 (1986) 25.
- Y.Kashiwase, M.Mori, M.Kogiso, M.Minoura, S.Sasaki and T.Ishikawa
Observation of Anomalous Transmission of Thermally Scattered X-Rays in a Germanium Crystal
J. Phys. Soc. Jpn., 55 (1986) 4172.
- H.Kato, T.Ishii, S.Masuda, Y.Harada, T.Miyano, T.Komeda, M.Onchi and Y.Sakisaka
Reply to 'Comment on 'Photoemission Study of the Existence of a Valence-band Satellite in Fe''
Phys. Rev. B., 34 (1986) 8973.
- K.Koto, H.Mori and Y.Ito
Oxygen Disorder in the Fluorite-type Conductors $(\text{Bi}_2\text{O}_3)_{1-x}(\text{Gd}_2\text{O}_3)_x$ by X-ray and EXAFS Analyses
Solid State Ionics, 18/19 (1986) 720.
- I.Maeda, K.Hieda, H.Maezawa, K.Kobayashi, T.Yamada and T.Ito
Single-strand Breaks in 5-bromouracil Substituted DNA by Monochromatic X-rays --- Effect of the K Shell Ionization of Bromine
J. Radiat. Res., 27 (1986) 17.
- H.Maruyama, K.Shirai, O.Yamada, H.Maeda, H.Terauchi and R.Pauthenet
Magnetic Anomaly and Local Structural Change as Premartensitic Phenomena in Fe-Pt Invar Alloys
Proc. ICOMAT-86, (1986) 144.
- M.Miyake, N.Nakagawa, H.Ohyangagi and T.Suzuki
EXAFS Study of Chromium Ions in the Mixed-Solvent System of Formamide and Ammonium Formate
Inorg. Chem., 25 (1986) 700.
- M.Miyake, O.Kaji, S.Nagahara and T.Suzuki
Coordination Structure of Zinc(II) Ions in a Mixed-solvent System of Formamide and Ammonium Formate; an EXAFS and RDF Investigation
J. Chem. Soc., Faraday Trans. 2, 82 (1986) 687.
- T.Murata and S.Emura
EXAFS Study of Relaxation of Cu^+ Impurities in Alkali Halides
J. Phys. (Paris), Colloq., 47 (1986) C8-795.
- K.Naito, Y.Onuki, T.Komatsubara, T.Miyahara, H.Kato, S.Sato, K.Soda, S.Asaoka and T.Ishii
Electronic States of $\text{Ce}_{1-x}\text{La}_x\text{Cu}_6$ Studied by Resonant Photoemission
J. Phys. Soc. Jpn., 55 (1986) 4351.
- M.Nomura and T.Yamaguchi
Solute Structure of Copper(II) Acetate Solutions in Liquid and Glassy States
J. Phys. (Paris), Colloq., 47 (1986) C8-619.
- K.Ohsumi, S.Sueno, I.Nakai, M.Imafuku, H.Morikawa, M.Kimata, M.Nomura and O.Shimomura
EXAFS Measurement under High Pressure by Diamond Anvil Cell
J. Phys. (Paris), Colloq., 47 (1986) C8-189.
- M.Sano, T.Maruo, Y.Masuda and H.Yamatera
EXAFS Studies on the Methanol and Ethanol Solutions of Cobalts(II) Bromides
J. Solution Chem., 15 (1986) 803.
- T.Tamegai, K.Tsutsumi and S.Kagoshima
Electric-field Induced Deformation of Sliding CDW in $\text{K}_{0.30}\text{MoO}_3$
Physica, 143B (1986) 114.
- H.Tanaka, T.Kobayashi, Y.Amemiya and K.Wakabayashi
Time-resolved X-ray Diffraction Studies of Frog Skeletal Muscle Isometrically Twitched by Two Successive Stimuli Using Synchrotron Radiation
Biophysical Chem., 25 (1986) 161.
- H.Terauchi, H.Maeda, K.Shirai, H.Maruyama, M.Hida, H.Sakashita, N.Kamijo and O.Yamada
EXAFS Study on Premartensitic Phase in AuCuZn_2
Proc. ICOMAT-86, (1986) 115.
- K.Wakabayashi, Y.Amemiya, H.Tanaka, H.Sugi and T.Mitsui
Two-dimensional X-ray Diffraction Studies on the Structural Change of Actin Filaments during Isometric Contraction of Frog Skeletal Muscle by Using a New Type of Integrating Area Detector (an

- Imaging Plate) and Synchrotron Radiation
J. Muscle Research and Cell Motility, 7 (1986) 276.
- A. Yagishita, S. Arai, C.E. Brion, T. Hayaishi, J. Murakami, Y. Sato and M. Ukai
Auger Decay of Core-Excited State of SiH₄ Molecules
Chem. Phys. Lett., 132 (1986) 437.
- O. Yamada, H. Maruyama, K. Shirai and H. Maeda
Local Structural Change of Premartensitic Transformation in Fe-Pt Invar Alloys
J. Phys. (Paris), Colloq., 47 (1986) C8-1041.
- M. Yanagihara, M. Niwano, T. Koide, S. Sato, T. Miyahara, Y. Iguchi, S. Yamaguchi and T. Sasaki
Soft X-ray Reflection from SiC, TiC, and WC Mirrors
Appl. Opt., 25 (1986) 4586.
- A. Yoshiasa, K. Koto, S. Emura and F. Kanamaru
Local Structure of the AgBr_{1-x}I_x Rock-salt Type Solid-solution
J. Phys. (Paris), Colloq., 47 (1986) C8-803.
- M. Yoshino, T. Hayaishi, Y. Itikawa, Y. Itoh, T. Koizumi, T. Nagata, Y. Sato, H. Shibata and A. Yagishita
Photoionisation of Cs Atoms in the 650-760 Å Wavelength Region
J. Phys. B., 19 (1986) L849.
- 1987
- I. Abe and M. Fujieda
Display System for Control Console of KEK PF Linac
Proc. of 6th Symp. on Accelerator Science and Technology, (1987) 227.
- Y. Akahama, W. Utsumi, S. Endo, T. Kikegawa, H. Iwasaki, O. Shimomura, T. Yagi and S. Akimoto
Melting Curve of Black Phosphorus
Phys. Lett. A, 122 (1987) 129.
- K. Akimoto, J. Mizuki, I. Hirose, T. Tatsumi, H. Hirayama, N. Aizaki and J. Matsui
Interfacial Super Structure between Epitaxial Si(111) Layers and B(√3×√3)/Si(111) Substrates Studied by Synchrotron X-Ray Diffraction
Extended Abstracts of the 19th Conf. on Solid State Devices and Materials, Tokyo, (1987) 463.
- K. Akimoto, J. Mizuki, T. Tatsumi, N. Aizaki and J. Matsui
Synchrotron X-Ray Diffraction Study of an Interfacial Super-Structure : a-Si on Ge_{0.2}Si_{0.8}(111)-5×5
Surf. Sci., 183 (1987) L297.
- S. Akimoto, T. Suzuki, T. Yagi and O. Shimomura
Phase Diagram of Iron Determined by High-Pressure/Temperature X-Ray Diffraction Using Synchrotron Radiation
High-Pressure Res. Miner. Phys., (1987) 149.
- Y. Amemiya and Y. Izumi
Synchrotron Radiation in Polymer Science
High Polymers, Jpn., 36 (1987) 590. (in Japanese).
- Y. Amemiya, K. Wakabayashi, H. Tanaka, Y. Ueno and J. Miyahara
Laser-Stimulated Luminescence Used to Measure X-ray Diffraction of Contracting Striated Muscle
Science, 237 (1987) 164.
- S. Arai, T. Kamozaki, M. Ukai
Detection of Radiation in the Atomic and Molecular Process and Its Application Using Synchrotron Radiation
Bunko Kenkyu, 36 (1987) 205. (in Japanese).
- A. Asami, S. Ohsawa, Y. Ogawa, A. Enomoto, S. Anami, M. Yokota, Y. Otake, S. Fukuda, I. Sato, G. Horikoshi, H. Iwata and O. Azuma
Acceleration Characteristics of the Positron Generator Injector at KEK
Proc. 6th Symp. on Accelerator Science and Technology, (1987) 192.
- Y. Chikaura, M. Imai and T. Ishikawa
Observation of Microdefects in Thin Silicon Crystals by Means of Plane-Wave Topography Using Synchrotron X-Radiation
Jpn. J. Appl. Phys., 26 (1987) L839.
- H. Endo and M. Yao
Selenium in the One-dimensional Pores of Zeolite Hyomen, 25 (1987) 394. (in Japanese).
- T. Fujisawa, T. Ueki, Y. Inoko and M. Kataoka
X-Ray Scattering from a Troponin C Solution and Its Interpretation with a Dumbbell-Shaped Molecule Model
J. Appl. Cryst., 20 (1987) 349.
- S. Fukuda, T. Shidara, Y. Saito, H. Hanaki, K. Nakao, H. Homma, S. Anami and J. Tanaka
Performance of High Power S-Band Klystrons Focused with Permanent Magnet
KEK Report, 86-9 (1987)
- K. Fukuyama, S. Hirota and T. Tsukihara
Crystallization and Preliminary X-ray Diffraction Studies of Tobacco Necrosis Virus
J. Mol. Biol., 196 (1987) 961.
- Y. Furusawa, H. Maezawa, K. Hieda, K. Kobayashi and K. Suzuki
Enhanced Killing Effect of X-Ray at K-Shell Absorption Wavelength on Dry Bacteriophage T1 Labeled with BUdR
J. Radiat. Res., 28 (1987) 40.
- Y. Gohshi, S. Aoki, A. Iida, S. Hayakawa, H. Yamaji and K. Sakurai
A Scanning X-Ray Fluorescence Microprobe with Synchrotron Radiation
Jpn. J. Appl. Phys., 26 (1987) L1260.
- T. Hayaishi, A. Yagishita, K. Ito, M. Kihara and Y. Morioka
Coincidence Spectra of Threshold Photoelectrons and Photoions near the B²B₂ States of H₂O⁺ and D₂O⁺
J. Phys. B, 20 (1987) L207.
- T. Hayaishi, T. Koizumi, T. Matsuo, T. Nagata, Y. Sato, H. Shibata and A. Yagishita
Dissociative Photoionization of SiH₄ in the

- 12-19eV Region
Chem. Phys., 116 (1987) 151.
- S.Hayashi, M.Suzuki, K.Hieda, I.Maeda, H.Maezawa, K.Kobayashi, T.Yamada and T.Ito
Radiation Induced Single-Strand Breaks of Bromouracil Substituted and Non-Substituted pBR322 DNA
J. Radiat. Res., 28 (1987) 40.
- K.Hieda
Spectroscopy in Biological Sciences IV. Use of Synchrotron Radiation in Biological Sciences
Bunko Kenkyu, 36 (1987) 295. (in Japanese).
- K.Higashiyama, S.Kono, T.Kinoshita, T.Miyahara, H.Kato, H.Ohsawa, Y.Enta, F.Maeda and Y.Yaegashi
Surface Core-level Shifts of the Si(111) $\sqrt{3}\times\sqrt{3}$ -Ga Surface
Surf. Sci., 186 (1987) L568.
- G.Horikoshi
Physical Understanding of Gas Desorption Mechanisms
J. Vac. Sci. Technol., A5(4) (1987) 2501.
- G.Horikoshi and Y.Kimura
Status of TRISTAN
Proc. on IEEE Particle Accelerator Conference, (1987) 34.
- G.Horikoshi
An Analysis and a Consideration of Molecular Flow in a Long Conduit Pipe
J. Vacuum Soc. Jpn., 30 (1987) 658. (in Japanese).
- T.Ishikawa, T.Kitano and J.Matsui
Equi-Lattice-Spacing Mapping X-Ray Topography
J. Appl. Cryst., 20 (1987) 344.
- K.Ito, K.Yoshino, Y.Morioka and T.Namioka
The $1s^2\ ^1S_0$ - $1snp\ ^1P_1^0$ Series of the Helium Spectrum
Physica Scripta, 36 (1987) 88.
- I.Iwasa, H.Suzuki, T.Nakajima, S.Suzuki, M.Ando, I.Yonenaga, M.Takebe and K.Sumino
Observation of Lattice Defects in Solid Helium by SR X-Ray Topography
J. Phys. Soc. Jpn., 56 (1987) 4225.
- H.Iwasaki
Photon Factory
Opt. Electro-Opt. Eng. Contact, 25 (1987) 635. (in Japanese).
- H.Iwasaki
Synchrotron Radiation for Materials Science
J. Atom. Energy Soc. Jpn., 29 (1987) 392. (in Japanese).
- M.Izawa, H.Kobayakawa, S.Sakanaka and S.Tokumoto
Higher-Order-Mode Damping Coupler for Beam Instability Suppression
Jpn. J. Appl. Phys., 26 (1987) 1733.
- M.Kanzaki, K.Kurita, T.Fujii, T.Kato, O.Shimomura and S.Akimoto
A New Technique to Measure the Viscosity and Density of Silicate Melts at High Pressure
High-Pressure Res. Miner. Phys., (1987) 195.
- T.Kikegawa
X-Ray Diamond Anvil Press for Structural Studies at High Pressure and High Temperature
High-Pressure Res. Miner. Phys., (1987) 61.
- T.Kikegawa, H.Iwasaki
Pressure-Induced Rhombohedral-Simple Cubic Structural Phase Transition in As
High-Pressure Res. Miner. Phys., 56 (1987) 3417.
- T.Kikegawa, H.Iwasaki, T.Fujimura, S.Endo, Y.Akahama, T.Akai, O.Shimomura, T.Yagi, S.Akimoto and I.Shiratori
Synchrotron-Radiation Study of Phase Transitions in Phosphorus at High Pressures and High Temperatures
J. Appl. Cryst., 20 (1987) 406.
- T.Kitano and M.Mizuta
Fluorescence EXAFS Study of AlGaAs Doped with Se Donor Impurities
Jpn. J. Appl. Phys., 26 (1987) L1806.
- T.Kitano, T.Ishikawa, J.Matsui, K.Akimoto, J.Mizuki and Y.Kawase
Synchrotron Plane Wave X-Ray Topography of 6 inch Diameter Si Crystal
Jpn. J. Appl. Phys., 26 (1987) L108.
- K.Kobayashi, N.Usami, K.Hieda, H.Maezawa, Y.Furusawa and T.Ito
Soft X-ray Wavelength Dependence of Inactivation and Induction of Mitotic Gene Conversion in Yeast Cells around the K-shell Absorption Edge of Phosphorus
J. Radiat. Res., 28 (1987) 41.
- K.Kobayashi, K.Hieda, H.Maezawa, M.Ando and T.Ito
Monochromatic X-Ray Irradiation System (0.08-0.4 nm) for Radiation Biology Studies Using Synchrotron Radiation at the Photon Factory
J. Radiat. Res., 28 (1987) 243.
- T.Koide, H.Fukutani, A.Fujimori, R.Suzuki, T.Shidara, T.Takahashi, S.Hosoya and M.Sato
Optical-reflectance Study of the Single-Crystal Superconductor $(La_{1-x}Sr_x)_2CuO_4$
Novel Superconductivity, (1987) 915.
- T.Koide, M.Yanagihara, Y.Aiura, S.Sato, T.Shidara, A.Fujimori, H.Fukutani, M.Niwano and H.Kato
Resuscitation of Carbon-Contaminated Mirrors and Gratings by Oxygen-Discharge Cleaning. I: Efficiency Recovery in the 4-40-eV Range
Appl. Optics, 26 (1987) 3884.
- T.Koide, M.Yanagihara, Y.Aiura, S.Sato, H.Kato and H.Fukutani
Glow-Discharge Cleaning in Oxygen of Carbon-Contaminated Optical Elements
Physica Scripta., 35 (1987) 313.
- T.Koizumi, T.Hayaishi, Y.Iitaka, T.Nagata, Y.Sato and A.Yagishita
Decay Channels after the Photoexcitation of 3d Electrons in Rb and Sr Studied by Photoion Yield Spectra
J. Phys. B, 20 (1987) 5393.

- T.Komeda, Y.Sakisaka, M.Onchi, H.Kato, S.Masuda and K.Yagi
Angle-Resolved Photoemission Study of the Interaction of Oxygen with a Ni(110) Surface II. Adsorption at 300 K
Surf. Sci., 188 (1987) 45.
- T.Komeda, Y.Sakisaka, M.Onchi, H.Kato, S.Masuda and K.Yagi
Angle-Resolved Photoemission Study of the Interaction of Oxygen with a Ni(110) Surface I. Adsorption at 80 K
Surf. Sci., 188 (1987) 32.
- T.Komeda, Y.Sakisaka, M.Onchi, H.Kato, S.Masuda and K.Yagi
Angle-Resolved Photoemission Study of the Ni(110)(1×2)-II Reconstructed Surface at 80K
Phys. Rev. B, 36 (1987) 922.
- S.Kono, K.Higashiyama, T.Kinoshita, T.Miyahara, H.Kato, H.Ohsawa, Y.Enta, F.Maeda and Y.Yaegashi
Surface and Bulk Core-Level Shifts of the Si(111) $\sqrt{3}\times\sqrt{3}$ -Ag Surface: Evidence for a Charged $\sqrt{3}\times\sqrt{3}$ Layer
Phys. Rev. Lett., 58 (1987) 1555.
- H.Kyuragi and T.Urisu
Synchrotron Radiation-excited Chemical Vapor Deposition of Si₃N₄H₂ Film
J. Appl. Phys., 61 (1987) 2035.
- H.Kyuragi and T.Urisu
Synchrotron Radiation-induced Etching of a Carbon Film in an Oxygen Gas
Appl. Phys. Lett., 50 (1987) 1254.
- H.Maezawa, A.Mikuni, M.Ando and T.Sasaki
Investigation on Optical Matching of a Soft X-Ray Undulator with Some Condenser Fresnel Zone Plates
Jpn. J. Appl. Phys., 26 (1987) L3.
- H.Maruyama, K.Shirai, H.Maeda, W.-L. Liu and L. O. Yamada
EXAFS Studies on the Local Structure of Phase Transition in Fe-Pt Invar Alloys. I. Premartensitic Phenomenon
J. Phys. Soc. Jpn., 56 (1987) 4377.
- T.Masujima, H.Kawata, Y.Amemiya, N.Kamiya, T.Katsura, T.Iwamoto, H.Yoshida, H.Imai and M.Ando
X-ray Photoacoustic Effect of Solid Materials
Chem. Lett., 1987 (1987) 973.
- H.Matsui, Y.Yoshioka, T.Morooka, K.Hasegawa and T.Nakajima
X-ray Stress Analysis in Textured Steels by Use of Synchrotron Radiation Source
J. Soc. Mater. Sci. Jpn., 36 (1987) 823. (in Japanese).
- N.Matuda, Y.Saito, S.Anami, S.Fukuda, T.Shidara, H.Hanaki, H.Horima, K.Nakao, A.Kinbara and J.Tanaka
Measurements of Secondary Electron Emission and Cathodoluminescence for Alumina Microwave Windows
J. Vacuum Soc. Jpn., 30 (1987) 226. (in Japanese).
- T.Miyahara, A.Fujimori, T.Koide, S.Sato, S.Shin, M.Ishigame, Y.Onuki and T.Komatsubara
Near-Normal Reflectance Spectra of CeO₂ and Ce_{1-x}La_xAl₂ System
J. Phys. Soc. Jpn., 56 (1987) 3689.
- M.Miyabe, K.Yagi, A.Yamada, Y.Aiura, T.Koide, T.Shidara, H.Kato and H.Fukutani
Piezoreflectance of Potassium Iodide in the Vacuum Ultraviolet Region from 5 to 30 eV
J. Phys. Soc. Jpn., 56 (1987) 378.
- E.Miyazaki, I.Kojima, M.Orita, K.Sawa, N.Sanada, K.Edamoto, T.Miyahara and H.Kato
Angle-Resolved Photoemission Study of NO Chemisorption on Pd(111)
J. Electron Spectrosc. Relat. Phenom., 43 (1987) 139.
- H.Morikawa, T.Osuka, C.D.Yin, M.Okuno and F.Marumo
An EXAFS Study of Coordination of Ag in AgI-Ag₂O-GeO₂ Glasses
Yogyoukyoukaishi, 95 (1987) 551. (in Japanese).
- T.Mukoyama, T.Tonuma, A.Yagishita, H.Shibata, T.Koizumi, T.Matsuo, K.Shima and H.Tawara
Charge Distribution of Xe Ions as a Result of Multiple Photoionisation of Xe Atoms between 4.1 and 8.0 keV
J. Phys. B, 20 (1987) 4453.
- T.Nakajima
Low Temperature SR X-ray Diffraction under External Fields at the Photon Factory
Nucl. Instrum. & Methods, A261 (1987) 308.
- H.Nakazawa, Y.Kanazawa, M.Kamo and K.Osumi
X-ray Section Topographs of a Vapour-grown Diamond Film on a Diamond Substrate
Thin Solid Films, 151 (1987) 199.
- D.Nerger, K.Kajiwar, H.Urakawa and Y.Hiragi
Structural Characteristic of Poly(vinylacetate) Microgel in Solution
Bull. Inst. Chem. Res., Kyoto Univ., 65 (1987) 97.
- M.Nomura
Documentation on the Operation of BL7C at Photon Factory
KEK Internal, 87-1 (1987) (in Japanese).
- M.Nomura, A.Kazusaka, N.Kakuta, Y.Ukisu and K.Miyahara
Structure of the Catalytic Site on a Silica-supported Catalyst Derived from Copper(II) Acetate
J. Chem. Soc., Faraday Trans. 1, 83 (1987) 1227.
- M.Nomura, A.Kazusaka, Y.Ukisu and N.Kakuta
Extended X-ray Absorption Fine Structure Study of the Reaction between Silica-supported Copper(II) Oxide Catalysts and Acetic Acid
J. Chem. Soc., Faraday Trans. 1, 83 (1987) 2635.
- Y.Ogawa, Y.Otake, M.Yokota and A.Asami
Remote Control of an Emission Current of a High-Current, Short-Pulse Electron Gun
Proc. of 6th Symp. on Accelerator Science and Technology, (1987) 62.
- S.Ohsawa, T.Mituhashi, A.Enomoto and A.Asami
Beam Emittance Measurement of the Positron Generator at KEK

- Proc. of 6th Symp. on Accelerator Science and Technology, (1987) 92.
- T.Osuka, H.Morikawa, F.Marumo, M.Yamane and Y.Suga
An EXAFS Study of Coordination of Ag in AgBr-CsBr-PbBr₂ Glasses
Yogyokyoukaishi, 95 (1987) 657. (in Japanese).
- Y.Otake, Y.Ogawa, S.Ohsawa, K.Nakahara and A.Asami
Short Pulse Grid Pulser for an Electron Gun of the KEK Positron Generator
Proc. 6th Symp. on Accelerator Science and Technology, (1987) 65.
- Y.Saito, N.Matuda, S.Anami, S.Fukuda, T.Shidara, H.Hanaki, H.Honma, K.Nakao, A.Kinbara and J.Tanaka
High Power Test of Microwave Window Using Resonant Ring
J. Vacuum Soc. Jpn., 30 (1987) 186. (in Japanese).
- S.Sakanaka, M.Izawa, H.Kobayakawa and M.Kobayashi
Differences in the Ion Trapping between Uniform and Partial Bunch Fillings
Nucl. Instrum. Methods, A256 (1987) 184.
- H.Sakashita, K.Kamon, H.Terauchi, N.Kamijo, H.Maeda, N.Toyota and T.Fukase
EXAFS Study on Premartensitic Phase in A-15 Compounds
Jpn. J. Appl. Phys., Suppl. 26-3 (1987) 909.
- H.Sakashita, K.Kamon, H.Terauchi, N.Kamijo, H.Maeda, N.Toyota and T.Fukase
EXAFS Study on Premartensitic Phase in Nb₃Sn
J. Phys. Soc. Jpn., 56 (1987) 4183.
- Y.Sakisaka, T.Komeda, M.Onchi, H.Kato, S.Masuda and K.Yagi
New Observation of the Valence-Band Satellite in Ni(110)
Phys. Rev. Lett., 58 (1987) 733.
- K.Sakurai, A.Iida and Y.Gohshi
Characterization of Co-O Thin Films by X-Ray Fluorescence Using Chemical Shifts of Absorption Edges
Jpn. J. Appl. Phys., 26 (1987) 1937.
- S.Sasaki
RADY: A FORTRAN Program for the Least-Squares Refinement of Crystal Structure
KEK Internal Report, 87-3 (1987)
- T.Sasaki
Synchrotron Radiation Spectroscopy of Atoms and Molecules at Photon Factory
Atomic Phys., 10 (1987) 283.
- S.Sasaki and K.Tsukimura
Atomic Positions of K-Shell Electrons in Crystals
J. Phys. Soc. Jpn., 56 (1987) 437.
- I.Sato
Design of Traveling Wave Proton Linac
Proc. of 6th Symp. on Accelerator Science and Technology, (1987) 98.
- S.Sato, J.Tanaka, K.Huke and J.Chikawa
Photon Factory: Status in 1986
Physica Scripta, 36 (1987) 49.
- I.Sato, K.Nakahara, A.Enomoto, T.Ohsawa, U.Ogawa, T.Ohoge, H.Kakihara, H.Hanaki, K.Furukawa, S.Fukuda, S.Anami, N.Yamaguchi, K.Inoue, Y.Iino, U.Kamouchi, Y.Tsuchiya, K.Taki and S.Fujie
High Gradient Acceleration by Recirculator
Proc. of 6th Symp. on Accelerator Science and Technology, (1987) 95.
- A.Shinohara, T.Saito, M.Shoji, A.Yokoyama, H.Baba, M.Ando and K.Taniguchi
Nuclear Excitation in ¹⁸⁹Os with Synchrotron Radiation
Nucl. Phys., A472 (1987) 151.
- H.Suzuki
Direct Observation of Dislocations in Solid Helium
Solid State Phys., 22 (1987) 983.
- H.Suzuki, I.Iwasa and T.Nakajima
Direct Observation of Dislocations in Solid Helium by SR X-Ray Topography
Jpn. J. Appl. Phys., 26 (1987) 405.
- M.Suzuki, K.Hieda, K.Kobayashi, H.Maezawa and Y.Furusawa
Induction of DNA Strand Breaks by Monochromatic X-Rays near P K-Shell Absorption Edge
J. Radiat. Res., 28 (1987) 40.
- T.Takahashi, S.Nakatani, T.Ishikawa and S.Kikuta
Surface Structure Analysis of Si(111) $\sqrt{3} \times \sqrt{3}$ -Bi by X-Ray Diffraction --- Approach to the Solution of the Phase Problem
Surf. Sci., 191 (1987) L825.
- T.Takahashi, K.Izumi, T.Ishikawa and S.Kikuta
Evidence for a Trimer in the $\sqrt{3} \times \sqrt{3}$ -Bi Structure on the Si(111) Surface by X-ray Diffraction under the Nearly Normal Incidence Condition
Surf. Sci., 183 (1987) L302.
- T.Takahashi, F.Maeda, H.Arai, H.Katayama-Yoshida, Y.Okabe, T.Suzuki, S.Hosoya, A.Fujimori, T.Shidara, T.Koide, T.Miyahara, M.Onda, S.Shamoto and M.Sato
Synchrotron-Radiation Photoemission Study of the High-*T_c* Superconductor YBa₂Cu₃O_{7- δ}
Phys. Rev. B, 36 (1987) 5686.
- T.Tamegai, K.Tsutsumi and S.Kagoshima
Transport and Structural Properties of CDW in K_{0.30}MoO₃
Synthetic Metals, 19 (1987) 923.
- T.Tanaka, Y.Nishimura, S.Kawasaki, T.Funabiki and S.Yoshida
X-ray Absorption Spectroscopy (EXAFS/XANES) Evidence for the Preferential Formation of Isolated VO₄ Species on Highly Photoactive V₂O₅/SiO₂ Catalysts
J. Chem. Soc., Chem. Commun., (1987) 506.
- N.Terada, H.Ihara, M.Hirabayashi, K.Senzaki, Y.Kimura, K.Murata, M.Tokumoto, O.Shimomura and T.Kikegawa
Lattice Parameter and Its Pressure Dependence of High *T_c* Sr₁La_{2-x}CuO_{4-y}(x=0.6) Prepared under Reducing Condition
Jpn. J. Appl. Phys., 26 (1987) L510.

- T.Tonuma, A.Yagishita, H.Shibata, T.Koizumi, T.Matsuo, K.Shima, T.Mukoyama and H.Tawara
Multiple Photoionization of Xe Atoms between 4.1-8.0 keV: Mean Charge
J. Phys. B, 20 (1987) L31.
- U.Ueno and K.Wakabayashi
Data Processing of X-ray Diffraction Diagram from Muscles Recorded by Imaging Plates
Kessho Kaiseki Kenkyu Senta Dayori, 8 (1987) 3.
(in Japanese).
- M.Ukai, A.Kimura, S.Arai, P.Lablanquie, K.Ito and A.Yagishita
Photoionization Cross Section of the $O_2^+(B^2\Sigma_g^-)$ State in the Energy Region of 20.3-23.8eV
Chem. Phys. Lett., 135 (1987) 51.
- N.Usami, K.Kobayashi and S.Ishizaka
Optimal Conditions of Labeling Yeast Cells' DNA by BrdUMP
J. Radiat. Res., 28 (1987) 22.
- K.Usuda, S.Yasumi, Y.Higashi, H.Kawata and M.Ando
Absolute Lattice Parameter Measurement of GaAs Crystals Using Monochromatic Synchrotron Radiation
Extended Abstracts of the 19th Conf. on Solid State Devices and Materials, Tokyo, (1987) 119.
- M.Wakagi, M.Chigasaki and M.Nomura
Structural Study of Amorphous Ge Using Extended X-Ray Absorption Fine Structure
J. Phys. Soc. Jpn., 56 (1987) 1765.
- M.Wakagi, T.Ohno, M.Chigasaki and M.Nomura
Structural Study of Amorphous SiGe Alloy Films Using Extended X-Ray Absorption Fine Structure
J. Phys. Soc. Jpn., 56 (1987) 2413.
- T.Yagi, M.Akaogi, O.Shimomura, T.Suzuki and S.Akimoto
In Situ Observation of the Olivine-Spinel Phase Transformation in Fe_2SiO_4 Using Synchrotron Radiation
J. Geophys. Res., 92 (1987) 6207.
- A.Yagishita
Absolute Photoionization Cross Sections for Argon, Krypton, and Xenon in the VUV Regions
KEK Report, 86-11 (1987)
- S.Yamamoto and H.Kitamura
Generation of Quasi-Circularly Polarized Undulator Radiation with Higher Harmonics
Jpn. J. Appl. Phys., 26 (1987) L1613.
- H.Yamashita, T.Tanaka, H.Mizutani, T.Funabiki and S.Yoshida
EXAFS Studies of the Local Structure of Transition Metal-based Amorphous Alloys
Abstract of the 6th Int. Conf. on the Phys. of Non-Crys. Solids, (1987) 157.
- K.Yokoi, N.Matsubayashi, T.Miyanaga, I.Watanabe, K.Murata and S.Ikeda
Studies on the Structure of Cationic Dimer of Molybdenum(VI) in Acidic Solution by XANES and EXAFS
Chem. Lett., (1987) 1453.

